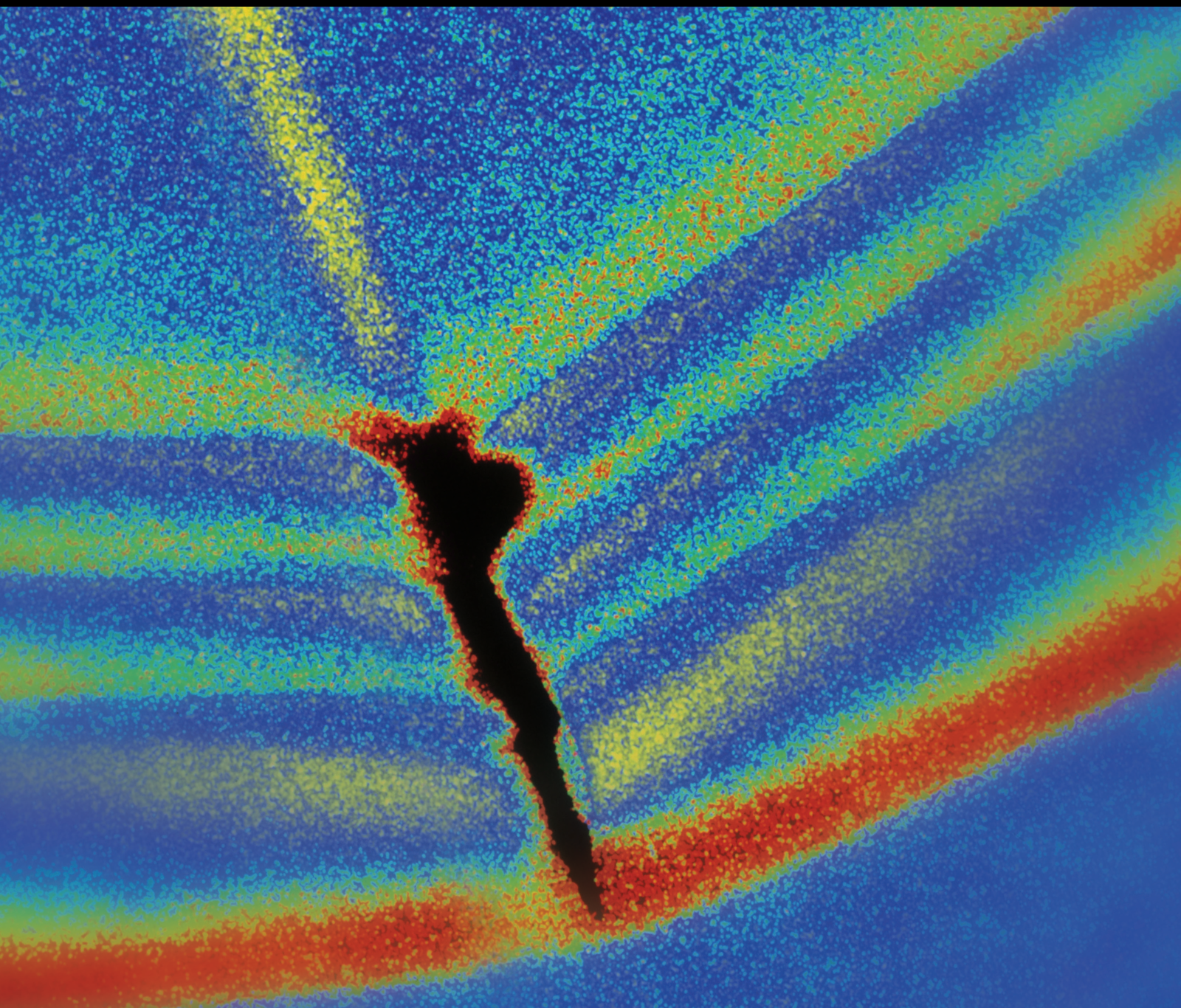


Shock and Vibration Induced by Mining Extraction

Guest Editors: Caiping Lu, Linming Dou, Nong Zhang,
Marcin Aleksander Lutyński, and Shimin Liu





Shock and Vibration Induced by Mining Extraction

Shock and Vibration

Shock and Vibration Induced by Mining Extraction

Guest Editors: Caiping Lu, Linming Dou, Nong Zhang,
Marcin Aleksander Lutyński, and Shimin Liu



Copyright © 2015 Hindawi Publishing Corporation. All rights reserved.

This is a special issue published in "Shock and Vibration." All articles are open access articles distributed under the Creative Commons Attribution License, which permits unrestricted use, distribution, and reproduction in any medium, provided the original work is properly cited.

Editor-in-Chief

Mehdi Ahmadian, Virginia Polytechnic Institute and State University, USA

Associate Editors

Brij N. Agrawal, USA
Marco Alfano, Italy
Farbod Alijani, Canada
Sumeet S. Aphale, UK
Hassan Askari, Canada
Matteo Aureli, USA
Ranjan Banerjee, UK
José Villanueva, Spain
Subhamoy Bhattacharya, UK
Ivo Caliò, Italy
Antonio Carcaterra, Italy
Dumitru I. Caruntu, USA
Noël Challamel, France
Peng Chen, Japan
Ashwin Chinnayya, France
Giorgio Dalpiaz, Italy
Farhang Daneshmand, Canada
Sergio De Rosa, Italy
Longjun Dong, China
Mohamed El badaoui, France
Mohammad Elahinia, USA
Francesco Franco, Italy
Alessandro Gasparetto, Italy
Anindya Ghoshal, USA

Alicia Gonzalez-Buelga, UK
Hassan Haddadpour, Iran
María I. Herreros, Spain
Hamid Hosseini, Japan
Reza Jazar, Australia
Sakdirat Kaewunruen, UK
Jeong-Hoi Koo, USA
Georges Kouroussis, Belgium
Mickaël Lallart, France
Kenneth J. Loh, USA
Nuno M. Maia, Portugal
Giuseppe C. Marano, Italy
Laurent Mevel, France
Emiliano Mucchi, Italy
Tony Murmu, UK
Sundararajan Natarajan, India
Toshiaki Natsuki, Japan
Miguel Neves, Portugal
Coral Ortiz, Spain
Gyuhae Park, Korea
Evgeny Petrov, UK
Antonina Pirrotta, Italy
Didier Rémond, France
Francesco Ripamonti, Italy

Salvatore Russo, Italy
Edoardo Sabbioni, Italy
Jerzy T. Sawicki, USA
Vadim V. Silberschmidt, UK
Kumar V. Singh, USA
Isabelle Sochet, France
Alba Sofi, Italy
Jussi Sopanen, Finland
Narakorn Srinil, UK
Salvatore Strano, Italy
Chao Tao, China
Mario Terzo, Italy
Tai Thai, Australia
Carlo Trigona, Italy
Federica Tubino, Italy
Nerio Tullini, Italy
Marcello Vanali, Italy
Jörg Wallaschek, Germany
Peijun Xu, USA
Zaili L. Yang, UK
Stana Živanović, UK
Lei Zuo, USA

Contents

Shock and Vibration Induced by Mining Extraction, Caiping Lu, Linming Dou, Nong Zhang, Marcin Aleksander Lutyński, and Shimin Liu
Volume 2015, Article ID 320804, 1 page

Numerical Tests on Failure Process of Rock Particle under Impact Loading, Yu-Jun Zuo, Qin Zhang, Tao Xu, Zhi-Hong Liu, Yue-Qin Qiu, and Wan-Cheng Zhu
Volume 2015, Article ID 678573, 12 pages

Study on Dynamic Disaster in Steeply Deep Rock Mass Condition in Urumchi Coalfield, Xing-Ping Lai, Mei-Feng Cai, Fen-Hua Ren, Peng-Fei Shan, Feng Cui, and Jian-Tao Cao
Volume 2015, Article ID 465017, 8 pages

An Experiment Monitoring Signals of Coal Bed Simulation under Forced Vibration Conditions, Chengwu Li, Po Hu, Tianbao Gao, Yingfeng Sun, Shengyang Shao, and Qifei Wang
Volume 2015, Article ID 693612, 23 pages

Simulation of the Load Evolution of an Anchoring System under a Blasting Impulse Load Using FLAC^{3D}, Xigui Zheng, Jinbo Hua, Nong Zhang, Xiaowei Feng, and Lei Zhang
Volume 2015, Article ID 972720, 7 pages

A Case Study of Damage Energy Analysis and an Early Warning by Microseismic Monitoring for Large Area Roof Caving in Shallow Depth Seams, Like Wei, Qingxin Qi, Hongyan Li, Bin Zhang, Yongren Wang, and Linghai Kong
Volume 2015, Article ID 709459, 9 pages

Mechanism of Roof Shock in Longwall Coal Mining under Surface Gully, Gangwei Fan, Dongsheng Zhang, and Xufeng Wang
Volume 2015, Article ID 803071, 8 pages

Damage Characteristics of Surrounding Rock Subjected to VCR Mining Blasting Shock, Nan Jiang, Chuanbo Zhou, Xuedong Luo, and Shiwei Lu
Volume 2015, Article ID 373021, 8 pages

A Comparison of Mine Seismic Discriminators Based on Features of Source Parameters to Waveform Characteristics, Ju Ma, Guoyan Zhao, Longjun Dong, Guanghui Chen, and Chuxuan Zhang
Volume 2015, Article ID 919143, 10 pages

The Mechanism and Application of Deep-Hole Pre-cracking Blasting on Rockburst Prevention, Zhenhua Ouyang, Qingxin Qi, Shankun Zhao, Baoyang Wu, and Ningbo Zhang
Volume 2015, Article ID 625691, 7 pages

Blast-Induced Damage on Millisecond Blasting Model Test with Multicircle Vertical Blastholes, Qin-yong Ma, Pu Yuan, Jing-shuang Zhang, Rui-qiu Ma, and Bo Han
Volume 2015, Article ID 504043, 6 pages

Multi-Index Monitoring and Evaluation on Rock Burst in Yangcheng Mine, Yunliang Tan, Yanchun Yin, Shitan Gu, and Zhiwei Tian
Volume 2015, Article ID 624893, 5 pages

Effects of Fine Gangue on Strength, Resistivity, and Microscopic Properties of Cemented Coal Gangue Backfill for Coal Mining, Tingye Qi, Guorui Feng, Yanrong Li, Yuxia Guo, Jun Guo, and Yujiang Zhang
Volume 2015, Article ID 752678, 11 pages

Study on Monitoring Rock Burst through Drill Pipe Torque, Zhonghua Li, Liyuan Zhu, Wanlei Yin, and Yanfang Song
Volume 2015, Article ID 371948, 8 pages

Warning Method of Coal Bursting Failure Danger by Electromagnetic Radiation, Guang-Jian Liu, Cai-Ping Lu, Hong-Yu Wang, Peng-Fei Liu, and Yang Liu
Volume 2015, Article ID 583862, 9 pages

Numerical Investigation of Rockburst Effect of Shock Wave on Underground Roadway, Cai-Ping Lu, Guang-Jian Liu, Hong-Yu Wang, and Jun-Hua Xue
Volume 2015, Article ID 867582, 10 pages

Distribution of Side Abutment Stress in Roadway Subjected to Dynamic Pressure and Its Engineering Application, Yao Qiangling, Zhou Jian, Li Yanan, Tan Yingming, and Jiang Zhigang
Volume 2015, Article ID 929836, 11 pages

Instantaneous Rock Blasting Wave and Its Microscopic Characteristics during Interaction with Concrete, Shaoqin Huang, Lifeng Luan, Wanli Xing, and Qunyi Liu
Volume 2015, Article ID 318286, 6 pages

Study on Low-Frequency TEM Effect of Coal during Dynamic Rupture, Cheng-wu Li, Chuan Wang, Bei-jing Xie, Xiao-yuan Sun, and Xiao-meng Xu
Volume 2015, Article ID 189569, 8 pages

Bolt Pull-Out Tests of Anchorage Body under Different Loading Rates, Tong-bin Zhao, Wei-yao Guo, Yan-chun Yin, and Yun-liang Tan
Volume 2015, Article ID 121673, 8 pages

Experimental Study on Anisotropic Strength and Deformation Behavior of a Coal Measure Shale under Room Dried and Water Saturated Conditions, Jingyi Cheng, Zhijun Wan, Yidong Zhang, Wenfeng Li, Syd S. Peng, and Peng Zhang
Volume 2015, Article ID 290293, 13 pages

Blasting Vibration Safety Criterion Analysis with Equivalent Elastic Boundary: Based on Accurate Loading Model, Qingwen Li, Lan Qiao, Gautam Dasgupta, Siwei Ma, Liping Wang, and Jianghui Dong
Volume 2015, Article ID 604683, 10 pages

Dynamic Effect and Control of Key Strata Break of Immediate Roof in Fully Mechanized Mining with Large Mining Height, Yuan Yong, Tu Shihao, Zhang Xiaogang, and Li Bo
Volume 2015, Article ID 657818, 11 pages

Acoustic Emission Behavior of Rock-Like Material Containing Two Flaws in the Process of Deformation Failure, Quan-Sheng Liu, Jie Xu, Bin Liu, and Jing-Dong Jiang
Volume 2015, Article ID 167580, 9 pages

Editorial

Shock and Vibration Induced by Mining Extraction

Caiping Lu,¹ Linming Dou,² Nong Zhang,¹ Marcin Aleksander Lutyński,³ and Shimin Liu⁴

¹School of Mines, China University of Mining and Technology, Xuzhou 221116, China

²State Key Laboratory of Coal Resources and Safe Mining, China University of Mining and Technology, Xuzhou 221116, China

³Institute of Mining Engineering, Faculty of Mining and Geology, Silesian University of Technology, Ulica Akademicka 2, 44-100 Gliwice, Poland

⁴Department of Energy and Mineral Engineering, School of Earth and Mineral Sciences, Pennsylvania State University, State College, PA 16802, USA

Correspondence should be addressed to Caiping Lu; cplucumt@126.com

Received 1 April 2015; Accepted 1 April 2015

Copyright © 2015 Caiping Lu et al. This is an open access article distributed under the Creative Commons Attribution License, which permits unrestricted use, distribution, and reproduction in any medium, provided the original work is properly cited.

With the increase of mining depth and intensity of coal resource, the rockburst and other dynamic disasters are aggravating, which seriously threaten the safety of coal mines. According to the convincing statistics, only 32 coal mines belonged to rockburst mines until 1985 in China; unfortunately, by the end of 2011, nearly 142 coal mines were classified as rockburst tendency. Simultaneously, the mining depth of about 50 coal mines reaches or surpasses 1000 m. In the period of 2006–2013, 35 fatal rockbursts occurred, which cruelly killed over 300 workers and caused a thousand of injures. In despite of lack of accurate data about rockburst in other countries, we can infer that the rockburst may be a ubiquitous dynamic disaster in deep coal mines in the world.

It is well known that the mining-induced shock or vibration can easily trigger strong tremor (even rockburst disaster). Therefore, it is very urgent to essentially understand the mining-induced shock and vibration waves in coal mines.

This special issue is dedicated to fundamental understanding of mining-induced shock and vibration waves mainly concentrated on mechanical principles, propagation and attenuation laws, monitoring and warning methods, and prevention of catastrophic shock. The special issue is mainly divided into 3 aspects that are the mechanism of rockburst, early warning based on microseism (MS) and electromagnetic emission (EME) methods, and prevention measures, respectively. The rest mainly discuss rock mechanics and some relevant rules, underground pressure behaviors, and innovative supporting technologies of roadway in deep coal

mines. By rigorous review and negotiation, two highlights are presented which are the numerical simulation method of roadway rockburst process recurrence and the comprehensive warning method of rockburst by MS and EME and acoustic emission (AE).

Rockburst in coal mines is a worldwide conundrum poorly understood; the prediction indexes are confusing and exasperating. In particular, its prevention is yet not effectively resolved. The satisfactory solution compulsorily requires the worldwide efforts and cooperation in mining and rock mechanics community.

Caiping Lu
Linming Dou
Nong Zhang
Marcin Aleksander Lutyński
Shimin Liu

Research Article

Numerical Tests on Failure Process of Rock Particle under Impact Loading

Yu-Jun Zuo,^{1,2,3,4} Qin Zhang,^{1,2,3,4} Tao Xu,⁵ Zhi-Hong Liu,^{1,2,3,4}
Yue-Qin Qiu,^{1,2,3,4} and Wan-Cheng Zhu⁵

¹Mining College, Guizhou University, Guiyang, Guizhou 550025, China

²Guizhou Key Laboratory of Comprehensive Utilization of Non-Metallic Mineral Resources, Guizhou University, Guiyang, Guizhou 550025, China

³Guizhou Engineering Lab of Mineral Resources, Guiyang, Guizhou 550025, China

⁴Engineering Center for Safe Mining Technology under Complex Geologic Condition, Guiyang, Guizhou 550025, China

⁵School of Resources & Civil Engineering, Northeastern University, Shenyang, Liaoning 110004, China

Correspondence should be addressed to Qin Zhang; zq6736@163.com

Received 14 July 2014; Accepted 28 September 2014

Academic Editor: Caiping Lu

Copyright © 2015 Yu-Jun Zuo et al. This is an open access article distributed under the Creative Commons Attribution License, which permits unrestricted use, distribution, and reproduction in any medium, provided the original work is properly cited.

By using numerical code RFPA^{2D} (dynamic version), numerical model is built to investigate the failure process of rock particle under impact loading, and the influence of different impact loading on crushing effect and consumed energy of rock particle sample is analyzed. Numerical results indicate that crushing effect is good when the stress wave amplitude is close to the dynamic strength of rock; it is difficult for rock particle to be broken under too low stress wave amplitude; on the other hand, when stress wave amplitude is too high, excessive fine particle is produced, and crushing effect is not very good on the whole, and more crushing energy is consumed. Secondly, in order to obtain good crushing effect, it should be avoided that wavelength of impact load be too short. Therefore, it is inappropriate to choose impact rusher with too high power and too fast impact frequency for ore particle.

1. Introduction

The purpose of crushing is to reduce the particle size of rock materials or to liberate valuable minerals from ores. In order to obtain higher efficiency of crushing, it is very important to select the appropriate crusher and crushing circuit. Research shows that the breakage of a brittle material is a very complex process, in which the results are influenced by loading conditions and the rock properties [1]. First of all, breakage of particles can be either single particle or interparticle [2]. The breakage behavior of single particle without constraint and stressing a large number of particles are not fully identical, because loading conditions on the surface of particles can be more complicated when stressing a large number of particles [3]. For this reason, when studying particle breakage behavior, single particle breakage conditions need to be adequately considered. If single particle is suffering loading from other adjacent particles, constraint condition in particle

beds should be taken into consideration. What is more, the particle can not only be crushed under static loading but also be broken under dynamic loading. Therefore, particle breakage will require consideration of material properties, particle shape, and particle size. With such complex requirements, it is unlikely that any analytical approach would be adequate. The use of computer simulations seems to be the appropriate tool to obtain some clarification [4]. If we can get the rock crushing mechanism, according to numerical tests, and design or choose different crusher to control crushing effect, then technological process of coarse crushing and fine crushing can be optimized.

So far, it is seldom to investigate the mechanism on particle crushing from point of mechanical analysis. Traditionally, the breakage of material in crushing is regarded as relying upon single particle breakage without considering the confinement condition, and the physical point of departure is the Griffith theory of brittle fracture. The understanding of this

breakage behaviour of a particle is based on the knowledge obtained in indirect tensile strength tests of rock, such as the Brazilian test or compression of an irregular specimen [5]. As for the breakage of material subjected to dynamic loading, researchers mainly focused on damage mechanism, fracture process, and dynamic fracture criterion of various materials in the past few decades [6]. Besides, the relationship between parameters such as modulus of elasticity, strength, and deformation rate is elucidated; therefore strength criterion and constitutive relation of rock particles are summarized under dynamic loading [7–9]. The finite element method and the finite difference method based on the traditional continuum mechanics are suitable for prediction of damages and failure, but they are difficult to be used for calculation and simulation of the complete failure process directly. Based on mesoscopic damage mechanics, numerical code RFPA^{2D} (dynamic version) is developed by Tang and Kou [2, 10] to simulate the failure process of a single particle breakage and interparticle breakage subjected to an unconfined or confined static compressive load, which provides a reasonable description of fundamental mechanisms of particles breakage. In fact, particle breakage is usually subjected to dynamic loading. In order to study the damage and breakage mechanism of rock particles under dynamic loading, RFPA^{2D} (dynamic version) was used to study dynamic fragmentation of rock, and the effect of loading rate on failure characteristics was discussed sketchily [11].

In this paper, by using numerical code RFPA^{2D} (dynamic version), the failure process of ore particle under impact loading is simulated, and the influence of different impact loading on crushing effect and consumed energy of ore particle sample is analyzed.

2. Numerical Simulator Description

The newly developed RFPA^{2D} (dynamic edition) is a two-dimensional code that can simulate the fracture and failure process of rock under static or dynamic loading conditions. To model the failure of rock material or rock mass, the rock medium is assumed to be composed of many mesoscopic elements whose material properties are different from one to another and are specified according to a Weibull distribution [12]. The finite element method is employed to obtain the stress fields in the mesoscopic elements. Elastic damage mechanics is used to describe the constitutive law of the mesoscale elements when the maximum tensile strain criterion and the Mohr-Coulomb criterion that incorporate the effect of stress rate are utilized as damage thresholds [13].

2.1. Assignment of Material Properties. In RFPA, the solid or structure is assumed to be composed of many mesoscopic elements with the same size, and the mechanical properties of these elements are assumed to conform to a given Weibull distribution as defined by the following probability density function (PDF):

$$f(u) = \frac{m}{u_0} \left(\frac{u}{u_0}\right)^{m-1} \exp\left[-\left(\frac{u}{u_0}\right)^m\right], \quad (1)$$

where u is the mechanical parameter of the element (such as strength or elastic modulus), the scale parameter u_0 is related to the average of the element parameters, and the parameter m defines the shape of the distribution function. From the properties of the Weibull distribution, a larger value of m implies a more homogeneous material and vice versa. Therefore, the parameter m is called the homogeneity index in our numerical simulations. In the definition of the Weibull distribution, the value of the parameter m must be larger than 1.0. Using the PDF, in a computer simulation of a medium composed of many mesoscopic elements, one can produce numerically a heterogeneous material. The computationally produced heterogeneous medium is analogous to a real specimen tested in the laboratory, so in this investigation it is referred to as a numerical specimen.

2.2. The Constitutive Model for the Mesoscopic Element. Initially an element is considered elastic, with elastic properties defined by Young's modulus and Poisson's ratio. The stress-strain relation for an element is considered linear elastic until the given damage threshold is attained and then is modified by softening. Under a dynamic stress state, the elements undergo damage when one of the following damage criteria is satisfied at the element level:

$$-\varepsilon_1 = \frac{kf_{c0}}{E_0}, \quad \sigma_1 - \frac{1 + \sin\phi}{1 - \sin\phi}\sigma_3 \geq f_{c0}, \quad (2)$$

where f_{c0} is the dynamic uniaxial compressive strength of the element, which is closely related to the strain rate (or stress rate) of dynamic loading condition, E_0 is initial elastic modulus of the element that is assumed to be not affected by the stress rate, k is the ratio of compressive and tensile strength, and ϕ is the internal frictional angle of the element. σ_1 and σ_3 are the major and minor principal stresses of the element.

In this study, the following relation between dynamic uniaxial compressive strength and loading rate, which has been proposed by Zhao [7], is used to reflect the effect of stress loading rate on the dynamic strength:

$$f_{c0} = A \log\left(\frac{\dot{\sigma}}{\dot{f}_{cso}}\right) + f_{cso}, \quad \dot{\sigma} > \dot{f}_{cso}, \quad (3)$$

where f_{c0} is also the dynamic uniaxial compressive strength (MPa), $\dot{\sigma}$ is the stress rate (MPa/s), f_{cso} is the uniaxial compressive strength at the quasistatic stress rate \dot{f}_{cso} that is approximately 5×10^{-2} MPa/s, and A is a parameter depending on the material. In addition, the experimental results of Zhao [7] also indicated that the ratio of tensile and compressive strength ($k = f_{c0}/f_{t0}$) and internal frictional angle ϕ are not influenced by the stress rate. In this respect, when the f_{c0} obtained from (3) is substituted into (2), the effect of strain rate on the strength of elements will be incorporated.

The first part of (2) is the maximum tensile strain criterion, whilst the second part is the classical Mohr-Coulomb failure criterion for tensile and shear damage thresholds, respectively. Thus, an element may be damaged in either tension (corresponding to the maximum tensile strain criterion)

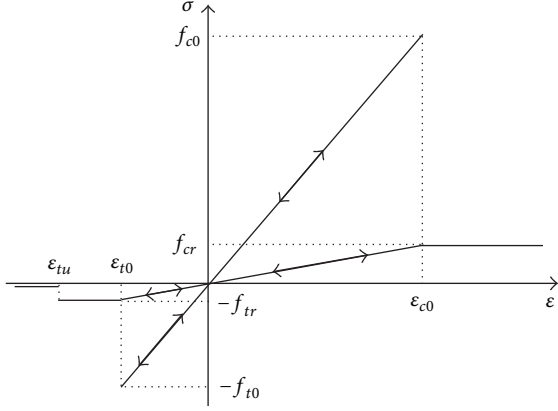


FIGURE 1: Elastic damage constitutive law of element under uniaxial stress state. (Here f_{t0} and f_{tr} are dynamic uniaxial tensile strength and residual uniaxial tensile strength of element, respectively. And f_{c0} and f_{cr} are dynamic uniaxial compressive strength and residual corresponding strength of element, resp.)

or shear (corresponding to the Mohr-Coulomb criterion). Once (2) is satisfied at the element level, the elastic modulus of the element is reduced according to the following expression:

$$E = (1 - \omega) E_0, \quad (4)$$

where ω represents a damage variable, E and E_0 are the elastic modulus of the damaged and the undamaged element, respectively. In the current method, the element and its damage are assumed isotropic, so the E , E_0 , and ω are all scalar quantities. The sign convention used throughout this paper is that compressive stress and strain are positive.

When the mesoscopic element is in a uniaxial stress state (both uniaxial compression and uniaxial tension), the constitutive relation of elements is as illustrated in Figure 1. Initially, the stress-strain curve is linear elastic and no damage exists; that is, $\omega = 0$. When the maximum tensile strain criterion is satisfied, damage occurs in the element in a brittle mode.

The constitutive relation of the mesoscopic element under uniaxial tension, as shown in the third quartile of Figure 1, can be expressed as

$$\omega = \begin{cases} 0, & \varepsilon > \varepsilon_{t0}, \\ 1 - \frac{\lambda \varepsilon_{t0}}{\varepsilon}, & \varepsilon_{tu} < \varepsilon \leq \varepsilon_{t0}, \\ 1, & \varepsilon \leq \varepsilon_{tu}, \end{cases} \quad (5)$$

where λ is the residual strength coefficient, which is given as $f_{tr} = \lambda f_{t0}$, and f_{t0} is the tensile strength of element. The parameter ε_{t0} is the strain at the elastic limit, which is called the threshold strain, and is calculated as

$$\varepsilon_{t0} = -\frac{f_{t0}}{E_0}. \quad (6)$$

From (6), it can be found that ε_{t0} also depends on the stress rate of element because f_{c0} is related to the stress rate according to (3). ε_{tu} is the ultimate tensile strain of the

element, describing the state at which the element would be completely damaged. The ultimate tensile strain is defined as $\varepsilon_{tu} = \eta \varepsilon_{t0}$, where η is called the ultimate strain coefficient. Both the residual strength coefficient (λ) and ultimate strain coefficient (η) are assumed to be independent of the stress rate.

Additionally, it is assumed that the damage of a mesoscopic element under multiaxial states of stress is also isotropic and elastic. The constitutive equation described above can be extended for application to 3D stress states when the tensile strain threshold is attained. In multiaxial stress states, the element is still subject to damage in the tensile mode when the equivalent major tensile strain $\bar{\varepsilon}$ attains the above threshold strain ε_{t0} . The equivalent principal strain $\bar{\varepsilon}$ is defined by

$$\bar{\varepsilon} = -\sqrt{\langle -\varepsilon_1 \rangle^2 + \langle \varepsilon_2 \rangle^2 + \langle \varepsilon_3 \rangle^2}, \quad (7)$$

where ε_1 , ε_2 , and ε_3 are three principal strains and $\langle \cdot \rangle$ is a function defined as follows:

$$\langle x \rangle = \begin{cases} x, & x \geq 0, \\ 0, & x < 0. \end{cases} \quad (8)$$

For an element subject to a multiaxial state of stress, the constitutive law can be easily obtained by substituting the strain ε in (5) with the equivalent strain $\bar{\varepsilon}$ defined by (7) and (8). The damage variable is expressed as

$$\omega = \begin{cases} 0, & \bar{\varepsilon} > \varepsilon_{t0}, \\ 1 - \frac{\lambda \varepsilon_{t0}}{\varepsilon}, & \varepsilon_{tu} < \bar{\varepsilon} \leq \varepsilon_{t0}, \\ 1, & \bar{\varepsilon} \leq \varepsilon_{tu}. \end{cases} \quad (9)$$

In the same way as for uniaxial tension, when the element is under uniaxial compression but damaged according to the Mohr-Coulomb criterion, the expression for damage variable ω can be described as

$$\omega = \begin{cases} 0, & \varepsilon < \varepsilon_{c0}, \\ 1 - \frac{\lambda \varepsilon_{c0}}{\varepsilon}, & \varepsilon \geq \varepsilon_{c0}; \end{cases} \quad (10)$$

λ is also the residual strength coefficient, and $f_{cr}/f_{c0} = f_{tr}/f_{t0} = \lambda$ is assumed to apply when the element is under either uniaxial compression or tension. Also, ε_{c0} is calculated as

$$\varepsilon_{c0} = \frac{f_{c0}}{E_0}. \quad (11)$$

If an element is under a multiaxial stress state and its strength satisfies the Mohr-Coulomb criterion, damage occurs, and it is necessary to consider the effect of the other principal stress in the model during damage evolution. When the Mohr-Coulomb criterion is satisfied, the maximum principal (compressive) strain ε_{c0} can be calculated at the peak value of the maximum principal (compressive) stress:

$$\varepsilon_{c0} = \frac{1}{E_0} \left[f_{c0} + \frac{1 + \sin \phi}{1 - \sin \phi} \sigma_3 - \mu (\sigma_1 + \sigma_2) \right]. \quad (12)$$

It is assumed that shear damage evolution is related only to the maximum compressive principal strain ε_1 . So the maximum compressive principal strain ε_1 of the damaged element is substituted for the uniaxial compressive strain ε in (10), extending the equation to represent shear damage under triaxial stress states:

$$\omega = \begin{cases} 0, & \varepsilon_1 < \varepsilon_{c0}, \\ 1 - \frac{\lambda \varepsilon_{c0}}{\varepsilon_1}, & \varepsilon_1 \geq \varepsilon_{c0}. \end{cases} \quad (13)$$

Based on the above equations, it can be found that the damage variable ω is related to the stress rate because it is calculated based on the values of ε_{c0} or ε_{t0} that are obtained directly according to the stress-rate dependent strength of the element (f_{c0} or f_{t0}) according to (6) or (11).

Of course, the above-mentioned constitutive law can be used to simulate the failure process of rock under static loading when the stress rate effect on the strength as expressed by (3) is not incorporated. Therefore, the stress-rate dependent constitutive law described above is based on the original one for static analysis and is also compatible with it.

2.3. Finite Element Implementation. As described above, the rock specimen is composed of many square elements with the same size. These elements are also acting as the four node parameter elements for finite element analysis. The equilibrium equations governing the linear dynamic response of a system of finite elements can be expressed in the following form:

$$M\ddot{U} + C\dot{U} + KU = R, \quad (14)$$

where M , C , and K are the mass, damping, and stiffness matrices; R is the vector of externally applied loads; and U , \dot{U} , and \ddot{U} are the displacement, velocity, and acceleration vectors of the finite elements. A direct step-by-step integration procedure is found suitable for solving the problem in which a body is subjected to a short duration impulse loading [14].

At initial condition, the elements are elastic, and their stresses can be calculated via step-by-step integration. At a time step, the principal stresses from the previous time step are subtracted from the current principal stresses and divided by the time step in order to calculate the stress rates of the elements. Similarly, when the current minor principal stress and corresponding stress rate are both negative, the increased strength of an element due to the increase of absolute value of this stress rate can also be obtained. When the effect of stress rate on the dynamic compressive strength is considered according to (3) and the stresses (or strains) of elements meet the maximum tensile strain criterion or Mohr-Coulomb criterion as given in (2), the elements are damaged according to the constitutive law given before, and then their stress will be reanalyzed iteratively for the current boundary conditions in order to reflect the stress redistribution at this time step. The program does not consider the analysis of the next time step until no new damaged elements are found for the iterative step of this time step. The above model described in the two preceding sections is implemented into the RFPA [15, 16], and therefore RFPA is extended for analysis of rock under dynamic loading.

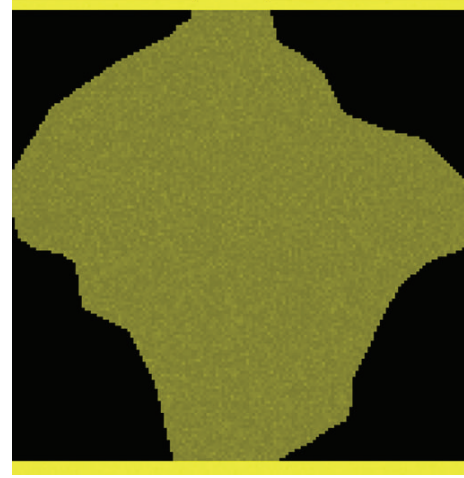


FIGURE 2: The numerical sample model of ore (generated by RFPA).

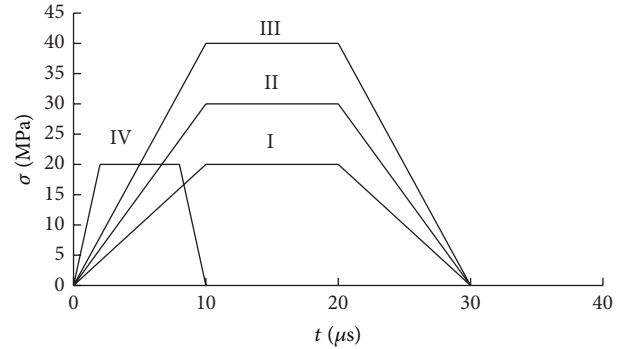


FIGURE 3: Different stress waves exerted on samples.

3. Numerical Model

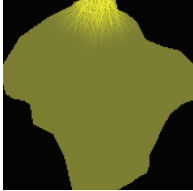
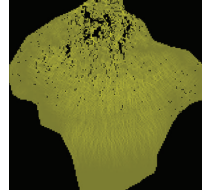
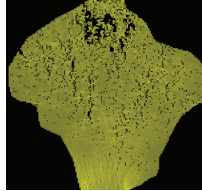
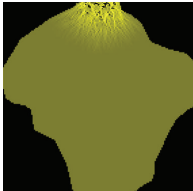
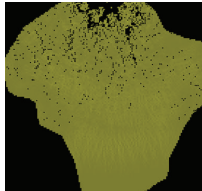
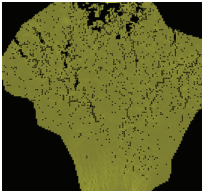
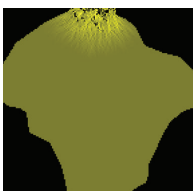
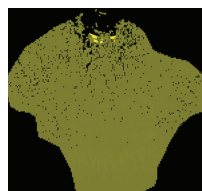
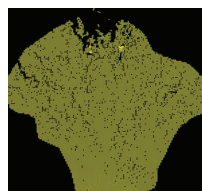
Research object is sample of ore particle, and the numerical sample model built with rock failure process analysis system RFPA is shown in Figure 2, which is 150 mm high and 150 mm wide. Loading plate, which is 5 mm thick, is uniform and elastic, and its elastic modulus is 200 GPa, and Poisson ratio is 0.25. The mechanical parameters of above-mentioned sample are close to phosphate. Moreover, assume that the mechanical property of the mesoscopic unit, which composes ore sample, is in accordance with Weibull distribution, and the mechanical property of the numerical sample is shown in Table 1.

In the process of dynamic loading, an impulsive load pulse is exerted on the loading plate of the sample. The pulse varies over time, which can be seen from Figure 3. On one hand, stress wave is exerted according to the three circumstances shown in segment I to segment III in Figure 3. In order to research the effect of amplitude on the failure model, three stress waves act on the sample. The wave crests are $\sigma_{\max} = 20$ MPa, 30 MPa, and 40 MPa, respectively. On the other hand, in order to investigate the effect of different wavelength on the failure model of the sample, stress waves are loaded according to I and IV shown in Figure 3.

TABLE 1: The mechanical property of the sample of ore particle.

The average value of elasticity modulus/GPa		The average value of uniaxial compressive strength/MPa		Poisson's ratio	The ratio of the compressive strength to tensile strength	Volume mass/kg/cm ³	Homogeneity index
Macroscopy	Mesocopy	Macroscopy	Mesocopy				
15	19	30	97	0.25	10	2.8	3

TABLE 2: Fracturing process of sample under stress waves with different amplitude.

		Propagation time of stress wave, $t/\mu\text{s}$		
		20	60	80
Amplitude of stress wave, /MPa	20			
	30			
	40			

There are two loading boundary conditions. (1) Bottom is fixed, both sides are free, and an impulsive load pulse is exerted on the area with specific width. This loading boundary condition is settled in order to discuss the failure behaviour of the particle under the condition of lateral freedom. (2) Both bottom and lateral are fixed, and an impulsive load pulse is exerted on the area with specific width. This loading boundary condition is settled for discussing the failure behaviour of the particle under constraint condition.

4. The Result and Analysis of the Numerical Simulation

4.1. The Effect of Different Dynamic Stress Wave Amplitudes

4.1.1. *The Failure Process Analysis of Ore Samples.* In numerical simulation, loading stress waves of which amplitude σ_{\max} is 20 MPa, 30 MPa, and 40 MPa, respectively, are adopted. Due to limitation of page, only the fracture processes for the shear stress field of the time steps are used, as shown in Table 2. Here, only some groups of typical simulated result maps are selected, which reflect the failure status of the sample at 20 μs , 60 μs , and 80 μs , respectively. In the following figure of stress distributions, the gray degree

denotes corresponding magnitude of element shear stress, that is, the brighter the point, the greater the shear stress of the element, and the black points indicate failure of elements. Table 2 shows the different failure processes of sample under different loading step.

When value of the exerted stress wave crest is at lower levels, such as wave crest $\sigma_{\max} = 20$ MPa, the value of the stress wave crest is less than the dynamic compressive strength of the ore. After the stress wave passes loading plate onto the top of the particle, it is not enough to crush ore into pieces. Therefore, the part of ore that touches loading plate is not destroyed, for example, when the propagation time $t = 20$ μs . When stress waves continue to propagate downward, stress wave reflection occurs as the stress wave reaches both sides of the particle. At this moment tensile fracture in particle is caused. As a result, tensile fracture area will be generated when stress waves arrive in the area. Stress wave attenuates rapidly when stress waves continue to propagate downward. Therefore, before stress wave propagates to the free surface below the particle, there is less elements fracture, shown in figure of propagation time $t = 60$ μs . So, when stress wave propagates to the free surface below the particle, extension wave is generated. When the amplitude of the extension wave is bigger than tensile strength of the ore element, tensile fracture is generated in the element of particle. Consequently,

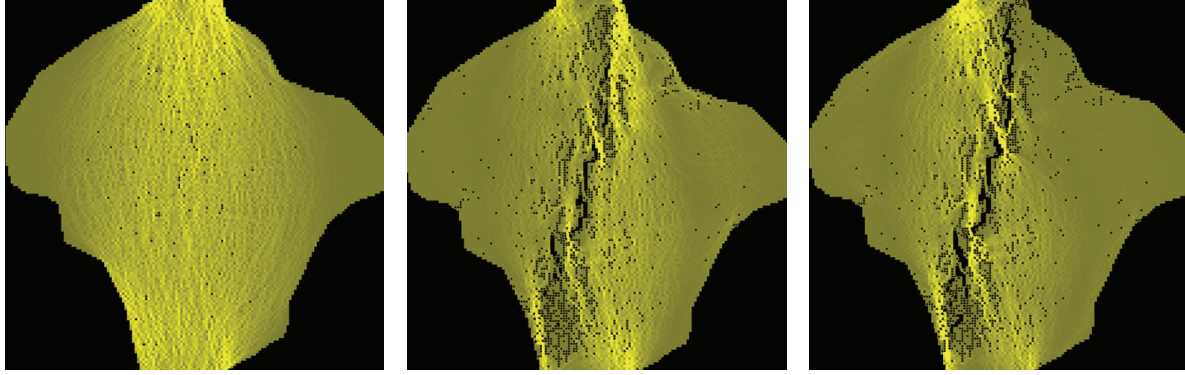


FIGURE 4: Maximum shear stress distribution map under static loading condition ((a)–(c) denote the order of rupture, and the stress unit is MPa).

a few number of elements will fracture near the bottom of particle, and when more failure elements occur, macroscopic tensile cracks may be generated, as shown in failure process at $t = 80 \mu\text{s}$. Comparing dynamic fracture model with fracture model under static loading, a principal crack runs through direction of the height of the samples under static loading, as shown in Figure 4; more cracks will be caused in the sample under dynamic loading, and more cracks coalesce into macroscopic cracks in the sample.

When value of the exerted stress wave crest increases to $\sigma_{\text{max}} = 30 \text{ MPa}$, the value of the stress wave crest is close to dynamic compressive strength of the ore. After the stress wave passes loading plate onto the top of the particle, the particle elements with lower strength which contact loading plate will be crushed, for example, when the propagation time $t = 20 \mu\text{s}$. When stress waves continue to propagate downward, stress wave reflection occurs as the stress wave reaches both sides of the particle. With the combined action of reflected wave and compressive stress wave, at this moment, tensile and crash fracture in particle are caused. As a result, obvious tensile fracture area will be generated when stress waves arrive in the area. Stress wave attenuates rapidly when stress waves continue to propagate downward. Therefore, before stress wave propagates to the free surface below the particle, there is also less elements fracture, shown in figure of propagation time $t = 60 \mu\text{s}$. When stress wave propagates to the free surface below the particle, extension wave is generated. At this moment the amplitude of the extension wave is bigger than amplitude of the stress wave $\sigma_{\text{max}} = 20 \text{ MPa}$. Consequently, there are also lots of fracture elements produced near the bottom of particle, and more macroscopic tensile cracks may be generated, as shown in failure process at $t = 80 \mu\text{s}$ period.

When value of the exerted stress wave crest increases to $\sigma_{\text{max}} = 40 \text{ MPa}$, the value of the stress wave crest is more than dynamic compressive strength of the ore. After the stress wave passes loading plate onto the top of the particle, the particle elements which contact loading plate will be crushed, for example, when the propagation time $t = 20 \mu\text{s}$. At this time, the ore is shattered with large energy consumption. When stress waves continue to propagate downward, stress wave reflection occurs as the stress wave reaches both sides

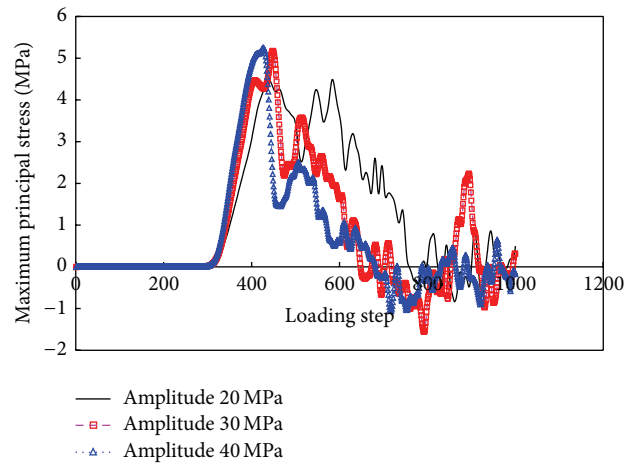


FIGURE 5: Variation law of maximum principle stress on numerical sample unit.

of the particle. With the combined action of reflected wave and compressive stress wave, at this moment, tensile and crash fracture in particle are caused. As a result, obvious tensile fracture area will be generated when stress waves arrive in the area. At this moment fracture area is larger than the two circumstances mentioned above. When stress wave continues to propagate downward until (75, 80), the variation law of stresses at this point is shown as in Figures 5, 6, and 7. Stress wave attenuates faster because stress wave consumes large amount of energy in crushing area before arriving at this point. Therefore, before stress wave propagates to the free surface below the particle, there is less elements fracture, shown in figure of propagation time $t = 60 \mu\text{s}$. When stress wave propagates to the free surface below the particle, extension wave is generated. At this moment the extension wave amplitude is less than the two stress waves' amplitude aforementioned. Consequently, a few number of elements will fracture near the bottom of particle, and when more failure elements occur, macroscopic tensile cracks may be generated in part area, as shown in failure process at $t = 80 \mu\text{s}$ period.

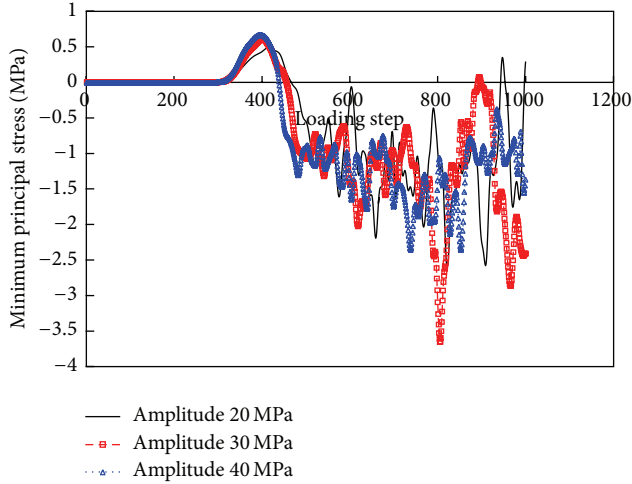


FIGURE 6: Variation law of minimum principle stress on numerical sample unit.

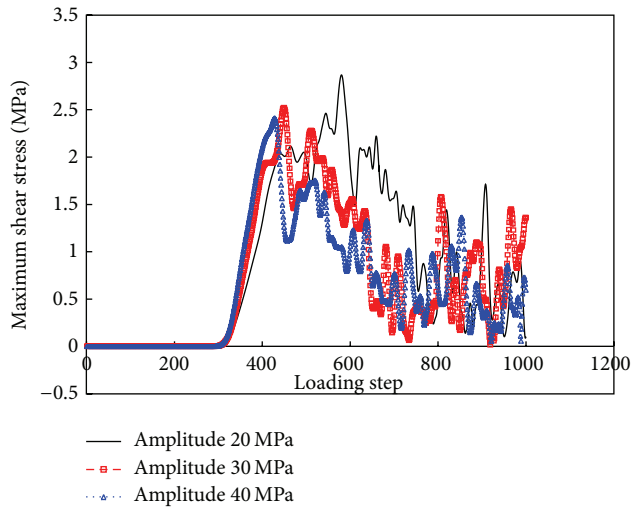


FIGURE 7: Variation law of maximum shear stress on numerical sample unit.

According to the above situation, it is better that the amplitude of stress wave be close to the dynamic strength of the ore subjected to impulsive loading; it is not enough to break the ore when amplitude of stress wave is too small. On the other hand, there will be more ore fines generated when the amplitude exceeds critical range, and crushing effect is generally not as good as desired.

4.1.2. Statistical Analysis of Accumulated Counts of Damaged Elements of Particle. When simulation sample is loaded with three stress waves with different amplitudes, there is a number of damaged elements occurrence in sample at two loading steps; for example, when $\sigma_{max} = 30$ MPa, the loading steps (i.e., the propagation time is $30 \mu s$ and $70 \mu s$, resp.) are numbers 300 and 700, respectively, as shown in Figure 8. Seen from failure process at different loading steps while a number of damaged elements occur, the less the stress wave amplitude

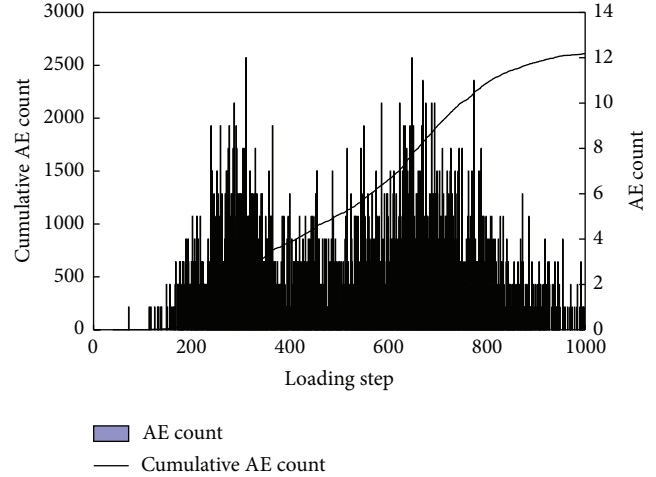


FIGURE 8: Accumulative damaged elements (AE) of sample in a different loading step ($\sigma_{max} = 30$ MPa).

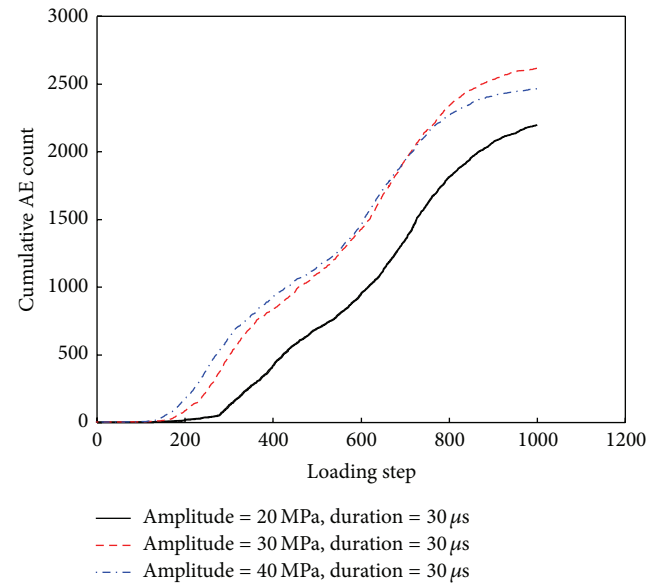
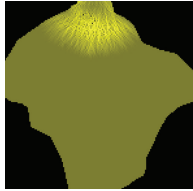
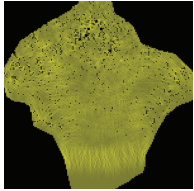
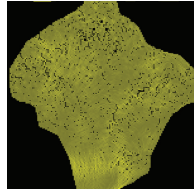
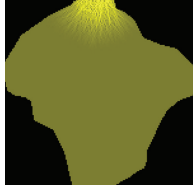
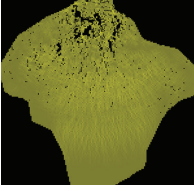
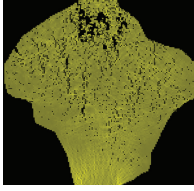


FIGURE 9: The variation of accumulated counts of AE under different stress wave amplitudes.

is, the later a number of damage elements failure occurs; the greater the stress wave amplitude is, the earlier a number of damage elements failure occurs.

When simulation sample is loaded with three stress waves with different amplitudes, the changing rule of accumulated counts of damaged elements of sample is shown in Figure 9. Seen from Figure 9, the less the stress wave amplitude, the less the accumulated counts of damaged elements of the sample at the same loading step; that is, the less the stress wave amplitude, the less cracks generated in sample; the greater the stress wave amplitude, the more the accumulated counts of damaged elements of the sample at the same loading step; that is, the greater the stress wave amplitude, the more cracks generated in the sample; however, if the stress wave amplitude is too high, the accumulated counts of damaged elements of

TABLE 3: Failure process of the sample under different wavelengths (stress amplitude is 20 MPa).

		Propagation time of stress wave, $t/\mu\text{s}$		
		20	60	80
Wavelength, μs	10			
	30			

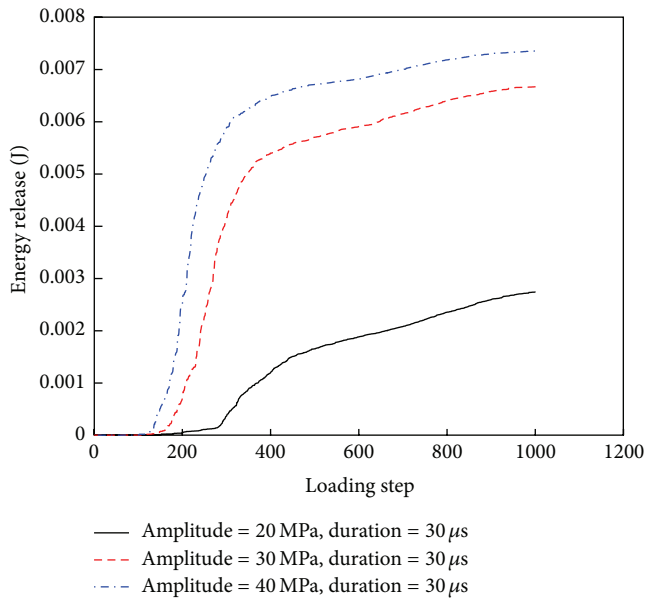


FIGURE 10: Variation of energy release of damaged elements of particle under different stress wave amplitudes.

the sample at the same loading step do not increase at large, but accumulated counts increase a little while stress wave propagates at the top of the sample, and accumulated counts are less than that of the less stress wave amplitude while stress wave propagates at the bottom of the sample, which indicate that the crushing effect is worse if stress wave amplitude is too large. This is due to comminuting at the top which consumes a lot of energy, so then stress wave attenuates fast when stress wave amplitude is too large.

4.1.3. Analysis of Energy Release of Damaged Elements of Particle. When simulation sample is loaded with stress waves with different amplitudes, the changing rule of energy release of damaged elements of particle is shown in Figure 10. Seen from Figure 10, the more the stress wave amplitude is, the

more the energy release of damaged elements of particle at the same loading step is. Analysis shows that the greater the stress wave amplitude, the more the energy consumption of damaged elements of particle.

Seen from the analysis results of the failure process of the sample under different stress wave amplitudes, it is better that the amplitude of stress wave be close to the dynamic strength of the ore subjected to impulsive loading; it is not enough to break the ore when amplitude of stress wave is too small. On the other hand, there will be more ore fines generated when the amplitude exceeds critical range, and crushing effect is generally not as good as desired. And if the stress amplitude is too large, not only desired crushing effect is not obtained, but also more energy in fragmentation is consumed. Therefore, too large power of crusher should not be selected for such ores.

4.2. The Effect of Different Wavelength of Dynamic Stress

4.2.1. Failure Process Analysis of Particles. When stress wave amplitude is 20 MPa and wavelength is different, the failure process of the sample is shown in Table 3. Seen from Table 3, there is no big change in failure mode except for amount of damaged elements when wavelength is different. Less amount of damaged element occurs when the wavelength is short, that is, caused by less input of crushing energy as a result of short wavelength; when the wavelength is long, more amount of damaged elements occurs. Therefore, in order to get good crushing effect, the wavelength of impact load should not be too short; that is, the impact frequency of crusher for this kind of ore should not be too fast.

4.2.2. Statistical Analysis of Accumulated Counts of Damaged Elements of Ore Particle. When simulation sample is loaded with stress waves with different wavelength, seen from failure process at different loading steps while a number of damaged elements occur, the shorter the stress wavelength is, the earlier a number of damaged elements failure occurs; the longer the stress wave amplitude is, the later a number of damaged elements failure occurs.

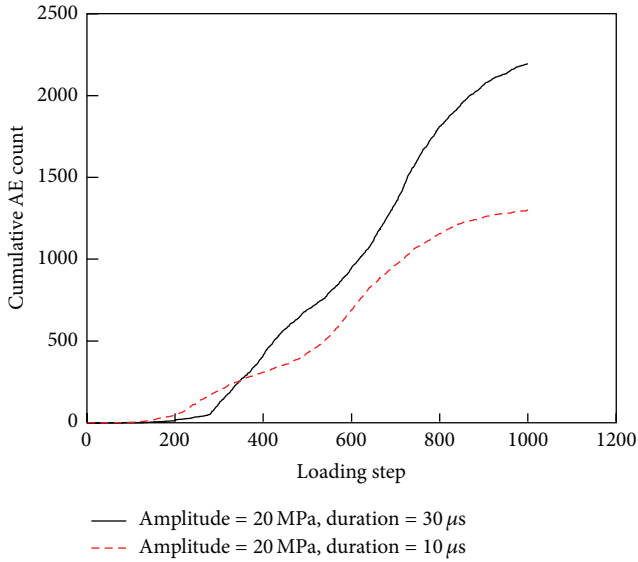


FIGURE 11: Variation of accumulated counts of failed elements (AE) of sample under different stress wavelength.

When simulation sample is loaded with stress waves with different wavelengths, the changing rule of accumulated counts of damaged elements of sample is shown in Figure 11. Seen from Figure 11, the shorter the stress wavelength is, the less the accumulated counts of damaged elements of sample at the same loading step (except for the beginning) are; that is, the shorter the stress wavelength, the less the cracks generated in the sample; the longer the stress wavelength, the more the accumulated counts of damaged elements of sample at the same loading step (except for the beginning); that is, the longer the stress wavelength, the more cracks generated in the sample. In the beginning of the stress wave propagation, accumulated counts of failed elements are relatively high while stress wave length is short. When the stress wave propagates to the border, stress wave reflection at free surface of boundary occurs, and because of the relatively short stress wavelength, more times of reflection occur and form more failed elements. This is consistent with aforementioned analysis results of a number of damaged elements occurring at some loading step. This fully indicates that there is a close relationship between the dynamic failure process and the stress wavelength.

4.2.3. Statistical Analysis of Energy Release of Damaged Elements of Particle. When simulation sample is loaded with stress waves with different wavelength, the changing rule of energy release of damaged elements of particle is shown in Figure 12. Seen from Figure 12, released energy in the failure process of sample increases with the increase of stress wavelength. It shows that more energy will be consumed for sample crushing with the increase of stress wavelength.

Seen from the analysis results of the failure process of the sample under different stress wavelength, in order to get good crushing effect, the wavelength of impact loads should not be

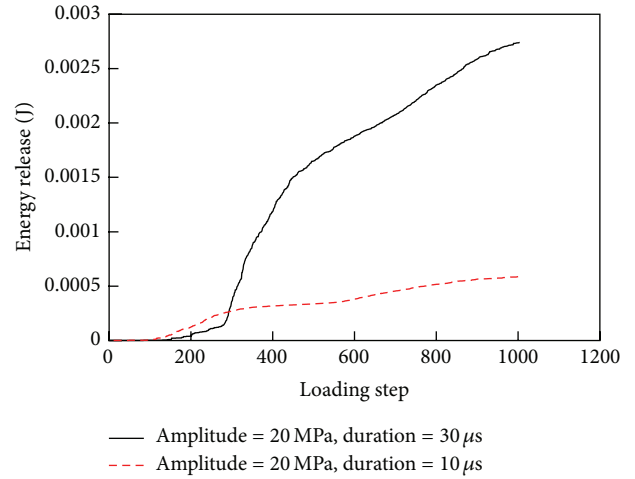


FIGURE 12: Variation of energy release of sample under different wavelength duration.

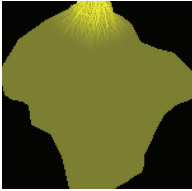
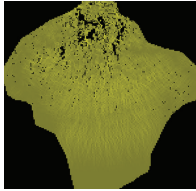
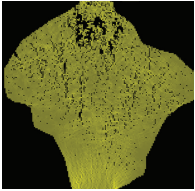
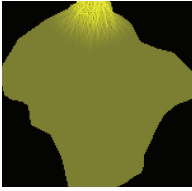
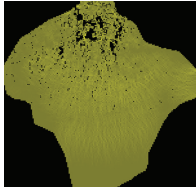
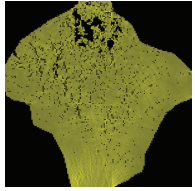
too short. Therefore, too high impact frequency of crushers should not be selected for such ores.

4.3. The Influence of Lateral Constraint on Breakage of Ore Particle

4.3.1. The Failure Process Analysis of Ore Particle. The breakage process of granular material, on which stress wave amplitude value is 20 MPa and wavelength is $30 \mu\text{s}$ and on both sides of which there is no constraint or constraint, is shown in Table 4. From Table 4, we know that the failure behavior of particle on both sides of which there is no constraint or constraint has nearly no change; only a small amount of change in the damage is extent. When there is no constraint on both sides of particle, the smaller the wavelength is, the larger the extent of damage is, but that is not obvious. This is rock-breaking effect using tensile stress wave under condition of no constraint. However, when there is constraint on both sides of particle, the extent of damage is lighter. So, in order to get the good effect of breakage, we need to consider the state of constraint of ore particle in the crushing chamber when we choose the proper crusher.

4.3.2. Statistical Analysis of Accumulated Counts of Damaged Elements of Ore Particle. When particle sample is constrained or unconstrained on both sides, damaged elements of ore particle at different loading step are shown in Figures 8 and 13. As shown in Figure 13, there are also obvious stages of elements damage of sample when the numerical sample is constrained but not sharper than that when it is unconstrained. When the numerical sample is constrained, the two times of a large number of damaged elements occurrence are $40 \mu\text{s}$ and $75 \mu\text{s}$, respectively. Compared with the two times of a large number of damaged elements occurrence ($t = 45 \mu\text{s}$ and $t = 75 \mu\text{s}$) of numerical sample with unconstrained, the time is earlier than that when numerical sample is constrained.

TABLE 4: The failure process of sample with no constraint and constraint.

	Propagation time $t = 20 \mu s$	$t = 60 \mu s$	$t = 80 \mu s$
No constraint			
Constraint			

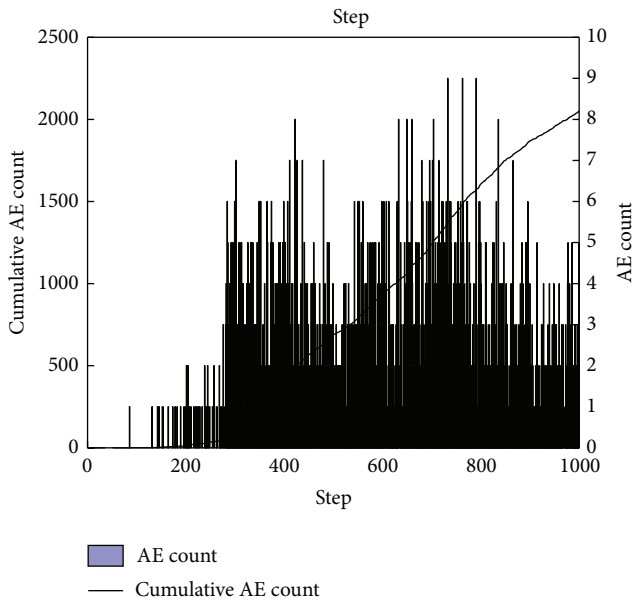


FIGURE 13: The counts of damaged elements of numerical sample with constraint at different loading step.

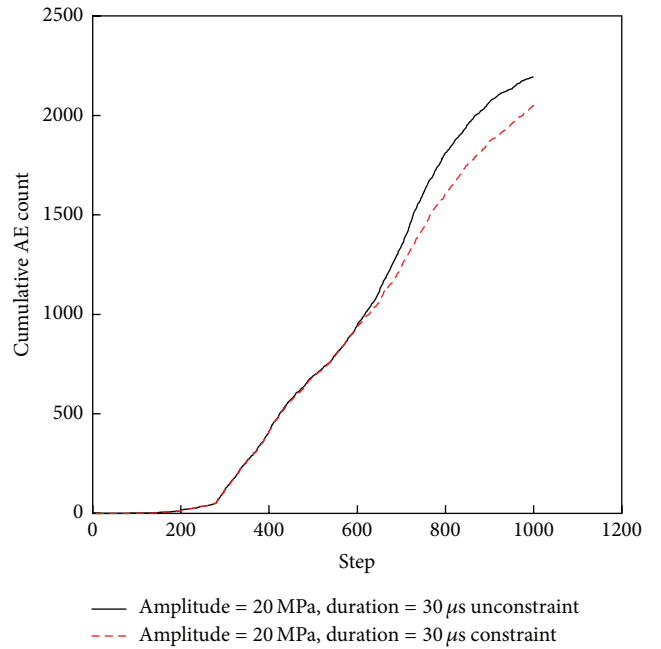


FIGURE 14: The accumulated counts of damaged elements of sample with unconstrained and constraint.

Under different constraints, the change rules of accumulated counts of damaged elements are shown in Figure 14. From Figure 14, we can see that accumulated counts of damaged elements at the same propagation time in the initial stages are approached. But when the stress wave propagates to the bottom of particle, compared with that having constraint, the accumulated counts of damaged elements are larger than those having no constraint. This shows that the free surface of particle may have some effect on crushing of particle. We can use tensile stress wave generated by reflection of stress wave at free surface to fracture rock. It reflects that the dynamic breakage process has a certain relationship with the constraint of ore particle.

4.3.3. *Statistical Analysis of Energy Release of Damaged Elements of Particle.* When the two sides of sample have constraint or no constraint, the damage energy release change rule is shown in Figure 15. As shown in Figure 15, the damage energy release of numerical sample with unconstrained is smaller than that when it has constraint.

From the failure process analysis results of the numerical sample with unconstrained and constrained, we know that when impacting load crushing ore, in order to obtain good crushing effect, particles do not need constraints, but from the point of energy-efficient, the particle should carry on the constraint.

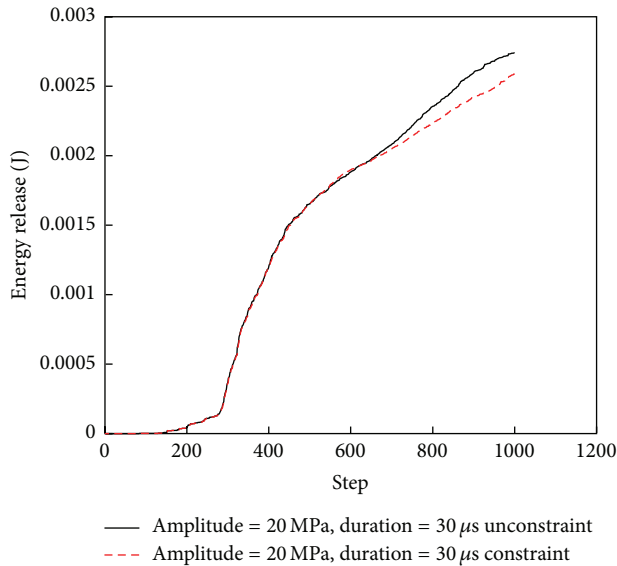


FIGURE 15: The damage energy release change rule of sample with unconstrained and constrained.

5. Conclusions

In this paper, the dynamic rock failure process analysis (RFPA) code is used to analyze failure process of ore particles under impact loading. Numerical simulations show that it is better to break rock when the amplitude of stress wave is close to the dynamic strength of the ore subjected to impact loading; it is not enough to break the ore when stress wave amplitude is too small; on the other hand, there will be more ore fines generated when the stress amplitude exceeds critical range, and crushing effect is generally not as good as desired. And if the stress amplitude is too large, not only desired crushing effect is not obtained, but also more energy in fragmentation is consumed. Therefore, too large power of crusher should not be selected for such ores. In order to get good crushing effect, the wavelength of impact loads should not be too short. Therefore, too high impact frequency of crushers should not be selected for such ores. It should be noted that the effect of geometry shape changes and homogeneity of the actual ore particles on failure process requires to be studied further more. In addition, the physical tests of the mineral particles are still in progress.

Conflict of Interests

The authors declare that there is no conflict of interests regarding the publication of this paper.

Acknowledgments

The study presented in this paper was jointly funded by the National Technology R&D Program for the 12th five-year plan (no. 2012BAB08B06), the National Natural Science Foundation of China (nos. 51164005, 51264005, 41172265, and 50874024), Project (GY(2011)3063) supported by Guizhou

Province Industry Tackles Key Problem Program, the Key Project for the Nature Science Research from the Guizhou Province Bureau of Education (2010003), the Governor Fund Project for Outstanding Scientific and Technological Education Talent from the Guizhou Province (2011-36), Special Project for Guizhou Province High-Level Personnel Scientific Research (TZJF-2010-044), and the Introducing Talents Project of Guizhou University (2010-008).

References

- [1] C. M. Evertsson, *Cone crusher performance [Ph.D. thesis]*, Chalmers University of Technology, Gothenburg, Sweden, 2000.
- [2] C. A. Tang, X. H. Xu, S. Q. Kou, P.-A. Lindqvist, and H. Y. Liu, "Numerical investigation of particle breakage as applied to mechanical crushing—part I: single-particle breakage," *International Journal of Rock Mechanics and Mining Sciences*, vol. 38, no. 8, pp. 1147–1162, 2001.
- [3] C. L. Prasher, *Crushing and Grinding Process Handbook*, John Wiley & Sons, New York, NY, USA, 1987.
- [4] O. Tsoungui, D. Vallet, and J.-C. Charmet, "Numerical model of crushing of grains inside two-dimensional granular materials," *Powder Technology*, vol. 105, no. 1–3, pp. 190–198, 1999.
- [5] V. S. Vutukri, R. D. Lama, and S. S. Saluja, *Handbook on Mechanical Properties of Rocks*, Trans Technical Publications, Rockport, Mass, USA, 1974.
- [6] Y.-J. Zuo, W.-C. Zhu, C.-A. Tang, X.-B. Li, and W.-H. Wang, "Numerical simulation on spallation process of inhomogeneous medium induced by reflection of stress wave," *Journal of Central South University (Science and Technology)*, vol. 37, no. 6, pp. 1177–1182, 2006.
- [7] J. Zhao, "Applicability of Mohr-Coulomb and Hoek-Brown strength criteria to the dynamic strength of brittle rock," *International Journal of Rock Mechanics and Mining Sciences*, vol. 37, no. 7, pp. 1115–1121, 2000.
- [8] W.-X. Gao, J. Yang, and F.-L. Huang, "The constitutive relation of rock under strong impact loading," *Transaction of Beijing Institute of Technology*, vol. 20, no. 2, pp. 165–170, 2000 (Chinese).
- [9] Y. Bin, L. Dianshu, Q. He et al., "Experimental study of granite's constitutive relation under blasting load," *Journal of China University of Mining and Technology*, vol. 28, no. 6, pp. 552–555, 1999 (Chinese).
- [10] S. Q. Kou, H. Y. Liu, P. A. Lindqvist, C. A. Tang, and X. H. Xu, "Numerical investigation of particle breakage as applied to mechanical crushing. Part II. Interparticle breakage," *International Journal of Rock Mechanics and Mining Sciences*, vol. 38, no. 8, pp. 1163–1172, 2001.
- [11] Z.-P. Huang, W.-C. Zhu, C.-A. Tang, and L.-X. Li, "Numerical simulation on breakage of rock particles under dynamic loading," *Journal of Shenyang Jianzhu University*, vol. 22, no. 1, pp. 91–95, 2006 (Chinese).
- [12] W. A. Weibull, "Statistical distribution function of wide applicability," *Journal of Applied Mechanics*, vol. 18, pp. 293–297, 1951.
- [13] W. C. Zhu and C. A. Tang, "Micromechanical model for simulating the fracture process of rock," *Rock Mechanics and Rock Engineering*, vol. 37, no. 1, pp. 25–56, 2004.
- [14] J. W. Tedesco, C. A. Ross, P. B. McGill, and B. P. O'Neil, "Numerical analysis of high strain rate concrete direct tension tests," *Computers and Structures*, vol. 40, no. 2, pp. 313–327, 1991.

- [15] C. A. Tang, "Numerical simulation of progressive rock failure and associated seismicity," *International Journal of Rock Mechanics and Mining Sciences & Geomechanics Abstracts*, vol. 34, no. 2, pp. 249–261, 1997.
- [16] C. A. Tang, H. Liu, P. K. K. Lee, Y. Tsui, and L. G. Tham, "Numerical studies of the influence of microstructure on rock failure in uniaxial compression—part I: effect of heterogeneity," *International Journal of Rock Mechanics and Mining Sciences*, vol. 37, no. 4, pp. 555–569, 2000.

Research Article

Study on Dynamic Disaster in Steeply Deep Rock Mass Condition in Urumchi Coalfield

Xing-Ping Lai,^{1,2} Mei-Feng Cai,³ Fen-Hua Ren,³ Peng-Fei Shan,^{1,2}
Feng Cui,^{1,2} and Jian-Tao Cao^{1,2}

¹School of Energy and Mining Engineering, Xi'an University of Science and Technology, Xi'an 710054, China

²Key Laboratory of Western Mines and Hazard Prevention, Ministry of Education of China, Xi'an 710054, China

³School of Civil and Environmental Engineering, University of Science and Technology Beijing, Beijing 100083, China

Correspondence should be addressed to Xing-Ping Lai; laixp@xust.edu.cn

Received 16 September 2014; Accepted 5 December 2014

Academic Editor: Shimin Liu

Copyright © 2015 Xing-Ping Lai et al. This is an open access article distributed under the Creative Commons Attribution License, which permits unrestricted use, distribution, and reproduction in any medium, provided the original work is properly cited.

The possible mining seismicity (MS) and its prediction are important for safety and recovery optimization of mining in steep-heavy-thick rock mass condition. The stress-lever-rotation-effect (SLRE) model of fault-like mobilization was proposed preliminarily. Some innovation monitoring technique approaches for mining seismicity assessment were successfully fulfilled at Wudong Mine of Urumchi Coalfield, China. The characteristics on acoustic-seismic-wave index indicated the spatial-temporal-strength and stress redistribution of steeply deeper-heavy thick coal and rock masses. Applications in field investigations showed that the innovation monitoring (in time and space) of these instruments could provide important information about the performance of mining disturbed structures (heading and steep pillar) during caving of competent overlying roof strata. The prediction and evaluation for mining seismicity were applicable and valid. Operating practice showed that mining efficiency was raised and conspicuous economic benefit was obtained. This approach provides essential data for assessing mining seismicity, coal burst, dynamic hazard prevention, and deep mining potential.

1. Introduction

There are many rock mechanics challenges related to the underground extraction of the western mining, China. Mining seismicity (MS) has a long history in Chinese coal mines [1]. Among them Urumchi Coalfield (UC) is a unique one in highly seismic region. The UC is an enrichment coalfield, as focal region of steep-heavy-thick coal seams, with the dip angle from 45° to 87°. Its deposits are 219 hundred million tons, consisting of 30 coal seams with various thicknesses. Wudong Mine is 19.5 km from east to west and about 3.0 km from south to north. The mine area is about 38 km². The seam thickness is varied from 30.0 m to 50.0 m. The present extraction depth is around 400 m. The dominant mining method was mechanized subhorizontal section top-coal caving (SSTCC) with annual production of 10 million tons [2]. Presently, its output is the highest among steep-heavy-thick coal seams of China.

Generally, the multi-narrow-space formed above the sub-horizontal section top-coal caving workings. The inclination length of working face is usually shorter. Hence, the variability of stress and deformation of steep-heavy-thick seams are obviously different from those of longwall top-coal caving (LTCC) of gently inclined coal seam [3–5]. Under the existing geological and mining conditions of the coal seam in the Dzungaria Basin, underground extraction of the coal mineral in the basin is typically accompanied by mining seismicity, which is also referred to as coal burst and dynamic collapse.

Formerly published literatures on the mining seismicity have mainly focused on understanding the mechanism of longwall top-coal caving workings involved and their impacts on the stress analysis, design and optimization, management, and policy-making [6–10]. It is novelty of the mining seismicity occurrence at Urumchi Coalfield. The field monitoring is one of crucial ways to predict mining seismicity and dynamic disaster [11]. The traditional prediction for mining seismicity

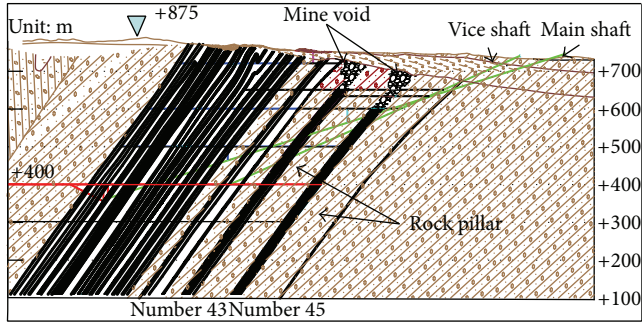


FIGURE 1: The existence of steep-heavy-thick coal seams in sectional view.

was inapplicable at Urumchi Coalfield and neither was analyzed nor studied acoustic-seismic-wave index and their implicit relations in detail. Particularly, the horizontal section coal caving multiple disturbed, the steep and broken coal-rock masses caved, the size and magnitude of broken or occurrence, and intensity related to the spatial-temporal-strength relation and mining disturbance, indicating stress redistribution of coal-rock masses.

In the present study, the stress-lever-rotation-effect (SLRE) model of fault-like mobilization was preliminarily proposed and the possible mining seismicity and its prediction were performed to steeply heavy-thick coal seam and rock mass. Specifically, innovation monitoring techniques relating to the acoustic-seismic-wave index were applied at Wudong Mine, China. The approach would provide essential data for assessing mining seismicity, coal burst, dynamic hazard prevention, and deep mining potential.

2. Site Details

2.1. Geology and Environment. The performance of safe mining depends on the geological environment, characterizations, and geomechanical prosperities of rock masses. The Urumchi Coalfield is located in the south of the Dzungaria Basin of China and at the south edge of Urumchi City. Historically, the earthquake frequently happened here. It is an enrichment coalfield adjacent to the Western-Mountain-Rupture Zone, which is an unwatered, ecological fragility, high ground stress region, and strong ground motion zone, known for the steep-heavy-thick coal seams. Its coal reserves are 219 hundred million tons, consisting of 30 coal seams with various thicknesses and interlayers (Figure 1). The bearing angle varies from 322° to 335° . The roof of the rock masses is mainly the siltstone, and the fine sandstone increases at shallow and reduces at deep strata. The coal and rock masses are very rigid.

2.2. Mining Method and Condition. With the dipping angle from 45° to 87° , the top-coal caving for steep coal seam in the horizontal section was evidently different from the gently inclined seam. Generally, the working face was arranged with short length when the thickness of coal seams ranges from 20.0 m to 50.0 m. Usually, the height of the horizontal section

was 20.0 m; it would successively extend from upper place to lower sections or workings and form the typical narrow-space mining and stress concentration conditions. As shown in Figure 1, the top-coal caving workings in the horizontal section located beneath the multilayer mined-out area all the while at Wudong Mine. During the horizontal section mining disturbed under weak and laminated conditions, dynamic hazard would easily induce the relating mining seismicity, rock outburst, pillar destabilization, dynamic roof collapse, and so forth.

2.3. MS Occurrence. In general, unique mining seismicity was dominant in the experience of limited mining space. In mines, such events were often referred to as rock bursts, tremors, coal occurrence, and acoustic events, depending on their frequency contents and the sizes of the source. There was previously no mining seismicity occurrence during shallow mining, with the depth of less than 350 m, while the coal-gas outburst ever happened. In particular, during the period of 2011–2013, the mining seismicity occurrences were severe, while mining at depths ranging from 300 m to 350 m, as several hazards happened at number 43 and number 45 working faces. Figure 2 illustrated the field calamitous collapse and the coal occurrence.

3. Proposal of the Stress-Lever-Structure Model

The structure of mining disturbed zone is shown in Figures 3(a) and 3(b); the advance heading of number 45 working face not only undertakes the compressive and shear stress from the roof, overburden, and top-coal dynamic effect, but also resists the pry rock pillar mobilization effect of the dip of a 50.0 m thickness caused by number. 43 coal seam. After heading and workings being excavated, overlying gravity of excavation space is transferred into the heading on both sides, then the stress redistributes, and two peak values of σ_{\max} present in the coal mass under the top-coal action of the roof and the floor. When the σ_{\max} is more than the compressive strength of the coal, regional fracture and damage occurred in the coal-rock mass; meanwhile, its strength reduces to the level of residual strength. During the top-coal caving, there appears the stress-lever-rotation-effect of fault-like mobilization in the roof of number 43 workings (Figure 3(b)).

The roof-floor of shallow stope is regarded as the arch of spanning strata with a certain thickness [12]. With mining advance and disturbance, the mobilization of the roof arch and the floor is enhanced. The peak stress of the roof and the floor appears underneath the support. The $\sigma_{1\max}$, the peak stress in the coal seam, and $\sigma'_{1\max}$, the peak stress in the rock mass, extend downward and migrate to lower strata to form the peak stresses $\sigma_{2\max}$ and $\sigma'_{2\max}$ in the lower section. The peak stress in the coal seam and the rock mass would be like this to migrate downwards successively. Mining disturbance would release stress, induce mining seismicity, or even cause dynamic hazard. It is a fundamental mechanism and a potential prediction of mining seismicity.

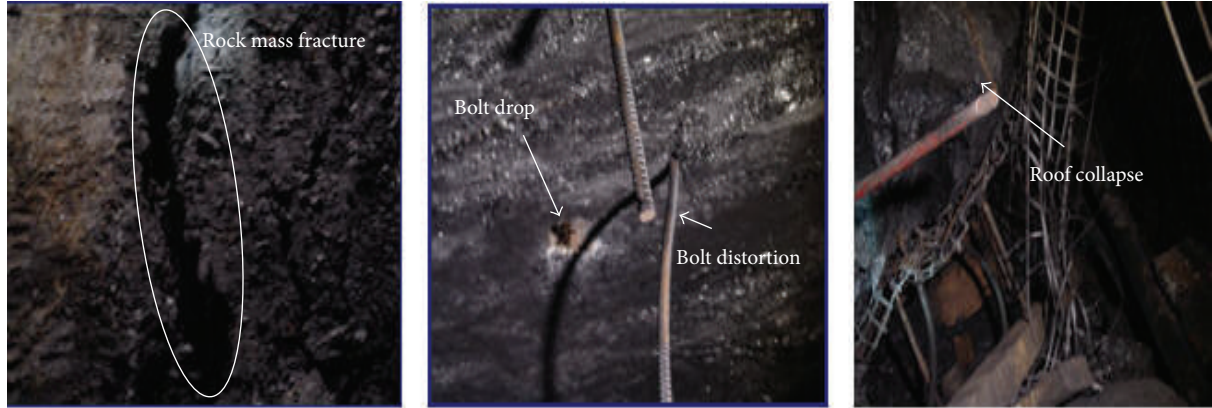


FIGURE 2: Field collapse and coal burst (2012.6.30).

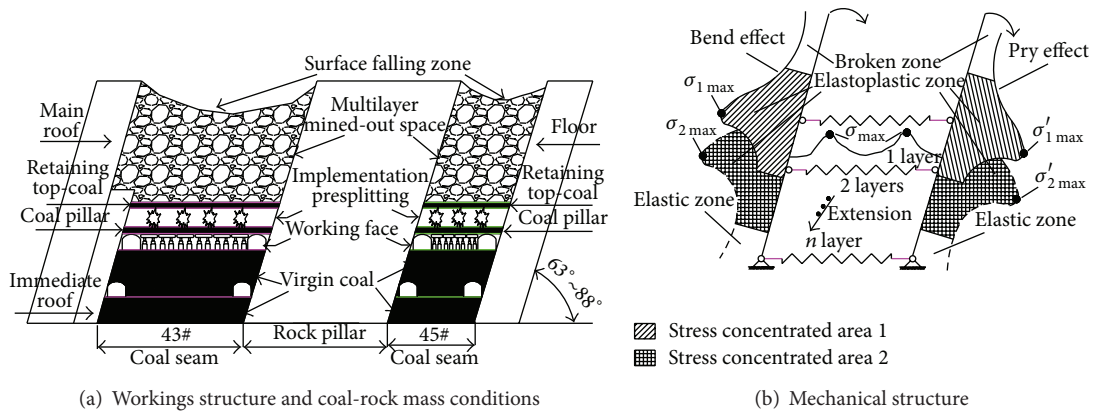


FIGURE 3: Descriptions of the structure with the steep-coal-seam working face.

The stress monitoring apparatus is installed at rock pillar between number 43 and number 45 working faces. The in situ stress distribution was obtained at various drilling depths (Figure 4(a)). The numerical computation resulted from quasi-static granular displacements in block caving, arch stress, dilatancy, or swelling effects and their illustrating intrinsic evolution on shapes with the FLAC^{3D} program (Figure 4(b)). Also, according to multiple mining disturbed zone interaction upon block caving by means of a large 3D physical model experiment [13, 14], the stress distribution had two crests, and the main reason was the action of large arch of spanning strata instability caused by stress-lever-rotation-effect from the roof and the floor coal-rock mass. Multicycles of top-coal caving induced a load which was bigger than the compressive strength to the coal pillars, increasing the number and the length of the fractures.

4. Field Acoustic-Seismic-Wave Index Monitoring

It is vital to obtain the in situ stress distribution, deformation, and fracture characteristics upon coal-rock masses at various depths under mining disturbed conditions [15–17]. The methods of acoustic-electromagnetic wave, optical

imaging and ground penetrating radar (GPR), and so forth are applicable, and the comprehensive field deformation monitoring of steeply dipping coal-rock masses provides the credible and quantitative information for the assessment mining seismicity affected by redistribution stress.

4.1. Acoustic-Wave. The quality of the surrounding rock can be determined by the value of velocity according to the principle of acoustic-wave propagation. Supposing that the coal-rock mass is elastic medium, the calculation formula of longitudinal wave is derived as follows:

$$v_p = \sqrt{\frac{E(1-\mu)}{\rho(1+\mu)(1-2\mu)}} \quad (1)$$

Here, v_p is preliminary wave velocity, E is elastic modulus of coal-rock mass, μ is Poisson's ratio, and ρ is the density of coal-rock mass. It is indicated that the intensity and elastic modulus for the surrounding rock are smaller at the same time. Based on the elastic modulus, Poisson ratio, and other parameters gained from rock mechanics experiments of the coal-rock mass, all parameters reduced with a certain proportion for the rock mass. The longitudinal wave velocity of the coal-rock mass was 2217 m/s and 1629 m/s obtained by

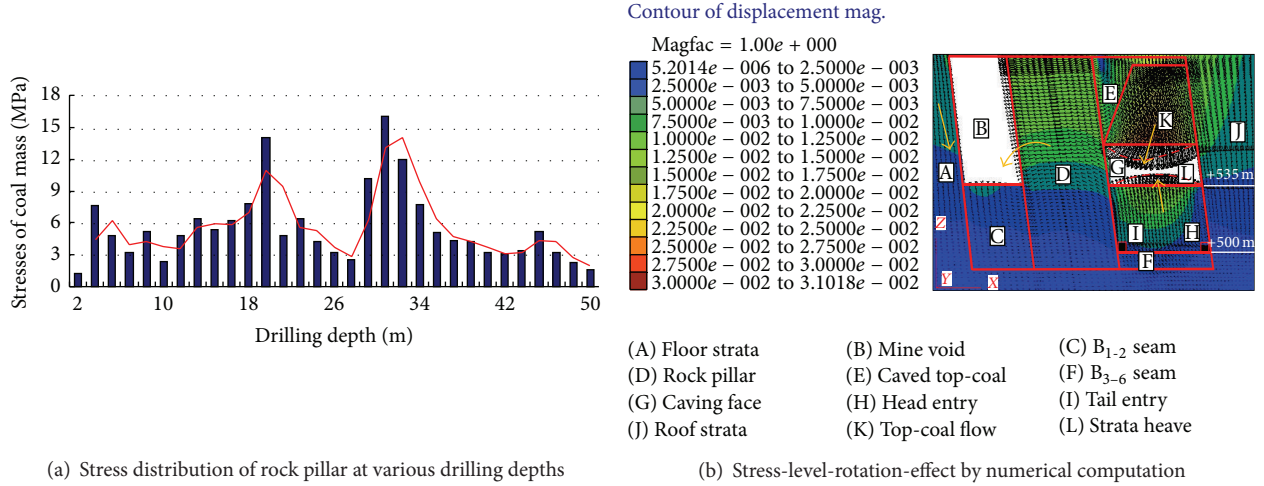


FIGURE 4: Relation between depths stress (a) and deformation distribution (b).

calculation, respectively. We proposed that the surrounding rock was fractured or ruptured when velocity of the received wave was lower than the corresponding v_p . Five test boreholes were arranged on the section of the roadway from left to right clockwise, with the angles of 0° , 45° , 90° , 135° , and 180° , respectively (Figure 5). The diameter of the borehole was 0.42 m with the depth of 10.0 m.

It was indicated that the velocity of longitudinal wave within the range of 0 to 1.5 m of coal-rock masses was less than that of analytic calculation, which means coal and rock masses qualities were poor. The acoustic velocity of the rock side was beyond that of the coal side, which showed that the stability of the rock mass side was better than that of the coal mass side. The sound velocity of measurement points was less than 2217 m/s and 1629 m/s in the measuring lines of 45° direction for two sides and roof in the roadway with the range of 2.5 m to 7.5 m. The main reason was the stress concentration effected by the nearby vertical roof bending and floor pry; the peaks $\sigma_{n,max}$ and $\sigma'_{n,max}$ were produced in the two ends of the working face, respectively. The depth of the fractured zone of the roadway was about 1.5 m, rock masses decreased within the depth of 2.5 m to 7.5 m, and the stability of the borehole wall was dreadful at the 45° direction for each side of the roadway. The velocity of longitudinal wave of the surrounding rock increased slightly after the distance of 7.5 m depth of rock masses, which indicated that the stability of roof rock masses increased. The acoustic-wave speed of the coal was less than 1629 m/s. It was indicated that the deformation and the fracture distribution were obviously asymmetric migration and localization.

4.2. Electromagnetic Wave. Delineation of mining seismicity and dynamical fractures with ground penetrating radar is an advanced way. The high frequency electromagnetic wave of ground penetrating radar launched from transmitting antenna is delivered into underground; the amplitude of electromagnetic wave changes when encountering discontinuous interface. The propagation velocity of electromagnetic wave

in underground rock masses can be obtained according to the following formula:

$$v = \frac{c}{\sqrt{\epsilon_r}}. \quad (2)$$

Here, c is 3×10^8 m/s and ϵ_r is the constant of medium. The travel time (T) of the reflected wave from the target can be tracked and measured. The depth of the underground object (H) can be determined based on the electromagnetic wave propagation in the medium velocity and the reflection time as follows:

$$H = \frac{T * V}{2}. \quad (3)$$

Here, T is the time of electromagnetic wave propagation; V is the electromagnetic wave velocity. SIR20 GPR (100 MHz) is applied. Four lines with the 50.0 m length strike and that of 12.0 m vertical depth were detected to rock pillar at roadway.

Figure 6 illustrates the electromagnetic wave results in the roadway roof. With the frequency of 0–350 scans and the energy of 0–59 ns, the left circle in this figure shows electromagnetic wave results in a broken cavity located at the strike of 630–650 m with the vertical depth of 350–360 m, and the observed results indicate that the fragmentation degree and the electromagnetic wave energy of the coal seam are lower in the cavity; with the frequency of 350–900 scans and the energy of 0–150 ns, the right circle shows electromagnetic wave results in the other place located at the strike of 650–700 m; with the vertical depth of 360–380 m, the observed results indicate that the coal-rock masses in this place are more stable and the reflected wave has not caused any large deflections and displacements. At the strike of 700–750 m with the vertical depth of 380–400 m, wave lineups sign of delaminating and damage are observed with the electromagnetic wave results of 0–350 scan frequency and 50–100 ns energy, which reflects obvious dislocation and mutual cross and indicates that more electromagnetic wave energy has been absorbed and the coal-rock is broken in

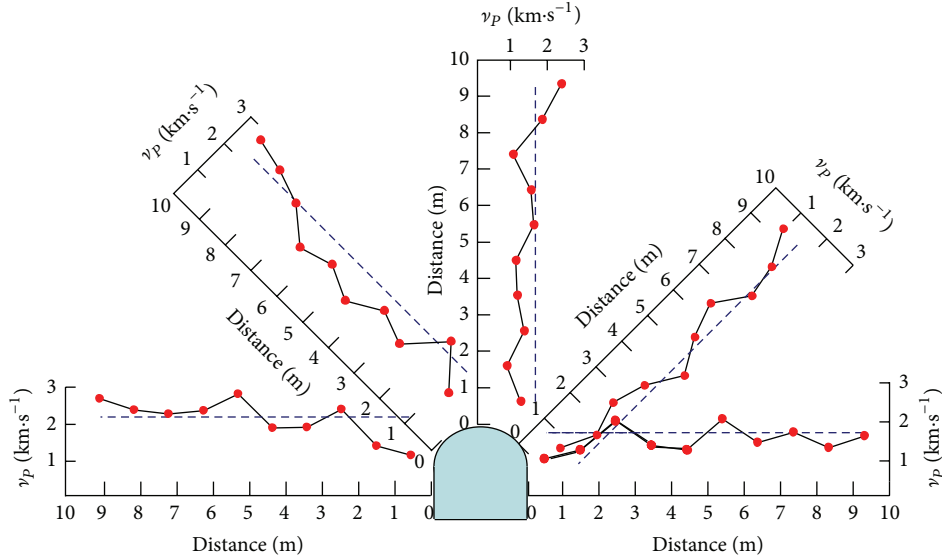


FIGURE 5: Relations of acoustic-wave velocities (v_p) and the distance of boreholes.

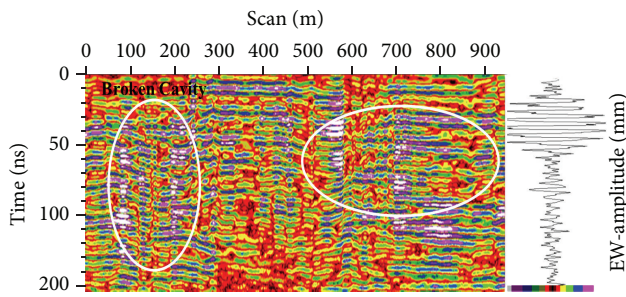


FIGURE 6: The in situ profile result of the electromagnetic wave.

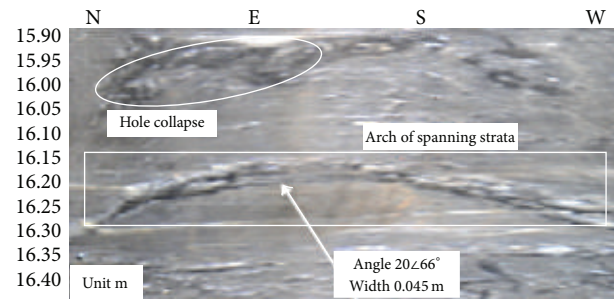


FIGURE 7: Observation by the borehole optical imaging TV.

this place. Plus the deflection acuteness wave, a small range of the broken cavity is detected, which was formed under the coupling action of the broken coal-rock masses. It is indicated that the energy intensity of the electromagnetic wave is remarkable at various mining depths and redisturbed ranges besides the dip angle and the lithology.

4.3. The Observation of the Borehole Optical Imaging TV. Parallel to its spanning coal seam, the arch structure of the spanning strata is verified above the working face in mining (Figure 7) by the in situ optical imaging TV. The in situ optical imaging TV can directly observe the crack propagation, fissure, and the fracture broken and the caving phenomena. Moreover, it provides the stress magnitude, orientation, and trend based on deeper dynamic swelling and shrinkage cavity of the borehole inner wall. We could indicate the fracture spatial-temporal-strength evolvement and distribution of the pillars. Sequentially, it was available for analysis of the characteristics of the mining seismicity and the definition of its potential to generate coal burst.

4.4. Mining Seismicity Monitoring. Paladin-TM mining seismicity monitoring has been adopted in Wudong Mine

for real-time field information. Specially, mining seismicity ($M_L = 3.2$) caused vast facility damage (Figure 8) that happened in +500 working face (mining depth 350 m) and its roadways at September 18, 2013. With analyzing the monitoring data from September 8 to September 22, 2013, amount of mining seismicity in B_{3-6} and B_{1-2} seams was 22 and 40, respectively. Energy release was more frequent. Major mining seismicity events emerged at coal mass near the rock pillar being advanced the working face. Simultaneously, mining seismicity events happened at coal mass which was lag excavation in B_{1-2} seams. In vertical direction, mining seismicity events mainly concentrated from +475 m to +510 m, while major mining seismicity seldom emerged above +550 m. Figure 9 illustrated that mining seismicity is focused from +500 m to +510 m and from +475 m to +485 m.

5. Results and Discussions

5.1. Mining Depth. The mining seismicity is akin to an artificial earthquake caused by mining disturbance. Mining seismicity was more frequent when the mining depth exceeds

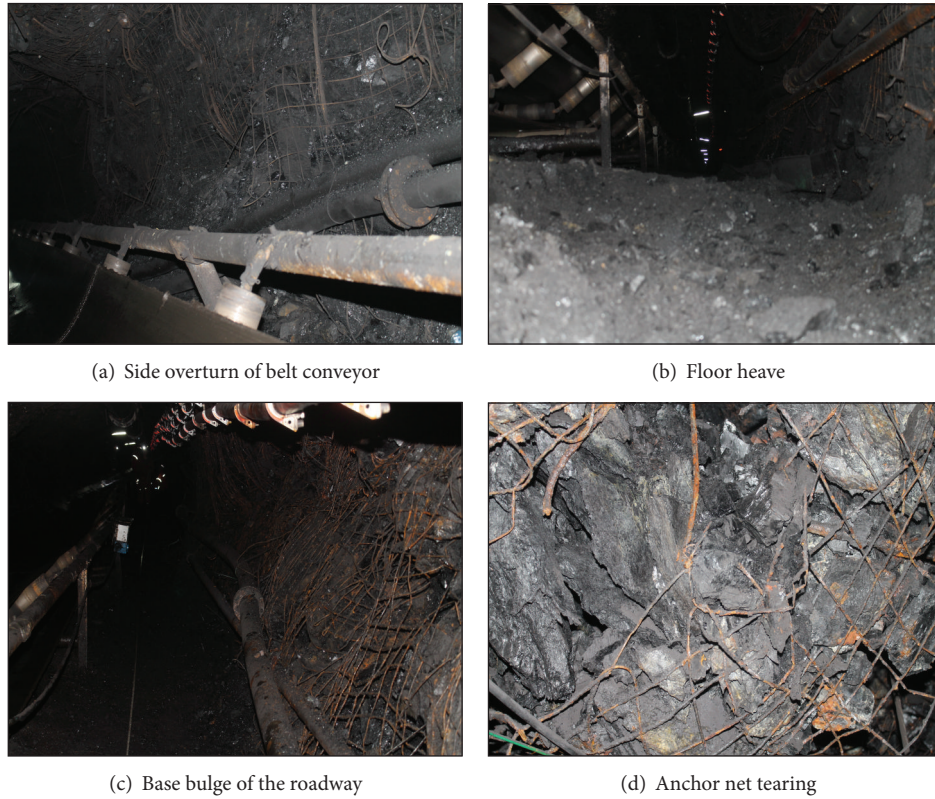


FIGURE 8: Description of destroying phenomena of the 9.18.

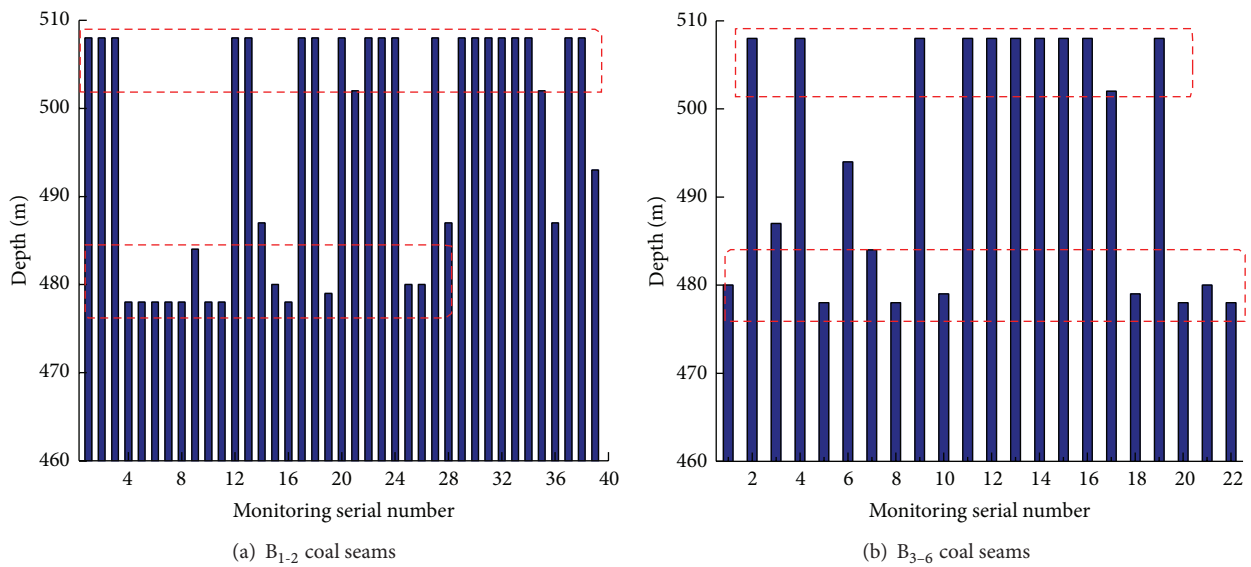


FIGURE 9: Distribution of mining seismicity (2013.9.8~9.22).

350 m. Deeper mining would result in high stress concentration so as to induce mining seismicity. In the unique geological and unwatered environment of the steep-heavy-thick coal, extraction of the coal seam in subhorizontal section would meet the multioverlying strata and the mined-out area which consists of a number of barrier pillars with high stress

concentrations at the depth of 350 m. The existence of these stressed pillars over the mining actives at deeper bed also becomes a contributing factor to the mining seismicity [18]. In general, the mining seismicity that happened in Urumchi coalfield is quite unique because it is rooted in a narrow mining space.

5.2. Coupling of Spatial-Temporal Strength Characteristics and Redisturbance. Indubitably, underground mining disturbance is a nonlinear dynamic evolution process related to the spatial-temporal-strength, and the stress concentration of the top-coal and rock masses is caused by the mobilization effect of the arch-pry and redisturbance from deep and complex structures in steeply dipping thick coal seams. Under the action of high stress concentration, the scale of the near field fractured zone sequentially migrates to the deeper roof of the roadway, which caused the aggregation of multiple fracture zones with a poor stability at the combination of the vertical wall and arch. It indicates that mining seismicity generation and occurrence are derived from multi-index coupling contribution patterns. Moreover, different depth and scope of fractured zones are formed in the far field stress released area during stress migration. Finally, spatial-temporal-strength evolution of the mining disturbed energy induces mining seismicity, coal-rock mass burst, and serious dynamic hazard.

5.3. Stress-Lever-Rotation-Effect (SLRE). According to the horizon of the coal seam thickness, the working face is arranged with a short length during the top-coal caving in horizontal section. However, no roof but top-coal and rock residues are reestablished above the working face during shallow mining. Instability of the arch of spanning strata (ASS) results in the top-coal sliding and structure instability.

After mining the deeper coal-seam and disturbing the rock pillar, the root segments of the steeply deeper rock pillar adjacent to both lower and upper working faces or headings were nonuniformly mobilized; then the effects of heterogeneity on equivalent modulus and failure were manifested by the upper additional dynamic load that stemmed from the upper broken strata. Accordingly, the stress-lever-rotation-effect (SLRE) of the fault-like mobilization would induce and even intensify dynamic hazard [19]. It is also applicable for the arch of spanning strata (ASS) in vertically inhomogeneous anisotropic rock masses.

5.4. Validity of Field Monitoring Index. On the basis of field experiences, it is observed that these advanced monitoring instruments to be preferably applied in and around SSTCC workings (coal, heading, and pillar) are less dependent upon the geomining conditions of the sites. Acoustic-wave and borehole imaging monitoring verifies the asymmetric characteristics of deformation and fracture distribution. The electromagnetic wave detection shows that broken strata will absorb large amounts of energy of electromagnetic wave. It would provide essential data to assess both dynamic hazard prevention and deep mining potential.

Above all, acoustic-seismic-wave index indicated the spatial-temporal-strength and mining disturbance and stress redistribution of the steep-heavy-thick coal and rock masses. The prediction and evaluation for mining seismicity are applicable and valid obviously. The shallow-focus earthquake (6.6 Ms) and aftershock happened on June 30, 2012. The advance heading of number 45 coal seam working face induced severe tremors and bolt-cables broken and a section of metal mesh located between 756.7 m and 762.0 m was split;

about 21 tons of coal was burst out. Fortunately it is none of mortalities. It is causal of previously applied methods of hydraulic fractured and preblasting, mining optimization, pillar reinforcement, and depressed stress along dipping angles. Operating practice shows that the environment, safety, and productions have been improved. The highest efficiency was 77 t/d, the average efficiency was 60.84 t/d, which was increased by 35.2%, the recovery rate was 85.21%, and the highest production was 6000 t/d. Gas concentration was below 0.1%, and dust concentration was reduced by 10.0% and hydrogen sulfide concentration was significantly reduced, all of which improve the environment better and reduce the labor intensity of workers.

6. Conclusions

(1) Mining seismicity is a typical dynamic hazard in high ground stress region of western China. Innovation of field monitoring is a crucial way to predict mining seismicity.

(2) The stress-lever-rotation-effect (SLRE) model of fault-like mobilization is preliminarily proposed. Based on the effect of the arch of spanning strata (ASS) and predisturbance, the crack distribution, and broken presented asymmetrical migration and localization, steeply deeper rock mass will induce stress concentration obviously when the fracture of the coal is larger. The stress-lever-effect of deeper rock pillar will induce dynamic hazard. It is also applicable for the vertically inhomogeneous anisotropic rock masses.

(3) The characteristics of acoustic-seismic-wave can indicate the spatial-temporal-strength, redisturbance, and stress redistribution of steeply deeper-heavy thick coal and rock masses. The prediction and evaluation for mining seismicity are applicable and valid.

Conflict of Interests

The authors declare that there is no conflict of interests regarding the publication of this paper.

Acknowledgments

Financial support for this work provided by 973 National Key Basic Research Development program (2015CB251600), 973 Preliminary National Key Basic Research Development program (2014CB260404), the Key National Natural Science Foundation of China (U13612030), Shaanxi Innovation Team Program (2013KCT-16), and the High Technology Development Program of Xinjiang Municipality (201432102) is gratefully acknowledged.

References

- [1] M. F. Cai, H. G. Ji, and J. A. Wang, "Study of the time-space-strength relation for mining seismicity at Laohutai coal mine and its prediction," *International Journal of Rock Mechanics and Mining Sciences*, vol. 42, no. 1, pp. 145–151, 2005.
- [2] X.-P. Lai, N.-B. Wang, H.-D. Xu, T. Qi, J.-T. Cao, and D.-H. Jiang, "Safety top-coal-caving of heavy and steep coal seams under

- complex environment,” *Journal of University of Science and Technology Beijing*, vol. 31, no. 3, pp. 277–280, 2009 (Chinese).
- [3] X.-P. Lai, F.-H. Ren, Y.-P. Wu, and M.-F. Cai, “Comprehensive assessment on dynamic roof instability under fractured rock mass conditions in the excavation disturbed zone,” *International Journal of Minerals, Metallurgy and Materials*, vol. 16, no. 1, pp. 12–18, 2009.
- [4] S.-J. Miao, X.-P. Lai, X.-G. Zhao, and F.-H. Ren, “Simulation experiment of AE-based localization damage and deformation characteristic on covering rock in mined-out area,” *International Journal of Minerals, Metallurgy and Materials*, vol. 16, no. 3, pp. 255–260, 2009.
- [5] X. Lai, P. Shan, J. Cao, H. Sun, Z. Suo, and F. Cui, “Hybrid assessment of pre-blasting weakening to horizontal section top coal caving (HSTCC) in steep and thick seams,” *International Journal of Mining Science and Technology*, vol. 24, no. 1, pp. 31–37, 2014.
- [6] J.-C. Wang, J.-L. Yang, H.-H. Liu, D.-P. Zhao, and L.-Y. Zheng, “The practical observation research on loose medium flow field theory on the top-coal caving,” *Journal of the China Coal Society*, vol. 35, no. 3, pp. 353–356, 2010 (Chinese).
- [7] H. Alehossein and B. A. Poulsen, “Stress analysis of longwall top coal caving,” *International Journal of Rock Mechanics and Mining Sciences*, vol. 47, no. 1, pp. 30–41, 2010.
- [8] S. Karekal, R. Das, L. Mosse, and P. W. Cleary, “Application of a mesh-free continuum method for simulation of rock caving processes,” *International Journal of Rock Mechanics and Mining Sciences*, vol. 48, no. 5, pp. 703–711, 2011.
- [9] Y.-S. Xie and Y.-S. Zhao, “Numerical simulation of the top coal caving process using the discrete element method,” *International Journal of Rock Mechanics and Mining Sciences*, vol. 46, no. 6, pp. 983–991, 2009.
- [10] F. Simsir and M. K. Ozfirat, “Determination of the most effective longwall equipment combination in longwall top coal caving (LTCC) method by simulation modelling,” *International Journal of Rock Mechanics and Mining Sciences*, vol. 45, no. 6, pp. 1015–1023, 2008.
- [11] C.-P. Lu and L.-M. Dou, “The relationship between vertical stress gradient, seismic, and electromagnetic emission signals at Sanhejian coal mine, China,” *International Journal of Rock Mechanics and Mining Sciences*, vol. 70, pp. 90–100, 2014.
- [12] P.-W. Shi and Y.-Z. Zhang, “Structural analysis of arch of spanning strata of top coal caving in steep seam,” *Chinese Journal of Rock Mechanics and Engineering*, vol. 25, no. 1, pp. 79–82, 2006.
- [13] L. Xingping, W. Yongping, C. Jiantao et al., *The Foundamental Research on Mechanics and Engineering of Safe and High Efficiency Mining for the Steeply Deeper Heavy-Thick Coal Seams*, Shan-xi Science Press, Xi’an, China, 2013.
- [14] X.-P. Lai, Y.-P. Wu, J.-T. Cao, Y.-N. Fan, Y.-L. Zhang, and F. Cui, “Experiment on rock-mass deformation of large scale 3D-simulation in complex environment,” *Journal of the China Coal Society*, vol. 35, no. 1, pp. 31–36, 2010 (Chinese).
- [15] C.-P. Lu, L.-M. Dou, N. Zhang et al., “Microseismic frequency-spectrum evolutionary rule of rockburst triggered by roof fall,” *International Journal of Rock Mechanics and Mining Sciences*, vol. 64, pp. 6–16, 2013.
- [16] C. P. Lu, L. M. Dou, H. Liu, H. S. Liu, B. Liu, and B. B. Du, “Case study on microseismic effect of coal and gas outburst process,” *International Journal of Rock Mechanics and Mining Sciences*, vol. 53, pp. 101–110, 2012.
- [17] C.-P. Lu, L.-M. Dou, X.-R. Wu, and Y.-S. Xie, “Case study of blast-induced shock wave propagation in coal and rock,” *International Journal of Rock Mechanics and Mining Sciences*, vol. 47, no. 6, pp. 1046–1054, 2010.
- [18] C. Feng, *Fundamental research on the coupled- fracture and application for coal-rock under complex environment [Ph.D. dissertation]*, Xi’an University of Science and Technology, 2014.
- [19] J. Cao, *Prediction and control research on mining seismicity occurrences under complex coal-rock masses [Ph.D. dissertation]*, Xi’an University of Science and Technology, 2014.

Research Article

An Experiment Monitoring Signals of Coal Bed Simulation under Forced Vibration Conditions

Chengwu Li,¹ Po Hu,¹ Tianbao Gao,² Yingfeng Sun,¹ Shengyang Shao,¹ and Qifei Wang¹

¹ Faculty of Resources & Safety Engineering, China University of Mining & Technology, Beijing, D11 Xuyuan Road, Haidian District, Beijing 100083, China

² School of Energy and Safety Engineering, Tianjin Chengjian University, Tianjin 300384, China

Correspondence should be addressed to Po Hu; ngd322hupo@gmail.com

Received 7 July 2014; Accepted 29 September 2014

Academic Editor: Caiping Lu

Copyright © 2015 Chengwu Li et al. This is an open access article distributed under the Creative Commons Attribution License, which permits unrestricted use, distribution, and reproduction in any medium, provided the original work is properly cited.

An experiment simulating coal seam under forced vibration conditions was conducted. Acceleration response and microseism signal during the experiment were collected and analyzed. It is found that, with an increasing amount of vibration, the natural frequency of the specimen decreases, and this phenomenon reflects fractures appearing in the specimen. Acceleration response signals show that peaks in shock excitation frequency and shock excitation acceleration affect the acceleration response, which reflects damage to the specimen. When shock excitation frequency nears natural frequency, the acceleration response first decreases and then increases. When resonance occurs, it reaches its maximum value. As shock excitation acceleration peaks increase, the acceleration response peak of the specimen also increases. We conclude that destruction is mainly concentrated in the coal seam evidenced by specimen destruction situation. Then shock excitation frequency and shock excitation acceleration influence on microseism signals were analyzed by Hilbert-Huang transform. By receiving these signals and analyzing their characteristics, it is beneficial to develop new methods to predict disasters underground dynamically in the future.

1. Introduction

An unexpected and violent simultaneous ejection of a large mass of gas and coal from an underground working face during mining is identified as “instantaneous coal outburst” [1, 2]. This, understandably, is a massive hazard for coal mining workers. To learn and predict outburst accidents, the factors contributing to outburst have been widely studied for decades. A wealth of hypotheses, such as the dynamic model [1, 3–5], the pocket model, spherical shell destabilization model [6], and gas phase transformation model [7], have been proposed to explain this phenomena. No single theory, however, can fully explain all the characteristics of outburst, because the phenomenon is so complex. Among these previously reported models, the effects of vibration and its potential to trigger an outburst have not been thoroughly explored. In the mining process, many different activities produce vibration. As previously reported by Zhou and He, 8362 of 8669 outbursts (96.5%) were related to human

activities such as drilling, blast mining, or coal dropping [8]. These activities cause vibration that alter the mechanical properties of coal and reduce coal strength [7, 9]. To this effect, this paper posits that vibration is a critical factor contributing to instantaneous outburst. Study of vibration characteristics and signals is crucial to a better understanding of outburst phenomena, and, ultimately, the reduction of outburst-related disasters.

Blasting is one process liable to cause outbursts. Millisecond delay blasting, a type of sectional blasting, is the primary method of roadway development in Chinese outburst mines. Every blast produces vibration, each of which forms a P wave (particle vibration direction is similar to wave propagation) as it moves through space, potentially quite far. In many coal mines, roadways exist horizontally in the coal bed, making the direction of vibration produced by blasting likewise horizontal. Earthquakes also cause horizontal coal bed vibration. In this experiment, the horizontal vibration of the specimen was produced by a vibration table.

TABLE 1: The vibration table characters.

Size	Maximum payload	Maximum overturn moment	Maximum eccentric torque	Maximum displacement	Frequency range	Acceleration at maximum load	Maximum speed
3 m × 3 m	10000 kg	300 KN·m	100 KN·m	±100 mm	0.2 Hz~50 Hz	1.2 g	1.0 m/s

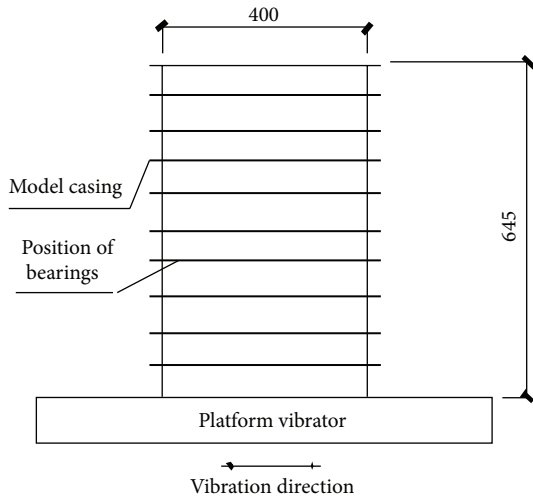


FIGURE 1: Sketch map of forced vibration specimen.



FIGURE 4: Steel frame of model box.

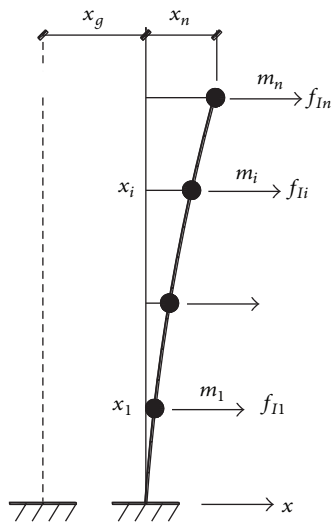


FIGURE 2: Deformation and force of multiple-degree-of-freedom forced vibration system.



FIGURE 5: Model specimen after completion.

TABLE 2: Material and mixing ratio.

	Cement	Lime	Coal powder	Medium sand	Gravel	Water
Coal floor	1	—	—	1.65	2.8	0.55
Coal bed	1	4	20	—	—	6
Coal roof	1	—	—	6.9	—	1.6



FIGURE 3: Vibrating table.

“In coal and rock failure processes, a variety of energies such as elastic energy, expansion energy of compressed gas, thermal energy, sound energy, and electromagnetic energy will be dissipated” [10]. By monitoring the system to receive these energy signals and analyze their characteristics, it is possible to methodically characterize, and therefore predict, natural disasters [11–16]. A simulation experiment of coal failure under forced vibration conditions was conducted in this paper. The acceleration response and microvibration signals during the experiment were collected and analyzed. To investigate the characteristics of these signals under forced

TABLE 3: Technical data of the acceleration sensor.

Main technical parameters			
Model	YD-32T	Linear	≤1%
Sensitivity V/ms ²	0.1	Transverse sensitivity	≤5%
Frequency range (Hz) (+10%)	10~6000	Output amplitude	±5 VP
Install resonance point (Hz)	23 K	Output offset voltage	8~12 VDC
Range m/s ² (+10%)	20	Supply current	2~20 mA
Resolution (m/s ²)	0.0002	Excitation voltage	9 V
Weight (g)	40	Output impedance	≤150 Ω
Geometry (mm)	Six party 18 × 18 × 23	Shell insulation resistance	>108 Ω
Output mode	Top output	Discharge time constant	≥0.2 s
Mounting screw	M5	Year stability	3%
Operating temperature range	-40°C~+80°C		

TABLE 4: Technical data of microseism sensor.

Index/model	Unit	SF1500S/SF1500SN
Linear output range	g peak value	±3
Sensitivity (differential)	V/g	1.2 (2.4)
Frequency response	Hz	DC to 1500
Frequency response (differential signal)	Hz	DC to 5000
Dynamic range (100 Hz BW)	dB	120
Noise (10 to 1000 Hz)	ngrms/ $\sqrt{\text{Hz}}$	300 to 500
Transverse impedance	dB	>40
Impact of restrictions	g peak value	1500
Vibration (20 Hz–2000 Hz)	g peak value	60
Operating temperature	°C	40 to +125
Temperature sensitivity coefficient	ppm/°C	75
Drift thermal coefficient	$\mu\text{g}/^\circ\text{C}$	±100
Linearity error	% full scale	±0.1
Input voltage	Volts DC	±6 to ±15
Static current	mA	11.6

vibration conditions as compared to site conditions is a beneficial resource for the formation of an effective method to predict and prevent outbursts.

2. Experimental Method

2.1. Basic Approach. While a variety of vibration forms exist in an underground coalface, a specific form of vibration was selected to conduct this experiment. Figure 1 shows the sketch map of forced vibration specimen. This design imitates the deformation and force of a multiple-degree-of-freedom forced vibration system, detailed in Figure 2. It can reflect the influence of vibration caused by seismic activity to natural



FIGURE 6: Acceleration transducer.

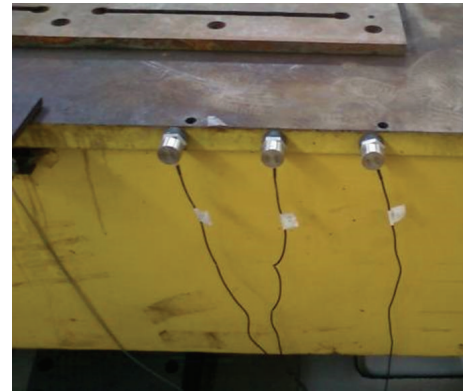


FIGURE 7: Calibration of acceleration transducer.

strata and coal beds. Other forms of vibrational influence will be explored in future research.

Different strata were simulated by a 10-layer steel frame located at different heights on a vibration table. The vibration table provided exciting force (with differing maximum acceleration peak and frequency sine wave load) in the horizontal

TABLE 5: Setting of experimental parameters.

Working condition	Frequency (hz)	Input acceleration	Vibration duration (s)	Vibration cycles	Working condition	Frequency (hz)	Input acceleration	Vibration duration (s)	Vibration cycles
1	White noise	0.02 g	15.0	—	43	30	0.5 g	8.0	240
2	1	0.02 g	30.0	30	44	White noise	0.02 g	15.0	—
3	5	0.02 g	6.0	30	45	32	0.5 g	7.5	240
4	10	0.02 g	6.0	60	46	White noise	0.02 g	15.0	—
5	15	0.02 g	4.0	60	47	34	0.5 g	7.1	240
6	20	0.02 g	3.0	60	48	White noise	0.02 g	15.0	—
7	24	0.02 g	5.0	120	49	24	0.75 g	10.0	240
8	White noise	0.02 g	15.0	—	50	White noise	0.02 g	15.0	—
9	1	0.1 g	30.0	30	51	27	0.75 g	8.9	240
10	White noise	0.02 g	15.0	—	52	White noise	0.02 g	15.0	—
11	5	0.1 g	6.0	30	53	30	0.75 g	8.0	240
12	White noise	0.02 g	15.0	—	54	White noise	0.02 g	15.0	—
13	10	0.1 g	12.0	120	55	32	0.75 g	7.5	240
14	White noise	0.02 g	15.0	—	56	White noise	0.02 g	15.0	—
15	15	0.1 g	8.0	120	57	34	0.75 g	7.1	240
16	White noise	0.02 g	15.0	—	58	White noise	0.02 g	15.0	—
17	20	0.1 g	6.0	120	59	28	1.5 g	8.6	240
18	White noise	0.02 g	15.0	—	60	White noise	0.02 g	15.0	—
19	24	0.1 g	5.0	120	61	29	1.5 g	8.3	240
20	White noise	0.02 g	15.0	—	62	White noise	0.02 g	15.0	—
21	27	0.1 g	4.4	120	63	30	1.5 g	8.0	240
22	White noise	0.02 g	15.0	—	64	White noise	0.02 g	15.0	—
23	30	0.1 g	4.0	120	65	31	1.5 g	7.7	240
24	White noise	0.02 g	15.0	—	66	White noise	0.02 g	15.0	—
25	32	0.1 g	3.8	120	67	32	1.5 g	7.5	240
26	White noise	0.02 g	15.0	—	68	White noise	0.02 g	15.0	—
27	34	0.1 g	3.5	120	69	33	1.5 g	7.3	240
28	White noise	0.02 g	15.0	—	70	White noise	0.02 g	15.0	—
29	2	0.5 g	15.0	30	71	34	1.5 g	7.1	240
30	White noise	0.02 g	15.0	—	72	White noise	0.02 g	15.0	—
31	5	0.5 g	6.0	30	73	36	1.5 g	6.7	240
32	White noise	0.02 g	15.0	—	74	White noise	0.02 g	15.0	—
33	10	0.5 g	12.0	120	75	35	1.5 g	57.1	2000
34	White noise	0.02 g	15.0	—	76	White noise	0.02 g	15.0	—
35	15	0.5 g	8.0	120	77	20	1.5 g	24.0	480
36	White noise	0.02 g	15.0	—	78	White noise	0.02 g	15.0	—
37	20	0.5 g	6.0	120	79	15	1.2 g	16.0	240
38	White noise	0.02 g	15.0	—	80	White noise	0.02 g	15.0	—
39	24	0.5 g	10.0	240	81	10	1.5 g	24.0	240
40	White noise	0.02 g	15.0	—	82	White noise	0.02 g	15.0	—
41	27	0.5 g	8.9	240	83	5	2.4 g	24.0	120
42	White noise	0.02 g	15.0	—					

TABLE 6: Natural vibration frequency of the specimen.

Work condition	Natural frequency (hz)						
1	49.76	26	42.48	46	42.39	66	37.67
8	49.72	28	42.48	48	42.37	68	39.16
10	49.73	30	42.39	50	42.49	70	39.19
12	49.71	32	42.38	52	42.37	72	39.19
14	49.76	34	42.48	54	42.37	74	39.18
16	44.50	36	42.35	56	42.37	76	39.20
18	44.80	38	42.47	58	42.47	78	26.85
20	44.80	40	42.46	60	39.17	80	28.80
22	44.50	42	42.49	62	37.68	82	28.95
24	42.48	44	42.37	64	39.18		

TABLE 7: Extreme and enhanced coefficient of acceleration response (0.02 g).

Shock excitation frequency (Hz)	$a0(g)$	$a1(g)$	$a2(g)$	$a3(g)$	$\mu1$	$\mu2$	$\mu3$
1	0.0191	0.00272	0.00274	0.00526	1.73	1.75	3.30
5	0.02435	0.00472	0.00508	0.00727	1.96	2.17	3.11
10	0.0177	0.00340	0.00376	0.00664	1.52	1.74	3.08
15	0.0179	0.00338	0.00377	0.00756	1.39	1.57	3.15
20	0.01757	0.00407	0.00443	0.00803	1.58	1.71	3.11
24	0.0193	0.00403	0.00418	0.00766	1.46	1.52	2.78



FIGURE 8: Speed sensor.

direction. The rolling bearing ensures steel frame motion repetition in one direction. Figures 4 and 5 show this design.

2.2. Experimental Set-Up

2.2.1. Vibration Table. The one-dimensional horizontal vibration table was provided by Heibei University of Engineering. It is shown in Figure 3. The acquisition system used was a 32-channel data acquisition system. The characters of the vibration table are shown in Table 1.



FIGURE 9: Microseism sensor.

2.2.2. Model Box. The model box was a 10-layer independent square steel framework stacking ensemble. Each layer of framework consisted of welded, four-groove steel. The groove steel section size was 60 mm × 30 mm × 3 mm (length × width × thickness, referred as L × W × H below). The overall internal size of the model box was 400 mm × 400 mm × 650 mm (L × W × H). Four rolling bearings were set up to form free rolling points to reduce friction and deflection between the two square steel frameworks. Clearance between the two layers was 6 mm. Among these 10 layers of independent square steel framework, 3 frameworks were selected for opening 3 square holes (45 mm × 45 mm) on the frame wall of every framework for installing sensors. In order to effectively lift the specimen after molding, steel bars (diameter 6 mm, spacing 100 mm) and hooks were welded on the bottom of the model box. According to this model box design, in-plane

TABLE 8: Extreme and enhancement coefficient of acceleration response (0.1 g).

Shock excitation frequency (Hz)	$a_0(g)$	$a_1(g)$	$a_2(g)$	$a_3(g)$	μ_1	μ_2	μ_3
1	0.0778	0.0107	0.01	0.027	1.65	1.54	4.16
5	0.107	0.0187	0.0193	0.04	1.77	1.88	3.89
10	0.11	0.022	0.0267	0.0503	1.58	1.99	3.75
15	0.13	0.0247	0.0287	0.0513	1.40	1.65	2.95
20	0.147	0.0247	0.0303	0.0603	1.18	1.44	2.87
24	0.104	0.02	0.0177	0.0403	1.35	1.19	2.71
27	0.0953	0.019	0.0193	0.0407	1.40	1.42	2.99
30	0.076	0.0173	0.0187	0.038	1.59	1.72	3.50
32	0.089	0.0197	0.0213	0.042	1.55	1.68	3.30
34	0.0854	0.0193	0.021	0.0423	1.58	1.72	3.47

lateral and torsion deformation is constrained, so only shear deformation along the vibration direction is present.

2.2.3. Specimen. For the purpose of this experiment, the specimen was divided into three parts: the coal roof, coal bed, and coal floor. These three parts consisted of a concrete mixture. Table 2 shows the material and mixing ratios.

500 mm of the mixture was poured in the coal roof, 80 mm in the coal bed, and 70 mm in the coal floor to simulate stress from overlying strata. The coal floor was cast by concrete and medium sand placement. The coal roof was cast layer-by-layer, where the thickness of each layer was 10~15 mm. Talc powder was added between every layer to create strata interface. The particle size of coal powder in the coal bed was 0–0.4 mm in diameter. A 100 mm long roadway (with a net sectional area of 60 mm × 60 mm) was established in the coal bed. Before the molding process, four rollers were installed along the direction of vibration between every two steel frames to reduce friction. Because the quality of the steel frame is much lower than the model, the steel frame was retained after molding. In the experiment, therefore, the shear deformation in the frame was limited and the specimen stiffness increased. This caused a vibration frequency greater than the actual, natural value in the measured model.

2.2.4. Sensors. Acceleration, speed and microseism sensor are used in this experiment. Figures 10 and 11 shows these sensors' distribution.

(1) Acceleration Sensor. A YD series voltage output piezoelectric acceleration sensor was used in this experiment which is shown in Figures 6 and 7. It is composed of a piezoelectric accelerometer and special imported ICP chip, which integrates a traditional piezoelectric acceleration sensor and amplifier and uses the same cable for power supply and output signals. Specific parameters of the YD series voltage output piezoelectric acceleration sensor are shown in Table 3.

Three YD-32T acceleration sensors were used in this experiment. These sensors were, respectively, arranged on the 3 different points (the bottom, middle, and top of the specimen) on the specimen's side. 1#, 2#, and 3# acceleration sensors correspond to the bottom of the model specimen,

the middle, and the top, respectively. Acceleration sensors are attached to the steel frame by magnet.

(2) Speed Sensor. A speed sensor measured the velocity response and then calculated the natural vibration frequency of the specimen. An 89.1-2 type speed sensor with high sensitivity was provided by Institute of Engineering Mechanics, China Earthquake Administration. The speed sensor which is shown in Figure 8 was fixed to the specimen's top center using Vaseline.

(3) Microseism Sensor. Eight SF1500MEMS capacitive acceleration microseism sensors (which is shown in Figure 9), produced by COLIBRYS Company, were attached to the specimen's surface using modified acrylate adhesive. The main components of the SF1500MEMS microseismic sensor are a silicon element by three-dimensional processing, low power DSP, microcontroller, and temperature sensor. Technical data of this kind microseism sensor is shown in Table 4.

2.2.5. Data Acquisition System

(1) Dynamic Acquisition Instrument. An amplifier and INV-306DF signal collecting tester were connected to the acceleration and speed sensors. DASP testing software was employed in the experiment to process signal data. There are 16 channels in the signal collecting tester. AD accuracy was 16, the maximum sampling frequency was 400 kHz, and magnification was 1–16 times.

(2) Coal and Rock Dynamic Disaster Experiment Simulation System of ZDKT-1 (ZDKT-1 System). Microseismic sensors were connected to the ZDKT-1 system [17, 18]. It has 12 microseismic channels. The maximum sampling frequency of this system is 51 kHz. In this experiment, the sampling frequency was set to 17067 Hz.

3. Determination of Specimen Nature Vibration Frequency

The specimen's natural vibration frequency is affected by material, density, size, and shape factors, reflecting the natural

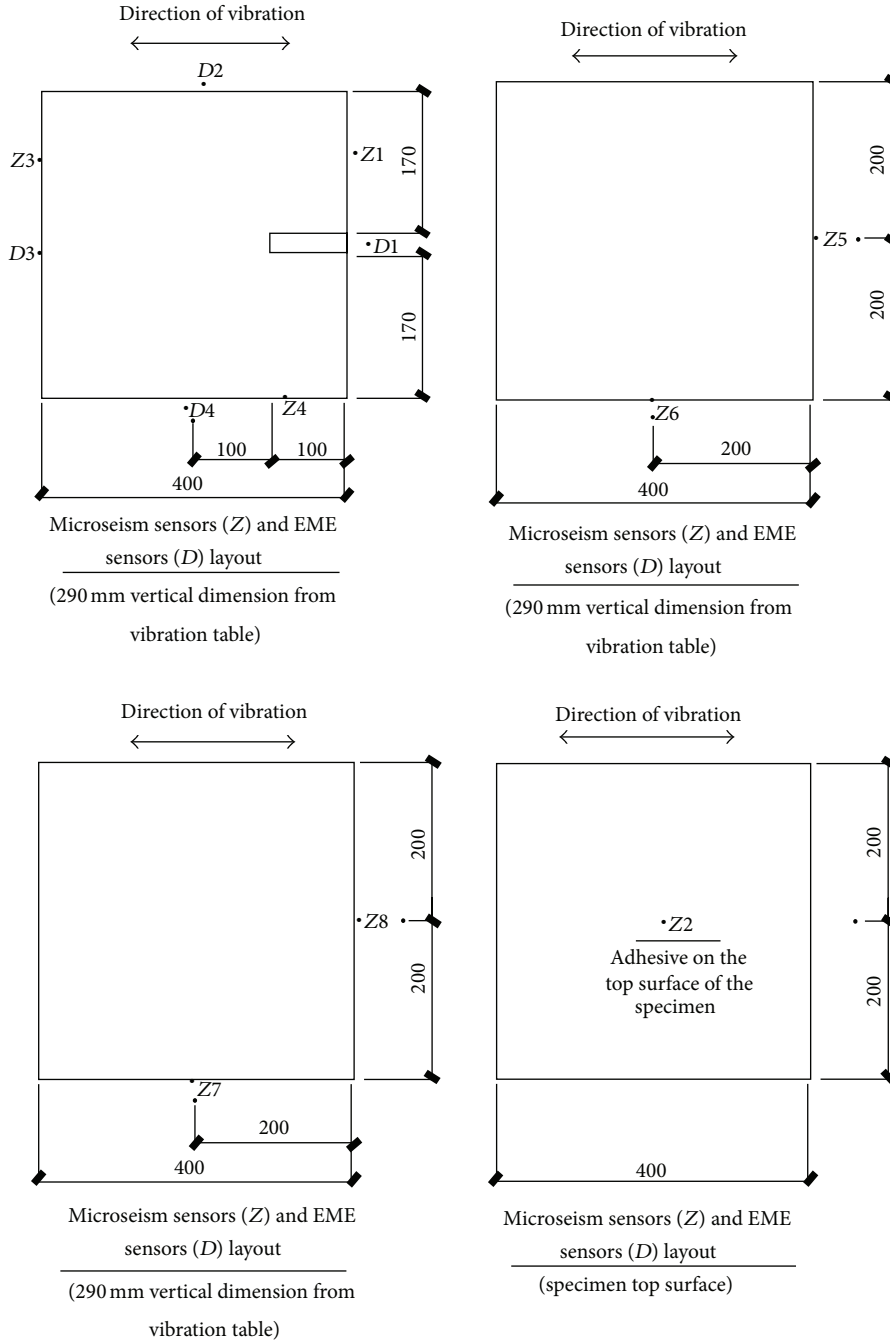


FIGURE 10: Microseism sensor and EME sensors (electromagnetic emission sensors are used for measuring EME signals which are not discussed in this paper) distribution.

dynamic characteristics of specimens. By taping the model specimens to the top, transverse free vibration was produced. The speed sensor fixed on top of the specimen collected vibration signals and then amplified and filtered them. Finally, the spectrum curve was obtained using the vibration signals by fast Fourier transform (FFT). In this experiment, data acquisition frequency was 1300 Hz. The results of the two experiments are as shown in Figure 12. The natural vibration frequency of the specimen was 49.7 Hz.

4. Experimental Process

White noise is known as a random signal with a constant power spectral density [19]. In this experiment, a horizontal one-way input shock excitation wave was produced by the synthesis of white noise and a sinusoidal wave (with differing peak acceleration and frequency). The white noise and sinusoidal wave were inputted alternately. White noise scanning acceleration was set to 0.02 g, 0.02 g, 0.1 g, 0.5 g,

TABLE 9: Extreme and enhanced coefficient of acceleration response (0.5 g).

Shock excitation frequency (Hz)	$a_0(g)$	$a_1(g)$	$a_2(g)$	$a_3(g)$	μ_1	μ_2	μ_3
2	0.546	0.056	0.05533	0.0787	1.24	1.24	1.73
5	0.5	0.0543	0.0527	0.0717	1.10	1.10	1.49
10	0.505	0.0697	0.057	0.1037	1.09	0.93	1.68
15	0.5196	0.08	0.093	0.1233	1.13	1.34	1.77
20	0.4272	0.122	0.1747	0.2357	1.94	2.78	3.75
24	0.511	0.0977	0.1083	0.1393	1.34	1.48	1.91
27	0.4959	0.107	0.0767	0.0937	1.51	1.08	1.32
30	0.501	0.0883	0.069	0.1007	1.23	0.96	1.41
32	0.5088	0.089	0.0523	0.0967	1.22	0.72	1.33
34	0.524	0.0963	0.0477	0.092	1.29	0.64	1.23

TABLE 10: Extreme and enhanced coefficient of acceleration response (0.75 g).

Shock excitation frequency (Hz)	$a_0(g)$	$a_1(g)$	$a_2(g)$	$a_3(g)$	μ_1	μ_2	μ_3
24	0.7719	0.133	0.1893	0.1687	1.21	1.72	1.53
27	0.8053	0.169	0.1153	0.1747	1.47	1.00	1.52
30	0.81	0.1673	0.0767	0.145	1.45	0.66	1.25
32	0.7636	0.1247	0.057	0.11	1.14	0.52	1.01
34	0.7904	0.1253	0.048	0.11	1.11	0.43	0.97



FIGURE 11: Arrangement of each sensor.

0.75 g, and 1.5 g peak acceleration, respectively. Experiments were carried out in 5 stages according to the different acceleration peaks. At each stage, the sine wave frequency of the shock excitation wave changed. Table 5 further details the experimental parameters.

These 83 working conditions were performed continuously. The specimen rupture process was such as (1) initial crack opening expansion, (2) derivative crack propagation, (3) crack coalescence, and (4) specimen destruction.

5. Result and Discussion

5.1. Specimen Nature Vibration Frequency. The natural vibration frequency of the specimen, which changes during the vibration period, reflects its natural dynamic characteristics.

The random vibration method, which scans white noise, was used in this experiment to measure the specimen's natural vibration frequency. White noise scanning acceleration was set to 0.02 g. The corresponding white noise frequency components were measured to be the same as natural vibration frequency and amplify in tandem. To obtain spectra, we collected signals in the speed sensor and processed these signals by fast Fourier transform (FFT). These spectra reveal the natural vibration frequency in detail.

Here working condition 1 is selected to measured (other working condition have similar process). The white noise signals set in vibration are shown in Figure 13. The result after FFT processing are shown in Figure 14. From this result, it can be known that the specimen's natural vibration frequency was 49.76 Hz, consistent with the result mentioned in Section 3. Table 6 shows the natural vibration frequency of the specimen in all conditions.

The specimen's natural frequency decreases alongside an increase in the amount of vibration. When the coal specimen begins to display obvious failure characteristics, the natural vibration frequency decreases rapidly. It can be seen from Figure 15. As shown in the single-degree-of-freedom forced vibration equation without damping, $f = (1/2\pi)\sqrt{k/m}$, natural vibration frequency is mainly related to mass and stiffness. In this experiment, the specimen quality was kept constant. As the amount of vibration increased, cracks began to appear in the coal specimen and gradually intensify. This decreased the specimen's lateral stiffness, reducing the natural vibration frequency.

5.2. Acceleration Response. A total of five acceleration levels, 0.02 g, 0.1 g, 0.5 g, 0.75 g, and 1.5 g, were put into the vibration table, respectively (see Table 5). Four groups of acceleration

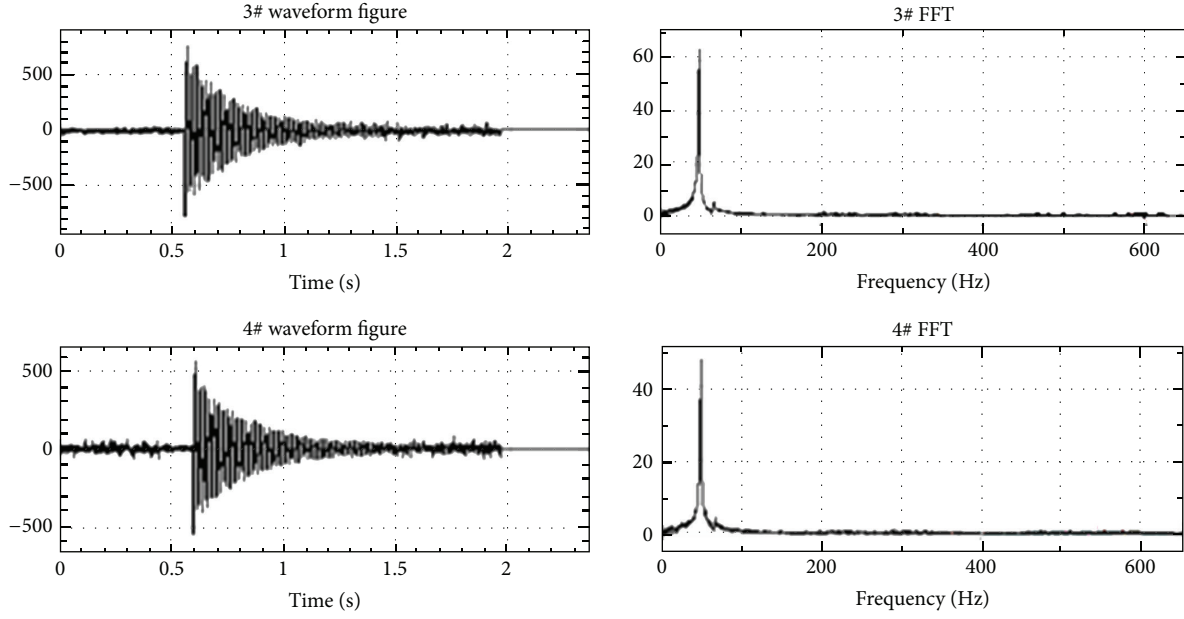


FIGURE 12: Free vibration curve and spectrogram.

TABLE 11: Extreme and enhanced coefficient of acceleration response (1.5 g).

Shock excitation frequency (Hz)	$a_0(\text{g})$	$a_1(\text{g})$	$a_2(\text{g})$	$a_3(\text{g})$	μ_1	μ_2	μ_3
28	1.585	0.3183	0.349	1.1753	1.41	1.54	5.19
29	1.5107	0.3103	0.2153	0.8097	1.44	1.00	3.75
30	1.4597	0.3043	0.1837	0.5517	1.46	0.88	2.65
31	1.471	0.2703	0.1393	0.3253	1.29	0.66	1.55
32	1.432	0.2513	0.1627	0.395	1.23	0.80	1.93
33	1.4934	0.292	0.1523	0.4393	1.37	0.71	2.06
34	1.4743	0.29	0.2407	0.623	1.38	1.14	2.96
36	1.5159	0.2917	0.2283	0.5117	1.35	1.05	2.36
35	1.5157	0.311	0.2237	0.5077	1.44	1.03	2.34
20	1.5256	0.2873	0.3037	0.8097	1.32	1.39	3.72
15	1.2108	0.2117	0.2387	0.6663	1.22	1.38	3.85
10	1.6187	0.214	0.483	0.7983	0.93	2.09	3.45

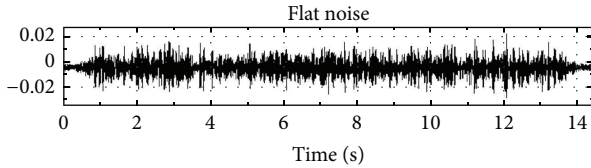


FIGURE 13: White noise signal of vibration table setting.

TABLE 12: Peak value of acceleration response.

Working condition	$a_0(\text{g})$	$a_1(\text{g})$	$a_2(\text{g})$	$a_3(\text{g})$
7	0.0193	0.0677	0.056	0.1797
19	0.104	0.14	0.1239	0.2821
39	0.511	0.6839	0.7581	0.9751
49	0.7719	0.931	1.3251	1.1809

data were collected for every working condition. Sampling frequency was set to 512 Hz. The 0# acceleration sensor indicated the actual acceleration on the vibration table surface. The 1#–3# sensors indicated the specimen's bottom, middle, and top acceleration, respectively.

5.2.1. Shock Excitation Frequency Influence on Acceleration Response. Because measured acceleration on the vibration

table was not completely consistent with input acceleration, a different value for altered shock excitation frequency was observed. To acquire shock excitation frequency influence on acceleration response, acceleration response enhancement coefficient μ is defined. Peak acceleration on the vibration table was set to a_0 (0# sensor measurement), and a_1 , a_2 , and a_3 were the peak acceleration from the bottom to top, respectively (1#–3# sensor measurements); then, $\mu_1 = a_1/a_0$,

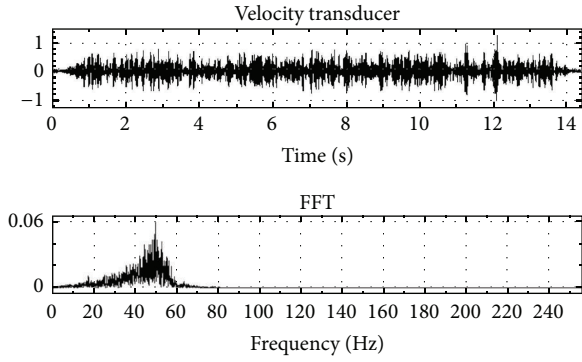


FIGURE 14: Time domain waveform and spectrogram of velocity response signal in working condition 1.

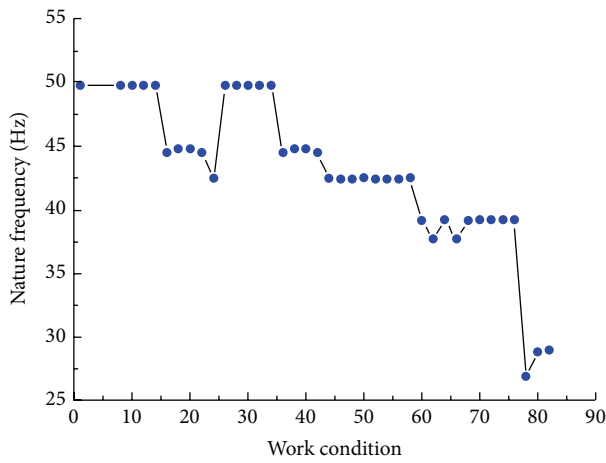


FIGURE 15: Natural vibration frequency change trend curve.

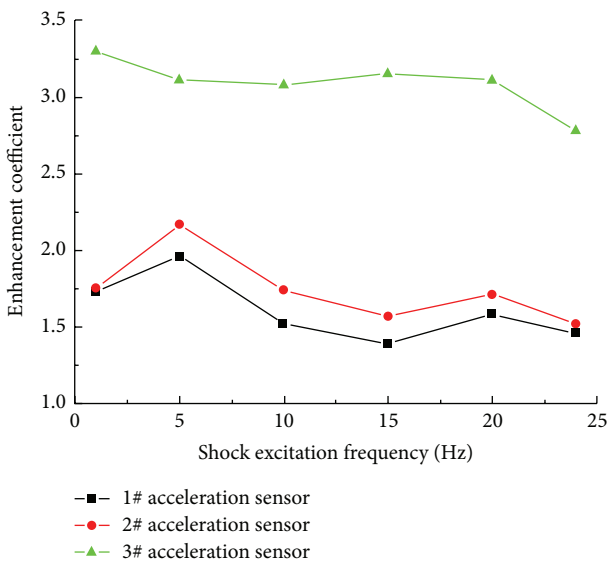


FIGURE 16: Enhancement coefficient curve of the acceleration response (0.02 g).

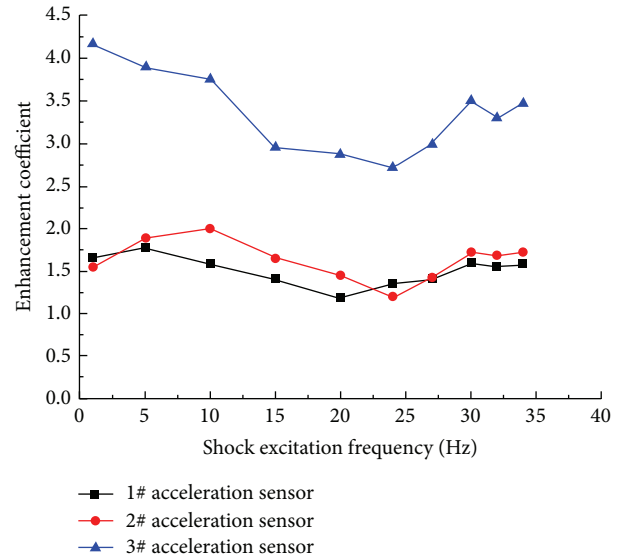


FIGURE 17: Enhancement coefficient curve of the acceleration response (0.1 g).

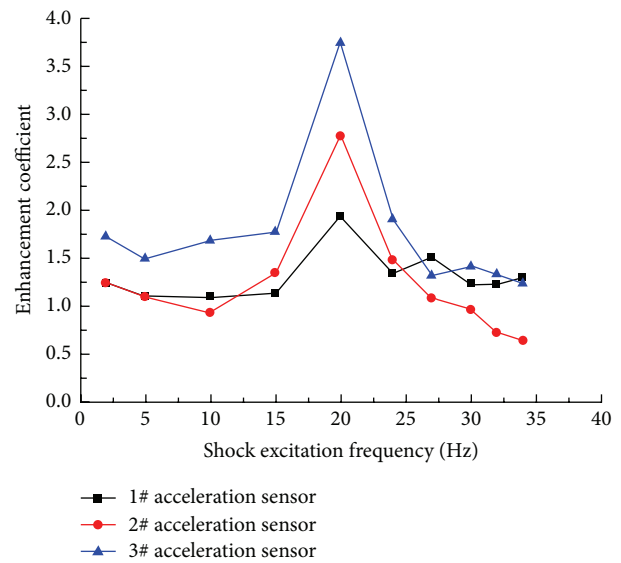


FIGURE 18: Enhancement coefficient curve of the acceleration response (0.5 g).

$\mu_2 = a_2/a_0$, and $\mu_3 = a_3/a_0$. By comparing different acceleration response enhancement coefficients under a variety of shock excitation frequency conditions, it is possible to obtain the change law at work. Peak acceleration was measured, and acceleration response enhancement coefficient μ was calculated under different shock excitation frequencies. The results are shown in Tables 7, 8, 9, 10, and 11.

(1) Result at Input 0.02 g Peak Acceleration of Vibration. Figure 16 shows that the enhancement coefficient had no obvious change as shock excitation vibration frequency increased. In this set of experiments, the shock excitation

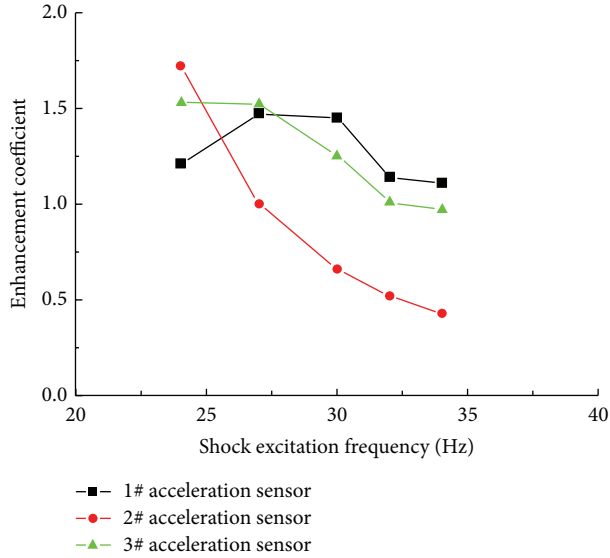


FIGURE 19: Enhancement coefficient curve of the acceleration response (0.75 g).

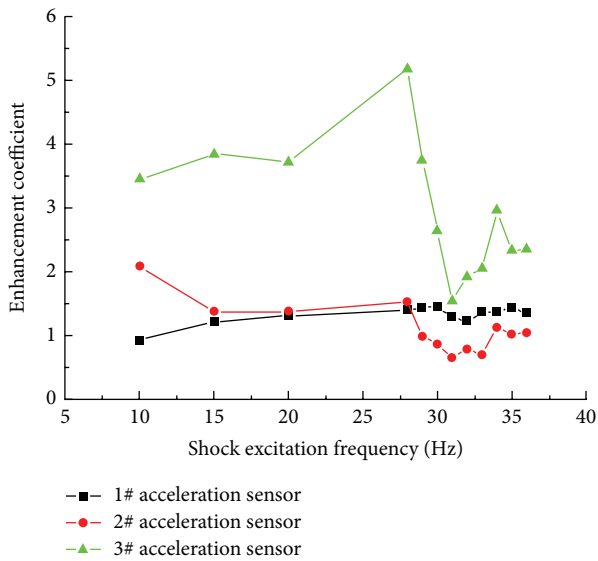


FIGURE 20: Enhancement coefficient curve of the acceleration response (1.5 g).

frequency was far lower than the natural frequencies of the specimen, preventing resonance phenomenon. Due to the small input acceleration to the vibration table combined with the data collected by microvibration sensor (no effective microvibration signal,) we deduced that the specimen was still in the elastic deformation stage, where no obvious damage occurred. Additionally, the enhancement coefficient increased from bottom to top.

(2) *Result at Input 0.1g Peak Acceleration of Vibration.* As shown in Figure 17, the enhancement coefficient declined

TABLE 13: IMF component percentage of energy of original micro-seism signals by EEMD in working condition 29.

IMF component	Energy percentage (%)
IMF_h1	51.1
IMF_h2	19.3
IMF_h3	12.4
IMF_h4	12.4
IMF_h5	3
IMF_h6	0.795
IMF_h7	0.324
IMF_h8	0.639
IMF_h9	0.273
IMF_h10	11.6
IMF_h11	0.0243
IMF_h12	0.02
IMF_h13	0.0191
IMF_h14	0.00991
IMF_h15	0.00378
IMF_h16	4.71E - 05
IMF_h17	1.03E - 05

TABLE 14: IMF component energy percentages of effective micro-seism signals by EEMD in working condition 29.

IMF component	Energy percentage (%)
IMF_h1	66.8
IMF_h2	15.6
IMF_h3	14.2
IMF_h4	2.88
IMF_h5	0.222
IMF_h6	0.115
IMF_h7	0.0434
IMF_h8	0.0249
IMF_h9	0.0356
IMF_h10	0.0218
IMF_h11	0.0113
IMF_h12	0.00279
IMF_h13	0.000226
IMF_h14	0.000126
IMF_h15	0.00023
IMF_h16	0.000115
IMF_h17	0.000104

when shock excitation frequency was less than 24 Hz and then rose when shock excitation frequency was greater than 24 Hz under 0.1 g acceleration input to the vibration table. In these stages, microfractures and a web of micropores began to appear, increasing the damping ratio and causing the enhancement coefficient to decline. When shock excitation frequency was greater than 24 Hz, it grew near to the specimen's natural vibration frequency (44.5 Hz). Though the



FIGURE 21: Destruction of the specimen side figure.

TABLE 15: IMF component energy percentage for selected effective microseism signals by EEMD.

IMF components	Working condition 29 (%)	Working condition 35 (%)	Working condition 37 (%)	Working condition 41 (%)	Working condition 47 (%)
IMF_h1	66.8	80.3	10	85.4	55.9
IMF_h2	15.6	10.4	11.3	13.6	42.4
IMF_h3	14.2	5.74	61.2	0.49	1.23
IMF_h4	2.88	3.05	16.3	0.311	0.293
IMF_h5	0.222	0.374	0.959	0.0857	0.0826
IMF_h6	0.115	0.0826	0.146	0.0317	0.0314
IMF_h7	0.0434	0.0449	0.0343	0.016	0.0161
IMF_h8	0.0249	0.0198	0.0222	0.0088	0.00861
IMF_h9	0.0356	0.00868	0.00808	0.00421	0.0042
IMF_h10	0.0218	0.00266	0.00393	0.00286	0.00213
IMF_h11	0.0113	0.000972	0.00388	0.00128	0.0012
IMF_h12	0.00279	0.000577	0.00114	0.000586	0.000455
IMF_h13	0.000226	0.000359	0.00086	0.000305	0.000322
IMF_h14	0.000126	0.000242	0.00114	0.000217	0.000105
IMF_h15	0.00023	0.000248	$1.78E - 05$	$4.52E - 05$	0.000184
IMF_h16	0.000115	$3.72E - 05$	—	$3.82E - 05$	—
IMF_h17	0.000104	—	—	—	—

resonance phenomenon was not observed, the acceleration response peak did enlarge according to resonance theory. Because a 0.1g acceleration peak is still not very high and microsensors do not collect any obvious rupture signals from the specimen, this paper assumes the specimen to have remained in an apparent linear elastic deformation stage.

The results also indicate that the enhancement coefficient increased from bottom to top.

(3) *Result at Input 0.5g Peak Acceleration of Vibration.* As shown in Figure 18, the enhancement coefficient inclined when shock excitation frequency is less than 20Hz and



FIGURE 22: Coal burst figure.

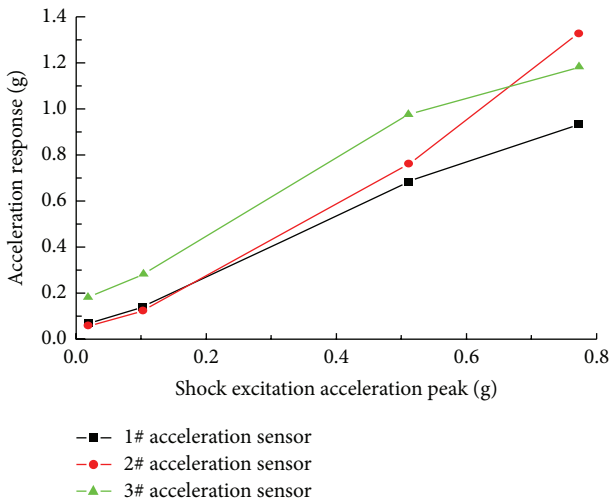


FIGURE 23: Relationship curve of acceleration response and shock excitation acceleration peak value.

declined when shock excitation frequency was greater than 20 Hz under 0.5 g acceleration input to the vibration table. The acceleration response amplitude at 20 Hz was greater than any other frequency. A resonance phenomenon was observed to occur in the specimen (where the specimen natural vibration frequency was 20 Hz in our experiment). This differs from the result in Section 5.1, 42.5 Hz, which was concluded as the specimen’s natural vibration. The difference can be attributed to the 0.5g acceleration input to the vibration table in this section of the experiment, 249 times greater than the 0.002 g used to measure natural vibration frequency by white noise scanning in Section 5.1. When the acceleration peak reached 0.5 g, damage occurred within the specimen. Crack propagation, damping ratio increases, and lateral stiffness decreases altogether caused the specimen’s natural vibration frequency to drop to 20 Hz. Damage to the specimen can be demonstrated by microseism signals. In addition, a_3 was larger than a_1 or a_2 when shock excitation was smaller than 24 Hz. When shock excitation exceeded 24 Hz, a_2 shrank significantly. This phenomenon differs from observations gathered at 0.02 or 0.1 g acceleration inputs to

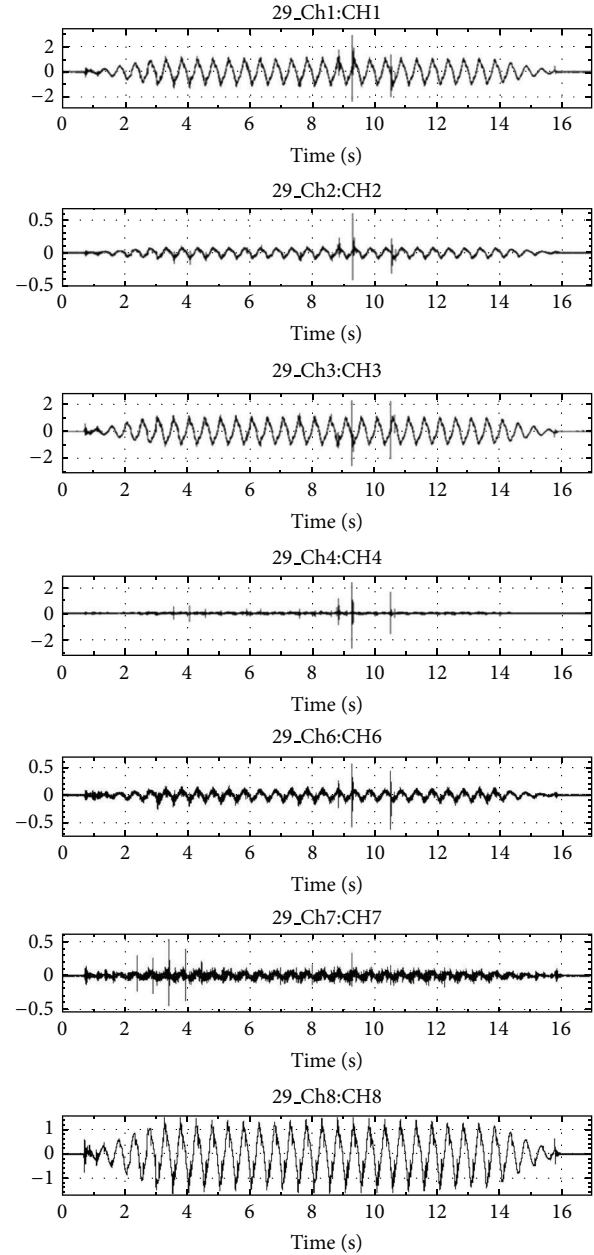


FIGURE 24: Microseism signals from different channels in working condition 29 (CH indicates the sensors’ serial numbers).

the vibration table and is not in accordance with the vibration response of an elastic system. We thus inferred that the specimen was no longer in the elastic deformation stage.

(4) *Result at Input 0.75 g Peak Acceleration of Vibration.* As shown in Figure 19, the enhancement coefficient declined as shock excitation frequency increased under 0.75 g acceleration input to the vibration table. The previous section allows us to conclude that the specimen’s natural vibration in this condition was less than 20 Hz. At this stage, shock excitation frequency varies considerably from natural frequency as it increases, and acceleration response decreases. Additionally,

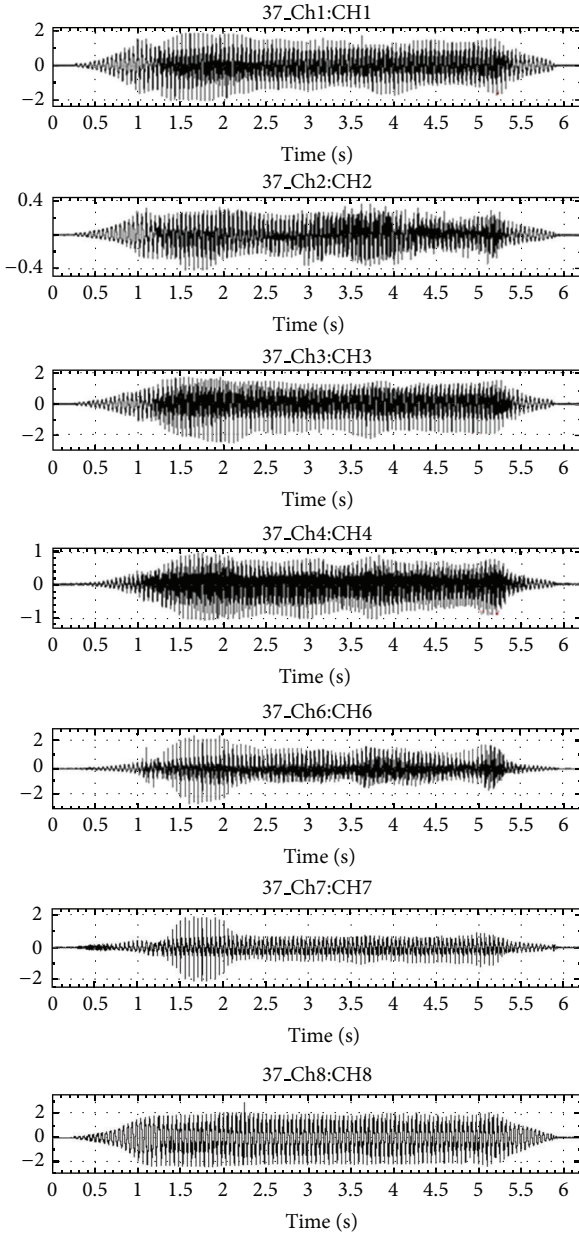


FIGURE 25: Microseism signals of working condition 37.

the a_3 value was not larger than a_1 or a_2 , indicating the specimen was not in the elastic deformation stage.

(5) *Result at Input 1.5g Peak Acceleration of Vibration.* Figure 20 shows enhancement coefficient curve of the acceleration response in this condition. When 1.5g shock excitation acceleration was inputted to the vibration table, the microseismic signal amplitude enlarged and a_2 and a_3 remained high. As vibration continued, coal specimen fractures became more serious. Horizontal cracks appeared in many locations, the coal loosened, and coal particles began to drop out of the specimen (Figure 21). During this process, smoke was observed where the crack opened and closed.

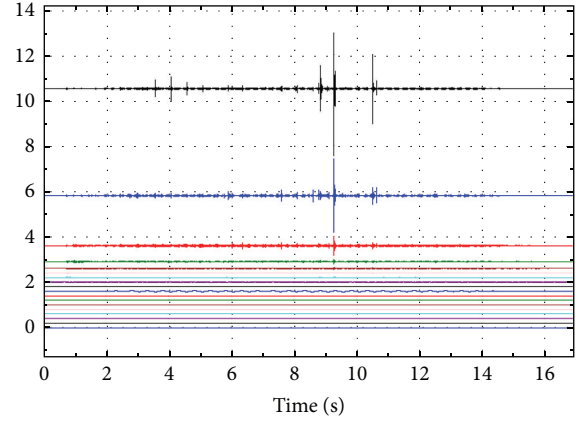


FIGURE 26: EEMD analysis results of original microseism signals from 4# sensor in working condition 29.

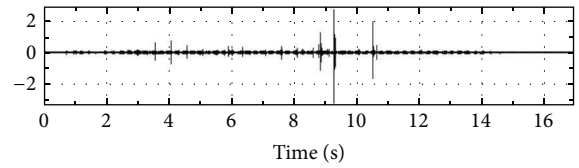


FIGURE 27: Effective microseism signals from 4# sensor in condition 29.

TABLE 16: IMF component energy percentages of effective microseism signals by EEMD.

IMF components	Working condition 43 (%)	Working condition 53 (%)	Working condition 63 (%)
IMF_h1	70.7	64.1	64.5
IMF_h2	27.4	29.4	32.8
IMF_h3	1.31	5.03	1.9
IMF_h4	0.384	1.07	0.414
IMF_h5	0.0921	0.207	0.157
IMF_h6	0.0296	0.0651	0.0773
IMF_h7	0.0149	0.0285	0.0465
IMF_h8	0.00777	0.0172	0.027
IMF_h9	0.00509	0.00983	0.0136
IMF_h10	0.0021	0.00427	0.00626
IMF_h11	0.00103	0.00192	0.00445
IMF_h12	0.000539	0.000885	0.00212
IMF_h13	0.000197	0.000562	0.000543
IMF_h14	0.000227	0.000847	0.001
IMF_h15	$7.32E-05$	0.000524	0.000759
IMF_h16	$6.79E-06$	$1.2E-05$	$9.34E-05$

Finally, when shock excitation acceleration reached 2.4g, severe destructive shaking occurred under shock excitation frequency of 5 Hz. After the experiment, the steel frame was demolished. Damage was mainly concentrated in the coal seam (Figure 22).

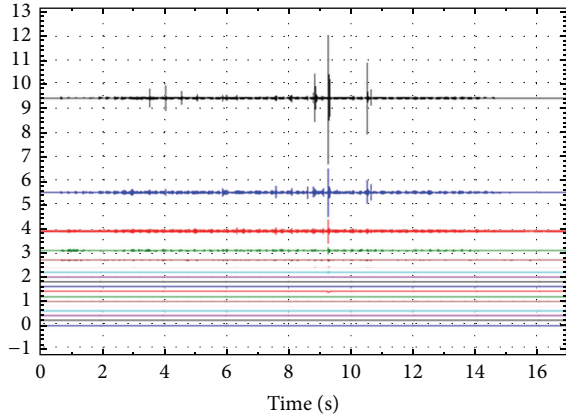


FIGURE 28: EEMD analysis results of effective microseism signals from 4# sensor in working condition 29.

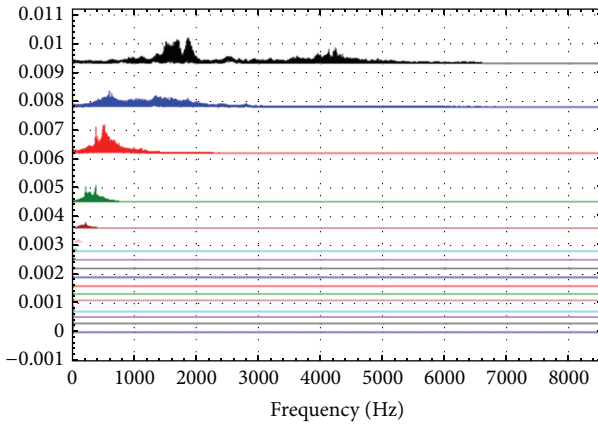


FIGURE 29: IMF components spectrum of effective microseism signals in working condition 29.

To summarize, the specimen stayed in the elastic deformation stage when the shock excitation acceleration peak was inputted at less than 0.5 g. If the shock excitation acceleration peak was inputted beyond 0.5 g, the specimen entered the inelastic deformation stage. Once shock excitation acceleration was determined, the shock excitation frequency's influence on acceleration response became obvious. When shock excitation frequency was close to the specimen's natural vibration, the acceleration response increased and a resonance phenomenon occurred once the shock excitation frequency and natural vibration were equal. During that time, the specimen grew prone to fracture due to the force of inertia.

5.2.2. Shock Excitation Acceleration Influence on Acceleration Response. To effectively study shock excitation acceleration peak influence on acceleration response, data measured under working conditions 7, 19, 39, and 49 were selected for analysis. For this set of data, shock excitation frequency is 24 Hz, and acceleration peaks are 0.02 g, 0.1 g, 0.5 g, and 0.75 g, respectively. The results are shown in Table 12 and Figure 23. Generally speaking, acceleration response

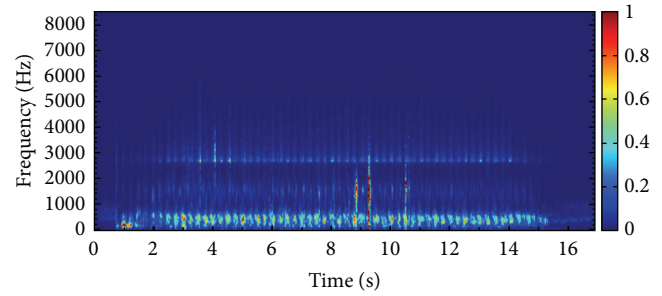


FIGURE 30: Hilbert energy spectrum of effective microseism signals in working condition 29.

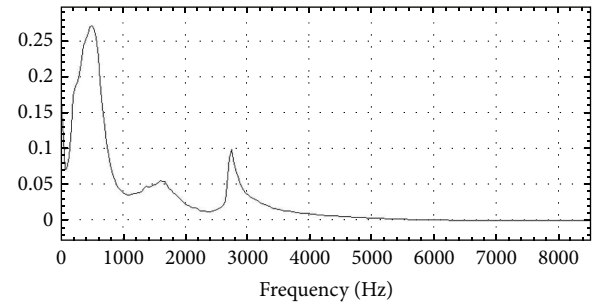


FIGURE 31: Hilbert marginal spectrum of effective microseism signals in working condition 29.

increases as shock excitation acceleration increases. Using the least square method, acceleration response data from a1 (reflecting the vibration of the bottom of the specimen) meets fitting equation $y = 1.1858x + 0.0388$ (where x represents $a0$ data reflecting shock excitation acceleration peak values,) and $R^2 = 0.9951$. Its law of change forms a linear relationship.

5.3. Microseism Signal Characters. Eight microseism signal sensors were installed in the specimen, detailed in Section 2. 1#, 3#, 5#, and 8# sensors measured microseism signals along the horizontal vibration direction, and 4#, 6#, and 7# sensors measured microseism signals perpendicular to the vibration table. 2# sensor sat atop the specimen. Sampling frequency was set to 17067 Hz for each working condition. Data from 5# sensor was discarded due to function failure.

5.3.1. Microseism Signal Characters at Specimen Start to Crack. Effective microseism signals began to appear in working condition 29, in which 0.5 g shock excitation acceleration and 2 Hz frequency were inputted to the vibration table, and vibration cycle was 30.

Microseism signals were concentrated at 9 s–11 s from Figure 24. Signal amplitude from 1#, 3#, and 4# sensors reached about 2.5, 0.6 from 2# and 6#, and 0.5 from 7# and 8#. This indicates that 1#, 3#, and 4# sensors were close to the fracture location. When the direction of sensors matched the vibration direction, such as with 1# and 3#, the signal from these sensors not only contained a high-frequency signal that caused the coal to burst, but also a low-frequency signal due

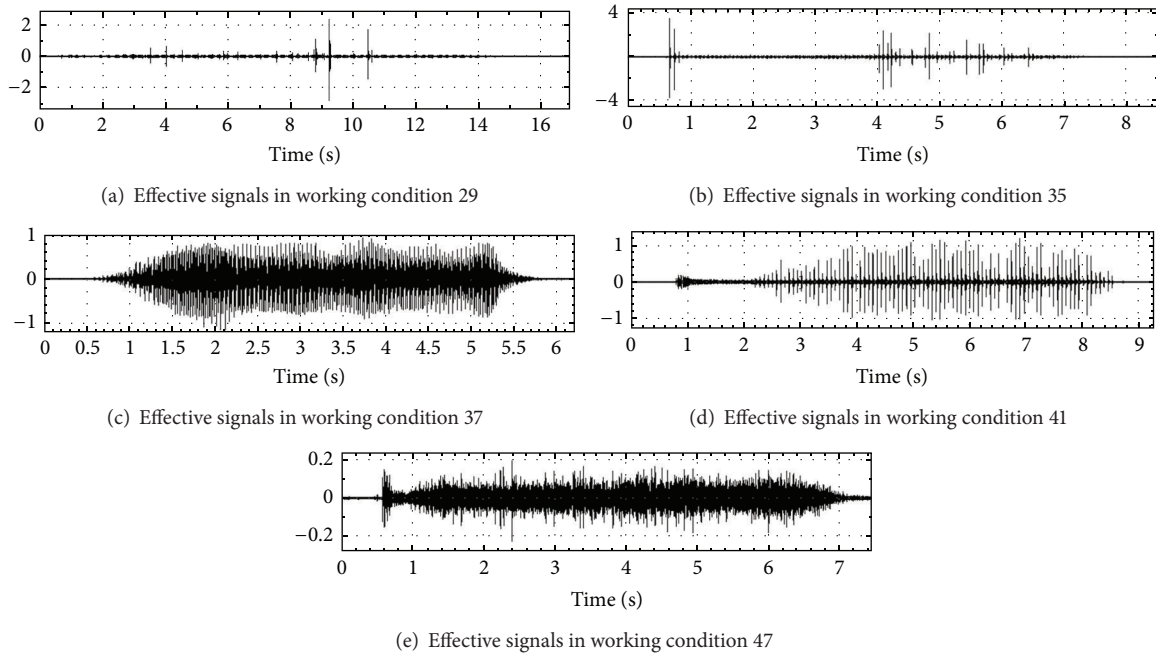


FIGURE 32: Effective microseism signals for certain working conditions (4# sensor).

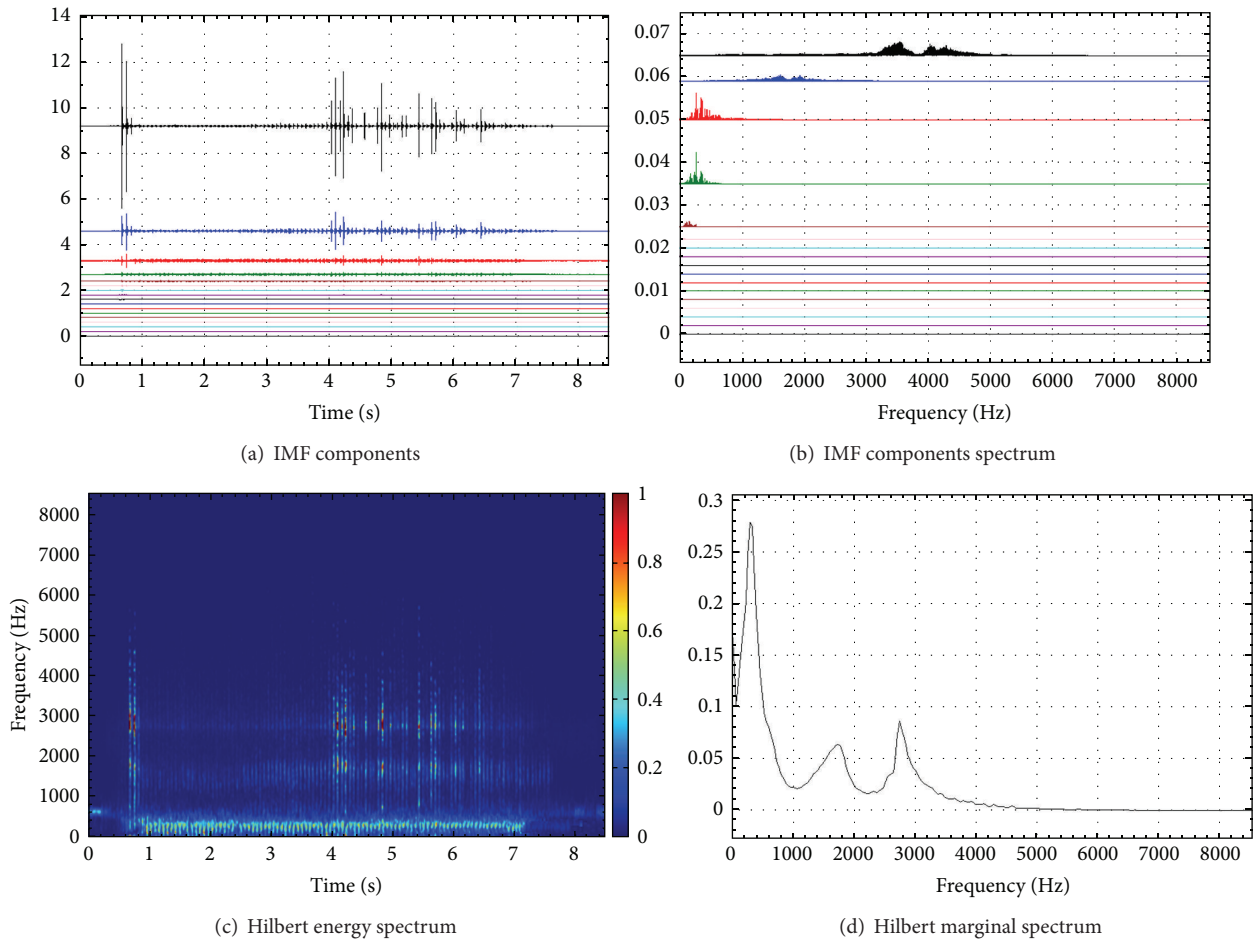


FIGURE 33: HHT analysis results in working condition 35.

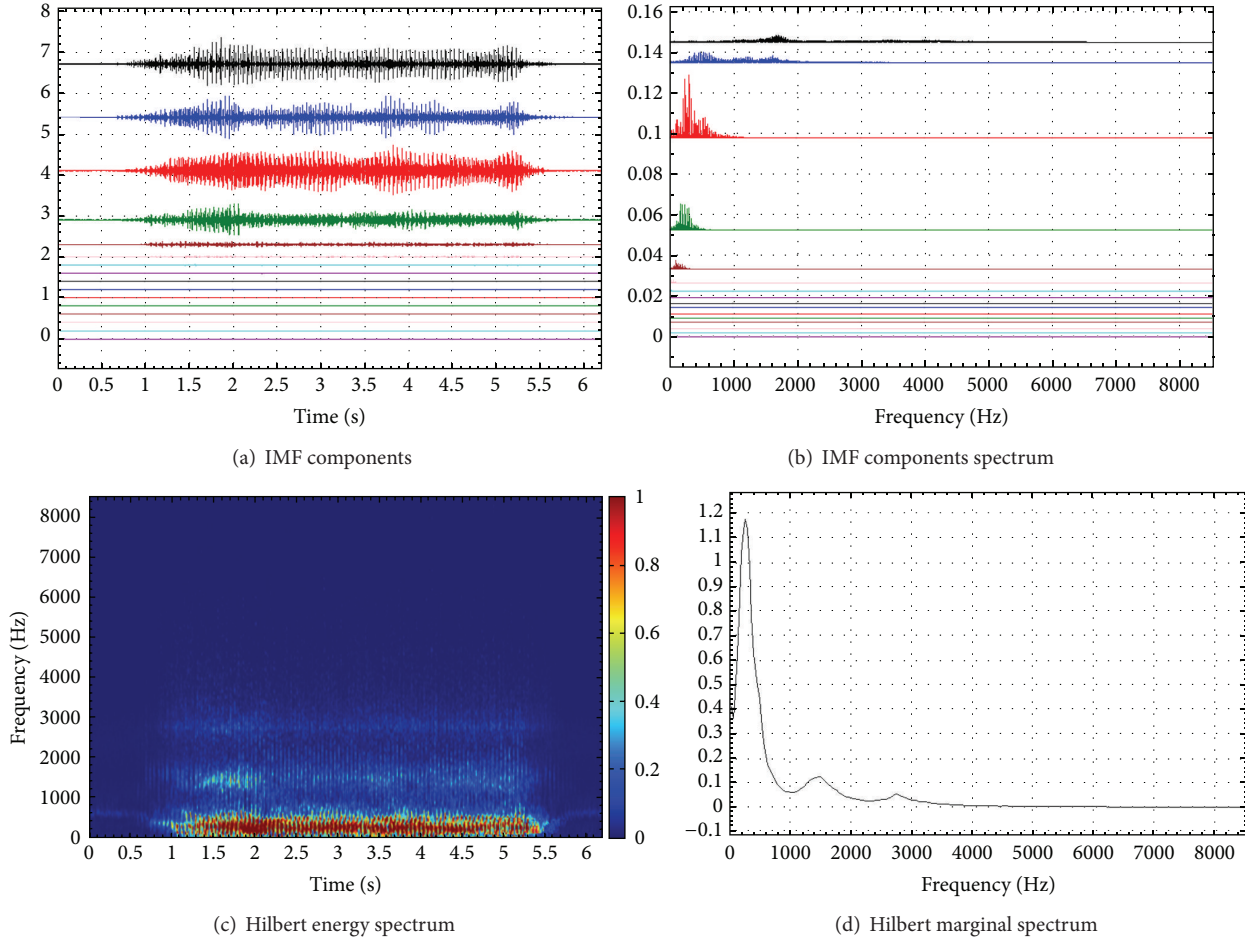


FIGURE 34: HHT analysis results in working condition 37.

to the specimen's vibration. These kinds of signals display the same characteristics as a carrier wave. Microseism signals from 1#, 3#, and 4# sensors, perpendicular to the direction of vibration, also presented carrier signal characteristics, partially due to installation deviation. The 2# sensor was on top of the specimen quite far from the coal seam, so its signal amplitude was the smallest, as we concluded that destruction was mainly concentrated in the coal seam.

5.3.2. Microseism Signal Characteristics When Resonance Occurs. Resonance occurred in working condition 37, evidenced by analyzing acceleration response data. In this condition, a 0.5 g shock excitation acceleration and 20 Hz frequency were inputted to the vibration table, and the vibration cycle was 120. The specimen's natural vibration frequency matched the result from Chapter 5.1 (which measured white noise and a shock excitation acceleration of 0.02 g) 42 Hz. When shock excitation acceleration changed, the state of destruction in the specimen also changed, causing the natural vibration frequency of the specimen to fluctuate.

Figure 25 shows that the microseism signal in working condition 37 was greater than in working condition 29. This indicates that the number of fractures increased when

resonance occurred. The acceleration response peak from the upper part of the specimen was bigger than the bottom. These signals also display carrier wave characteristics.

5.3.3. Microseism Signal Analysis Using Hilbert-Huang Transform Method

(1) Analyzing Microseism Signals in Working Condition 29 by Hilbert-Huang Transform Method. Hilbert-Huang transform (HHT) is a primary signal analysis method. By using the ensemble empirical mode decomposition (EEMD) method, it decomposes a signal into an intrinsic mode function (IMF). Instantaneous frequency data is also obtained through the Hilbert spectral analysis (HAS) method [20].

In working condition 29, the first original microseism signal appeared. The IMF component of the 4# sensor can be obtained by decomposing this original signal using the EEMD method. The following section aims to introduce the HHT method used in this experiment by processing microseism signal from the 4# sensor.

The original microseism signal decomposed into 17 IMF components. Shown in Table 13 and Figure 26, the frequency decreased from IMF 1 to IMF 17. By processing every IMF

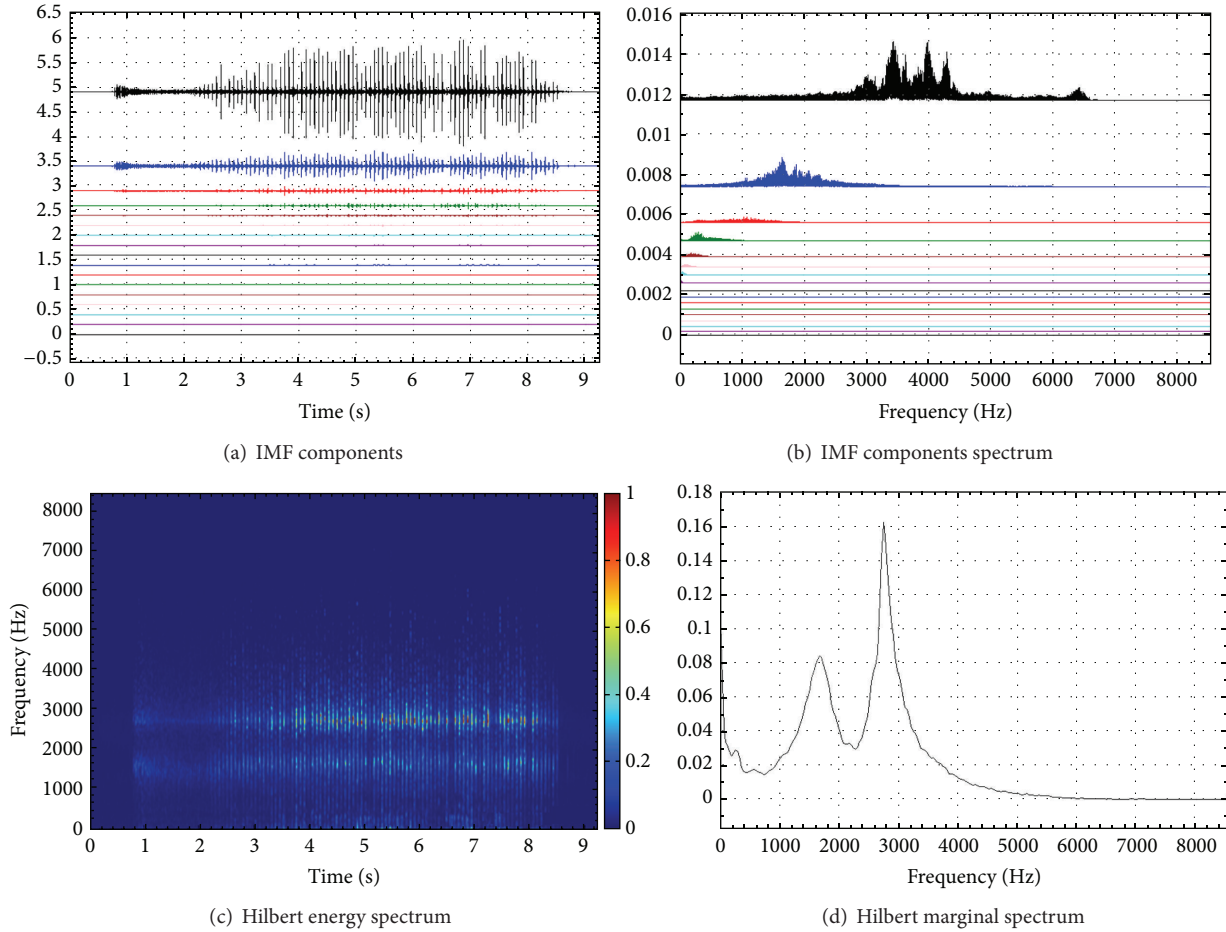


FIGURE 35: HHT analysis results in working condition 4I.

component using the fast Fourier transform (FFT) method, we find that IMF 10, 2 Hz, which accounted for 11.6% energy, is the sine signal caused by the vibration table's vibration due to input shock acceleration. IMF1-IMF4 components possess microseism signal characteristics of coal fracture and account for a considerable percentage of the energy. These IMF components are considered effective microseism signal components, and the other IMF components are attributed to environmental noise signals.

An effective microseism signal, shown in Figure 27, is composed of IMF1-IMF4 components and decomposed using the EEMD method.

17 new IMF components were obtained from the effective microseism signal (shown in Figure 28 and Table 14). The energy percentages of IMF1, IMF2, and IMF3 were far greater than any other components. These three components account for 96.6% of the energy, dominating the frequency of all components.

The FFT method was used to obtain spectra of IMF components. Shown in Figure 29, IMF1 has the widest range of frequency, from 1000–4500 Hz. Its frequency is concentrated at 1000–2000 Hz, and its peak appears at 1850 Hz. The range of IMF2 is from 500 to 2000 Hz, and its peak appears at

600 Hz. The IMF3 frequency range is 200–1000 Hz and peaks at 500 Hz. In conclusion, the dominant frequency due to coal fracture is 200–4500 Hz.

Hilbert energy spectrum and marginal spectrum are acquired by processing IMF components using Hilbert transform.

Figure 30 shows the relationship between frequency, time, and amplitude of effective microseism signals. In this figure, the deeper the color, the greater the energy. Energy is concentrated below 4000 Hz. Instantaneous frequency in this figure fluctuates up and down around a center frequency, maintaining a large amplitude. This indicates that the microseism signal has a wide frequency range.

The Hilbert marginal spectrum (Figure 31) expresses the range of the global frequency, representing an accumulation of all amplitudes in the statistical view. This indicates the possibility for some frequencies to appear. The signal of the frequency between 500 and 4000 Hz is most likely to appear. 500, 1700, and 2470 Hz are the main frequencies.

In conclusion, effective microseism has a frequency range between 200 and 4200 Hz while main frequencies are 500, 1700, and 2470 Hz under shock excitation acceleration 0.5 g and 2 Hz vibration input to the vibration table.

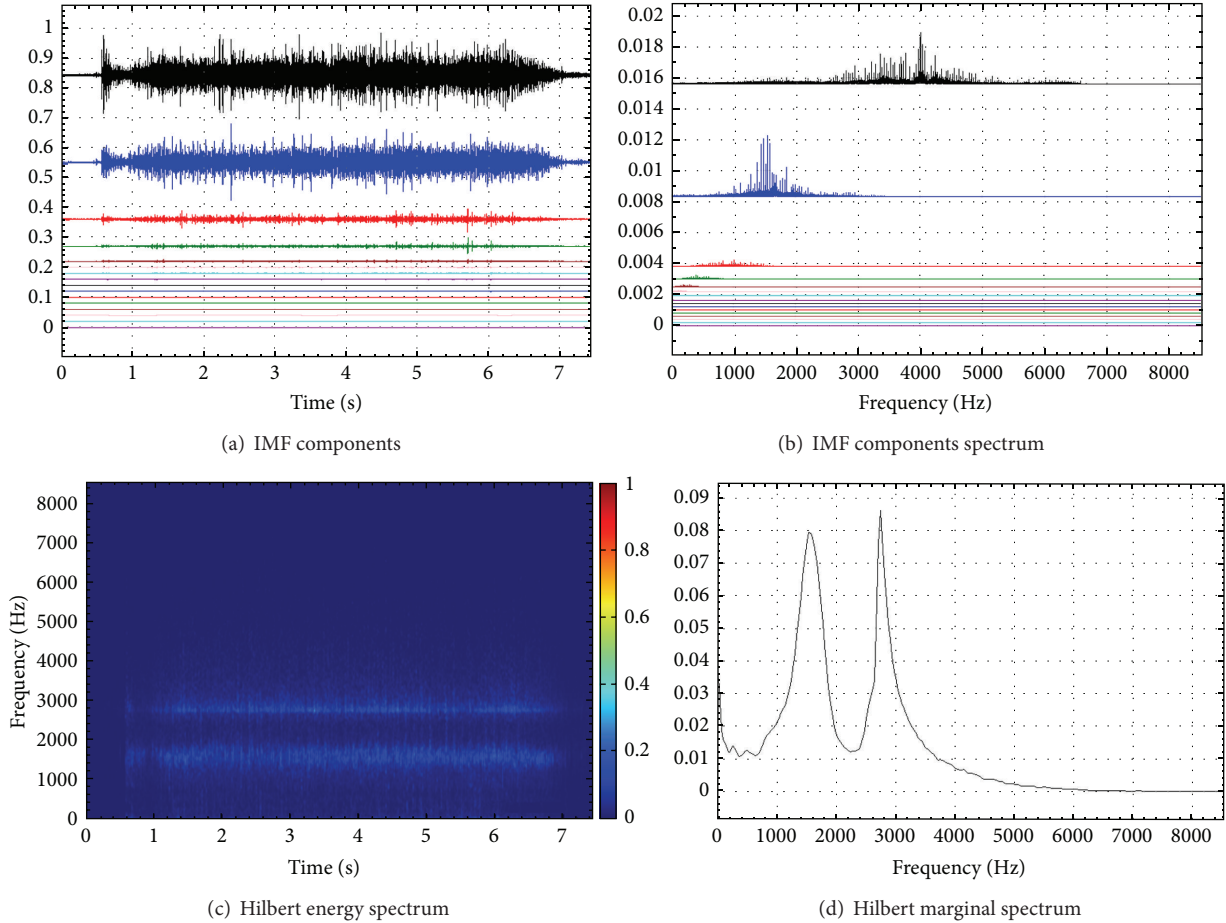


FIGURE 36: HHT analysis results in working condition 47.

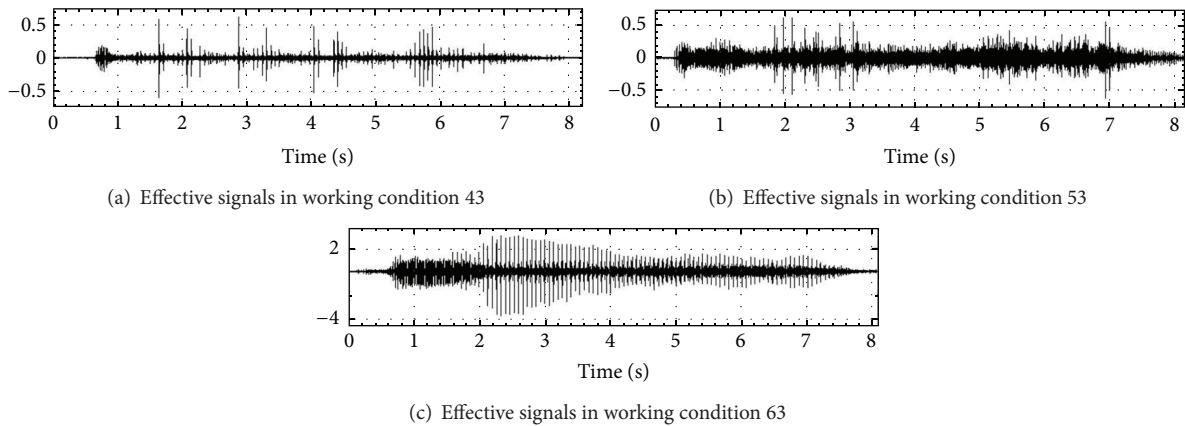


FIGURE 37: Effective microseism signals in certain working conditions.

(2) *Shock Excitation Frequency Influence on Microseism Signals.* We selected 0.5 g shock excitation acceleration conditions to analyze shock excitation frequency’s influence on microseism signals. Part analysis results are shown in Figures 32, 33, 34, 35, and 36 and Table 15. When input frequency is less than 20 Hz, microseism is relatively sparse,

and the amplitude of microseism signals varies widely. Maximum amplitude appears randomly. At a shock excitation frequency of 20 Hz, microseism signals become very dense and amplitude increases. When shock excitation frequency is over 20 Hz, the microseism signals become sparse again and amplitude decreases. Combining the results of Figure 18

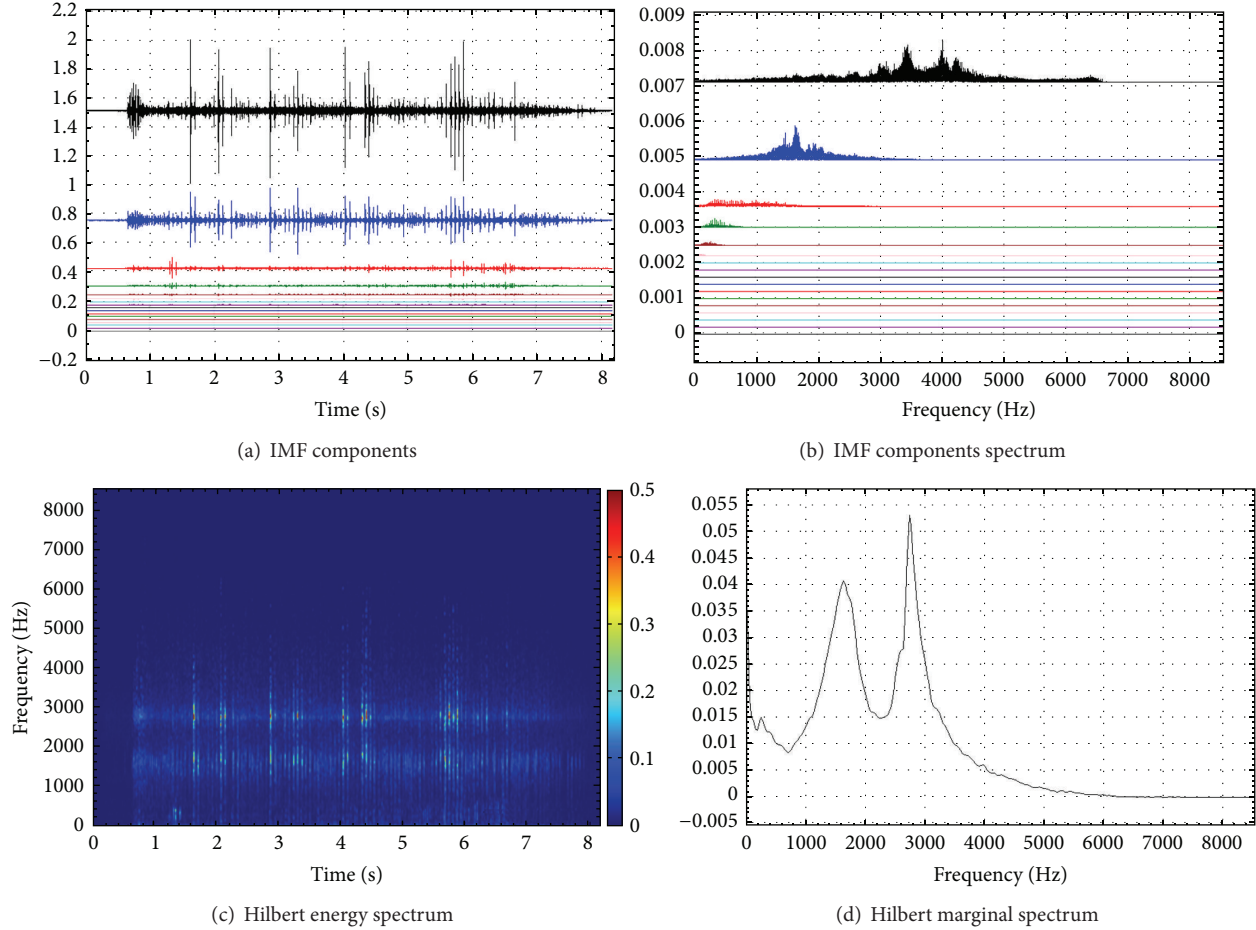


FIGURE 38: HHT analysis results of working condition 43.

result indicates that resonance has occurred, at which time the acceleration response peak reaches its maximum.

In working condition 37 (with a shock excitation frequency of 20 Hz) the IMF3 component accounts for most of the energy percentage, where the frequency range is 200 Hz–2000 Hz and the main frequencies are 300 and 1500 Hz. 37 differs from other working conditions in that IMF1 has the maximum energy percentage and a dominant microseism signal frequency range of 200 Hz–4500 Hz and 500, 1700, and 2740 Hz as main frequencies. The microseism signal frequency shifts from high to low likely due to the increased stress caused by inertia effect when resonance occurs.

In summary, shock excitation frequency has a clear influence on microseism signals. When shock excitation frequency is far from natural vibration frequency, coal fractures randomly occur once stress reaches a critical point. The specific cause of fractures or the amplitude of rupture duration time are unknown, demonstrating that microseism possesses the same characteristics. If shock excitation is close to natural vibration frequency, a large number of fractures are produced. Obvious microseism signals appear in every vibration cycle where frequency shifts lower.

(3) *Shock Excitation Acceleration Influence on Microseism Signals.* The previous section proved that the relationship between acceleration response and shock excitation acceleration peak changes from linear to nonlinear after the specimen cracks. This relationship affects microseism signals. Data from the 4# sensor under working condition 43 (at a shock excitation peak of 0.5 g,) 53 (shock excitation peak 0.75 g,) 63 (shock excitation peak 1.5 g,) were selected to study shock excitation acceleration's influence on microseism signals. The frequency of these three working conditions was 30 Hz. Figures 37 and 40 show HHT analysis results of the selected data.

As shown in Figure 37, sparse microseism appeared when shock excitation acceleration peak reached 0.5 g and amplitude 0.61. When shock excitation acceleration peak reached 0.75 g, the number of small peak microseism signals increased while the microseism signals with larger amplitude remained sparse. The maximum amplitude in this situation was 0.62. In working condition 63, the shock excitation acceleration reached 1.5 g, microseism increased significantly, and density was enhanced. The maximum amplitude was 3.08. We thus conclude that coal crack microseism signals

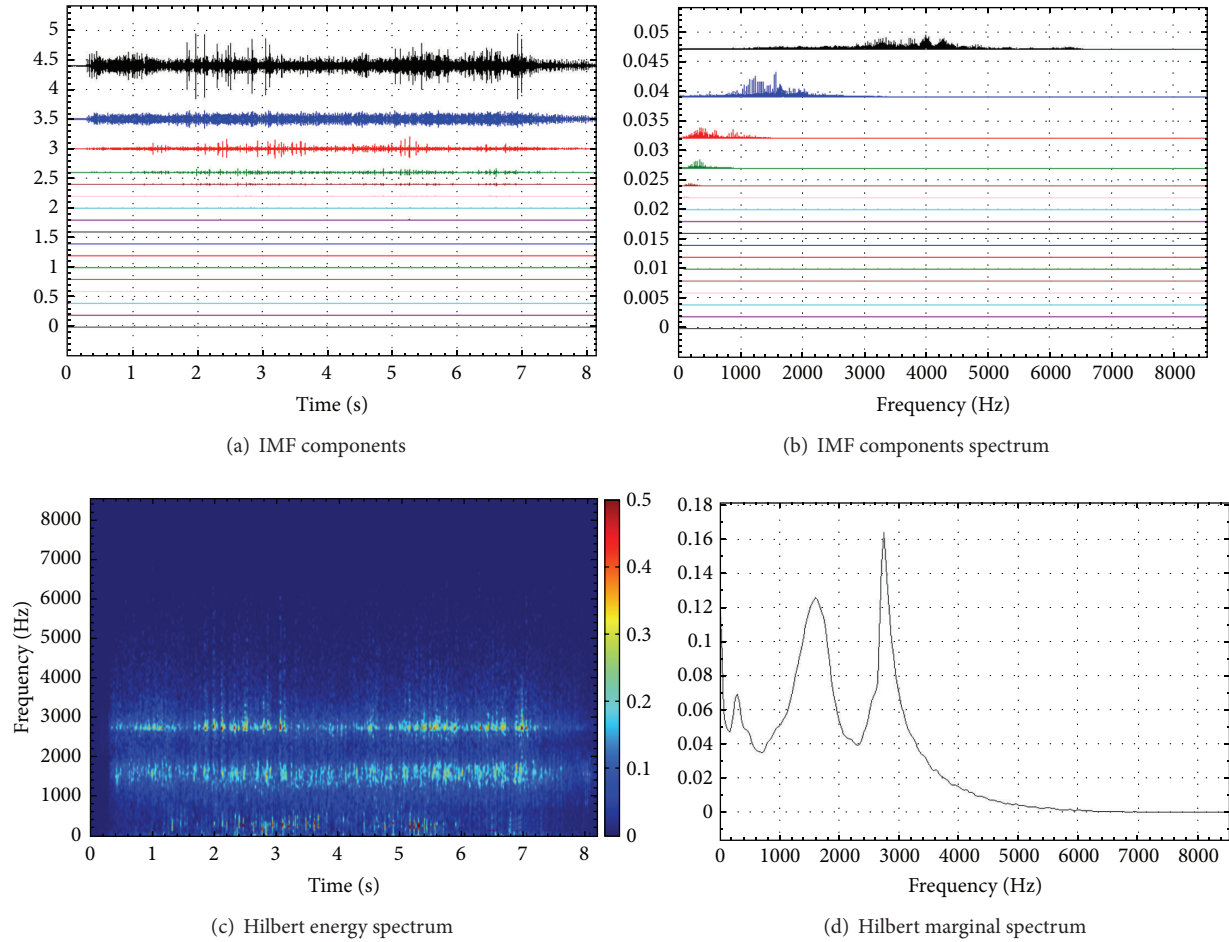


FIGURE 39: HHT analysis results of working condition 53.

amplitudes and number of fractures both increase as shock excitation acceleration peak increases.

From Figures 38, 39, and 40 and Table 16, it can be seen IMF1 and IMF2 are the main IMF components of effective microseism, and IMF1 accounts for the largest proportion of energy. As the shock excitation acceleration peak goes from 0.5, 0.75 g to 1.5 g, the frequency range also changes. IMF1 frequency range shifts from 3000 Hz–4000 Hz to 1000 Hz–4000 Hz, while IMF2 is unchanged. As evidenced by the IMF1 component, the microseism signal frequency range widens and the domain frequency shifts lower. Demonstrated by the Hilbert energy spectrum, microseism signal energy increases as shock excitation peaks incline. By forming an analysis which uses a combination of Hilbert energy spectrum and Hilbert marginal spectrum, we find that the instantaneous frequencies for these three signals are 1600 Hz or 2740 Hz. An instantaneous frequency of 2740 Hz appears more often than 1600 Hz when shock excitation frequency is 0.5 or 0.75 and hardly at all when excitation frequency is 1.5 g.

Based on these observations, we conclude that as shock acceleration and excitation peaks rise, the following phenomena occur: microseism signal density rises, amplitude enlarges, energy increases, number of fractures increases,

dominant frequency shifts lower, and frequency range expands.

6. Conclusion

Vibration, which can cause coal destruction, reduce coal strength, and induce coal outbursts, is a very common phenomenon inherent to coal mining processes. When vibration occurs, energy signals such as microseism and EMR signals are generated and propagate. By receiving these signals and analyzing their characteristics, it is possible to evaluate damage and, ultimately, to dynamically predict disaster conditions.

Because of the complexity of geological conditions, it is difficult to simulate site environments accurately. In this paper, a simple experiment specimen was designed to effectively simulate a coal seam. A destruction situation within the specimen was simulated, and its microseism signal characteristics were gathered by acceleration and microseism sensor. The experimental data was then thoroughly analyzed. It was observed that, (1) with increased vibration, the specimen's natural frequency decreases and fractures begin to appear. (2) Shock excitation frequency significantly affected the coal

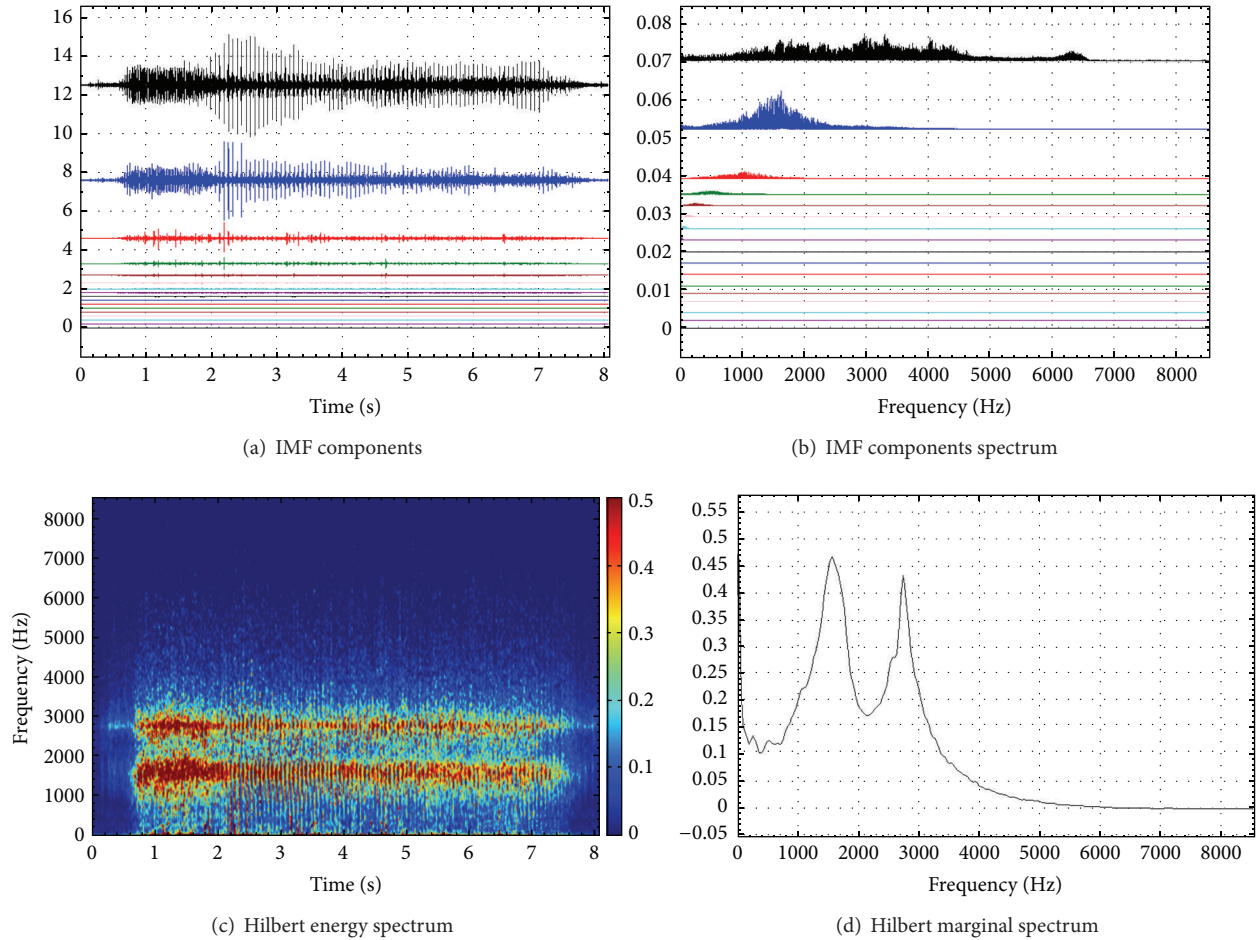


FIGURE 40: HHT analysis results of working condition 63.

specimen acceleration when the shock excitation acceleration peak remained unchanged. When shock excitation frequency nears the specimen's natural vibration frequency, the acceleration response peak increases and reaches its maximum when resonance occurs. (3) As shock excitation peak increases, the specimen's acceleration response peak also increases until the specimen enters an inelastic deformation stage. (4) When shock excitation acceleration is 0.5 g and input frequency is 2 Hz, effective microseism signals in the frequency range 200–4200 Hz begin to appear, while the main frequencies are 500, 1700, and 2470 Hz. (5) When shock vibration acceleration is 0.5 g and input frequency is less than 20 Hz, microseism is relatively sparse. The microseism signals begin to vary wildly, and maximum amplitude appears at random. When shock excitation frequency is 20 Hz, microseism signals become dense and amplitude increases. When shock excitation frequency is more than 20 Hz, microseism signals become sparse again and amplitude decreases. (6) When the input frequency is 30 Hz, microseism signal density rises, amplitude enlarges, energy increases, number of fractures grows, dominant frequency shifts low, and frequency range expands as shock acceleration and excitation acceleration peaks increase.

Notably, these results were all obtained in experimental conditions—in-site situations are more complex. In a real-life scenario, signals are affected by many other relevant factors, such as distance and varying vibration forms that would likely alter microseism signals significantly.

Conflict of Interests

The authors declare that there is no conflict of interests regarding the publication of this paper.

Acknowledgments

This research is supported by the National Natural Science Foundation of China (Grant no. 51274206) and Fundamental Research Funds for the Central Universities (Grant no. 2010YZ05). The authors would like to express their gratitude to these foundations.

References

- [1] J. Shepherd, L. K. Rixon, and L. Griffiths, "Outbursts and geological structures in coal mines: a review," *International Journal*

- of Rock Mechanics and Mining Sciences and*, vol. 18, no. 4, pp. 267–283, 1981.
- [2] K. P. Chen, “A new mechanistic model for prediction of instantaneous coal outbursts—dedicated to the memory of Prof. Daniel D. Joseph,” *International Journal of Coal Geology*, vol. 87, no. 2, pp. 72–79, 2011.
- [3] A. J. Hargraves, “Instantaneous outbursts of coal and gas: a review,” *Proceedings—Australasian Institute of Mining and Metallurgy*, no. 285, pp. 1–37, 1983.
- [4] R. D. Lama and J. Bodziony, “Management of outburst in underground coal mines,” *International Journal of Coal Geology*, vol. 35, no. 1–4, pp. 83–115, 1998.
- [5] P. Guan, H. Wang, and Y. Zhang, “Mechanism of instantaneous coal outbursts,” *Geology*, vol. 37, no. 10, pp. 915–918, 2009.
- [6] Q. Yu and C. Jiang, “Spherical shell destabilization hypothesis of coal and gas outburst,” *Safety in Coal Mines*, vol. 2, pp. 17–25, 1995.
- [7] J. Litwiniszyn, “A model for the initiation of coal-gas outbursts,” *International Journal of Rock Mechanics and Mining Sciences & Geomechanics Abstracts*, vol. 22, no. 1, pp. 39–46, 1985.
- [8] S. Zhou and X. He, “Rheological hypothesis of coal and methane outburst mechanism,” *Journal of China University of Mining & Technology*, vol. 19, no. 2, pp. 1–8, 1990.
- [9] Y.-D. Jiang, Y.-X. Zhao, Y.-Q. Song, W.-G. Liu, and D.-J. Zhu, “Analysis of blasting tremor impact on roadway stability in coal mining,” *Chinese Journal of Rock Mechanics and Engineering*, vol. 24, no. 17, pp. 3131–3136, 2005.
- [10] X. He, B. Nie, W. Chen et al., “Research progress on electromagnetic radiation in gas-containing coal and rock fracture and its applications,” *Safety Science*, vol. 50, no. 4, pp. 728–735, 2012.
- [11] P. Styles, S. J. Emsley, and T. Jowitt, “Microseismic monitoring for the prediction of outbursts at Cynheidre Colliery, Dyfed, S. Wales,” *Geological Society Engineering Geology Special Publication*, vol. 5, no. 1, pp. 423–433, 1988.
- [12] V. Frid, “Electromagnetic radiation method for rock and gas outburst forecast,” *Journal of Applied Geophysics*, vol. 38, no. 2, pp. 97–104, 1997.
- [13] X. X. Shi, S. R. Cai, H. Feng, and H. Li, “The prediction of coal and gas outburst using the acoustic emission technique,” *Coal Geology & Exploration*, vol. 26, no. 3, pp. 60–65, 1998.
- [14] X.-Q. He, E. Wang, and Z. Liu, “Experimental study on the electromagnetic radiation (EMR) during the fracture of coal or rock,” in *Proceedings of the International Symposium on Mining Science and Technology*, pp. 133–136, Science Press, Beijing, China, 1999.
- [15] V. Frid and K. Vozoff, “Electromagnetic radiation induced by mining rock failure,” *International Journal of Coal Geology*, vol. 64, no. 1–2, pp. 57–65, 2005.
- [16] S. Cao, Y. Liu, and L. Zhang, “Study on characteristics of acoustic emission in outburst coal,” *Chinese Journal of Rock Mechanics and Engineering*, vol. 26, no. 1, pp. 2794–2799, 2007.
- [17] C.-W. Li, W. Yang, S.-Y. Wei, T. Li, and L.-L. Chi, “Experimental research of influence scope of disaster gas after coal and gas outburst,” *Journal of China Coal Society*, vol. 39, no. 3, pp. 478–485, 2014.
- [18] C. Wang, C. Li, J. Wang, P. Hu, Y. Cui, and X. Xu, “Characteristics of electromagnetic signals obtained during blasting rupture of coal in excavating workface,” in *Progress in Mine Safety Science and Engineering II*, p. 63, CRC Press, 2014.
- [19] B. Carter and R. Mancini, *Op Amps for Everyone*, Texas Instruments, 2009.
- [20] Wikipedia, “Hilbert–Huang transform,” 2010, http://en.wikipedia.org/wiki/Hilbert%E2%80%93Huang_transform.

Research Article

Simulation of the Load Evolution of an Anchoring System under a Blasting Impulse Load Using FLAC^{3D}

Xigui Zheng, Jinbo Hua, Nong Zhang, Xiaowei Feng, and Lei Zhang

School of Mines, Key Laboratory of Deep Coal Resource Mining, Ministry of Education of China, China University of Mining and Technology, Xuzhou, Jiangsu 221116, China

Correspondence should be addressed to Nong Zhang; zhangnong@126.com

Received 1 August 2014; Accepted 28 November 2014

Academic Editor: Alicia Gonzalez-Buelga

Copyright © 2015 Xigui Zheng et al. This is an open access article distributed under the Creative Commons Attribution License, which permits unrestricted use, distribution, and reproduction in any medium, provided the original work is properly cited.

A limitation in research on bolt anchoring is the unknown relationship between dynamic perturbation and mechanical characteristics. This paper divides dynamic impulse loads into engineering loads and blasting loads and then employs numerical calculation software FLAC^{3D} to analyze the stability of an anchoring system perturbed by an impulse load. The evolution of the dynamic response of the axial force/shear stress in the anchoring system is thus obtained. It is revealed that the corners and middle of the anchoring system are strongly affected by the dynamic load, and the dynamic response of shear stress is distinctly stronger than that of the axial force in the anchoring system. Additionally, the perturbation of the impulse load reduces stress in the anchored rock mass and induces repeated tension and loosening of the rods in the anchoring system, thus reducing the stability of the anchoring system. The oscillation amplitude of the axial force in the anchored segment is mitigated far more than that in the free segment, demonstrating that extended/full-length anchoring is extremely stable and surpasses simple anchors with free ends.

1. Introduction

Prestressed anchoring technology, characterized by its high efficiency and profound economic benefits, has been widely applied and highly developed in various civil engineering applications [1]. This innovative methodology is theoretically based on an implied stress transfer mechanism under tension load and is widely used in collieries. Technicians and researchers worldwide have carried out many experiments and field tests to gain a detailed understanding of the mechanisms and performance of the technology.

The mechanism of mechanical transfer between a bolt/cable and grouting has been investigated [2–8]. Kang focused on the coupling relationship among the bolt prestress, bolt length, and prestressed field distribution using FLAC^{3D} software [9]. Lu et al. investigated the stability of a roadway that was affected by adjacent excavations, ultimately obtaining a relationship between the deformation of the roadway and the anchoring force [10]. Moosavi et al. tested the mechanism of anchor failure [11]. Nevertheless, the aforementioned results mainly focused on static mechanical analysis and ignored blasting effects, rock burst impacts,

seismic wave disturbance, and similar impulse loads induced by underground mining. Frequent periodic weighting, driving loads, and coal-mining cyclic loading greatly threaten the stability of the surrounding rock mass in mining. This threat is even more prominent for deep rock masses for which stress concentrations are higher and dynamic disturbances are fiercer [12, 13]. Anchoring units are thus affected and eventually destroyed by the evolution of the dynamic load. There is thus a scientific need to study the evolution of the anchoring system under different loads rather than conduct simple static mechanical analysis. Gao et al., for instance, investigated the evolution of the stress field of a rock mass, displacement field, and plastic zone under dynamic load disturbance, thus revealing the relevant mechanism that destabilizes or destroys a deep high-stress roadway in a mine [14]. The authors of this paper numerically studied the stress evolution of a bolt subjected to a dynamic load [15–17].

The present paper employs the dynamics module of FLAC^{3D} software to numerically simulate the transfer/evolution of stress along a bolt/cable and the mechanism of mutual stress transfer between an anchoring system and rock mass in the case of impulse dynamic load disturbances such as

TABLE 1: Initial parameters for fitting curves of shear stress.

Shear modulus of a different lithology/GPa			Shear modulus of resin/GPa	Radius of bolts/m	Radius of contact face/m	Elasticity modulus of cable/GPa
Stable	Moderate stable	Unstable				
5.6	2.8	1.4	1.2	0.011	0.025	195

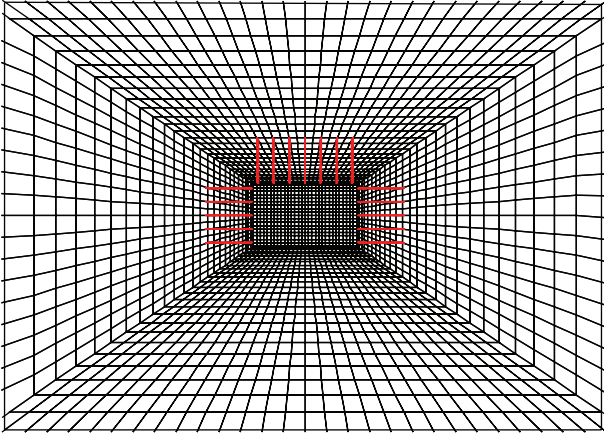


FIGURE 1: Schematic illustration of three-dimensional model.

those generated by blasting, seismic loading, and periodic weighting during mining.

2. Numerical Model and Schemes

2.1. Model and Parameter Initiation. A model is established using the Hoek-Brown yield criterion in FLAC^{3D}. The thickness and depth of the coal seam are specified as 20 and 800 m, respectively. The immediate surroundings and floor comprise moderate stable strata. Relevant parameters are given in Table 1.

The modeled roadway has a rectangular cross-section and is located at the center of the coal seam. The roadway has a width of 5.0 m and height of 3.0 m. The total model size is 50 m × 15 m × 60 m ($X \times Y \times Z$), as schematically illustrated in Figure 1. All free faces except the upper face are fixed. Incipient perpendicular stress is generated by the dead weight of overlying strata. The side pressure coefficient is 1. The roof of the roadway is supported by 2.8-meter-long bolts with an anchoring length of 1.6 m and exposed length of 100 mm. A pretension force is applied to the free segments of the bolts. The bolts are spaced 750 mm in rows that are spaced 1000 mm. The side walls of the roadway are supported by bolts in a scheme similar to that of the bolts supporting the roof but with bolt spacing of 650 mm and row spacing of 1000 mm. Note that the cell size in the dynamic calculation must be less than 1/8 to 1/10 of the wavelength corresponding to the highest frequency of the input waveform; hence, the maximal cell size is 1 m for the stress wave employed in this simulation.

The model is first built in a static state in FLAC^{3D} and the incipient stress field is equilibrated. The roadway is excavated for a length of 7 m and the prestressed bolt supporting

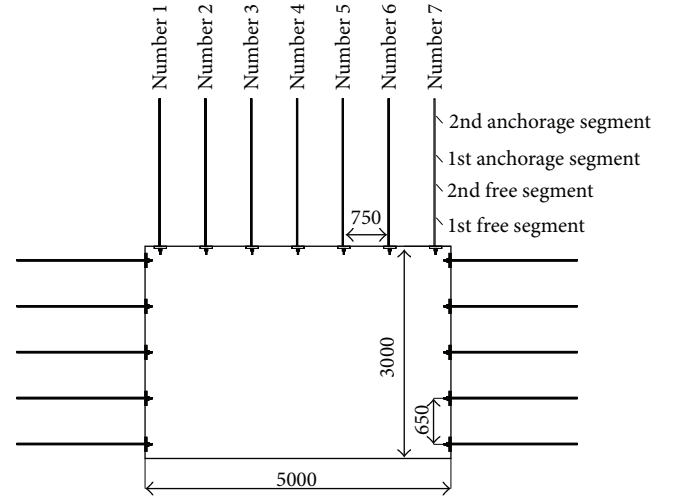


FIGURE 2: Arrangement and serial numbers of bolts.

scheme described above is then implemented. Each bolt has four units; the first and second free units are both 0.5 m in length, while the first and second anchoring units are 0.85 m in length. The anchoring scheme is specified as extended anchoring. A pretension force of 40 kN is applied to bolts and the simulation is allowed to run until equilibrium is reached. The initial fixed boundary is then replaced by a static boundary to begin the dynamic analysis module. An impulse load wave is imposed near the excavated head-on of the roadway so as to simulate the impact of a blasting load on antecedent installed bolts. Because the model and impulse load are symmetrically built and distributed, it is reasonable to analyze half of the roadway for the sake of simplicity. The arrangement and serial numbers of several bolts are presented in Figure 2.

2.2. Optimization of Dynamic Boundary Conditions. To absorb wave energy reflected from the model boundary as much as possible and thus guarantee calculation precision, relevant static boundary conditions and free-field boundary conditions are established.

A power source can be applied to the cells of a model directly to provide the impulse load. There is therefore no need to add an additional free-field boundary, and a static boundary is already capable of effectively reducing the reflection of wave energy. A static boundary and dynamic boundary are shown in Figure 3. All faces except the upper face are fixed to obtain the static solution. Stress of 20 MPa is applied to simulate the dead weight of overlying strata. In the next procedure of dynamic response model, all these

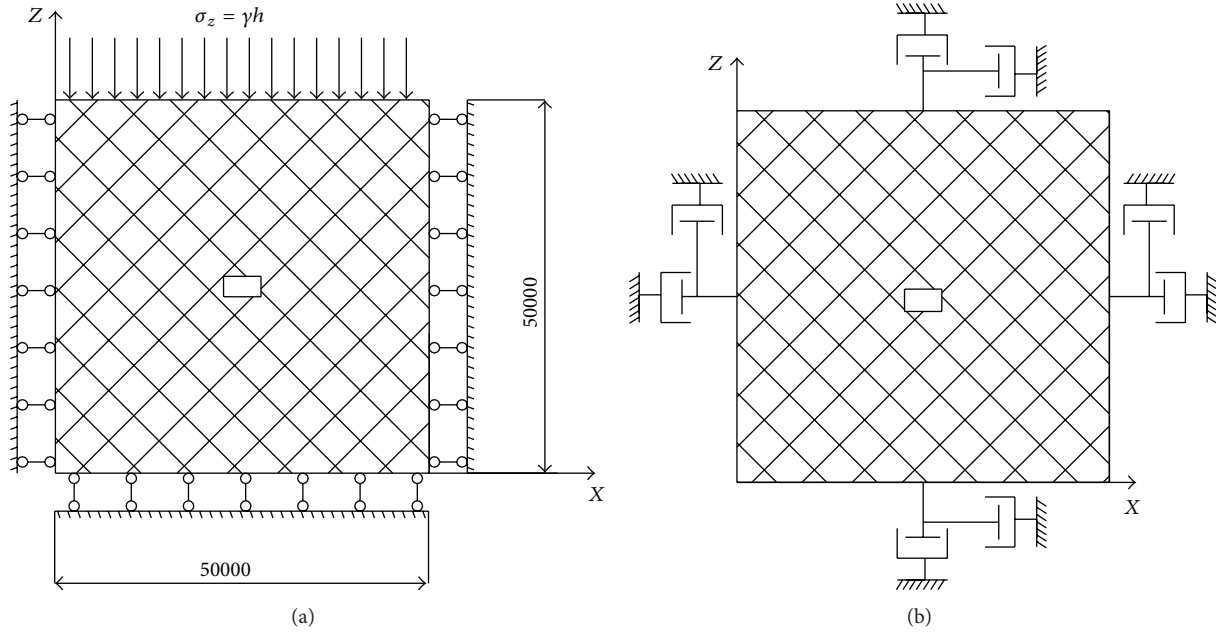


FIGURE 3: Boundary conditions of the static solution and dynamic solution; (a) boundary conditions of the static model; (b) boundary conditions of the dynamic model.

boundary conditions are removed and viscous boundary conditions are applied to all faces.

2.3. Damping Settings. All propagation media have damping characteristics relating to their inner friction and possible contact surfaces and interfaces. It is thus essential that the maximum extent of reappearing their own undisturbed damping properties and value should be reached during numerical simulation to ensure high reliability. However, the largest problem in dynamic numerical calculation is that damping differs for different values. $FLAC^{3D}$ provides Rayleigh damping, local damping, and hysteresis damping as damping schemes.

Rayleigh damping and hysteresis damping are generally applied in rock engineering [18]. The Rayleigh damping scheme involves two parameters: the critical damping ratio and central frequency of vibration. The critical damping ratio can typically be set as 2%–5% or obtained in a laboratory test. However, the application of an elastic-plastic model results in much energy being consumed in plastic flow and thus requires a small critical damping ratio, such as 1%. Local damping is widely applied to structural units in $FLAC^{3D}$; 8% is taken in this analysis. The central frequency is difficult to evaluate but may be obtained for a relatively simple model. The natural vibration frequency should first be determined for the model, and the value is then used as an approximation of the central frequency. This paper employs this methodology to obtain a central frequency of 50 Hz.

2.4. Processing of the Impulse Load. The so-called impulse load is a physical quantity that changes instantaneously and returns to its original value. Such a load is generated in events

such as blasting, the sudden breakage of a roof, and seismic activity. Much energy can be generated in the event of an impulse load. Part of the energy is released to adjacent rock mass and triggers the crushing and fracturing of the rock mass. The remainder enters the surrounding rock mass at the speed of splitting propagation, which is characterized by an extremely unstable dynamic wave. This dynamic wave destabilizes the anchoring system.

After a seismic wave has entered the rock mass, the rock not only undergoes compression but also a shear effect. There is thus shear failure within the rock mass; that is, there is a shear wave, or S wave, propagating at lower speed and mainly comprising horizontal fluctuation [19]. This paper focuses on the region close to the impulse source, and the seismic waves, wave speeds, and the like all relate to the primary wave, or P wave. The propagation speed and attenuation of the dynamic wave are strongly related to the mechanical properties of the rock mass. Commonly used equations for the velocities of the S and P waves are

$$V_P = \left[\frac{E(1-\mu)}{\rho(1+\mu)(1-2\mu)} \right]^{1/2}, \quad (1)$$

$$V_S = \left[\frac{E}{2\rho(1+\mu)} \right]^{1/2},$$

where E is the elastic modulus of the propagation medium, μ is Poisson's ratio, and ρ is the density of the medium.

An oscillogram has a high-frequency component during the postprocessing of impulse data because of the discrete

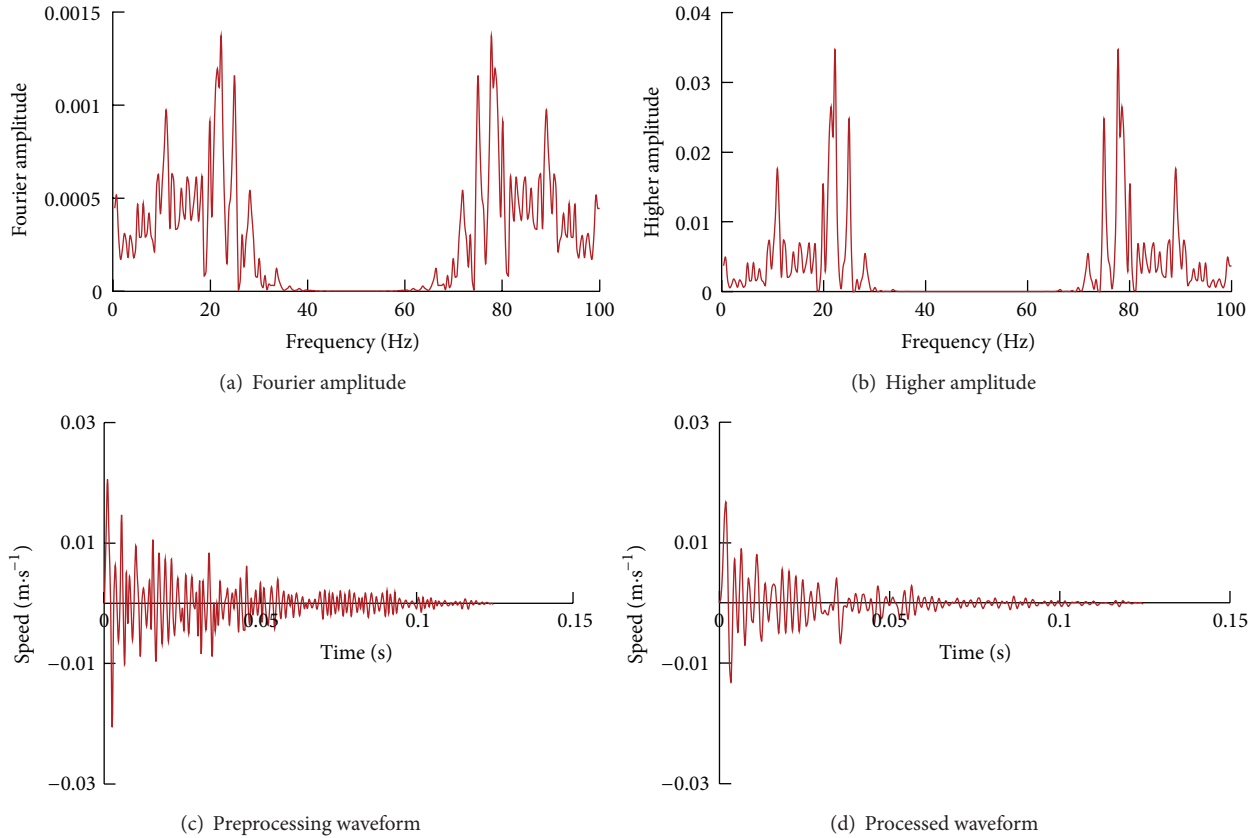


FIGURE 4: Filtering and baseline correction of the impulse wave source.

measurement of the initial load. The high-frequency component is detrimental to the calculation in the simulation, because as mentioned above the cell size of the grid must be less than $1/10$ of the wavelength. The component limits the size of a cell to a very tiny range, and the tiny value is impossible to calculate. It is thus necessary to execute baseline correction and filtering before applying the load so as to filter out the high-frequency component of the wave. It is eventually possible to increase the model cell size and thus reduce the calculation cost and simultaneously diminish potential residual deformation in the dynamic calculation of a plastic constitutive model.

Here Seismic Signal software is adopted for the filtering and baseline correction of the history of the perpendicular load speed [20]. The Butterworth filter is a linear filter that provides the required precision and has a smooth bandpass frequency-response curve and gentle amplitude-frequency curve.

Frequency bands of the primary wave are determined from the Fourier amplitude and higher amplitude in Figure 4 so as to define the chopping frequency. The figure shows that the chopping frequency of the impulse wave selected in this paper is approximately 30 Hz. This frequency is the criterion used in filtering and baseline correction; that is, only waves having frequency lower than 30 Hz are allowed to pass. The preprocessing data curve and processed data curve are shown in Figure 4.

3. Discussion and Analysis of Simulation Results

3.1. Dynamic Response of the Axial Force of the Anchoring System. It is commonly acknowledged that the amplitude of a wave decreases at a decreasing rate during the propagation of the wave in a medium. The attenuation rate is defined as the difference between the amplitude of two adjacent peaks of a wave divided by the amplitude of the first peak.

Figure 5 presents the evolution of the simulated axial force for four bolts placed from the roof center to the roof corner at a distance 0.5 m from the excavated head-on. As seen in Figure 5(a), the axial force of the free segment of each bolt increases while oscillating under the effect of the incipient impulse wave, and tension and loosening effects occur repeatedly. The rods thus must have high fatigue resistance. The duration of the process is short and the bolts regain their initial stability after approximately 0.05 s; thus, the high-frequency component is mainly concentrated within the first 0.05 s.

Increments in axial forces after applying an impulse load wave at the head-on of the roadway differ among the bolts, with the axial force of bolt number 4 undergoing the largest change because of the central position of bolt number 4 in the roof. Among the first row of bolts in the roof, the axial force of the free segment is the smallest for bolt number 1, having a value of 50.24 kN. The axial force of this bolt surges

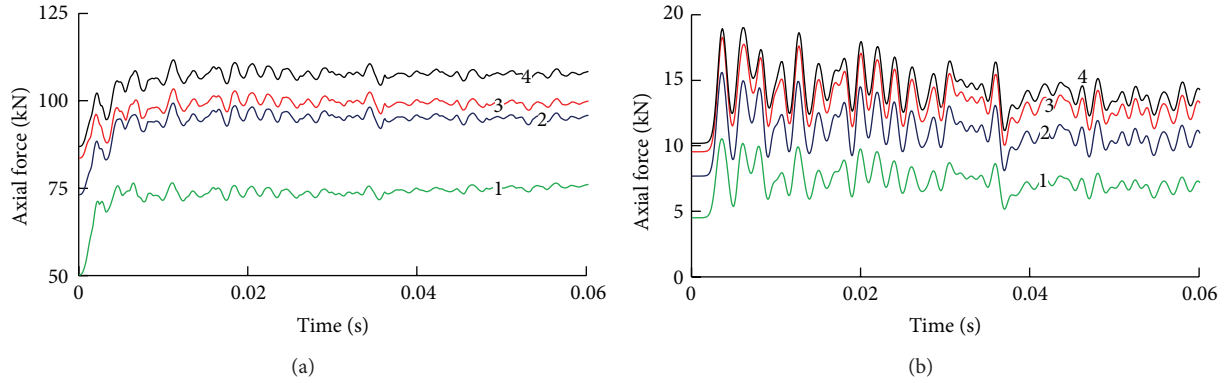


FIGURE 5: Evolution of axial forces of the first row of bolts in the roof; (a) free segment and (b) anchoring segment.

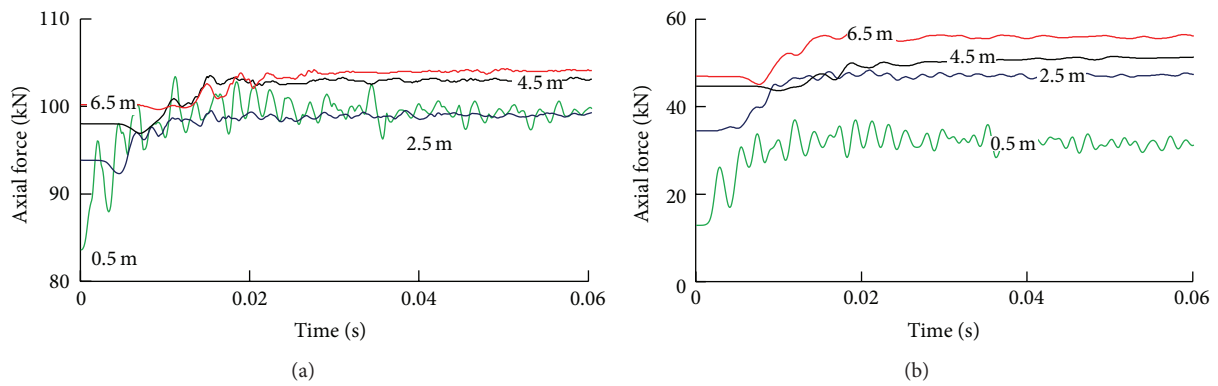


FIGURE 6: Evolution of the axial force in the simulated anchoring system; (a) evolution of the axial force along the free segment of bolt number 4; (b) evolution of the axial force along the anchored segment of bolt number 4.

by 49.56% to 75.14 kN after the application of the impulse load wave, and the attenuation rate of the first wave cycle is 65.06%. The axial forces of bolts numbers 2, 3, and 4, respectively, increase from initial values of 73.16, 83.61, and 86.93 kN to final values of 94.5, 8.61, and 107 kN (i.e., increases of 29.17%, 17.94%, and 23.08%). Apparently, an impulse blasting wave strongly affects the upper corners and central areas, where the anchoring system shows certain instability. The percentage increase in the axial force is greatest for corner bolt number 1; this increase is distinctly larger than that for central bolt number 4. This is explained by (1) the central bolt reaching a stable state earlier than the other bolts and its axial force only slowly increasing with an increase in roof subsidence and (2) bolt number 4 already being highly stressed before the application of the impulse load wave and thus responding little to the dynamic wave.

Figure 5(b) shows that the axial forces of the anchoring segments of the bolts in the first row have an overall increasing trend in response to roadway excavation. The axial force in the anchoring segment of bolt number 1 increases by 52.1% from 4.51 to 6.86 kN after the application of the impulse load wave, and the attenuation rate in the first wave cycle is 16.49%. Axial forces of bolts numbers 2, 3, and 4, respectively, increase from initial values of 7.69, 9.54, and 10.19 kN to final values of 10.42, 12.53, and 13.30 kN (i.e., increases of 35.50%,

31.34%, and 30.52%). Similar to the case for the free segments, the increment in the axial force is greater for bolt number 1 than for bolt number 4, and the difference is due to the wave attenuation rate dropping more dramatically than in the case of the free segment. This demonstrates that resin bonds the bolt and rock mass tightly, and the rock mass relieves the shockwave that should initially impact the anchoring system and thus prevents the system from being isolated.

Figure 6(a) presents the evolution of the axial force in the free segment of bolt number 4 for different distances to the entry's head-on (i.e., the central bolts in different rows). It is seen that all of the middlemost bolts in a certain range are affected by the blasting wave and their axial forces have an increasing trend. The increment ratio is a maximum 23.08% for the bolt 0.5 m from the head-on, while the ratios for the bolts 2.5, 4.5, and 6.5 m from the head-on are 5.42%, 4.23%, and 3.89%, respectively. The results reveal that a bolt further from the head-on is less affected by the impulse load and has the characteristics of a slower dynamic response, lower oscillation frequency, and lower oscillation amplitude.

Figure 6(b) presents the evolution of the axial force for the anchored segment at different distances to the entry's head-on. The characteristics of the evolution under the dynamic are similar to those of the free end shown in Figure 6(a), although the curves in Figure 6(b) have a lower frequency of oscillation

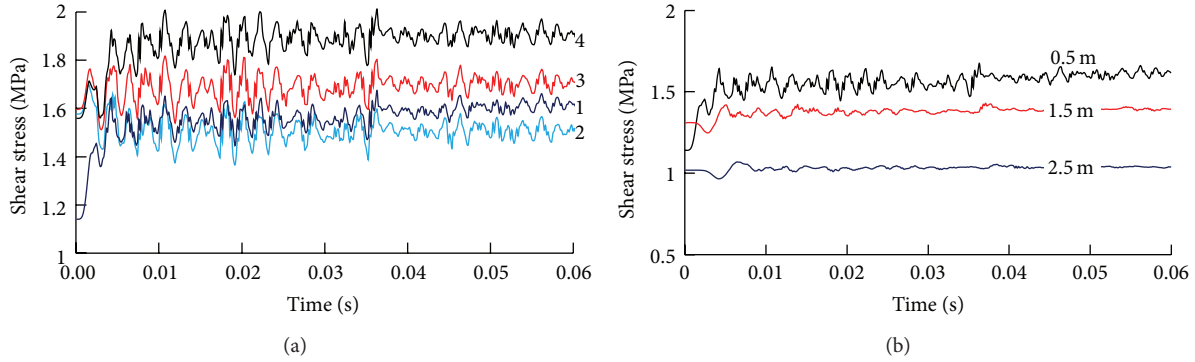


FIGURE 7: Dynamic response of shear stress along resin in the anchoring system; (a) evolution of shear stress in the anchoring segment of the first row of bolts; (b) evolution of shear stress in the anchoring segment of bolt number 1 for different distances to the head-on.

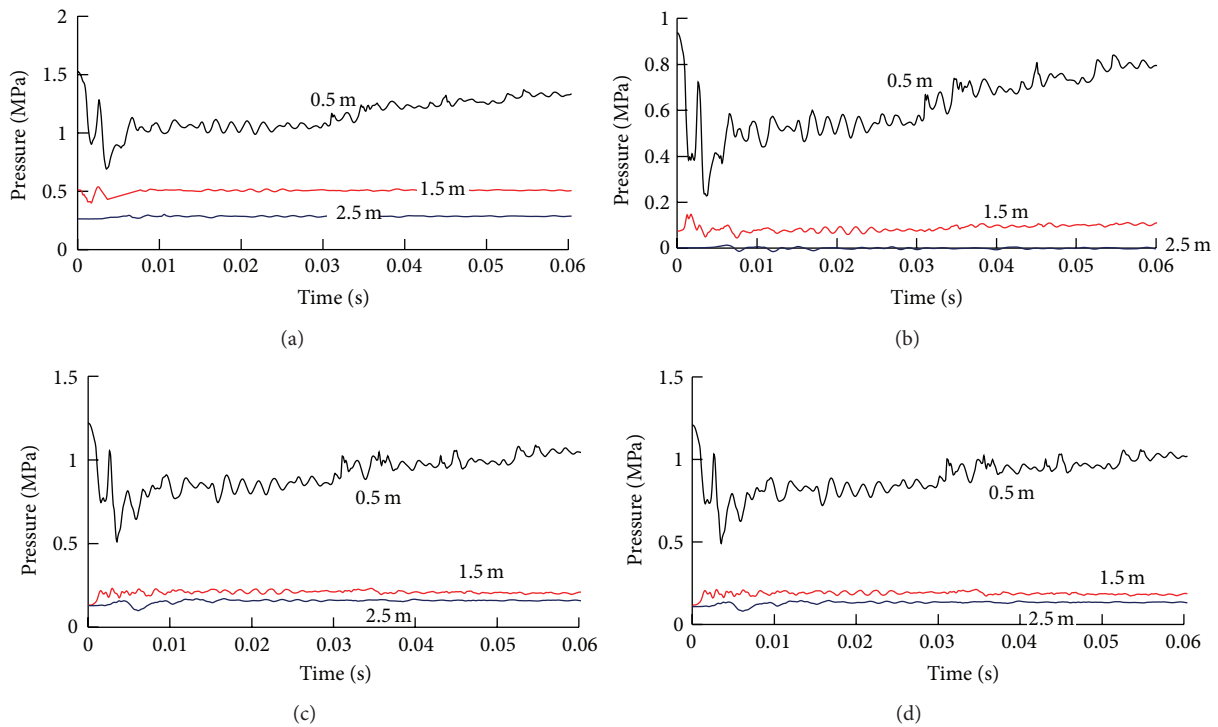


FIGURE 8: Dynamic response curves for the surrounding rock mass; (a) vertical stress in the roof, (b) vertical stress in the floor, (c) horizontal stress in the right wall, and (d) horizontal stress in the left wall.

and a weaker response, demonstrating that resin mitigates the effect of the blasting impulse load.

3.2. Dynamic Response of Shear Stress along Resin. The dynamic response of shear stress along the resin in a pre-stressed anchoring system under the effect of a blasting wave is illustrated in Figure 7(a). The shear stress for the anchoring segment of the first row of bolts oscillates dramatically and eventually stabilizes to a certain average value. The shear stress is maximal for central bolt number 4. Shear stress increment ratios of bolts numbers 1, 2, 3, and 4 are 41.37%, 4.50%, 6.64%, and 22%, respectively. Accordingly, the bolts most affected are the central and corner bolts, which match the evolution of the axial forces of the bolts. Figure 7(b)

presents the evolution of the shear stress in the anchoring segment of bolt number 1 for different distances to the head-on of the entry (i.e., the corner bolts in different rows). It is seen that the shear stress plummets and the vibration rate reduces as the distance to the head-on increases, revealing that the scope of the effect of excavation blasting on the anchoring system is approximately 1.5 m. The stability of the anchoring system thus requires special attention during blasting so as to guarantee the mechanical properties and active support of the system.

3.3. Dynamic Response Characteristics of Stress in an Anchored Rock Mass. Figure 8 presents dynamic load response curves for different positions in the anchored rock mass. It is

concluded that the rock pressure at all positions oscillates and attenuates with an increase in the distance to the head-on under the effect of a blasting impulse load. The reduction of the pressure amplitude is a maximum at a distance 0.5 m from the head-on of the entry. The reduction is 14.72% for the left wall of the roadway, 12.86% for the roof, 14.70% for the right wall, and 14.58% for the floor. Additionally, the decrease in amplitude of the stress in the anchored area plummets and almost reaches zero as the distance from the head-on increases; hence, the scope of the effect in the rock mass is approximately 1.5 m.

4. Conclusions

(1) Numerical calculation software FLAC^{3D} was employed to determine the load stability of an anchoring system under the action of an impulse load wave. The results show that the dynamic response of the axial force conforms to the pertinent waveform of the dynamic impulse load on the whole. The strength of the effects of this impulse perturbation depends on the position within the anchoring system, with the corners and middle being most affected. The dynamic response of shear stress also conforms to the corresponding evolution of the axial force on the whole; however, the oscillations of shear stress are larger and affect both the corners and middle of the anchoring system dramatically.

(2) Anchoring rods are greatly affected by repeated tension and loosening under the perturbation of an impulse load. This means that the rods must be highly resistant to such perturbation. The oscillation amplitude of the anchoring segment is much lower than that of the free segment, revealing that resin acts as an effective buffer that absorbs a certain amount of the impulse load. It is thus beneficial to employ extended or full-length anchoring and thus reduce interference in engineering.

(3) The stress state in an anchored rock mass may decrease under frequent effects, including blasting impulse loads, of head-on excavation. The effects are strongest close to the source of the blasting impulse load. There is eventually stress loss of the initially intact anchored rock mass that reduces the stability of the anchoring system.

Conflict of Interests

The authors declare that there is no conflict of interests regarding the publication of this paper.

Acknowledgments

Financial support for this paper was provided by the National Natural Science Foundation of China (51204159) and Fundamental Research Funds for the Central Universities (2011QNB05), and the Qing Lan project is gratefully acknowledged.

References

- [1] W. F. Cofer, D. S. Matthews, and D. I. McLean, "Effects of blast loading on prestressed girder bridges," *Shock and Vibration*, vol. 19, no. 1, pp. 1–18, 2012.
- [2] L. Lutz and P. Gergeley, "Mechanics of band and slip of deformed bars in concrete," *Journal of American Concrete Institute*, vol. 64, no. 11, pp. 711–721, 1967.
- [3] N. W. Hansor, "Influence of surface roughness of pre-stressing strand on band performance," *Journal of Pre-stressed Concrete Institute*, vol. 14, no. 1, pp. 32–45, 1969.
- [4] Y. Goto, "Cracks formed in concrete around deformed tension bars," *Journal of American Concrete Institute*, vol. 68, no. 4, pp. 244–251, 1971.
- [5] H. X. Jiang, C. L. Du, S. Y. Liu, and K. D. Gao, "Numerical simulation of rock fragmentation under the impact load of water jet," *Shock and Vibration*, vol. 2014, Article ID 219489, 11 pages, 2014.
- [6] X. Y. Wang, J. B. Bai, G. L. Guo, and Y. Yu, "Test and application of hydraulic expansion bolts in a roadway under goaf with ultra-close separation," *International Journal of Mining Science and Technology*, vol. 24, no. 6, pp. 839–845, 2014.
- [7] M. Ghadimi, K. Shahriar, and H. Jalalifar, "Analysis profile of the fully grouted rock bolt in jointed rock using analytical and numerical methods," *International Journal of Mining Science and Technology*, vol. 24, no. 5, pp. 609–615, 2014.
- [8] C. Cao, T. Ren, and C. Chris, "Introducing aggregate into grouting material and its influence on load transfer of the rock bolting system," *International Journal of Mining Science and Technology*, vol. 24, no. 3, pp. 325–328, 2014.
- [9] H. P. Kang, "Development and application of pre-stress anchored bolt supporting technology in coal mine," *Coal Mining Technology*, vol. 16, no. 3, pp. 25–30, 2011.
- [10] S. L. Lu, G. B. Fu, and L. Tang, "Regularity of deformation of rocks around roadway under mining influence and change of rockbolt resistance," *Journal of China University of Mining and Technology*, vol. 28, no. 3, pp. 201–203, 1999 (Chinese).
- [11] M. Moosavi, W. F. Bawden, and A. J. Hyett, "Mechanism of bond failure and load distribution along fully grouted cable-bolts," *Transactions of the Institution of Mining and Metallurgy, Section A: Mining Technology*, vol. 111, pp. A1–A12, 2002.
- [12] M.-Y. Wang, Z.-P. Zhou, and Q.-H. Qian, "Tectonic, deformation and failure problems of deep rock mass," *Chinese Journal of Rock Mechanics and Engineering*, vol. 25, no. 3, pp. 448–455, 2006 (Chinese).
- [13] M.-C. He, H.-P. Xie, S.-P. Peng, and Y.-D. Jiang, "Study on rock mechanics in deep mining engineering," *Chinese Journal of Rock Mechanics and Engineering*, vol. 24, no. 16, pp. 2803–2813, 2005 (Chinese).
- [14] F. Q. Gao, X. F. Gao, and H. P. Kang, "FLAC analysis of mechanical response of surrounding rock mass in deep tunnel," *Chinese Journal of Underground Space and Engineering*, vol. 5, no. 4, pp. 680–685, 2009 (Chinese).
- [15] X.-G. Zheng, L. Zhang, N. Zhang, and N. Liu, "Pre-stressed anchorage function and evolution in the roof of rectangular roadway in deep mine," *Journal of China University of Mining and Technology*, vol. 42, no. 6, pp. 929–934, 2013 (Chinese).
- [16] X. G. Zheng, *Evolutionary mechanism of Bolt's(Cable's) lift anchoring force and surrounding rock controlling technology of roadway in coalmine [Ph.D. thesis]*, China University of Mining and Technology, Xuzhou, China, 2013 (Chinese).
- [17] L. Zhang, *Anchorage load evolution mechanism and control technology under dynamic load in roadway [Master dissertation]*, China University of Mining and Technology, Xuzhou, China, 2014, (Chinese).

- [18] H.-Y. Han and S. Shuang, "Evolution of nonlinear seismic waves in microstructured earth crust," *Acta Physica Sinica*, vol. 61, no. 5, Article ID 059101, 6 pages, 2012 (Chinese).
- [19] G. Fang and B. Zhang, "Lagrangian dynamics and seismic wave align of elastic medium," *Acta Physica Sinica*, vol. 62, no. 15, Article ID 154502, pp. 1–6, 2013 (Chinese).
- [20] R. Zhang, X.-H. Zhao, Y.-J. Hu et al., "A new method of background elimination and baseline correction for the first harmonic," *Acta Physica Sinica*, vol. 63, no. 7, Article ID 070702, 8 pages, 2014 (Chinese).

Research Article

A Case Study of Damage Energy Analysis and an Early Warning by Microseismic Monitoring for Large Area Roof Caving in Shallow Depth Seams

Like Wei, Qingxin Qi, Hongyan Li, Bin Zhang, Yongren Wang, and Linghai Kong

China Coal Research Institute, Mine Safety Technology Branch, No. 5 Qingniangou Road, Chaoyang District, Beijing 100013, China

Correspondence should be addressed to Like Wei; wlkyo@qq.com

Received 12 November 2014; Accepted 17 February 2015

Academic Editor: Shimin Liu

Copyright © 2015 Like Wei et al. This is an open access article distributed under the Creative Commons Attribution License, which permits unrestricted use, distribution, and reproduction in any medium, provided the original work is properly cited.

Shallow depth coal seams are widely spread in Shendong mining area, which is located in the Northwestern region of China. When working face is advanced out of concentrated coal pillar in upper room and pillar goaf, strong strata behaviors often cause support crushing accidents, and potentially induce large area residual pillars instability and even wind blast disaster. In order to predict the precise time when the accident happens, guaranteeing life-safety of miner, microseismic monitoring system was for the first time applied in shallow coal seam. Based on damage mechanics correlation theory, the damage energy model is established to describe relationship between damage level and cumulative energy of microseismic events. According to microseismic monitoring data of two support crushing accidents, the damage energy model is verified and an effective early warning method of these accidents is proposed. The field application showed that the early warning method had avoided miners suffering from all support crushing accidents in Shigetai coal mine.

1. Introduction

The shallow depth coal seams which had been mined in the Shendong mining area have led to large area roof weighting frequently due to large thickness, high tensile strength, and small overlying load of the main roof. To prevent the large area roof weighting accidents, deep-hole presplit blasting technology for controlling roof caving is a suitable method and has been widely applied in some mines [1]. Furthermore, the mechanism and influence of these accidents have been exploited mainly by theoretical analysis, numerical simulation, and engineering verification [2–6], but prediction method of these accidents is barely analysed.

In geophysical techniques, seismic methods are widely applied to monitor and warn rock dynamic hazards in coal mines due to its abundant spectrum and broadband character, which can monitor the fracturing form of surrounding coal and rock, roof falls, and the high stress concentration distribution. During the past two decades, microseismic monitoring technique emerged from a pure research mean to a main stream industrial tool for daily safety monitoring at

various fields of geotechnical engineering. In recent years, it has been widely applied in China. A microseismic monitoring system was for the first time installed for stability analysis of a high steep rock slope in China [7]. It has been proven to be very promising in instability prediction of rock slope subject to identification and delineation of potential slip surface and failure regions. Dou et al. [8] improve mining safety for water inrush in the goaf by more effective monitoring and proposed a monitoring method using partitioning and time sharing. According to a case study, the energy emission rate of microseismic events can be used to analyze the microseismic activity in time and the energy spatial density in space. Jiang et al. [9] investigate the progressive failure of geological structures (faults, karst collapse columns) and predicted water inrush with microseismic activities. Liu et al. [10] use an operation microseismic monitoring system of ESG to understand the relation between background stress field of three-dimensional numerical simulation with microseismicity and water inrush probability, combined with an engineering case of grout curtain community for Zhangmatun iron mine. Then, the accumulated three-dimensional

geometry spaces of microrupture are delineated and the possible dangerous water inrush regions of grout curtain community are divided. Jiang et al. [11] analyzed and predicted that fracturing of high and thick strata of hard rocks causes strong dynamic response by theoretical calculation and microseismic monitoring based on high and thick strata of hard magmatic rock at working front 10416 in Yangliu coal mine. Lu and Dou [12] simulated and analyzed vertical stress concentration and gradient distribution rules by on-site monitoring of seismic, EME, and drilling bits volume for nearly a year in the whole mining process of 9202 working face in Sanhejian coal mine of Xuzhou coal mining group in China. Xia et al. [13] improved 5 risk forecasting indexes to predict coal mine rock burst with microseismic monitoring data. Zhu et al. [14] provided a new method for recognizing blasting vibration and rock fracture signals and use the calculated distribution feature of signals energy to recognize microseismic waveforms as feature index based on in situ microseismic data. Lu et al. [15] evaluated and monitor the danger and intensity of roof dynamic fracture by the evolution rules of frequency spectrum. With SOS MS monitoring system, the hard and weak roof fracture processes are measured in field. Yuan and Li [16] collected abundant microseismic signals by seismic monitoring system during the period of three pillar type rock bursts that occurred in number 11 mine of Pingmei group. The time sequence of microseismic signal in this period is obtained and the frequency spectrum and spatial distribution are analyzed by fast Fourier transformation (FFT) algorithm and fractal theory.

As an irreversible phenomenon, rock damage process was obtained by many experiments. Experimental study and theoretical research demonstrate that the damage evolution equation of rock based on analysis of energy dissipation can well characterize the damage evolution process of rock [17]. Wang et al. [18] proposed a rheological damage constitutive model for sandstone by using the damage theory and by introducing the concept of the whole process of damage into Burgers rheological model based on the Mazars damage evolution law. Zhang et al. [19] investigated the fatigue damage properties of intact sandstone samples subjected to axially cyclic loads with different frequencies at confining stress state and studied influence of frequency on dynamic mechanical features of sandstone by the MTS-815 rock and concrete test system. Acoustic emission tests under triaxial compression of limestone were carried out by MTS815 servo-controlled rock mechanical test system and AE21C acoustic emission monitor. Yang et al. [20] analyzed the characteristics of limestone damage evolution under triaxial compression through acoustic emission parameters.

Despite a great deal of work on application of microseismic monitoring system and analysis of rock damage process, there are a few reports about the relationship between rock damage process and the law of monitoring energy change by seismic monitoring system. In this paper, structure damage model will be established by damage mechanics theory based on the microseismic monitoring energy. Then, the damage characteristics of supporting-beam structure will provide

a theoretical basis for an early warning method for large area roof caving in shallow depth seams.

2. Accident Analysis

Room and pillar mining was applied in Shendong mining area before large-scale exploitation, which controlled roof and surface subsidence by the remaining coal pillars to support mining. But the room and pillar mining is a low mining rate method, and it not only wastes a lot of resources but also forms a large area of room and pillar goaf and residual coal pillar. The residual coal pillar would form local stress concentration areas and increase difficulty of below contiguous seam mining.

With the increasing exploitation of strength, first primary mineable coal bed in Shendong mining area has been mined out mainly by room and pillar mining. Currently, longwall fully mechanized mining method is applied in second primary mineable coal bed. Due to close coal seam interval, strong strata behaviors would happen in mining face and even cause support crushing accident, such as accident in Shigetai coal mine of Wulan group [1–3], accident in Daliuta coal mine of Shenhua group [4, 5], and accident in Bulianta coal mine of Shenhua group [6].

There is large area of room and pillar goaf in 2-2 coal seam above 31201 working face in 3-1 coal seam in Shigetai coal mine of Shenhua group. According to geological conditions in Shigetai coal mine which is shown in Table 1, the depth of room and pillar goaf in 2-2 coal seam is about 81.3 m. The distance between 2-2 coal seam and 3-1 coal seam is about 34.5~39 m.

The depth of 31201 working face was about 120 m and the width of 31201 working face was about 300 m. Three-dimensional structure of 31201 working face is shown in Figure 1. In Figure 1, the direction of black arrow is the direction of face advance and blue zones include concentrated coal pillar and residual room pillars. Support which had 18000 KN working resistance was applied in the face, but support crushing accident still happened in the midnight of December 16, 2013, when 31201 working face was mining 15.5 m out of concentrated coal pillar in upper room and pillar goaf. In the accident, 22#~142# support was crushed to death in less than 30 seconds and the descending amount of piston increased sharply to 1.3 m~1.5 m. Different field situations before and after accident are shown in Figure 2. The minimum oxygen concentration was 9% in return airflow corner and 14% in return airflow roadway. When the pressure was stable, the value of pressure gauge ranged from 45 MPa to 80 MPa (19300 KN~34000 KN). Fortunately, the accident did not happen in working time, and no one was hurt in the accident.

According to the accident, support load was much higher than supporting ability, and the instantaneous value of pressure gauge in working face jumped to 800 bar (34000 KN). Thus, there is no support which can resist the overwhelming pressure and the support crushing accident cannot be prevented only by support type choice. So, an early warning

TABLE 1: Stratigraphic column of Shigetai mine.

Stratigraphic order	Lithology	Average thickness/m	Depth/m	Lithological column
1	Aeolian sand	18.1	18.1	
2	Packsand	15.9	34	
3	Siltstone	16.2	50.2	
4	Packsand	12.7	62.9	
5	Medium granular sandstone	6.1	69	
6	Packsand	8.2	77.2	
7	2-2 coal seam	4.1	81.3	
8	Siltstone	12	93.3	
9	Medium granular sandstone	16	109.3	
10	Sandy mudstone	8	117.3	
11	3-1 coal seam	4	121.3	
12	Siltstone	7.6	128.9	

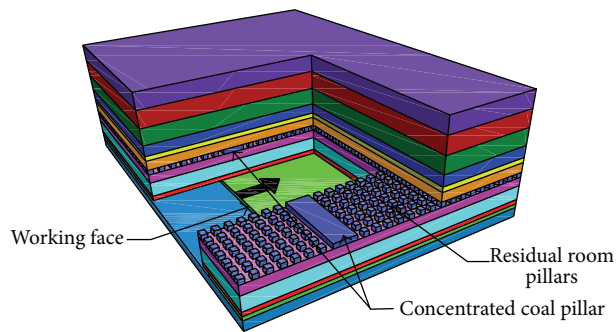


FIGURE 1: Three-dimensional structure of 31201 working face in Shigetai mine.

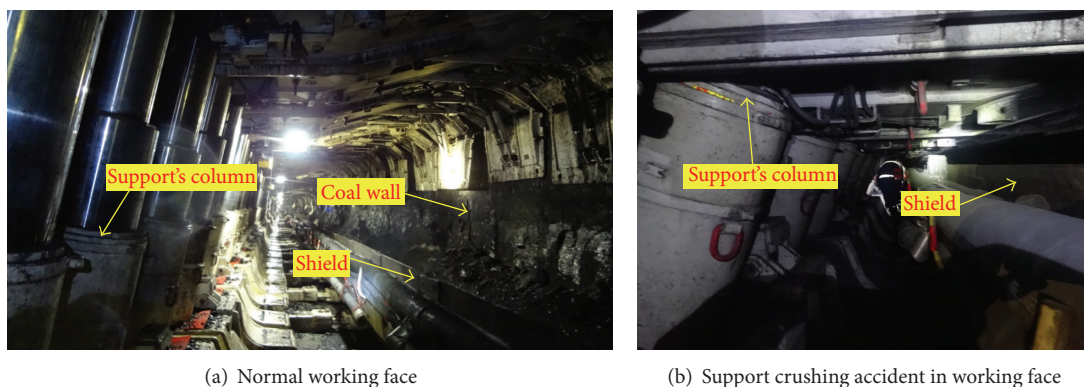


FIGURE 2: Comparison diagram in working face.

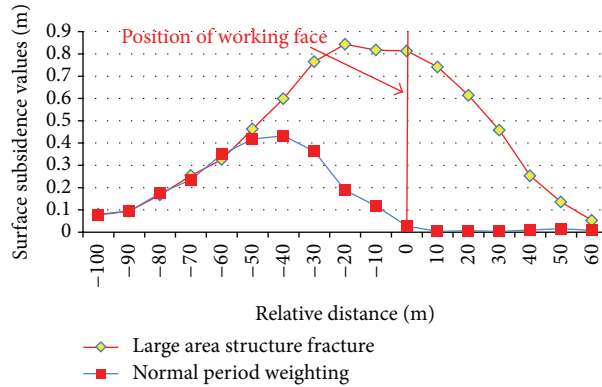


FIGURE 3: Surface subsidence values one day after two kinds of roof weighting.

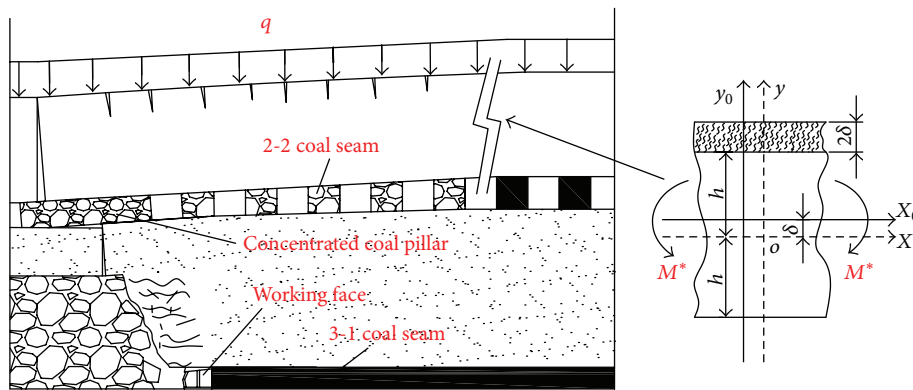


FIGURE 4: Supporting-beam structure damage model.

method will play an important role in guaranteeing life-safety of miners.

3. Damage Energy Model

3.1. Surface Subsidence Features. After roof weighting, surface subsidence values of this day can be obtained by the difference of measuring points altitude values in two neighboring days. For researching the difference between normal period weighting and large area roof weighting, the surface subsidence curve was used to measure roof sinking state in shallow depth seams. Along the middle line in the advancing direction above 31201 working face, measuring points in the surface subsidence curve were arrayed at intervals of 10 m from open-off cut to the stopping line. Figure 3 shows, respectively, curves of surface subsidence values one day after two kinds of roof weighting. It is obviously concluded from Figure 3 that when normal period weighting happens, only surface subsidence values of the measuring points behind the working face are obvious. But after large area structure fracture, obvious surface subsidence values will happen in measuring points in front of and behind the working face, and the values will be much bigger than the values caused by normal period weighting. Due to these phenomena, the difference of the two roof weighting is that large area roof

weighting will cause 2-2 coal seam roof fracturing in front of working face position.

3.2. Supporting-Beam Structure Damage Model. The process of large area roof weighting can be abstracted to a model in the left diagram of Figure 4. The concentrated coal pillar starts to collapse after first roof weighting while mining out of concentrated coal pillar. Due to the high stress transfer process from concentrated coal pillar to residual room pillars, the maximum bending moment value of 2-2 coal seam roof will be gradually increased to its limit. And then, with 2-2 coal seam roof collapsing, large area of bending and sinking would happen in the roof of room and pillar goaf, causing large area of residual room pillars collapse. The weight of concentrated coal pillar and its upper strata would force on all supports in working face suddenly. Finally, the whole process would cause support crushing accident. Thus, the 2-2 coal seam roof plays a key role in support crushing accidents. In order to determine mechanism of these accidents, continuum damage mechanics model is established in maximum bending moment cross section of 2-2 coal seam roof, which is shown in the right diagram of Figure 4.

3.3. Damage Process Energy Analysis. Plenty of researches show that rock will inevitably release energy in the form of acoustic or seismic signals before its irreversible damage.

Each seismic signal contains abundant information about the internal changes of rock mass. Seismic monitoring is a primary requirement for mining in rock burst coal mines. By analyzing the important parameters of seismic signals, such as seismic waves (P-wave and S-wave) initial arrival time, moment, magnitude, and the epicenter coordinates, the reliable and important information for determining coal and rock fracturing energy and the corresponding dynamic disasters warning can be obtained [12].

In the process of roof fracturing, part of energy which is doing work by external force transfers to elastic energy of the structure and another part of it is dissipated by creating new cracks. Energy which can be monitored by microseismic monitoring system is exactly a part of the fracturing energy. So, total energy which can be monitored by microseismic monitoring system is defined by the following function:

$$U = K(W - V), \quad (1)$$

where W denotes the supporting-beam structure doing work by external force and V is elastic energy which is transformed by part of W . K is proportional coefficient of total energy which can be monitored by microseismic monitoring system to total fracturing energy in one roof weighting.

According to fracture mechanics theory [21], the energy release rate formula can be defined as

$$G = \frac{dW}{d\tilde{A}} - \frac{dV}{d\tilde{A}}, \quad (2)$$

where \tilde{A} is the lost area.

Equation (3) can be easily derived from (2) and (1):

$$\frac{dU}{d\tilde{A}} = KG. \quad (3)$$

Damage variable of the supporting-beam structure is given by the relation

$$D = \frac{A_0 - A}{A_0}, \quad (4)$$

where A_0 denotes the initial area of the undamaged section in maximum bending moment cross section and A can be interpreted as the actual area of the cross section.

According to the beam geometry, the lost area \tilde{A} is related by

$$\tilde{A} = A_0 - A. \quad (5)$$

Taking into account (5), by the derivation of (4), (6) can be obtained:

$$\frac{d\tilde{A}}{dD} = A_0. \quad (6)$$

Taking into account (3) and (6), energy data monitored by microseismic monitoring system per unit time is

$$V_U = \frac{dU}{dt} = \frac{dU}{d\tilde{A}} \frac{d\tilde{A}}{dD} \frac{dD}{dt} = KG A_0 \frac{dD}{dt}. \quad (7)$$

In this paper, a formula of the damage evolution time of the supporting-beam structure with the exponential distribution is presented:

$$D(t) = \begin{cases} 0 & (t \leq t^*) \\ ae^{b(t-t^*)} & (t^* \leq t \leq t_{\max}), \end{cases} \quad (8)$$

where both a and b are materials constants, which are related to stress state. t^* is the moment when the stress at $y_0 = h_0$ is maximal and t_{\max} is the moment when h is equal to zero.

Based on the cumulative energy data of microseismic events, (8) and (9) lead to the damage energy model

$$\begin{aligned} U(t) &= \int_0^t V_U dt = KG A_0 D(t) \\ &= \begin{cases} 0 & (t \leq t^*) \\ K A_0 G a e^{b(t-t^*)} & (t^* \leq t \leq t_{\max}). \end{cases} \end{aligned} \quad (9)$$

Due to the fact that $D(t_{\max}) = 1$, $U(t_{\max}) = K_v G A_0 \cdot U(t_{\max})$ is the total cumulative energy which can be monitored by microseismic monitoring system in one roof weighting.

4. Field Applications Analysis

4.1. Microseismic Monitoring System. For monitoring seismic signal of supporting-beam structure while mining, a microseismic monitoring system, named KJ768, which is made by China coal research institution, was installed in 31201 working face. The KJ768 system has sophisticated hardware and powerful software features in data acquisition and data analysis. It is comprised of ground central station, GPS timer, exchanger, power, substation, and sensors. Series and parallel layout are shown in Figure 5.

Once the amount of sensors to be installed in 31201 working face is determined, it is necessary to conduct a reasonable arrangement of the sensors. Through theoretical analysis and field observation, the ultimate optimal arrangement and distribution of the twenty sensors are shown in Figure 6. Those twenty sensors are connected to three substations. With the advance of 31201 working face, the sensors will be moved forward one by one from one period to the next period and the width of every period is 210 m. In Figure 6, four black sensors in ground surface are connected to one substation, five blue sensors in coal wall of air-return roadway and two red sensors in roof of air-return roadway are connected to one substation, and five blue sensors in coal wall of belt roadway and two red sensors in roof of auxiliary haulage roadway are connected to one substation.

The processing system in the central station digitizes the data with a sampling frequency of 60 kHz and performs preliminary event detection when the recorded signals of three substations exceed a given threshold. Example waveforms of one artificial blasting test are shown in Figure 7, so constant P-wave and S-wave velocities are initially estimated from artificial blasting tests and used to calculate event locations. Then, the traces can be used to evaluate the energy size as well as the location of the event.

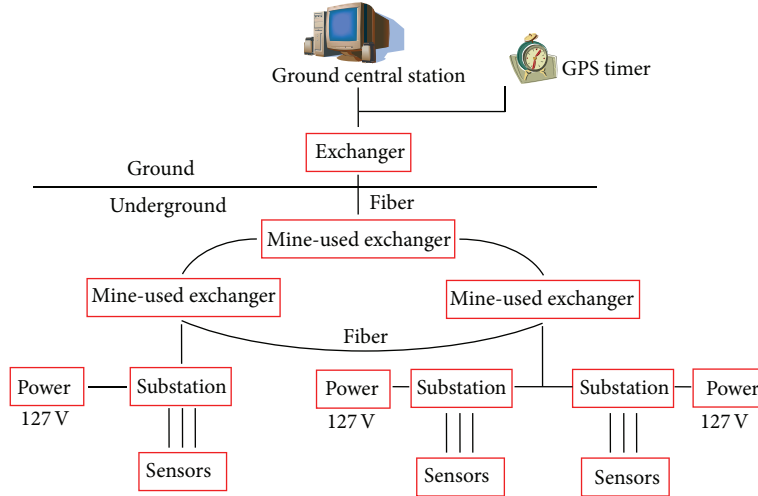


FIGURE 5: Example waveforms of a microseismic event recorded in artificial blasting test.

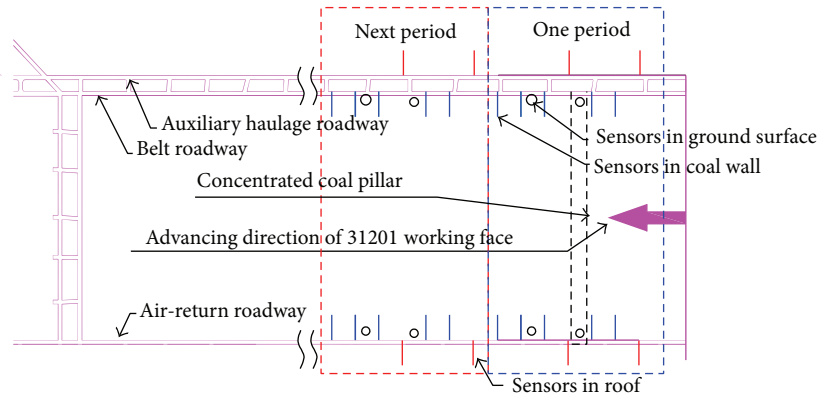


FIGURE 6: Sensors arrangement and distribution.

4.2. Damage Energy Application. The energy of microseismic events during the process of two supports crushing accidents that happened separately on the 20th of April and 22nd of April was monitored by KJ768. The relevant data of these processes are shown in Tables 2 and 3.

The curve of cumulative energy data of two large area roof weighting is described in Figure 8 by the data in Tables 2 and 3. The result of curve fit analysis by damage energy model is shown in Table 4. Indexes of SSE, *R*-square, and RMSE indicate that fitting effects are very satisfactory. So, the damage energy model is suitable for describing variation law of cumulative energy which can be monitored by microseismic monitoring system in one roof weighting.

According to Figure 8, when the cumulative energy value of microseismic events was more than max cumulative energy value of microseismic events $U_{P_{max}}$ in normal roof weighting, the field monitoring process entered into warning region. Because time in damage energy model obeyed exponential distributions, when the cumulative energy value of microseismic events was more than $U_{P_{max}}$ and condition which was $U(t_1) > U(t_2) > U(t_{max})$ satisfied $t_1 > t_2$, a warning message was sent to inform miners escaping from the dangerous area

in working face. After ending warning region, roof weighting appeared and caused supports crushing accident. Fortunately, thanks to the effective early warning method, life-safety of miners was guaranteed in these accidents. Thus, for life-safety of miners, warning time and escaping time must be sufficient in warning region.

4.3. Warning Area Analysis. For brittle material, damage evolution law equation can be assumed as follows:

$$\dot{D} = C \left(\frac{\sigma}{1-D} \right)^v, \quad (10)$$

where σ is the normal stress and both c and v are the materials constant.

According to supporting-beam structure damage model in Figure 4, at the stage of latent fracture, the normal stress in maximum bending moment cross section is given by

$$\sigma = \frac{M^*}{I_{m0}} y_0^u, \quad (11)$$

TABLE 2: Microseismic monitoring data on the 20th of April.

Time	Energy/J	Time	Energy/J	Time	Energy/J	Time	Energy/J
8:09:04	4.30E + 04	15:03:49	4.80E + 04	16:04:04	4.40E + 04	17:00:44	4.10E + 04
8:10:19	3.70E + 04	15:08:29	4.10E + 04	16:09:29	5.20E + 04	17:01:04	4.20E + 04
8:51:19	4.20E + 04	15:20:29	3.80E + 04	16:12:14	2.60E + 04	17:02:04	5.10E + 04
9:47:54	3.30E + 04	15:21:04	4.20E + 04	16:14:44	4.80E + 04	17:02:14	4.70E + 04
9:51:14	2.20E + 04	15:21:44	3.20E + 04	16:21:54	4.60E + 04	17:03:09	3.80E + 04
11:26:14	5.60E + 04	15:25:04	3.50E + 04	16:26:34	6.10E + 04	17:04:54	4.60E + 04
12:20:29	5.00E + 04	15:25:24	4.30E + 04	16:32:09	4.60E + 04	17:05:14	4.50E + 04
12:36:54	4.40E + 04	15:28:19	4.40E + 04	16:34:14	4.70E + 04	17:05:19	3.70E + 04
12:38:14	5.10E + 04	15:31:34	3.00E + 04	16:38:49	5.10E + 04	17:06:29	3.30E + 04
13:08:24	2.10E + 04	15:36:24	4.20E + 04	16:41:24	4.10E + 04	17:06:54	3.30E + 04
14:16:14	4.20E + 04	15:38:59	5.20E + 04	16:41:44	6.40E + 04	17:06:59	5.10E + 04
14:20:39	4.30E + 04	15:40:49	4.80E + 04	16:43:19	3.50E + 04	17:07:04	3.30E + 04
14:27:44	3.80E + 04	15:45:04	4.00E + 04	16:51:44	4.50E + 04	17:07:39	3.00E + 04
14:35:49	3.90E + 04	15:45:54	4.70E + 04	16:52:04	4.40E + 04	17:07:59	5.90E + 04
14:39:39	2.80E + 04	15:54:39	3.50E + 04	16:54:29	5.90E + 04	17:08:19	5.20E + 04
14:55:24	4.20E + 04	15:56:09	6.20E + 04	16:58:39	4.70E + 04	17:08:29	4.70E + 04
14:55:44	4.60E + 04	16:02:49	5.00E + 04	17:00:19	3.80E + 04	17:09:14	3.30E + 04

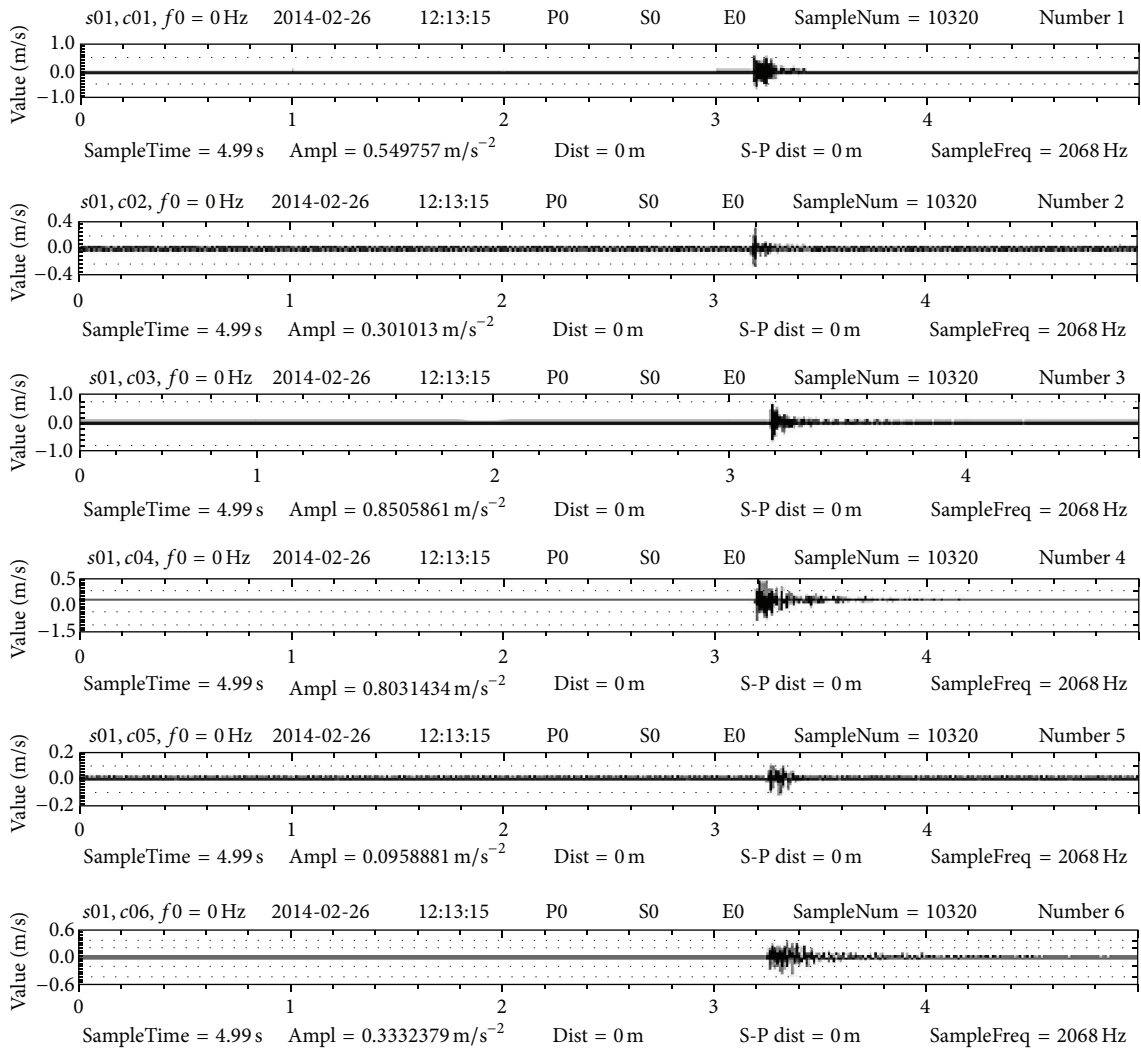


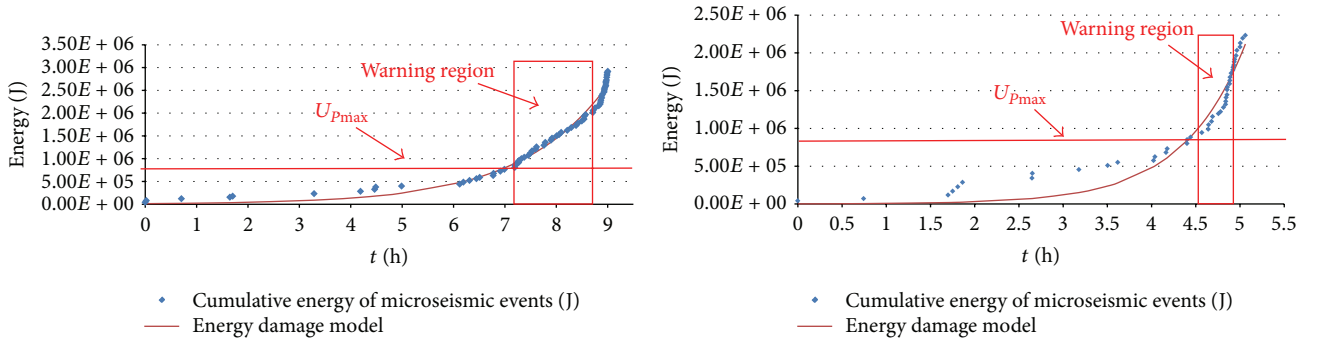
FIGURE 7: Example waveforms of a microseismic event recorded in artificial blasting test.

TABLE 3: Microseismic monitoring data on the 22nd of April.

Time	Energy/J	Time	Energy/J	Time	Energy/J	Time	Energy/J
17:38	4.20E + 04	21:40	5.00E + 04	22:25	2.60E + 04	22:33	4.20E + 04
18:23	2.90E + 04	21:48	5.70E + 04	22:27	5.70E + 04	22:33	3.50E + 04
19:20	4.80E + 04	21:49	5.00E + 04	22:28	3.90E + 04	22:34	3.00E + 04
19:23	5.00E + 04	22:02	6.90E + 04	22:28	4.00E + 04	22:34	4.30E + 04
19:27	5.80E + 04	22:02	5.10E + 04	22:29	5.20E + 04	22:35	3.30E + 04
19:30	6.00E + 04	22:05	3.20E + 04	22:29	3.60E + 04	22:35	5.00E + 04
20:17	5.60E + 04	22:12	6.10E + 04	22:29	6.60E + 04	22:36	6.90E + 04
20:17	6.30E + 04	22:17	4.50E + 04	22:30	3.60E + 04	22:38	4.40E + 04
20:49	5.00E + 04	22:17	5.80E + 04	22:31	4.30E + 04	22:38	5.30E + 04
21:08	5.40E + 04	22:19	4.50E + 04	22:31	4.40E + 04	22:40	6.40E + 04
21:15	4.10E + 04	22:19	6.40E + 04	22:31	4.40E + 04	22:42	3.80E + 04
21:39	2.40E + 04	22:23	3.90E + 04	22:32	5.30E + 04		

TABLE 4: Fitting parameters.

Date	$U(t_{\max})/J$	a	b	Goodness of fit		
				SSE	R-square	RMSE
20th of April	2.92e + 06	4.35e - 03	0.592	8.539e + 11	0.983	1.137e + 05
22nd of April	2.23e + 06	7.78e - 04	1.404	1.161e + 12	0.9401	1.606e + 05



(a) Large area structural instability process during low-speed mining on the 20th of April

(b) Large area structural instability process during high-speed mining on the 22nd of April

FIGURE 8: Energy damage process comparisons between low-speed mining and high-speed mining.

where M^* is the maximum bending moment in supporting-beam structure and u is the materials constant. I_{m0} is the generalized moment of inertia.

According to the damage mechanics theory [22], latent fracture time when the stress reaches maximum is

$$t^* = \left[(\nu + 1) C \left(\frac{M^*}{I_{m0}} \right)^\nu h_0^{u\nu} \right]^{-1}, \quad (12)$$

where h_0 is the initial height of the undamaged section in maximum bending moment cross section.

At $h = 0$, the beam structure is completely fractured, and the corresponding time of fracture is

$$t = \frac{2n+1}{2n-1} t^* = \frac{(2n+1) I_{m0}^\nu}{(2n-1) (\nu+1) C h_0^{u\nu} M^{*\nu}}. \quad (13)$$

According to formula (13), damage time which the beam structure needs to be completely fractured will be decreased

in exponential level with the increase of the max bending moment M^* . It can be concluded from Figure 8 that, in the process of high-speed mining, observation time in warning area was only about half an hour, but observation time in warning area was increased rapidly to an hour and a half in the process of low-speed mining. Therefore, for increasing the finite observation time in warning area, the method of decreasing the max bending moment increasing speed by controlling mining speed was applied to obtain more time in warning area in the next similar situation.

5. Conclusion

Aiming at strong strata behaviors in shallow coal seam while mining out of the concentrated coal pillar in Shigetai coal mine of Shenhua group, microseismic monitoring system is

for the first time applied in shallow coal seam. According to the features of ground surface subsidence, the supporting-beam structure damage model is established. Based on the damage mechanics correlation theory, formula of energy damage model is deduced to describe the change laws of cumulative energy of microseismic events. Using energy data of two support crushing accidents, parameters of the formula are obtained by fitting test and an effective early warning method of these accidents is determined by the laws of formula. By adopting the microseismic monitoring system and mining speed controlling method while mining out of the concentrated coal pillar, the early warning method has successfully avoided miner suffering from all support crushing accidents in Shigetai coal mine.

Conflict of Interests

The authors declare that there is no conflict of interests regarding the publication of this paper.

Acknowledgments

This work was financially supported by the National Science and Technology Major Program of China (2011ZX05040-002), the International Science & Technology Cooperation Program of China (2011DFA61790), and the National Natural Science Foundation of China (51174272).

References

- [1] F. Wang, S. Tu, Y. Yuan, Y. Feng, F. Chen, and H. Tu, "Deep-hole pre-split blasting mechanism and its application for controlled roof caving in shallow depth seams," *International Journal of Rock Mechanics and Mining Sciences*, vol. 64, pp. 112–121, 2013.
- [2] Q. Bai, S. Tu, F. Wang, and Y. Yuan, "Stress evolution and induced accidents mechanism in shallow coal seam in proximity underlying the room mining residual pillars," *Chinese Journal of Rock Mechanics and Engineering*, vol. 31, no. 2, pp. 3772–3778, 2012.
- [3] S. H. Tu, F. J. Dou, Z. J. Wan, F. T. Wang, and Y. Yuan, "Strata control technology of the fully mechanized face in shallow coal seam close to the above room-and-pillar gob," *Journal of the China Coal Society*, vol. 36, no. 3, pp. 366–370, 2011.
- [4] J.-F. Ju, J.-L. Xu, W.-B. Zhu, and X.-Z. Wang, "Mechanism of strong strata behaviors during the working face out of the upper dip coal pillar in contiguous seams," *Journal of the China Coal Society*, vol. 35, no. 1, pp. 15–20, 2010.
- [5] J.-F. Ju and J.-L. Xu, "Influence of leading instability in the upper dip coal pillar boundary to the strong strata behaviors during the working face out of the pillar," *Journal of the China Coal Society*, vol. 37, no. 7, pp. 1080–1087, 2012.
- [6] J.-F. Ju and J.-L. Xu, "Prevention measures for support crushing while mining out the upper coal pillar in close distance shallow seams," *Journal of Mining and Safety Engineering*, vol. 30, no. 3, pp. 323–330, 2013.
- [7] N. W. Xu, C. A. Tang, L. C. Li et al., "Microseismic monitoring and stability analysis of the left bank slope in Jinping first stage hydropower station in southwestern China," *International Journal of Rock Mechanics and Mining Sciences*, vol. 48, no. 6, pp. 950–963, 2011.
- [8] L.-M. Dou, J. He, S.-Y. Gong, Y.-F. Song, and H. Liu, "A case study of micro-seismic monitoring: goaf water-inrush dynamic hazards," *Journal of China University of Mining & Technology*, vol. 41, no. 1, pp. 20–25, 2012.
- [9] F. Jiang, G. Ye, C. Wang, D. Zhang, and Y. Guan, "Application of high-precision microseismic monitoring technique to water inrush monitoring in coal mine," *Chinese Journal of Rock Mechanics and Engineering*, vol. 27, no. 9, pp. 1932–1938, 2008.
- [10] C. Liu, C. Tang, L. Li, Z. Liang, and S. Zhang, "Analysis of probability of water inrush from grout curtain based on background stress field and microseismicity," *Chinese Journal of Rock Mechanics and Engineering*, vol. 28, no. 2, pp. 366–372, 2009.
- [11] J. Jiang, P. Zhang, L. Nie, H. Li, L. Xu, and W. Wang, "Fracturing and dynamic response of high and thick stratas of hard rocks," *Chinese Journal of Rock Mechanics and Engineering*, vol. 33, no. 7, pp. 1366–1374, 2014.
- [12] C.-P. Lu and L.-M. Dou, "The relationship between vertical stress gradient, seismic, and electromagnetic emission signals at Sanhejian coal mine, China," *International Journal of Rock Mechanics & Mining Sciences*, vol. 70, pp. 90–100, 2014.
- [13] Y.-X. Xia, L.-J. Kang, Q.-X. Qi et al., "Five indexes of microseismic and their application in rock burst forecastion," *Journal of the China Coal Society*, vol. 35, no. 12, pp. 2011–2016, 2010.
- [14] Q. Zhu, F. Jiang, Z. Yu, Y. Yin, and L. Lu, "Study on energy distribution characters about blasting vibration and rock fracture microseismic signal," *Chinese Journal of Rock Mechanics and Engineering*, vol. 31, no. 4, pp. 723–730, 2012.
- [15] C. Lu, L. Dou, X. Guo, B. Liu, Z. Lu, and J. Fan, "Frequency-spectrum characters of microseismic signals induced by roof stratum fracture," *Chinese Journal of Rock Mechanics and Engineering*, vol. 29, no. 5, pp. 1017–1022, 2010.
- [16] R. Yuan and H. Li, "Distribution of microseismic signal and discrimination of portentous information of pillar type rockburst," *Chinese Journal of Rock Mechanics and Engineering*, vol. 31, no. 1, pp. 80–85, 2012.
- [17] R. Peng, H. Xie, and Y. Ju, "Analysis of energy dissipation and damage evolution of sandstone during tensile process," *Chinese Journal of Rock Mechanics and Engineering*, vol. 26, no. 12, pp. 2526–2531, 2007.
- [18] W. Wang, J. Lu, H. Wang, and S. Sun, "A rheological damage model of sandstone and its application to engineering," *Chinese Journal of Rock Mechanics and Engineering*, vol. 31, no. 2, pp. 3650–3658, 2012.
- [19] S. Zhang, E. Liu, and J. Zhang, "Experimental study of fatigue damage properties of sandstone samples under cyclic loading with low frequencies," *Chinese Journal of Rock Mechanics and Engineering*, vol. 33, no. 1, pp. 3212–3218, 2014.
- [20] Y. Yang, D. Wang, M. Guo, and B. Li, "Study of rock damage characteristics based on acoustic emission tests under triaxial compression," *Chinese Journal of Rock Mechanics and Engineering*, vol. 33, no. 1, pp. 98–104, 2014.
- [21] C. Shen, *Fracture Mechanics*, Tongji University Press, Shanghai, China, 1996.
- [22] S. Yu and X. Feng, *Damage Mechanics*, Tsinghua University Press, Beijing, China, 1997.

Research Article

Mechanism of Roof Shock in Longwall Coal Mining under Surface Gully

Gangwei Fan, Dongsheng Zhang, and Xufeng Wang

School of Mines, Key Laboratory of Deep Coal Resource Mining, Ministry of Education of China, China University of Mining & Technology, Xuzhou 221116, China

Correspondence should be addressed to Dongsheng Zhang; zdscumt@126.com

Received 10 November 2014; Revised 21 February 2015; Accepted 23 February 2015

Academic Editor: Shimin Liu

Copyright © 2015 Gangwei Fan et al. This is an open access article distributed under the Creative Commons Attribution License, which permits unrestricted use, distribution, and reproduction in any medium, provided the original work is properly cited.

The paper presents an interpretation on the abnormal roof shock in longwall coal mining under gullies using physical modeling, numerical modeling, and mechanical analysis. The modeling results show that the roof movement causes the shock load onto the stope in longwall coal mining under surface gully. The triggering mechanism of shock load depends on the direction of the face retreat with respect to the bottom of the surface gully. The slope tends to slide along the interface plane with a long periodical weighting intervals when mining towards the bottom of the gully (downslope direction), while the overburden strata may be split into blocks and tend to topple towards the free face of gully when mining away from the bottom of the gully (upslope direction). The mechanical models showed that, during the period of mining in downslope direction, planar sliding and key fragmental blocks cause a sudden roof shearing off which could result in shock load and, during the period of mining in upslope direction, the overburden blocks may become unstable due to shearing off which could result in large shock pressure onto the stope.

1. Introduction

With the development of coal mining technology and equipment in China, the mining scale becomes larger and larger. And the center of coal resource exploitation has transferred to western coalfield, where there is rich coal resource [1, 2]. The coal is shallow, thick, and excellent in quality. For example, Shenfu-Dongsheng coalfield with 223.6 billion tons coal in proved reserves is the biggest coalfield in China and one of seven biggest coalfields in the world [3]. However, the ground surface is bare and has been subjected to serious water erosion for long time, resulting in that wide spread of surface gullies, especially in Northwest of China. The gully depth may exceed 100 m.

Abnormal phenomena such as coal bump and roof shock are observed in shallow longwalls under gullies. In Dongsheng coalfield, sudden spalling of barrier pillars and crushing of face hydraulic supports without warning frequently occurred in underground stopes (see Figure 1). These events cannot be explained according to traditional theories on coal mine ground pressure [4–6]. In general, coal and/or rock bump usually occurs in deep coal mining due to the super-high ground pressure [5–7]. As the mining depth in

this region is less than 200 m, the absolute ground pressure is not great enough to trigger a coal or rock bump. It is found that most of these dynamic events are involved in coal mines operated under surface gullies. Therefore, the slope movement of gullies is thought of as an additional factor resulting in the abnormal underground pressure.

Many researchers studied the influence of underground mining on surface slope [8–15]. It is accepted that underground mining may cause surface slope sliding or even geological disaster. The effect of surface topography on underground mining was rarely taken into consideration in the previous researches, but it is sensitive and strong and, at times, can play a dominant role on ground pressure in shallow coal seam mining under surface gully. Therefore, it is very urgent and important to clearly understand the mining-induced roof shock in gully areas.

2. Mechanisms of Overburden Movement

Based on the geological condition of Houhayewusu Gully at Nalinmiao number 2 Coal Mine, physical simulation and numerical modeling were conducted to analyze the effect of



FIGURE 1: The abnormal phenomena in underground mining under gullies. (a) Pillar gets inclined and spalls; (b) slope rock is broken and bare.

TABLE 1: Key properties of the overlying rock.

Lithology	Thickness /m	Density /kg·m ⁻³	Young's modulus /GPa	Cohesion /MPa	Friction angle /°	Poisson's ratio
Loess	10	1810	—	—	—	—
Mudstone	3.5	2500	15	1.5	30	0.3
Fine sandstone	8	2600	35	2.2	33	0.2
Sandy mudstone	11	2510	16	1.8	32	0.25
Fine sandstone	12	2545	23	2.1	34	0.22
Sandy mudstone	9	2510	16	1.6	32	0.25
Fine sandstone	20	2600	38	2.6	35	0.2
Sandy mudstone	2.5	2510	16	1.6	32	0.25
Fine sandstone	8	2600	38	2.6	35	0.2
Sandy mudstone	0.5	2510	16	1.6	32	0.25
Coal	6.5	1370	39	2.3	34	0.23
Siltstone	4	2580	42	2.6	36	0.22

underground coal mining on the overburden movement at gully area.

2.1. Geology. The coal measure is mainly as Jurassic formations which is covered with Quaternary unconsolidated layers. The coal seam is 6.5 m thick and the overlying bedrock is 74.5 m thick. A 10-meter-thick loess overlays the bedrock. The maximum depth of gully is 73.5 m and the average slope of gully is 30° (see Figure 2). The generalized stratigraphy at the studied area is shown in Figure 3. The overlying bedrock is predominantly composed of fine sandstone and sandy mudstone, and most of them are involved in the gully. The properties of overlying strata are shown in Table 1.

2.2. Physical Simulation. Physical modeling is a scale modeling in which rock strata and mine structures are simulated using scaled artificial materials. Physical simulation can realistically model the layered structures and their failure modes, much like that observed in underground coal mines, and strata movement can be observed directly in real time [5].

2.2.1. Model Setup. Simulated material selection is of great importance for modeling the mining-induced overburden



FIGURE 2: A photo of Houhayewusu Gully at underground mining area.

movement. The material is always mixed by the aggregate and the adhesive. Sand is generally used as the aggregate. The most popular materials used as the adhesives are gypsum, cement, calcium carbonate (CaCO₃), lime, and kaolin [16]. In this paper, sand, gypsum, and calcium carbonate were selected as the mixed materials in some given proportions. According to the widely accepted results on the mix proportions among sand, gypsum, and calcium carbonate [16], the mix design of

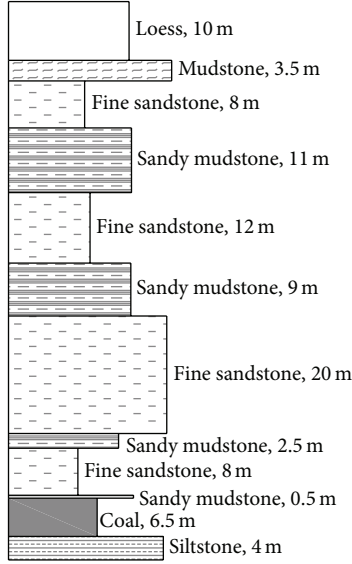


FIGURE 3: Generalized geological column at studied area.

TABLE 2: The mix proportion of simulated materials.

Lithology	Sand /kg	CaCO ₃ /kg	Gypsum /kg	Water /kg	Sawdust /kg
Loess	95.8	6.8	6.8	18.8	3.4
Mudstone	44.6	5.2	2.2	6.5	/
Fine sandstone	105.8	10.6	10.6	15.9	/
Sandy mudstone	160.4	22.5	9.6	24.1	/
Fine sandstone	175.3	40.9	17.5	33.4	/
Sandy mudstone	159.6	22.3	9.6	23.9	/
Fine sandstone	356.7	59.4	59.4	67.9	/
Sandy mudstone	53.1	7.4	3.2	8.0	/
Fine sandstone	153.0	25.5	25.5	29.1	/
Sandy mudstone	10.6	1.5	0.6	1.6	/
Coal	138.1	19.3	8.3	20.7	/
Siltstone	76.5	12.8	12.8	14.6	/

different layers is listed in Table 2. Wood sawdust was mixed with the above three materials to simulate loess material.

The geometric scale (α_l) of this model is defined as 1:100 to the real. The gully is shaped like “V” in the model. The model frame is 5 m long, 0.3 m wide, and 0.95 m high. The slope angle of gully is 30°. 5 cm × 5 cm grid was painted on the surface of model (see Figure 4). According to the scale model theory, the similarity scale of gravity (α_γ) is about 1:1.67, and the similarity scale of stress $\alpha_s = \alpha_l \times \alpha_\gamma = 1:167$. The excavation was conducted from the left to the right. The mining height is 6.5 cm and the excavation web is 5 cm. The total mining void is 420 cm long.

2.2.2. Modeling Result. The physical modeling was conducted in two stages (see Figure 4).

- (1) Downslope stage, in which the coalface is advancing in the downslope direction and the gob is getting close

with the bottom gully. Typical overburden movement was observed until the coalface is located underneath the slope. Figure 5 shows some scenes of overburden movement in downslope mining stage. When the coalface was at 160 m away from the setup line, a downward crack appeared at the surface. Meanwhile, the overlying slope subsided and slipped towards gully due to lack of horizontal confinement. The interfaces were seriously broken with significant planar sliding. The roof breakage interval became longer, which may result in a roof shock in underground if the roof suddenly collapses down (see Figure 5(a)). When the coalface approached the bottom of the gully, the roof sheared off along the coalface (see Figure 5(b)), which may also initiate a shock load onto the face support.

- (2) Upslope stage, in which the coalface is advancing in the upslope direction away from the gully. After the coalface passed the bottom of the gully and moved away from the gully, a crack linking the slope with the gob developed in the roof. Figure 6 shows a scene of overburden movement in upslope mining stage. The broken roof was cut into blocks by gully and mining-induced cracks. The formed blocks rotated towards the gob, and sometimes it is hinged above the retreating face. However, the hinged structure lost the stability in a short time as the broken block sheared off along the hinged point, which may also trigger a roof shock onto the face hydraulic support.

2.3. Numerical Modeling. FLAC (Fast Lagrangian Analysis of Continua) software was used to analyze the mechanism of slope movement. The constructed numerical model was shown in Figure 7. The geological column is based on the generalized stratigraphy shown in Figure 3. The Mohr-Coulomb criterion was employed to estimate the failure of rocks. The physical and mechanical parameters of the overlying strata used in FLAC model are listed in Table 1. The left, the right, and the bottom boundaries of the model are fixed, and the top boundary is free.

2.3.1. Model Calibration. The mechanical behavior of caved zone (gob) greatly affects the overburden movement. An appropriate gob model is crucial to analyze the mechanical mechanism of slope deformation in response to underground mining. Salamon’s model developed by Salamon is useful to understand the compaction characteristics of caved rock in gob [17], which is widely accepted by many researchers [5]. Salamon’s model assumes the following strain hardening model for gob material:

$$\sigma = \frac{E_0 \varepsilon}{1 - \varepsilon/\varepsilon_m},$$

$$\varepsilon_m = \frac{b-1}{b}, \quad (1)$$

$$E_0 = \frac{10.39 \sigma_c^{1.042}}{b^{7.7}},$$

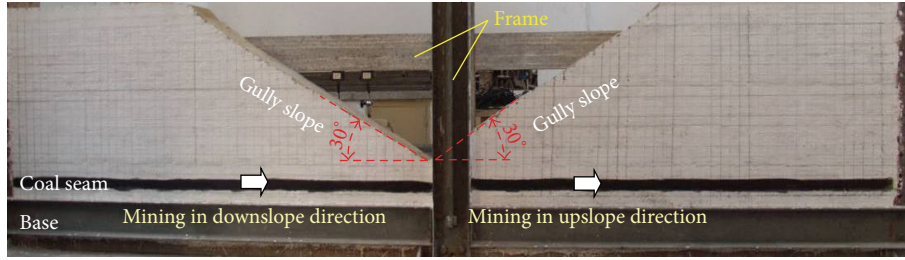


FIGURE 4: The original model for the physical experiment.

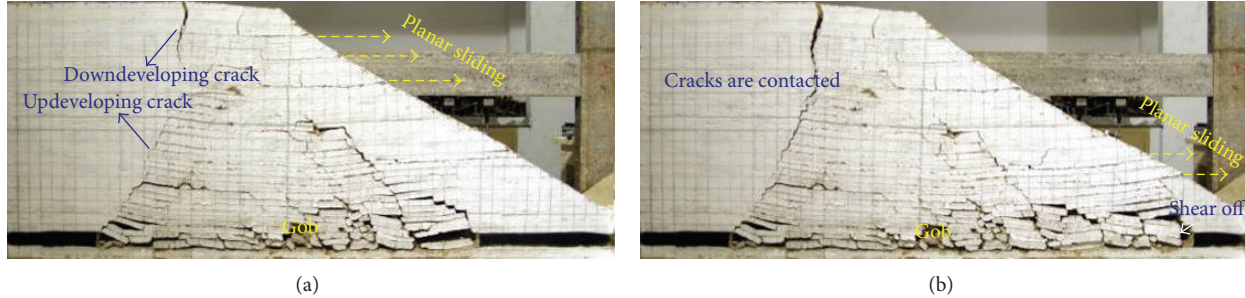


FIGURE 5: The overburden movement in response to underground mining in downslope direction. (a) The slope slid obviously layer by layer. (b) The roof sheared off along the coalface.

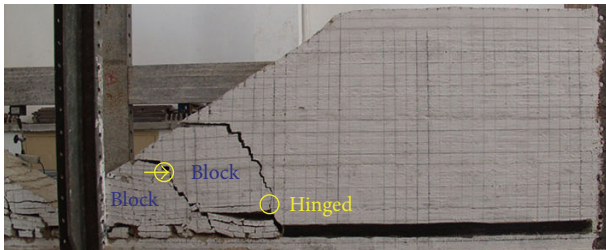


FIGURE 6: The overburden movement in response to underground mining in upslope direction.

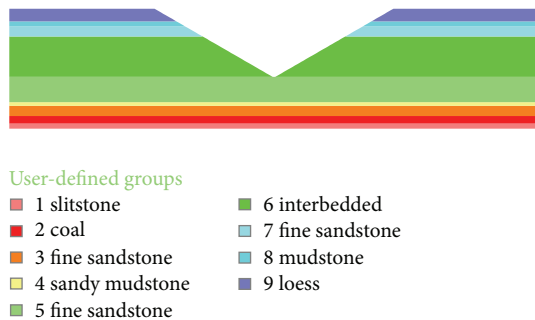


FIGURE 7: The model for FLAC modeling.

where b is the bulking factor, ϵ_0 is the compaction strain, and E_0 is the initial gob modulus.

However, there is no ready-made model for Salamon's model in FLAC. Double yield material model was selected to simulate Salamon's model. A process of trial and error is used to match the stress-strain curve of Salamon's model to

that of the double yield model [5], resulting in a set of input parameters for converting Salamon's model to the double yield model (Tables 3 and 4).

Figure 8 shows the stress-strain behavior of a simple cube gob model of 10 cm thick loaded at the top at a constant velocity using the input data listed in Tables 3 and 4. It shows a good match between the results of FLAC simulation and Salamon's model.

2.3.2. Modeling Result. Downslope stage: the distribution of equivalent plastic stain in the overlying strata was plotted in Figure 9(a) to analyze the fracture development. The fractures in the overlying strata developed upward from the gob, while the surface fractures extended downward. When the coalface was at 42 m away from the bottom of the gully, shear failure was observed at the slope of the gully associated with horizontal slippage at the bedding planes. When the coalface was at 12 m away from the bottom of the gully, the upward and downward fractures became connected and the fractures at bedding planes reached the slope of the gully. When the coalface was 6 m away from the bottom of gully, the overlying strata sheared off along the face line.

Upslope stage: after the coalface passed the gully, the overburden moved in different patterns (see Figure 9(b)). When the coalface advanced at 36 m away from the gully, most of rock overlying the coalface was fractured and yields in tension or shear. The angle between the fractured rock and the horizontal line is less than 20°. When the coalface is at 60 m away from the gully bottom, the overlying strata are split into polygons by a fractured zone which connects the slope surface with the coalface. The same phenomena repeated in every face retreat in the upslope stage.

TABLE 3: Input parameters for the double yield model.

Property	Density, kg/m ³	Shear modulus, Pa	Bulk modulus, Pa	Friction angle, °	Dilation angle, °
Value	2410	1.19e10	1.35e10	10	5

TABLE 4: Volumetric strain-hydrostatic pressure relationship of the gob material.

Volumetric strain	Hydrostatic pressure, Pa	Volumetric strain	Hydrostatic pressure, Pa
0	0	0.12	17725587.81
0.01	711498.289	0.13	21284942.79
0.02	1493364.541	0.14	25710086.82
0.03	2356581.038	0.15	31360655.35
0.04	3314540.81	0.16	38827478.06
0.05	4383747.523	0.17	49153934.99
0.06	5584774.241	0.18	64371871.52
0.07	6943600.091	0.19	89035423.82
0.08	8493510.825	0.20	135896173.2
0.09	10277861.84	0.21	259438148.8
0.10	10277861.84	0.22	1494857905
0.11	14800573.32		

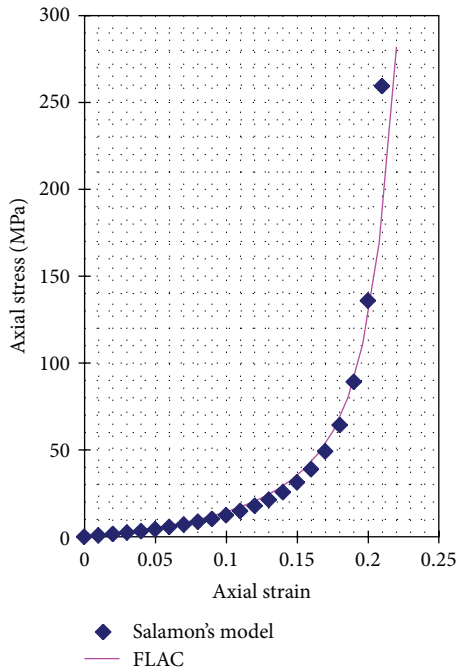


FIGURE 8: Stress-strain curve of the gob model.

3. Mechanisms and Control of Roof Shock

The roof shock and coal bump in this case are mainly caused by the sudden loss of roof structural stability. The mechanisms of roof shock can be understood after the mechanical analysis on roof structure.

Downslope stage: the physical and numerical modeling results show that when the coalface becomes underneath the gully, the overlying strata may slide towards the gully along the interface planes, and subsequently, the roof may shear off along the face line. The slope of the gully is considered

an additional free surface to the fractured blocks at overburden strata. The fractured zone in the overburden strata can be assumed as a beam which breaks into blocks (A, B, and C, Figure 10(a)) in response to underground mining [18]. Block B is stable due to the compressive forces applied from blocks C and A. Block A loses the horizontal confinement from the right side when the compressive force between blocks A and B is greater than the total shear strength at the upper and the lower interfaces. Block A may slide towards the gully and, hence, block B will lose the stability and shear off at the contact between blocks A and B. Consequently, a roof shock occurs.

In order to calculate the compressive forces, a free body diagram for blocks B and C was constructed as shown in Figure 10(b). P_B and P_C are the applied forces on blocks B and C, respectively. l_B and l_C identify the assumed positions of blocks B and C where forces P_B and P_C act on the blocks, respectively. Q_A , Q_B are the shear force at the hinged contacts between blocks. The lengths of blocks B and C are the periodical weighting interval, say l . R_C is the supporting force of caved rock onto block C. T is the horizontal compressive force between A and B. θ_B and θ_C are the rotation angles of blocks B and C, respectively. a is the height of contact face between blocks A and B.

According to the key strata theory [7] and mechanical analysis,

$$\begin{aligned}
 & Q_B [l \cos(\theta_B - \theta_C) + h \sin(\theta_B - \theta_C) + l] \\
 & + T [h - a - l(\sin \theta_B + \sin \theta_C)] \\
 & = P_B \left[l_B \cos \theta_B + \left(h - \frac{a}{2} \right) \sin \theta_B \right] \quad (2)
 \end{aligned}$$

$$Q_A + Q_B = P_B$$

$$Tl \sin \theta_C = Q_B l,$$

where h means the thickness of the studied roof beam.

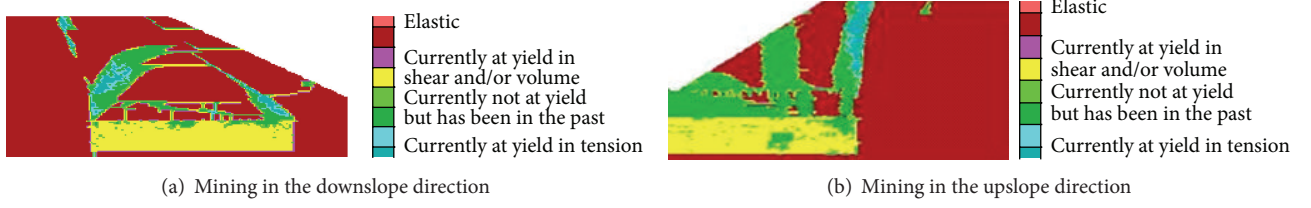


FIGURE 9: The failure status when mining under gully.

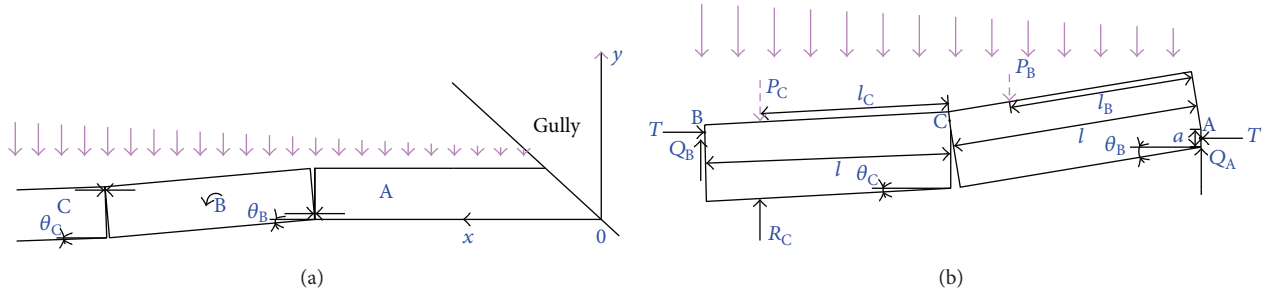


FIGURE 10: Mechanical model for roof beam when mining in downslope direction. (a) The assumed mechanical model; (b) mechanical analysis on blocks B and C.

Solving T from (2),

$$T = P_B \frac{3L + 2l}{6L + 3li + 2 \sin(\theta_B/4) - \sin \theta_B}, \quad (3)$$

where $\sin^2(\theta_B/8)$ approximates 0 and is thus omitted; i means the fragmentation degree of the block and is defined by $i = h/l$.

Focusing on block A, the maximum friction force or the shear strength of the interfaces can be estimated by [19]

$$F = cL + \frac{1}{2} \rho g L^2 \tan \alpha \tan \varphi, \quad (4)$$

where L is the length of block A, c is the cohesion of the interfaces, ρ is the density of block A, g is the gravity acceleration, α is the slope angle of gully, and φ is the friction angle of the interface.

In order to keep block A out of sliding, the shear strength of the interfaces between the adjacent strata and block A should be greater than the compressive force; then

$$\tan \alpha \leq \frac{2cL}{2\rho gl(3L + 2l)/3(i + 2 \sin(\theta_B/4) - \sin \theta_B) - \rho g L^2 \tan \varphi}. \quad (5)$$

According to (5), the smaller the gully angle or the rotation degree of block B gets, the less likely block sliding and roof shock occur. Therefore, the block sliding can be controlled by lowering the mining height which will reduce the rotation angle significantly [19].

Upslope stage: the above simulations show that the slope is cut into blocks by large mining-induced cracks and tends to topple when mining in the upslope direction. A hinged

structure forms but is less stable. As the face continues to advance, the block may shear off and the structure disappears, which may result in a serious shock in underground.

In order to understand the structure stability, a mechanical model focusing on two key blocks was constructed as Figure 11 shows. G_1 and G_2 are the self-gravity of blocks A and B, respectively. R_2 is the supporting force of caved rock onto block #2. θ is the rotation angle of block #2. a represents the height of the contact between blocks. Q_A , Q_B are the shear force at the hinged contacts between blocks. w is the subsidence of block #2. α is the slope angle. H_1 , H_2 , and H_3 are the heights of the blocks. L is the length of the blocks.

According to the key strata theory [7, 18],

$$\begin{aligned} \frac{T}{G_1} &= \left(\frac{1}{2} - \frac{\tan \alpha}{12i} \right) \\ &\cdot \left((i - \tan \alpha) \left(\frac{1}{2} + \tan \alpha \tan \theta \right) \right. \\ &\left. + \left(\frac{1}{\cos \theta} + \frac{\sin \theta}{2} \right) - \sin \theta_{\max} \right)^{-1}, \quad (6) \\ \frac{Q_A}{G_1} &= 1 - \frac{\tan \alpha}{\cos \theta} \cdot \frac{T}{G_1}, \end{aligned}$$

where i is the average fragmentation degree of the block and defined by $i = H_2/L + (1/2) \tan \alpha$.

Block A does not shear off at contact A only if

$$T \tan \varphi \geq Q_A. \quad (7)$$

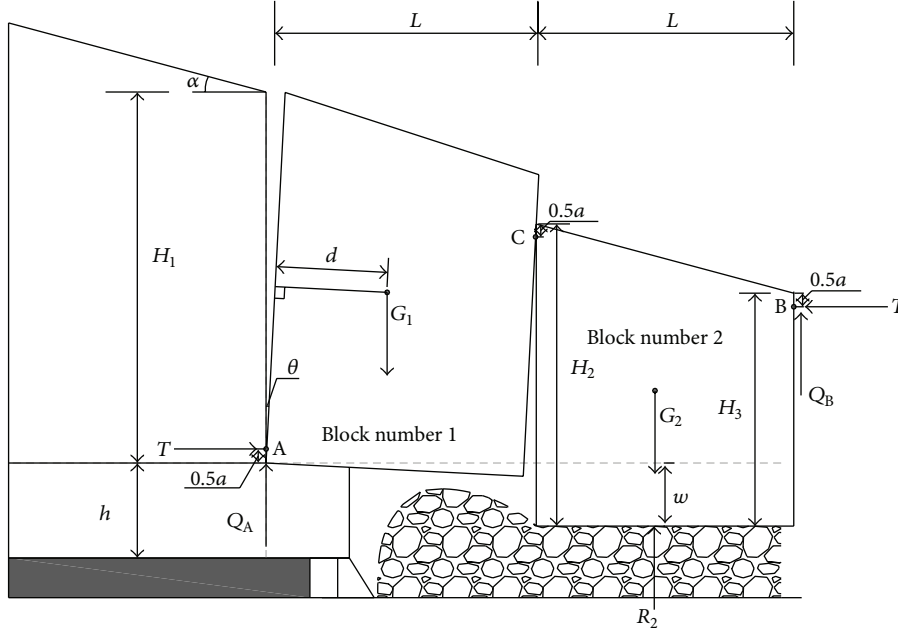


FIGURE 11: Mechanical model for key blocks in upslope mining.

Substituting (6) into (7), then

$$\begin{aligned} \frac{Q_A}{T} = & \left((i - \tan \alpha) \left(\frac{1}{2} + \tan \alpha \tan \theta \right) \right. \\ & + \left. \left(\frac{1}{\cos \theta} + \frac{\sin \theta}{2} \right) - \sin \theta_{\max} \right) \\ & \cdot \left(\frac{1}{2} - \frac{\tan \alpha}{12i} \right)^{-1} - \frac{\tan \alpha}{\cos \theta} \leq \tan \varphi. \end{aligned} \quad (8)$$

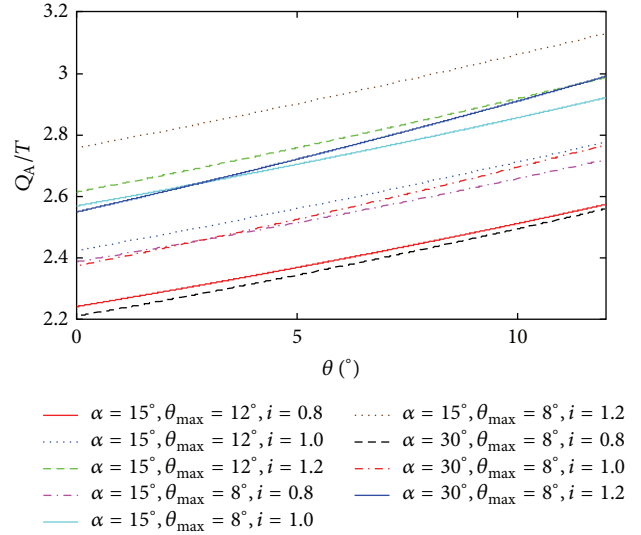
In order to analyze the block stability, a series of curves showing the relationship between Q_A/T and θ at different values of α , θ_{\max} , and i were drawn in Figure 12 based on (8). Generally, θ_{\max} values 8° to 12° , i values 0.8 to 1.2, and $\tan \varphi$ appropriate 0.5. According to Figure 12, all the Q_A/T values at the designed conditions are greater than 2, which means that the blocks may shear off with a large shock load onto the face support. Therefore, a reasonable support capacity is important to control the shock load and the stability of roof blocks.

For the structure to be stable, a reasonable support capacity R must be equal to or greater than the downward transferring loading; that is,

$$R + T \tan \varphi \geq Q_A. \quad (9)$$

Substituting (6) into (9),

$$\begin{aligned} R \geq & \left[1 - \left(\left(\frac{1}{2} - \frac{\tan \alpha}{12i} \right) \left(\tan \varphi + \frac{\tan \alpha}{\cos \theta} \right) \right) \right. \\ & \cdot \left((i - \tan \alpha) \left(\frac{1}{2} + \tan \alpha \tan \theta \right) \right. \\ & \left. \left. + \left(\frac{1}{\cos \theta} + \frac{\sin \theta}{2} \right) - \sin \theta_{\max} \right)^{-1} \right] G_1. \end{aligned} \quad (10)$$

FIGURE 12: Relationship between Q_A/T and θ .

According to (10), the greater the block fragmentation degree or the block rotation angle, the greater the needed support capacity. Based on the definition of block fragmentation degree i , the greater the slope angle or the less the block length, the greater the needed support capacity. In other words, if the support capacity cannot meet (10), the block may shear off and roof shock will happen at the coalface, which is hazardous to an underground coal mine. Therefore, strengthening the face support capacity or lowering the mining height may reduce the possibility of roof shock when mining in the upslope direction.

4. Conclusions

The paper presents the modeling results for understanding the mechanisms of roof shock in coal mining under surface gully. Two types of mining directions with respect to the bottom of gully were analyzed: (1) in downslope period where the face retreats towards the bottom of the gully, the slope of gully slid obviously layer by layer due to lack of horizontal confinement, with a resultant roof shearing off; (2) in upslope period, the overlying strata are split into polygon blocks which may suddenly become unstable and shear off with a large shock load onto face support. In order to avoid or control the roof shock in mining under gully, layer sliding should be controlled in downslope period and block shearing off should be avoided in upslope period.

The paper constructs mechanical models to analyze the roof structure stability in response to mining under gully. The mechanical analysis results show that, (1) in downslope period, the smaller the gully angle or the rotation degree of formed blocks gets, the less likely block sliding and roof shock occur; (2) in upslope period, the mining-induced blocks will lose the stability in many scenarios. The roof shock can be controlled by lowering the mining height and strengthening the face support capacity.

Conflict of Interests

The authors declare that there is no conflict of interests regarding the publication of this paper.

Acknowledgments

The authors would like to thank the Fundamental Research Funds for the Central Universities (Grant no. 2012QNA35), the National Key Basic Research Program of China (2015CB251600), the National Natural Science Foundation of China (Grant no. 51264035), and the Priority Academic Program Development of Jiangsu Higher Education Institutions (PAPD) for their financial support. Special thanks are given to Dr. Khaled M. Mohamed for language assistance.

References

- [1] G. Fan and D. Zhang, "Mechanisms of aquifer protection in underground coal mining," *Mine Water and the Environment*, vol. 34, no. 1, pp. 95–104, 2015.
- [2] D. Zhang, G. Fan, Y. Liu, and L. Ma, "Field trials of aquifer protection in longwall mining of shallow coal seams in China," *International Journal of Rock Mechanics & Mining Sciences*, vol. 47, no. 6, pp. 908–914, 2010.
- [3] D. Zhang, G. Fan, L. Ma, and X. F. Wang, "Aquifer protection during longwall mining of shallow coal seams: a case study in the Shendong Coalfield of China," *International Journal of Coal Geology*, vol. 86, no. 2-3, pp. 190–196, 2011.
- [4] G.-W. Fan, D.-S. Zhang, D.-Y. Zhai, X.-F. Wang, and L. U. Xin, "Laws and mechanisms of slope movement due to shallowly buried coal seam mining under ground gully," *Journal of Coal Science and Engineering (China)*, vol. 15, no. 4, pp. 346–350, 2009.
- [5] S. S. Peng, *Coal Mine Ground Control*, Syd S. Peng, Morgantown, Va, USA, 3rd edition, 2008.
- [6] M. Qian and P. Shi, *Coal Mine Ground Pressure and Control*, China University of Mining and Technology Press, 2003.
- [7] M. Qian, *Key Strata Theory in Strata Control*, China University of Mining and Technology Press, Xuzhou, China, 2000.
- [8] G. Chen, X. Cheng, W. Chen, X. Li, and L. Chen, "GPS-based slope monitoring systems and their applications in transition mining from open-pit to underground," *International Journal of Mining and Mineral Engineering*, vol. 5, no. 2, pp. 152–163, 2014.
- [9] A. W. Khair, M. K. Quinn, and R. D. Chaffins, "Effect of topography on ground movement due to longwall mining," *Mining Engineering*, vol. 40, no. 8, pp. 820–822, 1988.
- [10] M. Marschalko, I. Yilmaz, M. Bednárík, and K. Kubečka, "Deformation of slopes as a cause of underground mining activities: three case studies from Ostrava-Karviná coal field (Czech Republic)," *Environmental Monitoring and Assessment*, vol. 184, no. 11, pp. 6709–6733, 2012.
- [11] S. S. Peng and Y. Luo, "Slope stability under the influence of ground subsidence due to longwall mining," *Mining Science and Technology*, vol. 8, no. 2, pp. 89–95, 1989.
- [12] D. M. Ross-Brown, "Design considerations for excavated mine slopes in hard rock," *Quarterly Journal of Engineering Geology and Hydrogeology*, vol. 6, no. 3-4, pp. 315–334, 1973.
- [13] R. Singh, P. K. Mandal, A. K. Singh, R. Kumar, J. Maiti, and A. K. Ghosh, "Upshot of strata movement during underground mining of a thick coal seam below hilly terrain," *International Journal of Rock Mechanics and Mining Sciences*, vol. 45, no. 1, pp. 29–46, 2008.
- [14] T. N. Singh and D. P. Singh, "Slope behaviour in an opencast mine over old underground voids," *International Journal of Surface Mining & Reclamation*, vol. 5, no. 4, pp. 195–201, 1991.
- [15] S. Wang, C. Li, P. Liu, and J. Zhu, "Optimization parameters of the slope under open-underground combined mining," in *Transit Development in Rock Mechanics: Recognition, Thinking and Innovation*, chapter 41, pp. 229–234, CRC Press, Boca Raton, Fla, USA, 2014.
- [16] S. Tu, W. Ma, Z. Wan, and D. Zhang, *Experimental Method and Field Measurement on Strata Control*, China University of Mining and Technology Press, Xuzhou, China, 2010.
- [17] M. D. G. Salamon, "Mechanism of caving in longwall coal mining," in *Rock Mechanics Contributions and Challenges*, W. A. Hustrulid and G. A. Johnson, Eds., pp. 161–168, A A Balkema Publishers, Golden, Colo, USA, 1990.
- [18] D. Zhang, G. Fan, and X. Wang, "Characteristics and stability of slope movement response to underground mining of shallow coal seams away from gullies," *International Journal of Mining Science and Technology*, vol. 22, no. 1, pp. 47–50, 2012.
- [19] G. Fan, *Mechanism and Engineering Practice on Mutual Response between Underground Mining of Shallow Coal Seam and Protection of Fragile Ecological Environment*, China University of Mining and Technology, 2011.

Research Article

Damage Characteristics of Surrounding Rock Subjected to VCR Mining Blasting Shock

Nan Jiang,^{1,2} Chuanbo Zhou,^{1,2} Xuedong Luo,^{1,2} and Shiwei Lu^{1,2}

¹Engineering Research Center of Rock-Soil & Excavation and Protection, Ministry of Education, Wuhan 430074, China

²Faculty of Engineering, China University of Geosciences, Wuhan 430074, China

Correspondence should be addressed to Chuanbo Zhou; cbzhou@cug.edu.cn

Received 23 July 2014; Accepted 28 September 2014

Academic Editor: Caiping Lu

Copyright © 2015 Nan Jiang et al. This is an open access article distributed under the Creative Commons Attribution License, which permits unrestricted use, distribution, and reproduction in any medium, provided the original work is properly cited.

For limiting the damage range caused by explosive shock loads in vertical crater retreat (VCR) mining, the blasting damage characteristics of surrounding rock were studied by two methods: numerical simulation and ultrasonic testing. Combined with the mining blasting in Dongguashan Copper Mine of China, the VCR blasting shock characteristics under different conditions are obtained by using LSDYNA. Based on statistical fracture mechanics and damage mechanics theories, a damage constitutive model for rock mass subjected to blasting shock load was established. Then by using the fast Lagrange analysis codes (FLAC3D), the blasting damage characteristics of surrounding rock were analyzed by applying the blasting shock loads obtained from the VCR mining and the damage zone is obtained. At last, the relationship between the amount of explosives and the radius of damaged surrounding rock mass was discussed, and its formula was also derived. The research provides a theoretical basis for rationally controlling stope boundaries and optimizing mining blasting parameters.

1. Introduction

VCR (vertical crater retreat) mining technology is widely used in mine engineering because it possesses many better features, such as higher efficiency and more simple operation. In the mining process, the blasting shock originating simultaneously from the rock-fracturing blasting load also can damage surrounding rock. For better control of the stope boundary, it is a key prospect in engineering application to ascertain damage characteristics of surrounding rock under mining blasting shock load and to optimize blasting parameters.

Damage effects of rock mass under blasting load were extensively studied at home and abroad, but these researches were mostly based on in-site tests and laboratory experiments [1–4]. In recent years, with the development of computer technology, numerical simulation was increasingly adopted to study blasting damage of rock mass [5–8]. Hao et al. analyzed the rock damage under stress wave of blasting based on an anisotropic damage constitutive model [9, 10]. Wei et al. studied the damage of rock mass subjected to underground explosion [11]. Wang et al. analyzed the tensile damage of

brittle rock mass subjected to underground explosion and the evolution characteristics of craters [12].

Based on the theories in statistical fracture mechanics and damage mechanics, a damage model for rock mass subjected to blasting load was established. At the same time, damage characteristics of surrounding rock subjected to mining blasting shock load in VCR mining and conventional blasting shock load were analyzed by numerical simulations.

2. VCR Mining Blasting Shock Load

2.1. Numerical Model. Dongguashan Copper Mine is located in Tongling, Anhui, China. It has the ability to produce around 4.3 million tons of copper ore annually, and its service life is 28 years. As the largest copper mine of down-hole pit mining in Asia, its mining depth is more than 1000 meters, which ranks the first among the nonferrous metal mines in Asia. The deposit is as long as more than 1800 m in trend, more than 500 meters wide, and 20–70 m thick. It is divided into panels every 100 m, and there is an 18 m wide barrier pillar in each pair of adjacent panels. A panel is 100 m wide,

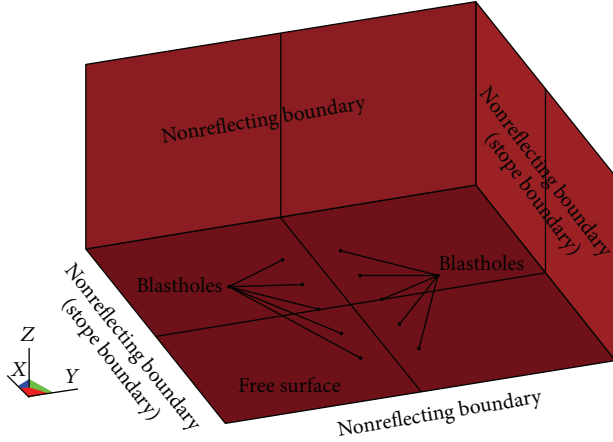


FIGURE 1: LSDYNA model.

TABLE 1: Parameters of the rock material.

Density ($\text{g}\cdot\text{cm}^{-3}$)	Elastic modulus (GPa)	Poisson's ratio	Cohesion (MPa)	Internal friction ($^\circ$)
3.22	69.00	0.31	21.43	56.21

whose length and height equal the width and the thickness of the deposit, respectively. Every panel consists of 20 stopes, which are arranged along the trend of the deposit and 18 m wide. The room stope and pillar stope are 82 m long and 78 m long, respectively. In the mining blasting process, it is significant to control the stope boundary for safety of underground mining construction in the mine.

VCR mining method was adopted for underground mining in Dongguashan Copper Mine. According to the reality, large-diameter deep-hole blasting is introduced. The blasthole diameter is 165 mm, the charge length is 1.5 m to 10.5 m, and the stemming length is 1.2 m to 2.0 m. In this study, a three-dimensional model is established using the software LS-DYNA, as shown in Figure 1, which is measuring 20 m in X -direction, 20 m in Y -direction, and 10 m in Z -direction. 10 blasting holes are equally divided into 2 rows. The distance between two rows is 3 m, and the distance between 2 adjacent holes in the same row is 2.8 m. Only the bottom surface is free, and the remaining surfaces are applied with nonreflecting boundary.

2.2. Calculation Parameters. In LSDYNA simulation, Mohr-Coulomb (M-C) model is selected as rock material's model [13]. According to the test results, parameters of stope rock mass are listed in Table 1.

The JWL state equation can simulate the relationship between pressure and specific volume in the explosion process [14]. The equation is as follows:

$$p = A \left(1 - \frac{w}{R_1 V} \right) e^{-R_1 V} + B \left(1 - \frac{w}{R_2 V} \right) e^{-R_2 V} + \frac{\omega E_0}{V}, \quad (1)$$

where A , B , R_1 , R_2 , and W are material constants, P is pressure, V is relative volume, and E_0 is specific internal energy. The physical and mechanical parameters of

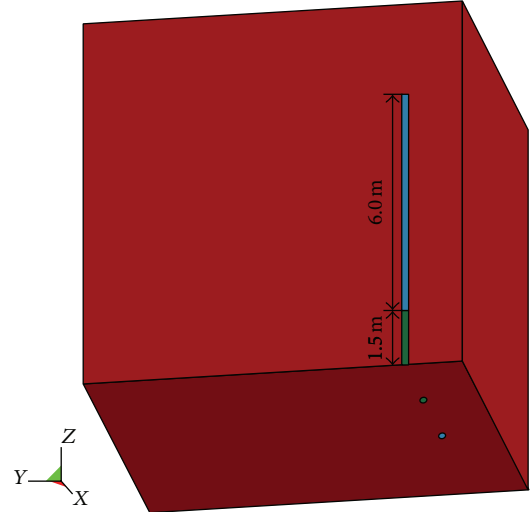


FIGURE 2: Numerical models with 6 m charging length.

TABLE 2: Parameters of the explosive.

Density ($\text{g}\cdot\text{cm}^{-3}$)	Detonation velocity ($\text{cm}\cdot\mu\text{s}^{-1}$)	A (GPa)	B (GPa)	R_1	R_2	ω	E_0 (GPa)
1.09	0.4	214.4	18.2	4.2	0.9	0.15	4.192

the dynamite are the same as those of the field test and are listed in Table 2.

2.3. Blasting Load. Due to the model which is built symmetrically, a quarter of the model is calculated to reduce the size of the research object. So the model was simplified as a 10 m cube, and the charge length is 3 m, 3.5 m, 4.0 m, 4.5 m, 5.0 m, 5.5 m, and 6.0 m, respectively. The charging length of 6.0 m is shown in Figure 2. The bottom surface is free; the front surface and the right surface are applied with normal displacement constraint. The remaining surfaces are applied with nonreflecting boundary, and the left sides are stope boundaries [15].

As illustrated in the rock blasting theory, the crushed zone radius is 2-3 times larger than the blasthole radius [16]. In order to obtain the blasting load applied on the crushed zone boundary, the monitoring element was selected at a horizontal distance of 0.33–0.50 m away from the center of the blasthole. For example, when the charge length is 6 m, Element H54050 was selected as the monitoring element, as shown in Figure 3.

Figure 4 shows the pressure curve with time at Element H54050. Shock wave pressure applied on the boundary of crushed zone under blasting load increases to its maximum within 0.5 ms, up to 1.74 GPa. In the same way, when the charge length is 3 m, 3.5 m, 4 m, 4.5 m, 5 m, and 5.5 m, the maximum shock wave pressure applied on the boundary of crushed zone under blasting load is 1.4 GPa, 1.43 GPa, 1.46 GPa, 1.52 GPa, 1.57 GPa, and 1.61 GPa, respectively.

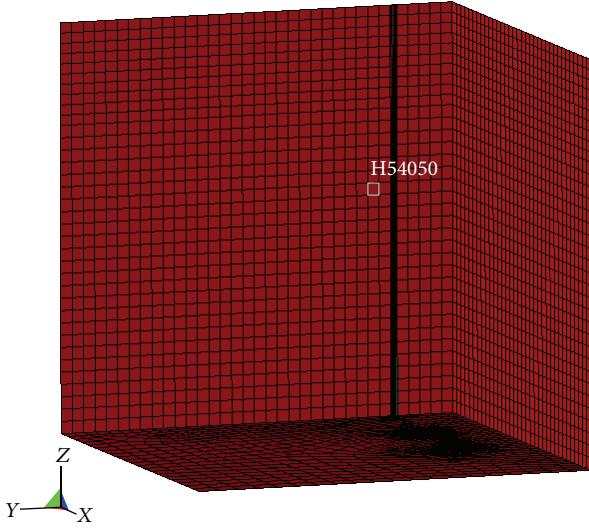


FIGURE 3: Monitoring element in the model with 6 m charging length.

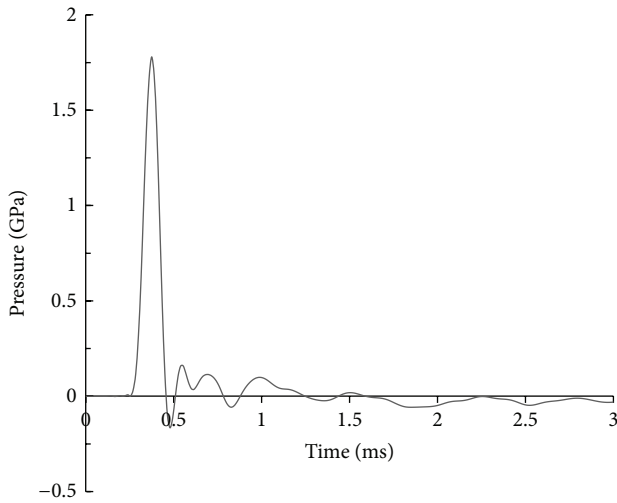


FIGURE 4: Pressure time history of Element H54050.

3. Rock Damage Model under Blasting Shock Load

According to statistical fractured mechanics [17], rock damage is believed to occur when the crack density reaches a given value, and the cumulation and growth of crack in rock can be demonstrated in probability terms. The following agreements have been achieved by the related research [18, 19]:

- (1) a rock material does not fail if the applied stress is lower than its static strength;
- (2) when a rock material is subjected to a stress higher than its static strength, a certain time duration is needed so that the fracture can take place;
- (3) the dynamic fracture stress of a rock material is higher than its static strength and is approximately cube root dependent on the strain rate.

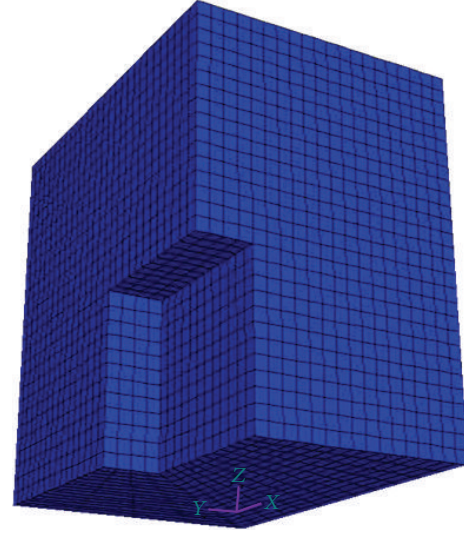


FIGURE 5: Numerical model with the charging length of 6 m.

TABLE 3: Damage zone radiuses with different charge weights.

Charging length (m)	Maximum one-stage charge weight (kg)	Damage zone radius (m)
3	696.75	5.504
3.5	812.875	5.942
4	929	6.478
4.5	1045.125	6.763
5	1161.25	7.065
5.5	1277.375	7.684
6	1393.5	8.141

So damage due to blasting loading can be defined as the probability of fracture, written as follows:

$$D_i = p_f = 1 - e^{-C_{di}^2}, \quad i = 1, 2, 3, \quad (2)$$

where p_f is the fail probability of damaged rock mass, C_{di} is the crack density in i direction, and D_i is damage value. Obviously D_i has a value between 0 and 1, to respond to the stiffness of the intact, undamaged rock with crack density $C_{di} = 0$, and the fully fragmented rock with an infinite C_{di} , respectively. Crack density is defined as follows:

$$C_{di} = \begin{cases} 0 & (\varepsilon_i \leq \varepsilon_{cri}) \\ \alpha_i (\varepsilon_i - \varepsilon_{cri})^{\beta_i} t & (\varepsilon_i > \varepsilon_{cri}), \end{cases} \quad (3)$$

where α_i , β_i are material constants, ε_i is the principle strain in i direction, ε_{cri} is the corresponding critical strain, and t is the time to reach fracture stress. In terms of isotropic damage, the principle strain would be equivalent volume modulus.

Tensile strain is a quite important index to evaluate whether rock mass is damaged or not [20], so generally uniaxial tensile test is adopted to approximately simulate rock

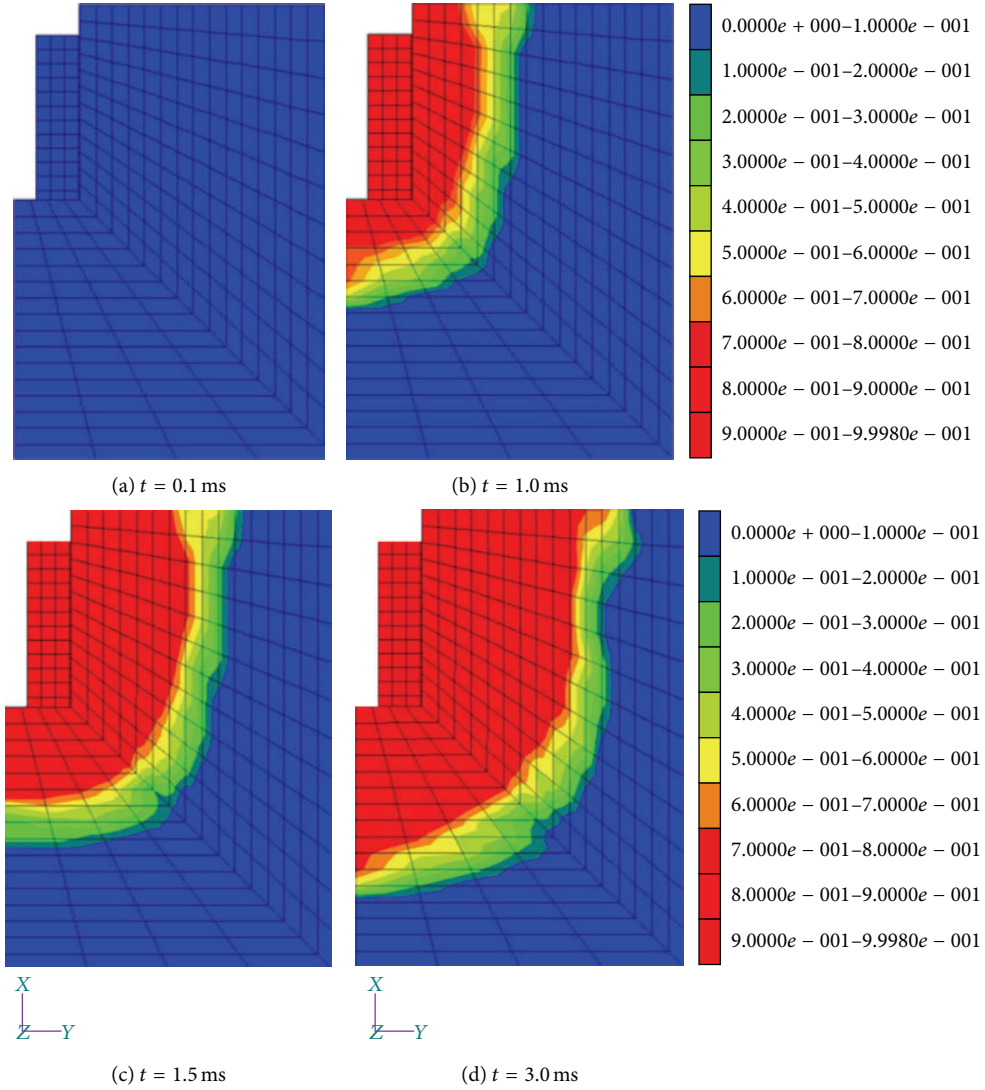


FIGURE 6: Damage growth on the bottom free surface.

damage. Critical strain can be obtained based on uniaxial tensile test as follows:

$$\varepsilon_{cri} = \frac{1-2\nu}{E_i} \sigma_{sti}, \quad i = 1, 2, 3, \quad (4)$$

where σ_{sti} is static tensile strength in i direction and E_i is equivalent elastic modulus. We define ε_{fi} and C_{dfi} as the tensile strain and crack density in i direction when rock mass is cracked. Then C_{dfi} can be expressed as follows:

$$C_{dfi} = \alpha_i (\varepsilon_{fi} - \varepsilon_{cri})^{\beta_i} (t_i - t_{ci}), \quad i = 1, 2, 3, \quad (5)$$

where t_i is the total time when the rock mass reaches the fracture stress and t_{ci} is the time duration when the tensile

strain reaches the critical value. Both of them can be obtained by

$$\begin{aligned} t_i &= \frac{\varepsilon_{fi}}{\dot{\varepsilon}_i}, \quad i = 1, 2, 3, \\ t_{ci} &= \frac{\varepsilon_{cri}}{\dot{\varepsilon}_i}, \quad i = 1, 2, 3, \end{aligned} \quad (6)$$

where $\dot{\varepsilon}_i$ is tensile strain rate. Accordingly, (5) can further be written as

$$C_{dfi} = \alpha_i (t_i \dot{\varepsilon}_i - t_{ci} \dot{\varepsilon}_i)^{\beta_i} (t_i - t_{ci}), \quad i = 1, 2, 3. \quad (7)$$

The time interval between the critical damage to the fracture of rock mass is given by

$$t = t_i - t_{ci} = \left(\frac{C_{dfi}}{\alpha_i} \right)^{1/(1+\beta_i)} \dot{\varepsilon}_i^{-\beta_i/(1+\beta_i)}, \quad i = 1, 2, 3. \quad (8)$$

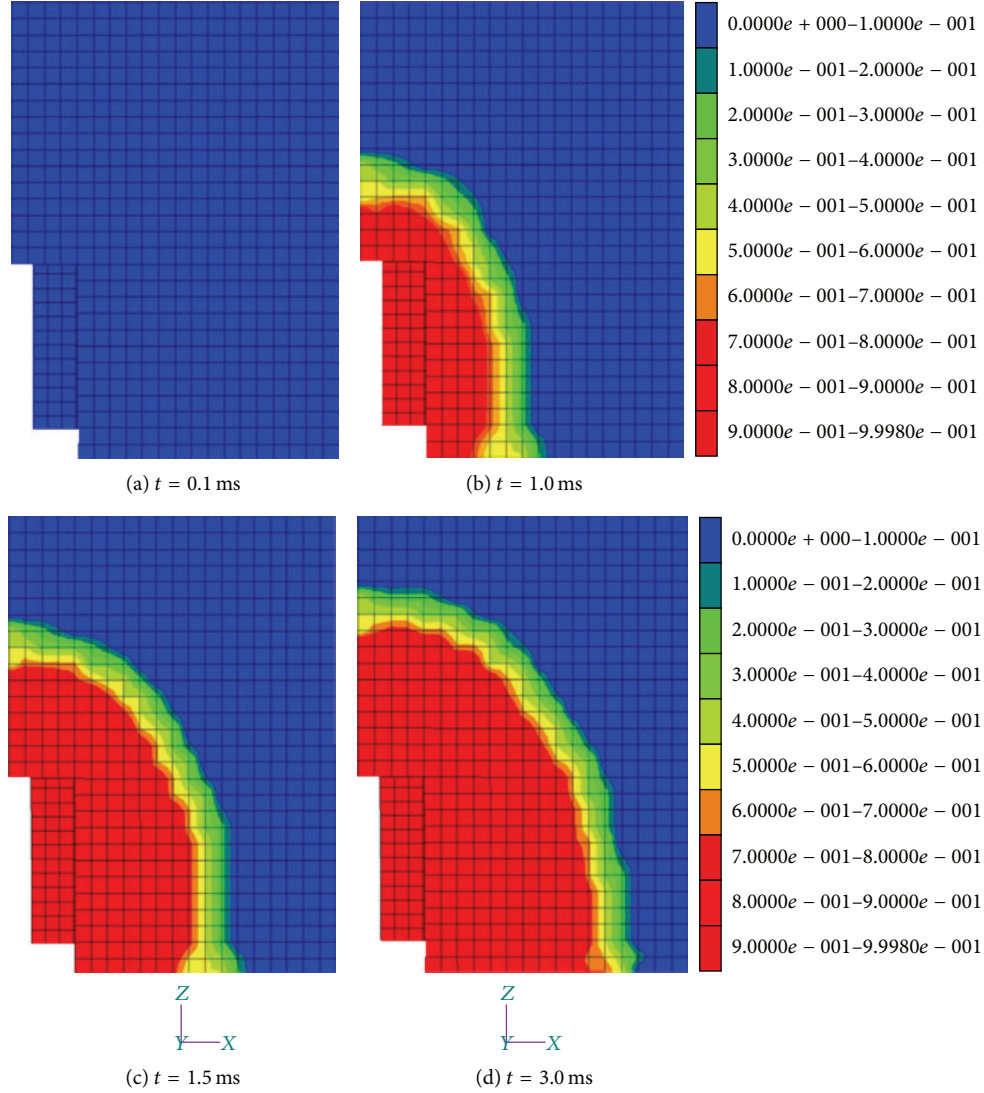


FIGURE 7: Damage growth along the height direction.

The relationship between the fracture stress and the corresponding strain is

$$\sigma_{fi} = \frac{E_i (1 - D_{fi})}{1 - 2\nu} \varepsilon_{fi}, \quad i = 1, 2, 3. \quad (9)$$

Submitting (4) and (8) to (9), the strain rate dependent constitutive relation is obtained:

$$\sigma_{fi} = (1 - D_{fi}) \sigma_{si} + \frac{E_i (1 - D_{fi})}{1 - 2\nu} \left(\frac{C_{dfi}}{\alpha_i} \right)^{1/(1+\beta_i)} \dot{\varepsilon}^{1/(1+\beta_i)}, \quad (10)$$

$$i = 1, 2, 3,$$

where D_{fi} is the damage variable under the fracture state and other variables are the same as previous meanings. Because the dynamic tensile strength of a rock material is higher than its static strength and is approximately cube root dependent on the strain rate, the value of β can be given as 2. For given D_{\min} and C_{df} , the material constant α_i can be calculated based on the blasting crater test results.

According to the *Construction Technical Specification on Rock-Foundation Excavation Engineering of Hydraulic Structure (SL47-94)*, D_{\min} should be 0.2 [21]. At the same time, based on the in-site tests, α_i is equal to 3.16×10^6 , and other parameters are listed in Table 1.

4. Numerical Analysis of Rock Damage Zone

4.1. Numerical Model. Like the blast model above, a 3D model was established using FLAC3D. Hexahedral solid element is selected when the model is meshed. Due to the model which is built symmetrically, a quarter of the model is calculated to reduce the size of the research object. For example, when the charge length is 6 m, a 10 m long, 14 m wide, and 14 m high model is established, as shown in Figure 5. The left side is the stope boundary, and the hollow part is the boundary of crushed zone of $2 \text{ m} \times 6 \text{ m} \times 7.5 \text{ m}$.

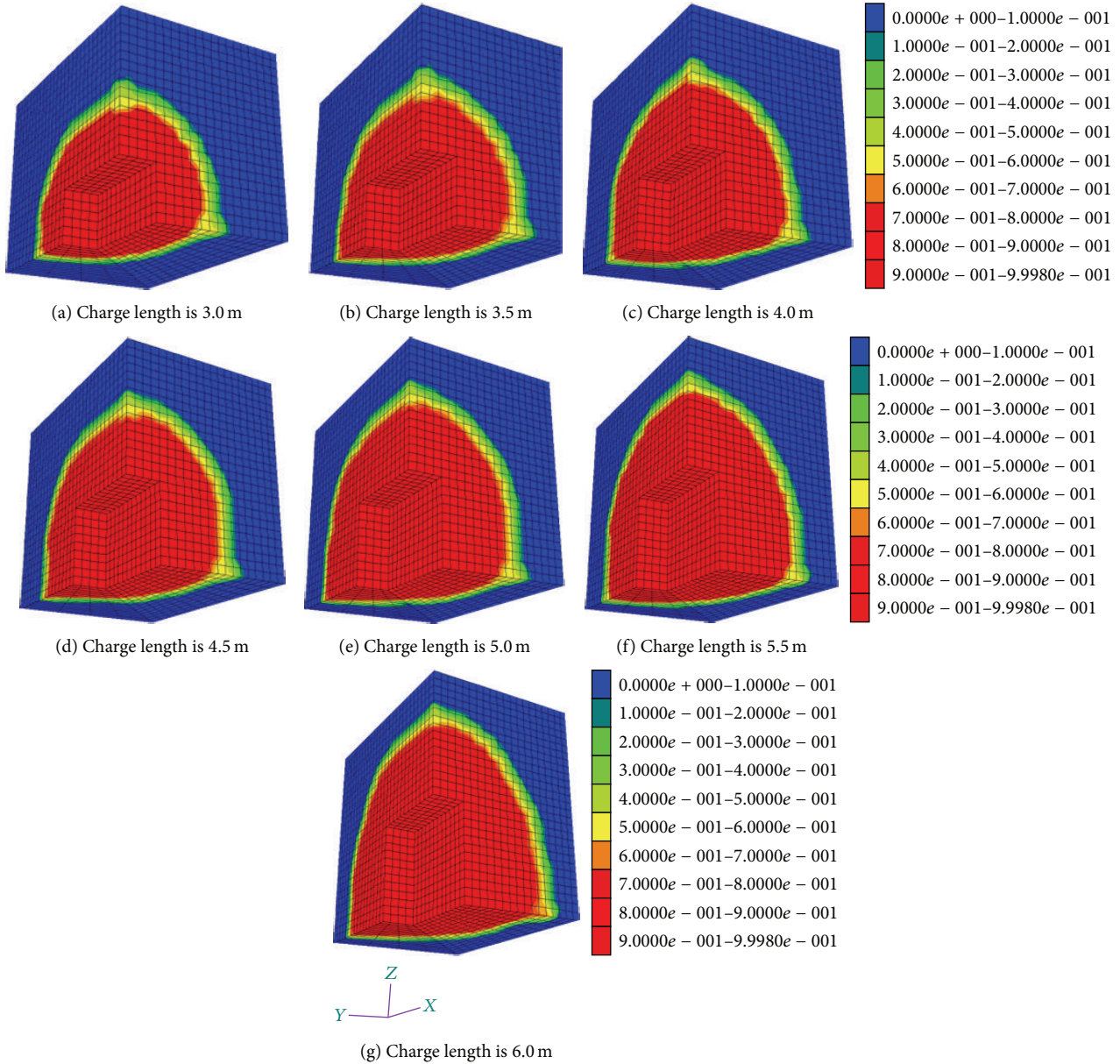


FIGURE 8: Damage zone after mining blasting.

The boundary conditions are the same as those in Section 2.3, because the maximum pressure varies depending on the charge and the blasting damage zone depending on the charge can be simulated by applying different pressure on the boundary of crushed zone. Mohr-Coulomb (M-C) model is considered the material model for numerical simulation [22], and the parameters are listed in Table 1. The applied dynamic loads are equal to the results calculated above.

4.2. Analysis of the Damage Characteristics. For example, when the charge length is 6 m, the damage growth on the free surface and along the height direction is shown in Figures 6 and 7.

Figures 6 and 7 show that the rock mass is not damaged yet in 0.1 ms after detonation whether on the free surface or along the height direction. The damage of rock subject to blasting load needs some time to develop. In the time interval between 0.1 ms and 1.5 ms, the damage zone radius is approximately 6.785 m and it reaches about 8.142 m in the time interval between 1.5 ms and 3.0 ms. Combined with the above analysis, the calculation results agree well with the first two agreements (1) and (2) which are presented in Section 3.

Using the same way, the damage zone with the charge length of 3 m, 3.5 m, 4.0 m, 4.5 m, 5.0 m, 5.5 m, and 6.0 m is shown in Figure 8. Damage under blasting loads grows faster within the first 1.5 ms after denotation than that in the latter 1.5 ms.

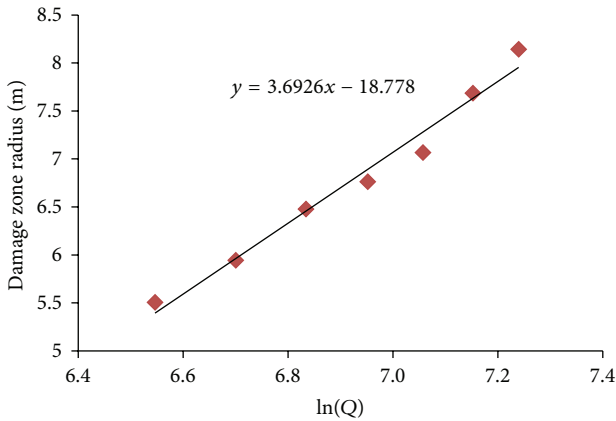


FIGURE 9: Fitting curve between damage zone radius and charge weight.

Figure 8 shows the crushed zone with the damage value of 0.2. The damage zone radiuses are listed in Table 3.

Based on the in-site parameters, the statistical relationship between charge amount and damage zone radius is established.

As shown in Figure 9, the function relation can be expressed by

$$r = 3.693 \ln Q - 18.778, \quad (11)$$

where r is damage zone radius of surrounding rock and Q is one-stage charge.

The rooms and barrier pillars are 18 m wide. As illustrated in (11), when $r = 9$ m, the maximum one-stage charge is 1848.26 kg. So the in-site maximum one-stage charge should be less than 1848.26 kg. The maximum one-stage charge can be precalculated by empirical formula when the blasting operation is performed at any location in the stope, so that the stope boundary can be under control, the surrounding rock mass can be stable, and the safe production can be ensured.

5. Conclusions

The following conclusions can be drawn.

- (1) Based on statistical fracture mechanics, damage due to blasting shock load can be defined in the probability form. The damage model was established. And the damage characteristics were obtained by numerical simulation.
- (2) Under blasting shock load, the rock mass is not damaged yet at the initial stage after detonation whether on the free surface or along the height direction. The damage of rock subject to blasting load needs some time to develop. Damage under blasting loads grows faster within the first 1.5 ms after denotation than that in the latter 1.5 ms.
- (3) According to the results in different blasting conditions, the statistical relationship between charge

amount and damage zone radius is established. Furthermore, the maximum one-stage charge was proposed to be less than 1848.26 kg on the purpose of controlling the stope damage boundary.

Conflict of Interests

The authors declare that there is no conflict of interests regarding the publication of this paper.

Acknowledgments

The study was sponsored by the National Natural Science Foundation of China (Grant nos. 41372312 and 51379194), the Fundamental Research Funds for the Central Universities, China, University of Geosciences (Wuhan) (Grant no. CUGL140817), and the China Postdoctoral Science Foundation (Grant no. 2014M552113). The authors are also grateful to the China Scholarship Council (CSC) for the support.

References

- [1] A. Palmström and R. Singh, "The deformation modulus of rock masses—comparisons between in situ tests and indirect estimates," *Tunnelling and Underground Space Technology*, vol. 16, no. 2, pp. 115–131, 2001.
- [2] P. K. Singh, "Blast vibration damage to underground coal mines from adjacent open-pit blasting," *International Journal of Rock Mechanics and Mining Sciences*, vol. 39, no. 8, pp. 959–973, 2002.
- [3] Y.-Q. Zhang, H. Hao, and Y. Lu, "Anisotropic dynamic damage and fragmentation of rock materials under explosive loading," *International Journal of Engineering Science*, vol. 41, no. 9, pp. 917–929, 2003.
- [4] M. Cai, P. K. Kaiser, Y. Tasaka, T. Maejima, H. Morioka, and M. Minami, "Generalized crack initiation and crack damage stress thresholds of brittle rock masses near underground excavations," *International Journal of Rock Mechanics and Mining Sciences*, vol. 41, no. 5, pp. 833–847, 2004.
- [5] C. Wu and H. Hao, "Numerical prediction of rock mass damage due to accidental explosions in an underground ammunition storage chamber," *Shock Waves*, vol. 15, no. 1, pp. 43–54, 2006.
- [6] G. W. Ma and X. M. An, "Numerical simulation of blasting-induced rock fractures," *International Journal of Rock Mechanics and Mining Sciences*, vol. 45, no. 6, pp. 966–975, 2008.
- [7] C. Wu, Y. Lu, and H. Hao, "Numerical prediction of blast-induced stress wave from large-scale underground explosion," *International Journal for Numerical and Analytical Methods in Geomechanics*, vol. 28, no. 1, pp. 93–109, 2004.
- [8] Z. Zhu, H. Xie, and B. Mohanty, "Numerical investigation of blasting-induced damage in cylindrical rocks," *International Journal of Rock Mechanics and Mining Sciences*, vol. 45, no. 2, pp. 111–121, 2008.
- [9] H. Hao, C. Wu, and C. C. Seah, "Numerical analysis of blast-induced stress waves in a rock mass with anisotropic continuum damage models Part 2: stochastic approach," *Rock Mechanics and Rock Engineering*, vol. 35, no. 2, pp. 95–108, 2002.
- [10] H. Hao, C. Wu, and Y. Zhou, "Numerical analysis of blast-induced stress waves in a rock mass with anisotropic continuum damage models Part 1: equivalent material property approach," *Rock Mechanics and Rock Engineering*, vol. 35, no. 2, pp. 79–94, 2002.

- [11] X. Y. Wei, Z. Y. Zhao, and J. Gu, "Numerical simulations of rock mass damage induced by underground explosion," *International Journal of Rock Mechanics and Mining Sciences*, vol. 46, no. 7, pp. 1206–1213, 2009.
- [12] Z.-L. Wang, Y.-C. Li, and R. F. Shen, "Numerical simulation of tensile damage and blast crater in brittle rock due to underground explosion," *International Journal of Rock Mechanics and Mining Sciences*, vol. 44, no. 5, pp. 730–738, 2007.
- [13] N. Jiang and C. Zhou, "Blasting vibration safety criterion for a tunnel liner structure," *Tunnelling and Underground Space Technology*, vol. 32, pp. 52–57, 2012.
- [14] J. O. Hallquist, *LS-DYNA Keyword User's Manual*, Livermore Software Technology Corporation, Livermore, Calif, USA, 2007.
- [15] M. Chen, W. B. Lu, and C. P. Yi, "Blasting vibration criterion for a rock-anchored beam in an underground powerhouse," *Tunnelling and Underground Space Technology*, vol. 22, no. 1, pp. 69–79, 2007.
- [16] P. A. Persson, R. Holmberg, and J. Lee, *Rock Blasting and Explosives Engineering*, CRC Press, New York, NY, USA, 1993.
- [17] L. Liu and P. D. Katsabanis, "Development of a continuum damage model for blasting analysis," *International Journal of Rock Mechanics and Mining Sciences*, vol. 34, no. 2, pp. 217–231, 1997.
- [18] R. Yang, W. F. Bawden, and P. D. Katsabanis, "A new constitutive model for blast damage," *International Journal of Rock Mechanics and Mining Sciences & Geomechanics*, vol. 33, no. 3, pp. 245–254, 1996.
- [19] L. Haibo, X. Xiang, L. Jianchun, Z. Jian, L. Bo, and L. Yaqun, "Rock damage control in bedrock blasting excavation for a nuclear power plant," *International Journal of Rock Mechanics and Mining Sciences*, vol. 48, no. 2, pp. 210–218, 2011.
- [20] J. S. Kuszmaul, *A New Constitutive Model for Fragmentation of Rock under Dynamic Loading*, Sandia National Laboratories, Albuquerque, NM, USA, 1987.
- [21] C. Zhou, N. Jiang, and G. Luo, "Study on blasting vibration cumulative damage effect of medium-length hole mining," *Disaster Advances*, vol. 5, no. 4, pp. 468–473, 2012.
- [22] Itasca Consulting Group, *Fast Lagrangian Analysis of Continua in 3 Dimensions, Version 4.0*, Itasca Consulting Group, Minneapolis, Minn, USA, 2009.

Research Article

A Comparison of Mine Seismic Discriminators Based on Features of Source Parameters to Waveform Characteristics

Ju Ma, Guoyan Zhao, Longjun Dong, Guanghui Chen, and Chuxuan Zhang

School of Resources and Safety Engineering, Central South University, Changsha 410083, China

Correspondence should be addressed to Longjun Dong; rydong001@csu.edu.cn

Received 2 October 2014; Accepted 27 December 2014

Academic Editor: Marcin A. Lutynski

Copyright © 2015 Ju Ma et al. This is an open access article distributed under the Creative Commons Attribution License, which permits unrestricted use, distribution, and reproduction in any medium, provided the original work is properly cited.

To find efficient methods for classifying mine seismic events, two features extraction approaches were proposed. Features of source parameters including the seismic moment, the seismic energy, the energy ratio of S- to P-wave, the static stress drop, time of occurrence, and the number of triggers were selected, counted, and analyzed in approach I. Waveform characteristics consisting of two slope values and the coordinates of the first peak and the maximum peak were extracted as the discriminating parameters in approach II. The discriminating performance of the two approaches was compared and discussed by applying the Bayes discriminant analysis to the characteristic parameters extracted. Classification results show that 83.5% of the original grouped cases are correctly classified by approach I, and 97.1% of original grouped cases are correctly classified by approach II. The advantages and limitations pertaining to each classifier were discussed by plotting the event magnitude versus sample number. Comparative analysis shows that the proposed method of approach II not only has a low misjudgment rate but also displays relative constancy when the testing samples fluctuate with seismic magnitude and energy.

1. Introduction

Mining excavations induce elastic and then inelastic deformation within the surrounding rock mass. A seismic event is a sudden inelastic deformation within a given volume of rock. Having recorded and processed a number of seismic events within a given volume of interest ΔV over time Δt , one can then quantify the changes in the strain and stress regimes and in the rheological properties of the rock mass deformation associated with the seismic radiation [1, 2]. However, a variety of dynamic processes in mines which radiate seismic waves are detected by the seismic monitoring systems and in general, seismograms generated by a development or production blast and a shear fracturing or a sudden slip on a surface of weakness are the majority of records [3–8]. As recorded quarry blasts may mislead scientific interpreting and lead to erroneous results in the analysis of seismic hazards in mines, standard processing of seismic monitoring data require these events to be separated. An automatic classifier is necessary to be developed to reduce the dramatically arduous task of finding to which class each recorded event belongs [9–17].

Many researches have been carried out on the topic of source location during the last decade. All techniques for source location methods can be classified under two conditions that require prior knowledge of the sonic speed of the structure [18] and methods that do not require such information [19–21]. However, few researches focused on the discrimination of mine seismic events in the past. Generally two steps, features extraction and statistical identification, could be separated from all those limited amount discriminators. Parameters characterizing the source (such as *magnitude, potency, moment, energy, static stress drop, apparent stress, and apparent volume*) and parameters directly extracted from the seismograms (including *amplitude, polarization, frequency, correlation coefficient, and travel time*) are the two categories of discriminating features. Statistical methodologies like *fisher discriminant classifier, logistic regression, unascertained measurement, and neural networks* have been occasionally carried out on mine seismic events identification and classification.

Malovichko selected the time of day, the repetition of waveforms, the high-frequency versus the low-frequency

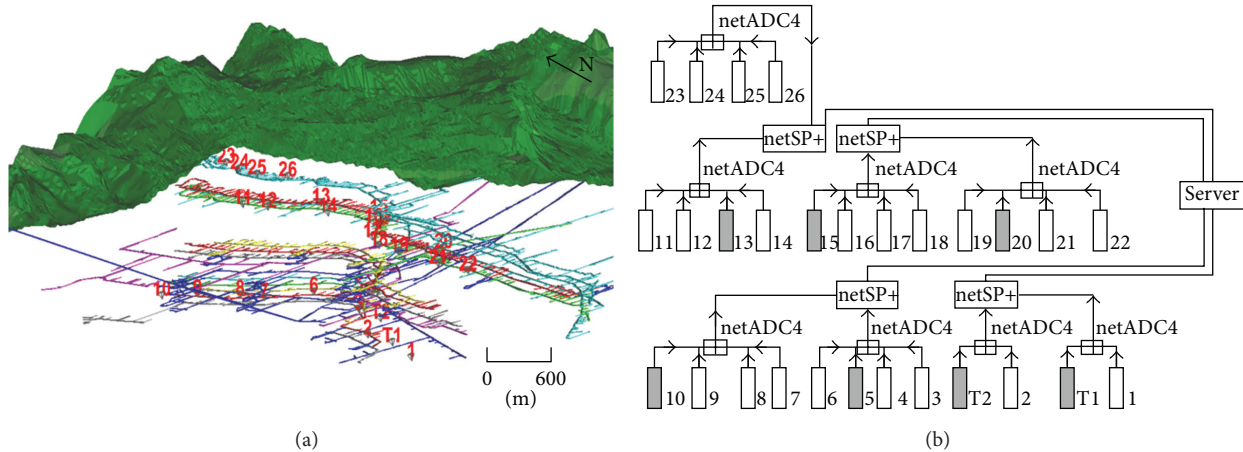


FIGURE 1: The microseismic monitoring system installed at Yongshaba mine: (a) isometric view of the ground surface, tunnels, and the microseismic monitoring system and (b) the configuration of the seismic network used in the project.

radiation and the radiation pattern as features and then established the Gaussian Maximum Likelihood Classification method for the classification [2]. This method provides a way to identify signals of different type, but the great amount of computation leads to low efficiency. Vallejos and McKinnon proposed the identification of seismic records in seismically active mines by considering the logistic regression and the neural network classification techniques. An efficient methodology was presented for applying these approaches to the classification of seismic records [3]. However, the calculation of seismic source parameters requires precise signal processing, namely expertise-required and time-consuming P- and S-wave hand-picking. Besides, the statistical classification models that only rely on source parameters show great difference in accuracy when applied to different mine sites.

Liu et al. proposed a synthesis method to identify microseismic event based on the triggering principle of short term average to long term average [9]. But very small fluctuations in the threshold would cause a great rate of misclassification since the threshold setting completely depends on experience. Zhu et al. decomposed the microseismic signals into 5 layers to gain specified frequency bands using wavelet analysis. Based on the box fractal dimensions and those specified frequency bands, 23-dimensional values of pattern recognition feature vector were established. The support vector machine, which was adopted to train, classify, and recognize, shows a correct identification rate of 94% [10]. Jiang et al. presented a three-step strategy to achieve the classifying of local multichannels microseismic waveforms. The author extracted the time-frequency, the amplitude distribution, and the correlation coefficient as features and established an effective judgment mechanism [11]. However, the studies did not provide much attention to the huge workload of calculation in practical application. Their input data could not be obtained directly from the monitoring system and their calculation algorithm is very complicated. The efficiency of identification still needs further improvement since any algorithm must be as simple as possible in order to run on a small low-power microprocessor.

A classification method of mine blasts and microseismic events using the starting-up features in seismograms was proposed. It is a method that presents less computation with a relatively low misjudgment rate. In this study, the Bayes discriminant classifier is applied to further analyse the “starting-up features.” The differential discriminating performances acquired by means of extracting the features of, respectively source parameters and waveform, were compared and discussed.

2. Data

2.1. Engineering Background. The Yongshaba Mine is located at Gaobang, which is about 85 km northeast of Guiyang ($26^{\circ}38'N$, $106^{\circ}37'E$), Guizhou Province, PR China. It is the main operation base of the Guizhou Kailin Co. Ltd. with phosphate production capacity over 200,000 tons/year. The current exploitation stopes are mainly scattered on levels of 1090 m to 840 m with a relative depth of 500 m to 700 m below the surface. Tens of millions of tons has cumulatively excavated employing open stoping mining method since initial operating in the 1950s.

The study region covers a volume of approximately $3000\text{ m} \times 300\text{ m} \times 350\text{ m}$, between the depths of 300 m and 700 m below the surface. The underground microseismic monitoring system, used to inform the evolution of the microfracture behavior, consists of 26 uniaxial and 2 triaxial geophones (Figure 1). The geophone manufactured by IMS holds a natural frequency of 14 Hz and a sampling rate of 6000 Hz. Signals from various dynamic processes, fracturing in rock mass, production and development blasts, impacts, and vibration of machinery, all are being recorded by the microseismic monitoring system.

2.2. Databases. The sample databases used in this study consist of two parts: the subset of the signals of blast events and the subset of the signals of normal microseismic events. Each of the signals in the blast subset has been confirmed to be consistent with the blast operations according to

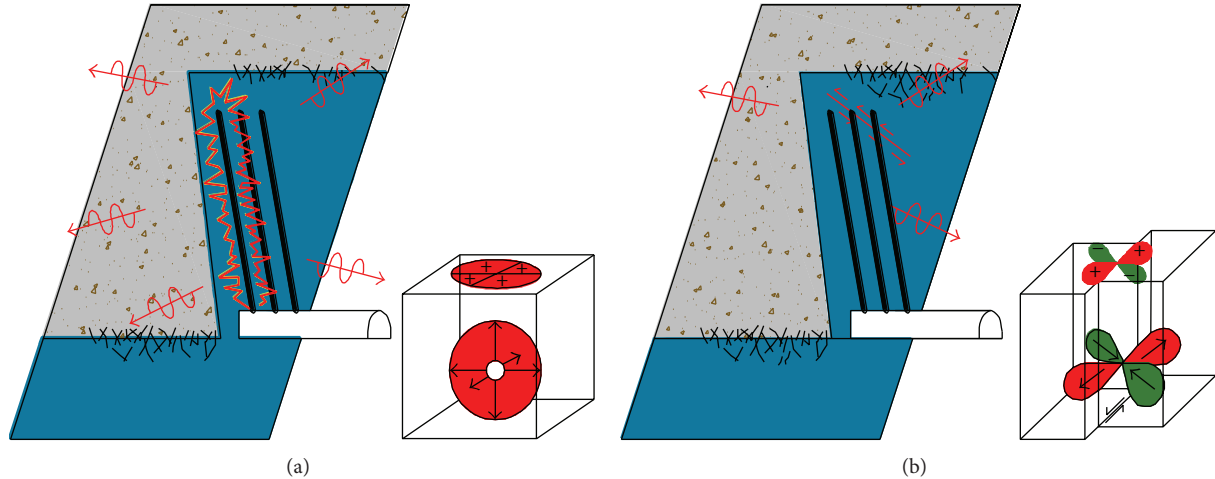


FIGURE 2: Two typical seismic source processes in mines, blast (a) and shear fracturing (b) (Malovichko 2012). Radiation pattern of an idealized explosion and of a strike-slip earthquake along a vertically dipping fault are shown correspondingly (Bormann, 2002). The arrows show the directions of compressional (outward, polarity +, red shaded) and dilatational (inward, polarity –, green shaded) motions in P-wave.

the time and location records provided by the mining workers. The subset of the microseismic events can be divided into two parts: those related to discrete, large-scale rock mass failures and those not resulting in observable rock mass damage. The observable ones also have been confirmed to be consistent with the fact. For the unobservable ones, they were processed manually by three independent processors. To aid in determining whether an event is a microseismic or not, the guide lines of an unequivocal classification were listed in Table 1. Only when the three discriminating results are exactly equivalent can the event be recruited into the database. Those events that could not be determined which type belongs to by manually approaches, were not enrolled into the sample database. The databases used in this paper contain a total of 103 seismic records with all seismic parameters calculated, from which 56 are labeled as normal events and the others are tagged as blasts.

3. Discriminating Features

3.1. Approach I: Source Parameters. A seismic event is the sudden release of potential or stored energy in the rock. The released energy is then radiated as seismic wave [7]. The two typical seismic source processes in mines (the blasts and the shear fracturing of the microseismic events) and its approximate radiation patterns are shown in Figure 2. It is obvious that the explosion radiates predominantly P-waves outward directing compressional directions while the shear fracturing or slip on a surface radiates S-waves that are stronger than P-waves. These characteristics can be used to identify the type of source process and to discriminate between blasts and microseismic events [2].

3.1.1. Seismic Moment. The basic characteristics of radiation can be described by a seismic moment tensor. This tensor

represents a set of fictitious dipoles acting on a point in the source area. The moment tensor makes it possible to describe the low-frequency amplitudes and polarities of seismic waves. Inverting the moment tensor from the observed waveforms and analysis of its components allows the discrimination of blasts from slip-type and, even, from crush-type events [2, 13, 14]. The logarithm of the seismic moment is considered as the feature of radiation.

Figure 3(a) shows that the values of the $\log(M)$ at the points with the highest probability density are 10.0 for blasts and 8.0 for microseismic events. The seismic moment is a relative useful performing discriminating feature as it provides a relatively large separation between normal events and blasts.

3.1.2. Seismic Energy. The energy release during rock fracturing and frictional sliding comes from the transformation of elastic strain into inelastic strain [14]. This transformation may occur at different rates ranging from slow creep-like events to very fast dynamic seismic events. The average velocity of deformation at the source is up to a few meters per second. Unlike the dynamic sources of the same size, the slow type events have long time duration at the source and thus radiate predominantly lower frequency waves. In terms of fracture mechanics, the slower the rupture velocity is, the less energy the event radiates. A quasi-static rupture would radiate practically no energy. Similarly for blasting, smaller blasts make smaller changes to the rock mass or more gradual stress changes, so that the response is less dynamic [12–16].

Observations from the probability density distribution (Figure 3(b)) indicate that the seismic energy is one of the best performing discriminating features. The value of $\log(E)$ distributed from -2 to 2 for microseismic events and 0 to 6 for blasts. More than 65% of the blasts events could be accurately identified in terms of this single indicator.

TABLE I: Guidelines for mine seismic events classification manually.

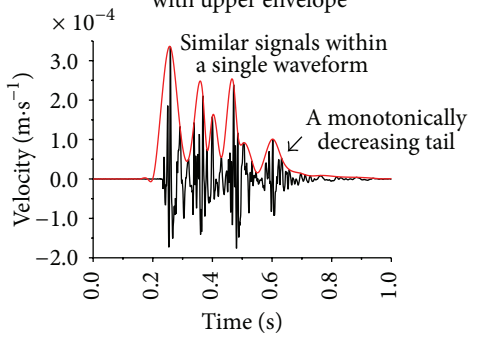
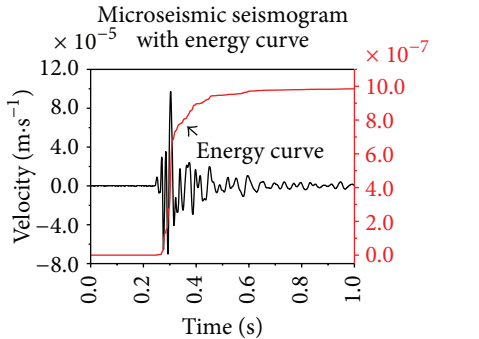
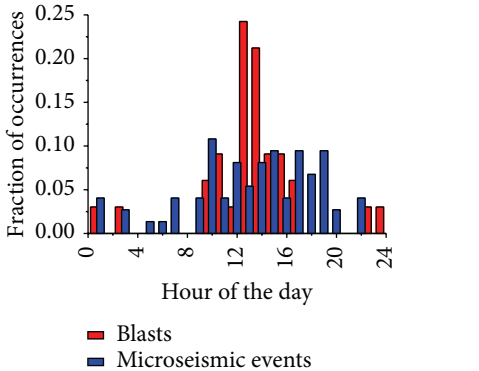
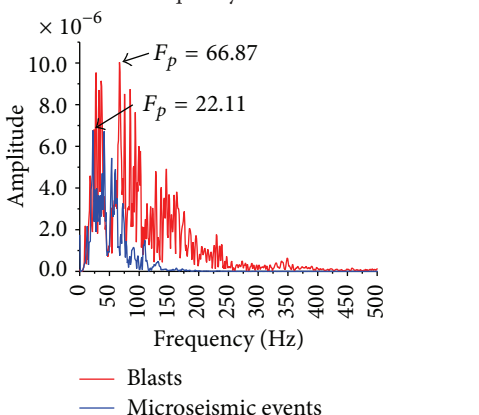
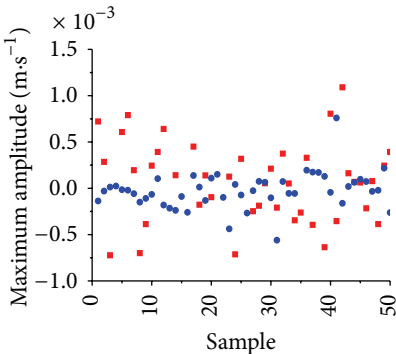
Characteristics	Description
<p>The presence of delays of the blast</p> <p>Blasting seismogram with upper envelope</p> 	<p>Blasts, especially stope firings, have multiple delays, which are expressed in the seismogram as similar signals repeating closely within a short time interval. The practice of decides whether an event is a blast or a microseismic event is based on the repetition feature. Besides, seismograms capturing a blast will have a monotonically decreasing tail commonly. For the waveform of a microseismic signal, a large amplitude difference exists between the maximum peak and the peak closest behind, without a gradual decrease.</p>
<p>The steeper rise in the energy curve of the normal event</p> <p>Microseismic seismogram with energy curve</p> 	<p>Seismograms capturing a microseismic event usually associated with shear fracturing and have an S-wave arrival more obvious than in the cases of blasts due to the source of the latter are usually in the focal mechanism of expansion and compression. Furthermore, blasting events will typically have a consistent gradual rise in their energy curve while seismic events will tend to have a steeper, more distinct, rise in the energy curve, and the energy curves for blasting events can be loosely compared to a positive sloping flat line.</p>
<p>The time of occurrence</p> 	<p>Another way to eliminate blasts from the microseismic catalogue is to apply the time filters (i.e., generally mines have prescribed blasting times, and the events that does not occur at the blasting time are marked as microseismic events). Two main daily blasting shifts are observed from the typical diurnal chart of Chinese mines, hours between 10~16 (stope firings) and 23~1 (development firings), each of which triggers an increase in seismicity. It has to be classified referring to other features for the cases that recorded during the blasting time and located close to the blasting area.</p>
<p>The dominant frequency</p> 	<p>A large number of actual observations and analysis show that blasts or explosions usually radiate higher frequency waves compared to normal microseismic events. The statistics show that the value of the dominant frequency of the microseismic events varies from 10 to 100 Hz and from 70 to 260 Hz for blasts. In addition, blasting events will typically not be well matched to the Brune's model curve as plotted in the Stacked Spectra Plot within TRACE (the software provided by IMS). Spectral analysis is often considered as a relative effective method to distinguish blasts from microseismic events.</p>

TABLE I: Continued.

Characteristics	Description
<p>The maximum amplitude</p>  <p>Maximum amplitude ($\text{m}\cdot\text{s}^{-1}$) $\times 10^{-3}$</p> <p>Sample</p> <ul style="list-style-type: none"> ▪ Blasts • Microseismic events 	<p>The maximum amplitude of the waveform, which characterizes the size of energy released, is also considered as an important reference for the recognition of blasts and microseismic events. Generally the maximum vibration velocity of microseismic events is about $10^{-5} \text{ m}\cdot\text{s}^{-1}$ far less than $10^{-3} \text{ m}\cdot\text{s}^{-1}$ of the blasting. However, this approach cannot be considered as universally applicable since it is possible to have a scenario where a blast triggers shear fracturing that radiates stronger seismic signals than the blast itself.</p>

3.1.3. S : P Energy Ratio. There are several seismic phases, but only S-waves and P-waves are commonly recorded in mining induced seismicity. P-waves, or compressive waves, are the first ones which arrive at receivers. When seismic waves propagate, they carry energy from the source of the shaking outward in all directions. The ratio between S-wave energy and P-wave energy can be an indicator of seismic source mechanism [4]. Seismic energy is proportional to the integral of the square of the vectorial sum of the velocity waveform and can be calculated separately for the P-wave and S-wave [7]. For fault-slip type events in seismology (earthquakes), there is considerably more energy in the S-wave than in the P-wave with the ratio of the S-wave energy to the P-wave energy frequently greater than 10 [12]. Urbancic et al. noted that for nonshear seismic source mechanisms, there would be a deficiency in S-wave energy or relatively more P-wave energy than for shearing events. For nonshearing event mechanisms, such as strain-bursting, tensile failure, and volumetric rock mass fracturing, the ratio of S-wave energy to P-wave energy is frequently in the range of 3 or less [14].

Observations from Figure 3(c) point out that the most probability of the $\log(E_S/E_P)$ falls in the interval of 0.0 to 2.0 for microseismic events and -1.0 to 4.0 for blasts. It was obvious that the S : P energy ratio performs not well in this mine site since too small separation was provided.

3.1.4. Static Stress Drop. Shearer defined the term-stress drop, $\Delta\sigma$, as the average difference between the stress across the fault before and after an earthquake [17]. There are several different methods of determining the stress drop, of which some use records of ground velocity and ground acceleration. Stress drops can vary considerably from event to event. For microseismic events in Yongshaba mine, the range of $\log(\text{SSD})$ is from 2.5 to 4.5 and 3.0 to 6.5 for blasts (Figure 3(d)). This parameter plays a tremendous role in Yongshaba mines seismic discrimination.

3.1.5. Time of Occurrence. Mining-induced seismic events occur most of the time in the ultimate proximity of mine workings and concentrate during blasting time. Statistical results show that almost all the blasts occur at 10:00 to 15:00 and rarely occur in other time (Figure 3(e)). However, a large number of microseismic events take place at this time simultaneously. The performance of the “time of occurrence” is discounted.

3.1.6. Number of Triggers. The Number of triggers is affected by many factors. Mine layout, geological features, seismic locations, and the sensor array all are likely to affect the number of triggered sensors. It should be guaranteed that the potential areas of microseismic occurring and blasting operations are enclosed inside the sensor array. Only in this way can the “number of triggers” reflect the pattern of seismic wave propagation and the scale of seismic energy. Figure 3(f) shows blasting events usually triggering more sensors than normal microseismic events. The discriminating feature of the “number of triggers” provides a relatively medium separation between normal events and blasts.

3.2. Approach II: Waveform Features. The classification method of mine blasts and microseismic events using the starting-up features in seismograms was proposed. Signals from databases of different event types were drawn into a unified coordinate system. All waveform sections are starting at the point of each P-wave first arrival and ending in their first peak points (Figure 4(a)). It is noticed that the starting-up angle of the two types tends to be concentrated into two different intervals. Since it is difficult to calculate the starting-up angle directly due to the inaccuracy of P-wave arrival’s picking, the slope value of the starting-up trend line obtained from linear regression was proposed to substitute the angle. Two slope values associated with the coordinates

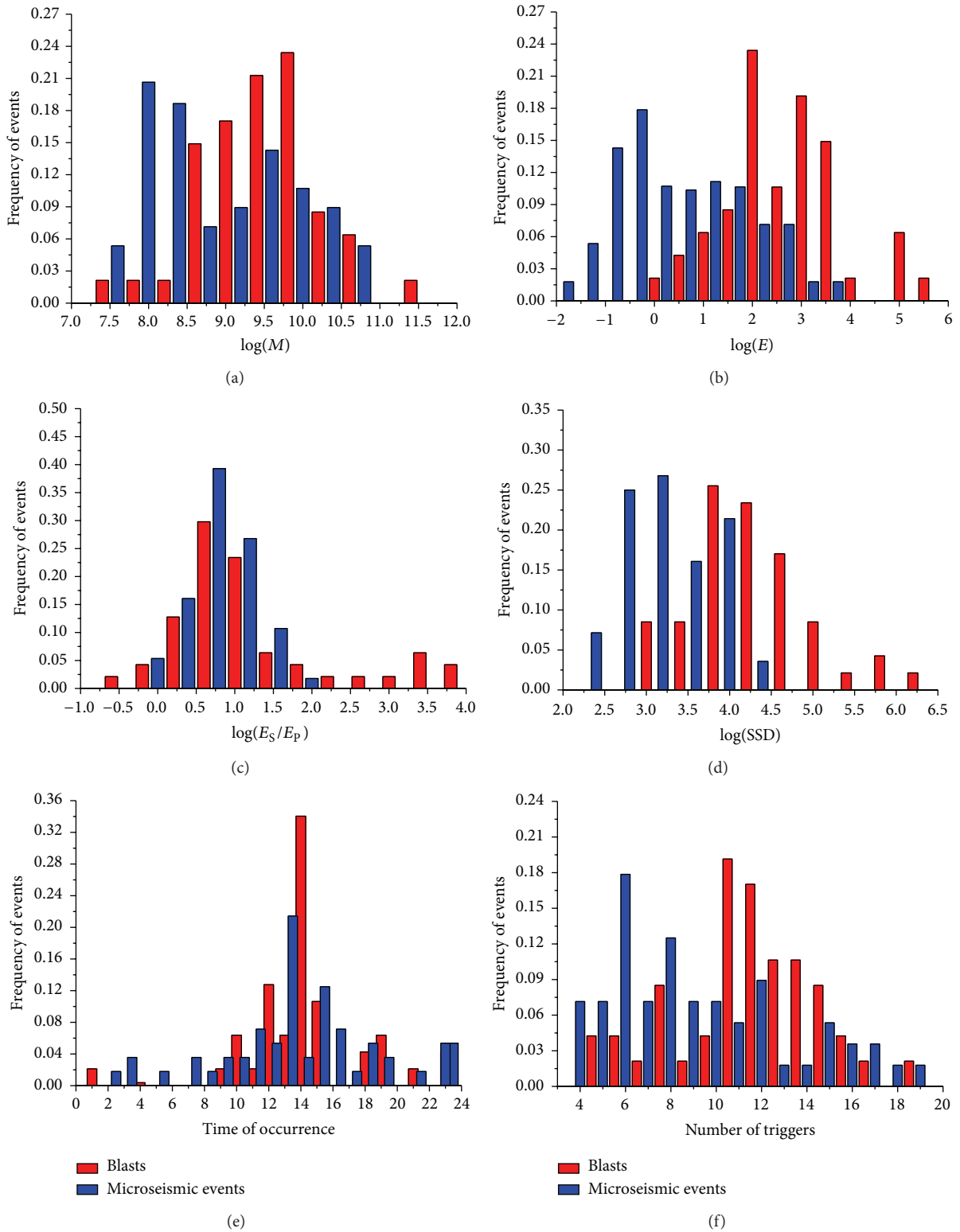


FIGURE 3: Distributions of the measured features for the database are displayed as histograms. The seismic energy is the best performing discriminating feature as it provides maximum separation between normal events and blasts. The feature “time of occurrence” provides the slightest separation between blasts and normal events.

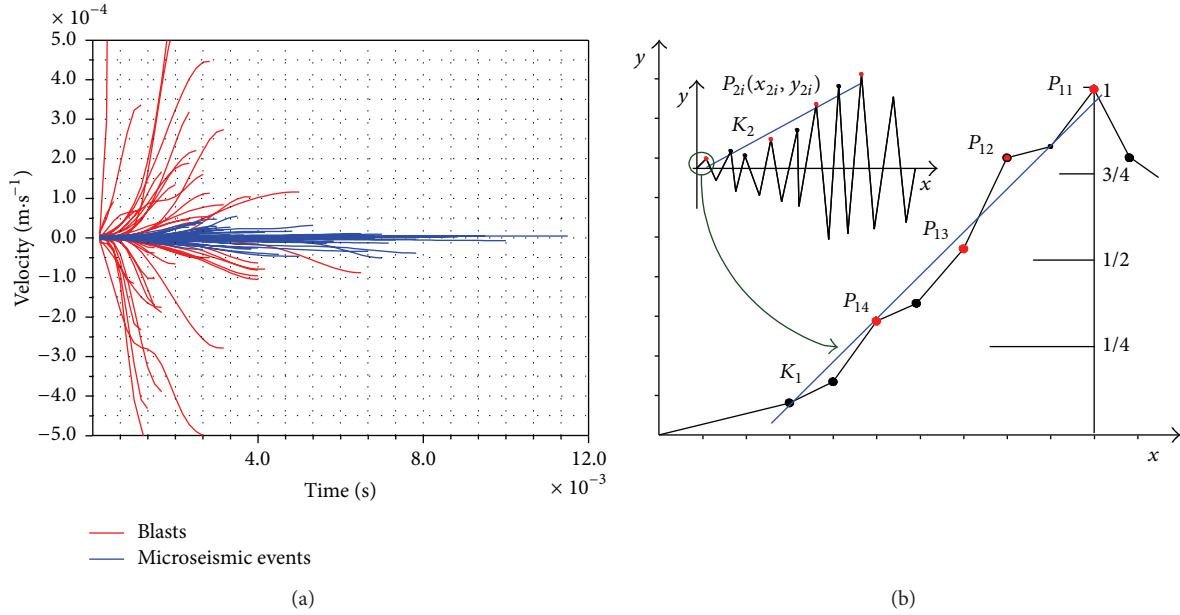


FIGURE 4: Comparison chart of signal starting-up before first peak within blasts and microseismic events (frame (a)) and the schematic diagram of data points selecting and the trend line constructed by linear regression (frame (b), solid circles represent sampling points, and the reds represent the selected). The x - and y -axis in frame (b) represent the time and the amplitude axis in frame (a).

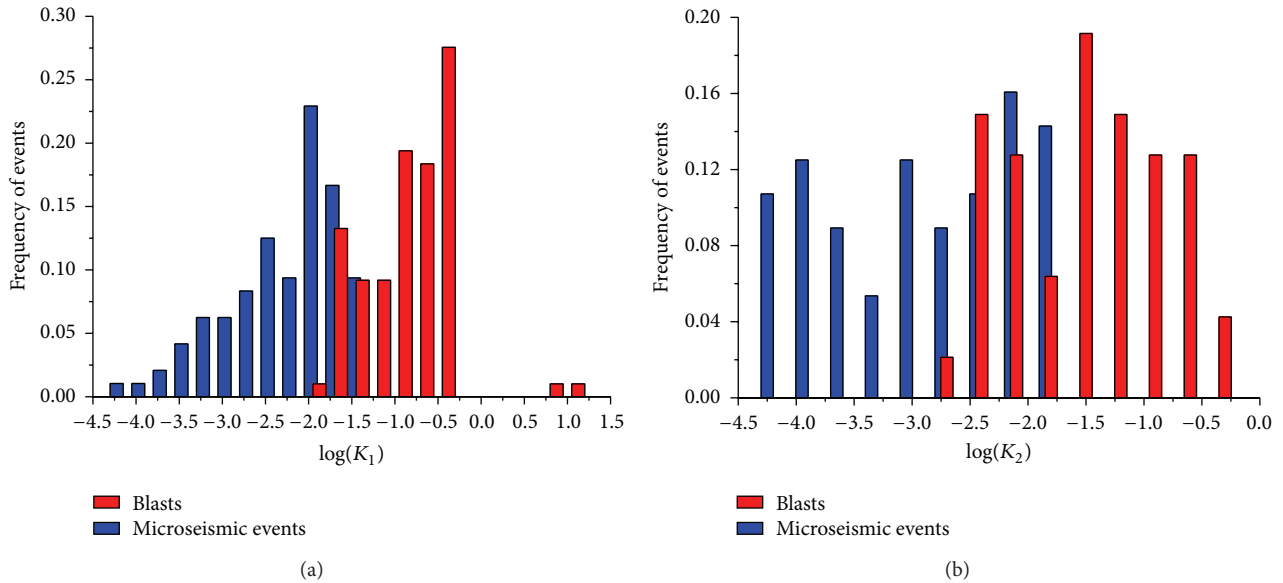


FIGURE 5: Comparison chart of slope value of the two starting-up trend lines within waveforms of blasts and microseismic events. Histograms are used to illustrate the behavior of the discriminating features.

of the first peak and the maximum peak were extracted as the characteristic parameters.

Set K_1 as the absolute value of the slope of the trend line of the waveform section that is from the P-wave arrival to the first peak, and set K_2 as the absolute value of the slope of the trend line of the waveform section that is from the P-wave arrival to the maximum peak. The two trend lines are constructed by linear regression based on four points. The method of the features extraction and their performance are displayed in Figures 4 and 5.

4. Method

Bayes discriminant is a branch of modern statistics with the basic hypothesis that some certain cognitions of the studying collectivity had been received before extracting samples. Generally using the priori probability to describe the level of awareness, and then the posterior probability was obtained by modifying it [22–26].

Suppose $\mathbf{G} = (\mathbf{X}_1, \mathbf{X}_2, \dots, \mathbf{X}_p)^T$ is a collectivity with p member indexes, and $f_1(\mathbf{X})$ and $f_2(\mathbf{X})$ are the distribution

density functions of the two collectivities: \mathbf{G}_1 which refers to blasts and \mathbf{G}_2 which refers to microseismic events. Indexes $\mathbf{X}_1, \mathbf{X}_2, \mathbf{X}_3, \mathbf{X}_4,$ and \mathbf{X}_5 represent the characteristic parameters, respectively.

The priori probability of \mathbf{G}_1 and \mathbf{G}_2 are calculated by the following formulas:

$$p_1 = P(\mathbf{G}_1) = \frac{n_1}{n_1 + n_2}, \quad p_2 = P(\mathbf{G}_2) = \frac{n_2}{n_1 + n_2}, \quad (1)$$

where n_1 and n_2 are the number of training samples belonged to the collectivity \mathbf{G}_1 and \mathbf{G}_2 .

Set $\Sigma_1, \Sigma_2,$ and Σ as the covariance matrix of $\mathbf{G}_1, \mathbf{G}_2,$ and \mathbf{G} . The Bayes discriminant function can be expressed as follows when $\Sigma_1 = \Sigma_2 = \Sigma$:

$$W_j(\mathbf{X}) = (\Sigma^{-1} \boldsymbol{\mu}_j)^T - 0.5 \boldsymbol{\mu}_j^T \Sigma^{-1} \boldsymbol{\mu}_j + \ln p_j, \quad j = 1, 2, \quad (2)$$

where $\boldsymbol{\mu}_j$ is the mean vectors of \mathbf{G}_j and the generalized squared distance function can be obtained as

$$d_j^2(\mathbf{X}) = (\mathbf{X} - \boldsymbol{\mu}_j)^T \Sigma^{-1} (\mathbf{X} - \boldsymbol{\mu}_j) - 2 \ln p_j. \quad (3)$$

The a posteriori probability function can be obtained as follows:

$$P(\mathbf{G}_j | \mathbf{X}) = \frac{p_j f_j(\mathbf{X})}{p_1 f_1(\mathbf{X}) + p_2 f_2(\mathbf{X})}. \quad (4)$$

Since $p_j f_j(\mathbf{X}) \propto \exp[-0.5 d_j^2(\mathbf{X})]$, then

$$P(\mathbf{G}_j | \mathbf{X}) = \frac{\exp[-0.5 d_j^2(\mathbf{X})]}{\exp[-0.5 d_1^2(\mathbf{X})] + \exp[-0.5 d_2^2(\mathbf{X})]}. \quad (5)$$

Normally $\boldsymbol{\mu}_1, \boldsymbol{\mu}_2,$ and Σ are unknown and their estimation values $\hat{\boldsymbol{\mu}}_1, \hat{\boldsymbol{\mu}}_2,$ and $\hat{\Sigma}$ can be obtained from the training samples; then

$$\hat{d}_j^2(\mathbf{X}) = (\mathbf{X} - \hat{\boldsymbol{\mu}}_j)^T \hat{\Sigma}^{-1} (\mathbf{X} - \hat{\boldsymbol{\mu}}_j) - 2 \ln p_j. \quad (6)$$

The estimation of a posteriori probability function is

$$\hat{P}(\mathbf{G}_j | \mathbf{X}) = \frac{\exp[-0.5 \hat{d}_j^2(\mathbf{X})]}{\exp[-0.5 \hat{d}_1^2(\mathbf{X})] + \exp[-0.5 \hat{d}_2^2(\mathbf{X})]}. \quad (7)$$

Bayes discriminant criterion can be expressed as

$$\begin{aligned} \mathbf{X} \in \mathbf{G}_1, \quad & \text{when } \hat{P}(\mathbf{G}_1 | \mathbf{X}) \geq \hat{P}(\mathbf{G}_2 | \mathbf{X}), \\ \mathbf{X} \in \mathbf{G}_2, \quad & \text{when } \hat{P}(\mathbf{G}_1 | \mathbf{X}) < \hat{P}(\mathbf{G}_2 | \mathbf{X}). \end{aligned} \quad (8)$$

To estimate the reliability of the discriminator, the resubstitution method was used to calculate the misdiscrimination rate. All the training samples were regarded as the new samples and resubstituted into the classifier. The rate of misjudgment can be evaluated by the following index $\hat{\alpha}$:

$$\hat{\alpha} = \frac{n_{12} + n_{21}}{n_1 + n_2}, \quad (9)$$

where n_{12} is the number of training samples regarded to be \mathbf{G}_2 which belong to collectivity of \mathbf{G}_1 actually and n_{21} is the number of training samples discriminated as \mathbf{G}_1 but belongs to \mathbf{G}_2 in fact.

TABLE 2: Prior probabilities for groups.

Type	Prior	Cases used in analysis	
		Unweight	Weighted
Blast	0.5	47	47.0
Microseismic event	0.5	56	56.0
Total	1.0	103	103.0

5. Results

The aim of the present study is to compare the two approaches for event accurate identification of different classes. The Bayes discriminant models for signal identification are established after developing the theory discussed above to the 103 sets of samples selected. The prior probabilities for different groups and the classification function coefficients are listed in Tables 2 and 3.

As can be seen from the classification functions coefficients, the features of source parameters are in the following order according to their importance in the accurate identification of microseismic events: the seismic moment, the static stress drop, the seismic energy, the S:P energy ratio, the number of triggers, and the time of occurrence. According to their importance in the accurate identification of microseismic events, the waveform characteristics are in order of the time of the first peak arrival (x_{11}), the amplitude of the maximum peak (y_{21}), the slope value of the first trend line (K_1), the slope value of the second trend line (K_2), the amplitude of the first peak (y_{11}), and the time of the maximum peak arrival (x_{21}).

The classification results show that 83.5% of original grouped cases are correctly classified by approach I, and 97.1% of original grouped cases are correctly classified by approach II (Table 4). The results show that the second features extraction approach (waveform characteristics) has higher accuracy. Although the input data used for classification in approach II cannot be given directly by the monitoring systems, the calculation process of those characteristic parameters are not complicated.

These misclassified events are labeled in Figure 6 according to the order of moment magnitude. Figure 6 shows the misclassified cases of both approaches falling without specific magnitude intervals. It is concluded that the error rate is not affected by the seismic magnitude or the scale of seismic energy. Although approach I has a higher misclassified rate with a more complex computation, it has been widely used in many mines. Approach II is a new straight-forward method with lower error rate and got very good application in the Yongshaba mine. But in other mines or in more complex cases (mines existing variety of dynamic processes which radiate seismic waves, such as shock and vibrations induced by orepass), the feasibility of this approach may need further improvements.

6. Conclusion

(1) The considerations and the criteria of manual identification of blasts and microseismic events were summarized

TABLE 3: Classification function coefficients.

Approach I	$\log(M)$	$\log(E)$	$\log(E_s/E_p)$	$\log(SSD)$	TOO ^a	NOT ^b	Constant
Blast	18.229	-9.827	2.964	18.790	0.625	-1.495	-11.242
Microseismic	18.248	-9.761	2.410	16.133	0.557	-1.596	-100.464
Approach II	$\log(x_{11})$	$\log(y_{11})$	$\log(K_1)$	$\log(x_{21})$	$\log(y_{21})$	$\log(K_2)$	Constant
Blast	-92.588	3.878	-8.471	-3.704	-33.644	-4.304	-186.187
Microseismic	-91.487	2.263	-10.915	-0.344	-32.830	-7.053	-193.783

^aTOO presents the time of occurrence; ^bNOT presents the number of triggers.

TABLE 4: Classification results.

Type	Predicted group membership (approach I)		Predicted group membership (approach II)		Total
	Blast	Microseismic events	Blast	Microseismic events	
Count					
Blasts	39	8	46	1	47
Microseismic events	9	47	2	54	56
%					
Blasts	83.0	17.0	97.9	2.4	100.0
Microseismic events	16.1	83.9	3.6	96.4	100.0

83.5% of original grouped cases are correctly classified by approach I, and 97.1% of original grouped cases are correctly classified by approach II.

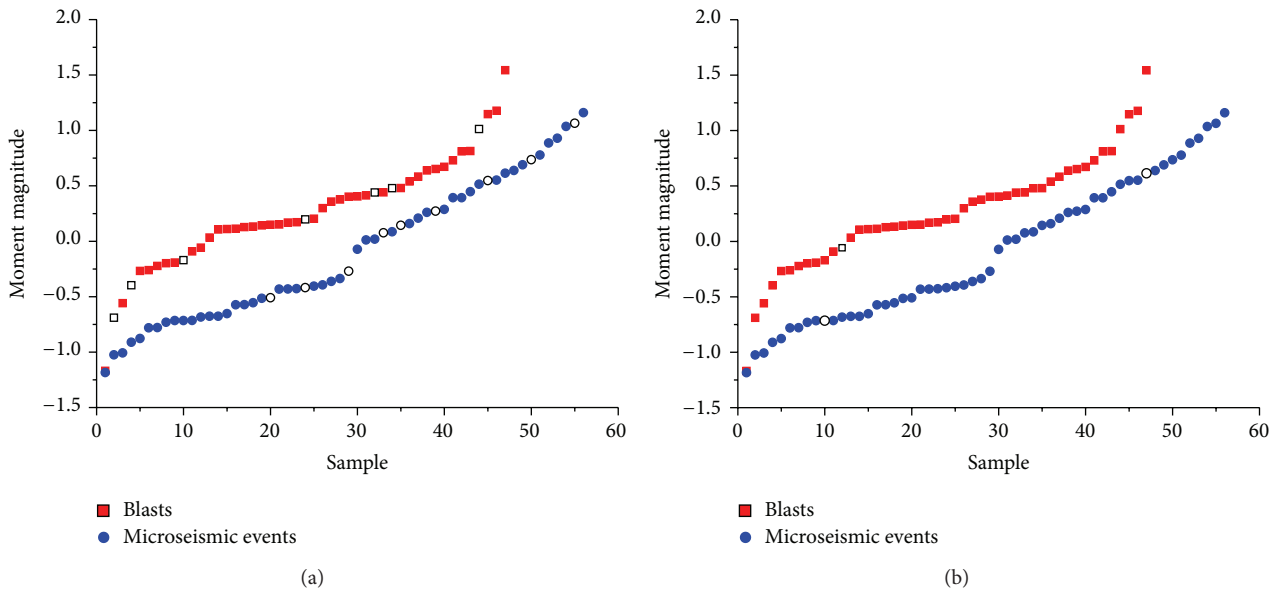


FIGURE 6: Events that are misclassified: frame (a) misclassified by approach I and frame (b) misclassified by approach II. The hollow ones represent the misclassified cases.

based on experiences. The guide lines listed in this study cover well the majority of all the encountered situations in seismic data processing. The sample databases of the two types' events were established by three independent processors with reference to these guidelines.

(2) Two features extraction approaches were proposed. Features of source parameters including the seismic moment, the seismic energy, the energy ratio of S- to P-wave, the static stress drop, the time of occurrence, and the number of triggers were selected, counted, and analyzed in approach I.

Waveform characteristics consisting of two slope values and the coordinates of the first peak and the maximum peak were extracted as the discriminating parameters in approach II.

(3) The discriminating performance of the two approaches were compared and discussed by applying the Bayes discriminant analysis to the characteristic parameters extracted. The classification results show that 83.5% of the original grouped cases were correctly classified by approach I, and 97.1% of original grouped cases were correctly classified by approach II.

(4) Comparative analysis shows that the misclassified cases of the two approaches all fall without specific magnitude intervals. The error rate is not affected by the seismic magnitude. Although approach II has got very good application in the Yongshaba mine, the feasibility of this approach may need further improvements in other mines or in more complex cases, mines existing in variety of dynamic processes which radiate seismic waves, such as shock and vibrations induced by orepass.

Conflict of Interests

The authors declare that there is no conflict of interests regarding the publication of this paper.

Acknowledgment

The authors gratefully acknowledge the financial support of National Natural Science Foundation of China (no. 51374244, 11447242) and the Fundamental Research Funds of Central South University (no. 2013zzts058).

References

- [1] A. J. Jager and J. A. Ryder, *A Handbook on Rock Engineering Practice for Tabular Hard Rock Mines*, Creda Communications, Cape Town, South Africa, 1999.
- [2] D. Malovichko, "Discrimination of blasts in mine seismology," in *Proceeding of the Deep Mining*, Australian Centre for Geomechanics, Perth, Australia, 2012.
- [3] J. A. Vallejos and S. D. McKinnon, "Logistic regression and neural network classification of seismic records," *International Journal of Rock Mechanics and Mining Sciences*, vol. 62, pp. 86–95, 2013.
- [4] S. J. Gibowicz and A. Kijko, *An Introduction to Mining Seismology*, Academic Press, San Diego, Calif, USA, 1994.
- [5] K. Larsson, *Seismicity in Mines: A Review*, Luleå University of Technology, 2004.
- [6] P. Bormann, *New Manual of Seismological Observatory Practice*, GFZ, Potsdam, Germany, 2002.
- [7] A. J. Mendecki, *Seismic Monitoring in Mines*, Chapman & Hall, London, UK, 1997.
- [8] L.-J. Dong, X.-B. Li, Z.-L. Zhou, G.-H. Chen, and J. Ma, "Three-dimensional analytical solution of acoustic emission source location for cuboid monitoring network without pre-measured wave velocity," *Transactions of Nonferrous Metals Society of China*, vol. 25, no. 1, pp. 293–302, 2015.
- [9] C. Liu, C.-A. Tang, J.-H. Xue, and G.-F. Yu, "Comprehensive analysis method of identifying and calibrating micro-seismic events attributes in coal and rock mass," *Journal of Mining & Safety Engineering*, vol. 28, no. 1, pp. 61–65, 2011.
- [10] Q.-J. Zhu, F.-X. Jiang, Y.-M. Yin, Z.-X. Yu, and J.-L. Wen, "Classification of mine microseismic events based on wavelet-fractal method and pattern recognition," *Chinese Journal of Geotechnical Engineering*, vol. 34, no. 11, pp. 2036–2042, 2012.
- [11] F.-X. Jiang, Y.-M. Yin, Q.-J. Zhu, S.-X. Li, and Z.-X. Yu, "Feature extraction and classification of mining microseismic waveforms via multi-channels analysis," *Journal of the China Coal Society*, vol. 39, no. 2, pp. 229–237, 2014.
- [12] P. Duplancic, *Characterization of caving mechanism through analysis of stress and seismicity [Ph.D. thesis]*, University of Western Australia, Perth, Australia, 2001.
- [13] Y. Abolfazlzadeh, *Application of Seismic Monitoring in Caving Mines Case Study of Telfer Gold Mine*, Laurentian University, Ontario, Canada, 2013.
- [14] T. I. Urbancic, B. Feignier, and R. P. Young, "Influence of source region properties on scaling relations for $M < 0$ events," *Pure and Applied Geophysics*, vol. 139, no. 3-4, pp. 721–739, 1992.
- [15] M. R. Hudyma, D. Heal, and P. Mikula, "Seismic monitoring in mines—oldtechnology—newapplications," in *Proceedings of the 1st Australasian Ground Control in Mining Conference*, pp. 201–218, University of New South Wales, Sydney, Australia, 2003.
- [16] J. Boatwright and J. B. Fletcher, "The partition of radiated energy between P and S waves," *Bulletin of the Seismological Society of America*, vol. 74, pp. 361–376, 1984.
- [17] P. M. Shearer, *Introduction to Seismology*, Cambridge University Press, Cambridge, Mass, USA, 1999.
- [18] L. J. Dong, X. B. Li, and G. Xie, "An analytical solution for acoustic emission source location for known P wave velocity system," *Mathematical Problems in Engineering*, vol. 2014, Article ID 290686, 8 pages, 2014.
- [19] X. B. Li and L. J. Dong, "An efficient closed-form solution for acoustic emission source location in three-dimensional structures," *AIP Advances*, vol. 4, no. 2, Article ID 027110, 2014.
- [20] L. J. Dong and X. B. Li, "Three-dimensional analytical solution of acoustic emission or microseismic source location under cube monitoring network," *Transactions of Nonferrous Metals Society of China*, vol. 22, no. 12, pp. 3087–3094, 2012.
- [21] L. Dong and X. Li, "A microseismic/acoustic emission source location method using arrival times of PS waves for unknown velocity system," *International Journal of Distributed Sensor Networks*, vol. 2013, Article ID 307489, 8 pages, 2013.
- [22] S. Weisberg, *Applied Linear Regression*, John Wiley & Sons, Hoboken, NJ, USA, 3rd edition, 2005.
- [23] L. Dong and X. Li, "Comprehensive models for evaluating rockmass stability based on statistical comparisons of multiple classifiers," *Mathematical Problems in Engineering*, vol. 2013, Article ID 395096, 9 pages, 2013.
- [24] Å. Björck, *Numerical Methods for Least Squares Problems*, SIAM, Philadelphia, Pa, USA, 1996.
- [25] A. R. Webb, *Statistical Pattern Recognition*, John Wiley & Sons, 2nd edition, 2002.
- [26] G. J. McLachlan, *Discriminant Analysis and Statistical Pattern Recognition*, John Wiley & Sons, Malvern, UK, 1992.

Research Article

The Mechanism and Application of Deep-Hole Precracking Blasting on Rockburst Prevention

Zhenhua Ouyang,^{1,2} Qingxin Qi,^{1,2} Shankun Zhao,^{1,2} Baoyang Wu,^{1,2} and Ningbo Zhang^{1,2}

¹China Coal Research Institute, Beijing 100013, China

²State Key Laboratory of Coal Mining and Clean Energy Utilization, Beijing 100013, China

Correspondence should be addressed to Zhenhua Ouyang; oyzhua@163.com

Received 13 November 2014; Revised 18 January 2015; Accepted 8 February 2015

Academic Editor: Marcin A. Lutynski

Copyright © 2015 Zhenhua Ouyang et al. This is an open access article distributed under the Creative Commons Attribution License, which permits unrestricted use, distribution, and reproduction in any medium, provided the original work is properly cited.

The mechanism of preventing rockburst through deep-hole precracking blasting was studied based on experimental test, numerical simulation, and field testing. The study results indicate that the deep-hole precracking could change the bursting proneness and stress state of coal-rock mass, thereby preventing the occurrence of rockburst. The bursting proneness of the whole composite structure could be weakened by the deep-hole precracking blasting. The change of stress state in the process of precracking blasting is achieved in two ways: (1) artificially break the roof apart, thus weakening the continuity of the roof strata, effectively inducing the roof caving while reducing its impact strength; and (2) the dynamic shattering and air pressure generated by the blasting can structurally change the properties of the coal-rock mass by mitigating the high stress generation and high elastic energy accumulation, thus breaking the conditions of energy transfer and rock burst occurrence.

1. Introduction

Rockburst is one of the major dynamic disasters in mining, tunneling, and other underground engineering since it causes numerous casualties and accidents in South Africa, Central Europe, North and South America, China, and other countries of the world. Since the first rockburst which occurred at Shengli coal mine in Fushun and was recorded in 1933, over 3,000 coal bursts had happened in nearly 140 coal mines in China over the past 80 years. Rockbursts and their secondary disasters have been associated with thousands of accidents and casualties. For instance, on June 5, 2008, November 3, 2011, and March 27, 2014, three serious rockbursts accidents happened in Qianqiu coal mine of Yima Coal Industry Group, killing a total of 29 people and injuring more than 80 people. Also, on February 14, 2005, 214 workers were killed in a gas explosion disaster induced by rockburst in Sunjiawan coal mine in Fuxin, Liaoning Province. Rockburst has become one of the major dynamic disasters in deep coal mining in China.

As of now, understanding of rockburst mechanism is not explicit because of so many uncertain factors such as

bursting proneness of coal and rock stratum, geological conditions, and mining technology. Over the years, many studies pertinent to evaluation [1–3], prediction, and prevention of rockbursts have been conducted. To effectively predict rockburst, various methods and/or models have been established, including fuzzy comprehensive evaluation method [4, 5], Bayes' discriminant analysis [6], unascertained measurement approach [7], Lyapunov index method [8], maximum entropy principle [9], rough set combined with genetic algorithm [10], judgment index classification [11], stress state determination [12], rough set theory [13], mining and seismological parameters [14–16], and optimal relative membership degree [9]. In the field, methods and measures of optimal mining layout, mining protection layer, coal seam water injection, hydraulic fracturing [17], destress blasting [18–20], rock blasting [21–24], deep-hole directional fracturing [25], destress drilling, and deep-hole precracking blasting, and so forth, have been developed and applied for burst prevention.

Deep-hole precracking blasting (DHPB) is conceptually defined as blasting in the coal-rock mass with a blast hole with a depth of more than 10 m to develop fractures in the coal-rock mass. A coal seam with thick hard roof strata, such

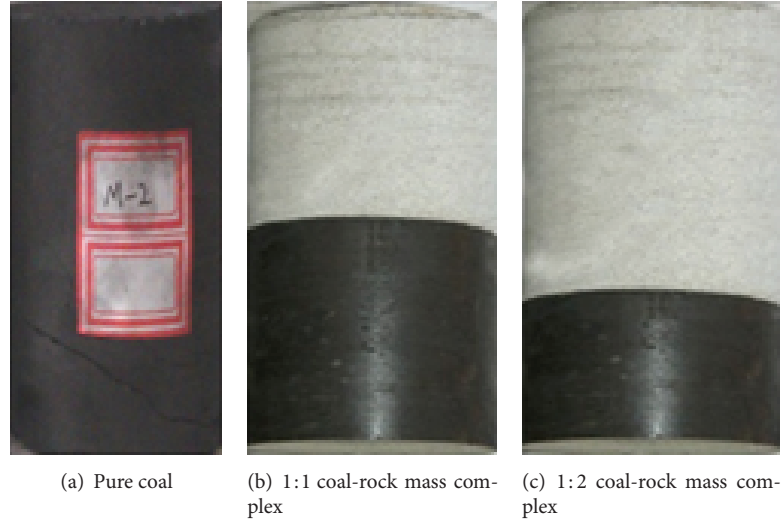


FIGURE 1: The bursting proneness test samples of coal-rock mass combination.

as Qianqiu mine of Yima Coal Industry Group and Huafeng coal mine of Xinwen Mining Group, uncaved roof strata in mined-out area could accumulate energy and incur potential rockburst. When adopting the approach of DHPB, the integrality and continuity of roof can be directly broken. As a simple process and effective rockburst preventing measure, it has been widely used in these burst-prone coal mines in China. To further study the rockburst mechanism of DHPB, experimental test, numerical simulation, and field testing were conducted and corresponding results were presented in this paper.

2. The Influence of DHPB on the Bursting Proneness of Coal-Rock Mass

2.1. Bursting Proneness Test of “Roof-Coal” Combination. The bursting proneness is an inherent property of coal-rock mass incurring bursting damage. In order to compare and study the bursting proneness of “roof-coal” combination, samples of roof stratum only, coal only, and two “roof-coal” combinations were tested with TAW-2000 microcomputer-controlled electrohydraulic servo rock triaxial testing machine in the lab. Figure 1 illustrates these three classified samples utilized in the test. Both roof rock and coal were taken from Yuejin coal mine of Yima Coal Industry Group and the samples of “roof-coal” combinations are glued together with columns of coal and roof rock. The finished cylindrical test specimens were about 50 mm in diameter and 100 mm in height.

The bursting proneness measurements of roof strata were conducted by following the Chinese national recommended standard GB/T25217.1-2010, which is named “Methods of test, monitoring and prevention of rockburst—part 1: Classification and laboratory test method on bursting liability of roof strata.” In this standard, bending energy index was expressed to determine and evaluate the bursting proneness of roof strata, just as Table 1 listed.

TABLE 1: Classification of bursting proneness of coal.

Classification	Type I	Type II	Type III
Bursting proneness	None	Weak	Strong
Bending energy index (U_{WQS})/kJ	$U_{WQS} \leq 15$	$15 < U_{WQS} \leq 120$	$U_{WQS} > 120$

The bursting proneness measurements of coal and “roof-coal” combinations were conducted by following the Chinese national recommended standard GB/T25217.2-2010, which is named “Methods of test, monitoring and prevention of rockburst—part 2: Classification and laboratory test method on bursting liability of coal.” To determine and evaluate the bursting proneness of coal, four indexes, including duration of dynamic fracture (DT), elastic strain energy (W_{ET}), bursting energy (K_E), and uniaxial compressive strength (R_c), were utilized in the testing and analysis. The classification of bursting proneness of coal is listed in Table 2.

2.2. Bursting Proneness Testing Results and Analysis. Based on measured uniaxial compressive strength, tensile strength, density, and elastic modulus of the roof stratum, the bending energy index of the roof was calculated as 22.09 kJ, which indicates that the bursting proneness of the roof stratum is weak.

Table 3 indicates sample group numbering, values of these four indexes of coal, and corresponding bursting proneness. Groups A, B, and C in Table 2 represent samples of coal, 1:1 coal-rock mass complex sample, and 1:2 coal-rock complex sample, respectively. The testing and calculation results indicate that the bursting proneness of these three group samples A, B, and C are weak, weak, and strong, respectively.

As indicated in Table 2, with the increase of roof stratum volume, the duration time of dynamic damage of the sample decreased, but the bursting energy, elastic energy, and uniaxial

TABLE 2: Classification of bursting proneness of coal.

Classification	Type I	Type II	Type III
Bursting proneness	None	Weak	Strong
Indexes			
Duration of dynamic fracture (DT)/ms	$DT > 500$	$50 < DT \leq 500$	$DT \leq 50$
Elastic strain energy index (W_{ET})	$W_{ET} < 2$	$2 \leq W_{ET} < 5$	$W_{ET} \geq 5$
Bursting energy index (K_E)	$K_E < 1.5$	$1.5 \leq K_E < 5$	$K_E \geq 5$
Uniaxial compressive strength (R_c)/MPa	$R_c < 7$	$7 \leq R_c < 14$	$R_c \geq 14$

TABLE 3: Bursting proneness testing results of coal and coal-rock mass combination.

Sample number	DT /ms	K_E	W_{ET}	R_c /MPa	Bursting proneness degree
A-1	316	1.44	3.10	10.08	Weak
A-2	358	1.55	2.37	13.64	
A-3	379	1.93	2.41	15.21	
Average	351	1.64	2.63	12.98	
B-1	218	2.06	5.49	15.89	Weak
B-2	132	3.82	2.74	16.98	
B-3	150	2.57	3.52	15.96	
Average	166	2.82	3.92	16.28	
C-1	16	7.83	6.62	17.26	Strong
C-2	8	10.83	4.50	21.23	
C-3	13	9.68	5.87	19.12	
Average	12.3	9.44	5.53	19.20	

compressive strength increased. When volume of roof stratum in the sample is two times large as the coal, the bursting proneness of the coal-rock mass became strong. It suggests that the roof stratum has a great influence on the bursting proneness of the coal seam. Although the bursting proneness of samples in Groups A and B is considered as weak, the average bursting proneness of coal-rock mass is greater than that of pure coal.

2.3. The Impact of DHPB on the Bursting Proneness of Roof-Coal Mass. As mentioned above, the roof stratum has a great impact on the bursting proneness of the coal seam. When assessing the bursting proneness of a specific coal mine merely using the bursting proneness result from a single seam or rock layer, the assessment result might lead to be conservative. The actual degree of bursting proneness of the coal seam in the active working, which is actually determined by the combination of roof strata and coal seam, is greater than that obtained from the lab testing. The lab testing results above indicate that the bursting proneness of the coal mass is actually greater with the increase of roof strata in the reality.

When applying the approach of DHPB, the integrity and continuity between the roof strata and coal seam are structurally broken, thus weakening and/or reducing their bursting proneness.

3. The Influence of DHPB on Changing Stress State

3.1. Numerical Simulation of DHPB. Based on the geotechnical condition of working face 25110 of Yuejin coal mine, the numerical analysis software FLAC was utilized to simulate the influence of DHPB on stress distribution in coal-rock mass.

The mechanical properties of coal-rock used in the numerical model are listed in Table 4. H is the thickness of the coal-rock strata, m; ρ is the density, $\text{kg}\cdot\text{m}^{-3}$; C is the adhesion stress, MPa; ϕ is the internal friction angle, $^\circ$; G is the bulk modulus, GPa; E is the shear modulus, GPa; and σ_c is the tensile strength, MPa. The simulation of the blasting influence on the coal-rock mass was achieved by weakening the mechanical property values of the coal-rock mass within the influencing area of the roof blasting, including density, elastic modulus, Poisson's ratio, tensile strength, cohesion, and frictional angle. There are multiple factors influencing the results of DHPB, such as blast hole angle, sealing length, and explosive dose. In this model, the depth and sealing length of the blasting hole are 20 m and 10 m, respectively. The blasting hole angles of 30° , 45° , and 60° were successively applied in the model as a comparison.

3.2. Numerical Simulation Results and Analysis. There are four cases simulated in this study.

- (i) Case-1: no blasting hole.
- (ii) Case-2: blasting angle is 30° .
- (iii) Case-3: blasting angle is 45° .
- (iv) Case-4: blasting angle is 60° .

Figure 2 indicates the distribution and change of the side-abutment pressure of these four cases. The numerical modeling results indicate that the peak side-abutment pressure is 83.7 MPa when not deploying precracking blasting. When applying the precracking blasting in the model, the peak side-abutment pressure decreases as the hole angle increases from 30° to 60° with decrements of 24.0%, 15.5%, and 9.2% as comparing with Case-1. In other words, the stress magnitude developed in the coal-rock mass can be effectively reduced/relieved by the precracking blasting with the effective blasting range. The degree of the stress reduction is mainly determined by the blasting hole angle when the rest of the parameters remain the same.

Furthermore, the main influences of DHPB on coal-rock mass stress environment can be summarized as follows.

TABLE 4: The physical and mechanics properties of rock layers in numerical simulation.

Rock layers	H/m	$\rho/kg\cdot m^{-3}$	C/MPa	$\phi/^\circ$	G/GPa	E/GPa	σ_c/MPa
Roof sandstone	40	2550	17	35	12	11	4.9
Roof mudstone	20	2700	13.5	29.2	8.2	7.8	2.6
Coal seam	10	1400	9	26.9	1.7	1.5	0.8
Backplane mudstone	4	2500	13.8	29.5	12.8	10	4.6
Backplane sandstone	26	2500	16.4	30.8	12.1	11.9	5.2

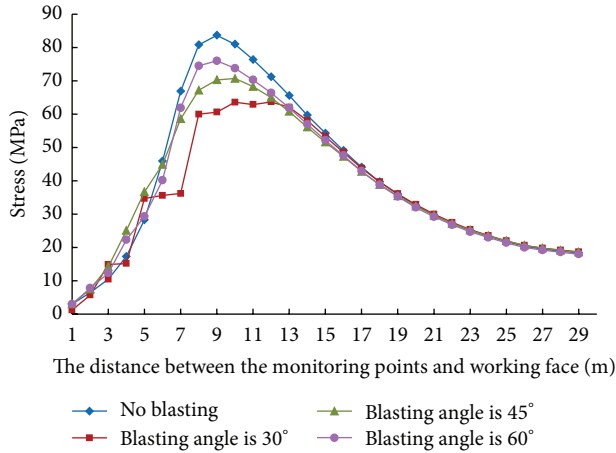


FIGURE 2: The changing curve of side-abutment pressure.

- (1) Properly applying DHPB can break the roof and effectively induce roof caving in the gob area. Also, it can weaken the integrity and continuity of the roof in the gob and ahead of the face, thus reducing the impact when roof pressure comes.
- (2) The dynamic shattering and air pressure generated by the blasting can structurally change the properties of the coal-rock mass by mitigating the high stress generation and high elastic energy accumulation, thus breaking the conditions of energy transfer and rockburst occurrence at a certain degree.

4. Case Study of DHPB Application

4.1. Basic Geotechnical Conditions of Yuejin Mine. Yuejin coal mine was constructed and put into operation in 1959; it is attached to Yima Coal Industry Group and located 2 km to the south of Yima City, Henan Province. The mine geographical coordinates are $111^\circ 50' 37'' \sim 111^\circ 56' 15''$ east longitude and $34^\circ 39' 00'' \sim 34^\circ 43' 13''$ north latitude; the area is about 21.4 km^2 .

The mining method utilized by Yuejin mine is fully mechanized retreat longwall. The cover depth varies from 580 m to 1,030 m. The overburden mainly consists of sandstone and hard conglomerate with a thickness of 400 m in average. Since the first rockburst occurred at face 25090 in 2000, the recorded bursting accidents are up to 40 times, causing entry damage as long as 2,500 m across the mine. Due to its strong

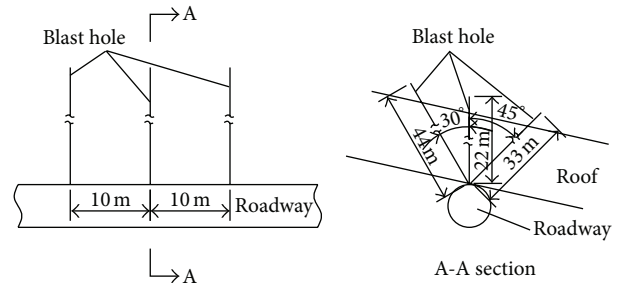


FIGURE 3: The schematic diagrams of DHPB.

bursting proneness, the roof needs to be caved in a well-managed way.

4.2. Rockburst Prevention Test with DHPB. The precracking blasting testing site is located at the tailgate, 330 m away from the stop line of longwall 25110. Three stations of DHPB testing site were determined for deploying these blast holes, which are 285 m, 320 m, and 345 m away from the longwall stop line, respectively. The spacing between these two adjacent stations is 10 m. In a fan-shaped arrangement, three blast holes with a hole spacing of 10 m for each station were drilled perpendicularly to the entry (Figure 3). The drilling angles of these two side blast holes are 30° and 45° relative to the coal seam, respectively. The depths of these two side blast holes are, respectively, 44 m and 33 m while the middle one is 22 m. The diameter of these blast holes is approximately 75 mm.

In order to detect and examine the rockburst prevention effectiveness of DHPB, the cuttings weight, mining induced stress, and working resistance of the hydraulic support were monitored. The arrangement of monitoring locations is shown in Figure 4. The three cuttings weight measuring points were 285 m, 320 m, and 345 m away from the terminal mining line. The two mining induced stress measuring points were 325 m and 345 m away from the terminal mining line. And the serial number of the 4 supports was 83, 103, 113, and 123.

4.3. Evaluation of Rockburst Prevention Effectiveness

4.3.1. Cuttings Weight. Shown in Figure 5 are the cutting weights before and after the blasting from these three monitoring stations. It can be seen that the cutting weight obtained from the middle station greatly decreased after the blasting conducted on November 17th. However, a minor change was

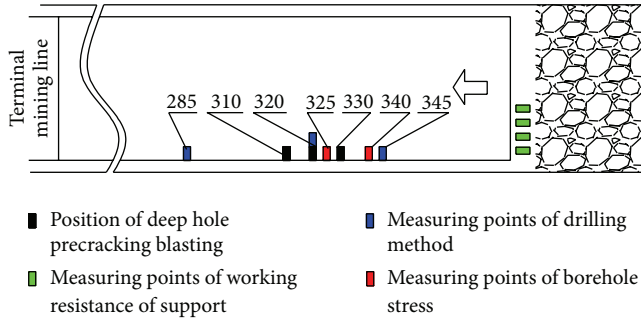


FIGURE 4: The arrangement of monitoring points.

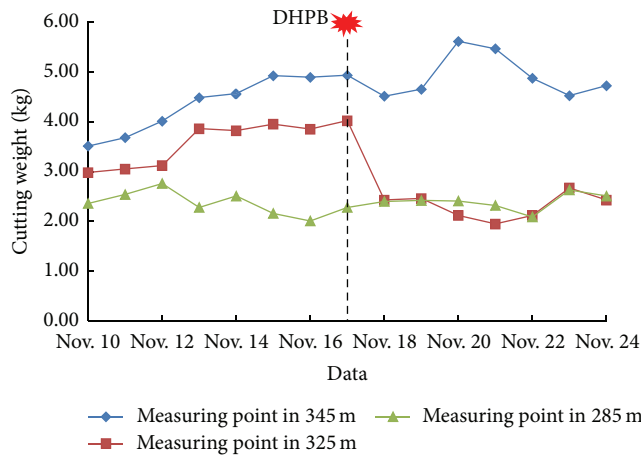


FIGURE 5: Cutting weight variation before and after blasting.

recorded in other two stations. Usually, there is a reliable correlation between the cutting weight of coal and the stress developed in the coal-rock mass. A decreasing cutting weight suggests the stress was relieved. It should be noted that the influence range of DHPB is not infinite. For the area that is out of the influence range, the cutting weight and stress developed in the coal-rock mass do not change much.

4.3.2. Mining Induced Stress. To monitor the vertical stress developed in the coal seam, two KSE-II borehole stress meters were installed at a distance of 325 m and 340 m apart away from the longwall stop line. The depth of the blast hole at 325 m is 12 m and the other one is 15 m. The stress variation before and after blasting is shown in Figure 6. It can be seen that the stresses from both locations became much lower after the first blasting on November 11th. The lower stress developed in the surrounding rock of the entry greatly decreased the bursting proneness as expected. As indicated in Figure 6, the stress was getting higher after the blasting on November 20th due to the longwall mining activity, but its peak value is lower comparing with the one obtained before the blasting.

4.3.3. Working Resistance of Hydraulic Support. The major purpose of DHPB is to make the strong roof from hard-to-cave to periodic caving as the longwall moves, reducing

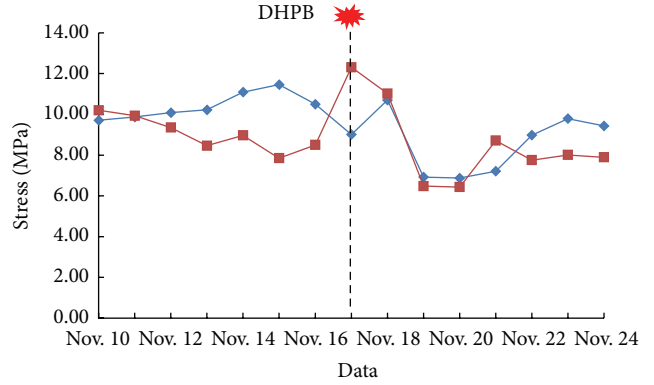


FIGURE 6: Borehole stresses variation before and after the blasting.

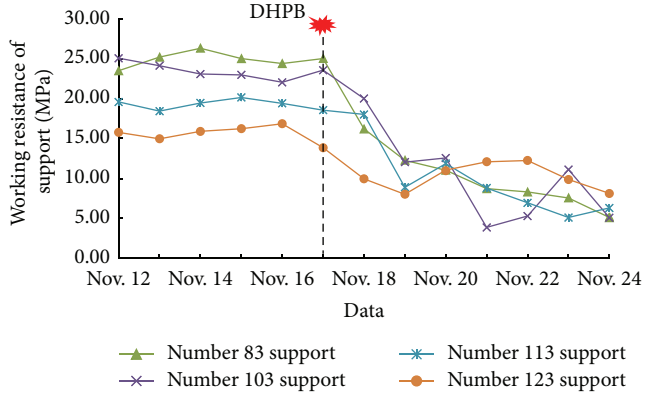


FIGURE 7: Working resistance variation of hydraulic supports before and after DHPB.

the span of the hanging roof and the pressure around the longwall face. Therefore, the pressure of the face support can be considered as another index indicating the effectiveness of DHPB.

There are 124 hydraulic supports installed in the longwall face 25110 of Yuejin mine. These supports were numbered from the head gate to the tailgate as #1, #2, ..., #124. As mentioned above, these blasting holes were drilled in the tailgate. When comparing the support resistances across the face, it can be seen that supports #1 to #80 experienced a minor pressure change while the rest evident. Figure 7 illustrates the working resistance variation of supports #83, #103, #113, and #123, which are closer to the tailgate, before and after the blasting. The recorded working resistance evidently indicates the pressure greatly reduced after applying DHPB. For the support #83, the pressure decreased by 73.6% from 25 MPa to 6.6 MPa. Additionally, the field observation indicated that, when the shearer was approaching the tailgate, the vibration generated from the drum was not visible and no coal squeezed out from the face, indicating a lower pressure from both the roof and the floor.

5. Conclusions

- (1) Roof strata has a great influence on the bursting proneness of coal seam. The bursting proneness tests of pure coal and coal-rock mass complex showed that, comparing with the pure coal, the duration of dynamic fracture of coal-rock mass complex was decreased from 351 ms to 12.3 ms, the elastic strain energy index was increased from 1.64 to 9.44, the bursting energy index was increased from 2.63 to 5.53, and the uniaxial compressive strength was increased from 12.98 MPa to 19.20 MPa. The bursting proneness of coal-rock mass combination is evidently higher than pure coal or rock strata only. The thicker the strong roof stratum, the higher the bursting proneness of coal-rock. The combination of roof rock and coal, both with weak bursting proneness, can form a coal-rock mass complex with a strong bursting proneness.
- (2) Properly applying DHPB can structurally break the original composition of the roof strata and coal, thus reducing its bursting proneness. The dynamic shattering and air pressure generated by the blasting can structurally change the properties of the coal-rock mass by mitigating the high stress generation and high elastic energy accumulation, thus breaking the conditions of energy transfer and rockburst occurrence.
- (3) The field testing data, including cutting weight, mining induced stress, working resistance of the hydraulic support, and microseismic events and energy from Yuejin coal mine, indicate that the stress concentration of coal-rock mass was greatly mitigated by DHPB. It can be conclusive that the approach of DHPB is applicable and reliable in reducing the bursting proneness for a burst-prone mine.

Conflict of Interests

The authors declare that there is no conflict of interests regarding the publication of this paper.

Acknowledgments

This work was financially supported by the State Key Development Program for Basic Research of China (Grant no. 2010CB226806), the International Science & Technology Cooperation Program of China (2011DFA61790), and the National Natural Science Foundation of China (Grants nos. 51174272, 51174112, and 51304117).

References

- [1] J. M. Alcott, P. K. Kaiser, and B. P. Simser, "Use of microseismic source parameters for rockburst hazard assessment," *Pure and Applied Geophysics*, vol. 152, no. 1, pp. 41–65, 1998.
- [2] J. Dubinski and W. Konopko, *Rockbursts—Assessment, Prediction and Control—Working Rules*, Central Mining Institute, Katowice, Poland, 2000 (Polish).
- [3] A. C. Adoko, C. Gokceoglu, L. Wu, and Q. J. Zuo, "Knowledge-based and data-driven fuzzy modeling for rockburst prediction," *International Journal of Rock Mechanics and Mining Sciences*, vol. 61, pp. 86–95, 2013.
- [4] Y. Wang, W. Li, and Q. Li, "Method of fuzzy comprehensive evaluations for rockburst prediction," *Chinese Journal of Rock Mechanics and Engineering*, vol. 17, pp. 493–501, 1998.
- [5] Y.-H. Guo and F.-X. Jiang, "Application of comprehensive fuzzy evaluation in burst-proneness risk of coal seam," in *Proceedings of the 2nd International Conference on Future Information Technology and Management Engineering (FITME '09)*, pp. 404–407, December 2009.
- [6] F.-Q. Gong, X.-B. Li, and W. Zhang, "Rockburst prediction of underground engineering based on Bayes discriminant analysis method," *Rock and Soil Mechanics*, vol. 31, no. 1, pp. 370–387, 2010.
- [7] X. Z. Shi, J. Zhou, L. Dong, H. Y. Hu, H. Wang, and S. R. Chen, "Application of unascertained measurement model to prediction of classification of rockburst intensity," *Chinese Journal of Rock Mechanics and Engineering*, vol. 29, no. 1, pp. 2720–2726, 2010.
- [8] H. Li, R.-Z. Dai, and J.-Q. Jiang, "Predicting Model of rock burst based on Lyapunov index," *Journal of Mining and Safety Engineering*, vol. 23, pp. 215–219, 2006 (Chinese).
- [9] J. Zeng, Y.-X. Zhang, and X.-G. Jin, "Prediction of rock burst using the method of optimal relative membership degree based on the maximum entropy principle," *Journal of Civil, Architectural and Environmental Engineering*, vol. 33, no. 1, pp. 93–97, 2011.
- [10] H.-C. Yu, H.-N. Liu, L. U. Xue-song, and H.-D. Liu, "Prediction method of rock burst proneness based on rough set and genetic algorithm," *Journal of Coal Science and Engineering (China)*, vol. 15, no. 4, pp. 367–373, 2009.
- [11] X. Chen, J. Sun, J. Zhang, and Q. Chen, "Judgment indexes and classification criteria of rock-burst with the extension judgment method," *China Civil Engineering Journal*, vol. 42, no. 9, pp. 82–88, 2009.
- [12] G. Takla, J. Ptacek, J. Holecko, and P. Konicek, "Stress state determination and prediction in rock mass with rockburst risk in Ostrava-Karvina coal basin," in *Proceedings of the International Symposium of the International Society for Rock Mechanics (Eurock '05)*, pp. 625–628, Brno, Czech Republic, May 2005.
- [13] J.-L. Yang, X. B. Li, Z.-L. Zhou, and H. Lin, "A fuzzy assessment method of rockburst prediction based on rough set theory," *Metal Mine*, vol. 408, pp. 26–29, 2010.
- [14] C. Srinivasan, S. K. Arora, and R. K. Yaji, "Use of mining and seismological parameters as premonitors of rockbursts," *International Journal of Rock Mechanics and Mining Sciences*, vol. 34, no. 6, pp. 1001–1008, 1997.
- [15] L.-Z. Tang and K. W. Xia, "Seismological method for prediction of areal rockbursts in deep mine with seismic source mechanism and unstable failure theory," *Journal of Central South University of Technology*, vol. 17, no. 5, pp. 947–953, 2010.
- [16] K. Holub, J. Rušajová, and J. Holečko, "Particle velocity generated by rockburst during exploitation of the longwall and its impact on the workings," *International Journal of Rock Mechanics and Mining Sciences*, vol. 48, no. 6, pp. 942–949, 2011.
- [17] Z. H. Ouyang, "Mechanism and experiment of hydraulic fracturing in rock burst prevention," in *Proceedings of the 1st International Conference on Rock Dynamics and Applications (RocDyn-1 '13)*, pp. 245–250, Lausanne, Switzerland, June 2013.

- [18] P. Konicek, K. Soucek, L. Stas, and R. Singh, "Long-hole destress blasting for rockburst control during deep underground coal mining," *International Journal of Rock Mechanics and Mining Sciences*, vol. 61, pp. 141–153, 2013.
- [19] P. Konicek, P. Konecny, and J. Ptacek, "Destress rock blasting as a rockburst control technique," in *Proceedings of the 12th International Congress on Rock Mechanics of the International Society for Rock Mechanics (ISRM '11)*, pp. 1221–1226, Beijing, China, October 2011.
- [20] P. Konicek, M. R. Saharan, and H. Mitri, "Destress blasting in coal mining - state-of-the-art review," in *Proceedings of the 1st International Symposium on Mine Safety Science and Engineering (ISMSSE '11)*, pp. 179–194, Beijing, China, October 2011.
- [21] P. Dvorsky, P. Konicek, E. Morkovska, and L. Palla, "Rock blasting as a rockburst control measures in the safety pillar of SW crosscuts at Lazy Colliery in Orlová," in *Proceedings of the 10th International Scientific-Technical Conference-Rockbursts*, pp. 37–45, Ustroń, Poland, November 2003.
- [22] P. Dvorsky and P. Konicek, "Systems of rock blasting as a rockburst measure in the Czech part of Upper Silesian Coal Basin," in *Proceedings of the 6th International Symposium on Rockburst and Seismicity in Mines*, pp. 493–496, Perth, Australia, March 2005.
- [23] A. Przewczek, P. Dvorsky, and P. Konicek, "System of rock blasting in boreholes diameter more than 100mm as a rock burst measure," in *Proceedings of the 12th International Scientific-Technical Conference-Rockbursts*, pp. 253–269, Ustroń, Poland, 2005.
- [24] P. Konicek and A. Przewczek, "Study of selected cases of local stress reduction due to rock blasting," in *Proceedings of the 15th International Scientific-Technical Conference (GZN '08)*, pp. 143–161, Targanice, Poland, November 2008.
- [25] H. He, L. Dou, J. Fan, T. Du, and X. Sun, "Deep-hole directional fracturing of thick hard roof for rockburst prevention," *Tunnelling and Underground Space Technology*, vol. 32, pp. 34–43, 2012.

Research Article

Blast-Induced Damage on Millisecond Blasting Model Test with Multicircle Vertical Blastholes

Qin-yong Ma, Pu Yuan, Jing-shuang Zhang, Rui-qiu Ma, and Bo Han

Research Center of Mine Underground Engineering, Ministry of Education, Anhui University of Science and Technology, Huainan, Anhui 232001, China

Correspondence should be addressed to Pu Yuan; puy2012@126.com

Received 12 November 2014; Accepted 26 January 2015

Academic Editor: Marcin A. Lutynski

Copyright © 2015 Qin-yong Ma et al. This is an open access article distributed under the Creative Commons Attribution License, which permits unrestricted use, distribution, and reproduction in any medium, provided the original work is properly cited.

To investigate the blast-induced damage effect on surrounding rock in vertical shaft excavation, 4 kinds of millisecond blasting model tests with three-circle blastholes were designed and carried out with excavation blasting in vertical shaft as the background. The longitudinal wave velocity on the side of concrete model was also measured before and after blasting. Then blast damage factor was then calculated by measuring longitudinal wave velocity before and after blasting. The test results show that the blast-induced damage factor attenuated gradually with the centre of three-circle blastholes as centre. With the threshold value of 0.19 for blast-induced damage factor, blast-induced damage zones for 4 kinds of model tests are described and there is an inverted cone blast-induced damage zone in concrete model. And analyses of cutting effect and blast-induced damage zone indicate that in order to minimize the blast-induced damage effect and ensure the cutting effect the reasonable blasting scheme for three-circle blastholes is the inner two-circle blastholes initiated simultaneously and the outer third circle blastholes initiated in a 25 ms delay.

1. Introduction

In recent decades, drilling blasting technology has been widely used in mining engineering, tunneling engineering, large slope engineering, underground engineering, and other kinds of rock engineering [1]. Only part of explosive energy is used to crush rocks to achieve the goal of rock mass excavation, while most of the energy is transferred into surrounding rock mass as heat, vibration, and air shock wave to make surrounding rock mass or structure damaged or even destroyed at the same time [2, 3]. Rock blasting damage affects the security, support, and reinforcement cost of underground engineering directly or indirectly.

The mechanical properties of blasting damaged rock and the regularities of rock damage by blasting have been investigated in various distances and blasting conditions with marble, and both spreading regularities of mesocrack and damaged properties of blasting damaged rock have also been analyzed by elastic-brittle mesodamage model [3]. The excavation damage zones of Renhechang tunnel resulting from blasting have been studied by an ultrasonic wave measurement, and blasting effect for two types of

detonators, nonel detonator and electronic detonator, have been compared. As the delay time of electronic detonator can be arbitrarily set up, the use of electronic detonator can lead to not only a small extent of excavation damage zones, but also a lower degree of rock breakage in excavation damage zones [4]. A new model for predicting the extent of blast-induced damage in rock mass has been proposed based on Langefors' theory of rock blasting [5]. The excavation damage of a granite tunnel resulting from blasting has been characterized by carrying out ultrasonic wave velocity and amplitude measurements around one quadrant of the test tunnel [6]. Blast design wants to cause minimum damage and overbreak with respect to existing in situ stress field and support system; then the controlling parameters for blast-induced damage and overbreak have been investigated [7]. The cumulative effect of blast-induced damage and damage evolutive law of rock mass have been researched by carrying out sound wave measurement for surrounding rock after blasting repeatedly; then a cumulative expanded model for predicting blast-induced damage has been put forward with the baseline of rock mass wave velocity reducing ratio [2, 8]. According to the similarity theory, blasting-induced damage

TABLE 1: Charging scheme.

Model number	CM-1	CM-2	CM-3	CM-4
Detonation delay	25 ms	50 ms	25 ms	50 ms
First circle	Electric detonator segment I	Electric detonator segment I	Electric detonator segment I	Electric detonator segment I
Second circle	Electric detonator segment I	Electric detonator segment I	Electric detonator segment II	Electric detonator segment III
Third circle	Electric detonator segment II	Electric detonator segment V	Electric detonator segment III	Electric detonator segment V

model test is conducted in simulated coal, and both ultrasonic wave velocity and blasting strain waves have been measured. The results indicate that the simulated coal damage is the results of the interaction of blasting shock wave, blasting stress wave, detonation gas, and coal gas [9, 10].

Excavation and surrounding rock protection are always a contradiction problem in blasting engineering. In order to investigate the blast-induced damage effect on surrounding rock in vertical shaft excavation, 4 kinds of millisecond blasting model tests with three-circle blastholes have been implemented, and the blast-induced damage of millisecond blasting to surrounding rock has also been investigated by ultrasonic wave velocity measurement. Then a reasonable blasting parameter for engineering blasting design and in situ blasting engineering construction has been put forward.

2. Design of Millisecond Blasting Model Test

In order to investigate the blast-induced damage on surrounding rock in vertical shaft excavation, 4 kinds of millisecond blasting model tests with three-circle blastholes in concrete model have been designed with parallel cut blasting in vertical shaft as prototype.

P.O 42.5 ordinary Portland cement was adopted to prepare the concrete specimen. The fine aggregate used in this study was natural river sand with a fineness modulus of 2.6, a silt content of 2.0%. The coarse aggregate used was gravel with continuous grading from 16 mm to 31.5 mm, a silt content of 0.6%. Moreover, HNT-K3 concrete waterproofing agent was mixed. The mix proportion of cement, water, sand, gravel, and admixture in concrete is 1.00, 0.43, 1.49, 2.89, and 0.08, respectively. The length of concrete model is 1000 mm, the width is 1000 mm, and the height is 600 mm. The basic mechanical test after curing 28 d shows that the cubic compressive strength of model concrete is 42.8 MPa, and its splitting tensile strength is 2.58 MPa. Ultrasonic wave velocity measurement indicates that the longitudinal wave velocity of model concrete is 4209 m/s [11].

Three-circle blastholes are arranged in the middle of concrete model. The diameter of first circle is 60 mm, and there are 4 blastholes in the first circle with a space of 43 mm. The diameter of second circle is 120 mm, and there are 6 blastholes in the second circle with a space of 60 mm. The diameter of third circle is 200 mm, and there are 10 blastholes in the third circle with a space of 62 mm. The depth of blastholes in the first circle and second circle is 180 mm, while the depth of blastholes in the third circle is 160 mm. Blastholes

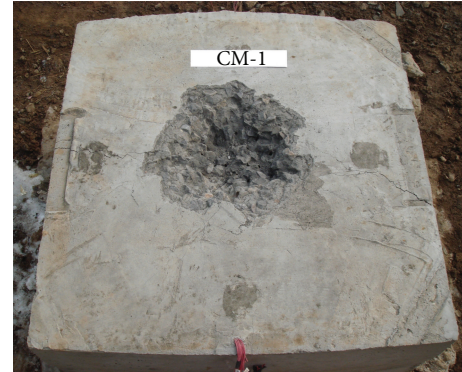


FIGURE 1: Blasting effect of concrete model with three-circle blastholes.

are formed by pulling out embedded circular steel bar after initial setting and before final setting. Each blasthole charges with one number 6 millisecond delay electric detonator. The 4 kinds of millisecond blasting model tests are named CM-1, CM-2, CM-3, and CM-4. The charging scheme for millisecond blasting model tests is shown in Table 1.

3. Blasting Effect in Concrete Model

After blasting, the cutting effect in concrete model is shown in Figure 1. Then the blasting cavity is cleaned and blasting fragments are gathered. The cutting depth is measured by ruler and its value is the mean of 4 measured depths. Delimiting the boundary of blasting cavity, the cavity radius is the mean of longest radius and shortest radius. After measuring cutting depth and cavity radius, put a plastic film on blasting cavity and fill blasting cavity with dry fine sand. The cutting volume of blasting cavity can be calculated by measuring the volume of dry sand in blasting cavity. The cutting depth, cavity radius, and cutting volume of 4 kinds of millisecond blasting model tests are shown in Table 2.

4. Blast-Induced Damage Measurement

4.1. Indicator for Blast-Induced Damage. The break and damage of rock mass resulting from blasting can be reflected by the deterioration of mechanical properties and initiation and development of inner crack. At present, damage variable is adopted to describe the blast-induced damage and the evolutive law of blast-induced damage. And damage variable

TABLE 2: Blasting effect of millisecond blasting model test.

Model number	Cutting depth/ mm	Cavity radius/ mm	Cutting volume/ cm ³
CM-1	64	260	3010
CM-2	57	290	2805
CM-3	49	369	4975
CM-4	118	427	10705

can be evaluated by damage area, density change, elastic modulus change, longitudinal wave velocity change, and CT value change before and after blasting [10, 12]. Since the longitudinal wave velocity is very sensitive about the joints and cracks in rock mass or concrete specimens, rock or concrete damage characteristics can be well described by longitudinal wave velocity change. And ultrasonic detection is a simple, undamaged, practicable, and widely used method for rock or concrete damage evaluation.

After comprehensive comparison, longitudinal wave velocity change before and after blasting is selected to evaluate the blast-induced damage in concrete model [12–14]. The blast-induced damage factor D can be calculated by the following equation:

$$D = 1 - \left(\frac{v}{v_0}\right)^2 = 1 - \eta^2, \quad (1)$$

where v_0 and v are the longitudinal wave velocity of concrete model before and after blasting, and its unit is m/s. η is the reduction rate of longitudinal wave velocity after blasting.

4.2. Arrangement of Measuring Points. To investigate the blast-induced damage effect on the model concrete, measuring points for longitudinal wave velocity test are arranged with horizontal and vertical lines at the center of the concrete model profile as the baselines. There are 36 measuring points in 4 lines and 9 rows with a space of 100 mm. The distance from the measuring points in the first line to the upper surface of concrete model is 150 mm which is a little higher than the charging center. The measuring points on concrete model can be seen in Figure 2.

The longitudinal wave velocity of concrete model is measured by NM-4A nonmetal ultrasonic detecting instrument. When measuring the longitudinal wave velocity of concrete model before and after blasting tests, the transmitter probe and receiver probe should be clingy on the concrete surface at measuring points with vaseline as couplant. During the test, the center of probe should be at the same position with the measuring points. The longitudinal wave velocity measurement is conducted in turn from top to bottom, from left to right. The value in stable waveform is the test result.

4.3. Measuring Results of Blast-Induced Damage. After analyzing the measuring results of longitudinal wave velocity of concrete model before and after blasting tests, the blast-induced damage factors for 4 kinds of concrete models are obtained, which can be seen in Table 3.

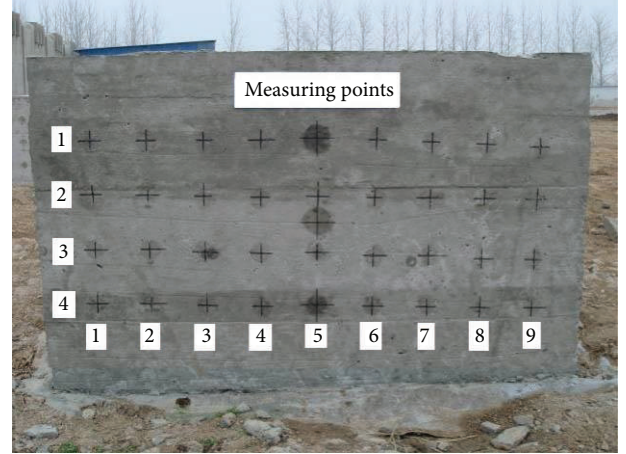


FIGURE 2: Measuring points of longitudinal wave velocity on concrete model.

According to the blast-induced damage results of millisecond blasting model test, the change curve of blast-induced damage factor in concrete model is drawn in Figure 3.

In CM-1, CM-2, and CM-3, the change trends of blast-induced damage factor in the first line and second line of CM-1 and the first line of CM-2 are obviously different from other lines. But both the peak value of blast-induced damage factor in the first line and second line of CM-1 and the peak value of blast-induced damage factor in the first line of CM-2 appear in the first row. The peak value of blast-induced damage factor in most of lines in CM-1, CM-2, and CM-3 appears in the fifth row which is the middle of concrete model. The singular change trend in CM-1 and CM-2 is the result of the blast-induced crack crossing the measuring points. The blast-induced damage factor attenuates with the center of three-circle blastholes as center.

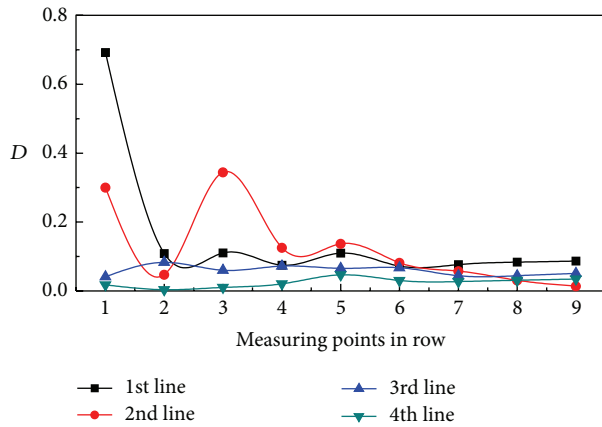
In CM-4, the concrete model has been broken and some large cracks have been extended to the model boundary. Thus the blast-induced damage factor is much bigger than other concrete models. And the change trend of blast-induced damage factor has been changed because of those large cracks.

5. Analyses of Blast-Induced Damage

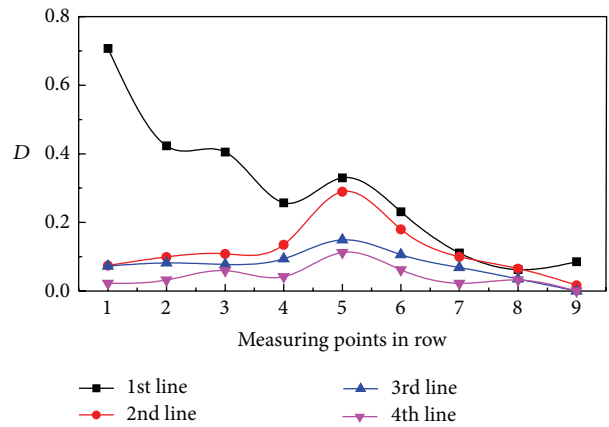
When the reduction rate of longitudinal wave velocity after blasting exceeds 10%, the rock mass can be regarded as damage and the critical blast-induced damage factor is 0.19 [12]. Then the threshold blast-induced damage factor, 0.19, is adopted to define the blast-induced damage zone. The blast-induced damage in CM-1 and CM-2 is mainly on the left side of concrete model. The depth of blast-induced damage for CM-1 is about 280 mm, seen in Figure 4(a). The depth of blast-induced damage for CM-2 is about 321 mm, and the blast-induced damage zone has extended to the left boundary of concrete model and extended to the right about 140 mm, as seen in Figure 4(b). The depth of blast-induced damage for CM-3 is about 273 mm, and the blast-induced damage zone

TABLE 3: Blast-induced damage factor in concrete model with three-circle blastholes.

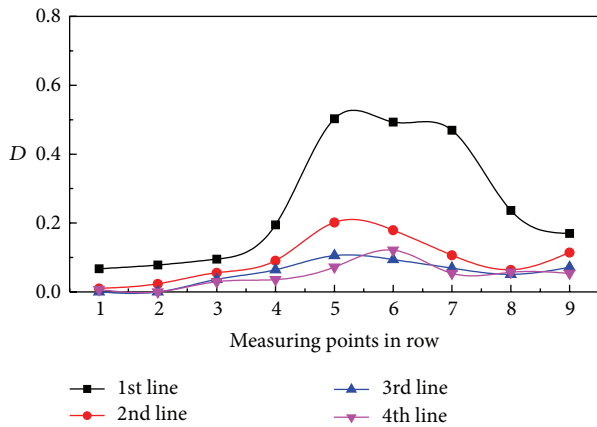
Model number	Line	Row								
		1	2	3	4	5	6	7	8	9
CM-1	1	0.692	0.109	0.110	0.075	0.110	0.072	0.077	0.084	0.087
	2	0.300	0.047	0.345	0.126	0.137	0.082	0.058	0.031	0.014
	3	0.041	0.083	0.060	0.072	0.066	0.067	0.044	0.044	0.051
	4	0.018	0.004	0.010	0.021	0.047	0.031	0.027	0.031	0.034
CM-2	1	0.707	0.423	0.405	0.257	0.330	0.231	0.111	0.063	0.086
	2	0.075	0.099	0.108	0.135	0.290	0.180	0.100	0.066	0.017
	3	0.073	0.082	0.078	0.094	0.150	0.106	0.069	0.035	0.000
	4	0.023	0.032	0.059	0.042	0.112	0.062	0.022	0.032	0.000
CM-3	1	0.067	0.078	0.095	0.195	0.503	0.493	0.470	0.236	0.170
	2	0.010	0.024	0.056	0.091	0.202	0.179	0.107	0.064	0.115
	3	0.000	0.000	0.037	0.064	0.105	0.094	0.069	0.051	0.071
	4	0.007	0.000	0.030	0.036	0.072	0.121	0.054	0.057	0.054
CM-4	1	0.774	0.809	0.793	0.878	0.917	0.876	0.870	0.846	0.806
	2	0.772	0.773	0.695	0.796	0.792	0.790	0.833	0.760	0.633
	3	0.609	0.659	0.673	0.802	0.811	0.512	0.698	0.865	0.539
	4	0.595	0.692	0.748	0.750	0.687	0.657	0.844	0.770	0.743



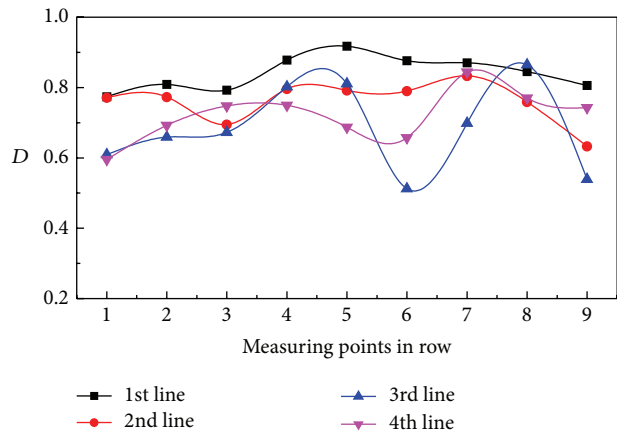
(a) CM-1



(b) CM-2



(c) CM-3



(d) CM-4

FIGURE 3: Curve of blast-induced damage factor D .

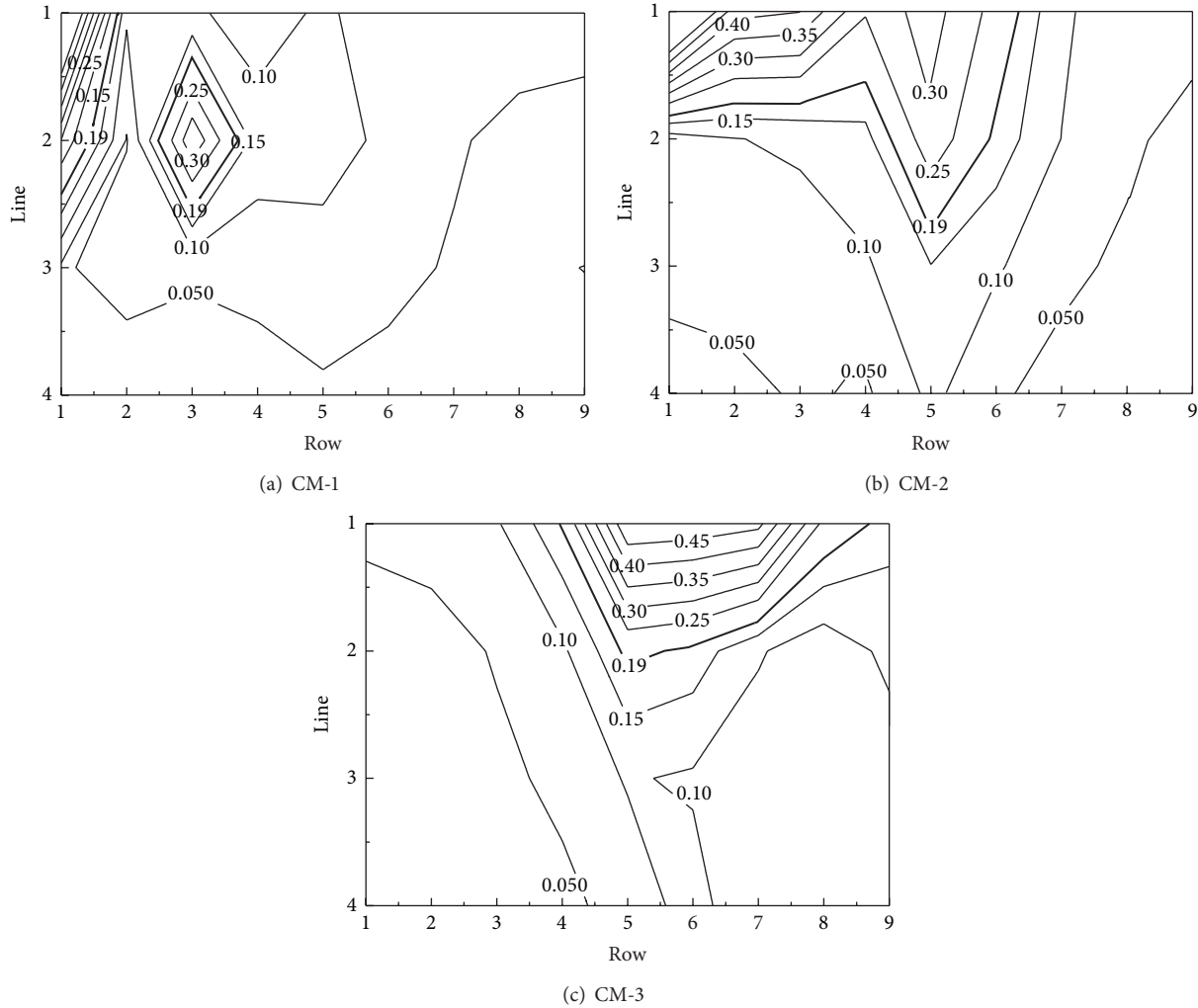


FIGURE 4: Blast-induced damage zone in model.

has extended to the left about 103 mm and to the right about 370 mm, as seen in Figure 4(c). For many cracks in CM-4, the blast-induced damage factor is much big and the smallest blast-induced damage factor is 0.512. So the whole concrete model in CM-4 is in blast-induced damage zone. The blast-induced damage zone is in an inverted cone distribution with the center line of three-circle blastholes as center line, as seen in Figure 4. The bold line in Figure 4 corresponds to the threshold value of blast-induced damage factor, 0.19.

It is considered that the left side of concrete model which has not been vibrated compactly for its longitudinal wave velocity is a little smaller than the right side. So the blast-induced damage zone in CM-1 is mainly on the left side of concrete model not in the blastholes area. And the blast-induced damage zone in CM-2 is mainly on blasthole areas and left side of concrete model, and the depth in blastholes areas is bigger than that in left side.

Comparing CM-1 with CM-2, the blast-induced damage factor in CM-2 is much bigger than that in CM-1, and its depth is about 1.15 times bigger than that for CM-1. And the cutting depth and cutting volume for CM-1 are better than

that in CM-2, and its cavity radius is smaller than that in CM-2, which means a light overbreak.

The blast-induced damage zone in CM-3 is mainly on the blastholes areas and right side of concrete model, in an inverted coned distribution. For the large blast-induced damage factor, the whole concrete model in CM-4 is in blast-induced damage zone. The cavity radius of CM-4 is 427 mm which is much bigger than the radius of the third circle blastholes, causing a heavy overbreak and damage to surrounding rock. Comparing CM-3 with CM-4, the cutting depth, cutting volume, and cavity radius of CM-4 are much bigger than that of CM-3, but its blast-induced damage effect is too large and a serious influence of surrounding rock stability presents. So the blasting parameters in CM-4 are not suggested to be adopted.

CM-3 shows that the cutting volume is big, and the cutting depth is small, which means an overbreak in CM-3. Comparing CM-1 and CM-3, the blast-induced damage factor for CM-1 is much smaller than that in CM-3.

After comprehensive consideration of the blast-induced damaged factor, blast-induced damage zone distribution, and

cutting effect in 4 kinds of millisecond blasting model tests, it is thought that the CM-1 presents not only a smaller blast-induced damage factor and blast-induced damage zone distribution but also a bigger cutting depth and smaller cavity radius. So in order to minimize the blast-induced damage effect on surrounding rock under the condition of good cutting effect, the reasonable blasting scheme for three-circle blastholes is the inner two-circle blastholes initiated simultaneously and the outer third circle blastholes initiated in a 25 ms delay.

6. Conclusions

- (1) The measured longitudinal wave velocity on the side of concrete model before and after blasting indicates that the blast-induced damage factor attenuates gradually with the centre of three-circle blastholes as centre.
- (2) With the threshold value of 0.19 for blast-induced damage factor, blast-induced damage zone for 4 kinds of model tests is in an inverted cone distribution with the center line of three-circle blastholes as center line.
- (3) In order to minimize the blast-induced damage effect on surrounding rock under the condition of good cutting effect, the reasonable blasting scheme for three-circle blastholes is the inner two-circle blastholes initiated simultaneously and the outer third circle blastholes initiated in a 25 ms delay.

Conflict of Interests

The authors declare that there is no conflict of interests regarding the publication of this paper.

References

- [1] B. Han, *Model Experimental Study and Application of Deep-Hole Blasting in Hard Rock for Mine Shaft*, Anhui University of Science and Technology, 2013 (Chinese).
- [2] C.-B. Yan, "Blasting damage cumulative effect of rock mass based on sound velocity variation," *Rock and Soil Mechanics*, vol. 31, supplement 1, pp. 187–192, 2010 (Chinese).
- [3] X.-L. Yang, X.-Y. Yuan, Z. Wu, and C.-D. Su, "The experimental study on mechanical properties of blast damaged rock," *Chinese Journal of Rock Mechanics and Engineering*, vol. 20, no. 4, pp. 436–439, 2001 (Chinese).
- [4] H.-X. Fu, L. N. Y. Wong, Y. Zhao, Z. Shen, C.-P. Zhang, and Y.-Z. Li, "Comparison of excavation damage zones resulting from blasting with nonel detonators and blasting with electronic detonators," *Rock Mechanics and Rock Engineering*, vol. 47, no. 2, pp. 809–816, 2014.
- [5] F. García Bastante, L. Alejano, and J. González-Cao, "Predicting the extent of blast-induced damage in rock masses," *International Journal of Rock Mechanics and Mining Sciences*, vol. 56, pp. 44–53, 2012.
- [6] I. L. Meglis, T. Chow, C. D. Martin, and R. P. Young, "Assessing in situ microcrack damage using ultrasonic velocity tomography," *International Journal of Rock Mechanics and Mining Sciences*, vol. 42, no. 1, pp. 25–34, 2005.
- [7] S. K. Mandal, "Parameters controlling blast-induced damage and overbreak," *Journal of Mines, Metals and Fuels*, vol. 60, no. 1-2, pp. 6–16, 2012.
- [8] C.-B. Yan, G.-Y. Xu, and F. Yang, "Measurement of sound waves to study cumulative damage effect on surrounding rock under blasting load," *Chinese Journal of Geotechnical Engineering*, vol. 29, no. 1, pp. 88–93, 2007 (Chinese).
- [9] H.-B. Chu, X.-L. Yang, W.-M. Liang, and Y.-Q. Yu, "Simulation experimental study on the coal blast mechanism," *Journal of the China Coal Society*, vol. 36, no. 9, pp. 1451–1456, 2011 (Chinese).
- [10] H.-B. Chu, X.-L. Yang, W.-M. Liang, Y.-Q. Yu, and L.-P. Wang, "Experimental study on the blast damage law of the simulated coal," *Journal of Mining and Safety Engineering*, vol. 28, no. 3, pp. 488–492, 2011 (Chinese).
- [11] Q.-Y. Ma, P. Yuan, B. Han, J.-S. Zhang, and H.-X. Liu, "Dynamic strain wave analyses of parallel cut blasting model tests for vertical shaft," in *Proceedings of the ISRM European Regional Symposium on Rock Engineering and Rock Mechanics: Structures in and on Rock Masses (EUROCK '14)*, pp. 1159–1164, Taylor & Francis, London, UK, May 2014.
- [12] W.-H. Zhu, F. Ming, and C.-Z. Song, "Fractal study of rock damage under blasting loading," *Rock and Soil Mechanics*, vol. 32, no. 10, pp. 3131–3135, 2011 (Chinese).
- [13] C.-Y. Zhu and S.-C. Yu, "Study on the criterion of rockmass damage caused by blasting," *Engineering Blasting*, vol. 7, no. 1, pp. 12–16, 2001 (Chinese).
- [14] J. Dai, *Dynamic Behaviors and Blasting Theory of Rock*, Metallurgical Industry Press, Beijing, China, 2nd edition, 2013, (Chinese).

Research Article

Multi-Index Monitoring and Evaluation on Rock Burst in Yangcheng Mine

Yunliang Tan,¹ Yanchun Yin,¹ Shitan Gu,¹ and Zhiwei Tian^{1,2}

¹State Key Laboratory of Mining Disaster Prevention and Control Co-Founded by Shandong Province and the Ministry of Science and Technology, Shandong University of Science and Technology, Qingdao, Shandong 266590, China

²Faculty of Earth Resources, China University of Geosciences, Wuhan 430074, China

Correspondence should be addressed to Yanchun Yin; yycrsd@163.com

Received 14 November 2014; Accepted 16 December 2014

Academic Editor: Shimin Liu

Copyright © 2015 Yunliang Tan et al. This is an open access article distributed under the Creative Commons Attribution License, which permits unrestricted use, distribution, and reproduction in any medium, provided the original work is properly cited.

Based on the foreboding information monitoring of the energy released in the developing process of rock burst, prediction system for rock burst can be established. By using microseismic method, electromagnetic radiation method, and drilling bits method, rock burst in Yangcheng Mine was monitored, and a system of multi-index monitoring and evaluation on rock burst was established. Microseismic monitoring and electromagnetic radiation monitoring were early warning method, and drilling bits monitoring was burst region identification method. There were three identifying indexes: silence period in microseismic monitoring, rising period of the intensity, and rising period of pulse count in electromagnetic radiation monitoring. If there is identified burst risk in the workface, drilling bits method was used to ascertain the burst region, and then pressure releasing methods were carried out to eliminate the disaster.

1. Introduction

Rock burst is one kind of typical dynamic disasters in coal mining. When the rock or coal is under ultimate strength state, energy in the rock will be released abruptly and severely. This will cause instantaneous rock burst damage, which threatens workers' life and the coal production [1–3]. Rock burst is difficult to research due to its complex occurrence conditions, multiple influence factors, and various fracture modes [4, 5].

In the developing process of rock burst, the rocks' stress state changes constantly, and energy releases accompanying with some physical effects, such as microseismic, acoustic emission, electromagnetic radiation, and so forth. By analyzing the foreboding information, monitoring system can be established to predict rock burst disaster [6–9]. At this stage, many rock burst monitoring methods are used in mining widely and popularly, such as pressure observation method, drilling method [10], electromagnetic radiation method [11–13], microseismic method [14–16], and seismic CT technology [17, 18].

Different monitoring methods have various monitoring principles, objectives, accuracy, and regions. In rock burst prediction, multiple methods should be combined together to establish more effective multi-index monitoring technology. In this paper, Yangcheng Mine in China was taken as the research site. Microseismic method, electromagnetic radiation method, and drilling bits method were combined to monitor rock burst. A system of multi-index monitoring and evaluation on rock burst was established, and field applications showed that this evaluation system predicted rock burst effectively.

2. Site Conditions

The coal seam's ground elevation of 1304 workface in Yangcheng Mine ranges from –535 m to –660 m, and the mining area is 159824 m². The coal seam dip angles change from 17° to 21°, and the average angle is 19°. The thickness ranges from 7.0 m to 8.2 m, and the average thickness is 7.5 m. The workface length is 184 m, and the mining distance is

870.5 m. The mining method is long-wall fully mechanized top-coal mining overall height all caving method.

The hardness coefficient of the coal is 1.5, and the coal seam is medium hard. The immediate roof is siltstone, and the main roof is grayish fine sandstone. The floor is siltstone. The upper coal seam shows strong burst trend, and the bottom seam shows light trend. The roof and floor show light burst trend.

3. Monitoring Approaches

3.1. Microseismic Monitoring. Energy of seismic wave can be generated and spread around when the underground rock mass fractures. Microseismic monitoring equipment is used to receive and record these seismic waves. According to monitoring results, various characteristics of the rock fracture can be analyzed, such as the amount, frequency, intensity, density, and dimension [19].

Microseismic monitoring system can identify and analyze the development of mine vibration according to the energy release, the center position and waveform diagram of the vibration, and so forth. And then the occurrence possibility of rock burst can be predicted. According to the seismology's basic equation of Gutenberg-Richter formula, the relation between the frequency and the number of microseismic can be expressed as [20]

$$\lg N = a - bM, \quad (1)$$

where N is the frequency of microseismic events; M is the number of microseismic events; a and b are constants.

The relation between the frequency of rock burst and its magnitude shows a linear correlation. According to this law, we can predict the maximum magnitude of rock burst based on the information of occurring rock burst. The detecting method is to take 1 for the Gutenberg-Richter formula, which means there is only one maximum rock burst, and the maximum magnitude M_m is

$$M_m = \frac{a}{b}. \quad (2)$$

According to the change rule of value b in the formula (2), the trend of rock burst's occurrence can be predicted. If b increases, the possibility of the large magnitude rock burst will decrease. If b decreases, the possibility of the large magnitude rock burst will increase.

3.2. Electromagnetic Radiation Monitoring. Electromagnetic radiation in coal or rock is a release expression of electromagnetic energy in the process of deformation, and it has a close relation with the deformation process [21]. The occurrence of rock burst is a process of instantaneous energy release. When the accumulated energy of coal or rock reaches the strength limit, rock burst will happen. In the fracture process of the rock under high stress, cracks and friction can produce electromagnetic radiation. High stress and intense fracture will release strong electromagnetic radiation. The strength of electromagnetic radiation signal indirectly reflects the degree of stress concentration in the coal and rock. The higher

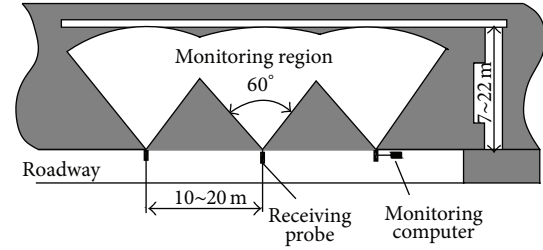


FIGURE 1: The region of electromagnetic radiation monitoring [21].

the degree of stress concentration is, the greater rock burst risk will be. We can predict the risk degree of rock burst by monitoring the intensity and changes of electromagnetic radiation signal.

The hardware of electromagnetic radiation monitoring system mainly includes the monitoring computer, receiving probes, conversion interface, and communication cable. It has characteristics of noncontact, regional, continuous monitoring. The main monitoring indicators are the intensity of amplitude and the number of pulses. In the application to monitor electromagnetic radiation in the mining area, noncontactable inductance type wideband directional receiving probe is usually used. The distance between the electromagnetic radiation instrument and the measured area is in the range of 0.6~1.0 m, and the station spacing is about 10 m. The effective monitoring depth ranges from 7 m to 22 m. The layout of the electromagnetic radiation monitoring positions is shown in Figure 1. Electromagnetic radiation signal is recorded according to the number of measuring points in sequence, and the monitoring time for the data at each point is 180 s.

3.3. Drilling Bits Monitoring. When drilling one hole in the high stress area of the coal seam, the drilling process can show dynamic characteristics, like the coal near the wall suddenly squeezing into the hole, accompanying with the phenomenon of vibration, noise, or microshock. Drilling bits method is a practical way to identify rock burst according to the coal dust amount and the relevant dynamic effect [22].

Indexes of drilling bits method for monitoring rock burst are coal dust amount, drilling depth, and dynamic effect. Coal dust amount is the discharged amount of the coal dust per meter. Drilling depth is the length between the coal wall and the dust amount measured location. Dynamic effect includes sticking of the drill, shock of the hole, and changes of particle size of the coal dust.

The danger of rock burst is often identified by dust amount index K [22]:

$$K = \frac{Q}{Q_0}, \quad (3)$$

where Q is the practical amount of the coal dust and Q_0 is the normal amount.

Identification standard of the coal dust amount is listed in Table 1. The higher rate of the coal dust than the calibration

TABLE 1: Coal dust index for identifying rock burst [22].

Drilling depth/mining thickness	1.5	1.5~3	3
Coal dust amount index	≥ 1.5	2~3	≥ 4

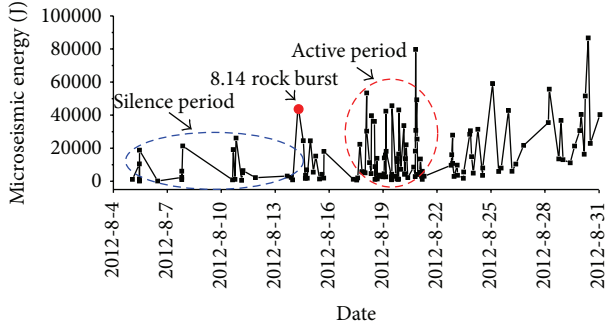


FIGURE 2: Microseismic events statistical data curve.

value shows the raised degree of stress concentration and the increased risk of rock burst.

For the convenience of calculation, the index of dust amount can be converted into an easily measured critical dust amount:

$$G_l = G \cdot K \cdot \alpha, \quad (4)$$

where G_l is the critical dust amount and G is the standard amount; K is the dust index; and α is the correction coefficient.

When using drilling bits method to monitor the danger of rock burst, if the actual amount of coal dust exceeds the critical value, there will be a trend of rock burst in the monitoring area. Measures of relieving pressure should be taken to prevent the occurrence of rock burst.

When drilling in the high stress area, there will be brittle fracture in the coal without the participation of the drill, because the coal around the drill has come into the ultimate limit state of stress. So the drill grinds the coal slightly, and particle sizes of dust are large. Therefore, the proportion of large-size particles (the diameter is larger than 3 mm generally) in the dust can be used as an index for predicting the local rock burst.

4. Results and Discussion

4.1. Microseismic Data. Microseismic data per time and per day were recorded and shown in Figures 2 and 3. Before "8.14 rock burst," the microseismic events were few, and the released energy was low, with the value smaller than 1.0×10^4 J mostly. This period was called microseismic silence period or energy accumulation period. After "8.14 rock burst," there was a high-incidence period of microseismic events, and it lasted four days. In this period, microseismic events occurred frequently, and the amount of released energy per day was very high. This period was called microseismic active period or energy release period.

Before rock burst, there is a silence period, in which microseismic events are few, and the total microseismic

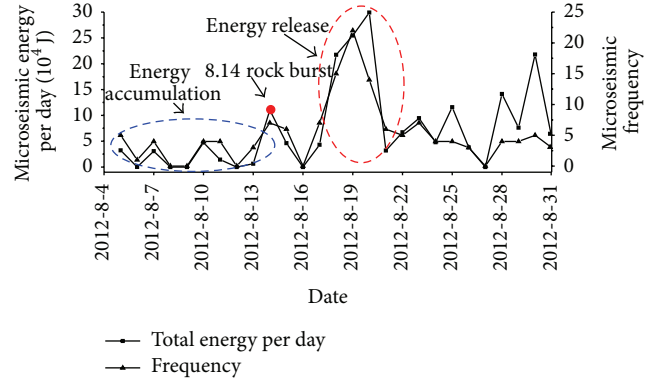


FIGURE 3: Total microseismic energy and frequency curves.

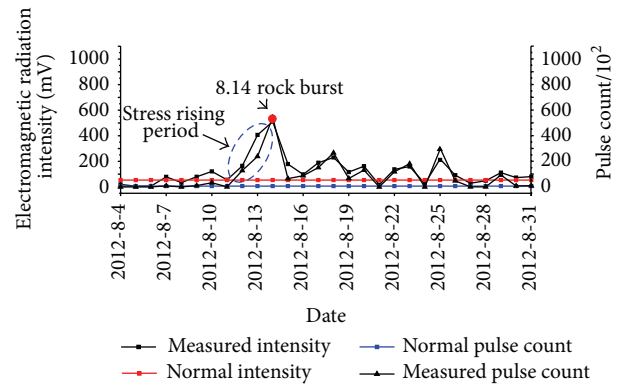


FIGURE 4: Electromagnetic radiation signal curves.

energy per day is smaller than 5×10^4 J. If the energy exceeds 5×10^4 J, the silence period ends, and burst risk should be warned. The lasting time of the silence period can be long or short and generally longer than five days. The longer the lasting time is, the greater the rock burst trend will be.

4.2. Electromagnetic Radiation Data. The electromagnetic radiation data in the workface was shown in Figure 4. From August 1 to August 8, the intensity and pulse count of the electromagnetic radiation fluctuated around the normal value, which showed that the stress distributed in the coal was stable. From August 11 to August 14, the intensity and pulse count of the electromagnetic radiation rose steadily. The increasing value was very large, nearly ten times of the normal value. The stress in the coal increased fast. High stress caused coal fracture and severe friction, accompanying with strong electromagnetic radiation signal. And then in August 14, rock burst happened.

Before "8.14 rock burst," there were a rising period of the intensity and a rising period of pulse count in electromagnetic radiation. The rising period reflected the increasing stress in the coal, and the steadily increasing stress caused rock burst.

4.3. Drilling Bits Data. At the beginning of the mining, five holes were drilled in the roadway of the workface, and the coal dust amount data was recorded in Figure 5. The dust amount

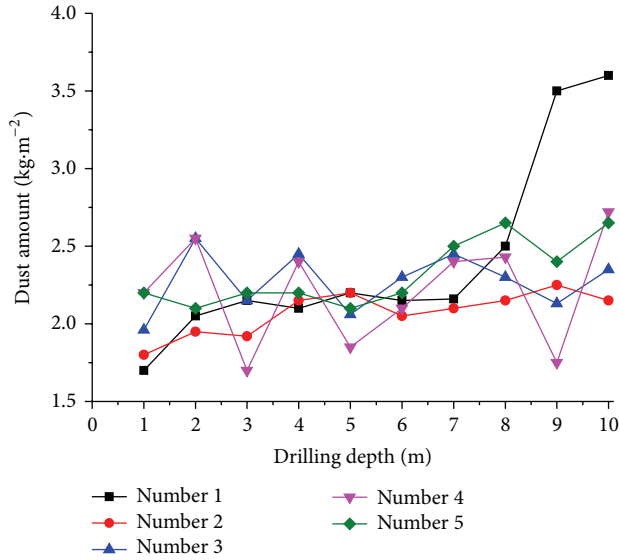


FIGURE 5: Coal dust amount changing curves.

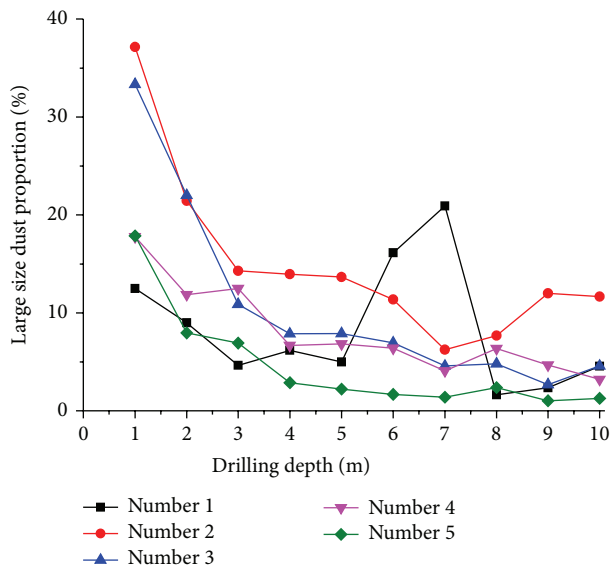


FIGURE 6: Large size dust proportion changing curves.

mainly ranged from 1.5 kg/m to 2.5 kg/m, and the max value was 3.6 kg/m. No. 1 drill was 15 m far from the workface, and the stress in the coal was high under the influence of advanced support pressure. When the dust amount reached 3.6 kg/m, there was dynamic effect like sticking of the drill.

The proportion of particles larger than 3 mm in the dust at different drilling depth in five holes was shown in Figure 6. At the coal wall, the coal was more fractured and bigger coal pieces dropped under the drill vibration, so the proportion at the drill outer end was high. The energy at the coal wall was already released, and there was no burst trend. The proportion at the wall could not be taken as monitoring index data.

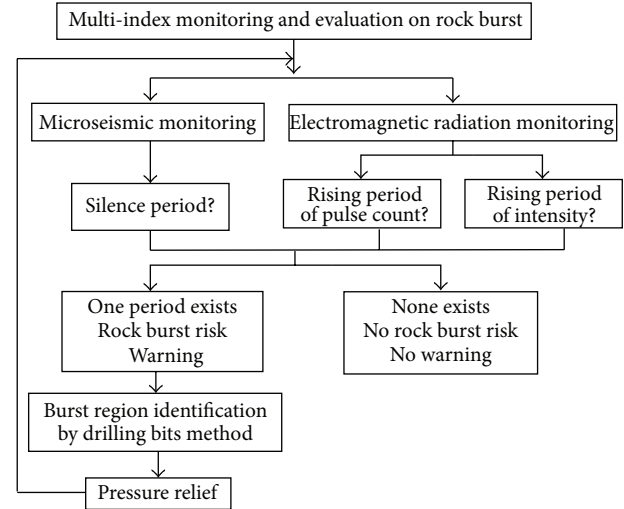


FIGURE 7: Flow chart of multi-index evaluation system on rock burst.

The average thickness of the coal seam is 7.5 m, so the critical dust amount is 3.68 kg/m, calculated from formula (4) by setting K to be 1.5 and α to be 1.1. If the actual amount of coal dust exceeds the critical value, there will be a trend of rock burst in the monitoring area. If there are dynamic effects like sticking of the drill, or the proportion of large-size particles in the dust is higher than 30%, there will be burst risk though the dust amount is smaller than the critical value. When using drilling bits method to monitor the risk of rock burst, multiple indexes should be considered together.

4.4. Multi-Index Evaluation. By analyzing the monitoring data, we found that there was a silence period in microseismic monitoring, as well as rising periods of intensity and pulse count of electromagnetic radiation monitoring. The foreboding information is taken as prediction index for rock burst, and a system of multi-index monitoring and evaluation is established, as shown in Figure 7.

There are three identifying indexes in the evaluation system. They are the silence period in the microseismic events and rising period of the intensity and rising period of pulse count in electromagnetic radiation. If any one of the three periods exists, it is identified burst risk. Only when the three periods all do not exist, there is no burst risk in the workface. If there is identified burst risk, the drilling bits method is used to ascertain the burst region. Then pressure releasing methods will be carried out to eliminate the disaster.

5. Conclusions

By using microseismic method, electromagnetic radiation method, and drilling method, rock burst in Yangcheng Mine was monitored, and a multi-index monitor and evaluation system for rock burst was established. The investigations show the following.

- (1) There is one microseismic silence period before rock burst, as well as one active period after burst. The

longer the silence period lasts, the greater the rock burst trend probability will be. The silence period is one index to identify burst risk.

- (2) There are steadily rising period of intensity and rising period of pulse count in electromagnetic radiation when the stress in the coal increases, which can cause rock burst. These two periods are other two indexes to identify burst risk.
- (3) Drilling bits method can ascertain the burst region after identifying burst risk. Coal dust amount, dynamic effect, and proportion of large-size particles should be considered together.

Conflict of Interests

The authors declare that there is no conflict of interests regarding the publication of this paper.

Acknowledgments

This work is supported by National Natural Science Foundation of China (51274133, 51474137, 51204102, and 51104133), Doctoral Scientific Fund Project of the Ministry of Education of China (no. 20123718110013), Shandong Province Natural Science Fund (no. ZR2012EEZ002), and Research Award Fund for Outstanding Young Scientists in Shandong Province (BS2012NJ007).

References

- [1] Y.-D. Jiang, Y.-S. Pan, F.-X. Jiang, L.-M. Dou, and Y. Ju, "State of the art review on mechanism and prevention of coal bumps in China," *Journal of the China Coal Society*, vol. 39, no. 2, pp. 205–213, 2014.
- [2] L. Dou, T. Chen, S. Gong, H. He, and S. Zhang, "Rockburst hazard determination by using computed tomography technology in deep workface," *Safety Science*, vol. 50, no. 4, pp. 736–740, 2012.
- [3] Z. Li, L. Dou, W. Cai et al., "Investigation and analysis of the rock burst mechanism induced within fault-pillars," *International Journal of Rock Mechanics and Mining Sciences*, vol. 70, pp. 192–200, 2014.
- [4] Q. M. Gong, L. J. Yin, S. Y. Wu, J. Zhao, and Y. Ting, "Rock burst and slabbing failure and its influence on TBM excavation at headrace tunnels in Jinping II hydropower station," *Engineering Geology*, vol. 124, no. 1, pp. 98–108, 2012.
- [5] X. P. Zhou, Q. H. Qian, and H. Q. Yang, "Rock burst of deep circular tunnels surrounded by weakened rock mass with cracks," *Theoretical and Applied Fracture Mechanics*, vol. 56, no. 2, pp. 79–88, 2011.
- [6] J.-H. Liu, M.-H. Zhai, X.-S. Guo, F.-X. Jiang, G.-J. Sun, and Z.-W. Zhang, "Theory of coal burst monitoring using technology of vibration field combined with stress field and its application," *Journal of the China Coal Society*, vol. 39, no. 2, pp. 353–363, 2014.
- [7] D.-Y. Zou and F.-X. Jiang, "Research of energy storing and gestation mechanism and forecasting of rockburst in the coal and rock mass," *Journal of the China Coal Society*, vol. 29, no. 2, pp. 159–162, 2004.
- [8] X. Y. Li, N. J. Ma, Y. P. Zhong, and Q. C. Gao, "Storage and release regular of elastic energy distribution in tight roof fracture," *Chinese Journal of Rock Mechanics and Engineering*, vol. 26, supplement 1, pp. 2786–2793, 2007.
- [9] P. P. Procházka, "Rock bursts due to gas explosion in deep mines based on hexagonal and boundary elements," *Advances in Engineering Software*, vol. 72, pp. 57–65, 2014.
- [10] X. Qu, F. Jiang, Z. Yu, and H. Ju, "Rockburst monitoring and precaution technology based on equivalent drilling research and its applications," *Chinese Journal of Rock Mechanics and Engineering*, vol. 30, no. 11, pp. 2346–2351, 2011.
- [11] C. Wang, J. Xu, X. Zhao, and M. Wei, "Fractal characteristics and its application in electromagnetic radiation signals during fracturing of coal or rock," *International Journal of Mining Science and Technology*, vol. 22, no. 2, pp. 255–258, 2012.
- [12] F. Freund and D. Sornette, "Electro-magnetic earthquake bursts and critical rupture of peroxy bond networks in rocks," *Tectonophysics*, vol. 431, no. 1–4, pp. 33–47, 2007.
- [13] E. Wang, X. He, J. Wei, B. Nie, and D. Song, "Electromagnetic emission graded warning model and its applications against coal rock dynamic collapses," *International Journal of Rock Mechanics and Mining Sciences*, vol. 48, no. 4, pp. 556–564, 2011.
- [14] M. K. Abdul-Wahed, M. Al Heib, and G. Senfaute, "Mining-induced seismicity: seismic measurement using multiplet approach and numerical modeling," *International Journal of Coal Geology*, vol. 66, no. 1–2, pp. 137–147, 2006.
- [15] X. Xu, L. Dou, C. Lu, and Y. Zhang, "Frequency spectrum analysis on micro-seismic signal of rock bursts induced by dynamic disturbance," *Mining Science and Technology*, vol. 20, no. 5, pp. 682–685, 2010.
- [16] X. He, W. Chen, B. Nie, and H. Mitri, "Electromagnetic emission theory and its application to dynamic phenomena in coal-rock," *International Journal of Rock Mechanics and Mining Sciences*, vol. 48, no. 8, pp. 1352–1358, 2011.
- [17] L. Du, X. Zhang, J. Niu, X. Wang, and G. Feng, "The seismic CT method in measuring rock bodies," *Applied Geophysics*, vol. 3, no. 3, pp. 192–195, 2006.
- [18] L.-M. Dou, W. Cai, S.-Y. Gong, R.-J. Han, and J. Liu, "Dynamic risk assessment of rock burst based on the technology of seismic computed tomography detection," *Journal of the China Coal Society*, vol. 39, no. 2, pp. 238–244, 2014.
- [19] Y. L. Liu, Y. Tian, X. Feng, Q. Zheng, and H. Z. Chi, "Review of microseism technology and its application," *Progress in Geophys*, vol. 28, no. 4, pp. 1801–1808, 2013.
- [20] Y. Zhao, Z. Wu, C. Jiang, and C. Zhu, "Present deep deformation along the longmenshan fault by seismic data and implications for the tectonic context of the Wenchuan earthquake," *Acta Geologica Sinica*, vol. 82, no. 12, pp. 1778–1787, 2008.
- [21] X. Q. He, E. Y. Wang, and B. S. Nie, *Electromagnetic Dynamics of Coal or Rock Rheology*, Science Press, Beijing, China, 2003.
- [22] B. J. Zhao and M. T. Zhang, "The study and application of the drilling method," *Journal of Fuxin Mining Institute*, vol. 51, pp. 13–28, 1985.

Research Article

Effects of Fine Gangue on Strength, Resistivity, and Microscopic Properties of Cemented Coal Gangue Backfill for Coal Mining

Tingye Qi, Guorui Feng, Yanrong Li, Yuxia Guo, Jun Guo, and Yujiang Zhang

College of Mineral Engineering, Taiyuan University of Technology, No. 79 Yingze Western Street, Taiyuan, Shanxi 030024, China

Correspondence should be addressed to Guorui Feng; fguorui@163.com

Received 6 October 2014; Revised 8 March 2015; Accepted 8 March 2015

Academic Editor: Shimin Liu

Copyright © 2015 Tingye Qi et al. This is an open access article distributed under the Creative Commons Attribution License, which permits unrestricted use, distribution, and reproduction in any medium, provided the original work is properly cited.

The cemented coal gangue backfill (CGB) in coal mining is normally made of gangue (particle size of 0–15 mm), fly ash, cement, and water. In this study, the effects of the weight content (ranging from 20% to 60%) of fine gangue (0–5 mm) on the microscopic characteristics, resistivity, and compressive strength of CGB were investigated at 3 d and 28 d curing times, respectively. The test results indicate that the strengths of the CGB, regardless of the curing time, increased with fine gangue content changing from 20% up to 40%. Further increase in fine gangue introduced a decrease in the strength. Another observation is that, at 3 days, a general increasing trend of CGB resistivity was noted with fine gangue content. At 28 days, the resistivity of CGB decreased with increase in the fine gangue content. Correlations between the resistivity and compression strength of CGB show a concave pattern, which attribute to the various micromechanism influenced on the resistivity and strength of CGB with different fine gangue content. It indicates that using resistivity to derive strength of CGB is not appropriate.

1. Introduction

Coal gangue is a solid waste discharged during coal mining and washing processes. The major chemical components of coal gangue are silica (SiO_2) and alumina (Al_2O_3), whereas the mineral components are quartz and feldspar [1]. In 2010, the world coal production was 7,273 Mt, with a waste yield of 1,455 Mt [2]. In China, coal gangue has accumulated to an amount of approximately 1,000 Mt, and the coal gangue discharge increases annually by 100 Mt/a. A vast area of land would be required to process such a large quantity of coal gangue, which would also cause serious environmental problems [3]. In addition, coal mining causes surface subsidence in the mining area. Cemented coal gangue backfill (CGB) produced from gangue is one of the solutions to support the overlying strata when transported to the underground goaf through pipelines [4, 5]; CGB can reduce landfill area requirements and help solve environmental problems.

CGB used for coal mining backfilling is an engineered mixture of milled gangues (75–85% solids by weight), fly ash, hydraulic binder (3–7% of total weight of dry paste), and water. Each component of CGB plays a significant role on

its short- and long-term performance (i.e., transportation, placement, strength, and stability) [6, 7].

Gangue is one of the most important components of CGB for coal mining; this is because crushed gangue exhibits a pozzolanic activity and a certain degree of strength [8–10]. However, considering the slurry transportation restriction and the compressive properties of the CGB, the maximum particle size of coal gangue is normally 15 mm at maximum. Previous researchers have evaluated the fine gangue (0–5 mm) content on the performance of CGB. According to Zheng et al. [10], increasing the fine gangue content may enhance the slump and pumpability of the paste. Fall et al. [11] found that fine tailings are not suitable for CGB because they provide much lower strength than CGB made of coarse tailings. The research on use of Na_2SO_4 as chemical activator for paste backfill was also carried out. Besides, the effect of desliming and pozzolans on paste backfill strength has been recently studied [12, 13].

The resistivity is an important character of cement matrix. It is related to the microstructure of the matrix (pore structure, porosity, and pore-size distribution). It is also a function of the concentration and mobility of ions in the pore solution

[14]. In concrete, resistivity was investigated to understand the corrosion resistance and the hydration reaction process [15, 16]. The change in the content of the raw material for concrete changes its resistivity. For instance, a decrease in the water/cement ratio causes an increase in the resistivity [17]. Adding rice husk ash to the concrete increases its resistivity [18]. An increase in the volume fraction of the aggregate facilitates the formation of current transport at the interface between the aggregate and the slurry, which results in an increase in the resistivity [19]. Compared with concrete, fewer studies focus on the resistivity of CGB.

Several authors have discussed the relationship between resistivity and compressive strength of concrete. Wei et al. [20] made several samples with different cements and measured their resistivity at 24 h, as well as the compressive strength at 28 d. They found that there existed a linear relationship between the two couples of values and concluded that the compressive strength and resistivity mainly depended on the pore structure and micromorphology of products, which were influenced by hydration. Lübeck et al. [21] used White Portland cement, ground granulated blast-furnace slag, and Na_2SO_4 to make different samples with three water-to-binder ratios and discovered that the resistivity and compressive strength with the same binder followed a nearly linear relationship owing to the compactness of the structure irrespective of the concrete saturation degree, together with the pore solution conductivity which imposed the influence on the resistivity. Ferreira and Jalali [22] observed a linear relationship between electrical resistivity and compressive strength for the concrete samples prepared by ordinary Portland cement and fly ash cement, because the variation of compressive strength and electrical resistivity depended on the pore structure and the sample geometry change caused by cement hydration. Ramezaniyanpour et al. [23] prepared 57 concrete mixtures by Portland cement with some supplementary materials including tuff, pumice, rice husk ash, metakaolin, and silica fume. Interestingly, the compressive strength and resistivity of concrete mixtures prepared with different cementitious materials presented no sensible correlation, because the interfacial transition zone (ITZ) only affected the compressive strength but had no obvious influence on the resistivity of concrete, whereas the chemical composition of the pore solution played an important role in resistivity but had little effect on the compressive strength of concrete.

In this study, the effects of fine gangue content on compressive strength, resistivity, and microstructure of CGB at 3 and 28 days curing times were investigated. Attempts were also made to link the strengths of CGB to the resistivity.

2. Materials and Methods

2.1. Materials

2.1.1. Coal Gangue. The coal gangue samples were obtained from Xinyang Colliery, which is situated in the west of Shanxi Province of China. The samples were mechanically crushed and then categorized into two groups based on particle size, fine gangue aggregate (0–5 mm), and coarse gangue

TABLE 1: Chemical composition and physical properties of the materials used.

Major element	Cement (%)	Fly ash (%)	Gangue (%)
SiO_2	22.27	52.42	28.46
Al_2O_3	5.59	32.48	16.11
Fe_2O_3	3.47	3.62	10.86
CaO	65.90	3.05	7.15
MgO	0.81	1.01	3.50
TiO_2	—	1.26	0.80
Specific gravity (g/cm^3)	3.1	2.2	2.0
Specific surface (m^2/kg)	349	415	499
Fineness ($>45 \mu\text{m}$) (%)	5	42.54	53.78
Moisture content (%)	—	0.56	8.0
Loss on ignition (%)	2	3.8	—

Notes: for measuring SiO_2 , samples were first burned at 800°C to remove organic matter and then measured in a NaOH solution at 650°C . All other oxides were measured from samples subject to sealed digestion in HF + HNO_3 at 185°C .

aggregate (5–15 mm). According to the Chinese Standard for Technical Requirements and Test Method of Sand and Crushed Stone (or Gravel) for Ordinary Concrete (JGJ52-2006), the sieving method was used to determine the particle size distribution of the gangue aggregates (Figure 1(a)). The fineness modulus μ of the fine gangue (0–5 mm) was 3.02. Table 1 lists the physical properties of the gangue samples. The X-ray diffraction (XRD) pattern of the mineral composition of the coal gangue samples was collected with a Bruker AXS D8 Advance diffractometer using Cu $K\alpha$ radiation (Figure 2(a)). A Thermo Fisher Scientific Thermo iCAP 6300 inductively coupled plasma optical emission spectrometer (ICP-OES) was used to determine the chemical composition of the gangue samples (Table 1).

2.1.2. Fly Ash. The fly ash samples were obtained from the power plant of Xinyang Colliery. A Malvern Mastersizer 2000 Particle Size Analyser was used to analyse the particle size of the fly ash samples (Figure 1(b)). The physical properties of the fly ash samples were analysed according to the Technical Specification for Fly Ash Used in Concrete and Mortar (JGJ28-86). An ICP-OES was used to analyse the chemical composition of the fly ash samples (Table 1). Figure 2(b) shows the mineral composition of the fly ash samples.

2.1.3. Cement and Water. Ordinary Portland cement (Grade 42.5) was used in this study. Table 1 lists the chemical composition and the physical properties of the cement (provided by the manufacturer). The initial and final setting times were 165 min and 231 min, respectively. The compressive strengths were 18.4 MPa (3 d curing time) and 46.4 MPa (28 d curing

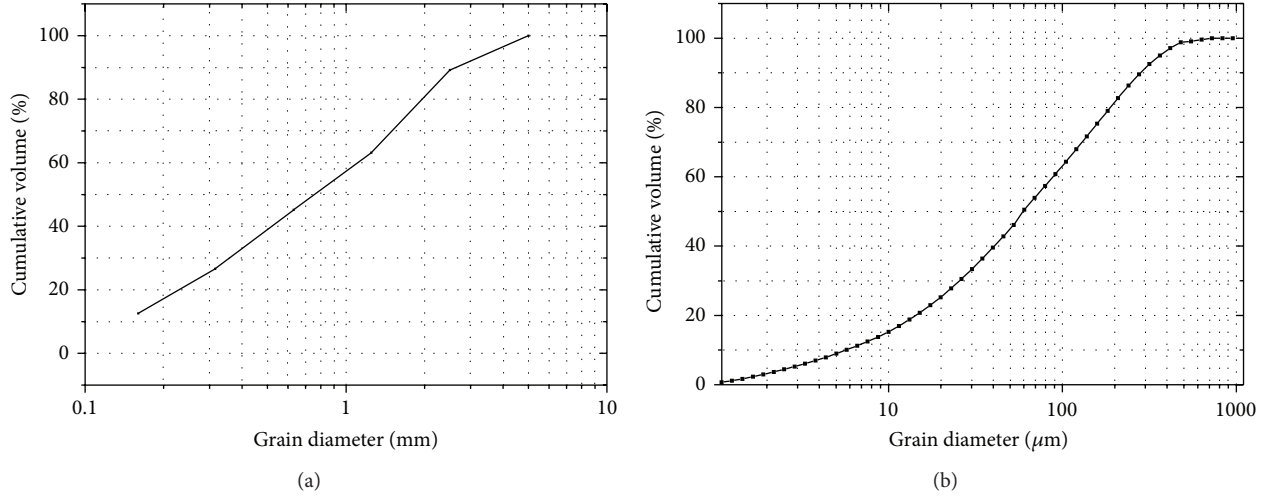


FIGURE 1: Particle size distribution curves: (a) fine gangue and (b) fly ash.

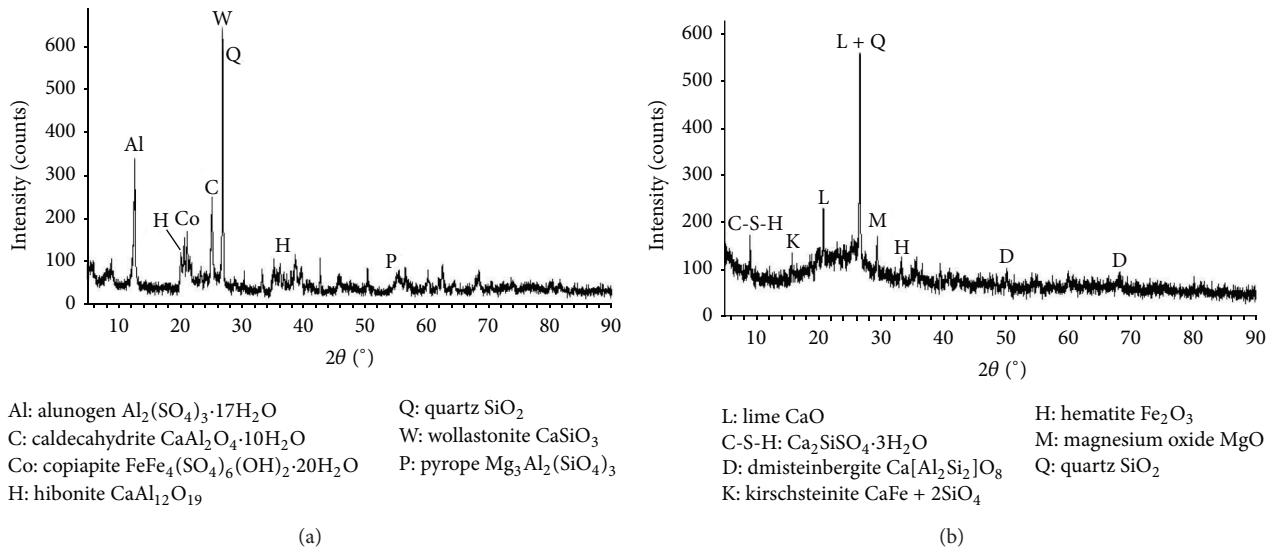


FIGURE 2: Mineral composition by XRD for (a) coal gangue and (b) fly ash.

time), respectively. The water source used in this study was tap water.

2.2. Sample Preparation and Test Methods

2.2.1. Sample Preparation. The raw materials used in the present study were ordinary Portland cement, coal gangue, fly ash, and water. The solid content of the paste mixtures was 80% by weight. The CGB samples were divided into five groups based on different fine gangue contents. The gangue content (including both fine and coarse gangues) in each group was constantly 950 kg/m^3 . The fine gangue (0–5 mm) occupied 20% (M1), 30% (M2), 40% (M3), 50% (M4), and 60% (M5) of the gangue (0–15 mm) content in each group, respectively. The detailed mixture is given in Table 2.

The raw materials were mixed according to the designed mix proportions and then mechanically stirred. Next, the

slurry was transferred into $10 \times 10 \times 10 \text{ cm}$ testing moulds. After casting, the specimens were cured in a curing room (temperature: $20 \pm 2^\circ\text{C}$; humidity: 40%) for periods of 3 and 28 days, respectively. To determine the mechanical strengths and electrical properties of CGB specimens after curing, the compressive strength and resistivity tests on the specimens were performed. After 3 and 28 days, samples were taken from the center of cured CGB specimens and immersed in anhydrous ethanol for 24 h. Then, the samples were put in an oven at a temperature of 105°C for 16 h for the following microscopic tests.

2.2.2. Compressive Strength and Resistivity Test. A Wenner dipole array was used to determine the resistivity of the specimens, which were cured for 3 d and 28 d, respectively. The test voltage was 1 V, and the frequency was 100 Hz. Referring to Gowers and Millard [24], contact resistance

TABLE 2: Proportions of the mix.

Mixture	Portland cement (kg/m ³)	Water (kg/m ³)	Fly ash (kg/m ³)	Gangue (kg/m ³)	
				Fine (0–5 mm)	Coarse (10–15 mm)
M1 (20%)	190	380	380	190	760
M2 (30%)	190	380	380	285	665
M3 (40%)	190	380	380	380	570
M4 (50%)	190	380	380	475	475
M5 (60%)	190	380	380	570	380

was a cause of unstable resistivity. To reduce the effect of contact resistance, copper papers were used as electrodes. A piece of cotton cloth that had been previously immersed in a saturated copper sulphate solution was placed between the copper papers and the specimen.

After resistivity tests, the compressive strength tests were performed on the same CGB samples using a computer-controlled mechanical press, which had a load capacity of 1000 kN and a pressure speed of 6.75 kN per minute according to GB50081. All the experiments were carried out in triplicate and the mean resistivity and compressive strength values were presented in the results.

2.2.3. Microscopic Test. After curing, the CGB particles were subjected to the porosity test using mercury intrusion porosimetry (MIP). A CE Pascal 140/240 porosimeter was used for this test. The CGB particles cured for 3 d and 28 d were ground into powder for the X-ray diffraction test. A field emission transmission electron microscopy (FETEM) unit (JSM-7001F) was used for the microscopic observation of the CGB particles cured for 28 d.

Gangue powder (0–160 μm) and fly ash were separately immersed in deionised water. The ratio of water to solid mass was 100 : 1. The solution was stirred using a magnetic stirrer for 10 min and then filtered. An ICP-OES was used to determine the concentrations of major ions in the filtrate.

Solution sample preparation was as follows: after curing for 3 d and 28 d, the processed CGB particles were ground into powder, which was then immersed in deionised water. The ratio of water to solid mass was 100 : 1. The solution was stirred using a magnetic stirrer for 10 min. To prevent the reaction between the particles and water, the solution was filtered. The concentrations of the major ions in the filtrate were immediately measured using the ICP-OES. The testing temperature of the solution was $20 \pm 1^\circ\text{C}$. The changing trend of the ion concentrations in the material solution was used to determine the changing regularity of the ion concentrations in the pore solution because of the correlation between the two solutions in pH and ion concentration [25, 26]. However, because of the difference in the pore water content caused by different curing times, there were differences between the ion concentrations of the pore solution and the material solution. The pore solution should not be collected using the high-pressure extraction method [27, 28], because the high pressure could cause the fragmentation of the gangue and the dissolution of active substances.

3. Results and Discussion

3.1. Effects of Fine Gangue Content on Microscopic Properties of CGB. The hydration and pozzolanic reaction occurred among the minerals in CGB. The hydration products contain hydrated calcium silicate (C-S-H) gel, calcium hydroxide (portlandite $\text{Ca}(\text{OH})_2$), AFt (ettringite, etc.), or AFm (mono-sulphate, etc.) phases. Then, the active Si^{4+} , Al^{3+} , Fe^{3+} ions, in which gangue and fly ash are enriched, react with portlandite to form AFt or AFm [29–31].

Figure 3 shows the XRD patterns of the mineral composition of the CGB samples with a fine gangue content of 20–60% cured for 3 d and 28 d, respectively. The diffraction angles of the mineral crystals with different fine gangue contents cured for the same time were approximately the same. However, their intensities differed, which indicated that the change in fine gangue content did not affect the material's mineral composition of the material but the mineral content differed among the samples. The reaction products C-S-H, AFt, and $\text{Ca}(\text{OH})_2$ were detected in the samples that were cured for 3 d (Figure 3(a)). The peak intensity of $\text{Ca}(\text{OH})_2$ crystals at 52° decreased with the increase in fine gangue content. The decrease in $\text{Ca}(\text{OH})_2$ content in material was related to the consumption of $\text{Ca}(\text{OH})_2$ in the pozzolanic reaction. The increasing fine gangue content led to amplifying the specific contact surface area between the gangue and $\text{Ca}(\text{OH})_2$. The mineral composition of the samples cured for 28 d (Figure 3(b)) included C-S-H and AFt. No $\text{Ca}(\text{OH})_2$ crystal was detected in the XRD because of the low cement content and high pozzolanic reaction degree after 28 d of curing time. The peak intensities of C-S-H gel at 22.3° and AFt phase at 31.8° increased with the increase in fine gangue content, due to the fact that increasing quantity of soluble active ions generates more pozzolanic products content.

Figure 4 shows surface morphology of the gangue particles in the CGB samples at 20%, 40%, and 60% fine gangue content. When the fine gangue content was 20%, the surface of gangue was covered by needle-like, columnar, floccus-like, and petal-like pozzolanic products (Figure 4(a)). When gangue was dissolved in water, active ions (Si^{4+} , Al^{3+} , and Fe^{3+}) precipitated on the gangue's surface. Then, a pozzolanic reaction occurred between these ions and $\text{Ca}(\text{OH})_2$, and the products of this reaction accumulated on the surface of the gangue particles. When the fine gangue content was 40% (Figure 4(b)), the surface of gangue was partially covered by floccus matter, whereas some lamellar minerals were

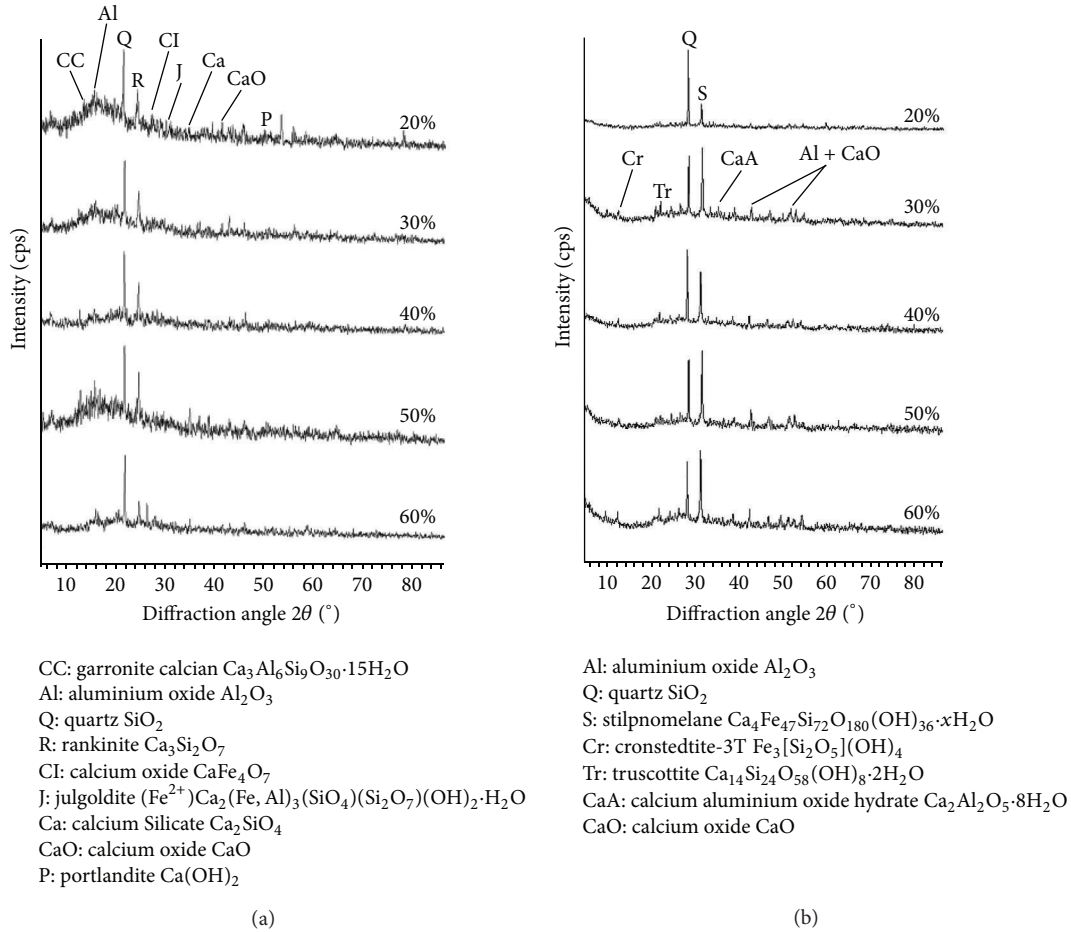


FIGURE 3: XRD results of samples at 20%–60% fine gangue dosage at (a) 3 d and (b) 28 d.

distributed on the surface. When the $\text{Ca}(\text{OH})_2$ content was fixed, the specific surface area of gangue of fine particle size increased, and the generated pozzolanic products could not fully cover the surface of gangue of fine particle size. When the fine gangue content was 60% (Figure 4(c)), lamellar and granular gangue in its initial form was observed on the surface of particles, which indicated that some minerals on the surface of gangue of fine particle size did not participate in the pozzolanic reaction. With the increase in fine gangue content, the exposed fine gangue minerals in CGB also increased.

Figure 5 shows that the porosity of the material cured for 28 d was smaller than that of the material cured for 3 d. Because the hydration and pozzolanic reaction products continuously filled up the pores between the cemented material and the gangue, the overall porosity decreased with the increasing curing time [32, 33].

The total porosity curve at 3 and 28 days is presented in Figure 5 which clearly showed that fine gangue addition produces less pores. At the fine gangue content between 20% and 40%, the porosity of the CGB samples of 3 and 28 days decreased from 39.97 and 34.34% to 35.28 and 30.16% corresponding to 11.72% and 12.19% losses of porosity. At the fine gangue content between 40% and 60%, the porosity

of the CGB samples of 3 and 28 days decreased from 35.28 and 30.16% to 32.91 and 28.30% corresponding to 6.72% and 3.62% losses of porosity. Fine gangue plays double roles during the pozzolanic reaction and pore structure formation processes. The bigger pore space among the coarse gangues is filled with finer gangues. The finer gangue content signified higher reaction degree and is related more to reaction products packing pattern.

Differential distribution curve (Figure 6) is presented in order to estimate and evaluate the pore structure of the CGB at 28 days. With the increase in fine gangue content, the volume of the capillary-size pores in the range of 0–2,000 nm gradually decreased. With the increase in porosity, the number of pores increased, which facilitated the connection of the pore solution. Additionally, a conductive network was formed inside the CGB, which enhanced the current transport capacity of the pore solution. To estimate the critical pore size (d_{cr}) the differential distribution curve was plotted where the critical pore size corresponds to the diameter that the distribution presents maximum. The critical pore size controls the transmissivity of the material [34]. The critical pore diameter is the most frequently occurring diameter in the interconnected pores that allows maximum percolation of chemical species through the CGB [35]. Figure 6

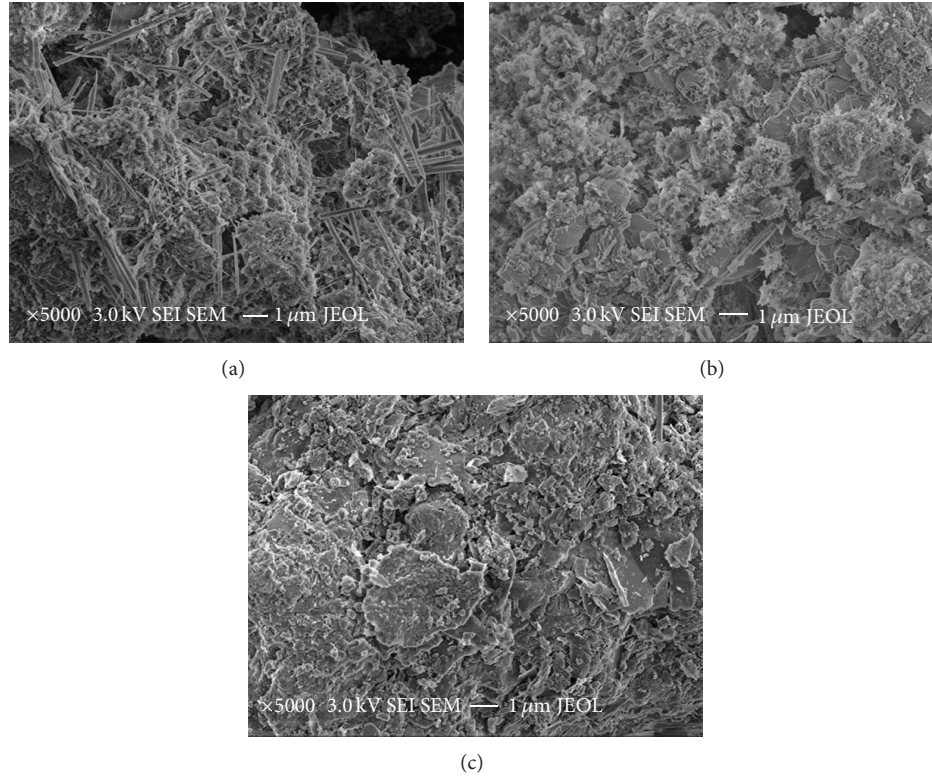


FIGURE 4: Surface morphology of the gangue particles in CGB samples at fine gangue contents of (a) 20%, (b) 40%, and (c) 60%.

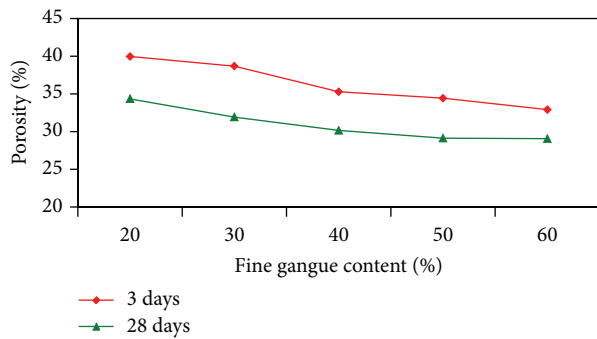


FIGURE 5: MIP porosity of CGB at 3 d and 28 d.

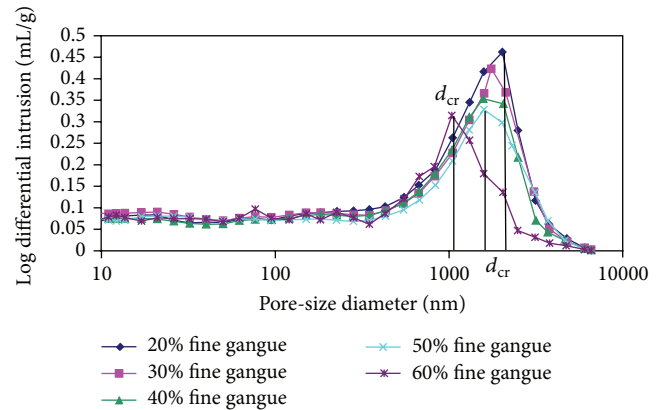


FIGURE 6: Differential distribution curve at 20–60% fine gangue content at 28 d.

indicates that as fine gangue content increases critical diameter decreased. This leads to the conclusion that fine gangue addition in CGB produces less interconnected pores in CGB but of the same magnitude.

Table 3 shows that the fly ash and the gangue solution contained Al^{3+} , Fe^{3+} , and Si^{4+} that could participate in the pozzolanic reaction. Al^{3+} , Fe^{3+} , and Si^{4+} contained independent cations and complex ions. The concentration of these cations and ions could be used to determine the active SiO_2 , Al_2O_3 , and Fe_2O_3 content. The concentration of Fe^{3+} reached 6.96 mg/L in the gangue solution, whereas the concentration of Al^{3+} reached 4.594 mg/L in the fly ash solution. The Ca^{2+} in the gangue and the fly ash solutions was relatively

concentrated. In addition, the concentrations of Na^+ and K^+ were similar.

The pore solution of the CGB primarily contained Na^+ , K^+ , Ca^{2+} , Mg^{2+} , Al^{3+} , Fe^{3+} , Si^{4+} , SO_4^{2-} , $\text{Al}(\text{OH})_4^-$, H_3SiO_4^- , OH^- , and $[\text{FeO}_2(\text{OH})]^{2-}$, which originated in the gangue, the dissolution of the fly ash, and the hydrolysis between the hydration and the pozzolanic reaction products [36].

Table 4 lists the change of the concentrations of seven major ions in the pore solution after curing for 3 d and 28 d. After curing for 3 d, the concentrations of Si^{4+} , Fe^{3+} , Al^{3+} , and

TABLE 3: Concentrations of major ions in the raw material solution.

Elements (mg/L)	Mg	Si	Fe	Al	Ca	K	Na
Coal gangue	3.07	0.36	6.96	0.284	233	0.409	0.986
Fly ash	1.20	0.413	0.006	4.594	47.7	0.426	1.08

TABLE 4: Active ion content at 3-day and 28-day curing times.

	Compound	Mg	Si	Fe	Al	Ca	K	Na
3 d (mg/L)	20%	0.664	1.76	0.447	6.966	86.5	2.28	2.94
	30%	0.596	1.69	0.438	6.758	77.6	2.43	2.77
	40%	0.650	1.70	0.412	6.638	74.3	2.34	2.82
	50%	0.601	1.56	0.387	6.495	72.1	2.18	2.88
	60%	0.624	1.47	0.342	5.786	63.7	2.08	2.68
28 d (mg/L)	20%	0.748	0.468	0.327	7.452	47.0	2.62	2.57
	30%	0.687	0.547	0.334	7.714	49.6	2.37	2.63
	40%	0.674	0.608	0.332	8.007	48.7	2.57	2.84
	50%	0.746	0.584	0.437	8.125	51.6	2.18	2.71
	60%	0.689	0.617	0.441	8.131	52.4	2.60	2.64

Ca^{2+} decreased with the increase in fine gangue content, the concentrations of K^+ , Na^+ , and Mg^{2+} did not change, and the overall ion concentration decreased. After curing for 28 d, the concentrations of Si^{4+} , Fe^{3+} , Al^{3+} , and Ca^{2+} increased and the overall ion concentration increased.

The hydration and the pozzolanic reactions are the primary reactions that occur in CGB. The dissolving and the reacting doses collectively affect the concentrations of the active ions. In the beginning, when the raw materials are mixed, a hydration reaction occurs in the cement. Active ions dissolve out and accumulate on the surface of gangue particles. The dissolving dose is greater than the reacting dose (24 h). When the hydration reaction continues, more $\text{Ca}(\text{OH})_2$ is generated. With the increase in fine gangue content, the specific surface area increases. Therefore, the reaction contact area between $\text{Ca}(\text{OH})_2$ and gangue increases. The concentrations of Ca^{2+} , OH^- , and active ions decrease. The gel generated from the reaction covers the surface of the particles, which prevents dissolution. At this time, the reacting dose is greater than the dissolving dose after curing for 3 d. After curing for 28 d, the hydration and the pozzolanic reaction level off. The change in the concentrations of the ions is primarily caused by precipitation. Therefore, with the increase in fine gangue content, the specific surface area increases, the quantity of the exposed minerals on the surface of gangue increases, and the number of dissolved ions increases.

3.2. Effects of Fine Gangue Content on Compressive Strength of CGB. Fine gangue content plays an important role in the mechanical behavior of CGB samples. Figure 7 shows the development of mechanical strength of CGB samples produced from 20%–60% fine gangue content at 3- and 28-day curing time. The increase in the strengths of the CGB samples was noted to peak at the fine gangue usage of 40%; thereafter, a trend of decline was apparent, irrespective

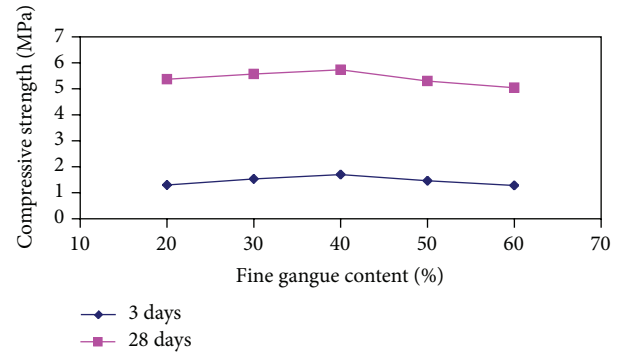


FIGURE 7: Compressive strength of CGB samples with 20–60% fine gangue contents at 3 and 28 days.

of curing time. At the fine gangue content between 20% and 40%, the strengths of the CGB samples of 3 and 28 days increased from 1.3 and 5.37 MPa to 1.7 and 5.73 MPa corresponding to 30.8% and 6.7% gains of strength. The reason is that increasing the gangues fineness leads to a lower porosity and more reaction products which reduce the porosity and enhance the bonding formation between the gangue particles. Previous research indicated that the surface texture of the aggregate plays an important role in compressive strength of mortars [37, 38]. The grip between the paste and the aggregate at the interfacial zone will be improved when a rougher texture aggregate is used, thereby leading to an increase in compressive strength [39]. As the fine gangue content increased from 40% to 60%, the strengths of the CGB samples of 3 and 28 days decreased from 1.7 and 5.73 MPa to 1.28 and 5.04 MPa corresponding to about 24.7% and 12% losses of strength. This is because the more products which covered the gangue particles surface exceed a threshold (Figure 4), which is not in favor of bonding with interspace between adjacent fine gangue grains. The rough

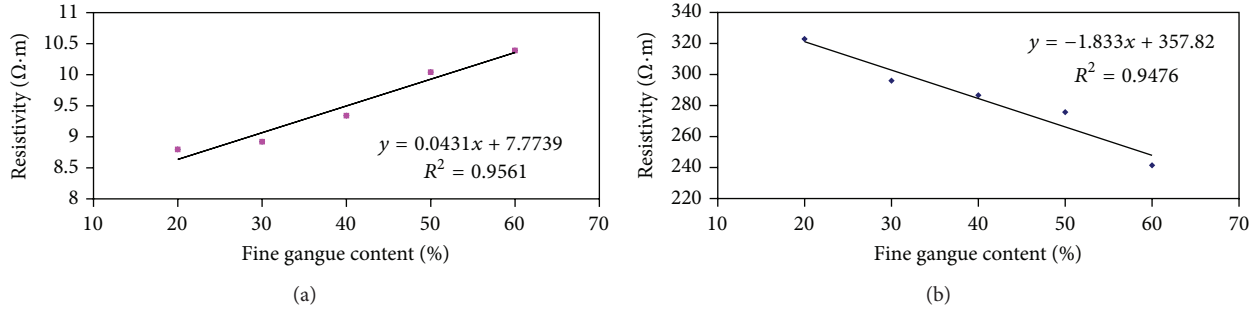


FIGURE 8: Relationship between resistivity and fine gangue content for CGB samples at curing times of (a) 3 d and (b) 28 d.

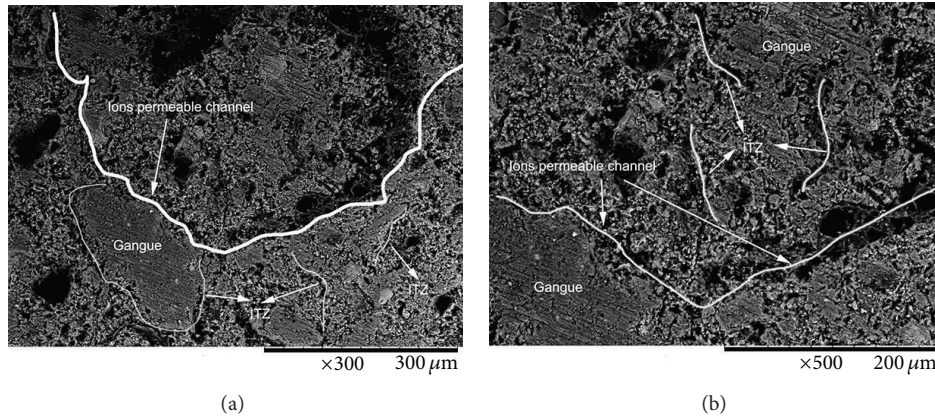


FIGURE 9: The interfacial transition zone (ITZ) between paste and gangue in CGB specimen at 28 days.

and angular nature of fine gangue affects the compaction of the mixes in the fresh state. Torkittikul and Chaipanich [40] explained that the decrease in strength when using fine gangue content at 40–60% of the total gangue by weight may be due to the difficulty in the compaction of the harsh mortar. The mechanical behaviour is taken into account; the optimum 40% fine gangue content is used in CGB.

3.3. Effect of Fine Gangue Content on the Resistivity of CGB.

Figure 8 shows the relationship between resistivity and fine gangue content after curing for 3 d and 28 d when the voltage was 1 V and the frequency was 100 Hz. Figure 8(a) shows that, with the increase in fine gangue content, the resistivity also increased after curing for 3 d. Figure 8(b) indicates that increasing fine gangue results in the reduction of resistivity in CGB samples after curing for 28 d. The resistivity of the gangue was measured to be $1 \times 10^7 \Omega \cdot m$, which is far greater than the resistivity of the measured CGB samples. The presence of gangues in the CGB matrix has two opposite effects on the transport properties [41]. The dilution and tortuosity effects reduce CGB permeability while the interface transition zone (ITZ) and percolation effects increase permeability (Figure 9). In addition, the diffusivity of CGB on pore structure can attribute to the effect of capillary porosity and connectivity of these capillary pores. Therefore, the resistivity of the CGB is related to the porosity, the pore-size distribution, the ion concentrations, and the ITZ effect [42–44].

After curing for 3 d, with the increase in fine gangue content, the concentrations of the ions in the pore solution decreased, which caused the decrease in the current transport capacity of the solution, and the current transport in the pore structure became more difficult, which caused the increase in resistivity. After curing for 28 d, because of the increase in the concentrations of the ions in the pore solution, the current transport capacity of the solution increased, which caused the decrease in resistivity. The pore structure had a limited impact on the resistivity of the CGB sample. However, when the gangue size decreased under a constant volume, the porous interfacial transition zone (ITZ) content would increase. The ITZ and percolation effects increase the CGB permeability; moreover, ions transport will be significantly enhanced [45].

3.4. Relationships between Compressive Strength and Resistivity.

The raw materials used in CGB of the present study resemble those used for concrete. However, the cement content for CGB is less than that for concrete, and the fine gangue for CGB acted as cementitious material and fine aggregate. As shown in Figures 7 and 8, the resistivity and strength of the tested CGB changed with increase in fine gangue content. The resistivity of the CGB is related to the porosity, pore-size distribution, ion concentration, and ITZ effect. At 3-day curing time, there were high porosity and much water in the pore space of CGB samples, which minimized the effect of ITZ on the current flow. The decreasing ion concentration (Table 4) and porosity with increase in fine

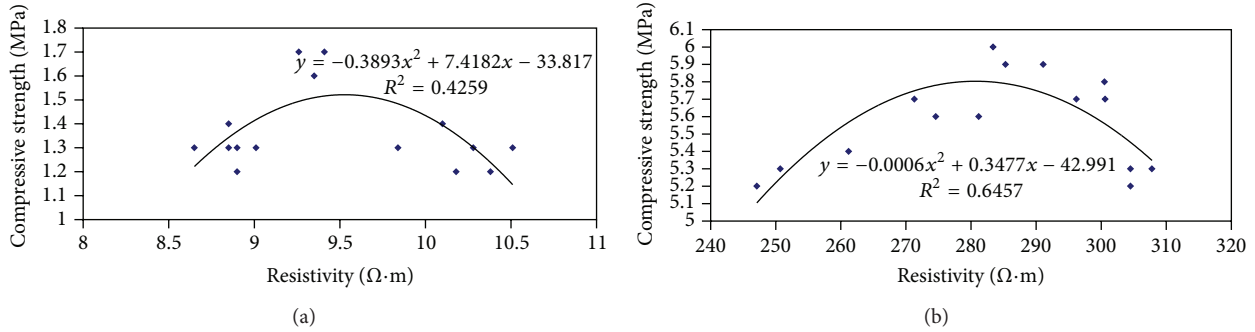


FIGURE 10: Relationships between strength and resistivity for CGB samples with 20–60% fine gangue content at (a) 3 and (b) 28 days.

gangue content might be the main cause for the increasing resistivity (Figure 8(a)), as the electrical resistivity of CGB is related to the porosity and the ions concentration of the pore solution. At 28 days, the degree of CGB saturation was lower than CGB saturation at early stage. The resistivity of CGB was influenced by the ions concentration of pore solution and ions transport channels. Ions transport channels consisted of pore structure and ITZ, the pore structure for MIP exhibits a statistical gradient of bulk paste of CGB which is outward from the actual paste-aggregate interface, and the effects of the ITZ are that the movement of water and ions through the “ITZ paste” is much more rapid than through the “bulk paste” [46]. In short, the ITZ would be the main factor on ions transport (Figure 9). With fine gangue content, the ITZ content increased and the fine gangues tended to be closely spaced so that the adjacent ITZs overlap in space. In addition, the ions concentration of pore solution increased with fine gangue content (Table 4). As a result, the capacity of ions transport was significantly enhanced and resistivity of CGB was decreased.

The factors influencing the compressive strength include interfacial zone, porosity, hydration, and content of pozzolanic reaction products. Increasing fine gangue content from 20% to 40% leads to a low porosity and many reaction products. This improves the CGB compaction and enhances the bonding formation between the gangue particles, causing increase in compressive strength. With further increase in fine gangue content from 40% up to 60%, the reaction products could not cover the surface of fine gangues, leading to reduction of bonding between gangue particles. This caused a reduction of compressive strength.

According to Wei et al. [20], Lübeck et al. [21], and Ferreira and Jalali [22], there is a linear relationship between compressive strength and concrete resistivity when concrete mixtures are made with the same cementitious materials. This is because both compressive strength and electrical resistivity are dependent on the continuous hydration of cement. In this study, however, there exists no sensible correlation between compressive strength and CGB resistivity as shown in Figure 10. On one hand, the compressive strength of CGB was influenced by reaction products, porosity, and surface of gangues. On the other hand, the resistivity of CGB was affected by ions concentration of pore solution and ITZ effects. The above two sides do not work in the same direction

during CGB curing periods. This may be the reason for the concave patterns in Figure 10. As there is no obvious correlation between the compressive strength and resistivity of CGB, it is thought not proper to use electrical resistivity as an indicator for evaluation of compressive strength of CGB in engineering practice.

4. Conclusions

In this study, the effect of fine gangue content on the strength, resistivity, and microscopic properties of CGB was evaluated. Based on the foregoing discussion, several main conclusions may be drawn as follows:

- (1) The compressive strength of CGB increases with fine gangue content increasing up to 40%. After that finer gangue leads to decrease in the compressive strength.
- (2) At 3 days of curing time, an increasing trend of CGB resistivity was noted with increase in fine gangue content, which could be attributed to the denser pore structure and higher ions concentrations of pore solution.
- (3) At 28 days, the resistivity of CGB decreased with increase in fine gangue content, which may be attributed to the enhanced interfacial transition zone and ion concentration of pore solution.
- (4) The nonlinear correlations between resistivity and compressive strength of CGB indicate that it is not proper to use the former to estimate the latter. This is different from what have been found in concrete study, where compressive strength seems proportional to resistivity. The fine gangue works not only as aggregates but also as cementitious materials in CGB. It influences not only the ITZ but also the ion concentration and content of chemical reaction products. The unbalanced change of these three with fine gangue content finally leads to a concave-shaped correlation between compressive strength and the resistivity of CGB.

Conflict of Interests

The authors declare that there is no conflict of interests regarding the publication of this paper.

Acknowledgments

This work was financially supported by the National Natural Science Foundation of China (51174142 and 51422404), National Science Support Panning of China (2009BAB48B02 and 2009BAB48B03), Program for New Century Excellent Talents in University of Chinese Ministry of Education (NCET-11-1036) and the Fok Ying Tung Education Foundation (132023), Scientific and Technological Industrialization Environment Construction Project of Shanxi Province (2013071050), and Postgraduate Innovate Project of Shanxi Province (02100489).

References

- [1] N. Zhang, H. H. Sun, X. M. Liu, and J. X. Zhang, "Early-age characteristics of red mud-coal gangue cementitious material," *Journal of Hazardous Materials*, vol. 167, no. 1–3, pp. 927–932, 2009.
- [2] Z. Bian, X. Miao, S. Lei, S.-E. Chen, W. Wang, and S. Struthers, "The challenges of reusing mining and mineral-processing wastes," *Science*, vol. 337, no. 6095, pp. 702–703, 2012.
- [3] C. Li, J. H. Wan, H. H. Sun, and L. T. Li, "Investigation on the activation of coal gangue by a new compound method," *Journal of Hazardous Materials*, vol. 179, no. 1–3, pp. 515–520, 2010.
- [4] D. Landriault, "Backfill in underground mining," in *Underground Mining Methods: Engineering Fundamentals and International Case Studies*, W. A. Hustrulid and R. L. Bullock, Eds., pp. 601–614, Society for Mining, Metallurgy and Exploration, Littleton, Colo, USA, 2001.
- [5] D. Hewitt, S. Allard, and P. Radziszewski, "Pipe lining abrasion testing for paste backfill operations," *Minerals Engineering*, vol. 22, no. 12, pp. 1088–1090, 2009.
- [6] A. Kesimal, B. Ercikdi, and E. Yilmaz, "The effect of desliming by sedimentation on paste backfill performance," *Minerals Engineering*, vol. 16, no. 10, pp. 1009–1011, 2003.
- [7] E. Yilmaz, A. Kesimal, and B. Ercikdi, "Strength properties in varying cement dosages for paste backfill samples," in *Proceedings of the 10th International Conference on Tailings and Mine Waste, Balkema, Swets and Zeitlinger*, pp. 109–114, Lisse, The Netherlands, October 2003.
- [8] W. Guo, D. X. Li, J. H. Chen, and N. R. Yang, "Structure and pozzolanic activity of calcined coal gangue during the process of mechanical activation," *Journal Wuhan University of Technology, Materials Science Edition*, vol. 24, no. 2, pp. 326–329, 2009.
- [9] Z.-D. Cui and H.-H. Sun, "The preparation and properties of coal gangue based sialite paste-like backfill material," *Journal of the China Coal Society*, vol. 35, no. 6, pp. 896–899, 2010.
- [10] B. C. Zheng, H. Q. Zhou, and R. J. He, "Experimental research on coal gangue paste filling material," *Journal of Mining and Safety Engineering*, vol. 23, no. 4, pp. 460–463, 2006.
- [11] M. Fall, J. C. Célestin, M. Pokharel, and M. Touré, "A contribution to understanding the effects of curing temperature on the mechanical properties of mine cemented tailings backfill," *Engineering Geology*, vol. 114, no. 3–4, pp. 397–413, 2010.
- [12] B. Ercikdi, H. Baki, and M. Izki, "Effect of desliming of sulphide-rich mill tailings on the long-term strength of cemented paste backfill," *Journal of Environmental Management*, vol. 115, pp. 5–13, 2013.
- [13] F. Cihangir, B. Ercikdi, A. Kesimal, A. Turan, and H. Deveci, "Utilisation of alkali-activated blast furnace slag in paste backfill of high-sulphide mill tailings: effect of binder type and dosage," *Minerals Engineering*, vol. 30, pp. 33–43, 2012.
- [14] R. B. Polder, "Test methods for on site measurement of resistivity of concrete—a RILEM TC-154 technical recommendation," *Construction and Building Materials*, vol. 15, no. 2–3, pp. 125–131, 2001.
- [15] C. Andrade, "Model for prediction of reinforced concrete service life based on electrical resistivity," *Ibracon Structures and Materials Journal*, vol. 1, no. 1, 2005.
- [16] L. Z. Xiao and Z. J. Li, "Early-age hydration of fresh concrete monitored by non-contact electrical resistivity measurement," *Cement and Concrete Research*, vol. 38, no. 3, pp. 312–319, 2008.
- [17] W.-M. Hou, P.-K. Chang, and C.-L. Hwang, "A study on anticorrosion effect in high-performance concrete by the pozzolanic reaction of slag," *Cement and Concrete Research*, vol. 34, no. 4, pp. 615–622, 2004.
- [18] A. L. G. Gastaldini, G. C. Isaia, T. F. Hoppe, F. Missau, and A. P. Saciloto, "Influence of the use of rice husk ash on the electrical resistivity of concrete: a technical and economic feasibility study," *Construction and Building Materials*, vol. 23, no. 11, pp. 3411–3419, 2009.
- [19] A. Princigallo, K. Van Breugel, and G. Levita, "Influence of the aggregate on the electrical conductivity of Portland cement concretes," *Cement and Concrete Research*, vol. 33, no. 11, pp. 1755–1763, 2003.
- [20] X. S. Wei, L. Z. Xiao, and Z. J. Li, "Prediction of standard compressive strength of cement by the electrical resistivity measurement," *Construction and Building Materials*, vol. 31, pp. 341–346, 2012.
- [21] A. Lübeck, A. L. G. Gastaldini, D. S. Barin, and H. C. Siqueira, "Compressive strength and electrical properties of concrete with white Portland cement and blast-furnace slag," *Cement and Concrete Composites*, vol. 34, no. 3, pp. 392–399, 2012.
- [22] R. M. Ferreira and S. Jalali, "NDT measurements for the prediction of 28-day compressive strength," *NDT & E International*, vol. 43, no. 3, pp. 55–61, 2010.
- [23] A. A. Ramezani-pour, A. Pilvar, M. Mahdikhani, and F. Moodi, "Practical evaluation of relationship between concrete resistivity, water penetration, rapid chloride penetration and compressive strength," *Construction and Building Materials*, vol. 25, no. 5, pp. 2472–2479, 2011.
- [24] K. R. Gowers and S. G. Millard, "Measurement of concrete resistivity for assessment of corrosion severity of steel using Wenner technique," *ACI Materials Journal*, vol. 96, no. 5, pp. 536–541, 1999.
- [25] Y. Xi, D. D. Siemer, and B. E. Scheetz, "Strength development, hydration reaction and pore structure of autoclaved slag cement with added silica fume," *Cement and Concrete Research*, vol. 27, no. 1, pp. 75–82, 1997.
- [26] Q. Pu, L. H. Jiang, J. X. Xu, H. Q. Chu, Y. Xu, and Y. Zhang, "Evolution of pH and chemical composition of pore solution in carbonated concrete," *Construction and Building Materials*, vol. 28, no. 1, pp. 519–524, 2012.
- [27] H. W. Whittington, J. McCarter, and M. C. Forde, "The conduction of electricity through concrete," *Magazine of Concrete Research*, vol. 33, no. 114, pp. 48–60, 1981.
- [28] F. Hunkeler, "The resistivity of pore water solution—a decisive parameter of rebar corrosion and repair methods," *Construction and Building Materials*, vol. 10, no. 5, pp. 381–389, 1996.
- [29] H. Xing, X. Yang, C. Xu, and G. B. Ye, "Strength characteristics and mechanisms of salt-rich soil-cement," *Engineering Geology*, vol. 103, no. 1–2, pp. 33–38, 2009.

- [30] W. Zhu, C. L. Zhang, and A. C. F. Chiu, "Soil-water transfer mechanism for solidified dredged materials," *Journal of Geotechnical and Geoenvironmental Engineering*, vol. 133, no. 5, pp. 588–598, 2007.
- [31] C. Jaturapitakkul and R. Cheerarot, "Development of bottom ash as pozzolanic material," *Journal of Materials in Civil Engineering*, vol. 15, no. 1, pp. 48–53, 2003.
- [32] M. Fall, M. Benzaazoua, and S. Ouellet, "Effect of tailings properties on paste backfill performance," in *Proceedings of the 8th International Symposia on Mining with Backfill*, pp. 193–202, Beijing, China, 2004.
- [33] A. C. Raymond and C. H. Kenneth, "Mercury porosimetry of hardened cement pastes," *Cement and Concrete Research*, vol. 29, no. 6, pp. 933–943, 1999.
- [34] K. Aligizaki, *Pore Structure of Cement-Based Materials*, Taylor & Francis, New York, NY, USA, 2006.
- [35] D. N. Winslow and S. Diamond, "A mercury porosimetry study of the evolution of porosity in Portland Cement," *Journal of Materials*, vol. 5, no. 3, 1970.
- [36] E. J. Reardon, "Problems and approaches to the prediction of the chemical composition in cement/water systems," *Waste Management*, vol. 12, no. 2-3, pp. 221–239, 1992.
- [37] M. Westerholm, B. Lagerblad, J. Silfwerbrand, and E. Forssberg, "Influence of fine aggregate characteristics on the rheological properties of mortars," *Cement and Concrete Composites*, vol. 30, no. 4, pp. 274–282, 2008.
- [38] Ö. Özkan and I. Yüksel, "Studies on mortars containing waste bottle glass and industrial by-products," *Construction and Building Materials*, vol. 22, no. 6, pp. 1288–1298, 2008.
- [39] A. M. Neville, *Properties of Concrete*, Addison Wesley Longman, Harlow, UK, 1997.
- [40] P. Torkittikul and A. Chaipanich, "Utilization of ceramic waste as fine aggregate within Portland cement and fly ash concretes," *Cement and Concrete Composites*, vol. 32, no. 6, pp. 440–449, 2010.
- [41] C. C. Yang, S. W. Cho, and L. C. Wang, "The relationship between pore structure and chloride diffusivity from ponding test in cement-based materials," *Materials Chemistry and Physics*, vol. 100, no. 2-3, pp. 203–210, 2006.
- [42] D. A. Koleva, O. Copuroglu, K. van Breugel, G. Ye, and J. H. W. de Wit, "Electrical resistivity and microstructural properties of concrete materials in conditions of current flow," *Cement and Concrete Composites*, vol. 30, no. 8, pp. 731–744, 2008.
- [43] K. A. Snyder, X. Feng, B. D. Keen, and T. O. Mason, "Estimating the electrical conductivity of cement paste pore solutions from OH^- , K^+ and Na^+ concentrations," *Cement and Concrete Research*, vol. 33, no. 6, pp. 793–798, 2003.
- [44] A. L. Horvath, *Handbook of Aqueous Electrolyte Solutions*, John Wiley & Sons, New York, NY, USA, 1985.
- [45] K. Wu, H. S. Shi, G. Shutter, G. Ye, X. L. Guo, and Y. Gao, "Effect of aggregate on chloride diffusivity of cement-based composite materials," *Journal of the Chinese Ceramic Society*, vol. 41, no. 11, pp. 1514–1520, 2013.
- [46] D. N. Winslow, M. D. Cohen, D. P. Bentz, K. A. Snyder, and E. J. Garboczi, "Percolation and pore structure in mortars and concrete," *Cement and Concrete Research*, vol. 24, no. 1, pp. 25–37, 1994.

Research Article

Study on Monitoring Rock Burst through Drill Pipe Torque

Zhonghua Li, Liyuan Zhu, Wanlei Yin, and Yanfang Song

Academy of Rock Burst, Liaoning Technical University, Fuxin 123000, China

Correspondence should be addressed to Zhonghua Li; 13941824411@139.com

Received 13 October 2014; Revised 5 January 2015; Accepted 5 January 2015

Academic Editor: Shimin Liu

Copyright © 2015 Zhonghua Li et al. This is an open access article distributed under the Creative Commons Attribution License, which permits unrestricted use, distribution, and reproduction in any medium, provided the original work is properly cited.

This paper presents a new method to identify the danger of rock burst from the response of drill pipe torque during drilling process to overcome many defects of the conventional volume of drilled coal rubble method. It is based on the relationship of rock burst with coal stress and coal strength. Through theoretic analysis, the change mechanism of drill pipe torque and the relationship of drill pipe torque with coal stress, coal strength, and drilling speed are investigated. In light of the analysis, a new device for testing drill pipe torque is developed and a series of experiments is performed under different conditions; the results show that drill pipe torque linearly increases with the increase of coal stress and coal strength; the faster the drilling speed, the larger the drill pipe torque, and vice versa. When monitoring rock burst by drill pipe torque method, the index of rock burst is regarded as a function in which coal stress index and coal strength index are principal variables. The results are important for the forecast of rock burst in coal mine.

1. Introduction

Nowadays, the threat of rock burst is increasingly intensifying with the increase of mining depth and intensity [1–4]. As a result, research on the prediction of rock burst is extremely urgent.

At present, the methods applied to the monitoring of rock burst can be classified into two classes [5–11]: one is geophysical method and the other is geomechanical method. Geophysical methods are circumstantial and use changes in the following physical parameters due to the stress increase in rocks near mine working: acoustic emission, the magnitude of “induced electromagnetic field,” and the value of rock self-potential. However, they are not very mature for their hard equipment maintenance management, high cost, hard data analyzing, and high requirements of technical conditions. At the present time there are no geophysical methods which can completely satisfy the requirements of minimal duration and maximal safety of prediction works [12]. At present the standard geomechanical method of estimating rock burst hazard in coal mines is based on measurement of a volume of “drilled coal rubble” [13, 14]. Drilling of a borehole leads to excitation of an intensive process of cracking in the zone of its influence. The volume of this zone depends on the hole diameter, the drilling rate, and especially the stress level. If the two first parameters remain constant, the volume of drilled

coal rubble formed due to drilling reflects an increase of the third. This method is widely used and already has a set of mature technologies. However, there are also different defects associated with this method; for example, it is not suitable for soft weak coal layer and coal stress crush exceeds the limit; on the other hand, monitoring rock burst by drilled coal rubble method is discontinuous, it is easy to cause loss of information, and both the fly out and residue of drilled coal rubble in the process of drilling can cause drilled coal rubble is not collected incompletely, thereby leading to measurement errors; moreover, the volume of drilled coal rubble has no correlation with coal strength, unable to determine the influence of coal strength on rock burst.

Hence, in this paper, in light of theoretical analysis, the self-designed device is used to test drill pipe torque under different coal stress, coal strength, and drilling speed, respectively, and the method to monitor rock burst by drill pipe torque is presented. The research results provide a new idea for rock burst prediction and have important significance for safety production in coal mine.

2. Drill Pipe Torque Analysis

When drilling in coal seam by electric-drill and twist drill pipe, the torque on drill pipe is mainly acted by electric-drill

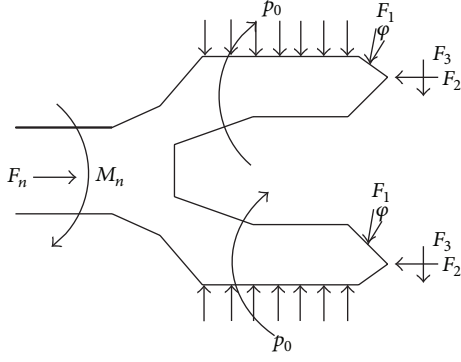


FIGURE 1: External forces of bit.

(M_0 , constant under rated power), bit (M_n), and drilled coal rubble (M_z) [15, 16]. “Drill pipe torque” in this paper refers to the torque in the junction of drill pipe tail end and drilling rig; it is equal to, in numeral, resultant force of M_n and M_z . Then

$$M_p = M_n + M_z. \quad (1)$$

2.1. Calculation of Torque Applied by Bit. During coal cutting operation, the forces on cutting tool include propulsion F_n and cutting force F_m acted by drill pipe, anti-cutting resistance F_1 , anti-incisiveness resistance F_2 acted by coal rock, and frictional resistance F_3 . In addition, there are also pressure p_0 and friction torque M_1 acted by hole wall on the side surface of bit, as is shown in Figure 1.

F_1 is corresponding with the force of coal shear body acted by tool specified in [17] as follows:

$$F_1 = P_1 = \frac{cbh \cos \phi}{\cos(\gamma + \phi + \psi) \cos \psi}, \quad (2)$$

where h is cutting depth, b is the width of cutting edge, c is cohesion, γ is negative anteversion angle of cutting tool, ϕ is internal friction angle, $\phi = \arctan \mu$ (μ is friction coefficient between clearance face and coal face), and ψ is the angle between cutting surface and shear plane. F_2 is corresponding with the normal pressure acting on the coal by cutting edge. Then

$$F_2 = P_c = \sigma_b S', \quad (3)$$

where σ_b is coal compressive strength and S' is the contacting area of cutting tool with coal. Now let the friction coefficient between cutting edge and coal be μ_1 ; then $F_3 = \mu_1 F_2$. Let the friction coefficient between coal on hole wall and surface of bit be μ_2 ; then

$$M_1 = \mu_2 \int_s p_0 \cdot R ds = \mu_2 p_0 \cdot R s, \quad (4)$$

where R is radius and s is the contacting area of one side surface of tool with hole wall. Since the bit contains two tools, the torque balance equation of the bit is represented by

$$M_n = 2F_1 \cos(\gamma + \phi) \cdot R' + 2\mu_1 F_2 \cdot R' + 2M_1, \quad (5)$$

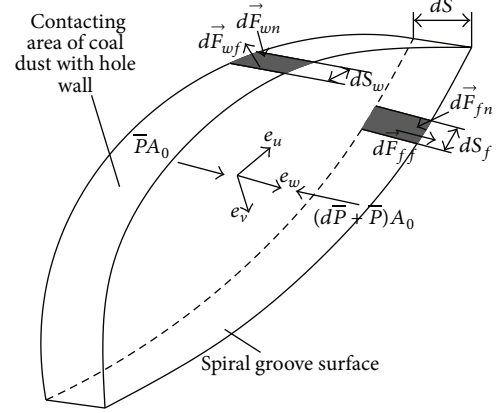


FIGURE 2: Mechanical mode of coal dust element.

where R' is the distance between equivalent concentrated force and medial axis of bit. Then, by substituting (2), (3), and (4) into (5), it is found that

$$M_n = 2 \frac{cbh \cos \phi}{\cos(\gamma + \phi + \psi) \cos \psi} \cos(\gamma + \phi) \cdot R' + 2\mu_1 \sigma_b S' \cdot R' + 2\mu_2 p_0 \cdot R s. \quad (6)$$

2.2. Calculation of Chip Removal Torque. Mechanical analysis of coal dust element drill pipe spiral groove is carried out, gravity and inertia force are neglected, and the external forces of coal dust are generalized as in Figure 2 [15, 18–20]. In Figure 2, dS_f denotes the unit width of the interface between coal dust element and the junk slot, dS denotes the thickness of coal dust in the direction of w , $d\vec{F}_{fn}$ and $d\vec{F}_{ff}$ denote the normal force and friction, respectively, which are acted by drill pipe spiral groove, and $d\vec{F}_{wn}$, $d\vec{F}_{wf}$, and $\bar{P}A_0$ denote the normal force, friction, and chip removal force, respectively, which are acted by hole wall on the outside surface of coal dust element.

During coal dust removing operation, the interaction of friction acted by coal wall and normal chip removal force acted by spiral groove results in a distribution of lateral pressure L on coal dust [17, 18, 20]. Then

$$d\vec{F}_{fn} = L dS_f dS \cdot \vec{e}_{fn}, \quad (7)$$

$$d\vec{F}_{ff} = \mu_3 |d\vec{F}_{fn}| \cdot \vec{e}_{ff} = \mu_3 L dS_f dS \cdot \vec{e}_{ff},$$

$$d\vec{F}_{wf} = \mu_4 \cdot d\vec{F}_{wn} = \mu_4 (L dS_w \cdot dS \cdot \vec{e}_\theta + p_0 dS_w \cdot dS \cdot \vec{e}_\theta), \quad (8)$$

where μ_3 is friction coefficient between coal dust and spiral groove, \vec{e}_{fn} is unit vector in the direction of $d\vec{F}_{fn}$, and \vec{e}_{ff} is unit vector in the direction of $d\vec{F}_{ff}$.

The balance equation of coal dust in the direction of u is [20]

$$L \Delta v dS - (dL + L) \Delta v dS + d\vec{F}_{wf} \cdot \vec{e}_u = 0, \quad (9)$$

where Δv is the difference between coal wall and profile of bottom spiral groove in the direction of v ; it is a function about u .

Then, by substituting (8) into (9), it is found that

$$L(u) = (k\bar{P} + p_0) \alpha e^{\mu_4 f(u)} - p_0, \quad (10)$$

where p_0 is the normal pressure acting on drill pipe by coal around borehole, the change block of u coordinate is $[u_a, u_b]$, which depends on the geometric parameters of drill pipe, μ_4 is the friction coefficient between clearance face and coal face, and k is a coefficient which depends on geometric parameters of drill pipe and drilling speed.

The balance equation of coal dust along the axial line of drill pipe is [20]

$$\begin{aligned} \bar{P} A_0 (\vec{e}_w \cdot \vec{k}) - (d\bar{P} + \bar{P}) A_0 (\vec{e}_w \cdot \vec{k}) \\ + \int d\vec{F}_{ff} \cdot \vec{k} + \int d\vec{F}_{fn} \cdot \vec{k} = 0. \end{aligned} \quad (11)$$

Then, by substituting (7) and (10) into (11), it is found that

$$\begin{aligned} \bar{P} = e^{\int_0^{z_c} (kAE/A_0)B(z_c)d\eta} \\ \cdot \int_0^{z_c} p_0(z_c) \frac{E}{A_0} [AB(z_c) - C(z_c)] e^{-\int_0^{z_c} (kAE/A_0)B(z_c)d\eta} d\eta, \end{aligned} \quad (12)$$

where

$$\begin{aligned} B(z_c) &= \int e^{\mu_4 f(u)} (\vec{e}_{fn} \cdot \vec{k}) dS_f + \mu_3 \int e^{\mu_4 f(u)} (\vec{e}_{ff} \cdot \vec{k}) dS_f; \\ C(z_c) &= \int (\vec{e}_{fn} \cdot \vec{k}) dS_f + \mu_3 \int (\vec{e}_{ff} \cdot \vec{k}) dS_f; \\ E &= \frac{1}{(\vec{e}_w \cdot \vec{k}) \cos \beta_h}. \end{aligned} \quad (13)$$

Let drilling depth be z_d ; then the removal force along the axial line of drill pipe is [18]

$$\vec{F}_z(z_d) = 2\bar{P}(z_d) A_0 \cdot \vec{e}_w \cdot \vec{k}. \quad (14)$$

By substituting (12) into (14) and expanding and rearranging,

$$\begin{aligned} F_z(z_d) &= 2A_0 \cos \beta_h e^{\int_0^{z_d} (k\alpha\delta/A_0)\beta(z_c)d\eta} \\ &\cdot \int_0^{z_d} p_0(z_c) \frac{\gamma}{A_0} [\alpha\beta(z_c) - \chi(z_c)] \\ &\cdot e^{-\int_0^{z_d} (k\alpha\delta/A_0)\beta(z_c)d\eta} dz_c. \end{aligned} \quad (15)$$

During drilling operation, the equation of chip removal torque is

$$M_z(z_d) = (\vec{r}_c(z_d) \times \vec{F}_w(z_d)) \cdot \vec{k} + \int_0^{z_d} dM_w(z_c), \quad (16)$$

where \vec{r}_c denotes the position vector at the center of coal dust element; $\vec{r}_c = R' \vec{e}_r$.

Now, by substituting (15) into (16) and expanding and rearranging,

$$M_z(z_d) = \bar{P}(z_d) A_0 \lambda + \psi \int_0^{z_d} p_0(z_c) \gamma dz_c + \psi \int_0^{z_d} k\bar{P} \gamma dz_c, \quad (17)$$

where $\lambda(z_d) = A_0 R' \sin \beta_h$; $\psi = \mu_4 AR / \cos \beta_h$; $\gamma(z_c) = \int e^{\mu_4 f(u)} dS_w$.

2.3. Calculation of Drill Pipe Torque. Then, by substituting (6) and (17) into (1), it can be simplified as

$$\begin{aligned} M_p &= A_1 b R' h + \sigma_b A_2 + p_0 A_3 + \bar{P}(z_d) K(z_d) \\ &+ G \int_0^{z_d} p_0(z_c) H dz_c + G \int_0^{z_d} k\bar{P} H dz_c, \end{aligned} \quad (18)$$

where $A_1 = 2(c \cos \phi / \cos(\gamma + \phi + \varphi + \psi) \cos \psi) \cos(\gamma + \varphi)$, $A_2 = 2\mu_1 S' R'$, and $A_3 = 2\mu_2 R s_2$. \bar{P} increases with the increase of coal stress, A_1 increases with the increase of coal strength, both b and h increase with the increase of drilling speed, S' , A_2 , and A_3 all have something to do with geometric parameters of bit, and K , G , and H all have something to do with geometric parameters of drill pipe.

3. Principle of Monitoring Rock Burst by Drill Pipe Torque Method

A degree of rock burst is inevitably associated both with the stress level near mine working and with the strength of coal. There is precursor information of stress concentration (high stress) and mutation (high stress mutation) in local area before rock burst [21, 22]. Therefore, the stress is reliable for monitoring rock burst; monitoring means such as AE method and volume of drilled coal rubble method reflect coal stress state through certain physical quantity and then judge rock burst risk based on stress trend. Coal strength is an important mechanical character parameter and also a significant indicator of coal seam burst tendency judgment. Coal strength and its variation have a great influence on rock burst hazard. The change of stress in the laneway periphery with the increase of mining depth is different depending on the compressive strength of coal rock mass; if covered depth exceeds the critical depth, coal mass will meet various degrees of violation; it provides condition for occurrence of rock burst. The larger the compressive strength and the sustained forces before failure, the larger the elastic energy accumulated in coal mass; then it is much easier to induce rock burst.

Based on the relationship of rock burst with coal stress and coal strength, monitoring rock burst by drill pipe torque method is designed. It can be known from the calculation results of Section 2 that there is a positive correlation of drill pipe torque and coal stress and coal strength in the course of drilling, if the drilling equipment and drilling speed are constant. Thus, when drilling with constant speed, coal stress and coal strength can be reflected by drill pipe torque, and

TABLE 1: Loading and drilling conditions of the samples.

Sample number	Loading pressure/kN	Coal stress/MPa	Coal strength/MPa	Drilling speed/m/min	Drilling time/s	Drilling depth/mm
1	1500	6.0	15	0.22	120	440
2	2000	8.0	15	0.22	120	440
3	2500	10.0	15	0.22	120	440
4	3000	12.0	15	0.22	120	440
5	3500	14.0	15	0.22	120	440
6	2500	10.0	7	0.4	60	400
7	2500	10.0	10	0.4	60	400
8	2500	10.0	15	0.4	60	400
9	2500	10.0	19	0.4	60	400
10	2500	10.0	24	0.4	60	400
11	2500	10.0	15	0.15	192	480
12	2500	10.0	15	0.2	144	480
13	2500	10.0	15	0.3	96	480

then quantitative relation of drill pipe torque with coal stress and coal strength is established and rock burst hazard is judged; the goal of forecasting rock burst is achieved.

4. Drill Pipe Torque Experiments

4.1. Experiments Device. The test system consists of drilling equipment, test device of torque, data acquisition and recording system, and other assistive devices (Figure 3). Drilling equipment includes 1.2kw hand-held electric coal drill, ϕ 42 hollow twist drill rods, and bit; test device of torque is the central unit of the test system, which is independently developed with a torque sensor mounted at the output terminal of electric coal drill. It can be continuously used to measure a real-time torque. YJZ-8/16 type digital strain gauge is chosen as the data acquisition and recording device, and results can be displayed on computers.

4.2. Experiments Scheme. Large size coal specimens collected from scene were put into iron cases which have dimension of 500 mm \times 500 mm \times 500 mm and thickness of 30 mm, and the surrounding areas were packed with cement mortar. The backs of specimens were pasted on the inner lining of the iron cases. Thus, the distortion in this direction was limited under force. The space exists between the left and right sides of the samples and iron cases were packed with S-588 sealing colloid. It has little effect on lateral deformation of coal under force, since S-588 colloid is elastic after solidifying. This allowed the acting form of the samples to be similar to that of coal body ahead of mining face; then coal stress ahead of mining face was simulated through pressuring the samples vertically.

13 specimens were made in all; among them, samples 1~5 were used to study the relationship between drill pipe torque and coal stress; in this experiment, drilled coal rubble was collected while drilling and was weighed after drilling; samples 6~10 were used to study the relationship between coal strength and drill pipe torque; samples 11~13 were used

to study the influence of drilling speed on drill pipe torque. The loading and drilling conditions of the samples are listed in Table 1.

When testing, the torque sensor was mounted on the junction of drill pipe tail end and drilling rig; wires were leaded out by rotary joint connected to the data acquisition device connected to computer. To keep the electric-drill running horizontally and uniformly in drilling process, the electric-drill was mounted on the self-designed support with scales on its horizontal guide; it controlled drilling speed constant combined with timer during the drilling operation. In order to make the stress of the specimens uniform, a 500 mm \times 500 mm \times 15 mm plate was put on the upper surface of the specimen, and a cushion block was put on the plate. The data acquisition and recording system was booted to acquire and record test data synchronously and automatically, testing machine was booted to pressure the specimens according to the test conditions, and electric-drill was booted to drill at the reference speed combined with stopwatch. When the procedure finished, data acquisition was stopped and then the testing machine was turned off.

4.3. Analysis of Experiments Results

4.3.1. Relationship between Drill Pipe Torque and Coal Stress. The change curve of drill pipe under different coal stress during drilling operating is obtained from the results of the recording (Figure 4). As it can be seen in Figure 4, under the same drilling speed, drill pipe torque under different coal stress fluctuates in a certain magnitude due to factors such as cracks and shake, but analyzing the entire tendency, the larger the coal stress, the larger the drill pipe torque.

The practice of prediction of mine dynamic disaster shows that coal stress can be reflected by volume of drilled coal rubble. When coal stress increases, the risk of rock burst increases and the volume of drilled coal rubble also increased. In order to verify that the magnitude and variation regularity of the coal stress can be reflected by drill pipe

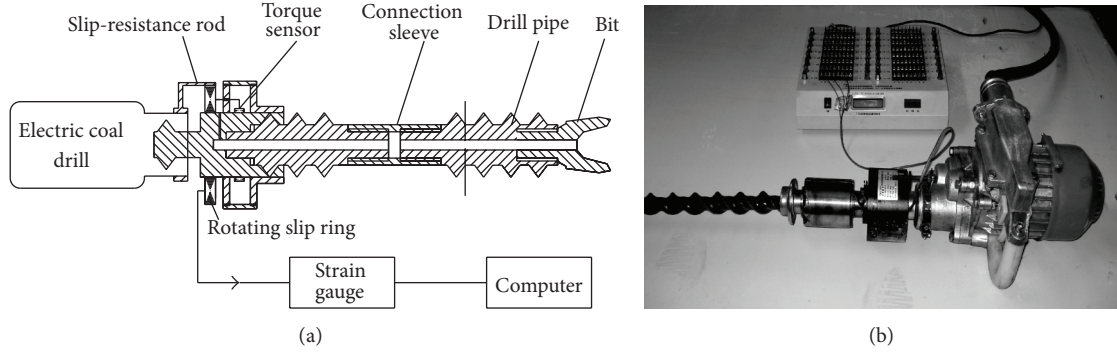


FIGURE 3: Drill pipe torque test equipment.

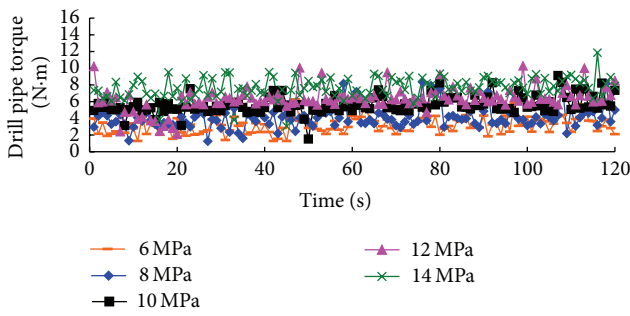


FIGURE 4: History time curve of drill pipe torque under different coal stress.

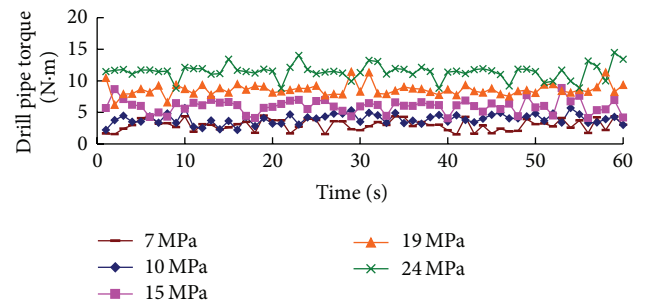


FIGURE 6: Time history curve of drill pipe torque under different coal strength.

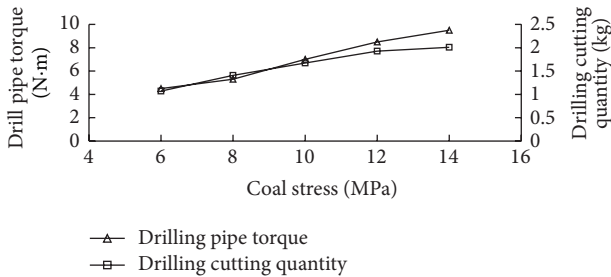


FIGURE 5: The comparison of drill pipe torque, volume of drilled coal rubble, and coal stress.

torque further, the relationship of coal stress with volume of drilled coal rubble and drill pipe torque was comparatively analyzed (Figure 5). As it can be seen in Figure 5, drill pipe torque had a similar changing trend to the volume of drilled coal rubble. We also fit the curve and gain the fitting relation of coal stress with volume of drilled coal rubble and drill pipe torque:

$$\begin{aligned} M_p &= 0.66\sigma + 0.36, \quad (R^2 = 0.9882), \\ G_0 &= 0.1199\sigma + 0.4195, \quad (R^2 = 0.9648), \end{aligned} \quad (19)$$

where M_p is drill pipe torque and σ is coal stress; G_0 is volume of drilled coal rubble.

Thus, it can be seen that both volume of drilled coal rubble and drill pipe torque linearly increase with the increase of

coal stress, and they have good correspondences. It indicates that drill pipe torque can reflect the magnitude and variation regularity of the coal stress and then monitor rock burst.

4.3.2. Relationship between Drill Pipe Torque and Coal Strength. Outcome of drill pipe torque under different coal strength is presented in Figure 6. As it can be seen in Figure 6, coal strength has significant effect on drill pipe torque though with a little fluctuation in it. Under the same coal stress and drilling speed, the larger the coal strength, the larger the drill pipe torque.

During the drilling process, when coal strength is 7 MPa, average value of drill pipe torque is 3.28 N·m; when coal strength is 10 MPa, average value of drill pipe torque is 4.30 N·m; when coal strength is 15 MPa, average value of drill pipe torque is 6.75 N·m; when coal strength is 19 MPa, average value of drill pipe torque is 7.25 N·m; when coal strength is 24 MPa, average value of drill pipe torque is 10.86 N·m. Outcome of regression analysis is presented in Figure 7. As it can be seen in Figure 7, drill pipe torque linearly increases with the increase of coal strength; they have good interrelations; the curve relation of them is

$$M_p = 0.4306\sigma_c + 0.0822, \quad (R^2 = 0.9763), \quad (20)$$

where σ_c is coal strength.

4.3.3. Influence of Drilling Speed on Drill Pipe Torque. Taking time as the abscissa axis and drill pipe torque as the ordinate

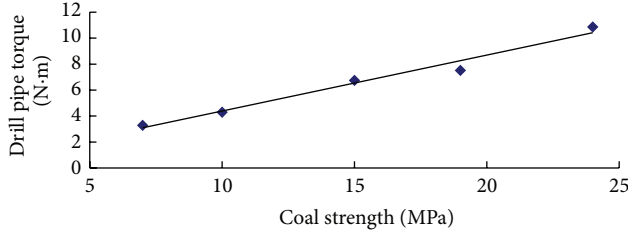


FIGURE 7: The curve relation between drill pipe torque and coal strength.

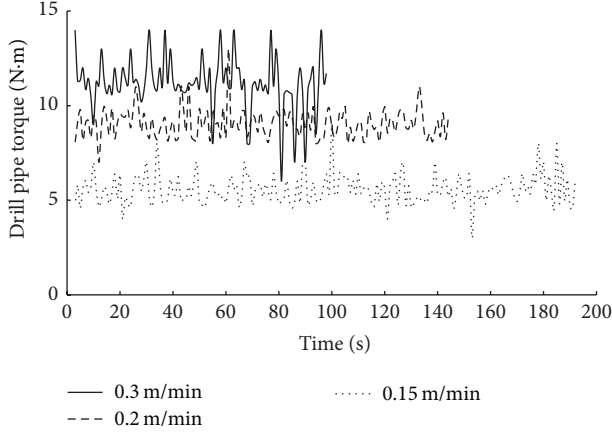


FIGURE 8: History time curve of drill pipe torque under different drilling speed.

axis, the curve relation between drill pipe torque and drilling time under different drilling speed was obtained (Figure 8).

As it can be seen in Figure 8, for the same material and pressure, drill pipe torques tested under different drilling speed have a great difference: when drilling speed is 0.15 m/min, average value of drill pipe torque is 5.21 N·m; when drilling speed is 0.20 m/min, average value of drill pipe torque is 8.44 N·m; when drilling speed is 0.30 m/min, average value of drill pipe torque is 10.16 N·m.

Therefore, drilling speed should be strictly controlled and should always keep pace while monitoring rock burst by drill pipe torque method.

5. Monitoring Rock Burst by Drill Pipe Torque Method

In order to determine the possibility of rock burst occurrence quantitatively, the paper regards the index of rock burst I as a function in which coal stress index I_s and coal strength index I_c are principal variables; namely, the index of rock burst can be expressed as

$$I = f(I_s, I_c), \quad (21)$$

where I_s is the membership degree of judging the danger of rock burst by coal stress and I_c is the membership degree of judging the danger of rock burst by coal strength.

5.1. Determination of Coal Stress Index I_s . As the high stress concentration and mutation are essential conditions of rock burst, coal stress varies in a greater range for a period of time before rock burst occurrence, and the studies in previous paper have proved that there exists a close relationship between coal stress and drill pipe torque. Therefore, coal changes can be reflected through drill pipe torque and then forecast rock burst.

The procedure of determining coal stress index I_s is carried out as follows: when the drill pipe torque at a certain depth reached or exceeded the forecasting and warning value M_0 (M_0 depends on conditions of workface), taking the moment as starting point, work out increment amplitude of drill pipe torque in interval time and then determine coal stress index I_s by increment amplitude of drill pipe torque. The relationship between coal stress index I_s and increment amplitude of drill pipe torque is

$$\Delta M = \frac{M(t_n) - M(t_{n-1})}{M(t_{n-1})}, \quad (22)$$

$$I_s = \begin{cases} \frac{\Delta M}{\gamma_0}, & (0 < \Delta M(t_n) < \gamma_0), \\ 1, & (\Delta M(t_n) \geq \gamma_0), \end{cases}$$

where $t_n = nt_0$, $M(t_n)$ is the drill pipe torque at the moment of t_n , γ_0 is the critical value of increment amplitude of drill pipe torque (the value of γ_0 can be modified according to field condition), and n is integer.

5.2. Determination of Coal Strength Index I_c . As coal strength is a major factor of rock burst, it is reasonable to judge the probability of rock burst by coal strength; the judgment formula is

$$C_0 = \begin{cases} \frac{\sigma}{\sigma_0}, & (\sigma < \sigma_0), \\ 1, & (\sigma \geq \sigma_0), \end{cases} \quad (23)$$

where σ is strength of bored coal and σ_0 is strength critical value of rock burst forecast. In terms of the expression for relationship between drill pipe torque and coal strength in Section 4.3.2, different coal strengths correspond to different drill pipe torques; it is then possible to get coal strength index by the simplified equation (23):

$$I_c = \begin{cases} \frac{M}{M_0}, & (M < M_0), \\ 1, & (M \geq M_0), \end{cases} \quad (24)$$

where M is drill pipe torque measured by drilling (average value) and M_0 is forecast critical value for judging coal stress by drill pipe torque. When the drill pipe torque is greater than or equal to critical value, the probability of rock burst occurrence is considered to be 1; when the drill pipe torque is less than critical value, coal strength index I_c is a linear function which takes the reciprocal of drill pipe torque forecast critical value as slope and drill pipe torque as variable.

TABLE 2: The possibility of evaluation index of the rock burst occurrence evaluated by the drill pipe torque method.

Possibility of rock burst occurrence	Impossible	Possible	Probably	Extremely large possibility
Evaluation indicator I	0~0.4	0.4~0.6	0.6~0.8	0.8~1.0

5.3. *Determination of Rock Burst Index I.* After coal stress index I_s and coal strength index I_c are determined, index I that monitors rock burst by drill pipe torque method can be expressed as

$$I = aI_s + bI_c, \quad (25)$$

where a and b are, respectively, the weights for I_s and I_c in prediction of rock burst, different mining condition endows different weights for a , b , and the sum of a , b is 1. Based on the value of I rock burst index can be divided into 4 classes of impossible, possible, probably, and extremely large possibility; they are relative to the possibility of the impact rock pressure occurrence, as shown in Table 2. Due to the high difference on geological, mining conditions and complicated reasons of rock burst, the evaluation indexes put forward in this paper need to be further modified and perfected.

6. Conclusion

In this paper, the authors make a test research with the independently developed system on characteristics of drill pipe torque under different coal stress, coal strength, and drilling speed on the basis of theoretical analysis and illustrate how to monitor rock burst through drill pipe torque. The major conclusions are as follows.

- (1) Through theoretic analysis, the formula for calculating drill pipe torque was derived, the conclusion that drill pipe torque can reflect coal stress and coal strength and is influenced by drilling speed was drawn, and the principle of monitoring rock burst by drill pipe torque was revealed.
- (2) The results of experiments show that drill pipe torque linearly increases with the increase of coal stress and coal strength; the faster the drilling speed, the larger the drill pipe torque, and vice versa.
- (3) While monitoring rock burst by drill pipe torque method, coal stress factor and coal strength factor are comprehensively considered; drill pipe torque method is simple and convenient, can realize real-time and continuous monitoring, and can overcome the defects of volume of drilled coal rubble method. The indicator of drill pipe torque can be tested in the same hole with indicators such as drilled coal rubble and can reach the goal of multiobjective prediction; it is a promising method of rock burst prediction.

Drill pipe torque method is a new rock burst prediction method; present studies on it are not satisfactory; this paper investigates it only from theoretical and laboratory experiment aspects. Future work should involve locale experiments to determine its critical index; furthermore, more complex experimental systems should be investigated.

Conflict of Interests

The authors declare that there is no conflict of interests regarding the publication of this paper.

Acknowledgments

The authors would like to acknowledge the financial support of National Natural Science Foundation of China (Grant no. 51174107) and National Program on Key Basic Research Project (Grant no. 2010CB0226803).

References

- [1] T. Li, M. F. Cai, and M. Cai, "A review of mining-induced seismicity in China," *International Journal of Rock Mechanics and Mining Sciences*, vol. 44, no. 8, pp. 1149–1171, 2007.
- [2] V. S. Kuksenko, I. E. Inzhevatin, B. T. Manzhikov, S. A. Stanchits, N. G. Tomilin, and D. I. Frolov, "Physical and methodological principles of rock burst prediction," *Soviet Mining*, vol. 23, no. 1, pp. 6–17, 1987.
- [3] Z. T. Bieniawski, H. G. Denkhous, and U. W. Vogler, "Failure of fractured rock," *International Journal of Rock Mechanics and Mining Sciences and*, vol. 6, no. 3, pp. 323–341, 1969.
- [4] N. G. W. Cook, "A note on rockbursts considered as a problem of stability," *The Southern African Institute of Mining and Metallurgy*, vol. 65, pp. 437–446, 1965.
- [5] J. P. Bardet, "Finite element analysis of rockburst as surface instability," *Computers and Geotechnics*, vol. 8, no. 3, pp. 177–193, 1989.
- [6] H. Wang and M. Ge, "Acoustic emission/microseismic source location analysis for a limestone mine exhibiting high horizontal stresses," *International Journal of Rock Mechanics and Mining Sciences*, vol. 45, no. 5, pp. 720–728, 2008.
- [7] M. Ge, "Efficient mine microseismic monitoring," *International Journal of Coal Geology*, vol. 64, no. 1-2, pp. 44–56, 2005.
- [8] P. R. Young, *Rock Bursts Andseismicity in Mines*, Balkema, Rotterdam, The Netherlands, 1993.
- [9] A. Leśniak and Z. Isakqw, "Space-time clustering of seismic events and hazard assessment in the Zabrze-Bielszowice coal mine, Poland," *International Journal of Rock Mechanics and Mining Sciences*, vol. 46, no. 5, pp. 918–928, 2009.
- [10] V. A. Mansurov, "Prediction of rockbursts by analysis of induced seismicity data," *International Journal of Rock Mechanics and Mining Sciences*, vol. 38, no. 6, pp. 893–901, 2001.
- [11] J.-A. Wang and H. D. Park, "Comprehensive prediction of rockburst based on analysis of strain energy in rocks," *Tunnelling and Underground Space Technology*, vol. 16, no. 1, pp. 49–57, 2001.
- [12] V. Frid, "Rockburst hazard forecast by electromagnetic radiation excited by rock fracture," *Rock Mechanics and Rock Engineering*, vol. 30, no. 4, pp. 229–236, 1997.
- [13] B. J. Zhao and M. T. Zhang, "The study and application of the drilling method," *Journal of Fuxin Mining Institute*, vol. S1, pp. 13–28, 1985 (Chinese).

- [14] C. G. Wen and Y. X. Wang, "Discussion of value of drilling cuttings weight index," *Journal of Mining Safety and Environment Protection*, vol. 3, p. 32, 1998.
- [15] J. C. Mellinger, O. B. Ozdoganlar, R. E. Decor, and S. G. Kapoor, "Modeling chip-evacuation forces and prediction of chip-clogging in drilling," *Journal of Manufacturing Science and Engineering*, vol. 124, no. 3, pp. 605–614, 2002.
- [16] J. C. Mellinger, O. B. Ozdoganlar, R. E. DeVor, and S. G. Kapoor, "Modeling chip-evacuation forces in drilling for various flute geometries," *Journal of Manufacturing Science and Engineering, Transactions of the ASME*, vol. 125, no. 3, pp. 405–415, 2003.
- [17] F. Zhao, *Theoretical and experimental research on rock fragmentation under coupling dynamic and static loads [Ph.D. thesis]*, Central South University, 2004 (Chinese).
- [18] Q. Yu and G.-H. Hu, "Development of a helical coordinate system and its application to analysis of polymer flow in screw extruders part I. The balance equations in a helical coordinate system," *Journal of Non-Newtonian Fluid Mechanics*, vol. 69, no. 2-3, pp. 155–167, 1997.
- [19] K. Ren and J. Ni, "Analyses of drill flute and cutting angles," *The International Journal of Advanced Manufacturing Technology*, vol. 15, no. 8, pp. 546–553, 1999.
- [20] X. Wan, *Study on new drilling force model of vibration drilling and vibration drilling with invariable parameter and variable parameter [Ph.D. thesis]*, Jilin University, 2004, (Chinese).
- [21] B. Amadei and O. Stephansson, *Rock Stress and Its Measurement*, Chapman & Hall, London, UK, 1997.
- [22] J. Franklin, "Suggested methods for pressure monitoring using hydraulic cells," *International Journal of Rock Mechanics and Mining Sciences & Geomechanics Abstracts*, vol. 17, no. 2, pp. 117–127, 1980.

Research Article

Warning Method of Coal Bursting Failure Danger by Electromagnetic Radiation

Guang-Jian Liu, Cai-Ping Lu, Hong-Yu Wang, Peng-Fei Liu, and Yang Liu

School of Mining Engineering, Key Laboratory of Deep Coal Resource Mining (Ministry of Education), China University of Mining and Technology, Xuzhou, Jiangsu 221116, China

Correspondence should be addressed to Cai-Ping Lu; cplucumt@126.com

Received 3 November 2014; Accepted 24 November 2014

Academic Editor: Shimin Liu

Copyright © 2015 Guang-Jian Liu et al. This is an open access article distributed under the Creative Commons Attribution License, which permits unrestricted use, distribution, and reproduction in any medium, provided the original work is properly cited.

Electromagnetic radiation (EMR) can reflect the stress state and deformation level of coal, yet its warning indexes correlated with coal properties and roof caving is poorly understood. The laboratory observations of EMR effects of coal samples bursting failure and in situ investigations in the process of roof caving are presented in this paper. EMR peak with increasing stress is discussed when the failure of coal samples happens, which provides an explanation to EMR signals positively correlated well with the stress loaded. The linearly increasing relation is also found between EMR intensity and the uniaxial compressive strength, and EMR maximum amplitudes and pulses behave a logarithmic accretion tendency with bursting energy indexes of coal. By in situ investigations, it is well found that EMR amplitude can effectively warn coal deformation and failure based on the critical value 120 mV proposed from experiments.

1. Introduction

Coal/rock undergoing deformation and failure emits many forms of energy, among which is electromagnetic radiation (EMR). The electromagnetic activity that is detected during the deformation and before failure of inhomogeneous materials, such as rocks, is of particular interest. This EMR is detectable not only in the laboratory but also in geophysical scale. Cohen first proposed the term EMR in the 1920 [1]. The EMR phenomenon was first observed to occur by researchers in the USSR prior to earthquake events, and EMR from material fractured under stress was first investigated in laboratory by Stepanov in 1933 [2]. Hanson and Rowell found EMR phenomenon during rock failure [3]. Studies on EMR produced by the deformation and failure of coal and other low strength rocks in coal-bearing strata started from 1990s. EMR from rocks and other brittle materials has been extensively investigated.

Presently, the physical mechanism of EMR is still unknown. Several attempts to explain the EMR mechanism are made including the acceleration and deceleration of dislocations and the movement of charged crack sides and electrical breakdown. Unfortunately, none of these was able to explain the properties of the detected EMR [4–6].

Numerous investigations show a relationship between applied stress and EMR emitted from rock material [7–9]. Therefore, the geogenic EMR, thus, merits its classification as an important sign of rockburst triggered by stress concentration. Many observations of electromagnetic anomalies associated with coal-rock mass deformation or bursting failure have been reported. For example, Muto et al. believed that the frictional discharges might be one of the sources of the seismoelectromagnetic emission based on an experiment simulating the motion of an asperity on a fault surface [10]. Rabinovitch et al. presented a viable model of EMR, according to which EMR was emitted by an oscillating dipole created by ions moving collectively as a surface wave on both sides of rock crack [11]. Morgounov and Malzev interpreted the data of electromagnetic precursors in terms of a multiple fracture model and discussed the possibility of constructing a physical model for the generation of a quasistable field and EMR on the basis of the deformation process [12]. Wang et al. established the coal-rock EMR electromechanical coupling model and conducted a series of experiments on coal-rock samples of lower strength to study the characteristics of ultralow frequency EMR signals, which verified that EMR were well correlated with stress in coal mass [13–15]. Liu

and He proposed an EMR model for predicting outbursts based on an experimental system composed of a differential pressure gauge and an electromagnetic field generator [16]. Jiang et al. investigated EMR of roadways to determine the zones of intensive roof deformation [17, 18]. Lichtenberger found that orientations and magnitudes of the horizontal principal stresses derived from the measurements of EMR correlated well with conventional stress measurements [19]. Mallik et al. presented an application of EMR technique for deciphering the directions of principal horizontal stress and identifying active fracture planes [20]. Carcione et al. found the shape of the grains in the rock has a significant influence on the EMR properties [21]. Frid proposed a new modern method of rock and gas outburst forecast, relying on registration of EMR caused by rock fracture, and employed an EMR method associated with rock fracture to study water infusion in rockburst-prone coal strata [22, 23]. Jiang et al. monitored the roadway nearby fault stability by the means of EMR instrument and fully obtained the coal and rock mass internal energy accumulation and release rules [17, 18]. He et al. described EMR method as a preliminary effort to provide a tool capable of predicting the stress concentration condition in coal-rock [24]. Nardi and Caputo believed experimentally that EMR that were possibly caused by fracturing may also be used to monitor the stress conditions of rocks for geological purposes [25]. Lu et al. proposed to warn gas outburst hazard induced by coal and rock bursting failure using microseismic (MS) and acoustic emission (AE) associated with EMR [26].

The main monitoring indicators of EMR include its intensity, pulse number, and dynamic trends. At present, although coal/rock EMR has been extensively studied both experimentally and theoretically, many issues still remain unresolved, such as its characteristics, spatial distribution, affecting factors, and characteristics under different sample scales, in particular if coal/rock is under complex loading conditions.

By the experimental investigations of EMR of coal in the deformation and failure processes, the amplitude and pulse evolutionary rules along with stress were analyzed, and the relationships between EMR intensity, the uniaxial compressive strength, and bursting energy index of coal samples were revealed. In particular, the critical index of EMR amplitude was obtained to evaluate the stress concentration and rockburst danger at Longgu coal mine with weak rockburst tendency.

2. Experiment on EMR Effects of Coal Samples Subject to Stress

2.1. Coal Samples. 7303 working face excavates 7# seam at west panel of Longgu coal mine, where the rockburst phenomenon begins to manifest along with the increasing mining depth. According to the principle of coal samples processing, the lump coal without obvious fissures or fractures was carefully collected and sealed.

According to the standard *ISRM*, coal materials were drilled into samples with 50 mm in diameter, then sawn into about 100 mm high segments, and grinded precisely at both ends. Nonparallelism of both ends was required to less

than 0.01 mm, and the deviation in diameter was less than 0.02 mm. Total 4 Φ 50 mm \times 100 mm coal samples were prepared.

2.2. Test Equipment and the Corresponding Parameters. Experimental system is classified into load device and monitoring apparatus. Load device uses MTS 815 press machine which is a high-precision electrohydraulic servo material testing system. It can precisely control the loading speed, and the complete stress-strain curves of coal and rock sample deformation until failure can be clearly recorded. EMR acquisition was accomplished by Disp-24 acoustic emission (AE) workstation developed by American Physical Acoustics Corporation and EMR sensors. The system contains 24 channels, 12 of which can record waveform and analyze the real-time or postfrequency-spectrum characteristics. AE and EMR signals can be simultaneously collected by the corresponding sensors.

Total 2 channels are used, and 1# and 2# channels record AE and EMR signals, respectively. The preamplifier coefficients of AE and EMR signals both are 40 dB. The center frequency value of AE sensor is 7.5 kHz, and the threshold value is 55 dB. The center frequency value of EMR dot-frequency antenna is 20 kHz, and the threshold value is 92 dB. The sampling rates of both AE and EME signals are 2000 kHz, and the sample length is 5 K. The copper network whose dimension is less than 0.5 mm as the shielding system is adopted to reduce the effect of external EMR interference. During the experiment, the AE and EMR sensors and the press ram are together put into the shielding system.

Figure 1 shows the schematic arrangement of load device, AE and EMR sensors, and Disp-24 AE workstation. Figure 2 is Disp-24 AE data acquisition system.

In this experiment, the uniaxial loading mode was tested, and the loading rate was about 0.5 kN/s until sample failure. The complete stress-strain curves were recorded. Simultaneously, the EMR signals were recorded in the whole period of sample deformation and failure. Main measured parameters included the amplitude (mV) and pulse (N) of EMR signals and so forth. Figure 3 shows the photographs of LM3# coal sample before and after failure.

2.3. Results and Analysis. Table 1 is the physical and mechanical parameters experimentally measured of 4 coal samples.

From Table 1, the uniaxial compressive strength of coal is less than 15 MPa, and the bursting energy indexes of 4 samples are less than 5, which indicate that 7# seam belongs to weak rockburst tendency. In the experiment, the phenomenon that coal debris eject or splash intensively is not observed during the process of coal samples deformation and failure. However, EMR signals are significantly produced. Therefore, EMR can be used to warn coal-rock deformation and failure, especially the rockburst danger.

The EMR signals were collected simultaneously along with the deformation and failure of coal samples, and the main monitoring indicators of EMR include its amplitude and pulse. Figures 4, 5, 6, and 7 are the curves of stress-time, EMR amplitude-time, and pulse-time of 4 coal samples.

TABLE 1: Physical and mechanical parameters of 4 coal samples.

Sample label	Height/mm	Diameter/mm	Uniaxial compressive strength/MPa	Bursting energy index	Elastic modulus/MPa
LM2#	98.16	49.12	6.801	1.182	3024.1
LM3#	90.4	49.22	13.824	1.875	3572.6
LM4#	80.68	49.3	4.622	1.022	1119.6
LM5#	99.12	49.22	9.811	1.541	3735.5

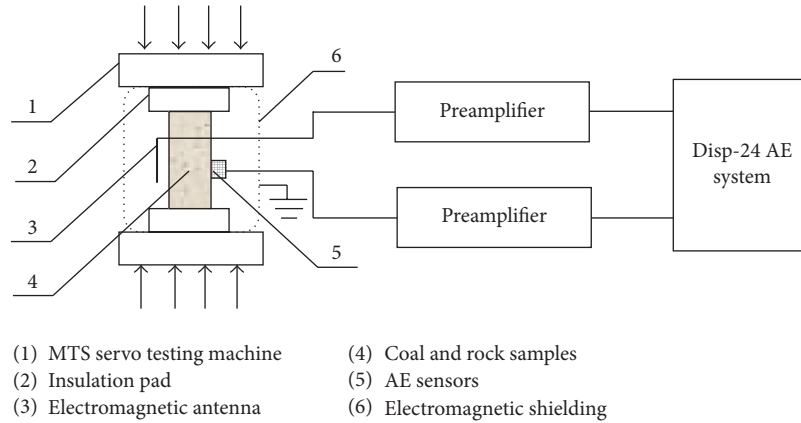


FIGURE 1: Schematic diagram of the experimental system.



FIGURE 2: Disp-24 AE data acquisition system.



(a) Before loading



(b) After failure

FIGURE 3: Photographs of LM3# coal sample before and after failure.

Obviously, the measured amplitude and pulse of EMR signals positively correlate well with the applied stress. In particular, when the failure of coal samples occurs, the amplitude and pulse simultaneously reach the maximum and after that gradually decrease along with the stress.

In order to further reveal EMR effects in the process of deformation and failure of coal samples, the correlations between the maximum amplitude and pulse of EMR, the uniaxial compressive strength, and bursting energy index were regressively analyzed. Figure 8 is the regressive curves of EMR maximum amplitude, the uniaxial compressive strength, and bursting energy index of samples. Figure 9 is the regressive curves of maximum pulse, the uniaxial compressive strength, and bursting energy index.

Theoretically, the amplitude and pulse of EMR increase linearly with the electron charge and acceleration of charged particles in the process of deformation and fracture of coal-rock. And the amplitude and pulse of EMR are associated with the density of charged particles, the larger the particles

number is, and the higher the strength of EMR is. Generally, the higher the uniaxial compressive strength of coal-rock is, the more the formed microcracks is, and the larger the number of particles accumulated in the tip of microcracks per unit time is. In other words, the higher the uniaxial compressive strength is, the more the intensity of deformation

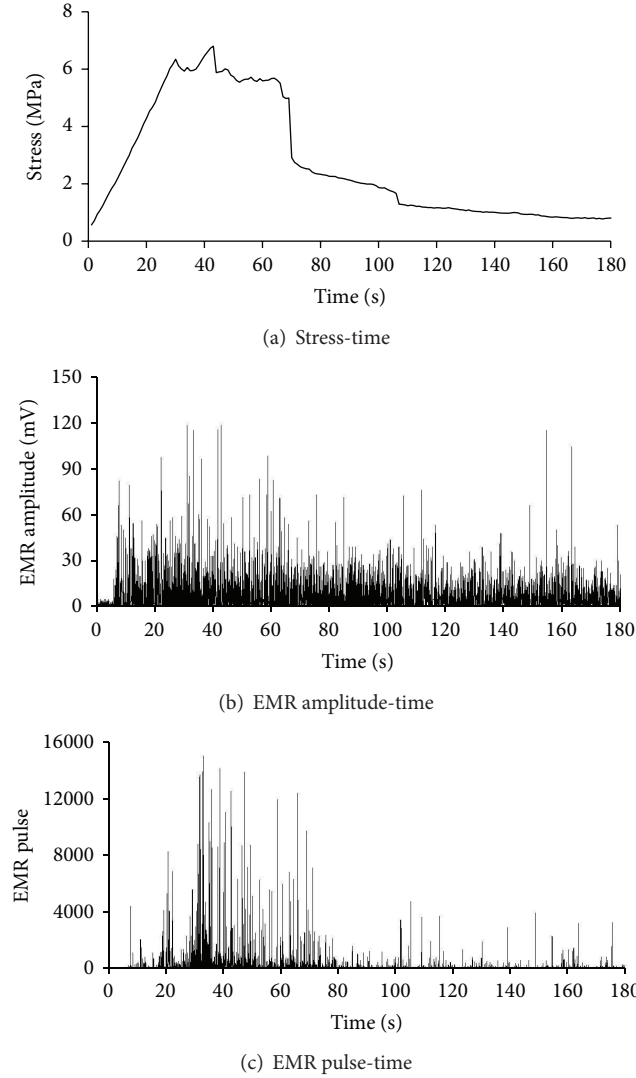


FIGURE 4: The measured stress and EMR of LM2# coal sample.

TABLE 2: The measured maximum amplitudes of EMR.

Sample label	LM2#	LM3#	LM4#	LM5#
Maximum amplitude	118 mV	163 mV	61 mV	132 mV
Average	118.5 mV			
Application index	120 mV			

and failure is, and the higher the velocity and acceleration of charged particles is. So, the larger the uniaxial compressive strength of coal-rock is, the higher the amplitude and pulse of EMR are, and the greater the bursting energy indexes are. It can be found from Figures 8 and 9, when the failure of coal sample occurs, the maximum amplitudes and pulses of the EMR increase linearly along with the increasing uniaxial compressive strength values. In addition, for bursting energy indexes of coal samples, the maximum amplitudes and pulses behave a logarithmic accretion tendency with it.

In Table 2, it is shown that EMR maximum amplitude values of 4 coal samples are 118 mV, 163 mV, 61 mV, and

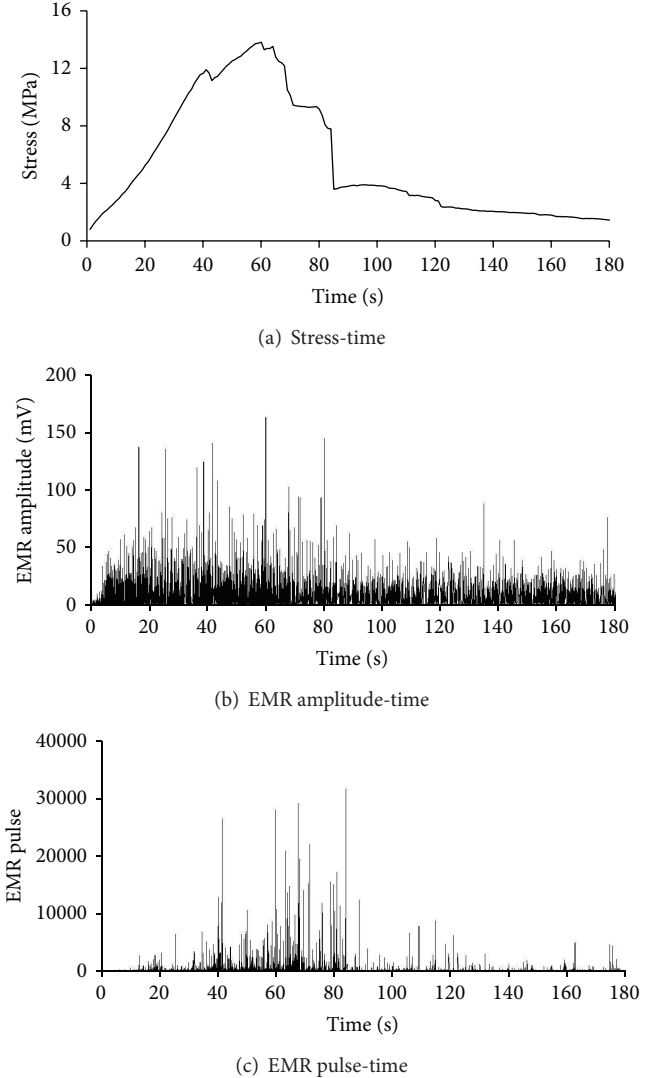


FIGURE 5: The measured stress and EMR of LM3# coal sample.

132 mV, respectively, when the failure occurs. The average ($\sum \max E = 118.5$ mV) is calculated and obtained, to propose the critical index of EMR amplitude for totally evaluating the stress state and deformation intensity of coal mass. The application index of EMR amplitude should be appropriately enlarged to be 120 mV, by taking the external inevitable electromagnetic interference in field into account.

3. EMR Measurement in Process of Roof Caving and Subsidence

To evaluate and warn rockburst risk of 7303 working face, EMR signal was measured in the whole mining period by KBD5 portable apparatus developed by China University of Mining and Technology (CUMT). The apparatus is mainly composed of a wideband and high-sensitivity directional receiving antenna, the mainframe and the remote communication interface, and so forth. In order to reduce the interference from other electromagnetic signals in the

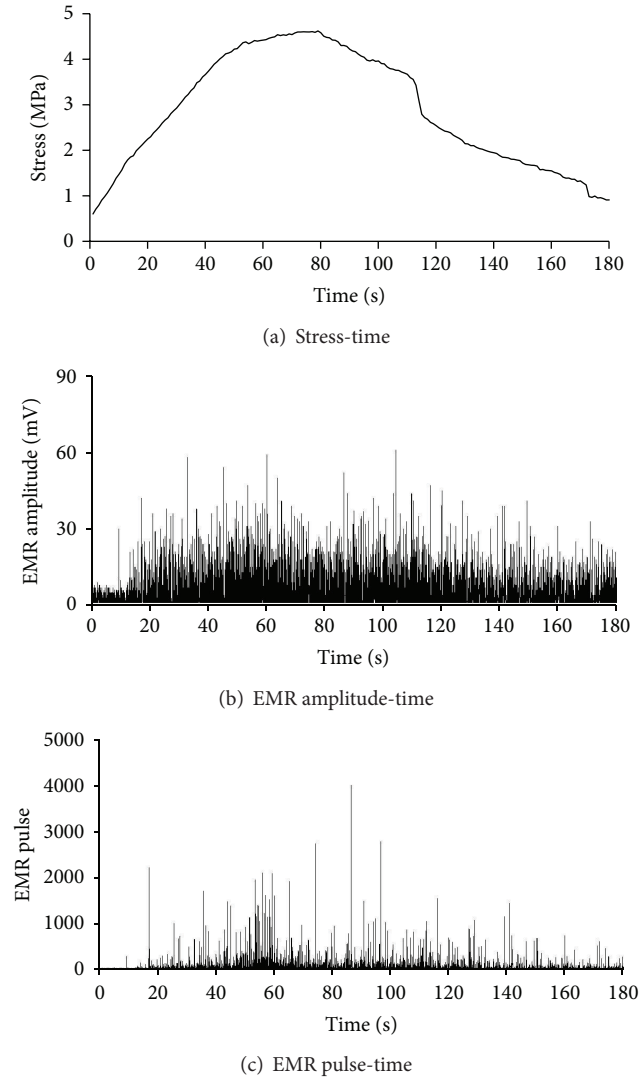


FIGURE 6: The measured stress and EMR of LM4# coal sample.

testing environment, the antenna adopts a special shielding technique. One end of antenna is shielded and adequately grounded, which can significantly reduce the sensitivity out of the effective receiving scope and actually guarantee the monitoring reliability. Adjustable gain preamplifier is designed for the different load-electromagnetic property of coal and rock material.

A large number of studies have shown that EMR amplitude is strongly related to the level and variation of stress, especially in correspondence with sharp stress drops or the final collapse. Based on experimental conclusions and on-site monitoring experience, the critical value (120 mV) and its variation trend (sharp drops or rises) of EMR amplitude can be used together for stress concentration evaluation in 7303 working face.

3.1. Geological and Mining Conditions of 7303 Working Face. The 7303 working face locates at the west wing of mine field, extracting 7# coal seam with average thickness of 4.4 m from August 1, 2004, and the average dip angle of 7# seam is 8–10°.

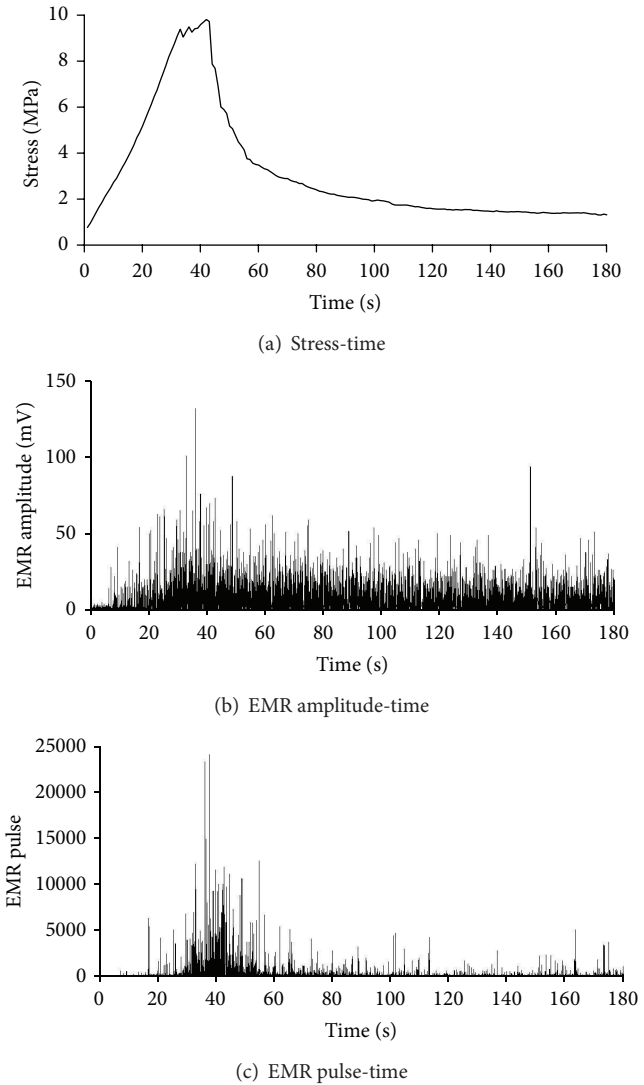
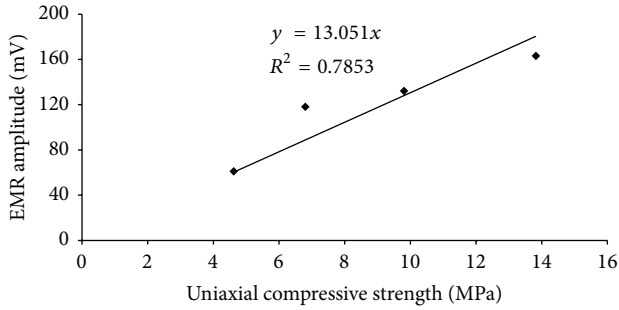


FIGURE 7: The measured stress and EMR of LM5# coal sample.

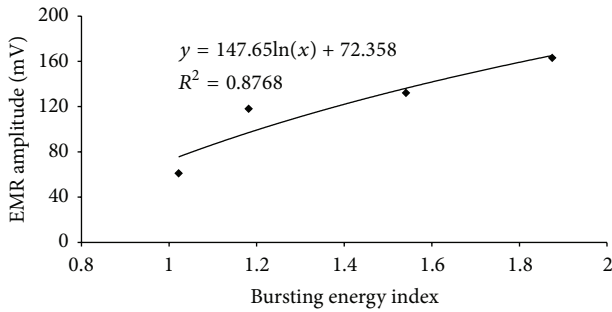
The geological condition of working face is relatively simple, only 11 faults whose throws are between 2.0 m and 15.0 m are disclosed in 7303 working face, and the fully mechanized top coal caving mining method is adopted. As the mining depth is larger than 760 m, there might be coal and rock dynamic disasters appearance in process of 7303 working face mining. According to the borehole data, the roof strata of 7# coal seam from bottom to up are as follows: siltstone (2.0 m), medium sandstone (10.6 m) so-called key stratum, siltstone (3.3 m), fine sandstone (2.0 m), and siltstone (12.6 m). Figure 10 shows the layout diagram of the 7303 working face.

3.2. Monitoring Scheme

3.2.1. Monitoring Method. For in situ measurement in coal mines, the antenna is fixed and the receiving end is vertically towards the medium-upper part of coal wall within 5 m. The amplitude and pulse indexes and their variations of EMR are measured. The fixed monitoring points in headentry

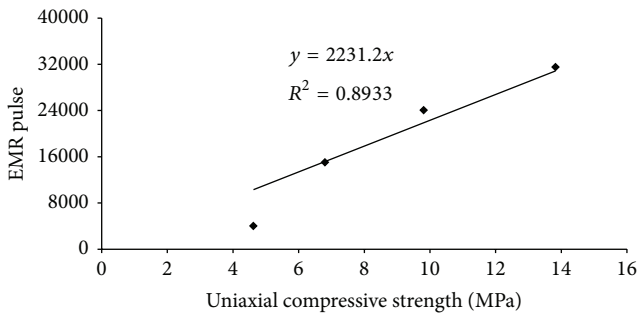


(a) Regressive curve between EMR maximum amplitude and the uniaxial compressive strength

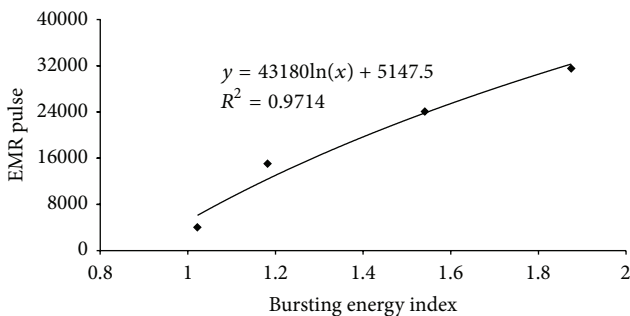


(b) Regressive curve between EMR maximum amplitude and bursting energy index

FIGURE 8: Correlations between EMR maximum amplitude, uniaxial compressive strength, and bursting energy index.



(a) Regressive curve between EMR maximum pulse and the uniaxial compressive strength



(b) Regressive curve between EMR maximum pulse and bursting energy index

FIGURE 9: Correlations between EMR maximum pulse, uniaxial compressive strength, and bursting energy index.

and tailentry combined with general investigation were conducted due to the high stress concentration of roadways.

3.2.2. Arrangement of Monitoring Points. Total 12 points were outward located in headentry 10 m from the cut of 7303 working face, and the interval of points was principally set to be 10 m. In addition, total 10 points were outward located in tailentry 20 m from the cut, and the interval of points was principally set to be 20 m. All points will move forward correspondingly with the advance of working face, and the interval can be adjusted according to in situ observation requirements, therefore, the relative positions of which are fixed. In particular, for the rest locations characterized higher stress concentration, such as fault and roadway junction areas, the density of points arrangement should be appropriately increased.

3.2.3. Monitoring Frequency. Daily monitoring frequency is three times including morning, noon, and night shifts, and the monitoring time of each shift for one point is 2 min.

3.3. Conclusions and Analysis

3.3.1. At the Stage of Initial Mining. Figure 11 shows the measured EMR amplitude variation of different points in tailentry and headentry at the stage of initial mining.

From Figure 11, it is obviously shown that the stress concentration level is not obvious and the risk of rockburst is lower due to the smaller EMR amplitude (much less than the critical value 120 mV), and the stress of the surrounding coal and rock of tailentry and headentry is lower. As 7303 working face firstly arranged in west panel is in the original stress state, where no any mining-induced stress interference exists. Moreover, due to the initial stage of 7303 working face mining, the fracturing and caving of overlying rock strata do not obviously occur. Therefore, the stress concentration level of 7303 working face is relatively lower, and the monitoring value of EMR amplitude is smaller.

3.3.2. The Initial Caving of Primary Roof. On August 21, 2004, when the total advancing distance of 7303 working face reached 35 m so-called first caving interval, the primary roof began to fall and the pressuring process approximately lasted 2 days based on in situ observation. Figure 12 shows the EMR amplitude variation in tailentry and headentry at morning shift on August 21.

In Figure 12, compared with initial mining, the measured EMR amplitude in tailentry and headentry obviously increased, which indicated that the stress of coal and rock surrounding 7303 working face correspondingly rose due to the primary roof caving. In particular, the amplitudes of 3 monitoring points located at 42 m, 85 m, and 105 m ahead of the cut in tailentry seriously exceeded the critical value 120 mV, which demonstrated that there might be rockburst risk induced by higher stress concentration. By implementing relieve-shot, EMR amplitude suddenly and sharply dropped, and the higher stress was transferred and further rebalanced. For headentry, the amplitude totally kept less than the critical

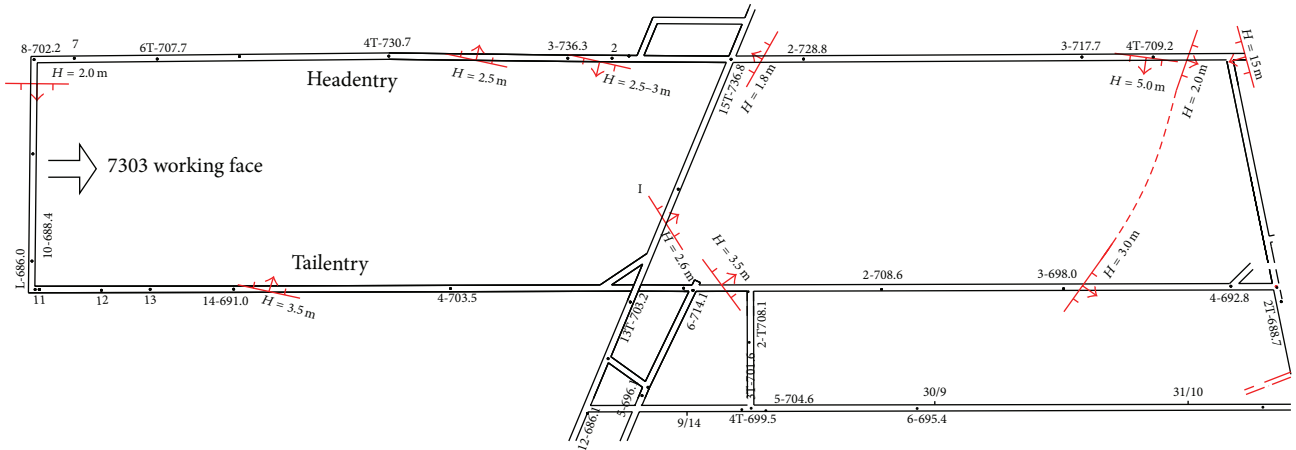
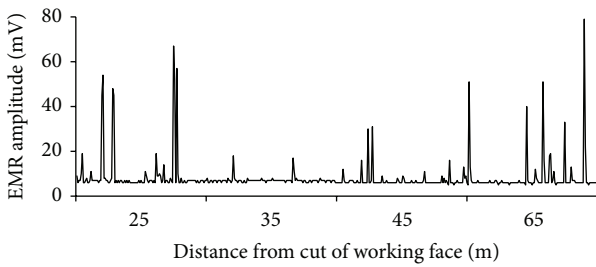
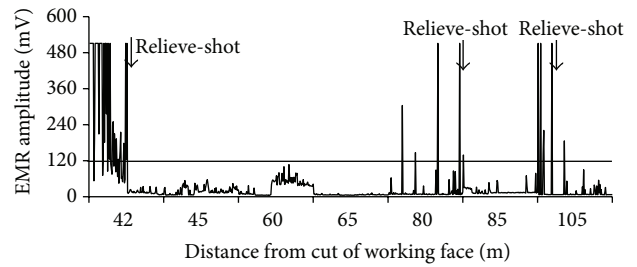


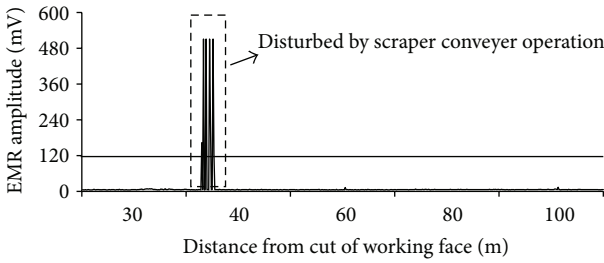
FIGURE 10: The layout diagram of 7303 working face.



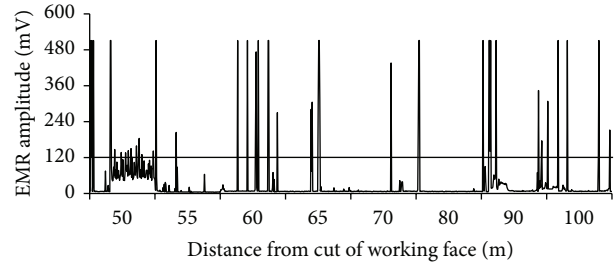
(a) In tailentry



(a) In tailentry



(b) In headentry



(b) In headentry

FIGURE 11: The monitoring result of EMR amplitude at the stage of initial mining.

FIGURE 12: The monitoring result of EMR amplitude at morning shift on Aug 21.

value. Therefore, the stress of headentry was relatively smaller than that of tailentry due to its shallower burial depth.

3.3.3. *The Periodic Caving of Primary Roof.* Along with further advancing of 7303 working face, the primary roof will experience periodic caving process after first caving. According to the advancing distances from initial caving to first periodic caving, the caving interval of primary roof was approximately 20 m. By the statistical analysis, the caving intervals of primary roof distributed in the range of 17 to 23 m based on 3 periodic caving. Figures 13–15 show EMR amplitude variations measured in tailentry at the stages of the first periodic caving, the second periodic caving, and the third periodic caving of primary roof, respectively.

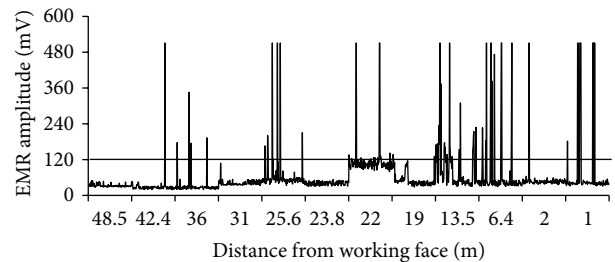


FIGURE 13: EMR amplitude variation in tailentry at the stage of first periodic caving. Note: the caving interval is 20 m, and the pressing intensity is not obvious according to in situ observation of roadway deformation.

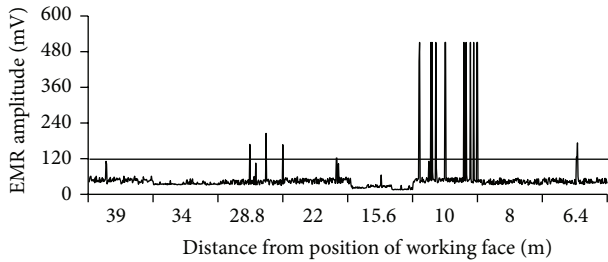


FIGURE 14: EMR amplitude variation in headentry at the stage of second periodic caving. Note: the caving interval is 17 m, and the pressuring intensity is weaker according to in situ observation of roadway deformation.

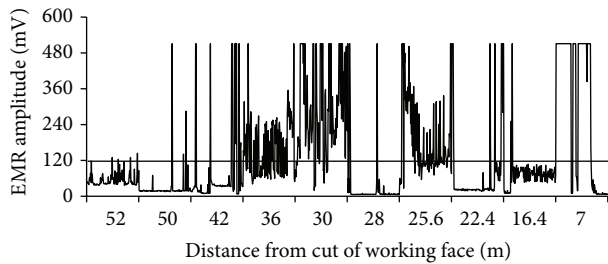


FIGURE 15: EMR amplitude variation in tailentry at the stage of third periodic caving. Note: the caving interval is 23 m, and the pressuring intensity is stronger based on in situ observation of roadway deformation and support resistance.

In process of the first periodic caving of primary roof (in Figure 13), the overall level of EMR amplitude is less than the critical value 120 mV. However, the amplitude fluctuation is intensive within the scope of 13.5 m ahead of working face in tailentry, which indicates the stress concentration and the deformation and failure of coal and rock. In process of the second periodic caving (in Figure 14), the overall level of EMR amplitude is smaller than the critical value except for electromagnetic interference of the monitoring point located 10 m ahead of working face in headentry. For the third periodic caving (in Figure 15), EMR amplitudes of a majority of monitoring points significantly exceed the critical value. In particular, within the scope of 42 m ahead of working face in tailentry, the amplitude variation and fluctuation is abnormal intensive. In conclusion, based on the caving intervals and EMR amplitudes, it can be verified that EMR remarkably increases with the periodic caving interval of primary roof. In particular, the influencing range of stress concentration also increases in accordance with the periodic caving intervals. Therefore, EMR amplitude can be used to check the results of conventional pressuring monitoring and warn the risk of dynamic hazard induced by roof caving.

3.3.4. Large-Scale Movement and Subsidence of Primary Roof.

From September 21 to 24, 2004, when 7303 working face advanced nearby a fault, the immediate and primary roof strata began to intensively move and subside due to the diastrophism and slippage of fault triggered by mining

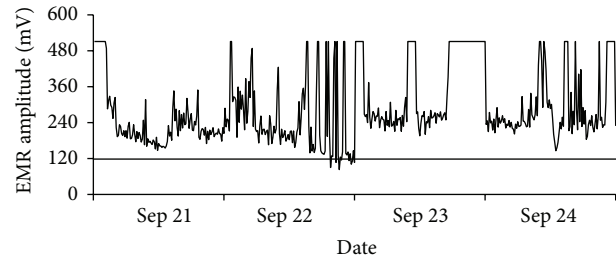


FIGURE 16: EMR amplitude of monitoring point located 20 m ahead of working face in tailentry from September 21 to 24.

activity. Based on in situ investigation and measurement, it can be found that tailentry seriously deformed and part of bolts and anchor cables became invalid. Figure 16 shows EMR amplitude of the monitoring point located 20 m ahead of working face in tailentry.

From Figure 16, during the period of roof movement and subsidence, EMR amplitude significantly exceeds the critical value 120 mV, which indicates that the higher EMR amplitude is attributed to the violent deformation of coal and rock induced by slippage of fault. In addition, it might be confirmed that the fault can easily generate the higher stress concentration and accumulate a large amount of energy.

In summary, comparison with past investigations, the highlight of in situ measurement mainly, manifests the complete observations of EMR signals in whole period of primary roof caving in 7303 working face, such as the initial and periodic caving and the large-scale movement and subsidence of primary roof induced by tectonic stress concentration.

4. Conclusions

- (1) The amplitude and pulse of EMR signals positively correlate well with stress. In particular, when the failure of coal samples occurs, the amplitude and pulse simultaneously reach the peak and after that gradually reduce along with the decreasing stress.
- (2) The maximum amplitude and pulse of EMR increase linearly with the uniaxial compressive strength of coal and behaves logarithmic accretion tendency with bursting energy indexes.
- (3) By in situ investigation of 7303 working face, it is well found that EMR amplitude can effectively reflect the stress state and rockburst failure level of coal subjected to roof loading based on the critical value 120 mV proposed from experiments.

Conflict of Interests

The authors declare that there is no conflict of interests regarding the publication of this paper.

Acknowledgments

The authors gratefully wish to acknowledge the collaborative funding support from the Foundation for the Author of National Excellent Doctoral Dissertation of PR China (201167), the Fundamental Research Funds for the Central Universities (no. 2014XT01), and a Project Funded by the Priority Academic Program Development of Jiangsu Higher Education Institutions (PAPD).

References

- [1] L. Cohen, "Electromagnetic radiation," *Journal of the Franklin Institute*, vol. 177, no. 4, pp. 409–418, 1914.
- [2] A. A. Urusovskaja, "Electric effects associated with plastic deformation of ionic crystals," *Soviet Physics Uspekhi*, vol. 11, no. 5, pp. 631–643, 1969.
- [3] D. R. Hanson and G. A. Rowell, "Electromagnetic radiation from rock failure," 1982.
- [4] C.-Y. King, "Earthquake prediction: electromagnetic emissions before earthquakes," *Nature*, vol. 301, no. 5899, article 377, 1983.
- [5] A. Rabinovitch, D. Bahat, and V. Frid, "Comparison of electromagnetic radiation and acoustic emission in granite fracturing," *International Journal of Fracture*, vol. 71, no. 2, pp. R33–R41, 1995.
- [6] A. Rabinovitch, D. Bahat, and V. Frid, "Emission of electromagnetic radiation by rock fracturing," *Zeitschrift für Geologische Wissenschaften*, vol. 24, pp. 361–368, 1996.
- [7] V. Hadjicontis and C. Mavromatou, "Transient electric signals prior to rock failure under aniaxial compression," *Geophysical Research Letters*, vol. 21, no. 16, pp. 1687–1690, 1994.
- [8] S. M. Krylov and N. N. Nikiforova, "On ultralow frequency electromagnetic emission from an active geological medium," *Physics of the Solid Earth*, vol. 31, no. 6, pp. 499–512, 1996.
- [9] C. Reuther, H. Obermeyer, K. Reicherter et al., "Neotektonik und aktive Krustenspannungen in Südost-Sizilien und ihre Beziehungen zur regionalen Tektonik im Zentralen Mittelmeer," in *Mitteilungen aus dem Geologisch-Paläontologischen Institut der Universität Hamburg*, vol. 86, pp. 1–24, 2002.
- [10] J. Muto, H. Nagahama, T. Miura, and I. Arakawa, "Frictional discharge plasma and seismo-electromagnetic phenomena," *Physics of the Earth and Planetary Interiors*, vol. 168, no. 1–2, pp. 1–5, 2008.
- [11] A. Rabinovitch, V. Frid, and D. Bahat, "Surface oscillations—a possible source of fracture induced electromagnetic radiation," *Tectonophysics*, vol. 431, no. 1–4, pp. 15–21, 2007.
- [12] V. A. Morgounov and S. A. Malzev, "A multiple fracture model of pre-seismic electromagnetic phenomena," *Tectonophysics*, vol. 431, no. 1–4, pp. 61–72, 2007.
- [13] E. Wang, X. He, J. Wei, B. Nie, and D. Song, "Electromagnetic emission graded warning model and its applications against coal rock dynamic collapses," *International Journal of Rock Mechanics and Mining Sciences*, vol. 48, no. 4, pp. 556–564, 2011.
- [14] E.-Y. Wang and E.-L. Zhao, "Numerical simulation of electromagnetic radiation caused by coal/rock deformation and failure," *International Journal of Rock Mechanics and Mining Sciences*, vol. 57, pp. 57–63, 2013.
- [15] E. Wang, H. Jia, D. Song, N. Li, and W. Qian, "Use of ultralow-frequency electromagnetic emission to monitor stress and failure in coal mines," *International Journal of Rock Mechanics and Mining Sciences*, vol. 70, pp. 16–25, 2014.
- [16] M. Liu and X. He, "Electromagnetics response of outburst-prone coal," *International Journal of Coal Geology*, vol. 45, no. 2–3, pp. 155–162, 2001.
- [17] Y. D. Jiang, Y. K. Lv, and Y. X. Zhao, "Principal component analysis on electromagnetic radiation rules while fully mechanized coal face passing through fault," *Procedia Environmental Sciences*, vol. 12, pp. 751–757, 2012.
- [18] Y. Jiang, H. Wang, S. Xue, Y. Zhao, J. Zhu, and X. Pang, "Assessment and mitigation of coal bump risk during extraction of an island longwall panel," *International Journal of Coal Geology*, vol. 95, pp. 20–33, 2012.
- [19] M. Lichtenberger, "Regional stress field as determined from electromagnetic radiation in a tunnel," *Journal of Structural Geology*, vol. 27, no. 12, pp. 2150–2158, 2005.
- [20] J. Mallik, G. Mathew, T. Angerer, and R. O. Greiling, "Determination of directions of horizontal principal stress and identification of active faults in Kachchh (India) by electromagnetic radiation (EMR)," *Journal of Geodynamics*, vol. 45, no. 4–5, pp. 234–245, 2008.
- [21] J. M. Carcione, G. Seriani, and D. Gei, "Acoustic and electromagnetic properties of soils saturated with salt water and NAPL," *Journal of Applied Geophysics*, vol. 52, no. 4, pp. 177–191, 2003.
- [22] V. Frid, "Electromagnetic radiation method for rock and gas outburst forecast," *Journal of Applied Geophysics*, vol. 38, no. 2, pp. 97–104, 1997.
- [23] V. Frid, "Electromagnetic radiation method water-infusion control in rockburst-prone strata," *Journal of Applied Geophysics*, vol. 43, no. 1, pp. 5–13, 2000.
- [24] X. He, W. Chen, B. Nie, and H. Mitri, "Electromagnetic emission theory and its application to dynamic phenomena in coal-rock," *International Journal of Rock Mechanics and Mining Sciences*, vol. 48, no. 8, pp. 1352–1358, 2011.
- [25] A. Nardi and M. Caputo, "Monitoring the mechanical stress of rocks through the electromagnetic emission produced by fracturing," *International Journal of Rock Mechanics and Mining Sciences*, vol. 46, no. 5, pp. 940–945, 2009.
- [26] C.-P. Lu, L.-M. Dou, N. Zhang, J.-H. Xue, and G.-J. Liu, "Microseismic and acoustic emission effect on gas outburst hazard triggered by shock wave: a case study," *Natural Hazards*, vol. 73, pp. 1715–1731, 2014.

Research Article

Numerical Investigation of Rockburst Effect of Shock Wave on Underground Roadway

Cai-Ping Lu,^{1,2} Guang-Jian Liu,² Hong-Yu Wang,² and Jun-Hua Xue³

¹Key Laboratory of Safety and High-Efficiency Coal Mining, Ministry of Education, Anhui University of Science and Technology, Huainan, Anhui 232001, China

²School of Mining Engineering, Key Laboratory of Deep Coal Resource Mining, Ministry of Education, China University of Mining and Technology, Xuzhou, Jiangsu 221116, China

³State Key Laboratory of Deep Coal Mining and Environment Protection, Huainan Mining Industry Group, Huainan, Anhui 232001, China

Correspondence should be addressed to Hong-Yu Wang; gjliucumt@126.com

Received 13 November 2014; Accepted 28 December 2014

Academic Editor: Shimin Liu

Copyright © 2015 Cai-Ping Lu et al. This is an open access article distributed under the Creative Commons Attribution License, which permits unrestricted use, distribution, and reproduction in any medium, provided the original work is properly cited.

Using UDEC discrete element numerical simulation software and a cosine wave as vibration source, the whole process of rockburst failure and the propagation and attenuation characteristics of shock wave in coal-rock medium were investigated in detail based on the geological and mining conditions of 1111(1) working face at Zhuji coal mine. Simultaneously, by changing the thickness and strength of immediate roof overlying the mining coal seam, the whole process of rockburst failure of roadway and the attenuation properties of shock wave were understood clearly. The presented conclusions can provide some important references to prevent and control rockburst hazards triggered by shock wave interferences in deep coal mines.

1. Introduction

Coal mining is closely related to blasting, transportation, mechanical operation, and other activities; therefore, the whole process of mining is accompanied with the generation and interference of shock wave. Due to diversity of vibration source and uncertainty of position, these dynamic loads will inevitably exert mutual interference in the process of coal-rock deformation and failure, and the disturbance effects on surrounding rock are very significant, especially for the surrounding rock with a free surface. Once the dynamic load is exerted, the surrounding rock may not generate macrodamage, but under the condition of stress wave disturbance, the cumulative damage of surrounding rock will rapidly increase and the local stress environment will be worsened on microcosmic or mesoscopic scale. Eventually, the instantaneous dynamic extension of crack is caused, and the transient strain energy rapidly releases in the form of kinetic energy by coal-rock violent ejection.

Once the mechanical system composed of coal and rock mass reaches its ultimate strength limit, the rockburst will

inevitably occur, and the vast majority of strain energy accumulated in coal and rock mass will, suddenly and sharply, be released, which can cause the instantaneous destruction of coal and rock in roadway, equipment damage, and miner casualty. Part of the energy will be released in the form of shock waves, which can generate dynamic impact on the surrounding coal and rock medium. In particular, shock waves might cause the deformation and damage of underground structures in far field. Once the residual shock wave intensity gets higher after attenuation, the energy input of coal and rock in higher stress concentration state can induce rockburst. In addition, rockburst may directly or indirectly trigger serious accidents such as coal/gas outburst, gas explosion, and water inrush. Increasingly, for gas-contained coal seam, the harm of rockburst is more remarkable [1, 2].

Because the rockburst occurrence relates closely to the dynamic instability of surrounding rock in higher static stress concentration state, the static stress combined with shock wave interference is extensively used to reveal the mechanism and influencing factors of rockburst failure of coal-rock, and many fruitful results have been obtained. In particular, a large

TABLE 1: Mechanical parameters of rock strata.

Stratum	Thickness/m	Density/(Kg·m ⁻³)	Bulk modulus/GPa	Shear modulus/GPa	Cohesion/MPa	Friction angle/°	Tensile strength/MPa
Tinea mudstone	11.5	2640	8	4.8	2.3	35	5
Finestone/siltstone	3.2	2700	12	8.1	4.0	37	7
Mudstone	10.0	2640	8	4.8	2.3	35	5
11 ⁻² coal seam	1.2	1300	8.5	4	0.5	28	2
Mudstone	4.5	2640	8	4.8	2.3	35	5
11 ⁻¹ coal seam	0.8	1300	8.5	4	0.5	28	2
Mudstone	9.0	2640	8	4.8	2.3	35	5

number of researches have been conducted by the numerical simulation methods. For example, Qin and Mao [3] simulated rockburst induced by disturbing stress wave and analyzed the influence of depth and peak of stress wave on rockburst by using the software UDEC. Gao et al. [4] found that the energy attenuation index η was considerably small in the rock and soil media but apparently much larger in weak or soft media. According to the law of micromechanics of impact fracture on coal-rock, Grady and Kipp [5] studied the transmission characteristics of shock waves in sandstone and mudstone and so forth. As stated by Zhao et al. [6], the calibration work of UDEC modelling on P-wave propagation across single linearly and nonlinearly deformable fractures was conducted. Park and Jeon [7] proposed an air-deck method for attenuating blast-induced vibration waves in the direction of tunneling. Uysal et al. [8] aimed at investigating the effect of empty barrier holes alone on seismic vibration and detected a decrease in the peak particle velocity (PPV) of up to 18% just behind the barrier holes. Li et al. [9] proposed experimentally that the shock wave propagation will be reflected, refracted, and absorbed by the discontinuity in coal and rock mass. Brown et al. [10] presented methods for modeling rock fractures and their influence on rock masses has been a distinctive feature of rock mechanics and rock engineering. Schoenberg [11] and Pyrak-Nolte et al. [12] derived solutions of reflection and transmission coefficients for obliquely incident P-wave or S-wave on a dry or liquid-filled fracture between two dissimilar media. Nakagawa et al. [13] found that wave conversion occurs when P-wave or S-wave is normally incident on a fracture subjected to a shear movement. Meanwhile, Gu et al. [14] pointed out that an inhomogeneous P-interface wave appears when an SV-wave is incident upon a fracture at or beyond the critical angle, which is determined by Poisson's ratio of rock material. Pyrak-Nolte and Nolte [15] performed a wavelet analysis on experimental results of interface wave propagating along a single fracture. Cai and Zhao [16] and Zhao et al. [17] used the method of characteristics to study wave attenuation across the linearly deformable fractures, in which the multiple reflections have been considered. Later, the theoretical results obtained by Zhao et al. [18] were verified by a series of tests on ultrasonic wave attenuation across parallel artificial fractures. A detailed description of UDEC simulation can be found in the software manual [19]. Brady et al. [20] conducted a two-dimensional UDEC modelling on the slip at a single fracture under an explosive linear source. The numerical results were

accordant with theoretical solutions presented by Day [21]. Gao et al. [22] revealed that compressive shear failure, rather than tensile failure, is the dominant failure mechanism in the caved strata above the mined-out area by a UDEC model.

The purpose of our research is to provide the certain basis and reference for prevention of rockburst by using the UDEC numerical simulation modelling. Based on the geological and mining conditions of 1111(1) working face at Zhuji coal mine, the whole process of rockburst failure of surrounding rock in roadway subjected to the disturbance of shock wave was simulated and recurred, and the effect rules of the immediate roof thickness and strength overlying the mining coal seam and with or without bolt support on rockburst failure of roadway were analyzed in detail.

2. Numerical Modelling and Analysis

2.1. Modelling. The numerical model is established based on the actual geological conditions of 1111(1) working face of Zhuji coal mine. The size (length \times height) of model is 60 m \times 40.2 m, and the shape of inside roadway is the semicircular arch with arch radius of 2 m and the size (width \times height) of roadway is 4 m \times 4 m. Mechanical parameters of the rock strata are shown in Table 1, and the models with or without bolt reinforcement are shown in Figure 1. Total 11 anchor rods were added in roadway, 5 of which were installed in semicircular arch area, and the rest were installed at left and right sides of roadway, respectively. The length of bolt is 2.4 m, the sectional area is $314e^{-6}$ m², and its pretightening force is set to be 40 KN.

The boundary conditions of model are as follows: the horizontal boundaries at left and right sides are constrained, the bottom boundary is fixed, and the upper boundary is free with the uniform load ($q = r \times H$), in which the average density r is 25 KN/m³ and the buried depth H of the upper boundary is 900 m. For the model of shock wave, in order to reduce the reflection effects of boundaries under the condition of dynamic loading, the boundaries were set up to be viscous to simulate infinity. The exerted shock was a cosine wave ($y = 20e^6 \times \cos(2\pi \times 10)$) with the peak stress of 20 MPa and the frequency of 10 Hz, and the source was located in 20–40 m scope of the upper boundary, respectively. Ten symmetrical points for monitoring the deformation and displacement in the vertical and horizontal directions were located at both sides of roadway (Figure 1(c)) as follows: (1) 5 points labeled A, B, C, D, and E were arranged at left side, and the

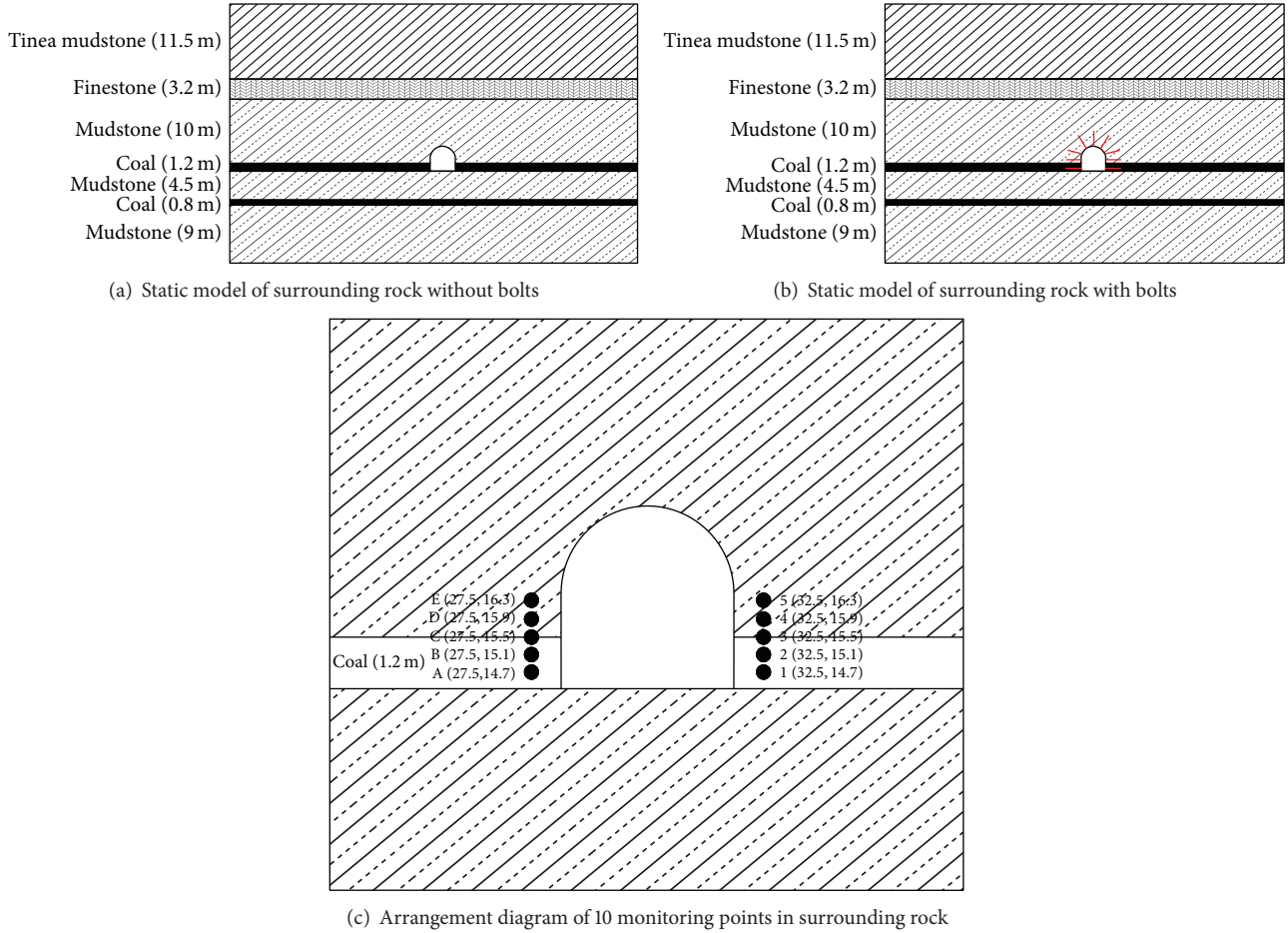


FIGURE 1: The mechanical models of surrounding rock with or without bolts.

two-dimensional coordinates were (27.5, 14.7), (27.5, 15.1), (27.5, 15.5), (27.5, 15.9), and (27.5, 16.3), respectively. (2) The rest labeled 1, 2, 3, 4, and 5 were arranged at right side, and the two-dimensional coordinates were (32.5, 14.7), (32.5, 15.1), (32.5, 15.5), (32.5, 15.9), and (32.5, 16.3), respectively. The critical damping ratio ε of the artificial shock as Rayleigh wave was set to be 0.1.

2.2. Simulation Scheme. According to the geological and mining conditions of IIII(1) working face, the original stress of surrounding rock of model was simulated and calculated firstly, and then the roadway was excavated; after that, the artificial shock wave was exerted. Eventually, by collecting the displacement and stress of monitoring points, the effect rules of dynamic stress disturbance on the stability of surrounding rock were analyzed in detail. The simulation scheme was as follows.

- (1) Under the conditions of the artificial shock wave, the effect rules of surrounding rock stability of roadway with and without bolt reinforcement were simulated and analyzed.
- (2) The effect rules of immediate roof thickness on the stability of roadway were simulated and analyzed.

- (3) The effect rules of immediate roof strength on the stability of roadway were simulated and analyzed.

3. Simulation Results and Analysis

3.1. Process Simulation of Rockburst Failure of Roadway Surrounding Rock. In the primitive condition of surrounding rock without bolt, the buried depth of roadway is about 900 m, and the peak stress of the exerted shock wave is 20 MPa. The simulation results are shown in Figure 2.

From Figure 2, the whole process of rockburst failure of surrounding rock in roadway induced by shock wave disturbance clearly recurred, and the impact time is 1.5 s. It is obviously observed that cracks firstly began nearby both sides of roadway as the high stress concentration areas, and the failure points located at two junctions between the arch and both sides. With further disturbance of shock wave, cracks began to expand rapidly from the starting positions to deep coal and rock mass of two sides and formed two macrocracks symmetrically distributed at both sides, respectively. Meanwhile, due to the effects of shock wave, coal and rock were firstly ejected outward from the top of roadway and gradually evolved to two sides and thrown into roadway at a certain velocity when the rockburst is triggered.

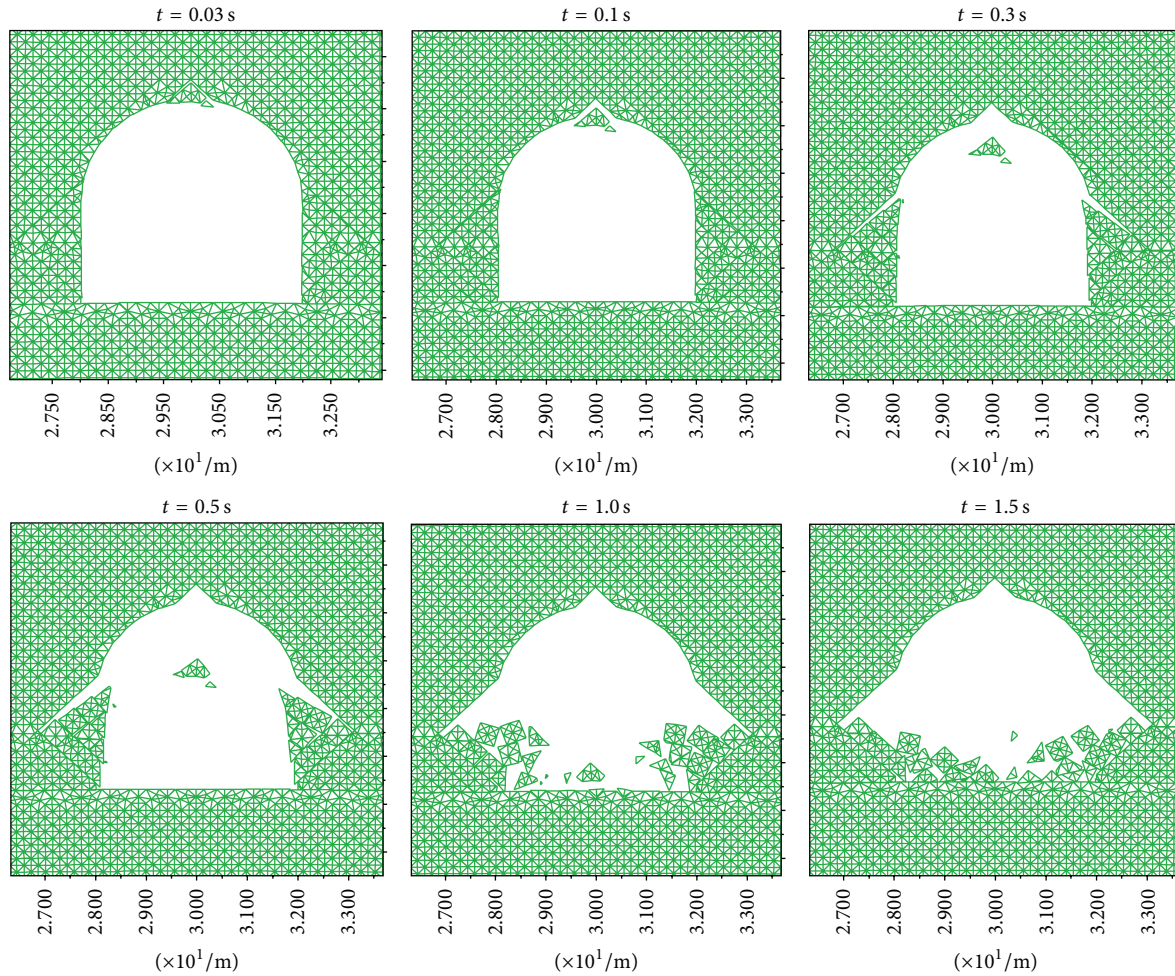


FIGURE 2: Process simulation of rockburst in the primitive condition.

Because the symmetrical dynamic stress is correspondingly generated, the deformation and failure distribution of roadway are also basically symmetrical. To reveal the positions of coal and rock failure once rockburst occurs, the displacements of 5 monitoring points at the right side were obtained and analyzed, as shown in Figure 3.

From Figure 3, the x - and y -directional displacements of monitoring points 1 and 5 are approximately the same, and their curves almost overlap. Comparatively, the displacement of point 2 is relatively bigger, and the displacements of points 3 and 4 are the biggest with the peak value of 0.8 m. Therefore, it is concluded that the coal and rock mass eject outward mainly from the interface between coal seam and its overlying stratum once rockburst occurs for the thin coal seam. Because the mechanical parameters of interface are smaller, the rockburst failure is easily induced by shock wave.

3.2. Simulation of Rockburst Failure of Roadway with Bolt Supporting. Bolts at the top and two sides of roadway were installed, and the pretightening force was exerted. Under the same conditions of the buried depth of 900 m, peak stress of 20 MPa, and the impact time of 1.5 s, the simulation results are shown in Figure 4.

At the different acting time of shock wave, the shear force and y -directional displacement of each bolt are shown in Figures 5 and 6, respectively.

In Figures 5 and 6, the numbers from 1# to 11# represent the serial numbers of bolts. For the roadway with bolt supporting, when it is disturbed by shock wave, the following conclusions can be drawn: (1) for the geological and mining conditions of III(1) working face, bolt supporting can reinforce the stability of surrounding rock mass in roadway and improve its ability to undergo shock wave, (2) for the semicircular arch roadway in shape, the shear stress of bolts in arch is smaller, and its distribution is basically symmetrical, and (3) y -directional displacements of each bolt along with shock time ($t = 0.5$ s and 1.0 s) are approximately symmetrical.

In summary, for roadway without bolt supporting, the resonant effect commonly triggering rockburst failure of surrounding rock will form when the dominant frequency of residual shock wave reaches or approaches the natural vibration frequency of surrounding rock of roadway. After installing bolts as deformation constraint and antishear structure, the integrity and strength of surrounding rock can be significantly enhanced. Simultaneously, the natural vibration frequency of surrounding rock obviously reduces,

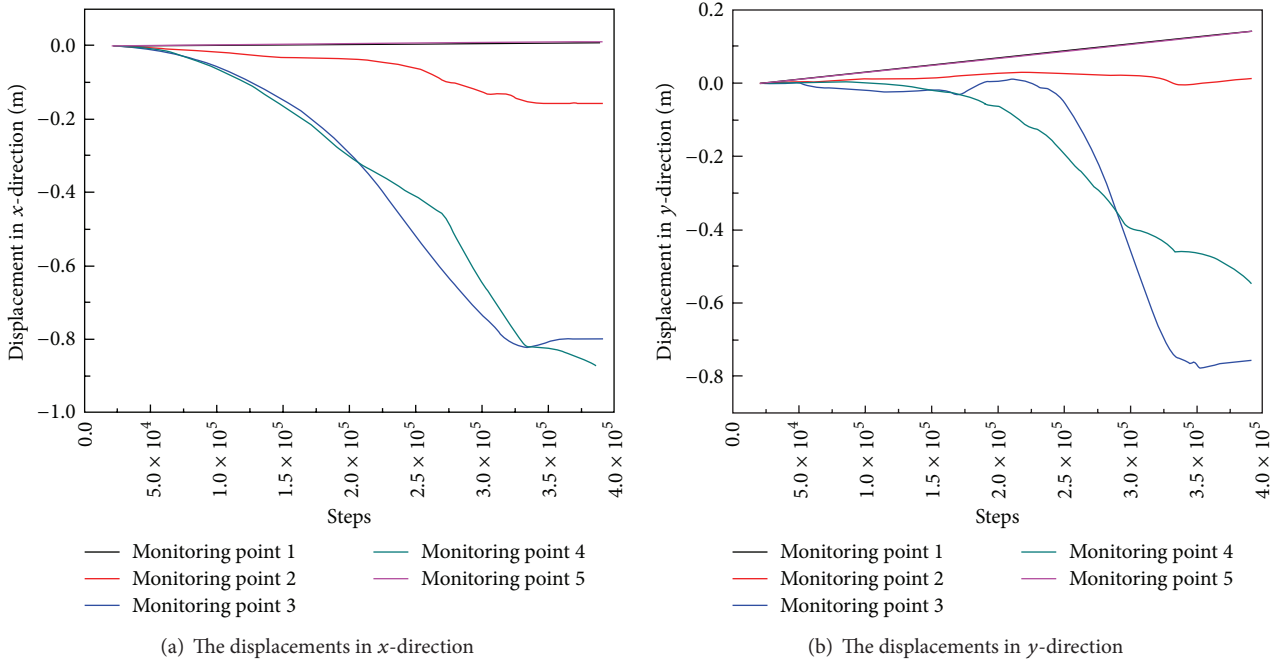


FIGURE 3: The displacement curves of 5 monitoring points at the right side.

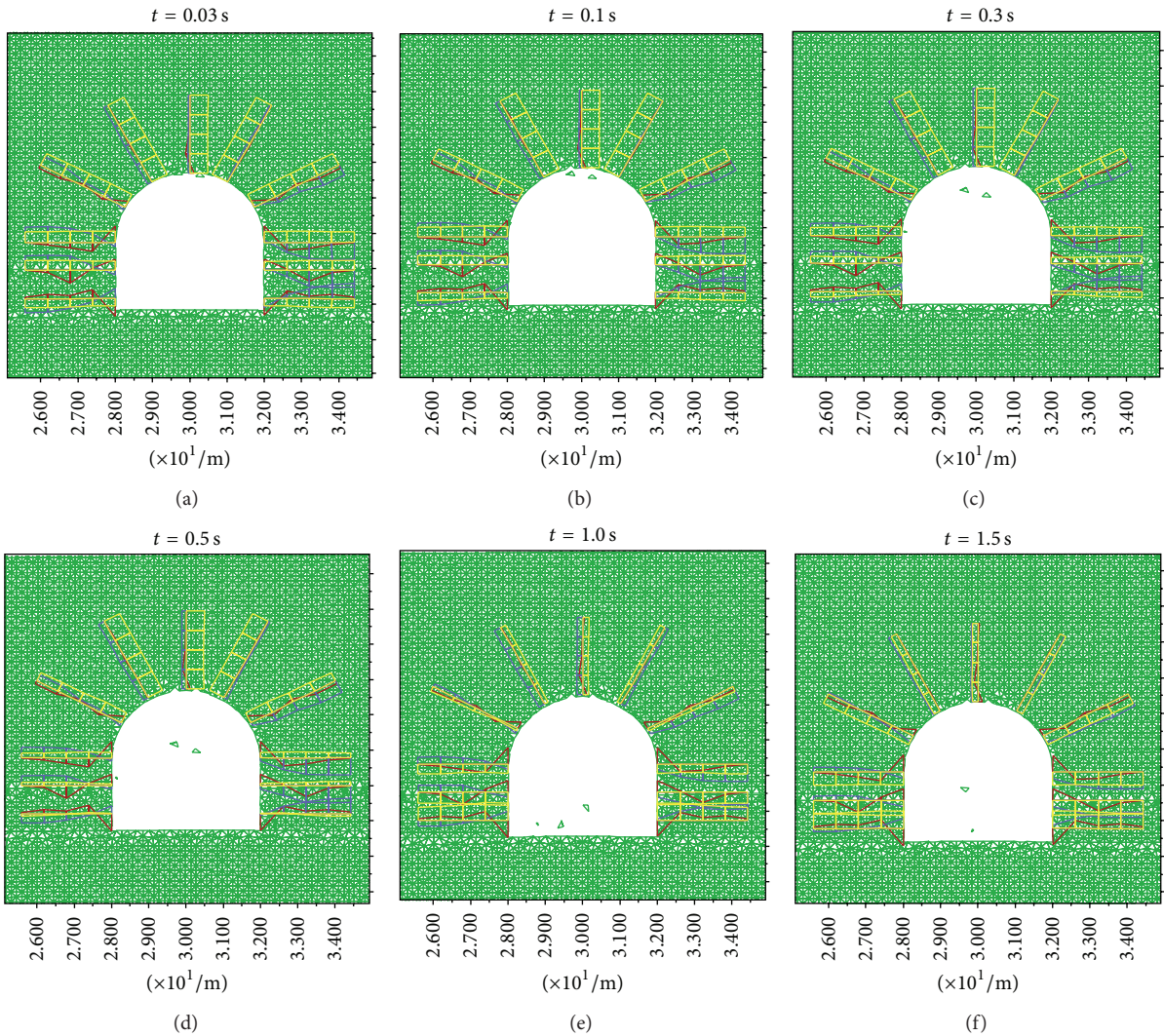


FIGURE 4: The disappearance of rockburst failure of roadway with bolt supporting.

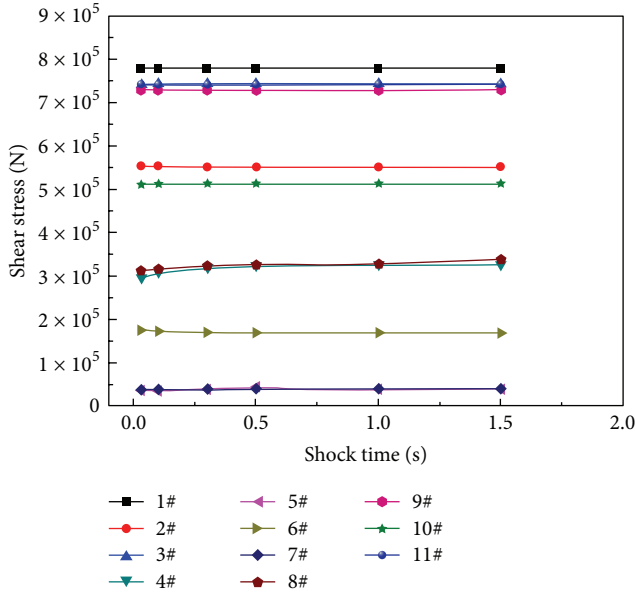


FIGURE 5: Shear stress curves with shock time of each bolt.

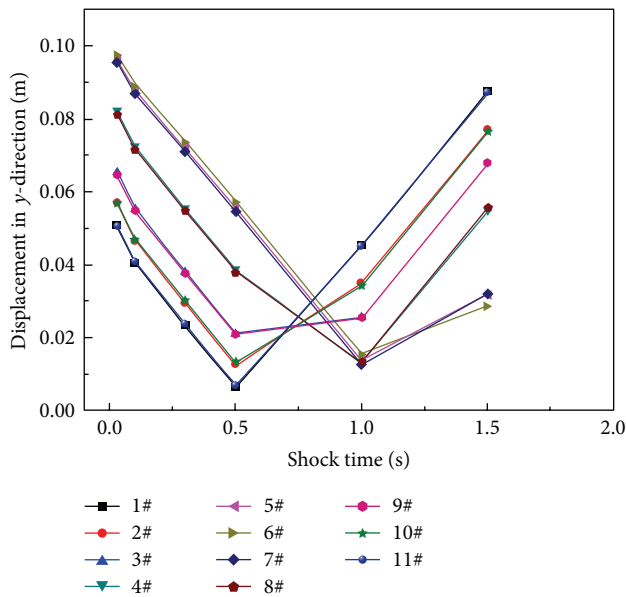


FIGURE 6: y -directional displacement curves with shock time of each bolt.

and thus the dominant frequency of the residual shock wave is higher than the natural vibration frequency. Therefore, the resonant effect does not occur, and rockburst failure of roadway is also not induced. In addition, if the resonant frequency of the surrounding rock increases by relief-shots, the dominant frequency of residual shock wave will be smaller than resonant frequency of roadway, and thus both resonant effect and rockburst do not occur. In conclusion, without bolt supporting, the resonant effect of roadway will induce rockburst failure of surrounding rock. When roadway is reinforced by bolt supporting, its integrity and strength are enhanced, and the natural vibration frequency obviously reduces to avoid resonant effect. Therefore, under the certain

conditions, bolt supporting can improve the stability of surrounding rock and prevent the occurrence of rockburst.

3.3. Effect of Immediate Roof Thickness on Rockburst Failure of Roadway. To discover the influences of immediate roof thickness on propagation and attenuation characteristics of shock wave, we keep the mechanical parameters of rock strata unchanged, only adjust the thickness of immediate roof to be 2 m, 6 m, and 10 m, respectively, and analyze the deformation and failure characteristics of surrounding rock under the conditions of different immediate roof thickness.

According to the simulation results, under the conditions of the buried depth of 900 m and the cosine wave with peak stress of 20 MPa, when the immediate roof thickness is set to be 2 m, 6 m, and 10 m, respectively, the rockburst failure form of roadway is approximately the same and is similar with the original condition. Figure 7 shows the rockburst failure of roadway at $t = 0.3$ s and 0.5 s of shock wave acting time, respectively.

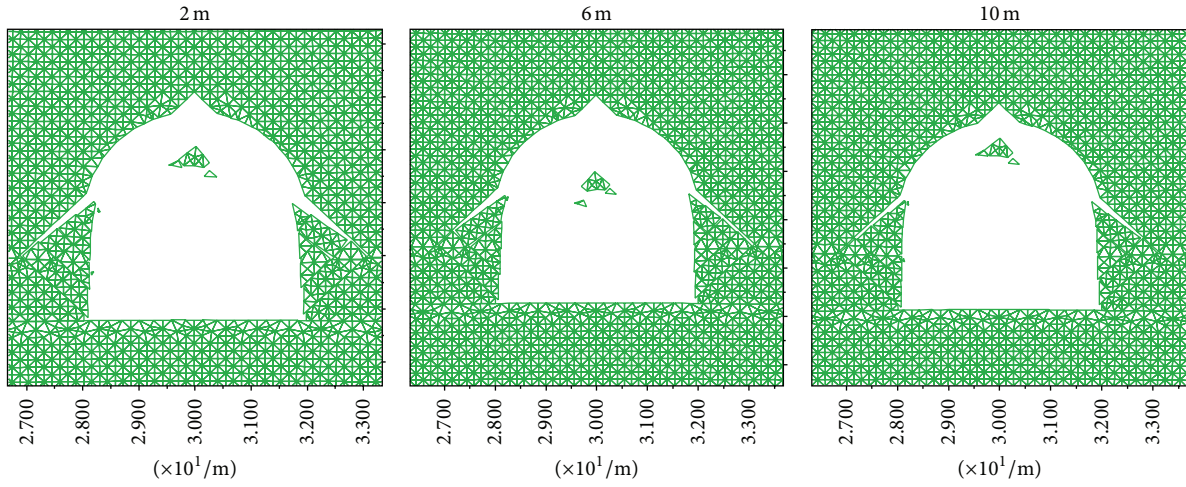
From Figure 7, it is well known that the smaller the immediate roof thickness is, the stronger rockburst failure intensity of roadway is. Based on the histogram of 1111(1) working face, the overlying two strata from downward to upward of 11^{-2} coal seam are mudstone with thickness of 10 m and finestone with thickness of 3.2 m, respectively. Based on the simulated fact that the total thickness of two strata is fixed, when the thickness of immediate roof mudstone decreases, the thickness of finestone will accordingly increase. Because the mechanical parameters of finestone are commonly larger than those of mudstone, the attenuation index of shock wave propagated in finestone is smaller compared with mudstone. So, under the condition of the same shock wave, the smaller the thickness of immediate roof mudstone is, the higher the residual shock wave intensity is and, accordingly, the stronger rockburst failure intensity of roadway is.

In summary, for the certain geological and mining conditions of 1111(1) working face, the smaller the immediate roof thickness is, the weaker the attenuation level of shock wave is, and the stronger rockburst failure of roadway is.

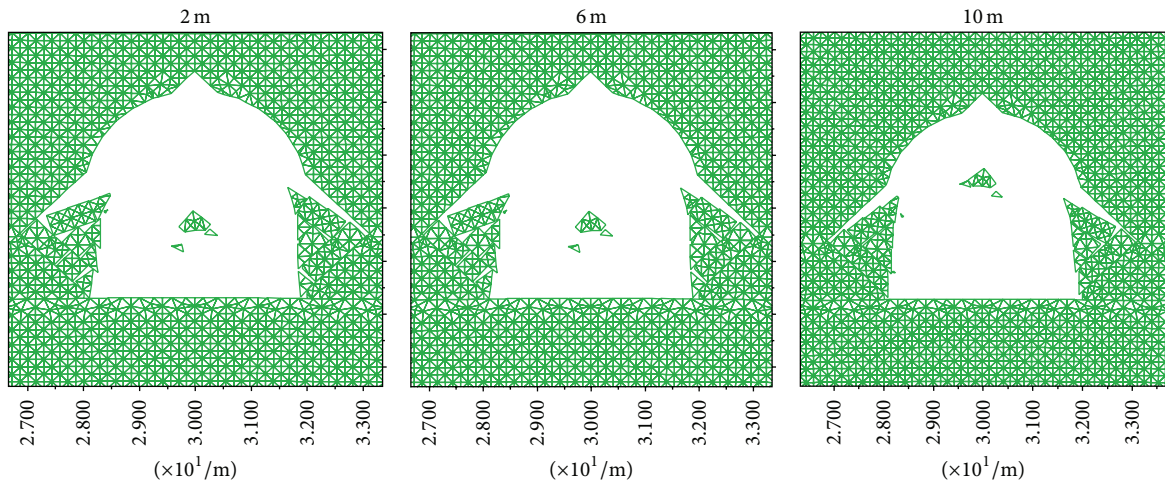
Figure 8 shows the changing curves of y -dimensional displacements of monitoring points 3 and 4.

From Figure 8, for the monitoring points 3 and 4 located at the right side of roadway, under the condition of the same calculation step, the displacement of immediate roof with thickness of 2 m is the largest, followed by immediate roof with thickness of 6 m, and the immediate roof with thickness of 10 m is the smallest. Based on the above-mentioned fact that the thickness of immediate roof mudstone is smaller and the corresponding thickness of overlying finestone is larger, due to the bigger mechanical parameters of finestone, the attenuation coefficient of shock wave propagated in overlying strata increases along with the increase of immediate roof thickness, and the intensity of residual shock wave decreases. Therefore, the displacement of surrounding rock of roadway will obviously reduce along with the increase of immediate roof thickness from 2 m to 10 m.

3.4. Effect of Immediate Roof Strength on Rockburst Failure of Roadway. To reveal the effect of immediate roof strength on

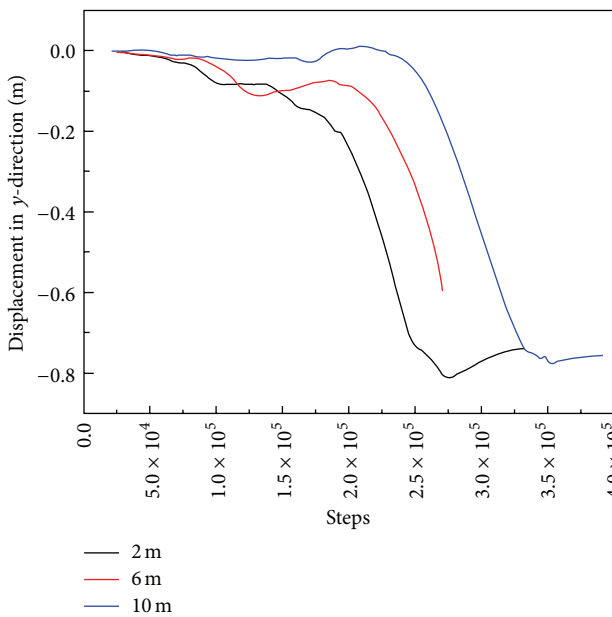


(a) The acting time of shock wave is $t = 0.3$ s

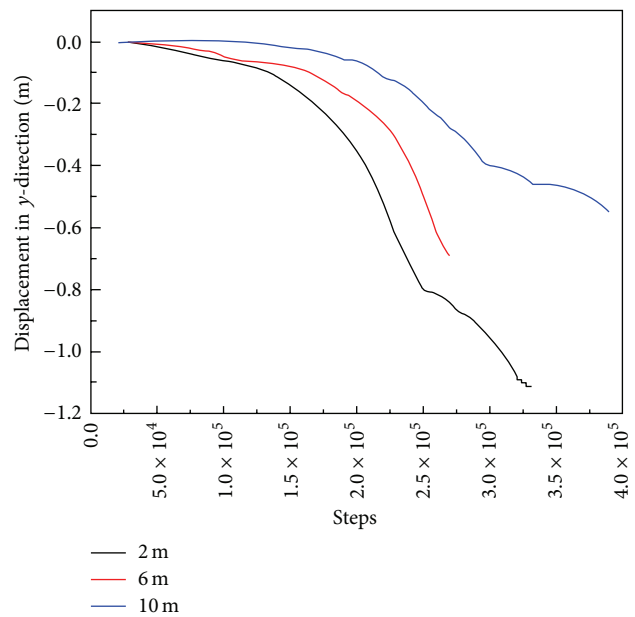


(b) The acting time of shock wave is $t = 0.5$ s

FIGURE 7: Rockburst failure of roadway at $t = 0.3$ s and 0.5 s of shock wave acting time. Note: 2 m, 6 m, and 10 m represent the immediate roof thickness, respectively.



(a) The y -dimensional displacement curves recorded by point 3



(b) The y -dimensional displacement curves recorded by point 4

FIGURE 8: The changing curves of y -dimensional displacements of monitoring points 3 and 4. 2 m, 6 m, and 10 m in legend represent the immediate roof thickness, respectively.

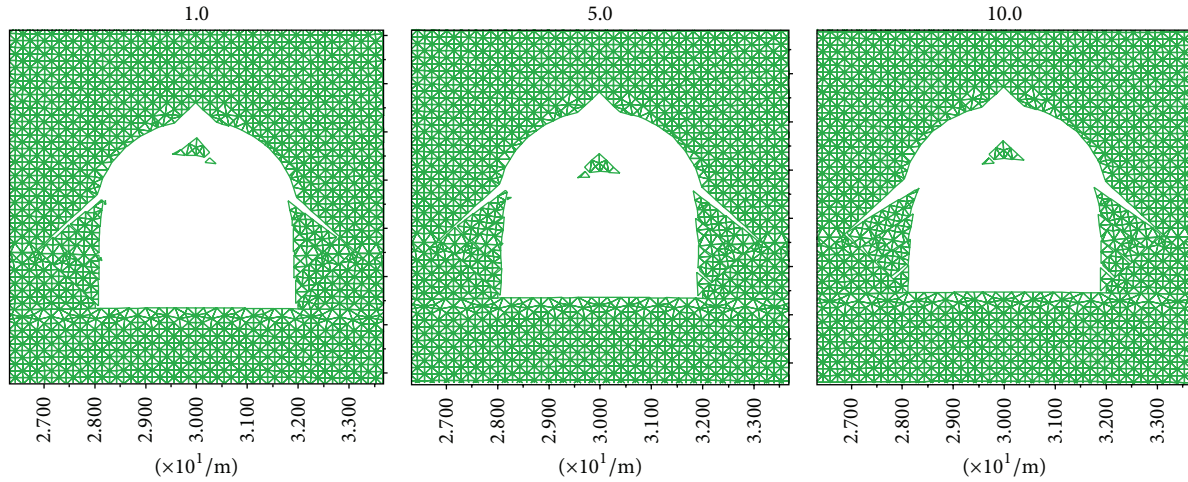
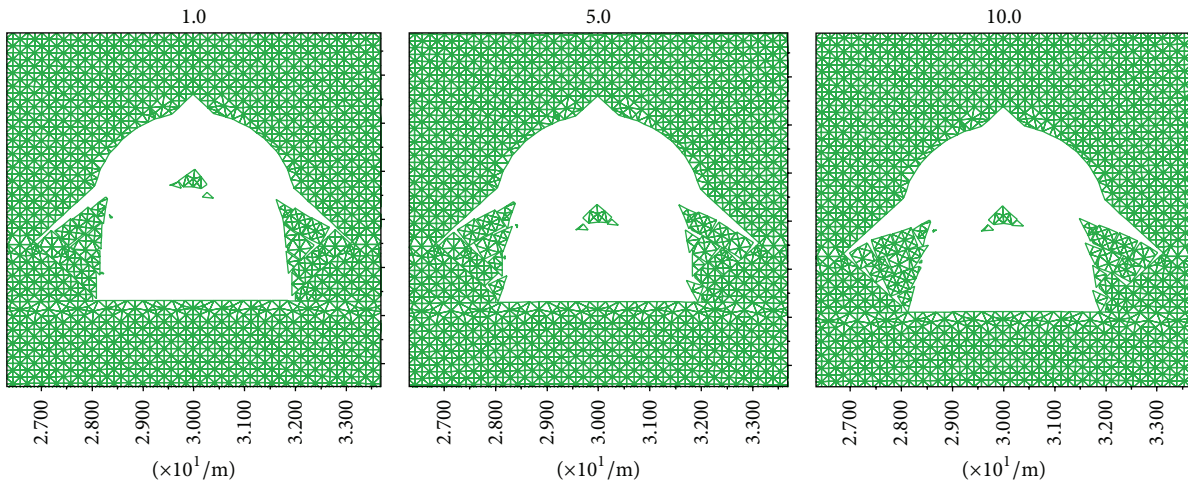
(a) The acting time of shock wave is $t = 0.3$ s(b) The acting time of shock wave is $t = 0.5$ s

FIGURE 9: Rockburst failure of roadway at $t = 0.3$ s and 0.5 s of shock wave acting time. Note: the numbers of 1.0, 5.0, and 10.0 m represent the multiple of the original uniaxial tensile strength of immediate roof, respectively.

attenuation characteristics of shock wave, we maintain the thickness of overlying roof strata unchanged, only adjust the uniaxial tensile strength of immediate roof mudstone to be 5 times and 10 times of the original value, respectively, and analyze the deformation and failure of roadway under the conditions of different immediate roof strength.

According to the simulation results, under the conditions of the buried depth of 900 m and the cosine wave with peak stress of 20 MPa, when the uniaxial tensile strength of immediate roof is set to be the original value, 5 times and 10 times of the original value, respectively, the rockburst failure form of roadway is basically the same and is similar to the original condition. Figure 9 shows the rockburst failure of roadway at $t = 0.3$ s and 0.5 s of shock wave acting time, respectively.

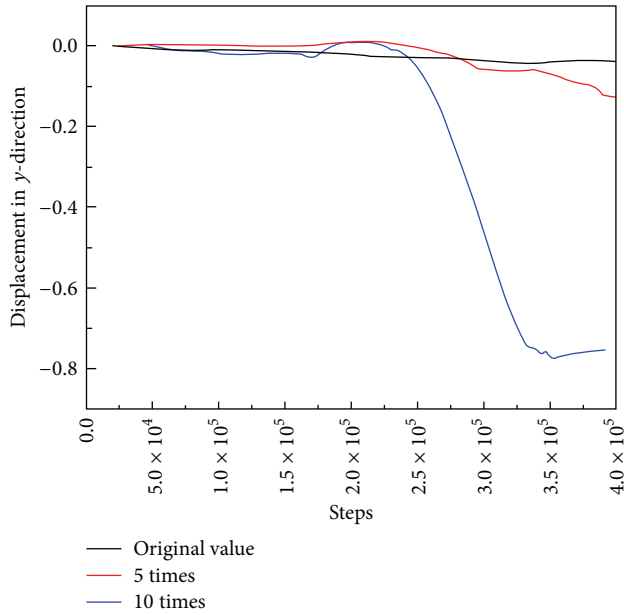
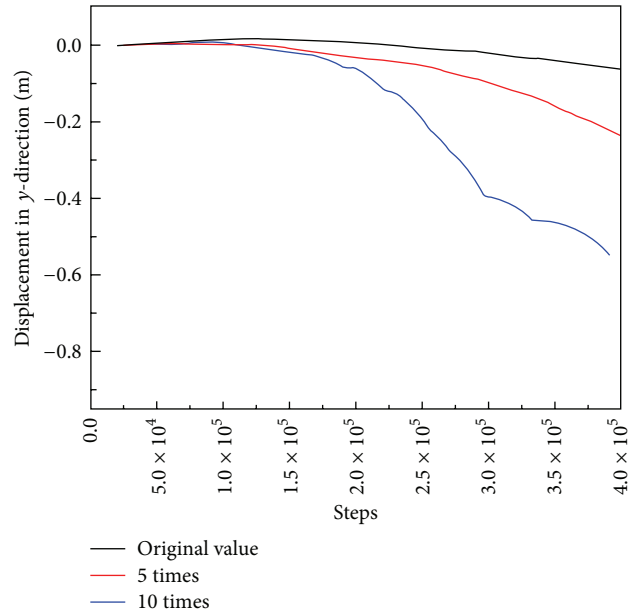
From Figure 9, it is well known that the smaller the uniaxial tensile strength of immediate roof is, the weaker the rockburst failure intensity of roadway is. The evident reason is that the attenuation index of shock wave gradually reduces

with the increase of immediate roof strength. Therefore, the dynamic stress of surrounding rock of roadway will rise along with the increase of immediate roof strength, and thus rockburst is easily triggered. Meanwhile, when the strength of immediate roof increases, it will be easier to accumulate a large amount of elastic energy in surrounding rock. Once the stored energy reaches or exceeds its limit, rockburst failure of roadway will inevitably occur.

In summary, for the certain geological and mining conditions of III(1) working face, the smaller the immediate roof strength is, the larger the attenuation index of shock wave is and thus the weaker rockburst failure intensity of roadway is.

Figure 10 shows the changing curves of y -dimensional displacements of monitoring points 3 and 4.

From Figure 10, it is obviously shown that the displacement of surrounding rock significantly rises along with the increase of uniaxial tensile strength of immediate roof. Due to the decreasing attenuation index of shock wave with the increase of immediate roof strength, the residual

(a) The y -dimensional displacement curves recorded by point 3(b) The y -dimensional displacement curves recorded by point 4FIGURE 10: The changing curves of y -dimensional displacements of monitoring points 3 and 4.

shock wave intensity will significantly improve, and thus the displacement of surrounding rock rapidly rises. Ultimately, the rockburst failure is easily induced.

4. Conclusions

- (1) For roadway without bolt support, due to the small mechanical parameters of interface between coal seam and its overlying stratum, the coal and rock mass will eject outward mainly from the interface once rockburst induced by shock wave occurs.
- (2) For roadway with bolt support, its integrity and strength are obviously enhanced, and the natural vibration frequency of surrounding rock significantly reduces to avoid the resonant effect triggering rockburst.
- (3) The smaller the immediate roof thickness is, the higher the intensity of the residual shock wave is and, accordingly, the stronger rockburst failure intensity of roadway is. Moreover, the displacement of roadway obviously reduces with the increase of immediate roof thickness.
- (4) The attenuation index of shock wave gradually reduces with the increase of immediate roof strength, and the dynamic stress accretion of surrounding rock correspondingly rises, and thus rockburst failure is easily triggered. In other words, the higher the immediate roof strength is, the stronger rockburst failure of roadway is.

Conflict of Interests

The authors declare that there is no conflict of interests regarding the publication of this paper.

Acknowledgments

The authors gratefully wish to acknowledge the collaborative funding support from the Foundation for the Author of National Excellent Doctoral Dissertation of PR China (201167), the Fundamental Research Funds for the Central Universities (2014XT01), the Open Research Program of Key Laboratory of Safety and High-Efficiency Coal Mining, Ministry of Education (Anhui University of Science and Technology) (JYBSYS2014203), and a Project Funded by the Priority Academic Program Development of Jiangsu Higher Education Institutions (PAPD).

References

- [1] L.-M. Dou and X.-Q. He, *Theory and Technique on Rockburst Prevention*, China University of Mining & Technology Press, Xuzhou, China, 2001.
- [2] L.-M. Dou and C.-G. Zhao, *Mining-Induced Rockburst Disaster Prevention*, China University of Mining & Technology Press, Xuzhou, China, 2006.
- [3] H. Qin and X.-B. Mao, "Numerical simulation of stress wave induced rockburst," *Journal of Mining & Safety Engineering*, vol. 25, no. 2, pp. 127–131, 2008.
- [4] M.-S. Gao, L.-M. Dou, N. Zhang, Z.-L. Mu, K. Wang, and B.-S. Yang, "Experimental study on earthquake tremor for transmitting law of rockburst in geomaterials," *Chinese Journal of Rock Mechanics and Engineering*, vol. 26, no. 7, pp. 1365–1371, 2007.

- [5] D. E. Grady and M. E. Kipp, "The micromechanics of impact fracture of rock," *International Journal of Rock Mechanics and Mining Sciences*, vol. 16, no. 5, pp. 293–302, 1979.
- [6] X. B. Zhao, J. Zhao, J. G. Cai, and A. M. Hefny, "UDEC modelling on wave propagation across fractured rock masses," *Computers and Geotechnics*, vol. 35, no. 1, pp. 97–104, 2008.
- [7] D. H. Park and S. W. Jeon, "Reduction of blast-induced vibration in the direction of tunneling using an air-deck at the bottom of a blasthole," *International Journal of Rock Mechanics and Mining Sciences*, vol. 47, no. 5, pp. 752–761, 2010.
- [8] O. Uysal, K. Erarslan, M. A. Cebi, and H. Akcakoca, "Effect of barrier holes on blast induced vibration," *International Journal of Rock Mechanics and Mining Sciences*, vol. 45, no. 5, pp. 712–719, 2008.
- [9] Z.-H. Li, L.-M. Dou, C.-P. Lu, A.-Y. Cao, M.-W. Zhang, and J. He, "Frequency spectrum analysis on micro-seismic signal of similar simulation test of fault rock burst," *Journal of Shandong University of Science Technology*, vol. 29, no. 4, pp. 51–56, 2010.
- [10] E. T. Brown, J. Bray, and C. Bray, *Analytical and Computational Methods in Engineering Rock Mechanics*, Allen and Unwin, London, UK, 1987.
- [11] M. Schoenberg, "Elastic wave behaviour across linear slip interfaces," *Journal of the Acoustical Society of America*, vol. 68, no. 5, pp. 1516–1521, 1980.
- [12] L. J. Pyrak-Nolte, L. R. Myer, and N. G. W. Cook, "Transmission of seismic waves across single natural fractures," *Journal of Geophysical Research*, vol. 95, no. 6, pp. 8617–8638, 1990.
- [13] S. Nakagawa, K. T. Nihei, and L. R. Myer, "Shear-induced conversion of seismic waves across single fractures," *International Journal of Rock Mechanics and Mining Sciences*, vol. 37, no. 1-2, pp. 203–218, 2000.
- [14] B. Gu, R. Suárez-Rivera, K. T. Nihei, and L. R. Myer, "Incidence of plane waves upon a fracture," *Journal of Geophysical Research B: Solid Earth*, vol. 101, no. 11, pp. 25337–25346, 1996.
- [15] L. J. Pyrak-Nolte and D. D. Nolte, "Wavelet analysis of velocity dispersion of elastic interface waves propagating along a fracture," *Geophysical Research Letters*, vol. 22, no. 11, pp. 1329–1332, 1995.
- [16] J.-G. Cai and J. Zhao, "Effects of multiple parallel fractures on apparent attenuation of stress waves in rock masses," *International Journal of Rock Mechanics and Mining Sciences*, vol. 37, no. 4, pp. 661–682, 2000.
- [17] J. Zhao, X. B. Zhao, and J. G. Cai, "A further study of P-wave attenuation across parallel fractures with linear deformational behaviour," *International Journal of Rock Mechanics and Mining Sciences*, vol. 43, no. 5, pp. 776–788, 2006.
- [18] J. Zhao, J.-G. Cai, X.-B. Zhao, and H.-B. Li, "Experimental study of ultrasonic wave attenuation across parallel fractures," *Geomechanics and Geoengineering*, vol. 1, no. 2, pp. 87–103, 2006.
- [19] Itasca, *UDEC User's Manual*, Itasca Consulting Group, Minneapolis, Minn, USA, 1996.
- [20] B. H. Brady, S. H. Hsiung, A. H. Chowdhury, and J. Philip, "Verification studies on the UDEC computational model of jointed rock," *International Journal of Rock Mechanics and Mining Sciences & Geomechanics Abstracts*, vol. 29, pp. 551–558, 1992.
- [21] S. M. Day, "Test problem for plane strain block motion codes," S-Cubed Memorandum to Itasca, 1985.
- [22] F. Gao, D. Stead, and J. Coggan, "Evaluation of coal long-wall caving characteristics using an innovative UDEC Trigon approach," *Computers and Geotechnics*, vol. 55, pp. 448–460, 2014.

Research Article

Distribution of Side Abutment Stress in Roadway Subjected to Dynamic Pressure and Its Engineering Application

Yao Qiangling,^{1,2} Zhou Jian,^{1,2} Li Yanan,^{1,2} Tan Yingming,^{1,2} and Jiang Zhigang^{1,2}

¹School of Mines, China University of Mining and Technology, Xuzhou 221008, China

²Key Laboratory of Deep Coal Resource Mining, CUMT, Ministry of Education, Xuzhou 221008, China

Correspondence should be addressed to Zhou Jian; zhou136090@126.com

Received 12 September 2014; Accepted 20 December 2014

Academic Editor: Shimin Liu

Copyright © 2015 Yao Qiangling et al. This is an open access article distributed under the Creative Commons Attribution License, which permits unrestricted use, distribution, and reproduction in any medium, provided the original work is properly cited.

The borehole stress-meter was employed in this study to investigate the distribution of the side abutment stress in roadway subjected to dynamic pressure. The results demonstrate that the side abutment stress of the mining roadway reaches a peak value when the distance to the gob is 8 m and the distribution curve of the side abutment stress can be divided into three zones: stress rising zone, stress stabilizing zone, and stress decreasing zone. Further numerical investigation was carried out to study the effect of the coal mass strength, coal seam depth, immediate roof strength, and thickness on the distribution of the side abutment stress. Based on the research results, we determined the reasonable position of the mining roadway and the optimal width of the barrier pillar. The engineering application demonstrates that the retention of the barrier pillar with a width of 5 m along the gob as the haulage roadway for the next panel is feasible, which delivers favorable technological and economic benefits.

1. Introduction

As the coal in a longwall panel is being extracted, the surrounding strata are forced to move toward and fill the voids left by the extracted coal [1]. This process induces a series of intensive activities which include movements of the overlying strata, abutment stress on both sides of the panel, abutment stress in front and rear of the panel, and the severe deformation of the adjacent roadways. A key issue in longwall mining is to understand the distribution characteristics of the abutment stress, including side abutment stress, front and rear abutment stress, providing some basis for the layout of the adjacent roadways.

Researches on the distribution characteristics of the abutment stress at a longwall mining face were done by a lot of scholars, achieving fruitful and useful results [2–7]. Zhang et al. (2011) studied the effects of coal hardness, coal seam thickness, and advancing speed of the panel on the position of the maximum abutment stress and obtained the empirical formulas used for determining the peak position [8]. Xu et al. (2012) studied the front abutment stress of a fully mechanized coalface of 11061 soft coal isolated islands of Liangbei Coal Mine using a self-developed mining-induced

stress monitoring system associated with electromagnetic radiation technology and discussed the effects of abutment stress distribution on strata behavior [9]. Qin and Wang analyzed and studied the distribution of abutment stress and its transmission law in floor at the fully mechanized caving face of isolated island in 4303 deep shaft of Dongtan Coal Mine [10]. Zhang et al. studied the distribution of lateral floor abutment stress at a working face. Firstly, they used elasticity theory to establish a distribution model of lateral floor abutment stress and then analyzed its distribution characteristics. Secondly, they established a three-dimensional numerical simulation model by using FLAC3D (ITASCA Consulting Group) software [11]. Whittaker and Potts (1974) developed an empirical approach to calculate the vertical stress ahead of the longwall face for rock conditions prevailing in the UK. In his approach, a yield zone exists ahead of the face. The vertical stress is zero both at the face and at the rib side. It increases quickly with the distance from the face [12].

Therefore, it is very important to make clear the distribution characteristics and scope of influence of the abutment stress, because it can provide the references for adopting reasonable supporting patterns, determining the position

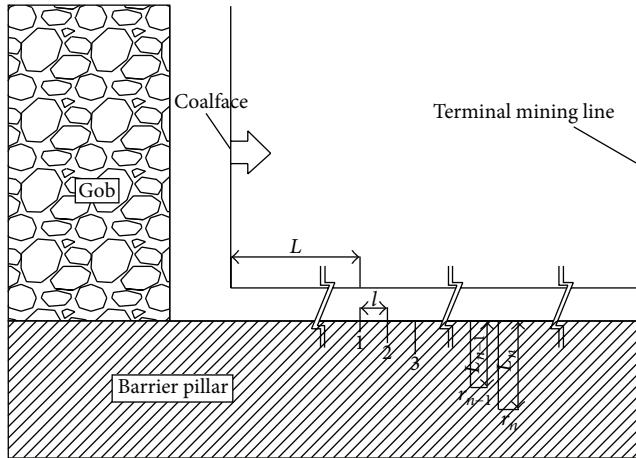
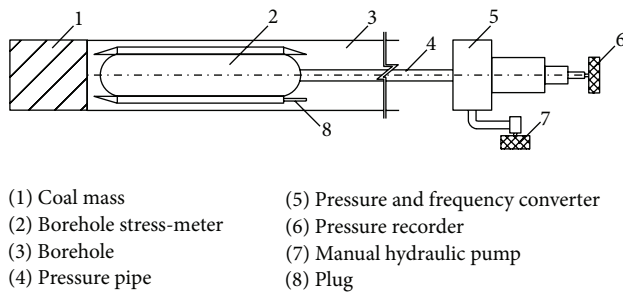


FIGURE 1: Layout of the side abutment stress observation station. L represents the distance of the first borehole stress-meter to the coalface, which should be larger than the scope of influence of the front abutment stress; r_n represents the number of the observation station; L_n represents the length of the borehole stress-meter, which is in general 1~2 m; l represents the space between the boreholes, which is in general 2~3 m.



(1) Coal mass
(2) Borehole stress-meter
(3) Borehole
(4) Pressure pipe
(5) Pressure and frequency converter
(6) Pressure recorder
(7) Manual hydraulic pump
(8) Plug

FIGURE 2: Installation drawing for the borehole stress-meter.

of the adjacent roadway, preventing the dynamic disasters induced by mining, and so forth. Some instruments and methods are adopted to investigate the distribution of the abutment stress [13, 14], of which borehole stress-meter is the most commonly used [15]. Thus, in this study, we firstly use the borehole stress-meter to monitor the distribution characteristics of the side abutment stress during the extraction of the longwall panel in Qianyingzi mine, China. Then we use the UDEC numerical simulation software to investigate the factors affecting the distribution of the side abutment stress. Based on the field monitoring and simulation results, we determined the reasonable layout position of the mining roadway and the optimal width of the barrier pillar between panels. Finally, a field application was carried out. The final engineering application further validates the reliability of the field monitoring and numerical simulation results. Therefore, this study could provide some beneficial references to the designing of the barrier coal pillar in roadway subjected to dynamic pressure.

2. Field Monitoring Principles and the Observation Instrument

2.1. Field Monitoring Principles for Side Abutment Stress. The borehole stress-meter is used to monitor the distribution of the abutment stress in roadway subjected to dynamic pressure. Firstly, we lay out the stress observation borehole in areas free from the impact of the moveable front abutment stress. The parameters of the boreholes mainly include space between the boreholes and depth of the borehole. Secondly, we install the stress-meters on these boreholes to monitor the stress changes with the advance of the coalface. The pressure recorder connected to the borehole stress-meter can record all the changes of the stress values, from which we can obtain the curve representing the relation between the side abutment stress and the distance to the gob. The layout of the side abutment stress observation station is illustrated in Figure 1. The specific number and depth of the boreholes are adjusted in line with the in situ geological settings.

As shown in Figure 1, r_n borehole stress-meter observation stations are laid out within the barrier pillar between panels. The specific numbers of the stations are closely related to the actual engineering requirements and the required precision of the acquired data. The boreholes in each observation station are installed with a stress-meter. The diameter of each borehole is 48 mm and the space between boreholes is 2 m. The borehole is perpendicular to the roadway rib with 1.5 m distance to the roadway floor.

2.2. Observation Instrument. The instruments used for monitoring the distribution of the side abutment stress mainly include the borehole stress-meter with a model number of KSE-II-1, the string wire pressure recorder with a model number of KSE-III, the steel wire data acquisition system with a model number of KSE-III, and the manual hydraulic pump. All of these instruments are made by Shandong Haozhou Mining Safety Equipment Corporation, China. The installation drawing for the borehole stress-meter is illustrated in Figure 2.

The installation steps for the observation instruments are as follows: (1) use the special drill rod to insert the plug (as shown in Figure 2) and slowly push the borehole stress-meter into the borehole; (2) connect the pressure pipe, the pressure and frequency converter, and manual hydraulic pump to the borehole stress-meter, respectively; (3) inject the oil into the borehole stress-meter through the manual hydraulic pump; during the injection, the pump pressure should be slowly increased until the borehole stress-meter fills the borehole; (4) the pump pressure should be continuously increased to make sure that the reading of the pressure gauge of the manual hydraulic pump stabilizes at a preset initial pressure value and maintains the value for 5~10 min; (5) release the pump pressure and observe the changes of the pressure gauge reading; if the reading cannot stabilize at the preset initial pressure value (for measuring the rising value of the abutment stress, the initial pressure is 4.0~5.0 MPa), then steps 3 and 4 should be repeated until the initial pressure reaches stable; (6) install and activate the pressure recorder to record the borehole stress values; the pressure recorder can record the

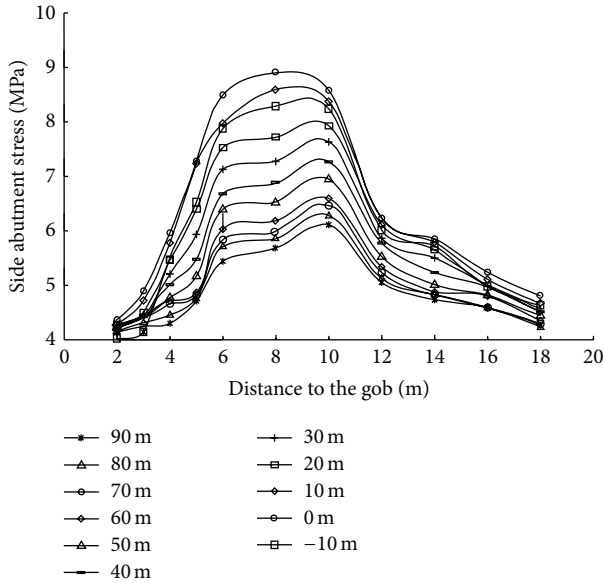


FIGURE 3: Measured curve of the distribution of the side abutment stress in Qianyingzi mine. In the figure: -10 m, 0 m, 10 m, . . . , 90 m represents the horizontal distance of the borehole stress-meter to the gob, respectively; the initial pressure of the borehole stress-meter is 4.0 MPa.

data automatically and the recording interval can be adjusted according to actual requirements. After the installation, the user should use the steel wire data acquisition system to gather the recorded data every day or every other day and import the acquired data to the computer for data processing.

3. Field Monitoring of the Side Abutment Stress

The borehole stress-meter was adopted to investigate the distribution of the side abutment stress in the 3₂12 coalface of Qianyingzi coal mine, China, where mining activity is carried out in the 3₂ coal seam. The characteristics of the coal seam are shown in Table 1.

In processing the acquired data, we plot the abutment stress obtained from the points with the same distance to the coalface in the seam plane in order to clearly present the distribution characteristics of the side abutment stress. Figure 3 shows the “side abutment stress versus distance to the gob” curve with the advance of the 3₂12 coalface. Due to the restrictions imposed by the coal seam strength and its intactness, the borehole stress-meter cannot reach the area where the stress is in a primitive state. Thus the pressure values presented in Figure 3 are relative values representing the rising side abutment stress. The significance of this curve lies in that it can help us to gain a better understanding of the distribution characteristics of the side abutment stress and to obtain some key parameters related to the side abutment stress, such as the stress rising zones at the coal wall side and the peak value of the side abutment stress, providing a basis for the retention of the barrier coal pillar between panels.

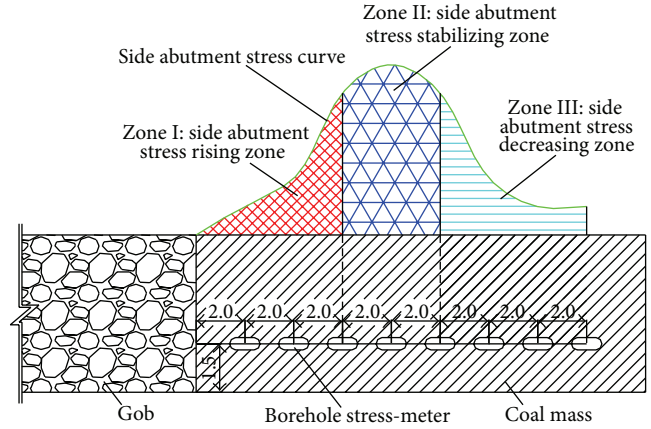


FIGURE 4: Zone chart of the distribution of the side abutment stress.

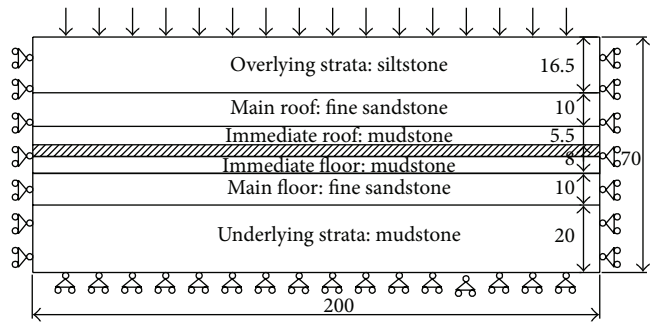


FIGURE 5: Numerical simulation model.

Figures 3 and 4 show the following. (1) With the advance of the coalface (the advancing direction can be referred to in Figure 1), the side abutment stress gradually increases; (2) Zone I, also termed pillar plastic zone, is 2~6 m in width, where the side abutment stress is on the rise; (3) Zone II, also called limit elastic zone, is 6~10 m in width, where the side abutment stress reaches stable; the side abutment stress reaches a peak value of 9.0 Mpa when the distance to the gob is 8 m; this should be taken into adequate consideration while laying out the roadway; (4) Zone III is in general 10 m away from the gob, where the side abutment stress is smaller than the peak value and gradually decreases until reaching the primitive stress; this zone is called side abutment stress decreasing zone.

4. Numerical Investigation into the Factors Affecting the Side Abutment Stress

Selecting the geological setting in Qianyingzi mine as the study site, we adopt the UDEC numerical simulation software to investigate the factors influencing the distribution characteristics of the side abutment stress. The numerical simulation model is illustrated in Figure 5. The physical and mechanical properties of various strata were initially acquired from drilling log and exploration results. Then, the borehole camera was employed to examine the integrity of the rock mass. The final simulation parameters in this study were

TABLE 1: Characteristics of the 3₂ coal seam.

Coal mine	Coal seam	Geologic age	Average depth/m	Average thickness/m	Roof and floor strata
Qianyingzi	3 ₂ seam	Permo-carboniferous period Lower Shihezi formation	600	3.3	Immediate roof: 4.3-meter-thick mudstone; Main roof: 11.5-meter-thick fine sandstone; Immediate floor: 2.9-meter-thick mudstone; Main floor: 9.5-meter-thick fine sandstone

TABLE 2: Physical and mechanical properties of various strata.

Stratum name	Rock type	Thickness/m	Bulk modulus/GPa	Shear modulus/GPa	Density/kg·m ⁻³	Friction angle/°	Cohesion/MPa	Tensile strength/MPa
Overlying strata	Siltstone	16.5	8.4	4.8	2450	32	5.6	3.6
Main roof	Fine sandstone	10	10	5.8	2580	38	7.8	4.5
Immediate roof	Mudstone	5.5	3.2	2.5	2460	32	2.6	2.8
Coal seam	Coal	3.5	2.3	1.2	1340	24	1.6	2
Immediate floor	Mudstone	4.5	2.8	1.5	2480	28	3.5	4.2
Main floor	Fine sandstone	10	5.2	2.3	2520	28	9.6	3.8
Underlying strata	Mudstone	20	4.7	2.7	2500	30	7.5	1.6

determined from the experience of Shen (2014) and Gao et al. (2014), which are given in Table 2 [16, 17].

Considering the speed of the numerical calculation, we reasonably simplify the model size in order to slash the calculation time. Based on the engineering experience, we select a reasonable influencing depth and width and determine the model size as 200 × 70 m, as shown in Figure 5. As we mentioned before, the coal seam has a depth of 600 m. Thus an equivalent vertical stress of 15.0 MPa is applied to the upper boundary of the model. The left, right, and bottom boundary are all fixed. So they have no vertical velocity and vertical displacement. The constitutive relation used in this model is Mohr-Coulomb model. During the simulation, the panel is stepwise excavated, with the excavation step being 4 m, which could effectively simulate the progressive caving of the overlying strata. We establish this model in an attempt to investigate the distribution characteristics of the side abutment stress with the advance of the former panel and compare the abutment stress before mining and after mining, thus providing some basis for the designing of the roadway subjected to dynamic pressure.

Previous studies demonstrate that [15, 18, 19] factors that heavily influence the distribution characteristics of the side abutment stress mainly include coal mass strength, coal seam depth, immediate roof strength and thickness, and breakage position of the main roof. In addition, key parameters that are commonly used to represent the distribution characteristics of the side abutment stress generally include the position and

magnitude of the peak stress and the stress concentration coefficient and the scope of influence of the stress.

4.1. Influences of the Coal Mass Strength. In terms of its strength, the coal mass can be divided into three categories: soft coal, medium hard coal, and hard coal [20]. This classification has gained wide recognition and practicality in China. The mechanical parameters for the coal of different category are shown in Table 3. These parameters are in line with Mohr-Coulomb criterion, which are used by most of the scholars and can still reflect the essence of the research problem. The parameters for other strata are given in Table 2. The distributions of the side abutment stress for soft coal, medium hard coal, and hard coal are illustrated in Figure 6.

Figure 6 shows that (1) the strength of the coal mass exerts a significant influence on the position of the peak value of the side abutment stress, while having no pronounced impact on its peak value and the influence of scope; (2) for the hard coal, the stress reaches a peak value when the distance to the gob is 7.2 m, while it is 9.2 m and 16.5 m for the medium hard coal and soft coal, increasing 27.8% and 129.2%, respectively; (3) the lower the coal mass strength, the larger the stress decreasing zone in the solid coal mass; the stress decreasing zone is caused by the side abutment stress during the advance of the former panel; (4) the width of the stress decreasing zone for soft coal is 6 times larger than that for hard coal, indicating the significant influences of the coal mass strength on the layout of the mining roadway.

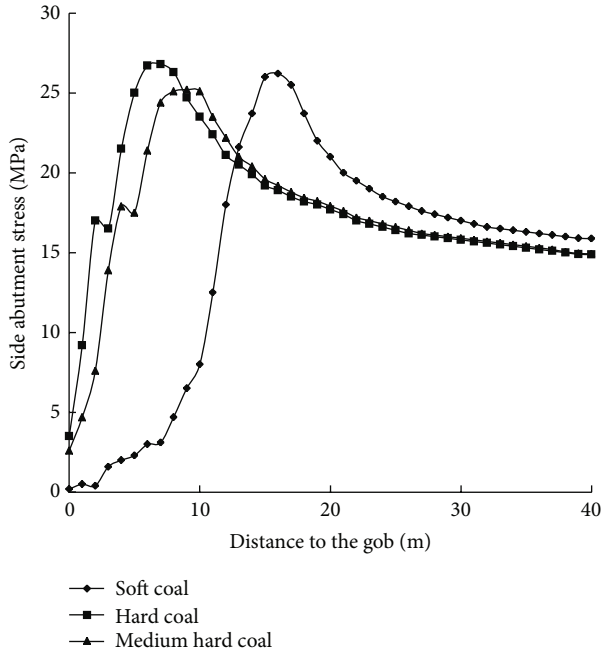


FIGURE 6: Distribution of the side abutment stress for coal of different category.

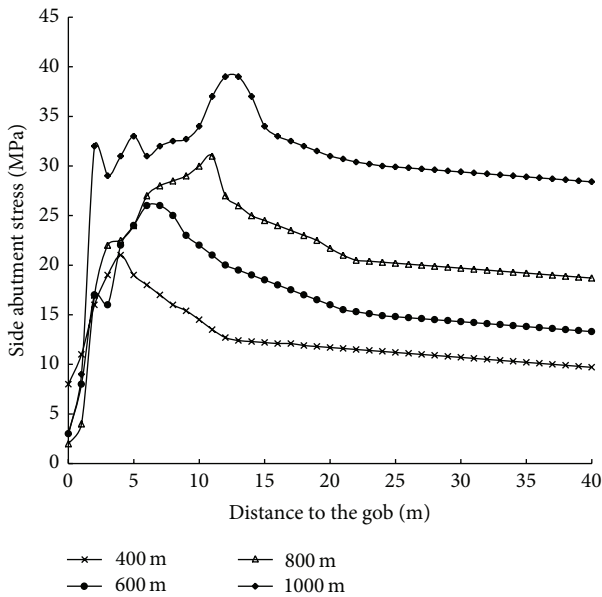


FIGURE 7: Distribution of the side abutment stress for coal seams with different depth.

4.2. *Influences of the Coal Seam Depth.* The average depth of the coal mines in China is about 600 m, with the deepest reaching 1400 m. In addition, coal mines in China are advancing to the deep area with a speed of 8~12 m per year [21, 22]. We select the representative depth of the coal seam in this study as 400 m, 600 m, and 1000 m, respectively. The distribution of the side abutment stress for coal seams with different depth is shown in Figure 7.

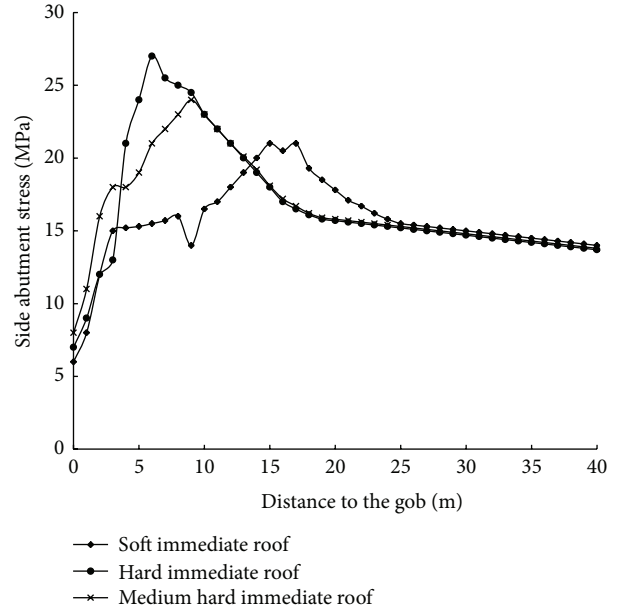


FIGURE 8: Distribution of the side abutment stress for the immediate roof with different strength.

Figure 7 shows that (1) with the increase of the depth, both the position and value of the peak stress have changed; (2) when the depth of the coal seam is 400 m, 600 m, 800 m, and 1000 m, the concentration coefficient of the corresponding side abutment stress is 2.2, 1.78, 1.62, and 1.59, respectively, demonstrating a decreasing trend; the position of the corresponding peak stress is 5.0 m, 7.5 m, 10 m, and 10 m to the gob, respectively.

4.3. *Influences of the Immediate Roof Strength and Thickness*

4.3.1. *The Strength of the Immediate Roof.* The physical and mechanical properties of other strata remain unchanged, which can be referred to in Table 2. Table 4 shows the physical and mechanical properties of the immediate roof. Selection of these parameters is in line with the Mohr-Coulomb criteria. Then we run the numerical simulation to investigate the influences of the changes of the immediate roof strength on the distribution characteristics of the side abutment stress. The distribution of the side abutment stress for the immediate roof with different strength is illustrated in Figure 8.

Figure 8 shows that (1) with the change from the hard immediate roof to soft immediate roof, the value of the peak side abutment stress gradually diminishes with the position of the peak stress getting away from the gob; (2) when the immediate roof is soft rock, medium hard rock, and hard rock, the distance of the position of the peak stress to the coal wall at the gob is 12.3 m, 9.2 m, and 5.2 m, respectively, demonstrating a decreasing trend; compared to the hard immediate roof, this distance for the soft immediate roof and medium hard immediate roof increases to 136.5% and 76.9%, respectively; (3) when the immediate roof is soft rock, medium hard rock, and hard rock, the concentration coefficient of the corresponding side abutment stress is 1.51,

TABLE 3: Mechanical parameters for the coal of different category.

Category	Bulk modulus/GPa	Shear modulus/GPa	Friction angle/ $^{\circ}$	Cohesion/MPa	Tensile strength/MPa
Soft coal	1.4	0.8	22	1.2	1.6
Medium hard coal	2.3	1.2	24	1.6	2
Hard coal	4.8	2.5	32	4.6	3.2

TABLE 4: Physical and mechanical properties of the immediate roof with different strength.

Category	Bulk modulus/GPa	Shear modulus/GPa	Friction angle ($^{\circ}$)	Cohesion/MPa	Tensile strength/MPa
Soft immediate roof	1.8	1.2	28	1.8	1.2
Medium hard immediate roof	3.2	2.5	32	2.6	2.8
Hard immediate roof	6.4	3.6	35	3.6	3.2

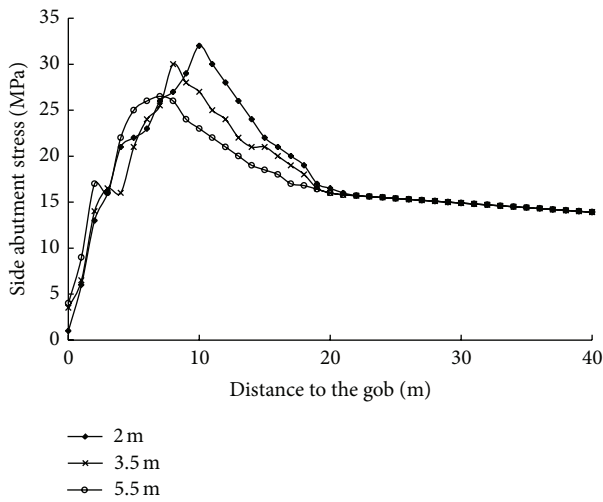


FIGURE 9: Distribution of the side abutment stress for the immediate roof with different thickness.

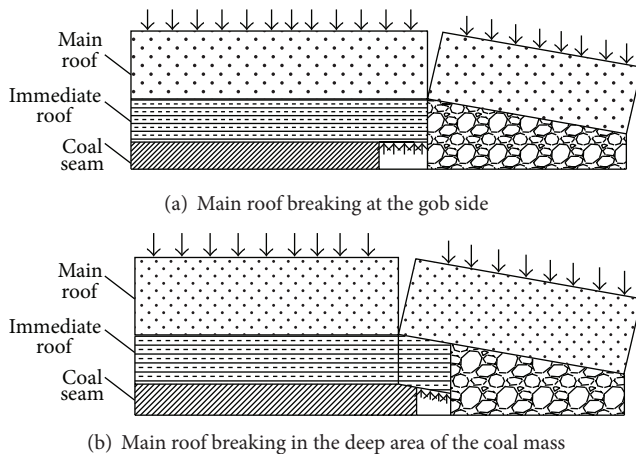


FIGURE 10: Schematic diagram of the breakage position of the main roof.

1.63, and 1.82, respectively, signifying an increasing trend; compared to the soft immediate roof, the concentration coefficient for the medium hard immediate roof and hard immediate roof increases to 7.9% and 20.5%, respectively.

4.3.2. The Thickness of the Immediate Roof. According to the geological characteristics of the immediate roof in China, we select the representative thickness of the immediate roof in this study as 2 m, 3.5 m, and 5.5 m, respectively. Then we run the numerical simulation to investigate the influences of the thickness of the immediate roof on the distribution characteristics of the side abutment stress. The distribution of the side abutment stress for the immediate roof with different thickness is illustrated in Figure 9.

Figure 9 shows that (1) with the increase of the thickness of the immediate roof, the distance of the position of the peak side abutment stress to the coal wall at the gob increases, while the value of the peak side abutment stress decreases; (2) when the thickness of the immediate roof is 2 m, 3.5 m, and 5.5 m, the distance of the peak side abutment stress to the gob is 10.3 m, 8.2 m, and 7.2 m, respectively, and the corresponding concentration coefficient for the side abutment stress is 2.1, 2.0, and 1.78, showing a decreasing trend.

4.4. Influences of the Breakage Position of the Main Roof. According to the field monitoring results of the hydraulic support pressure, we get to know that the breakage position of the main roof after the extraction of the coalface is roughly divided into two kinds, the main roof breaking at the gob side and the main roof breaking in the deep area of the coal mass, as shown in Figure 10. Then, we split the grid blocks based on the field monitoring results when we construct the simulation model, which could control the breakage position of the main roof. The distribution of the side abutment stress for the main roof with different breakage position is illustrated in Figure 11.

Figure 11 shows that the breakage position of the main roof exerts minor influences on the peak value of the side abutment stress. When the main roof breaks at the gob side, the distance of the position of the peak side abutment stress to the gob is further compared to the main roof breaks in the deep area of the coal mass, indicating that the width of the stress decreasing zone is larger. Based on the above results, we summarize the factors affecting the distribution of the side abutment stress, as shown in Table 5.

5. Engineering Application

5.1. Description of the Study Site. The 3₂14 coalface is 235 m on its dip and 2036 m on its strike. The haulage roadway is

TABLE 5: Factors affecting the distribution of the side abutment stress.

Influential factor	Position of the peak side abutment stress	Peak value of the side abutment stress	Scope of influence of side abutment stress	Stress concentration coefficient
Coal strength	Inverse ratio	Minor influence	Minor influence	Minor influence
Breakage position of the main roof	Minor influence	Minor influence	Minor influence	Minor influence
Depth	Direct ratio	Direct ratio	Minor influence	Inverse ratio
Immediate roof strength	Inverse ratio	Direct ratio	Minor influence	Direct ratio
Immediate roof thickness	Inverse ratio	Inverse ratio	Minor influence	Inverse ratio

Note: the position of the peak side abutment stress refers to the distance of the side abutment stress to the gob.

laid out along the gob of the 3_214 coalface, as illustrated in Figure 12. The average depth of the haulage roadway is 600 m and mining activity is carried out on the 3_2 coal seam. The 3_2 coal seam belongs to the semibright vitrain, with an average thickness of 3.3 m. The barrier pillar was previously designed as 30 m in width. In order to improve the recovery ratio of the coal resources and to mitigate the tension of the mining plan for the next panel, we propose the idea of retaining the narrow coal pillar through gob-side entry driving and put it into an engineering practice.

5.2. Designing of the Barrier Pillar between Panels

5.2.1. Layout of the Reasonable Position of the Barrier Pillar.

In general, the retaining width of the barrier pillar is related to the seam thickness, seam depth, and its roof and floor properties. For the present, most of the countries engaged in coal mining retain the barrier pillar with a width of 25~35 m [23]. The theoretical foundation lies in the fact that when laying out the roadway for the next panel the roadway is out of the influence scope of the abutment stress induced by the former panel, which could not only control the safety and stability of the roadway but also effectively prevent the occurrences of gob water and gas hazards.

However, in China, numerous practices demonstrate that it is feasible for driving the roadway by retaining the narrow coal pillar with a width of 3~5 m along the gob. Figure 4 shows that Zone I is the side abutment stress rising zone. Numerical studies prove that the width of this zone is related to the coal strength, coal seam depth, and immediate roof strength. Zone III is the side abutment stress decreasing zone, which is beneficial to the layout of the mining roadway. After adopting reasonable support pattern, roadway laid out in this zone can be effectively controlled during its service life.

5.2.2. Designing of the Width of the Barrier Pillar. The strain of the coal mass on the strike of the panel can be ignored due to the fact that the length of the panel on its strike is far larger than the width of the mining-induced fracture zone and plastic zone within the coal mass. Thus the stress state of the microunits within the fracture zone and plastic zone can be reduced to a plane stress problem. Figure 13 illustrates the mechanical model for the stress analysis.

Under the action of the side abutment stress, the coal mass has the tendency of being extruded towards the roadway with respect to the roof and floor. Therefore, the shear

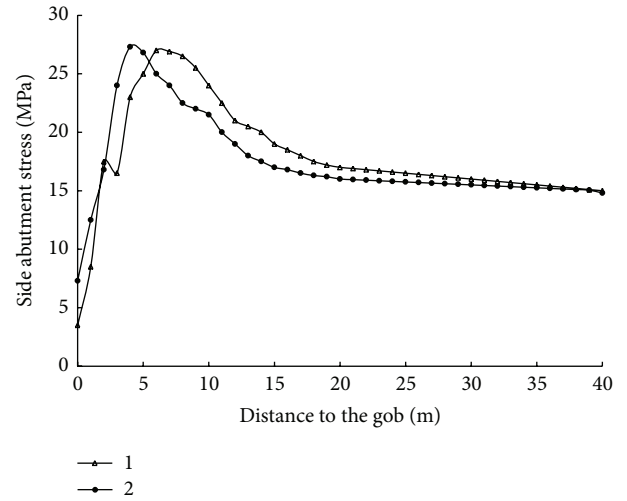


FIGURE 11: Distribution of the side abutment stress for the main roof with different breakage position. 1—main roof breaking in the deep area of the coal mass; 2—main roof breaking at the gob side.

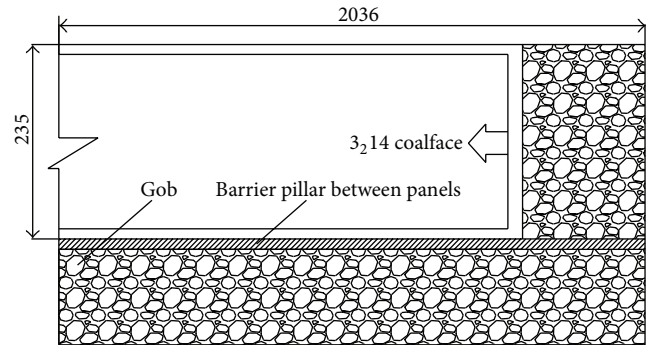


FIGURE 12: Layout of the 3_214 coalface and relevant roadways.

between the roof and floor interface could result in the sliding failure of the coal mass. The relation between the normal stress and the shear stress can be expressed as follows:

$$\tau_{yx} = -(\sigma_y \tan \varphi_0 + C_0), \quad (1)$$

where σ_y and τ_{yx} are the normal stress and shear stress on the roof and floor interface, respectively, and C_0 and φ_0 are the cohesion and internal friction angle of the rocks on the roof and floor interface, respectively.

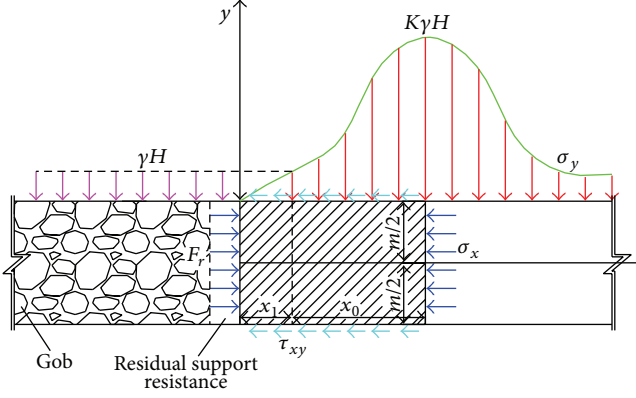


FIGURE 13: Mechanical model for the analysis of the stress around the gob.

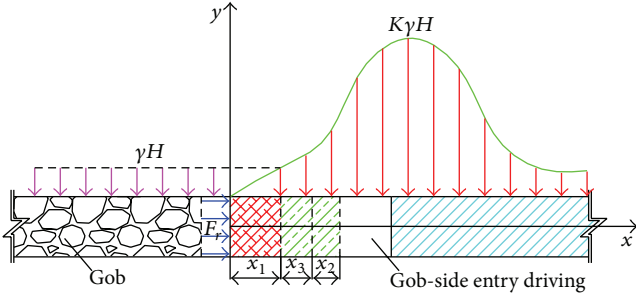


FIGURE 14: Diagram for the calculation of the reasonable width of the narrow coal pillar.

Without considering the body force, we establish the mechanical calculation model (Figure 13) and the coordinate system. The stress for the microunits at the roof and floor interface follows the following stress equilibrium differential equation:

$$\begin{aligned} \frac{\partial \sigma_x}{\partial x} + \frac{\partial \tau_{xy}}{\partial y} &= 0, \\ \frac{\partial \tau_{yx}}{\partial x} + \frac{\partial \sigma_y}{\partial y} &= 0, \end{aligned} \quad (2)$$

$$\tau_{yx} = -(\sigma_y \tan \varphi_0 + C_0).$$

As shown in Figure 13, x_1 represents the width of the fracture zone. The boundary condition for the stress in the fracture zone is as follows:

$$\begin{aligned} \sigma_y|_{x=0} &= 0, \\ \sigma_x|_{x=0} &= P_x, \\ \sigma_y|_{x=x_1} &= \gamma H, \\ \sigma_x|_{x=x_1} &= \lambda \gamma H, \end{aligned} \quad (3)$$

where P_x is the residual support resistance of the rib rock bolt adopted in the roadway of the former panel and λ is the

coefficient of horizontal pressure. λ is calculated through the equation $\lambda = \mu/(1 - \mu)$, where μ is Poisson's ratio.

Choosing all the rock mass within the fracture zone as the research object and given $\sum F_x = 0$, we can obtain

$$m\lambda\sigma_y|_{x=x_1} + 2 \int_0^{x_1} \tau_{yx} dx - mP_x = 0. \quad (4)$$

Based on the theory of the elastic mechanics [24] and considering (2), (3), and (4), we can calculate the width of the fracture zone:

$$x_1 = \frac{m\lambda}{2 \tan \varphi_0} \ln \left(\frac{\gamma H + C_0 / \tan \varphi_0}{C_0 / \tan \varphi_0 + P_x / \lambda} \right), \quad (5)$$

where m is the thickness of the coal seam; k is the concentration factor of the side abutment stress; γ is the average density of the overlying strata; H is the depth of the coal seam.

In a similar way, we can also obtain the calculation equation for x_0 , the width of the plastic zone

$$x_0 = \frac{m\lambda}{2 \tan \varphi_0} \ln \left(\frac{k\gamma H + C_0 / \tan \varphi_0}{C_0 / \tan \varphi_0 + \lambda\gamma H / \lambda} \right). \quad (6)$$

There is an optimal width of the narrow coal pillar in gob-side entry driving. Firstly, we should lay out the roadway in the stress decreasing zone in order to mitigate the convergence of the surrounding rocks, to control the stability of the surrounding rocks and to improve the recovery ratio of the coal resource. This will require us to design the width of the narrow coal pillar as small as possible. However, if the width of the narrow coal pillar is too small, excavating-induced fissures will connect and coalesce with the original fissures, resulting in the lack of anchoring foundation for the rock bolt. Therefore, the effectiveness of the bolt support system will diminish and the narrow coal pillar is prone to lose stability. Moreover, coal mass with large fracture zone becomes ineffective in preventing the air leaking problem and in avoiding the leakage of the hazardous air from the gob of the former panel, posing a great threat to the safe extraction of the current panel. Thus the reasonable width of the coal pillar, W , should be calculated through the calculation diagram as shown in Figure 14.

Figure 14 shows that the width of the narrow coal pillar is comprised of three parts, as illustrated in

$$W = x_1 + x_2 + x_3, \quad (7)$$

where x_1 , the width of the fracture zone caused by the side abutment stress during the advance of the former panel, can be calculated by (5); x_2 is the effective length of the rib bolt within the narrow coal pillar; x_3 , the safety width in considering the anchoring of the rock bolt to the stable coal, can be calculated by $(0.2 \sim 0.4) \times (x_1 + x_2)$. $0.2 \sim 0.4$ is the safety factor.

5.3. Roadway Support Pattern. Through above analysis, we advance the haulage roadway along the gob, retaining the narrow coal pillar with a width of 5.0 m. A corresponding support pattern, consisting of rock bolt, anchor cable, steel

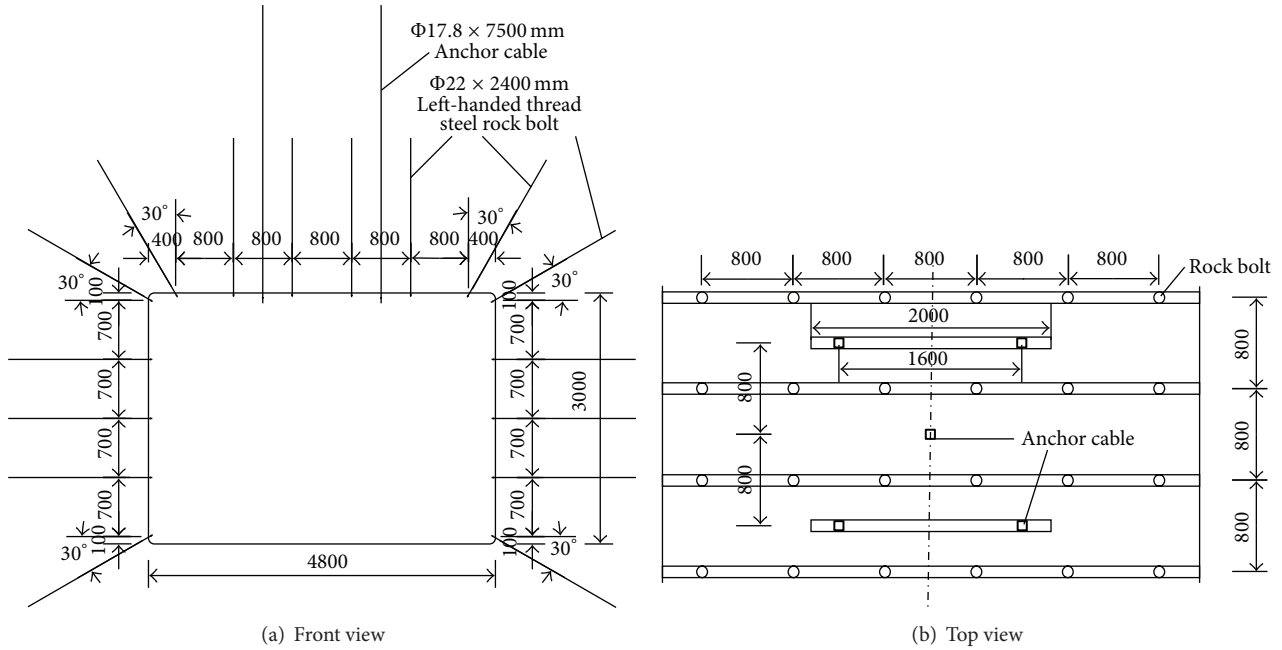


FIGURE 15: Schematic diagram of roadway support pattern.

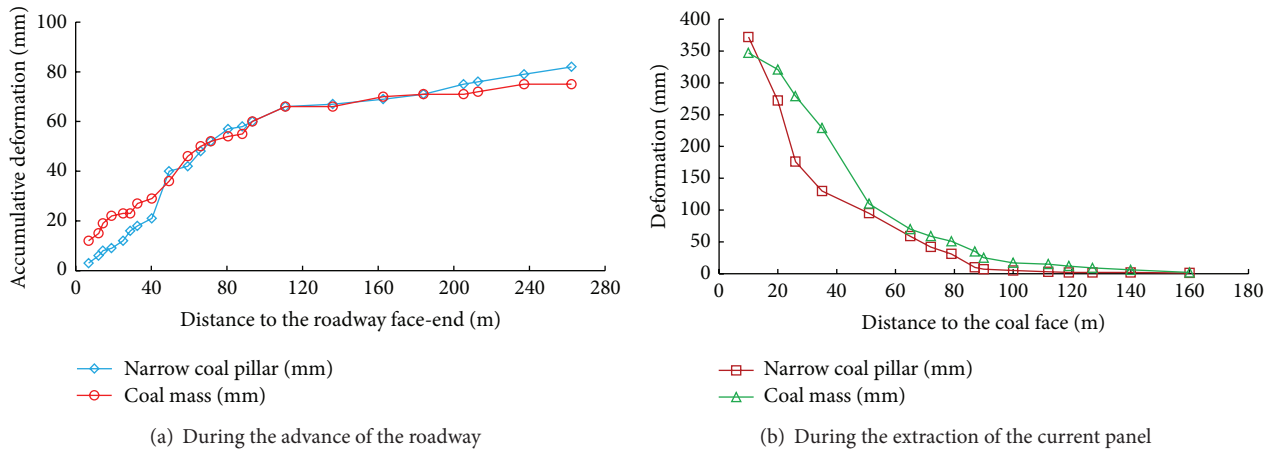


FIGURE 16: Monitoring results of the roadway deformation of the surrounding rocks.

strap and rhombic metal mesh, and so forth, was proposed to reinforce the roadway, as illustrated in Figure 15. The detailed support parameters are as follows.

- (1) The rock bolt and anchor cable use 2 and 4 resin cartridges of the Z2350 type.
- (2) The roof bolts are connected to a steel beam, which has six holes and is 4.8 m long. The rib bolts are connected with two steel straps, which have three holes and are 1.8 m long.
- (3) The screen mesh for the roof is steel mesh with rhombic holes, while, for the two ribs, plastic mesh is adopted. Both the steel mesh and plastic mesh are 1000 × 5000 mm mesh. In the upper corner of the roadway, steel wire is used to bind the steel mesh

with the plastic mesh. The overlapping width of the two meshes is larger than 100 mm, while the binding interval is less than 150 mm.

- (4) The pretightening torque of the roof and rib bolts is higher than 200 N·m. The pretension of the anchor cable is higher than 160 kN.

5.4. Support Effect and Economic Benefit

5.4.1. Roadway Support Effect. Field monitoring of the roadway deformation was carried out to validate the rationality of the proposed pillar width and effectiveness of the support pattern. The results are shown in Figure 16.

Figure 16 shows that (1) the deformation volume of the narrow coal pillar and coal mass is 82 mm and 75 mm,

respectively, during the advance of the haulage roadway and is 372 mm and 347 mm, respectively, during the extraction of the current panel; during these two stages, the roadway can maintain a sufficient profile for the transportation and ventilation requirements; (2) during the advance of the haulage roadway and the extraction of the current panel, both the narrow coal pillar and coal mass demonstrate the same deformation characteristics and both deformations reach stability when the driving face is 90 m away, while during the extraction of the current panel, the narrow coal pillar and coal mass are subjected to the influences of the front abutment stress when the coalface is 80 m away.

5.4.2. Yielded Economic Benefit. It is the first time for Qianyingzi coal mine to adopt the gob-side entry driving technology. The barrier pillar was previously designed as 30 m in width. Through comprehensive researches, we determine the width of the narrow coal pillar as 5.0 m. The 3_214 coalface is 2036 m long on the strike and 235 m long on the dip. The density of the coal seam is 1.4 t/m^3 and its thickness is 3.3 m. After adopting the gob-side entry driving technology, the recovery ratio of the coal is up to 218696.9 t ($25 \times 2036 \times 3.3 \times 1.4 \times 0.93 = 218696.9 \text{ t}$). In 2013, the average price of the coal of Qianyingzi mine is 500 Yuan/t, about 83.3\$. Therefore, this technology can yield 109348450 Yuan ($500 \times 218696.9 = 109348450$), about 18224741.7\$.

6. Main Conclusions

- (1) In this paper, the borehole stress-meter is used to monitor the distribution characteristics of the side abutment stress during the extraction of the longwall panel in Qianyingzi mine, China. The monitoring results demonstrate that the side abutment stress can be divided into three zones: Zone I, side abutment stress rising zone; Zone II, side abutment stress stabilizing zone; and Zone III, side abutment stress decreasing zone.
- (2) In line with the geological setting in Qianyingzi mine, we carried out numerical investigations into the factors that influence the distribution of the side abutment stress. The research results show that the position and value of the peak side abutment stress are closely related to the coal mass strength, immediate roof strength, and immediate roof thickness.
- (3) Based on the field monitoring and numerical research results, we put forward the idea of laying out the mining roadway using gob-side entry driving technology. We determined the reasonable position of the mining roadway and the optimal width of the barrier pillar between panels. The engineering application demonstrates that the retention of the barrier pillar with a width of 5 m along the gob as the haulage roadway for the next panel is feasible, which delivers favorable technological and economic benefits.

Conflict of Interests

The authors declare that there is no conflict of interests regarding the publication of this paper.

Acknowledgments

Financial support for this work, provided by the National Natural Science Foundation of China (Grant nos. 51304208 and 51474208) and the Priority Academic Program Development of Jiangsu Higher Education Institutions, is gratefully acknowledged.

References

- [1] S. S. Peng and H. S. Chiange, *Longwall Mining*, John Wiley & Sons, New York, NY, USA, 1984.
- [2] J. C. Chang, "Distribution laws of abutment pressure around fully mechanized top-coal caving face by in-situ measurement," *Journal of Coal Science and Engineering*, vol. 17, no. 1, pp. 1–5, 2011.
- [3] F. Gao, D. Stead, and J. Coggan, "Evaluation of coal longwall caving characteristics using an innovative UDEC Trigon approach," *Computers and Geotechnics*, vol. 55, pp. 448–460, 2014.
- [4] M. Shabanimashcool and C. C. Li, "A numerical study of stress changes in barrier pillars and a border area in a longwall coal mine," *International Journal of Coal Geology*, vol. 106, pp. 39–47, 2013.
- [5] Z.-H. Ouyang, C.-H. Li, W.-C. Xu, and H.-J. Li, "Measurements of in situ stress and mining-induced stress in Beiminghe Iron Mine of China," *Journal of Central South University of Technology*, vol. 16, no. 1, pp. 85–90, 2009.
- [6] M. Gao, W. Jin, Z. Dai, and J. Xie, "Relevance between abutment pressure and fractal dimension of crack network induced by mining," *International Journal of Mining Science and Technology*, vol. 23, no. 6, pp. 925–930, 2013.
- [7] L.-G. Wang, Y. Song, X.-H. He, and J. Zhang, "Side abutment pressure distribution by field measurement," *Journal of China University of Mining and Technology*, vol. 18, no. 4, pp. 527–530, 2008.
- [8] C. Zhang, Z. Y. Ti, and Z. X. Li, "Theoretical and regressive analysis of the position of peak stress on fully mechanized caving mining," *China Safety Science Journal*, vol. 21, no. 9, pp. 88–93, 2011.
- [9] W. Xu, E. Wang, R. Shen, D. Z. Song, and J. M. Zhang, "Distribution pattern of front abutment pressure of fully-mechanized working face of soft coal isolated island," *International Journal of Mining Science and Technology*, vol. 22, no. 2, pp. 279–284, 2012.
- [10] Z. C. Qin and T. X. Wang, "Abutment stress distribution and its transfer law in floor of deep isolated fully-mechanized mining face using sublevel caving," *Chinese Journal of Rock Mechanics and Engineering*, vol. 23, no. 7, pp. 1127–1131, 2004.
- [11] Z. Hualei, W. Lianguo, and S. Jian, "Distribution of lateral floor abutment pressure in a stope," *Mining Science and Technology*, vol. 21, no. 2, pp. 217–221, 2011.
- [12] B. N. Whittaker and E. L. Potts, "Appraisal of strata control practice: discussion on by BN Whittaker, and authors reply," *International Journal of Rock Mechanics and Mining Sciences & Geomechanics Abstracts*, vol. 11, no. 11, p. A225, 1974.

- [13] Y.-X. Xia, H. Lan, D.-B. Mao, and J.-F. Pan, "Study of the lead abutment pressure distribution base on microseismic monitoring," *Journal of China University of Mining and Technology*, vol. 40, no. 6, pp. 868–873, 2011.
- [14] N. Hosseini, K. Oraee, K. Shahriar, and K. Goshtasbi, "Studying the stress redistribution around the longwall mining panel using passive seismic velocity tomography and geostatistical estimation," *Arabian Journal of Geosciences*, vol. 6, no. 5, pp. 1407–1416, 2013.
- [15] N. Zhang, N. C. Zhang, C. L. Han, D. Y. Qian, and F. Xue, "Borehole stress monitoring analysis on advanced abutment pressure induced by Longwall Mining," *Arabian Journal of Geosciences*, vol. 7, no. 2, pp. 457–463, 2014.
- [16] B. Shen, "Coal mine roadway stability in soft rock: a case study," *Rock Mechanics and Rock Engineering*, vol. 47, no. 6, pp. 2225–2238, 2014.
- [17] F. Gao, D. Stead, and H. Kang, "Numerical simulation of squeezing failure in a coal mine roadway due to mining-induced stresses," *Rock Mechanics and Rock Engineering*, vol. 44, no. 9, pp. 1–11, 2014.
- [18] J. Coggan, F. Q. Gao, D. Stead, and D. Elmo, "Numerical modelling of the effects of weak immediate roof lithology on coal mine roadway stability," *International Journal of Coal Geology*, vol. 90-91, pp. 100–109, 2012.
- [19] W.-J. Wang, L.-Q. Luo, W.-J. Yu, H. Wu, and Y.-S. Qu, "Study of dynamic pressure roadway supporting scheme under condition of thick composite roof," *Journal of Coal Science and Engineering*, vol. 19, no. 2, pp. 119–125, 2013.
- [20] M. G. Qian and P. W. Shi, *Mining Pressure and Strata Control*, China University of Mining and Technology Press, Xuzhou, China, 2003.
- [21] P. Liu and Y. J. Zhao, "Technology status and development trend of shearer for difficult mining coal seam," *Colliery Mechanical and Electrical Technology*, vol. 1, pp. 48–50, 2011.
- [22] L. J. Zhu, H. X. Li, and J. J. Chen, "Probing into problems and countermeasures about mining in deep-lying," *Coal Technology*, vol. 26, no. 6, pp. 146–147, 2007.
- [23] M. Shabanimashcool and C. C. Li, "A numerical study of stress changes in barrier pillars and a border area in a longwall coal mine," *International Journal of Coal Geology*, vol. 106, pp. 39–47, 2013.
- [24] Z. L. Xu, *Elastic Mechanics*, Higher Education Press, Beijing, China, 2006.

Research Article

Instantaneous Rock Blasting Wave and Its Microscopic Characteristics during Interaction with Concrete

Shaoqin Huang,¹ Lifeng Luan,¹ Wanli Xing,² and Qunyi Liu²

¹*School of Earth Sciences and Resources, China University of Geosciences, Beijing 100083, China*

²*Institute of Mineral Resources, Chinese Academy of Geological Sciences, Beijing 100037, China*

Correspondence should be addressed to Wanli Xing; xingwanlicsgs@126.com

Received 30 September 2014; Revised 7 January 2015; Accepted 7 January 2015

Academic Editor: Shimin Liu

Copyright © 2015 Shaoqin Huang et al. This is an open access article distributed under the Creative Commons Attribution License, which permits unrestricted use, distribution, and reproduction in any medium, provided the original work is properly cited.

This paper uses improved technology for dynamic strain measurement to investigate the dynamic strain signals of blasting wave action tested in the range of 8–16 cm from the central blast. Based on the blasting mechanism and on the analysis of signal characteristics, blasting waves are recognized and divided into three zones, namely, shock wave zone, stress wave zone, and gas-expanding zone. This paper studies the relationships between stress, strain, and time of every zone. The tensile and compressive stresses of stress wave are considered. After the blasting test, four cracks from the borehole center toward the minimum burden appear at the model surface. The relationship between blasting wave and concrete damage is analyzed.

1. Introduction

Concrete is often used to reinforce mine tunnels. In a mining excavation, the blasting excavation method is often applied. This method may damage the concrete reinforcement and consequently change the stress-strain response of concrete under static load. According to the mechanism of rock blasting, the combined effects of blasting shock wave, stress wave, and gas expansion (collectively called blasting wave in this paper) will be exerted on the area adjacent to the contact structure at the instant of blasting [1, 2]. These waves are distinct from one another in terms of action time, action area, characteristics of loading and unloading, time-frequency distributions, allocation of energy, attenuation, and contribution to damage. Studies on the essential characteristics of blasting waves based on real-time tests are significant in many fields, such as mining engineering, as well as studies on stress-strain relations of rock mass [3–5], the characteristics of the source of blasting seismic wave [2, 6], and so on.

Thus far, some studies have investigated blasting waves at the instant of detonation or blasting [7–9]. Wen et al. [10] obtained the peak values of the shock wave between 0.81 and 22.3 GPa in different positions. These references mainly investigated the detonations or the shock wave in the medium, thereby promoting understanding of the blasting

mechanism. However, because of the complexity of blasting, the limitations of equipment to experiment on the adjacent area, and the constraints in technology, among others, only a few studies have investigated the tension phase after shock wave [11, 12]. Few studies have made progress in the study of the combined effects of blasting shock wave, stress wave, and gas expansion on the adjacent area at the instant of blasting; the separation of each wave from the result; and the essential characteristics of these waves because of the difficulty in obtaining the blasting wave signals.

Based on laboratory tests, the transient blasting wave strain signals in the concrete model are tested using resistance strain gauges with a highly dynamic strain testing system. This study also quantitatively examines the blasting wave and the essential characteristics of the separated blasting shock wave, stress wave, and gas expansion, considering such factors as action time, action area, dynamic strain variation, characteristics of loading and unloading, velocity and acceleration of test points, and features of time-frequency energy.

2. Blasting Test Results

The specimens are precast concrete with size of 500 mm × 500 mm × 350 mm cuboid, as shown in Figure 1, at the center



FIGURE 1: Concrete test model.

of which there is a borehole 250 mm deep and 8 mm in diameter. Six radial strain gauges are preburied in each model, and the test points ① and ② are 9 cm deep located along the direction of the minimum free face, 8 and 16 cm away from the center line of the borehole, respectively. To eliminate the influence of the free face surrounding the model, butter is coated onto the protective plate to constrict concrete block during the blasting.

A total of 108 test points of 18 models are tested for dynamic strain wave in this paper. The relationship between voltage signal U_0 and dynamic strain ε_d is as follows:

$$\varepsilon_d = \frac{4U_0}{KU_1A}, \quad (1)$$

where U_0 is the output voltage (V), U_1 is the bridge voltage (V), K is the sensitivity coefficient of the strain gauge, ε_d is the dynamic strain of the strain gauge, and A is the gain.

Assuming the specimens are in the elastic stage, the strain value can be obtained by $\sigma = E\varepsilon_d$. The time-strain curves of the test points ① and ②, which are 8 cm and 16 cm away from the center line of the borehole, respectively, in different conditions, are shown in Figure 2 after being transformed by formula (1). Based on the test results, other blasting waves obtained in the test have the same forms as in Figure 2, indicating that the waveform in Figure 2 is universal and representative.

3. Relation of the Division and the Detonation Structure

The blasting wave division in concrete is fairly related to the detonation wave structure. According to ZND detonation theory [13–15], the spread of the shock wave in the dynamite will become the detonation wave. Additionally, the detonation wave structure can be divided into three parts: shock front compressive zone 0-1, reaction zone 2-2, and gas-expanding zone.

- (1) The shock front compressive zone is about 10^{-4} mm wide and has the highest pressure and density, where values suddenly surge.

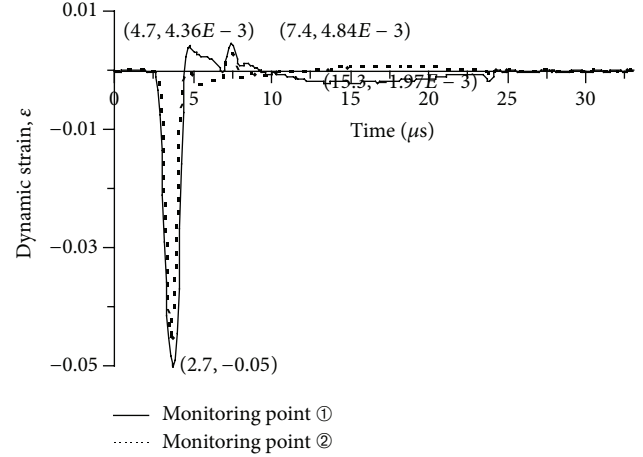


FIGURE 2: Complete time-strain curves of blasting waves.

- (2) The reaction zone is about 10^{-1} mm wide. The action time is in the order of magnitude of 10^{-1} μ s. The head face pressure P_H (i.e., pressure of C-J plane) at 2-2 is about 1/2 of the wave front pressure P_Z at 0-1, and the density at 2-2 is about 1/3 of the density at 0-1.
- (3) In the gas-expanding zone, the expansion of the detonation products is isentropic, and the air pressure, density, and temperature continue to fall.

As pointed out by Ramulu et al. [16], when the blasting occurs in the concrete, the effect of blasting wave on the concrete is similar to the detonation wave in an explosive and depends on the detonation design parameters. As proven by experiments, the shock wave in rocks is a disturbance at supersonic speed. The medium states (pressure, density, and temperature) at the wave front mutate in fractions of 1μ s, and the particles at the wave front move fast. The result agrees well with those shown in Figure 2, which means that the blasting shock wave in the concrete is the result of the sudden jump in detonation pressure at the wave front compressive zone. However, because the blasting shock wave spreads in the nonexplosion medium, the flowing velocity of the particles right behind the shock front is lower than the spreading velocity of the disturbance. Furthermore, because the shock wave lacks external support, some rarefaction waves exist, leading to an aperiodic decay of each parameter after the shock front in the concrete at 3–4 μ s. Therefore, the shock wave turns into the stress wave. The stress wave amplitude is much smaller than the shock wave amplitude. The stress wave front is also flatter, its action time equals that of the shock wave, and the time of the stress value ascending lasts shorter than when the stress value is descending. The stress wave zone in the concrete may be related to the continuous falling of the pressure and the density between the 1-1 front plane and the 2-2 (C-J) plane in the reaction zone. A certain concrete point in the stress zone may also correspond with a point at the C-J plane in the detonation wave. The gas-expanding zone in the concrete is caused by the amorphous isentropic expansion and flow of the detonation product after the C-J plane. And the gas-expanding action mainly causes

the deformation, compression, and tension in the rocks, as well as the formation of cracks.

4. Relation of the Wave Division and the Mechanism of Rock Blasting

To summarize various perspectives on the mechanism of rock blasting, Yang et al. [17] considered that the stress wave plays a dominant role in the whole rock blasting process. In terms of time, the shock wave activates the original microcracks in rocks and generates the crushed zone and radial cracks around the borehole first; then the following stress wave widens these cracks, which leads to a reflected tension stress wave failure at the free face; and the explosion gas wedges in the cracks may connect the cracks together. Finally, the rock fragments are thrown out. Owing to the separation of the free face reflected wave and the blasting wave in the temporal domain, the gas-expanding zone right after the shock wave zone being the reflected tension stress wave is impossible, as proven by the measured reflected tension stress wave from the free face. The wave division in this test agrees well with the result of the study by Yang et al. [17], who supposed that the reflected tension stress wave from the free face is negligible.

In terms of space, when a coupling explosion occurs in an infinite rock, three zones will appear around the borehole. These zones are the crushed zone (near area), which is $3\text{--}7R_0$ (R_0 is the charge radius) radius around the borehole and caused by the shock wave; the crack zone (middle area), which is $8\text{--}150R_0$ radius around the borehole and caused by the stress wave; and the elastic vibration zone (far area), which is more than $150R_0$ radius around the borehole and caused by the gas expansion. In this test, the monitoring points are located in the blasting center area at $20R_0$, $31R_0$, and $40R_0$ away from the center. The test results demonstrate that the blasting shock wave action still affects this area, and the fissures in the rocks at the center area are caused by the combined effects of blasting shock wave, stress wave, and gas expansion.

Therefore, the effects of coupling explosive blasting waves in the concrete can be divided into three phases in terms of time.

- (1) The shock wave from the blasting wave front affects the concrete medium by the overpressure and violent shock at a loading or unloading strain rate of more than $10^4/\text{s}$, which can be drawn from the phenomenon that at $2.4\text{--}3.7\ \mu\text{s}$ the concrete is under loading compression, at $2.4\text{--}3.7\ \mu\text{s}$ the blasting cavity is under unloading and resilience, and at $4.7\text{--}5.6\ \mu\text{s}$ the remaining weak shock wave is decaying with oscillation.
- (2) The stress wave affects the concrete medium through the compression and tension stress at a loading or unloading strain rate several times higher than $10^4/\text{s}$, which can be drawn from the phenomenon that the concrete is under loading and unloading again at $5.6\text{--}8.6\ \mu\text{s}$, and the peak values of the compression stress,

the tension stress, and the strain rate at the broken boundary are much higher than before.

- (3) The isentropic expansion of gas affects the medium by continuous approximate static tension or compression stress, which can be drawn from the phenomenon that at $8.6\text{--}24.7\ \mu\text{s}$ the concrete is still under continuous tension and compression, and decaying with oscillation occurs in the end lasting for about $1\ \mu\text{s}$.

In terms of space, these three actions exist in the study area at the same time, and they are independent of one another, contrary to the traditional view. The shock wave is previously thought to be in the near area, and the stress wave that decays rapidly with distance is in the middle area of the rock blasting area division. These two mechanical processes are two blasting loading forms in the medium because of their different distances from the blasting center, instead of being independent of each other.

5. Verification of Blasting Wave Division

To further verify the blasting wave division, the reflected blasting wave and the contacting blasting wave from the free face are tested on the same type of concrete. In the free face reflected wave, the protective plate is uncovered to prevent absorbing the energy. The sampling precision is $0.1\ \mu\text{s}$, and the sampling time lasts $20\ 000\ \mu\text{s}$; thus, $200\ 000$ data sets of each point are recorded to form a blasting waveform during each blasting. A part of the original measured waveform can be seen in Figure 3, and other analogous waveforms during the whole test appeared. In Figure 3, two conspicuous sudden jumps are recorded. A zoomed-in image of the waveform of jump ① is shown in Figure 2. The waveforms of the two monitoring points of jump ② are found in Figure 3(a) and zoomed in in Figure 4. The time in Figure 4 starts from the $4025\ \mu\text{s}$ in Figure 3(a), and the action time of the reflected wave is about $25\ \mu\text{s}$. As shown in the test result, the reflected wave cannot follow right after the shock wave zone and the stress wave zone. Additionally, the properties of the reflected waveform are entirely distinct from those of the waveform in the gas-expanding zone. Besides, no reference has ever proven that the free face reflected wave follows right after the blasting shock wave.

In the free face contacting blasting test, the charge is moved to the free face along the least resistance line, and everything is kept constant except for the blasting position. The measured waveform and the variations in loading strain rate with time in every contacting blasting can be found in Figure 5.

Based on Figure 5, the third zone of the blasting wave signal obviously disappears as the energy dissipates because of the rapid expansion in the air of the explosion gas. This expansion leads to a decrease in stress at the interface, such that the dynamic strain of the point in the medium is not high enough to be measured. If the blasting reflected wave is the one measured in the zone, the zone will not disappear because the free face stays and the reflected wave continues; the second zone, which is the stress wave zone, obviously

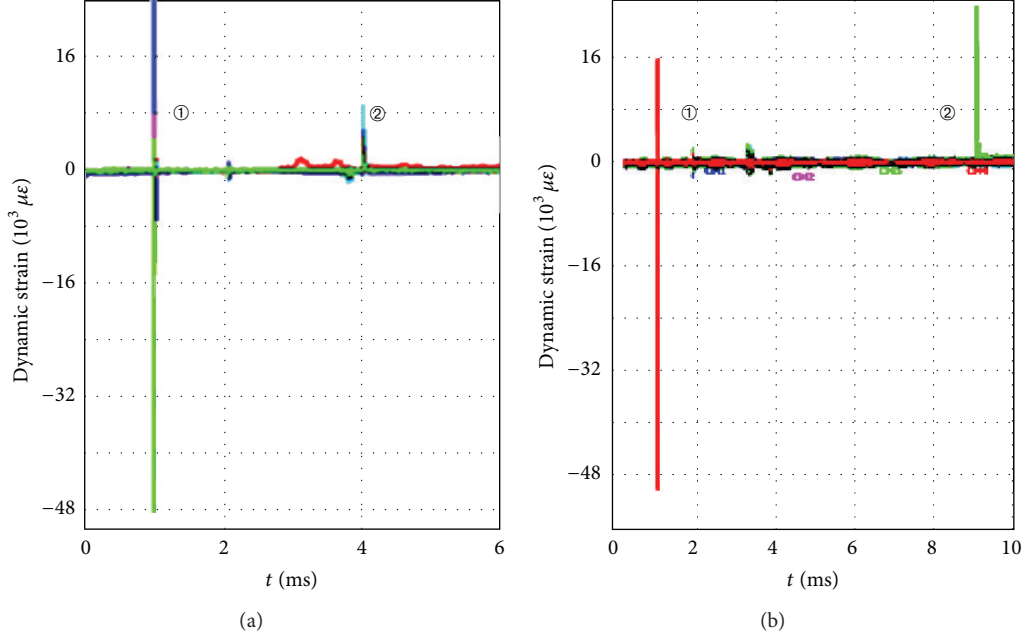


FIGURE 3: Measured curves of the blasting wave and the reflected wave from the free face.

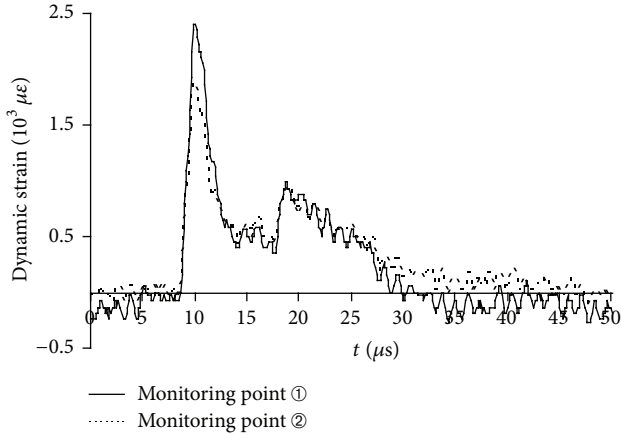


FIGURE 4: Measured curves of the reflected wave from the free face.

decreases and even disappears. If the loading and unloading properties of the whole blasting are considered, different results will be generated. If the unloading and the resilience of the shock wave are the ones measured in the zone, the zone should have the characteristics of the stress wave zone in the blasting wave division. However, as presented in numerous tests, the phenomenon of decreasing and disappearing exists in the second zone during the contacting blasting.

If the gas expansion causes a shock wave in the first zone, the effect of the wave front and the reaction zone must be ignored, a result which does not match detonation theory. Furthermore, no reference has ever recorded that the peak value of the gas expansion can reach more than 1 GPa. If the blasting cavity resilience and the second gas expansion occur in the second zone, then the time when the gas-expanding loading affects the blasting cavity should be determined.

However, only the loading of the blasting wave front and the reaction zone can affect the first zone, and there is no time for the explosion gas to expand and load in the first zone.

Therefore, based on ZND detonation theory, the mechanism of rock blasting, and the evidence of the blasting wave division in the test results, the shock wave zone in concrete results from the sudden jump in detonation pressure at the wave front compressive zone. Furthermore, the gas-expanding zone is caused by the amorphous isentropic expansion and flow of the detonation product after the C-J plane, and the mechanism in the stress wave zone in concrete is very complex. An in-depth discussion concerning the waves disappearing after the shock front of brittle materials, such as K9 glass, under high-speed loading was carried out by Zhao et al. [18]. After the blasting test, four cracks from the borehole center toward the minimum burden appear at the model surface (Figure 6).

The mechanical properties of materials are related to the strain rate and are different from the static mechanical properties. In the blasting wave, the function of the energy for concrete deformation is [19]

$$E = F(E_e, E_p, E_\Omega, E_x), \quad (2)$$

where E_e is the elastic potential energy, E_p is the plastic potential energy, E_Ω is the surface energy of newly formed surfaces, and E_x includes the other kinds of energy.

In this test, assuming that $E_x = 0$, then the process of energy transfer is as follows: (1) the phase of shock wave ascending: the concrete obtains energy E_{sh} ($E_{sh} = E_e + E_p$) from the shock wave. If the energy E_{sh} is higher than the threshold value E_{cri} of crack development, new surface cracks will be formed; when $E_{sh} < E_{cri}$, no surface cracks appear and only the amount of microcracks in the concrete increases;

TABLE 1: Peak values and calculations in each region.

	Test point number	Shock wave zone	Stress wave zone	Gas-expanding zone	Total
①	$t/\mu\text{s}$	2.4–5.6/3.3	5.6–8.6/3	8.6–24.7/16.1	22.4
	f/KHz	0–829	0–743	0–514	×
	$\sigma_{\text{max}}/\text{MPa}$	–1650	159.72	–65.01	×
	$\dot{\epsilon}_{\text{max}}/10^4 \text{ s}^{-1}$	–7.58/10.5	1.43/–1.14	Approximate static load	×
	$u_{\text{max}}/\text{m}\cdot\text{s}^{-1}$	–151.6/210	28.5/–22.7	Approximate static state	×
	$a_{\text{max}}/\text{m}\cdot\text{s}^{-2}$	612/–505	125/–142	0	×
	E_i	0.0157	0.0016	0.0054	0.0231
	$\eta_i/\%$	68.0	6.9	23.4	98.3
②	$t/\mu\text{s}$	2.4–5.6/3.3	5.6–8.6/3	8.6–24.7/16.1	22.4
	f/KHz	0–1000	0–686	0–227	×
	$\sigma_{\text{max}}/\text{MPa}$	–1518	101.31	25.476	×
	$\dot{\epsilon}_{\text{max}}/10^4 \text{ s}^{-1}$	–7.52/8.9	1.24/–1.12	Approximate static load	×
	$u_{\text{max}}/\text{m}\cdot\text{s}^{-1}$	–148/178	24.8/–19.2	Approximate static state	×
	$a_{\text{max}}/\text{m}\cdot\text{s}^{-2}$	608/–413.5	87/–137.5	0	×
	E_i	0.0106	0.0012	0.0016	0.0137
	$\eta_i/\%$	77.3	8.8	11.7	97.8

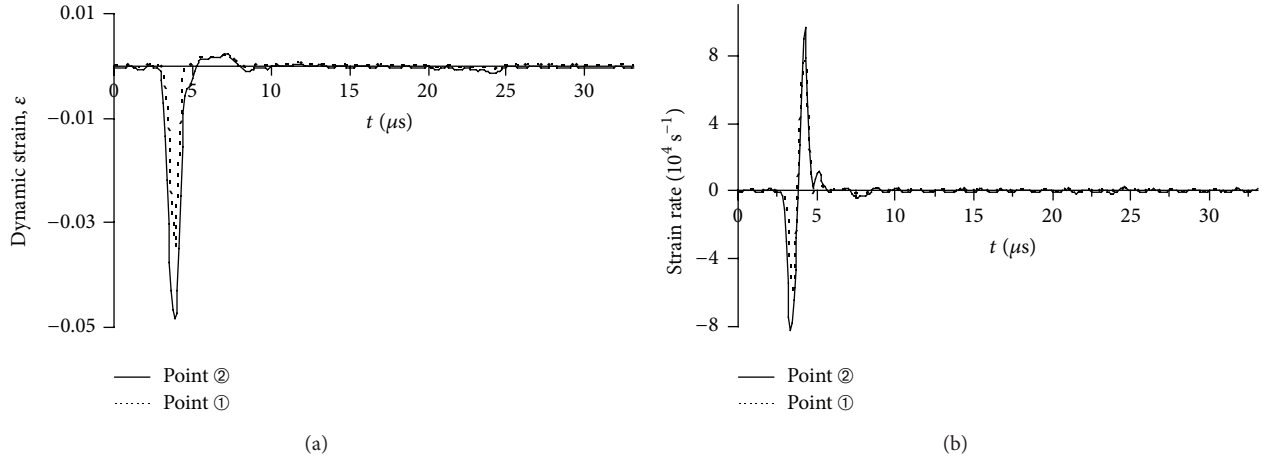


FIGURE 5: Measured curve of contacting blasting waveform.

FIGURE 6: Distribution of blasting cracks in the $\phi 8$ mm model.

(2) the phase of shock wave unloading: two types of energy, namely, deformation reversion energy E_r and wasted energy E_d , are released from E_{sh} , between which E_d is the main

cause of formation of new surface cracks or microcracks; (3) the phase of the effects of stress wave and explosion gas: the types of energy the concrete gets from the stress wave and the explosion gas are E_{st} and E_g , respectively. If $E_{st} > E_{cri}$ or $E_g > E_{cri}$, then new surface cracks will form; otherwise, only the existing cracks caused by E_{sh} can develop further. Based on the calculations in Table 1, E_{st} and E_g are much smaller than E_{sh} , and the effect of E_{sh} is mainly reflected in the crack development.

6. Conclusions

- (1) In the test of blasting wave in concrete with coupling charge, the following may be concluded in terms of space: the monitoring area, which is $20R_0$ – $40R_0$ away from the blasting center, is subjected to the combined effects of blasting shock wave, stress wave, and gas expansion. In terms of time, the three waves affect

the points. Concrete damage results from a complex process under shock compression and tension of the blasting shock wave, as well as the blasting stress wave at a strain rate of more than $10^4/s$, and the effect of gas expansion at an approximate static state.

- (2) The relationship between the effected process of blasting wave and the concrete damage is quantitatively analyzed in terms of energy. If the shock wave energy is greater than the releasing rate of energy for crack development, new surface cracks appear; otherwise, only microcracks appear, and the energy of the stress wave and that of the gas expansion are much smaller than the shock wave energy whose effect is mainly reflected in the crack development.

Conflict of Interests

The authors declare that there is no conflict of interests regarding the publication of this paper.

Acknowledgment

The research project was supported by National Natural Science Foundation of China (41202057).

References

- [1] J. Latham, A. Munjiza, and P. Lu, "Components in an understanding of rock blasting," in *Proceedings of the 6th International Symposium on Rock Fragmentation by Blasting*, pp. 173–182, Johannesburg, South Africa, 1999.
- [2] J. A. Sanchidrián, P. Segarra, and L. M. López, "Energy components in rock blasting," *International Journal of Rock Mechanics and Mining Sciences*, vol. 44, no. 1, pp. 130–147, 2007.
- [3] H. Lin, Z. Xiong, T. Liu, R. Cao, and P. Cao, "Numerical simulations of the effect of bolt inclination on the shear strength of rock joints," *International Journal of Rock Mechanics and Mining Sciences*, vol. 66, pp. 49–56, 2014.
- [4] O. S. Dinc, H. Sonmez, C. Tunusluoglu, and K. E. Kasapoglu, "A new general empirical approach for the prediction of rock mass strengths of soft to hard rock masses," *International Journal of Rock Mechanics and Mining Sciences*, vol. 48, no. 4, pp. 650–665, 2011.
- [5] J. González-Cao, F. Varas, F. G. Bastante, and L. R. Alejano, "Ground reaction curves for circular excavations in non-homogeneous, axisymmetric strain-softening rock masses," *Journal of Rock Mechanics and Geotechnical Engineering*, vol. 5, no. 6, pp. 431–442, 2013.
- [6] I.-S. Ha, "Estimation of shear wave velocity of earth dam materials using artificial blasting test," *Soil Dynamics and Earthquake Engineering*, vol. 55, pp. 120–129, 2013.
- [7] A. K. Chakraborty, J. L. Jethwa, and A. G. Paithankar, "Effects of joint orientation and rock mass quality on tunnel blasting," *Engineering Geology*, vol. 37, no. 3-4, pp. 247–262, 1994.
- [8] R. P. Dhakal and T.-C. Pan, "Response characteristics of structures subjected to blasting-induced ground motion," *International Journal of Impact Engineering*, vol. 28, no. 8, pp. 813–828, 2003.
- [9] A. Mortazavi and P. D. Katsabanis, "Modelling burden size and strata dip effects on the surface blasting process," *International Journal of Rock Mechanics and Mining Sciences*, vol. 38, no. 4, pp. 481–498, 2001.
- [10] S.-G. Wen, Y.-Q. Gong, S.-N. Dong, S.-Y. Wang, and S.-Y. Tang, "Application of wide range pressure gauge to DDT experiments on energetic materials," *Chinese Journal of Energetic Materials*, vol. 15, no. 2, pp. 165–168, 2007.
- [11] S. Bhandari, "On the role of stress waves and quasi-static gas pressure in rock fragmentation by blasting," *Acta Astronautica*, vol. 6, no. 3-4, pp. 365–383, 1979.
- [12] J. C. Jhanwar, J. L. Jethwa, and A. H. Reddy, "Influence of air-deck blasting on fragmentation in jointed rocks in an open-pit manganese mine," *Engineering Geology*, vol. 57, no. 1-2, pp. 13–29, 2000.
- [13] M. Zbikowski, D. Makarov, and V. Molkov, "LES model of large scale hydrogen-air planar detonations: verification by the ZND theory," *International Journal of Hydrogen Energy*, vol. 33, no. 18, pp. 4884–4892, 2008.
- [14] G. Lyng and K. Zumbun, "A stability index for detonation waves in Majda's model for reacting flow," *Physica D: Nonlinear Phenomena*, vol. 194, no. 1-2, pp. 1–29, 2004.
- [15] G. D. Roy, S. M. Frolov, A. A. Borisov, and D. W. Netzer, "Pulse detonation propulsion: challenges, current status, and future perspective," *Progress in Energy and Combustion Science*, vol. 30, no. 6, pp. 545–672, 2004.
- [16] M. Ramulu, A. K. Chakraborty, and T. G. Sitharam, "Damage assessment of basaltic rock mass due to repeated blasting in a railway tunnelling project—a case study," *Tunnelling and Underground Space Technology*, vol. 24, no. 2, pp. 208–221, 2009.
- [17] J. Yang, Q. K. Jin, and F. L. Huang, *Theoretical Models of Rock Blasting and Numerical Calculation*, Science Press, Beijing, China, 1999.
- [18] J.-H. Zhao, Z.-P. Duan, X.-X. Tan et al., "Investigations of failure waves in K9 glass using shadowgraph," *Explosion and Shock Waves*, vol. 21, no. 2, pp. 150–156, 2001.
- [19] H. Schuler, C. Mayrhofer, and K. Thoma, "Spall experiments for the measurement of the tensile strength and fracture energy of concrete at high strain rates," *International Journal of Impact Engineering*, vol. 32, no. 10, pp. 1635–1650, 2006.

Research Article

Study on Low-Frequency TEM Effect of Coal during Dynamic Rupture

Cheng-wu Li, Chuan Wang, Bei-jing Xie, Xiao-yuan Sun, and Xiao-meng Xu

School of Resource and Safety Engineering, China University of Mining and Technology (Beijing), Beijing 100083, China

Correspondence should be addressed to Chuan Wang; wangchuan010bj@163.com and Bei-jing Xie; bxjie1984@163.com

Received 24 June 2014; Revised 29 August 2014; Accepted 12 September 2014

Academic Editor: Caiping Lu

Copyright © 2015 Cheng-wu Li et al. This is an open access article distributed under the Creative Commons Attribution License, which permits unrestricted use, distribution, and reproduction in any medium, provided the original work is properly cited.

Dynamic loads provided by the SHPB test system were applied to coal specimens, and the TEM signals that emerged during coal rupture were recorded by the TMVT system. Experiments on coal-mass blasting rupture in excavating workface were also carried out, and the emerged TEM signal was analyzed. The results indicate that the low-frequency TEM signals were detected close to the coal specimens under high strain dynamic load applied by the SHPB, initially rising sharply and dropping rapidly, followed by a small tailing turbulence. And the field test results obtained during coal blasting process coincided with the results from the SHPB tests. Furthermore, its initial part shaped like a pulse cluster had a more pronounced tail and lasted even longer. And the generation mechanism of the low-frequency TEM effect was analyzed. It suggests that the low-frequency TEM effect of coal during dynamic rupture is contributed by the fractoemission mechanism and the resonance or waveguide effects. Because its wavelength is longer than the higher ones, the low-frequency TEM has a good anti-interference performance. That can expand the scope and performance of the coal-rock dynamic disaster electromagnetic monitoring technique.

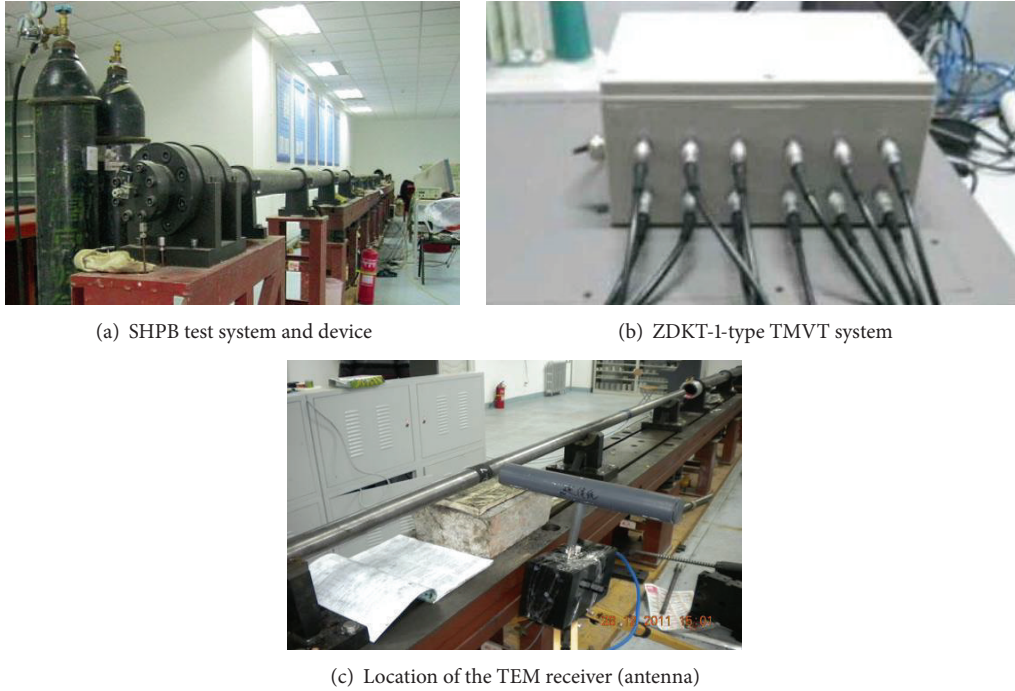
1. Introduction

In deep mining engineering, coal and rock masses have always been exposed to intense dynamic loading, while dynamic disasters such as rock burst, coal and gas outburst can occur [1–3]. The destruction of the coal-rock structure reveals features consistent with quick rupture at high strain rates. This is reflected in significant characteristics of nonlinear dynamics, accompanied by sound, electricity, magnetism, vibration, and other physical effects [4–8]. The phenomenon of electromagnetic radiation (EMR) is considered to be closely related to the deformation and fracture of coal or rock under load [9, 10]. Also the transient electromagnetic (TEM) effect near to coal subjected to dynamic loads has been initially confirmed [11–13]. Therefore, EMR has become a very effective method for coal-rock activity monitoring [14–16].

Studies on EMR produced during the process of coal-rock deformation or fracture show that the frequency of EMR has a wide bandwidth. The main frequency band is variable [17, 18]. EMR signals of different frequencies are generated by different mechanisms and have different waveforms.

Currently, the EMR detectors [19] for detecting coal and rock dynamic disasters were developed on the basis of EMR of medium-high-frequency (≥ 5 kHz). But in actual mining environments, the wavelength of medium-high-frequency EMR signal is too short to propagate more than 20 m. Also it is vulnerable to the high-frequency interference from mechanical and electrical equipment [20]. However, low-frequency electromagnetic wave can propagate a longer distance (around 3.5 km), with a small attenuation [21], and will be less affected by mining equipment. So, it is very important to study the characteristics of low-frequency EMR from coal under dynamic loading, to develop monitoring and early warning technology for coal and rock mines.

On the basis of previous work, this paper focuses on low-frequency TEM effect that emerges during coal rupture under dynamic loading. Considering the high strain rate of dynamic loading, mainly obtained by using SHPB [22] or blasting process [14], the methods of SHPB and in situ blasting tests were adopted to obtain the TEM signals during coal rupture. By combining basic theories such as charge separation, transfer theory [23, 24], and coal structure



(a) SHPB test system and device

(b) ZDKT-1-type TMVT system

(c) Location of the TEM receiver (antenna)

FIGURE 1: Test systems and their location.

resonance theory [25], the characteristics of the TEM effect and its generation mechanism are analyzed and presented by the following sections of this paper.

2. Experiments on TEM Effect of Coal Rupture under Dynamic Load

2.1. Experimental Systems and Specimen. The setup used in the experiment was based on the SHPB test system and the TMVT system.

Coal impact damage experiments under dynamic load were performed on the $\Phi 50$ mm SHPB test system in the China University of Mining (Beijing) Rock Dynamics Laboratory. Before the test, grease lubrication was applied to the interface between the elastic rod and the specimen to reduce the interfacial friction effect. Meanwhile, the ZDKT-1-type transient magnetic vibration test (TMVT) system was placed at 4 cm from the specimen, so as to record the TEM signal. The SHPB test system and the ZDKT-1-type TMVT system and devices used in the experiment are shown in Figure 1.

The SHPB test system contains the following: an impacting rod, two pressure bars, a gun system, ultradynamic strain gauges, and a data storage system. The impactor is a $\Phi 50$ mm \times 400 mm round steel rod, and the impact velocity is measured by a velocimeter. The TMVT system contains the following: an antenna (internal resistance is 21.8 ohms), a signal amplifier, and a data acquisition recorder.

The specimens tested in the test were obtained from a lump of coal from the excavating workface of number 10 mine of Pingdingshan Coal Group Co., Ltd. According to the optimum length-diameter ratio formula [26], cut cylindrical



FIGURE 2: Coal specimens.

samples of 50 mm in diameter and 100 mm in length (of 2 times diameter) for SHPB test. The coal specimens are shown in Figure 2.

2.2. Experiment of TEM Signals during Coal Deformation under Dynamic Impact Load. Before the test, the SHPB test system should be adjusted [27] to meet the Stress Equilibrium principle. 14 specimens were tested at impact velocities of 4.174, 4.534, 5.001, 6.709, 6.951, 8.714, 9.004, 10.700, 12.730, 12.746, 14.503, 14.847, 17.559, and 17.652 m/s.

During the experiment, the TEM signals were collected by the TMVT system. Some test results are shown in Figure 3.

From Figure 3, all the electromagnetic signals present abrupt part, with a short duration. They also contain a lot of noise which may come from the environment or the system itself.

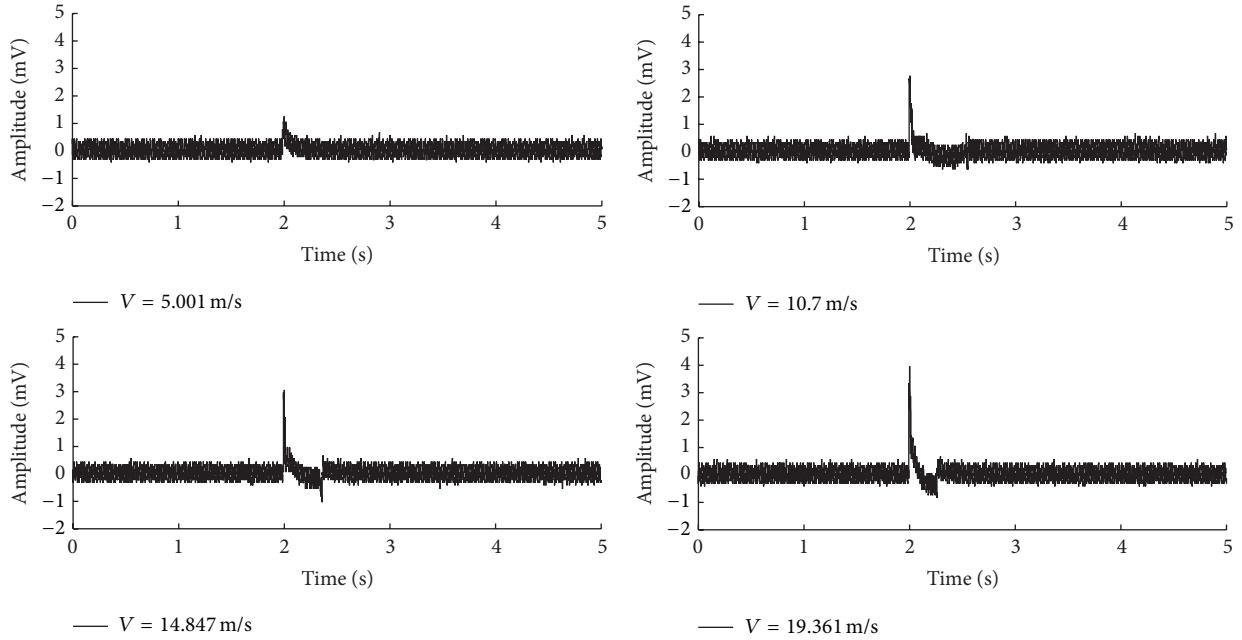


FIGURE 3: Original signals.

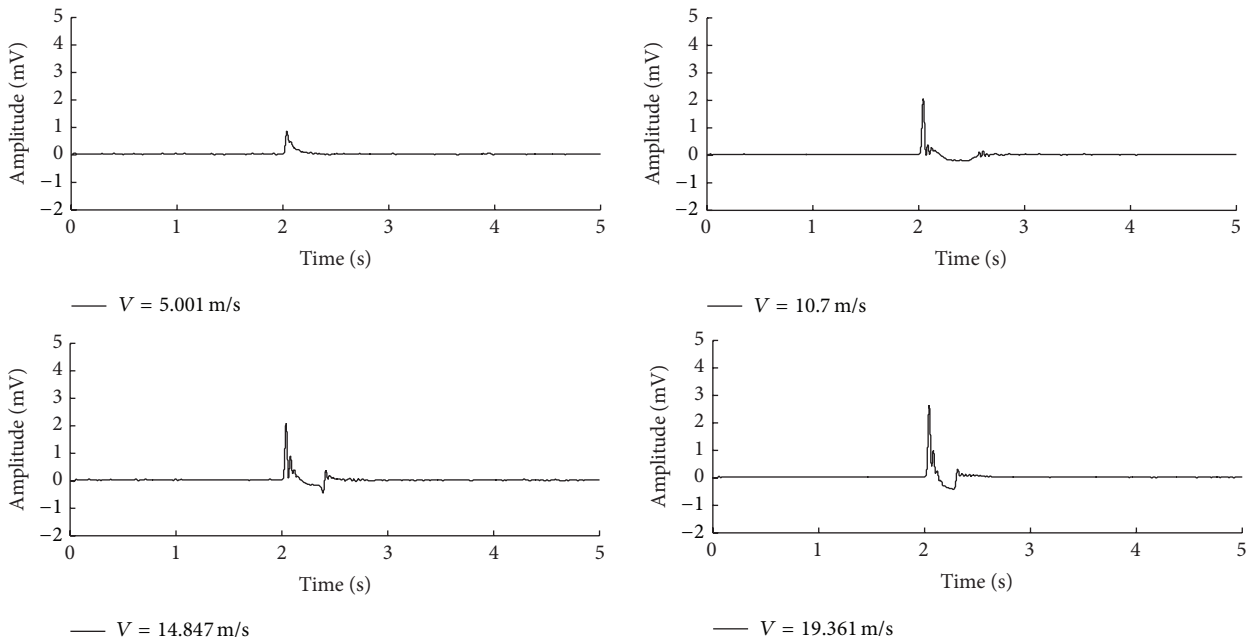


FIGURE 4: Processed signals.

In order to obtain a more realistic representation of the TEM signals, Data-Demon software was used to process them. The results are shown in Figure 4.

Figure 4 shows that, when processed by the “ensemble empirical mode decomposition” (EEMD) method [28], the noise in the recorded signals was filtered out, and then the true TEM signal was clearly retained. The true TEM signals rose quickly and then decreased rapidly with a slight tailing oscillation. FFT spectrum analysis results are shown in Figure 5.

Figure 5 shows that the TEM signal emerged during SHPB impact of coal as a low-frequency signal, with frequencies less than 40 Hz.

2.3. *Analysis and Discussion.* The peak values (maximum amplitude) of each signal were obtained (see Figure 6). The maximum amplitude of the signal can be seen to increase linearly with the impact velocity.

But that can be obviously divided into three regions. (1) When the impact velocity is small (under 5 m/s), the peak

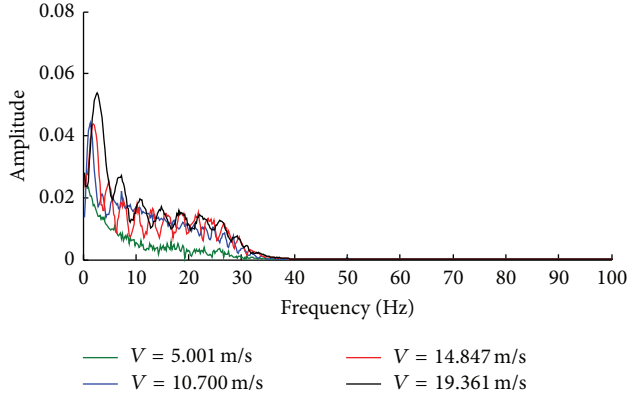


FIGURE 5: FFT spectrum of some signals.

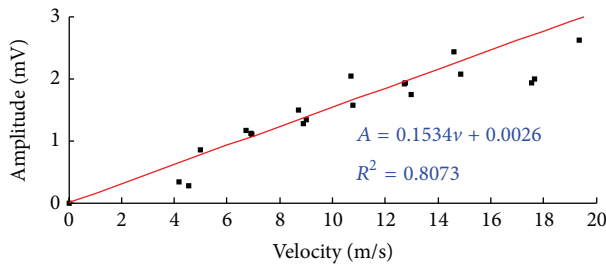


FIGURE 6: Relationship between the true TEM peak value and the impact velocity.

value is smaller than that given by the line. (2) While at the medium velocity (5~15 m/s), the peak value has a very good linear relationship with the velocity. (3) At the high velocity (greater than 15 m/s), the peak value also lies under the line.

That means, in the low velocity stage, the peak value increases quickly with velocity, and in the high velocity stage, the peak value grows more slowly. Since less data was obtained at high velocity, whether the peak value continues to increase or not, this needs further research.

The energy of the TEM signal can be described by

$$E = \frac{U^2}{R} = \frac{1}{R} \sum_{i=1}^N u_i^2, \quad (1)$$

where E is the energy of the TEM signal, R is the internal resistance, $R = 21.8 \Omega$, and U is the induced electromotive force, equal to the immediate detected value, mV.

A quadratic fit to the data is presented in Figure 7.

It can be seen that a quadratic relationship has a similar pattern as the linear one as shown in Figure 6. At the high velocity, the energy data deviates significantly.

3. Field Test of TEM Signals during Coal Rupture under Blasting Shock

The ZDKT-1-type transient magnetic vibration detection (TMVD) system was set up in the 21180# excavating workforce, in number 10 mine of Pingdingshan Coal Group, to carry

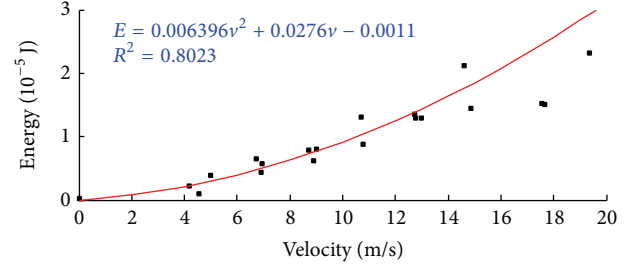


FIGURE 7: Relationship between the true TEM energy and the impact velocity.

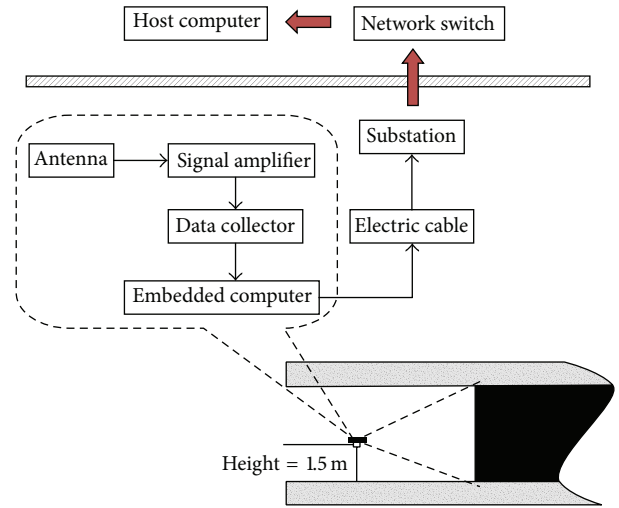


FIGURE 8: The field test TMVD system diagram.

out a field test of TEM produced by large-scale coal-mass dynamic rupture under actual blasting loads.

3.1. Field Test System. The TMVD system consists of a TEM detector, an electric cable, a substation of monitoring (underground), and a network switch and a host computer (above ground). The detector consists of a TEM signal receiving antenna, a signal amplifier, and a data acquisition card.

The detector was placed 300 m away from the tunnel opening (during the test period it remains about 200 m away from the workforce). The TEM signal produced during coal blasting rupture was received by the antenna, converted into an electrical signal, which was amplified by the signal amplifier, converted into a digital signal via the data acquisition card, and, finally, transmitted to the ground host computer by an underground cable.

Figure 8 is a schematic diagram of the field test system.

3.2. Field Test Result Analysis and Discussion. 22 blasting tests were performed in the field. Figure 9 shows a typical TEM signal collected by the system during blasting excavating.

It can be seen from Figure 9 that the TEM signal obtained is nonstationary, is of weak strength, and contains a lot of noise. A more distinct signal was extracted from the original signal by the EEMD method, as shown in Figure 10.

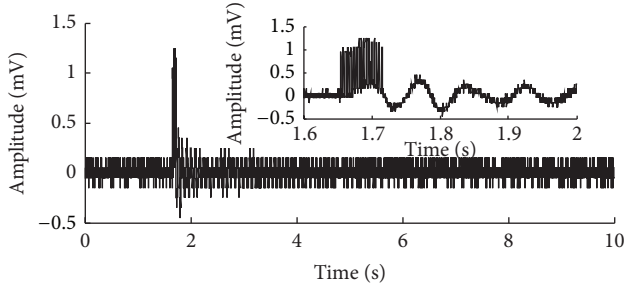


FIGURE 9: Original TEM signal obtained during coal blasting rupture.

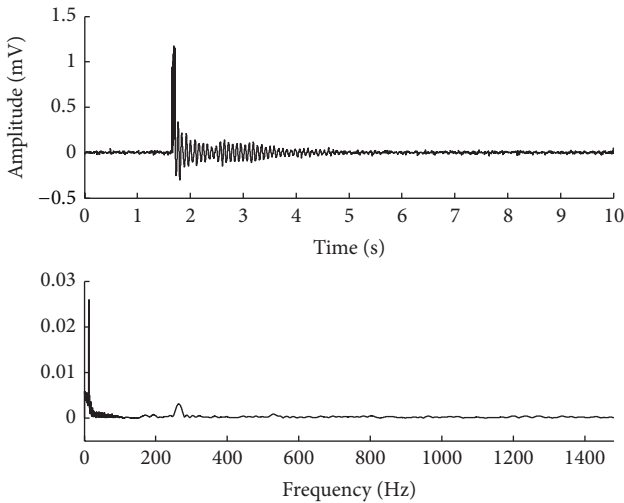


FIGURE 10: TEM signal processed by EEMD.

Comparing Figures 9 and 10, the interference component in the original signal was filtered. Its time domain feature became much clearer, and its FFT spectrum showed that the frequency of the signal was mainly focused around 0–25 Hz. Another frequency band is around 250–280 Hz.

From Figures 9 and 10, it can be seen that the TEM signal produced during coal blasting rupture presents two phases, a pulse rise and a trailing shock, which confirm the SHPB test result (Figure 3).

One difference from the single-pulse from the SHPB results is that the TEM signal obtained in the field performs as pulse clusters. The amplitude of the trailing shock is much higher than the SHPB results, and the duration is longer. An analysis of the 22 group signals showed that all the results coincide with the aforementioned characteristics.

4. Low-Frequency TEM Effect Generation Mechanism Analysis and Discussion

4.1. Mechanistic Analysis of the Pulse Part of TEM Signal. Dynamic analysis results of small-scale coal specimens tested in the SHPB suggested that, in a certain strain rate range, the dynamic response of coal changes from hardening to softening as the strain rate increasing. The peak value increased as

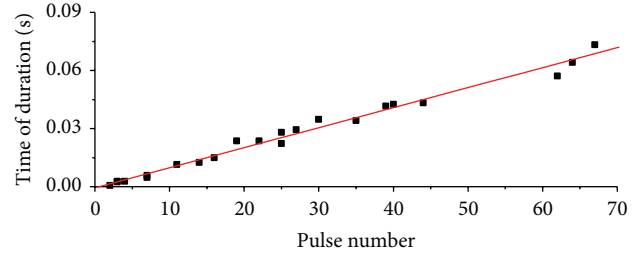


FIGURE 11: Relationship between N_{pulse} and T_{duration} .

the impact velocity, the strain rate, and the fracture stress limit value increased.

According to the SHPB test principle [29], the incident wave reverberates in the coal specimen 9–10 times or more. The shock wave reverberation in the coal specimen produces compression and tensile deformation.

And on the basis of fractoemission theory [30, 31] and the theories about the strain rate sensitivity of coal [22, 32], with the impact loading, the stress waves compress or stretch the coal-mass; internal cracks expand quickly and will be closed and opened in this process. A concussion capacitor can be formed at the fracture surface, leading to charge separation and transfer. High concentration of electrical charge at the surface transferred instantaneously and the energy was given out transiently, in the form of electromagnetic waves.

This is considered as a significant cause for the generation of pulsed electromagnetic anomalies.

In order to explain this phenomenon in detail, both the numbers of pulses in the cluster (N_{pulse}) and their duration (T_{duration}) were calculated. A plot of the two parameters is shown in Figure 11.

Figure 11 shows that there is a good linear relationship between the pulse number and pulse duration, which indicate that the pulse duration of the cluster increases with pulse number.

Analysis suggests that a blasting hole causes coal rupture and induces a single TEM pulse, and multiple holes blasting induces pulse clusters. But, if some holes blast simultaneously, the TEM pulses will merge together.

4.2. Mechanistic Analysis of the Trailing Part of the Signal. Research has shown that when coal is deformed by dynamic loads in the SHPB, as the increase of the impact velocity is increased, the change in duration of the TEM signal increase is not obvious. As the velocity increases to a certain extent, its duration remains substantially constant. And as to the midvelocity, the trailing part is obvious, but as to the low or high velocity, the trailing part is not obvious.

Initial analysis suggests the following. (1) Since coal material is a weakly conductive, high resistivity medium, at low impact velocity, the TEM signal amplitude decays rapidly and cannot produce obvious attenuation concussion. (2) While at high velocity, coal specimens fragment very quickly. As the shock waves transportation time is very short, the detector cannot capture the attenuation signal. (3) While for medium velocity, the trailing part of the TEM signal was

due to electromagnetic oscillation effects caused by shock stress unloading, coal crushing, crushed coal-mass friction, and the expansion of cracks produced during fragmentation rotating, vibrating, so the amplitude of the trailing part is much lower than the initial peak.

Compared with the laboratory test results, the trailing shock of the TEM signals during coal blasting is more obvious and lasts longer. Such changes may be caused by the coal-rock-mass structure and the overlaying of dynamic load is caused by multiple holes blasting.

Firstly, according to the triboluminescence theory [33], the blasting shock waves propagating in the coal seam in the form of dilatation or shear waves produce compressive, tensile, and shear deformation in the coal-mass, which causes extrusion, friction, and vibration at the preexisting and fresh cracks or fissures and thus produce variable motion free charges. Energy is converted into electromagnetic wave which is radiated outward. But due to the special structural, mechanical, and electrical properties, the electromagnetic emission of coal would be at low frequency.

Secondly, due to the different impedance of coal seam and rock, blasting shock waves are reflected between roof or floor coal-rock seam, producing a planar waveguide effect or surface oscillations effect [23]. That will even induce resonance of coal-mass. Researches on coal resonance damage indicate that the natural frequency of coal is below 50 Hz, and when the coal-mass is excited to resonance, the frequency of the electromagnetic radiation signals coincides with the excitation frequency. By the resonance effect, the TEM signal can be controlled by the variable motion of free charges generated by friction in the coal-mass. In addition, because the vibration damage lags behind the blasting damage effect and its intensity is much weaker than the latter, the TEM signal has a low-frequency trailing turbulence following the initial pulse.

4.3. Discussion on the Surroundings and the Piezoelectric Effect. In terms of usage, it is necessary to discuss the interference of the electromagnetic wave from the environments and the contribution of piezoelectric effect on the low-frequency TEM signal.

(1) As the literature [20] reported, the frequency bands of the electromagnetic environments in roadways of underground coal mines are relatively specific and high-frequency ones. And studies on EMR produced during the process of coal-rock deformation or fracture show that the frequency of EMR has a wide bandwidth. But the medium-high-frequency EMR signal is vulnerable to the effect of surrounding such as the high-frequency interference from mechanical and electrical equipment. So, the low-frequency electromagnetic technique has an advantage to avoid the surrounding interference in coal mine.

(2) The piezoelectric effect of rocks has been reported in various literatures [34]. However, the researches by Warwick et al. [35] and Maxwell et al. [36] indicated whether rocks contain piezoelectric materials or not; EMR phenomenon has been investigated. And researches by Cress et al. [37] and Zhu and Luo [38] revealed that the piezoelectric effect was

not the true mechanism or not the main role of rock EMR. Considering the transient time of the TEM signal produced by the piezoelectric effect is about 10^{-5} s and the spectral content shifts to higher frequencies as grain size decreases, it could be concluded that the piezoelectric effect may not be the main cause of the low-frequency TEM.

There is no doubt that the low-frequency TEM is related to coal-rock deformation and has potential application for monitoring coal mine dynamic disasters.

5. Conclusions

- (1) Transient electromagnetic radiation signals emerge during the damage of coal under dynamic load, and its wave form presents as a rising pulse and rapid dropping with a slight tailing oscillation. Its frequency ranges below 40 Hz, and the signal duration and peak value increase with impact velocity.
- (2) Coal fragments quickly while it is impacted by dynamic load, and cracks can expand rapidly, and high concentrations of free charge are generated at crack surfaces. Energy radiates outward in the form of electromagnetic waves while free charges are discharged and then form the TEM pulse. With the fragmentation of coal, the shock stress unloads quickly, and the TEM pulse decays rapidly. During the fragments rotating and translating, the emerged cracks continually expand. Accompanied with the friction between broken pieces, a low-frequency electromagnetic oscillation wave emerges. Unloading of the shock stress results in the intensity of the oscillation being much weaker than the initial pulse.
- (3) Characteristics of the TEM signal produced during coal blasting agree with the SHPB test results. But affected by the multiple holes blasting, the blasting produces a pulse cluster in the initial part, and the pulse number increases with the number of holes.
- (4) Affected by the blasting shock wave and the resonance caused by waveguide effects, the coal deformation lags behind the blasting damage effects, and its intensity is much weaker than the latter. Therefore, the TEM of coal blasting rupture is a low-frequency signal with a longer duration.
- (5) The low-frequency TEM is related to coal deformation and has potential application for monitoring coal mine dynamic disasters.

Conflict of Interests

The authors declare that there is no conflict of interests regarding the publication of this paper.

Acknowledgments

This research is supported by National Natural Science Foundation Project (51274206, 51404277) and the Program of Central Universities Fundamental Research Funds from

the Ministry of Education of China (2010YZ05, 2014QZ05). These supports are greatly acknowledged and appreciated.

References

- [1] M.-C. He, H.-P. Xie, S.-P. Peng, and Y.-D. Jiang, "Study on rock mechanics in deep mining engineering," *Chinese Journal of Rock Mechanics and Engineering*, vol. 24, no. 16, pp. 2803–2813, 2005 (Chinese).
- [2] Q. Qi and L. Dou, *Theory and Technology of Rockburst*, China University of Mining and Technology Press, Xuzhou, China, 2008 (Chinese).
- [3] Y.-D. Jiang, Y.-S. Pan, F.-X. Jiang, L.-M. Dou, and Y. Ju, "State of the art review on mechanism and prevention of coal bumps in China," *Journal of the China Coal Society*, vol. 39, no. 2, pp. 205–213, 2014 (Chinese).
- [4] B. T. Brady and G. A. Rowell, "Laboratory investigation of the electrostatics of rock fracture," *Nature*, vol. 321, no. 6069, pp. 488–492, 1986.
- [5] S. C. Langford, J. T. Dickinson, and L. C. Jensen, "Simultaneous measurements of the electron and photon emission accompanying fracture of single-crystal MgO," *Journal of Applied Physics*, vol. 62, no. 4, pp. 1437–1449, 1987.
- [6] X. He and M. Liu, *Electromagnetic Dynamics of Coal Containing Gas Destruction*, China University of Mining and Technology Press, Xuzhou, China, 1995 (Chinese).
- [7] V. Frid, J. Goldbaum, A. Rabinovitch, and D. Bahat, "Electric polarization induced by mechanical loading of solnhofen limestone," *Philosophical Magazine Letters*, vol. 89, no. 7, pp. 453–463, 2009.
- [8] C.-P. Lu, L.-M. Dou, A.-Y. Cao, and X.-R. Wu, "Research on microseismic activity rules in Sanhejian Coal Mine," *Journal of Coal Science & Engineering*, vol. 14, no. 3, pp. 373–377, 2008 (Chinese).
- [9] S. G. O'Keefe and D. V. Thiel, "A mechanism for the production of electromagnetic radiation during fracture of brittle materials," *Physics of the Earth and Planetary Interiors*, vol. 89, no. 1-2, pp. 127–135, 1995.
- [10] V. Frid, D. Bahat, J. Goldbaum, and A. Rabinovitch, "Experimental and theoretical investigations of electromagnetic radiation induced by rock fracture," *Israel Journal of Earth Sciences*, vol. 49, no. 1, pp. 9–19, 2000.
- [11] J. T. Dickinson, L. C. Jensen, S. Lee, L. Scudiero, and S. C. Langford, "Fracto-emission and electrical transients due to interfacial failure," *Journal of Adhesion Science and Technology*, vol. 8, no. 11, pp. 1285–1309, 1994.
- [12] M. V. Kurlenya, A. G. Vostretsov, M. M. Pynzar, and G. E. Yakovitskaya, "Electromagnetic signals during static and dynamic loading of rock samples," *Journal of Mining Science*, vol. 38, no. 1, pp. 20–24, 2002.
- [13] C.-W. Li, B.-J. Xie, W. Yang, and S. Wei, "Characteristics of transient magnetic nearby field in process of coal impact damage," *Chinese Journal of Rock Mechanics and Engineering*, vol. 31, no. 5, pp. 973–981, 2012 (Chinese).
- [14] N. Djordjevic, J. Esterle, D. Thornton, and D. la Rosa, "A new approach for prediction of blast induced coal fragmentation," in *Proceedings of the Mine to Mill Conference*, pp. 175–181, The Australasian Institute of Mining and Metallurgy, Brisbane, Australia, 1998.
- [15] V. Frid, "Rockburst hazard forecast by electromagnetic radiation excited by rock fracture," *Rock Mechanics and Rock Engineering*, vol. 30, no. 4, pp. 229–236, 1997.
- [16] W. Enyuan, H. Xueqiu, L. Zhentang et al., "Electromagnetic radiation detector of coal or rock dynamic disasters and its application," *Journal of China Coal Society*, vol. 28, no. 4, pp. 366–369, 2003.
- [17] S.-Q. Qian, K.-X. Ren, and Z. Lü, "Experimental study of the features of VLF, MF, HF and VHF electromagnetic radiation accompanying rock fracture," *Acta Seismologica Sinica*, vol. 9, no. 3, pp. 447–454, 1996.
- [18] W. Enyuan, H. Xueqiu, and L. Zhonghui, *Coal and Rock EMR Technology and Its Application*, Science Press, Beijing, China, 2009, (Chinese).
- [19] E.-Y. Wang, X.-Q. He, Z.-T. Liu, L.-M. Dou, S.-N. Zhou, and B.-S. Nie, "Electromagnetic radiation detector of coal or rock dynamic disasters and its application," *Journal of the China Coal Society*, vol. 28, no. 4, pp. 366–369, 2003 (Chinese).
- [20] J. Sun, F. Wang, T. Pan, L. Tang, S. Wang, and Y. Ming, "Electromagnetic environments in roadways of underground coal mines and a novel testing method," *Mining Science and Technology*, vol. 20, no. 2, pp. 244–247, 2010.
- [21] A. Rabinovitch, V. Frid, D. Bahat, and J. Goldbaum, "Decay mechanism of fracture induced electromagnetic pulses," *Journal of Applied Physics*, vol. 93, no. 9, pp. 5085–5090, 2003.
- [22] V. M. Kosenkov and A. R. Rizun, "Characterization of the pulse destruction of black coal using the Kolsky method," *Surface Engineering and Applied Electrochemistry*, vol. 47, no. 2, pp. 189–195, 2011.
- [23] A. Rabinovitch, V. Frid, and D. Bahat, "Surface oscillations—a possible source of fracture induced electromagnetic radiation," *Tectonophysics*, vol. 431, no. 1–4, pp. 15–21, 2007.
- [24] X.-Q. He, B.-S. Nie, E.-Y. Wang, L.-M. Dou, M.-J. Liu, and Z.-T. Liu, "Electromagnetic emission forecasting technology of coal or rock dynamic disasters in mine," *Journal of the China Coal Society*, vol. 32, no. 1, pp. 56–59, 2007 (Chinese).
- [25] G. Tianbao, *Coal Experiment Study on Forced Vibration Response and Fracture Characteristics*, China University of Mining and Technology, Beijing, China, 2013, (Chinese).
- [26] E. D. H. Davies and S. C. Hunter, "The dynamic compression testing of solids by the method of the split Hopkinson pressure bar," *Journal of the Mechanics and Physics of Solids*, vol. 11, no. 3, pp. 155–179, 1963.
- [27] X. J. Wu and D. A. Gorham, "Stress equilibrium in the split Hopkinson pressure bar test," *Le Journal de Physique IV*, vol. 7, no. C3, pp. 91–96, 1997.
- [28] Z. Wu and N. E. Huang, "Ensemble empirical mode decomposition: a noise-assisted data analysis method," *Advances in Adaptive Data Analysis*, vol. 1, no. 1, pp. 1–41, 2009.
- [29] C. Bacon, "An experimental method for considering dispersion and attenuation in a viscoelastic hopkinson bar," *Experimental Mechanics*, vol. 38, no. 4, pp. 242–249, 1998.
- [30] J. T. Dickinson, "Fractoemission," in *Encyclopedia of Materials: Science and Technology*, K. H. J. Buschow, R. W. Cahn, M. C. Flemings et al., Eds., pp. 3254–3257, Elsevier, 2001.
- [31] J. T. Dickinson, C. L. Jensen, and A. Jahan-Latibari, "Fracto-emission: the role of charge separation," *Journal of Vacuum Science & Technology A*, vol. 2, no. 2, pp. 1112–1116, 1984.
- [32] J. R. Klepaczko, "On the role of microcracking inertia in rate sensitivity of coal at high strain rates," *Archives of Mechanics*, vol. 40, no. 4, pp. 345–358, 1988.
- [33] A. J. Walton, "Triboluminescence," *Advances in Physics*, vol. 26, no. 6, pp. 887–948, 1977.

- [34] U. Nitsan, "Electromagnetic emission accompanying fracture of quartz-bearing rocks," *Geophysical Research Letters*, vol. 4, no. 8, pp. 333–336, 1977.
- [35] J. W. Warwick, C. Stoker, and T. R. Meyer, "Radio emission associated with rock fracture: possible application to the great Chilean Earthquake of May 22, 1960," *Journal of Geophysical Research*, vol. 87, no. 4, pp. 2851–2859, 1982.
- [36] M. Maxwell, R. D. Russell, A. W. Kepic, and K. E. Butler, "Electromagnetic responses from seismically excited targets B: non-piezoelectric phenomena," *Exploration Geophysics*, vol. 23, no. 2, pp. 201–208, 1992.
- [37] G. O. Cress, B. T. Brady, and G. A. Rowell, "Sources of electromagnetic radiation from fracture of rock samples in the laboratory," *Geophysical Research Letters*, vol. 14, no. 4, pp. 331–334, 1987.
- [38] Y.-Q. Zhu and X.-L. Luo, "A study of mechanism on electromagnetic emission associated with rock fracture," *Acta Geophysica Sinica*, vol. 34, no. 5, pp. 594–601, 1991 (Chinese).

Research Article

Bolt Pull-Out Tests of Anchorage Body under Different Loading Rates

Tong-bin Zhao,^{1,2,3} Wei-yao Guo,^{1,3} Yan-chun Yin,^{1,3} and Yun-liang Tan^{1,3}

¹State Key Laboratory of Mining Disaster Prevention and Control Co-Founded by Shandong Province and the Ministry of Science and Technology, Shandong University of Science and Technology, Qingdao 266590, China

²State Key Laboratory of Safe and Effective Coal Mining, Anhui University of Science and Technology, Huainan 232001, China

³School of Mining and Safety Engineering, Shandong University of Science and Technology, Qingdao 266590, China

Correspondence should be addressed to Wei-yao Guo; 363216782@qq.com

Received 13 November 2014; Accepted 9 January 2015

Academic Editor: Shimin Liu

Copyright © 2015 Tong-bin Zhao et al. This is an open access article distributed under the Creative Commons Attribution License, which permits unrestricted use, distribution, and reproduction in any medium, provided the original work is properly cited.

Based on the force analysis and mechanical transmission mechanism of grouting bolts, the self-developed test apparatus for interfacial mechanics is used to study the distribution rule of axial force and interfacial stress of bolts in anchorage body. At the same time, pull-out tests of anchorage body are simulated with the particle flow code software (PFC^{2D}), and stress distribution and failure patterns are researched under different loading rates. The results show that the distribution of axial force and interfacial shear stress is nonuniform along the anchorage section: axial force decreases, shear force increases first and then decreases, and the maximum value of both of them is closed to the pull-out side; with the increase of loading rates, both of axial force and interfacial shear stress show a trend of increase in the upper anchorage section but changes are not obvious in the lower anchorage section, which causes serious stress concentration; failure strength of pull-out and loading rates show a linear correlation; according to loading rates' impact on the anchoring effect, the loading rates' scope can be divided into soft scope ($v < 10$ mm/s), moderate scope (10 mm/s $< v < 100$ mm/s), and strong scope ($v > 100$ mm/s).

1. Introduction

Rock burst is a special form of mine pressure. It is a dynamic failure phenomenon due to the instantaneous release of energy caused by the accumulated energy that exceeds the strength of coal and rock under high stress of surrounding rock of roadways or working faces, and it can bring serious threats to the safety production of coal mines [1–3]. In order to reduce the damage caused by rock burst, international academics have done a deep study in the field of rock burst, such as occurrence mechanism [4, 5], monitoring [6, 7], and control technique [8, 9]. What is more, new technique of roadway support and design have been put forward, such as support technique of rigid and flexible energy storage [10], the high pretension and intensive bolts with U-shaped steel [11], and large deformation bolt cable [12]. These support methods effectively reduce the harm of rock burst. All of these support techniques contain bolt support which is an essential part.

Therefore, the study of anchorage mechanism of bolts under shock load has an important role in the design of roadway support.

Bolt supporting technology is an effective reinforcement technique for roadway surrounding rock, and it has been widely used in coalmine production [13, 14]. The research of interaction between bolts surrounding rock and anchorage mechanism is essential for the effectiveness of the anchorage design and the stable control of roadway surrounding rock. Many international scholars did lots of research work in this area [15–17]. Lots of field tests and laboratory tests show that the failure of anchorage body mostly appears in the bonding interface, so the distribution of interfacial shear stress is one of the focuses for researching the anchorage mechanism. There are three main ideas about the distribution pattern of interfacial shear stress: power function theory [18], “neutral point” theory [19], and shear stress distribution based on Mindlin solution [20]. The results above have been got

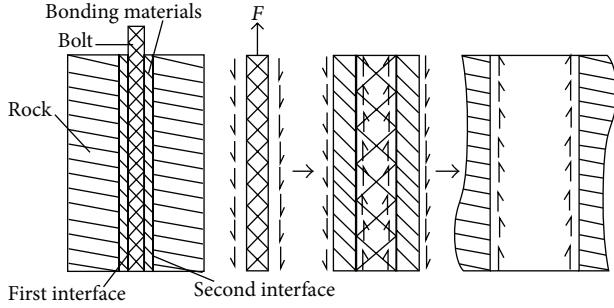


FIGURE 1: The structure of anchorage body and its stress distribution.

through the analysis of bolts under static load, but in mines of rock burst, bolts of roadway surrounding rock are often pulled out fast and then lead to anchorage failure. Therefore, the research of mechanical behaviors of anchorage structure under different loading rates is of importance to guide the rock-burst roadway support. In this paper, the test apparatus for interfacial mechanics based on self-development is used to study the distribution rule of axial force and interfacial shear stress of the anchorage structure. Using the PFC^{2D} software, bolt drawing tests are simulated to study the stress distribution characteristics of anchorage structure under different loading rates and analyze the failure patterns of anchorage body.

2. Testing Theory for Interfacial Stress of Anchorage Structure

In the bolt supporting system of roadways, under the influence of deformation and stress of surrounding rock, bolt plates move and deform with the rock mass's surface. At the same time, the plate pulls the bolt, which makes the bolt in tension. The analysis of the bolt's mechanics characteristics and its relationship with the surrounding rock under pull-out condition is significant for the research of anchorage support and anchorage mechanism.

The bolt and anchoring rock mass in the roadway's surrounding rock can be called anchorage body, which is composed of three mediums (bolt, bonding materials, and rock mass) and two bonding interfaces (the first interface: the contact area between bolts and bonding material; the second interface: the contact area between rock mass and bonding materials) [21], as is shown in Figure 1. When the bolt is pulled, the transmission of force is from the bolt body to bonding materials and then to rock mass. Therefore, the research of stress distribution of the surface is the premise and foundation for establishing anchorage design and theory.

During the test, the end of the bolt is exerted by a force F , under the action of the external force; the bolt body bar will produce a tensile mechanical response. The bolt body is pulled, which will produce shear mechanical effects between bolts and bonding materials, and its mechanical model is shown in Figure 2 [21]. The corresponding points' axial force can be calculated by the strain value of the bolt body:

$$N_i = E\varepsilon_i A, \quad (1)$$

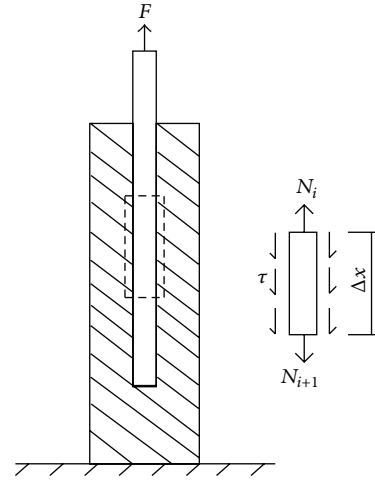


FIGURE 2: Interfacial mechanics model between bolts and bonding materials.

where N_i is the axial force of the strain gauge of point i , E is the elastic modulus of the steel bolt body, ε_i is the strain value of point i , and A is the area of cross section of the steel bolt body.

The analysis of bolt body's balance conditions is shown in Figure 2, where the axial force difference between two ends of the bolt body is balanced by the longitudinal shear stress in the surface and this kind of shear stress is bonding stress provided by bonding materials around. The axial shear stress distribution along the bolt can be got through formulas (2). From the equilibrium relation, we can get

$$\begin{aligned} N_i - N_{i+1} &= \tau_{i,i+1} \pi d \Delta x, \\ \tau_{i,i+1} &= \frac{N_i - N_{i+1}}{\pi d \Delta x}, \end{aligned} \quad (2)$$

where $\tau_{i,i+1}$ is the average interfacial shear stress between points i and point $i + 1$, d is the diameter of the bolt body, and Δx is distance between strain gauges.

3. Pull-Out Test Method

3.1. Development of Indoor Test Apparatus. The test apparatus for interfacial mechanics is based on RLJW-2000 servo testing machine, using the original hardware facilities and control system, and so forth, and through specific technical means (changing the oil-way, increasing the number of acquisition systems, making the anchorage body, and designing connective device) to achieve pull-out tests of anchorage body. The test apparatus for interfacial mechanics is shown in Figure 3; the connective device between each component is mainly connected by screws. The end of anchorage body is connected with the oil cylinder of the test through eye nuts, knuckle bearing, and junction plate, and the other end of the anchorage body is connected with the bearing-pull board through screws.

The anchorage body mainly includes the bolt, the matrix, and bonding materials, as is shown in Figure 4. The anchorage matrix is concrete materials, and three steel bars are

TABLE 1: Micromechanical parameters of anchorage body's pull-out test.

Properties	Density (kg/m ³)	Radius (mm)	Friction coefficient	Radius of parallel bond (mm)	Elasticity modulus (GPa)	Bonding strength (MPa)
Bolt	7500	10	0.5	1	220	500
Bonding materials	3000	1.3~1.7	0.5	1	12	30
Matrix	2500	1.3~1.7	0.5	1	10	20

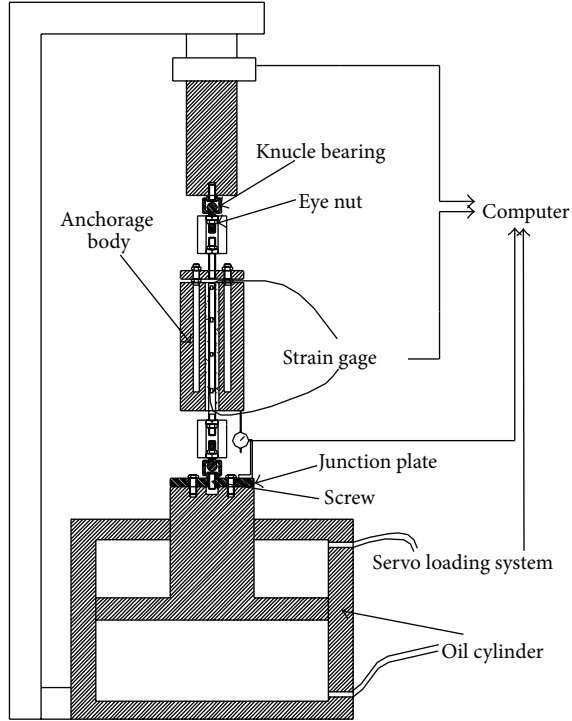


FIGURE 3: Pull-out test apparatus of anchorage body.

embedded in the concrete column for fixing the matrix when testing. The bolt is screw-thread steel, two symmetric cuttings are designed in the bolt anchorage section, and strain gauges are arranged in cuttings. The force bolt is inserted into the concrete matrix with resin to bond them.

The alternated RLJW-2000 testing machine is loading system for pull-out tests of the anchorage body, the DH3815N strain gauge is stress testing system for interfacial stress, and dial indicators are used to record pulling displacement of the bolt end. The loading rate is 5 mm/min.

3.2. Numerical Tests of Particle Flow. Preparations of the anchorage body are complex, mechanical properties between anchorage models are discrete, and the machine's loading rate fluctuates in a limited range, so dynamic loading tests cannot be carried out, although laboratory pull-out tests of anchorage body are effective means for studying the interfacial mechanics characteristics. Therefore, PFC^{2D} software is used to establish a pull-out test model of the anchorage body (the basic numerical model's establishment was based on the laboratory tests' results), and then numerical tests are used

to research the anchorage mechanical characteristics under different loading rates.

The PFC^{2D} is used as the numerical software, which is an effective means for the study of rock and soil mechanical failure mechanism [22]. The parallel bond model in the particle flow program represents the bonding between particles, which is often used to simulate dense materials, such as rock. Parameters in the parallel bond model which need to be set are grain friction coefficient (μ), bond stiffness (k_n and k_s), parallel bond stiffness (\bar{k}_n and \bar{k}_s), parallel bond strength (σ_n and σ_s), and radius coefficient of parallel bond (λ). These parameters can be obtained from the following [23]:

$$\begin{aligned}
 k_n &= 2E_c, \\
 k_s &= \frac{k_n}{k_n/k_s}, \\
 \bar{k}_n &= \frac{\bar{E}_c}{2\bar{r}}, \\
 \bar{k}_s &= \frac{\bar{k}_n}{k_n/k_s},
 \end{aligned} \tag{3}$$

where E_c and \bar{E}_c are Young's modulus of grain contact and parallel grain contact, respectively; both (k_n/k_s) and (\bar{k}_n/\bar{k}_s) are set to be 2.5 generally; \bar{r} is the mean radius between two grains; λ is often set to be 1. Generally, E_c and \bar{E}_c are equal, σ_n and σ_s are equal, and the four parameters can be obtained by the method of micromechanical parameters calibration.

In this paper, the parallel bond model to simulate the bolt pull-out test is used and the basic model is shown in Figure 5. The model size is 300 × 300 mm; the bolt is composed of particles of the same radius, recording the vertical force of bolt particles as bolt axial force during the operating process. Measuring circles are arranged in the bonding materials for recording the interfacial shear stress. Micromechanical parameters are listed in Table 1.

3.3. Testing Scheme. According to strain rates, deformation can be divided into five degrees [24], which is shown in Table 2. In order to quantify different loading rates' effects on the anchorage body, static load and quasi-dynamic load are selected, loading rate levels are 10^{-1} , 10^0 , 10^1 , 10^2 , and 10^3 , respectively, and the loading rates are 0.5 mm/s, 1.0 mm/s, 5.0 mm/s, 10.0 mm/s, 50.0 mm/s, 100.0 mm/s, 500.0 mm/s, and 1000 mm/s for simulation.

Tests are to study the loading rates' effect on the anchorage strength with the loading rate as the only variable during the simulating process. Loading rates' influence on the anchoring

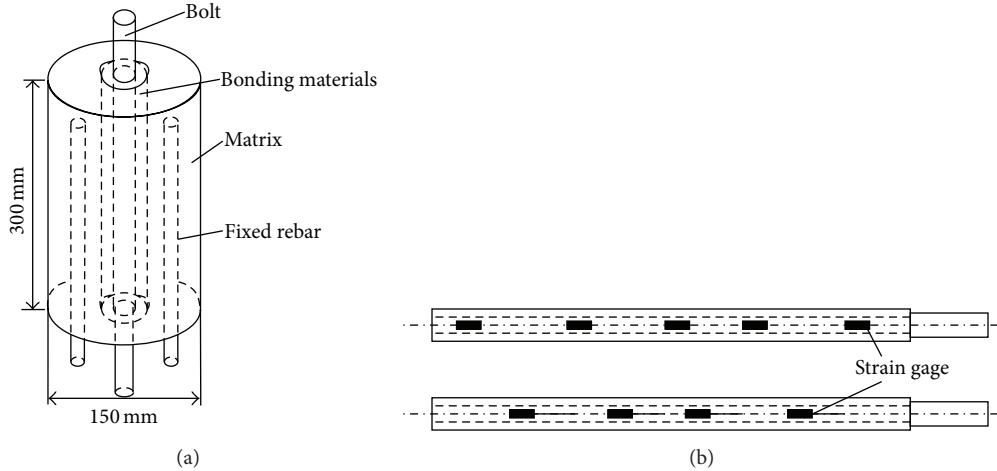


FIGURE 4: Structure model of anchorage body. (a) Integral structure. (b) Force anchor.

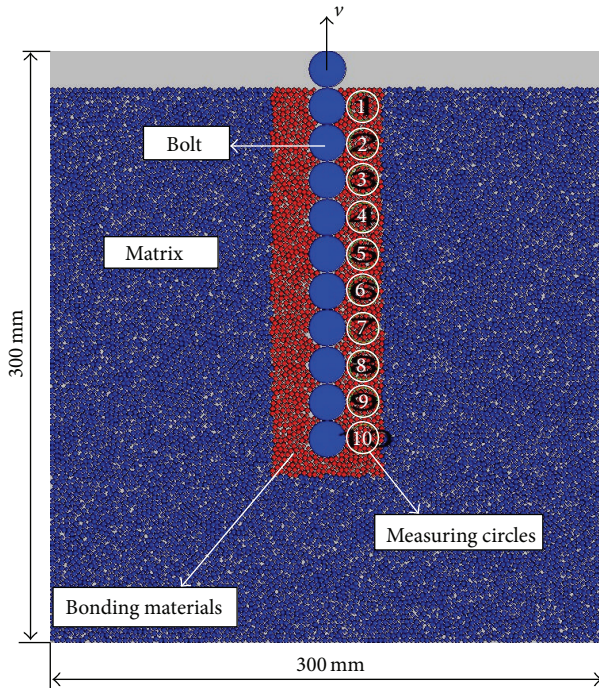


FIGURE 5: Micromechanical model of anchorage body's pull-out test.

TABLE 2: Rank classification of strain rates and loading rates [24].

Loading cases	Strain rates (s^{-1})	Loading rates (mm/s)
Creep	$<10^{-5}$	$<10^{-3}$
Static	$10^{-5} \sim 10^{-1}$	$10^{-3} \sim 10^1$
Quasi-dynamic	$10^{-1} \sim 10^1$	$10^1 \sim 10^3$
Dynamic	$10^1 \sim 10^4$	$10^3 \sim 10^6$
Superdynamic	$>10^4$	$>10^6$

effect is illustrated through changes of failure strength, failure patterns, axial force, and shear stress.

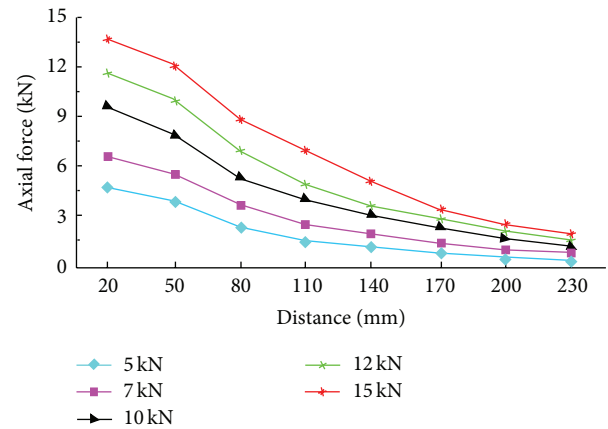


FIGURE 6: Axial force distribution.

4. Results and Discussion

4.1. Influence of Loading Rates on Axial Force Distribution.

As is shown in Figure 6, axial force's distribution curves of bolts along the anchorage section could be got by pull-out tests of anchorage body. The distribution of axial force is nonuniform—on the pull-out side exists an obvious stress concentration, and it decreases gradually along the anchorage section. With the increase of pull-out force, the axial force of anchorage section increases gradually, and the largest force is on the pull-out side, while the amplitude of axial force's increase decreases along the anchorage section. Therefore, the scope of axial force's influence is certain, which means a length of effective anchorage exists.

The change of bolt axial force under different loading rates obtained from numerical simulation is shown in Figure 7, and its distribution is similar to the indoor test—the axial force decreases along the anchorage section. If $v < 10$ mm/s, its change on the influence of axial force can be ignored; if 10 mm/s $< v < 100$ mm/s, with the increase of loading rates, the axial force increases slowly between the pull-out side and

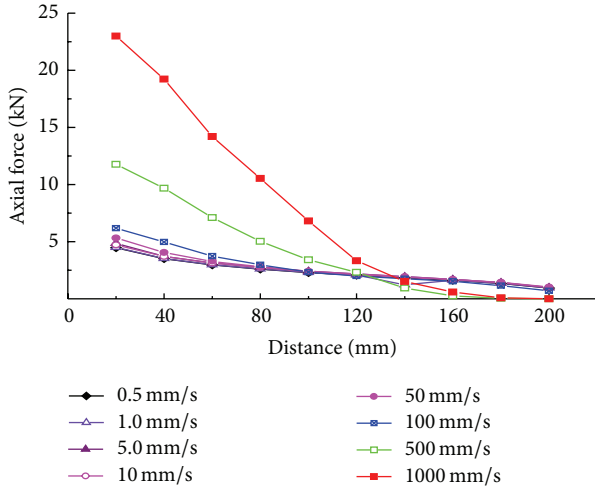


FIGURE 7: Changes of axial force under different loading rates.

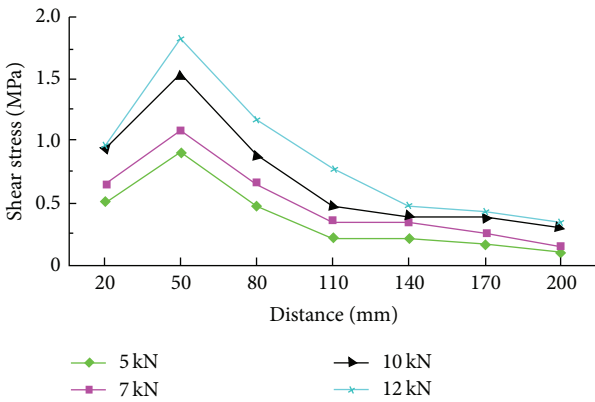


FIGURE 8: Shear stress distribution.

the middle, while it has no obvious changes between the middle and the bottom; if $v > 100$ mm/s, the axial force is much larger between the pull-out side and the middle than that of other loading rates ($v < 100$ mm/s) whereas axial force is almost zero along the distance between the middle and the bottom. Therefore, if the loading rate $v > 100$ mm/s, the larger the loading rates, the more steep the curve of axial force distribution, and that is prone to causing the impact damage of anchorage body.

4.2. Influence of Loading Rates on Interfacial Shear Stress Distribution. The curve of shear stress's distribution along the anchoring section is shown in Figure 8. The distribution of interfacial shear stress is nonuniform—shear stress is small at the orifice of the pull-out side but reaches peak after a certain distance away from the orifice and then drops rapidly. The shear stress under the middle of anchorage section changes a little, which means shear stress has a certain influencing scope as the axial force. With the increase of pull-out force, interfacial shear stress increases gradually, and the scope of its influence also increases, but its concentration remains mainly on the pull-out part of anchorage section.

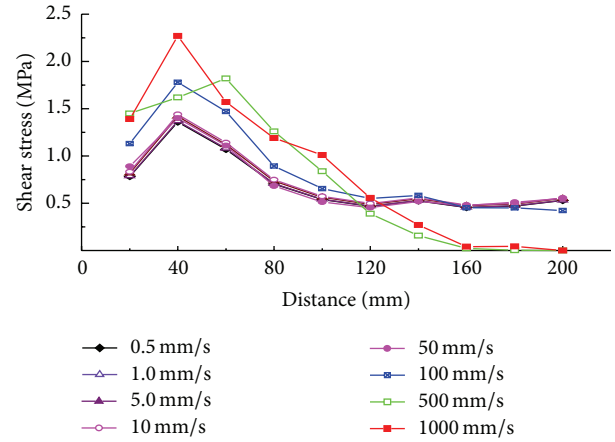


FIGURE 9: Changes of shear stress under different loading rates.

The change of interfacial shear stress under different loading rates is shown in Figure 9. When the loading rate v is the same, the distribution of shear stress is nonuniform—the shear stress increases firstly and then decreases with the increase of anchorage length. If $v < 10$ mm/s, its change on the influence of shear stress can be ignored; if 10 mm/s $< v < 100$ mm/s, with the increase of loading rates, the shear stress increases slowly; if $v > 100$ mm/s, the shear stress is larger between the pull-out part and the middle part of the anchorage section, while it is almost zero on the other part. Obviously, high loading rates cause apparent concentration of shear stress and its serious nonuniform distribution.

4.3. Influence of Loading Rates on the Pull-Out Force. According to pull-out tests of PFC scheme, different loading rates have been exerted at the end of bolt until the body's failure. Curves of pull-out load versus displacement and curves of failure load versus loading rates are shown in Figures 10 and 11, respectively.

As is shown from the two figures, if the loading rate $v < 10$ mm/s, the pull-out load is not affected obviously; if the loading rate $v > 10$ mm/s, the increase of loading rates will influence the pull-out load more and more obviously. The pull-out load of anchorage body's failure and loading rates show a linear correlation (the fitting curve: $y = 64.10188 + 0.27055x$).

4.4. Influence of Loading Rates on Failure Patterns. Final failure patterns of the model under different loading rates are shown in Figure 12, and we can find that if the loading rate $v < 10$ mm/s, the failure mode of the model is matrix cracking with a main crack, which crosses the bottom of the matrix; if the loading rate $v > 10$ mm/s, cracks grow in the upper part in addition to the main crossing crack; when the loading rate $v > 100$ mm/s, with the continuous increase of loading rates, cracks grow rapidly along the middle and upper parts of the bolt until the matrix cracking destruction evolves the bolt pull-out failure with large fracture zone. That means the higher the loading rate gets, the higher the anchorage body's broken degree will be. According to the influence degree

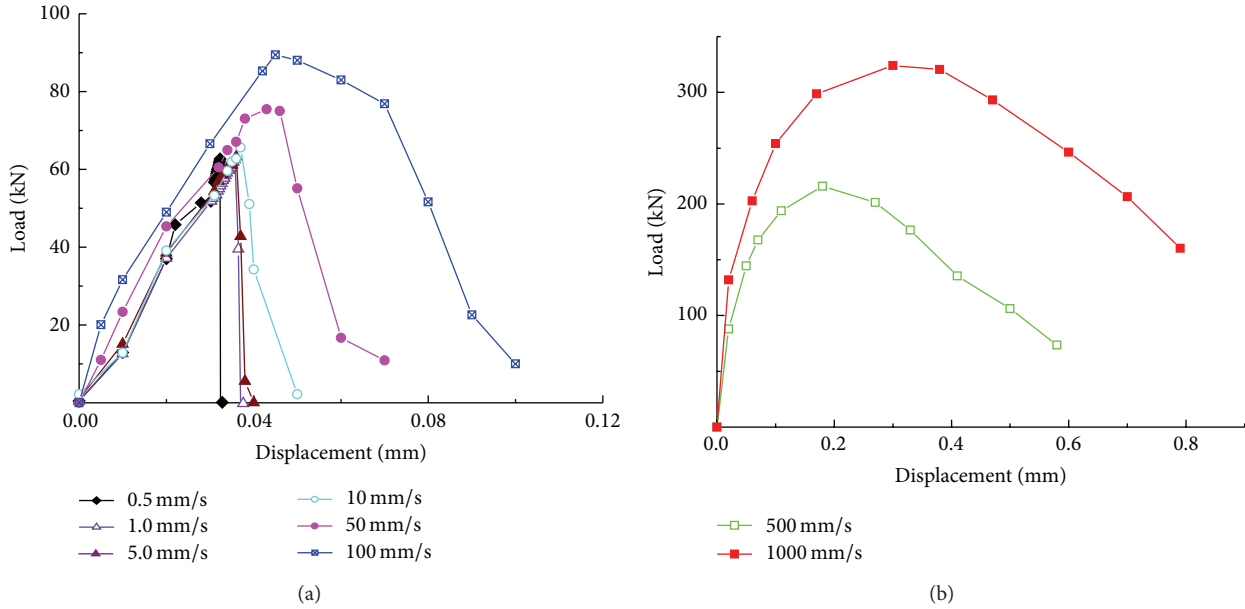


FIGURE 10: Load versus displacement. (a) $v \leq 100$ mm/s; (b) $v > 100$ mm/s.

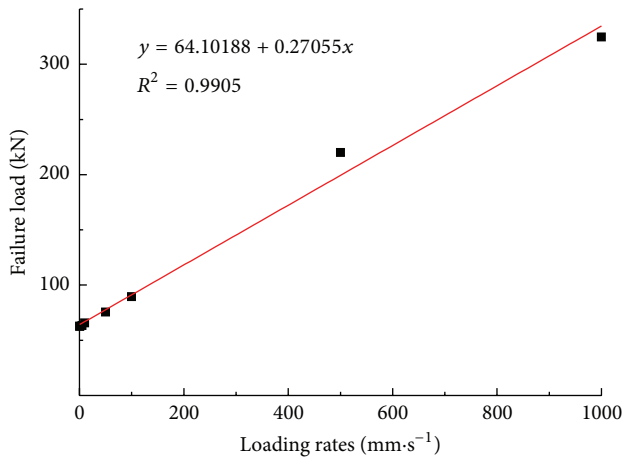


FIGURE 11: Failure load versus loading rate.

of loading rates, loading rates' scope can be divided into three conditions: soft scope ($v < 10$ mm/s), moderate scope ($10 \text{ mm/s} < v < 100$ mm/s), and strong scope ($v > 100$ mm/s).

The larger the loading rates are, the greater force the anchor stressed. Under high loading rates, the serious stress concentration along the upper anchorage section causes the broken of bonding materials and matrix around the bolt, which eventually leads to the bolt-out alone as the failure pattern of anchorage body.

5. Conclusions

Through the self-developed test apparatus for interfacial mechanics to study the distribution rule of axial force and

interfacial stress of bolts in the anchorage body, PFC^{2D} software is employed to simulate pull-out tests of the anchorage body to research stress distribution under different loading rates. Some conclusions are as follows.

(1) In the pull-out test of anchorage body, the distribution of axial force is nonuniform. On the pull-out side exists an obvious stress concentration, and it decreases gradually along the anchorage section. With the increase of loading rates, axial force between the pull-out side and the middle of anchorage section increases, but, between the middle and the bottom, changes of axial force are not obvious. That causes the distribution curve of axial force to become more steep with the increase of loading rates, which means the axial force is greater in the upper anchorage section than that in the lower anchorage section.

(2) The distribution of interfacial shear stress is nonuniform. Shear stress is small at the orifice of the pull-out section but reaches peak after a certain distance away from the orifice and then drops rapidly. With the increase of loading rates, interfacial shear stress between the pull-out side and the middle of anchorage section shows a trend of increase, but changes are not obvious in the lower anchorage section. That causes serious stress concentration of the upper anchorage section and its nonuniform distribution.

(3) According to loading rates' impact on anchoring effect, the loading rates' scope can be divided into the soft scope ($v < 10$ mm/s), the moderate scope ($10 \text{ mm/s} < v < 100$ mm/s), and the strong scope ($v > 100$ mm/s). Pull-out load will increase with the increase of loading rates, and they show a linear correlation. With the increase of loading rates, failure patterns will come into a trend of bolt pull-out only with wide broken zone due to serious stress concentration of the upper part of anchorage section.

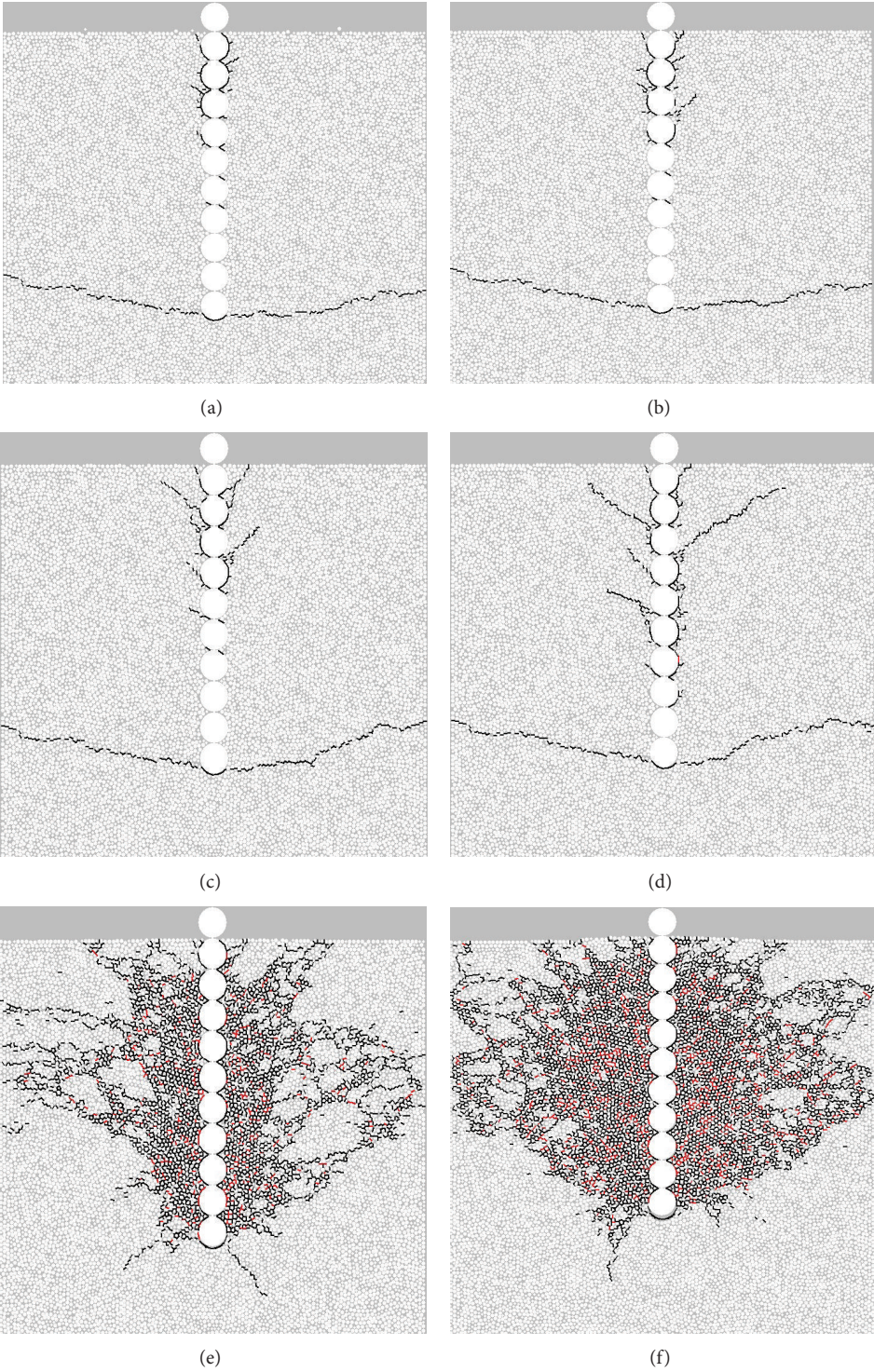


FIGURE 12: Failure patterns under different loading rates. (a) 5 mm/s; (b) 10 mm/s; (c) 50 mm/s; (d) 100 mm/s; (e) 500 mm/s; (f) 1000 mm/s.

Conflict of Interests

The authors declare that there is no conflict of interests regarding the publication of this paper.

Acknowledgments

The work was supported by the Natural Science Foundation of China (no. 51474136), the open fund of State Key Laboratory of Mining Disaster Prevention and Control Co-founded by Shandong Province and the Ministry of Science and Technology (MDPC2013KF06), and the open fund of State Key Laboratory of Safe and Effective Coal Mining (JYB-SYS2014202). The authors would like to thank them.

References

- [1] Y.-L. Tan, Z. Zhang, and C.-L. Ma, "Rock burst disaster induced by mining abutment pressure," *Disaster Advances*, vol. 5, no. 4, pp. 378–382, 2012.
- [2] Y. Tan, F. Li, Z. Hui et al., "Analysis on acoustic emission pattern for rock burst," *Chinese Journal of Rock Mechanics and Engineering*, vol. 19, no. 4, pp. 425–428, 2000.
- [3] Z.-L. Li, L.-M. Dou, W. Cai et al., "Investigation and analysis of the rock burst mechanism induced within fault-pillars," *International Journal of Rock Mechanics and Mining Sciences*, vol. 70, pp. 192–200, 2014.
- [4] L. Wang, Z.-L. Lu, and Q. Gao, "A numerical study of rock burst development and strain energy release," *International Journal of Mining Science and Technology*, vol. 22, no. 5, pp. 675–680, 2012.
- [5] S.-H. Liu, "Nonlinear catastrophe model and chaotic dynamic mechanism of compound coal-rock unstable failure under coupled static-dynamic loading," *Journal of the China Coal Society*, vol. 39, no. 2, pp. 292–300, 2014.
- [6] L.-M. Dou, W. Cai, S.-Y. Gong, R.-J. Han, and J. Liu, "Dynamic risk assessment of rock burst based on the technology of seismic computed tomography detection," *Journal of the China Coal Society*, vol. 39, no. 2, pp. 238–244, 2014.
- [7] L.-M. Dou, T.-J. Chen, S.-Y. Gong, H. He, and S. Zhang, "Rock-burst hazard determination by using computed tomography technology in deep workplace," *Safety Science*, vol. 50, no. 4, pp. 736–740, 2012.
- [8] H. Lan, Q.-X. Qi, J.-F. Pan et al., "Study status and prospects of mine pressure bumping control technology in China," *Coal Science and Technology*, vol. 39, no. 1, pp. 11–15, 2011.
- [9] M.-S. Gao, L.-M. Dou, N. Zhang, K. Wang, and B.-S. Zheng, "Strong-soft-strong mechanical model for controlling roadway surrounding rock subjected to rock burst and its application," *Rock and Soil Mechanics*, vol. 29, no. 2, pp. 359–364, 2008.
- [10] X.-F. Lü and Y.-S. Pan, "Simulation and numerical analysis of impact failure law of coal roadway under rigid-flexible energy absorbing support," *Chinese Journal of Geotechnical Engineering*, vol. 34, no. 3, pp. 477–482, 2012.
- [11] W.-J. Wang, G. Peng, and J. Huang, "Research on high-strength coupling support technology of high stress extremely soft rock roadway," *Journal of the China Coal Society*, vol. 36, no. 2, pp. 223–228, 2011.
- [12] M.-C. He, J. Wang, X.-M. Sun, and X.-J. Yang, "Mechanics characteristics and applications of prevention and control rock bursts of the negative poisson's ratio effect anchor," *Journal of the China Coal Society*, vol. 39, no. 2, pp. 214–221, 2014.
- [13] L. V. Rabcewicz, "The new Austrian tunneling method," *Water Power*, vol. 17, no. 1, pp. 511–515, 1964.
- [14] A.-H. Lu, J.-H. Xu, and H.-S. Liu, "Effect of a preload force on anchor system frequency," *International Journal of Mining Science and Technology*, vol. 23, no. 1, pp. 135–138, 2013.
- [15] Y.-S. Kang, Q.-S. Liu, G.-Q. Gong, and H.-C. Wang, "Application of a combined support system to the weak floor reinforcement in deep underground coal mine," *International Journal of Rock Mechanics and Mining Sciences*, vol. 71, pp. 143–150, 2014.
- [16] T.-B. Zhao, Y.-C. Yin, Y.-L. Tan, and Y. Qiu, "Mechanical test of bolt interface and microscopic simulation of transfer law for shear stress," *Journal of Mining and Safety Engineering*, vol. 28, no. 2, pp. 220–224, 2011.
- [17] T.-B. Zhao, Y.-L. Tan, S.-S. Liu, and Y.-X. Xiao, "Analysis of rheological properties and control mechanism of anchored rock," *Rock and Soil Mechanics*, vol. 33, no. 6, pp. 1730–1734, 2012.
- [18] S. H. E. Phillips, *Factors Affecting the Design of Anchorages in Rock*, Cementation Research, London, UK, 1970.
- [19] M.-S. Wang, H.-R. He, and Y.-T. Zheng, "Mechanical model of full grouting bolt and its application," *Metal Mine*, no. 4, pp. 21–24, 1983.
- [20] C.-A. You, M. Gao, L.-M. Zhang, Y.-B. Zhan, and J.-H. Wang, "Experimental research on stress distribution in anchorage body," *Rock and Soil Mechanics*, vol. 25, supplement 1, pp. 63–66, 2004.
- [21] T.-B. Zhao, *Creep Properties Test and Anchorage Control Time-Dependency of Surrounding Rock in Deep Mine*, Shandong University of Science and Technology, Qingdao, China, 2009.
- [22] Y.-C. Yin, T.-B. Zhao, Y.-L. Tan, and Z. Zhang, "Research of stress distribution evolution law and influencing factors," *Journal of Mining and Safety Engineering*, vol. 30, no. 5, pp. 712–716, 2013.
- [23] D. O. Potyondy and P. A. Cundall, "A bonded-particle model for rock," *International Journal of Rock Mechanics & Mining Sciences*, vol. 41, no. 8, pp. 1329–1364, 2004.
- [24] M.-R. Shen and J.-F. Chen, *Rock Mechanics*, Tongji University Press, Shanghai, China, 2006.

Research Article

Experimental Study on Anisotropic Strength and Deformation Behavior of a Coal Measure Shale under Room Dried and Water Saturated Conditions

Jingyi Cheng,^{1,2} Zhijun Wan,¹ Yidong Zhang,³ Wenfeng Li,^{1,2}
Syd S. Peng,² and Peng Zhang²

¹School of Mines, Key Laboratory of Deep Coal Resource Mining, Ministry of Education of China, China University of Mining and Technology, Xuzhou, Jiangsu 221116, China

²Department of Mining Engineering, West Virginia University, Morgantown, WV 26505, USA

³State Key Laboratory of Coal Resources and Safe Mining, China University of Mining and Technology, Xuzhou, Jiangsu 221116, China

Correspondence should be addressed to Zhijun Wan; zhjwumt@hotmail.com

Received 2 October 2014; Revised 26 January 2015; Accepted 29 January 2015

Academic Editor: Marcin A. Lutyński

Copyright © 2015 Jingyi Cheng et al. This is an open access article distributed under the Creative Commons Attribution License, which permits unrestricted use, distribution, and reproduction in any medium, provided the original work is properly cited.

This paper presents an experimental investigation of anisotropic strength and deformation behavior of coal measure shale. The effect of two factors (i.e., anisotropy and water content) on shale strength and deformation behavior was studied. A series of uniaxial and triaxial compression tests were conducted on both room dried and water saturated samples for different lamination angles. The test results indicate that (1) the compressive strength, cohesion, internal friction angle, tangent Young's modulus, and axial strain corresponding to the peak and residual strengths of room dried specimens exhibit anisotropic behavior that strongly depends on the orientation angle (β); (2) in comparison to the room dried samples, the compressive strength and Young's modulus as well as the anisotropy are all reduced for water saturated specimens; and (3) the failure mechanism of the samples can be summarized into two categories: sliding along lamination and shearing of rock material, with the type occurring in a particular situation depending strongly on the lamination orientation angles with respect to the major principal stress. According to the findings, it is strongly recommended that the effect of anisotropy and water content on the strength and deformation behavior of the rock must be considered in ground control designs.

1. Introduction

Shale is one of the most abundant rock materials in coal mines and forms the bulk of the roofs and floors of underground coal mines. Consequently, most cases of ground control failure are associated with shale. Among the 36 cases with detailed descriptions of geological conditions depicted by Peng [1], there were 32 cases with the immediate roof being shale, and all 9 roof fall cases occurred in shale strata.

Being the weakest part of shale, laminations play a key role in many kinds of ground control failures but its role in controlling rock mass behavior has been mostly ignored by researchers and engineers of the coal mining industry [2]. Current research on ground control design and analysis of the causes of ground control failures using computer

modeling and physical simulation are largely based on the assumption that the mechanical response of shale is isotropic [3]. However, because of the presence of laminations, the behavior of sedimentary rock is anisotropic. During mining, the stresses in the roof strata redistribute continuously. The orientation of the major principal stress (σ_1) with respect to the laminations or foliation of sedimentary rock may not be in the vertical or horizontal directions, and the failure strength of the rock mass is highly dependent on the anisotropic properties of the sedimentary rock. Hence, anisotropy must be taken into consideration in the dynamic analysis of geologic structure or in the prediction of dynamic disasters in engineering projects [4].

In the past few decades, the strength anisotropy of many kinds of rock has been investigated, such as shale and slates

in [4–8], gneisses and schists in [9–11], phyllites in [12], sandstone in [7, 13], and artificial transversely isotropic rock in [14–16]. Their works demonstrate that the failure strength of anisotropic material is related to the inclination angle (β) of the specimen laminations with respect to the direction of the major principal stress. Ramamurthy [12] stated that the maximum failure compressive strength is at $\beta = 0^\circ$ or $\beta = 90^\circ$ and the minimum value is around $\beta = 30^\circ$. Meanwhile, several investigators [8, 12, 16–19] have proposed a series of failure criteria to predict the strength of anisotropic rocks. By observing the failure processes and modes, several failure mechanisms have been proposed by researchers on different kinds of rock [5, 8, 14]. In spite of those attempts to investigate the mechanical properties of shale, the anisotropic strength and deformation behavior, especially the failure mechanism and the postfailure behavior of coal measure shale, remain obscure.

In addition to the presence of laminations, another important factor controlling shale behavior in coal mines is water content, including liquid water (manmade or natural, e.g., water inrush from the roof and flooding) and high moisture content ventilation air. It must be pointed out that because of the abundance of roof water, this issue is more serious in Chinese coal mines [20–22] than those in most other countries. In the past, some researchers [6, 23–26] have investigated the impact of ventilation air moisture on shale. Their work demonstrated that the properties of shale changed greatly as the water content increased. However, those studies dealt with the special situation when the rock surface was exposed to moisture carried by ventilation air, instead of the more general case where underground shale tends to be immersed in water most of the time. Furthermore, the detrimental effects of high water content on the mechanical properties of different types of rock have been investigated in [27–33]. But most of these tests were conducted under unconfined conditions, and few tests were performed on shale, especially coal measure shale, and none of them considered the effect of water content on rock anisotropy. Hence, it is of great value to conduct triaxial tests on the water saturated samples to evaluate the effect of water.

In this research, the uniaxial and triaxial compression tests were conducted with the confinement in the range of engineering interests to study the transverse anisotropy behavior of coal measure shale over the entire range of β under either the room dried or the saturated conditions.

2. Coal Measure Shale

A well laminated shale block was obtained from the roof strata of Pittsburgh Seam of a surface mine in Frostburg, Maryland, USA. To minimize variations in the natural moisture content of shale samples and in order to obtain conditions similar to in-situ, the samples were kept wrapped in plastic sheets until specimen preparation. The procedure used for preparation followed the ASTM Standard D7012-10 [34]. Cylindrical specimens 50 mm in diameter with length-to-diameter ratio of 2 were cored at different angles ($\beta = 0^\circ, 15^\circ, 30^\circ, 45^\circ, 60^\circ, 75^\circ, \text{ and } 90^\circ$) to the lamination.

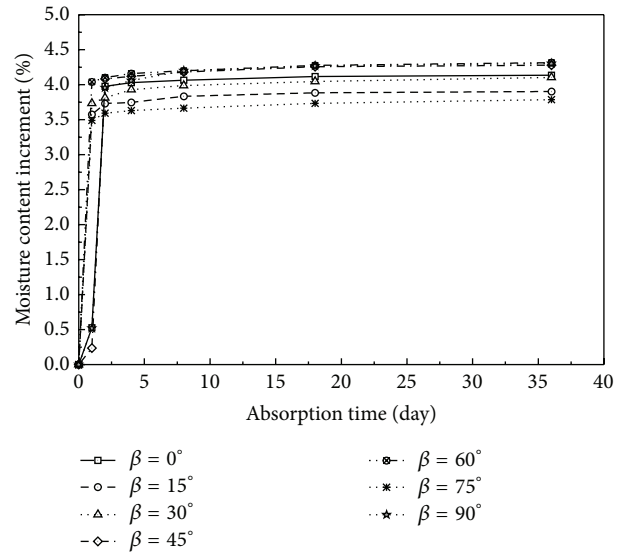


FIGURE 1: The moisture content increment of the specimens in the water saturated group.

Two groups of tests, room dried and water saturated, were performed at different values of β ($0^\circ, 15^\circ, 30^\circ, 45^\circ, 60^\circ, 75^\circ, \text{ and } 90^\circ$). With respect to the confining pressure applied to the samples during testing, Brady and Brown [35] collected data for about 900 in situ stresses measured by various investigators in various parts of the world and found that the maximum horizontal stress was 30 MPa for depths up to 1000 m. Since most coal mines in the USA and China range from 101 to 1000 m in depth, a maximum confining pressure of 30 MPa should cover the stress conditions encountered. Hence, the confining pressure applied to the specimens for this research was no more than 30 MPa, that is, 0 MPa, 10 MPa, 20 MPa, and 30 MPa for room dried specimens.

Although the shale blocks were wrapped with plastic sheets during transport from the site to the laboratory, the specimens were unavoidably watered during the coring, cutting, and grinding processes. Hence, before the tests started, all the specimens in the room dried group were placed in the laboratory at room temperature for at least 2 weeks to release most of the moisture absorbed during specimen preparation. The moisture content for the specimens in the room dried group was obtained by performing standard tests. Small pieces of sample were dried at a temperature of $110^\circ\text{C} \pm 5^\circ$ for at least 16 h. By dividing the mass of lost moisture by the mass of solid particles, the moisture content was obtained. The test results show that the moisture content for the ready-to-test specimens in the room dried group was 0.79%.

All the specimens in the water saturated group underwent the same procedure as those in the air-dry group before they were immersed in water for about 36 days. For the specimens in this group, the moisture content increased to 3.79–4.23% due to immersion in water (Figure 1). Note that the terms “saturated” or “saturation” in this paper simply refer to the state achieved by immersing the specimens as described in this paper; it is difficult to achieve a full water saturation in this way.

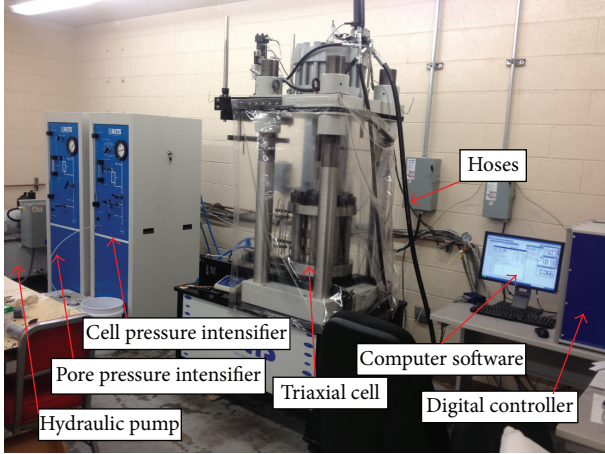


FIGURE 2: The GCTS triaxial rock test system.

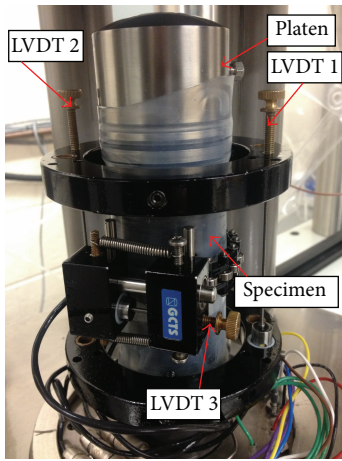


FIGURE 3: The layout of all 3 linear variable differential transformers (LVDTs).

3. Apparatus and Testing Procedures

The tests were carried out with the GCTS triaxial rock test system (RTX-1500) (Figure 2) housed in the Department of Mining Engineering of West Virginia University, Morgantown, WV, The United States. The testing system is equipped with two loading subsystems, a servo-controlled vertical loading subsystem with capacity of 1500 kN, and a servo-controlled confining pressure subsystem with capacity of 200 MPa. The stiffness of the testing frame is 1750 kN/mm.

The axial and lateral strains were determined from data obtained by the linear variable differential transformers (LVDTs) shown in Figure 3. The LVDT 1 and LVDT 2 were used to measure the axial displacements and LVDT 3 was a circumferential lateral deformation measurement device using a chain to measure the lateral/circumferential strain of the specimens. All 3 LVDTs were calibrated before testing.

Before testing, the sample was placed between the base cap and the top end cap inside the triaxial cell and jacketed with the polyolefin heat shrink tube to seal the sample from the confining fluid. Then, LVDTs and various sensors were

installed and the triaxial cell was placed onto the testing platform. A small differential stress ($\sigma_1 - \sigma_3$) of 0.5 MPa was applied to ensure that the sample was in good contact with the upper platen. In other words, in the initial part of loading sequence, the axial stress is consistently 0.5 MPa larger than the gradually increased confining pressure until reaching the planned level of confining pressure. During this period, the axial load was applied from a hydraulic pump with a constant strain rate of 0.002%/s until the test was finished.

4. Test Results

Figure 4 presents the variations of axial strain (ϵ_a) and lateral strain (ϵ_r) versus the differential stress ($\sigma_1 - \sigma_3$) of room dried specimens (RD) under confining pressures of 0 MPa, 10 MPa, 20 MPa, and 30 MPa for different orientation angles (β). The complete stress-strain curves corresponding to the water saturated specimens (WS) are also shown in Figure 4 marked with pink dots. For different orientation angles, the stress-strain curves, including both the prefailure and postfailure stages, exhibit different characteristics. The jagged portion of the stress-strain curves will be discussed in Section 5.4. Figure 4 shows that the water saturated samples have a lower compressive strength and Young's modulus as compared to the room dried ones.

5. Discussion

5.1. Effect of Anisotropy and Confining Pressure on Compressive Strength of Room Dried Samples

5.1.1. Peak Compressive Strength. Figure 5 shows the variation of the differential stress at failure ($\sigma_1 - \sigma_3$) and the corresponding sample orientation (β) at different confining pressures (σ_3) for room dried specimens. The compressive strength of shale is anisotropic and depends on its orientation angle (β). It reaches the maximum at $\beta = 0^\circ$ for confining pressures 10 MPa and 20 MPa and at $\beta = 90^\circ$ for confining pressure 0 MPa and 30 MPa. The minimum strength always occurs for samples with β between 30° and 45° under all confining pressures except uniaxial compressive tests. Similar results have been obtained by several researchers [5, 8] for other kinds of rock.

Nasseri et al. [10] defined the intensity of anisotropy for the strength of transversely isotropic materials with the following two parameters:

$$k_1 = \frac{(\sigma_1 - \sigma_3)_{\max}}{(\sigma_1 - \sigma_3)_{\min}} \quad (1)$$

$$k_2 = \frac{(\sigma_1 - \sigma_3)_{11}}{(\sigma_1 - \sigma_3)_{\perp}},$$

where k_1 defines the ratio of the maximum to the minimum strength and k_2 is the ratio of the failure stress for the samples parallel to the laminations to those perpendicular to the laminations.

k_1 is 3.5, 2.93, 2.45, and 2.14 for confining pressures 0, 10, 20, and 30 MPa, respectively (Figure 6). In other words,

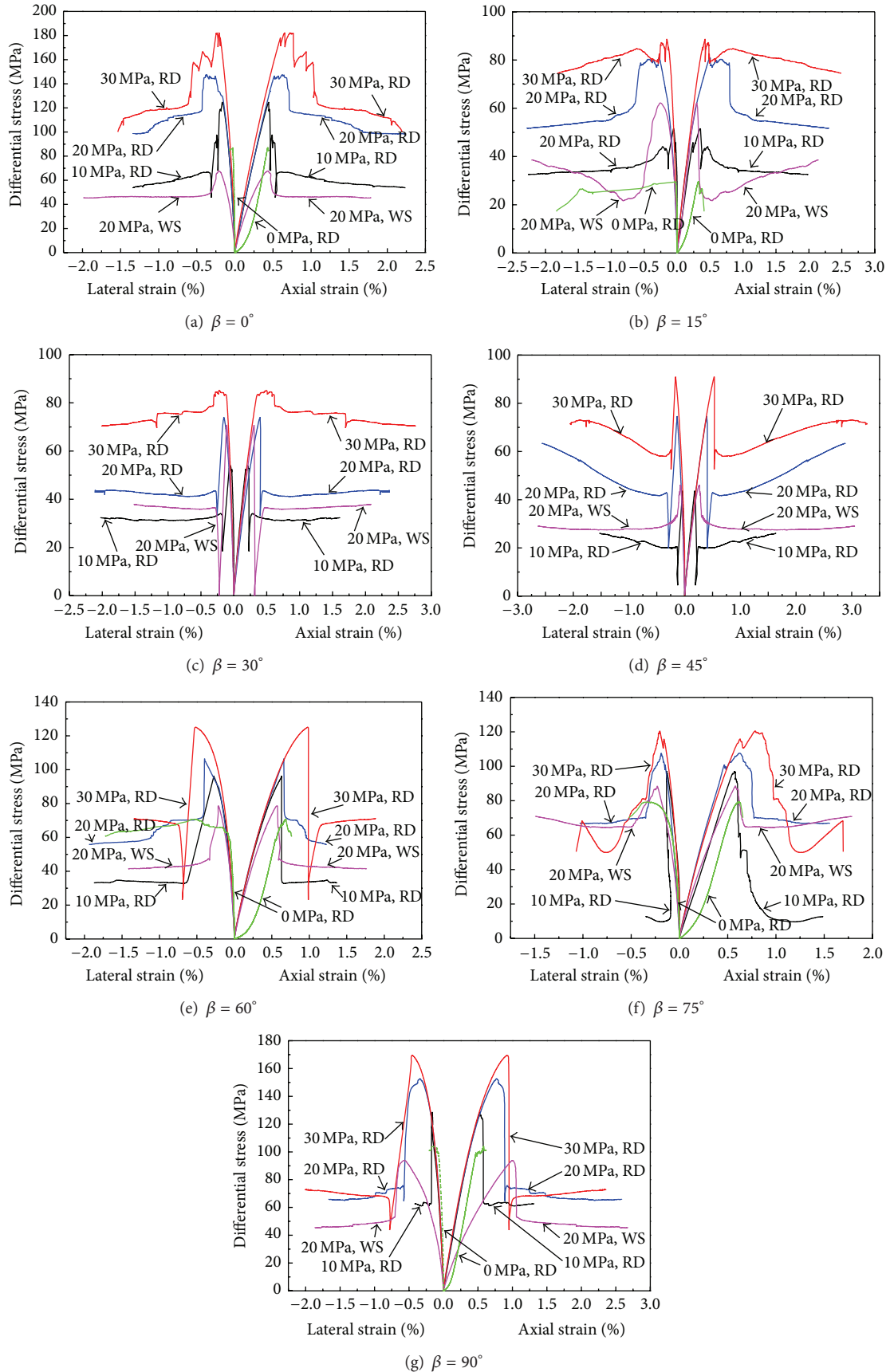


FIGURE 4: The complete stress-strain curves of dry and saturated shale samples of various angles (β), tested under different confining pressures.

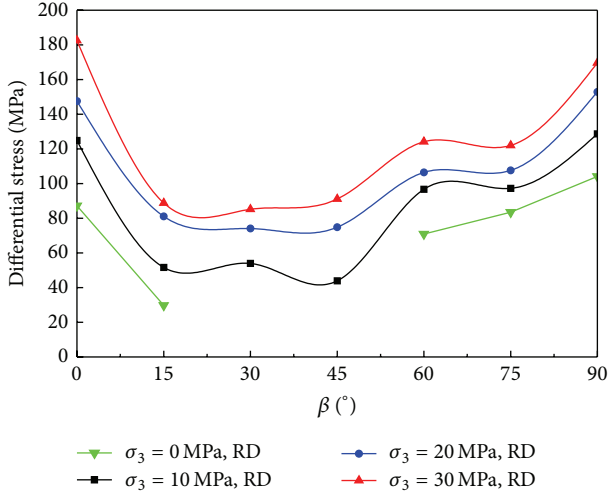


FIGURE 5: Differential stress at failure ($\sigma_1 - \sigma_3$) versus β at different confining pressures (σ_3).

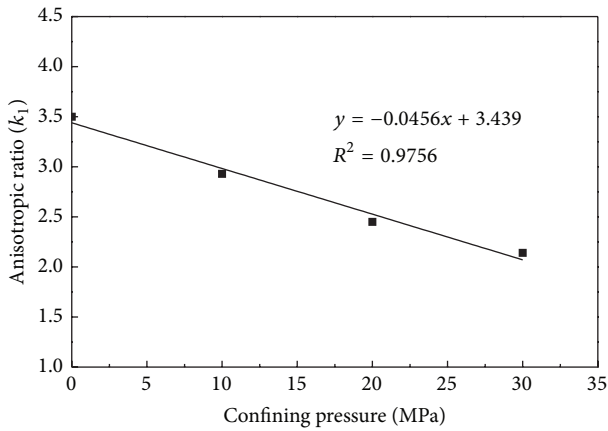


FIGURE 6: The relationship between anisotropic ratio k_1 and the confining pressure.

strength anisotropy decreases continuously as the confining pressure increases. Meanwhile, Figure 6 also shows that the relationship between k_1 and the confining pressure is linear and that the anisotropic effect of the failure strength will disappear at a sufficiently high confining pressure. When the confining pressure increases, rocks become more ductile, thereby inhibiting rock anisotropy. The same trend was also noted by other researchers [5, 8]. For confining pressures 0, 10, 20, and 30 MPa, k_2 is 0.84, 0.97, 0.96, and 1.07, respectively. Hence, the anisotropy of the samples parallel to the laminations is not markedly different to that of those perpendicular to the laminations. Figure 7 shows that the differential stress increases linearly with the confining pressure σ_3 for all correlation coefficients (R^2) more than 0.9.

5.1.2. The Mohr-Coulomb Failure Criterion. The Mohr-Coulomb failure criterion is widely used in ground control design

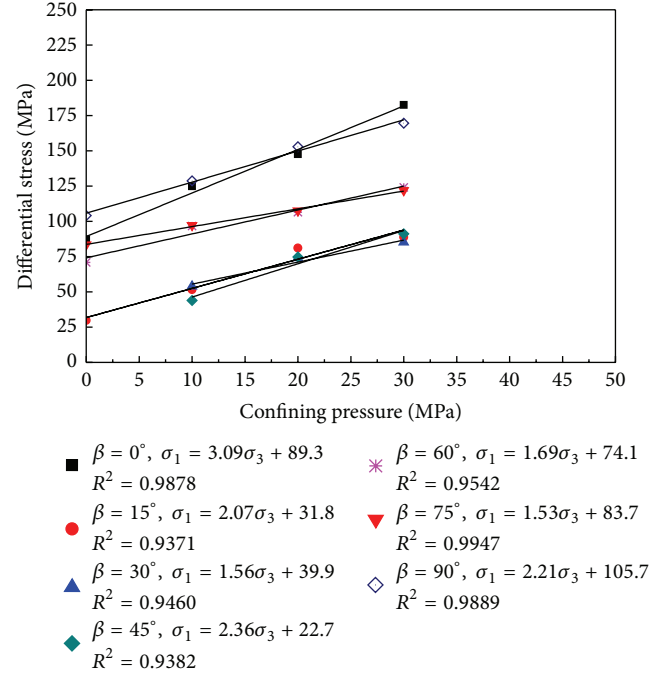


FIGURE 7: Differential stress at failure ($\sigma_1 - \sigma_3$) versus confining pressure (σ_3) at various orientation angles (β).

[23]. The cohesion (c) and internal friction angle (φ) can be determined using (2) [35] as shown below:

$$\tan \psi = \frac{1 + \sin \varphi}{1 - \sin \varphi} \quad (2)$$

$$\sigma_c = \frac{2c \cos \varphi}{1 - \sin \varphi},$$

where $\tan \psi$ = the slope of Mohr's envelope and σ_c = the uniaxial compressive strength.

The slope and intercept of the lines in Figure 7 were used to determine the cohesion (c) and internal friction angle (φ) of room dried samples with different β . The results are plotted in Figure 8. Based on the constructed Mohr-Coulomb curves, the peak strength envelope of normal stress (σ) and shear stress (τ) for different β was obtained and shown below. It can be seen from Figure 8 that cohesion exhibits obvious anisotropic behavior and strongly depends on the loading orientation. Specifically, the cohesion of samples with β between 15° and 45° is much smaller than others. This is because the failure mode of samples with β between 15° and 45° is shearing along the laminations (Section 5.4). Obviously, the required force of shearing failure along the rock material is higher than that of shearing along the laminations.

Figure 8 indicates that the internal friction angle follows a "W-shaped" curve, which is neither consistent with the concave curve nor remaining constant as reported in [4, 8]. The internal friction angle is anomalously high for $\beta = 45^\circ$. After a closer examination of the fracture planes for $\beta = 45^\circ$, the discrepancy could be attributed to differences in rock material variability even over a very short distance, even

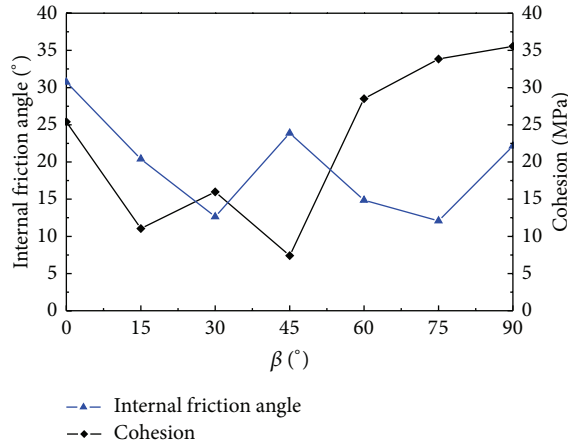


FIGURE 8: The friction angle and cohesion at various orientation angles were determined by plotting the linear Mohr-Coulomb failure envelopes.

though all specimens were drilled from the same block. Tiny sandstone streaks were found on the main fracture planes for $\beta = 45^\circ$ and the granularity of sandstone is coarser than that of shale. Consider

$$\begin{aligned}
 \text{For } \beta = 0^\circ, \quad \tau &= \sigma \tan 30.73^\circ + 25.4, \\
 \text{For } \beta = 15^\circ, \quad \tau &= \sigma \tan 20.39^\circ + 11.05, \\
 \text{For } \beta = 30^\circ, \quad \tau &= \sigma \tan 12.64^\circ + 15.97, \\
 \text{For } \beta = 45^\circ, \quad \tau &= \sigma \tan 23.88^\circ + 7.4, \\
 \text{For } \beta = 60^\circ, \quad \tau &= \sigma \tan 14.86^\circ + 28.5, \\
 \text{For } \beta = 75^\circ, \quad \tau &= \sigma \tan 12.09^\circ + 33.83, \\
 \text{For } \beta = 90^\circ, \quad \tau &= \sigma \tan 22.14^\circ + 35.55.
 \end{aligned} \tag{3}$$

5.2. Effect of Anisotropy and Confining Pressure on Deformability of Room Dried Samples

5.2.1. Young's Modulus. In accordance with the recommended method by ASTM [34], the tangent Young modulus (E_t) was calculated using the average slope of the axial stress-axial strain curve (Figure 4) at 50% of the peak strength. The relationship between the tangent Young modulus and the corresponding orientation (β) at different confining pressures (σ_3) for room dried specimens is presented in Figure 9. Note that the highest Young's modulus was always obtained at $\beta = 0^\circ$ no matter what confining pressure was applied, while lower values of Young's modulus occurred for samples with β in the range of 45° – 75° . This is because the axial deformation for specimens in that angle range is mainly controlled by the laminations.

Similar to the relationship between the peak strength and the orientation angle of the laminations (i.e., β), a correlation has been obtained between Young's modulus and β , as shown in Figure 9. As the confining pressure increases, Young's modulus fluctuates only slightly overall.

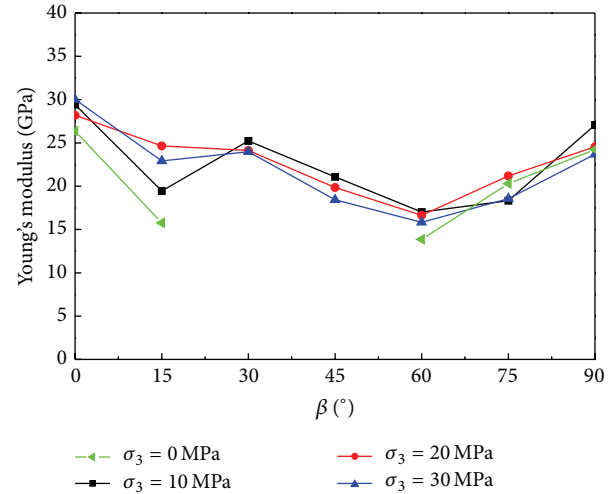


FIGURE 9: Tangent Young's modulus versus β at different confining pressures (σ_3).

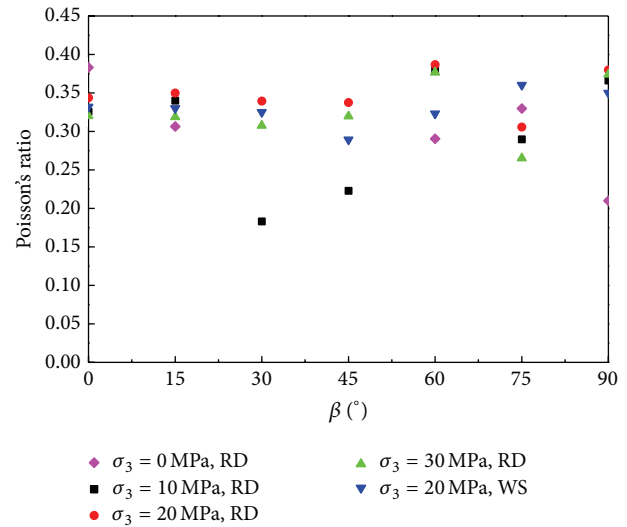


FIGURE 10: Poisson's ratio versus β at different confining pressures (σ_3).

5.2.2. Poisson's Ratio. Poisson's ratio was calculated from (4) based on the ASTM Standard [34], as shown in Figure 10. Most of the ratios range from 0.3 to 0.4 with small variations except when $\beta = 30^\circ$ and 45° . It can be seen that Poisson's ratio does not exhibit apparent anisotropic behavior with respect to the orientation angle within the range of confining pressures tested. In fact, the ratio tends to vary only slightly. In addition, it also can be seen from Figure 10 that Poisson's ratio of the water saturated samples is generally smaller than that of room dried specimens except for those with $\beta = 75^\circ$:

$$\nu = -\frac{\text{slope of axial curve}}{\text{slope of lateral curve}} = -\frac{E_t}{\text{slope of lateral curve}}, \tag{4}$$

where the slope of the lateral curve of the complete stress-strain curve (Figure 4) is determined in the same manner as was done for tangent Young's modulus, E_t .

5.2.3. Volumetric Strain. Figure 11 shows the variation of differential stress versus volumetric strain of room dried and saturated specimens under different confining pressures. When the axial load is initially applied, specimen tends to be compressed. As the differential stress approaches or just reaches the peak strength, the volume of the specimen starts to increase due to internal fracturing. This phenomenon is called specimen dilation. Shortly after the peak strength is reached, the net volumetric strain of the specimen becomes negative, which means the dilation continues in the postpeak stage. Note that, for the two specimens with $\beta = 75^\circ$ and $\beta = 90^\circ$ and both tested under confining pressure = 10 MPa, the result is invalid because the lateral deformation measurement device (LVDT 3) failed during tests. Meanwhile, since small cracks are gradually closed with the applied confining pressure, the amount of volume compression for specimens in triaxial compression is much smaller than that of the specimens in uniaxial compression.

5.3. Effect of Water Content on Anisotropic Strength and Deformation Behavior. Figure 12 shows compressive strength curves plotted against the orientation at confining pressure 20 MPa for the room dried and saturated specimens. The cohesion and internal friction angle could not be determined directly for the water saturated specimens because tests were performed at a single confining pressure of 20 MPa.

In comparison to the room dried specimens, the intensity of anisotropy is obviously suppressed for water saturated specimens. The curve for the saturated specimens in Figure 12 is flat instead of shoulder-shaped. The compressive strength is maximum at $\beta = 90^\circ$, followed by 75° , and the minimum is at $\beta = 45^\circ$. Figure 12 also indicates that water has some impact on the compressive strength of shale. The average compressive strength of saturated specimens is 28.9% lower than that of the room dried specimens. The largest reduction of 54% occurs at $\beta = 0^\circ$. Similar results were reported in [25, 27, 28, 30]. In addition, it is quite interesting to note that strength reduction is sensitive to the orientation angle (β); that is, water content has the greatest effect on compressive strength when the load is applied perpendicular and parallel to the laminations, while the minimum effect occurs when the orientation angle is around 30° .

Figure 13 compares Young's modulus of the room dried and saturated specimens under confining pressure of 20 MPa. The average and maximum reductions in Young's modulus of the water saturated samples are 26.1% and 62% (at $\beta = 90^\circ$), respectively. Similar to the effect of water content on compressive strength, the proportion of reduction of Young's modulus (i.e., shadow area in Figure 13) is related to the orientation angle (β) of specimen laminations; that is, reduction in Young's modulus increases gradually from the middle ($\beta = 45^\circ$) to both ends ($\beta = 0^\circ$ and 90°). In other words, water has the largest effect on stiffness of shale specimen when the applied load is perpendicular and parallel

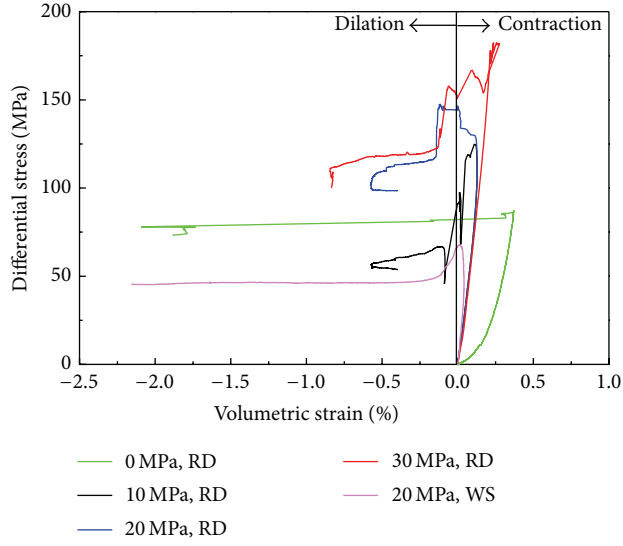
to the laminations, but it has the minimum effect when the orientation angle is around 45° .

Li et al. [31] claimed that although various hypotheses including fracture energy reduction, capillary tension decrease, frictional reduction, chemical and corrosive deterioration, and effective stress decrease due to pore pressure have been put forward in an attempt to interpret the effect of water content, none of them provides a reliable and quantitative approach to the problem. Based on Li's theory, when rock contains sufficient water-sensitive constituents such as clay and silt, both cohesive strength and internal friction angle will be reduced due to the presence of water, which means that the shear strength of the potential failure plane decreases. Hence, the water saturated specimen will fail at a lower compressive strength than that of the dry specimen. van Eeckhout and Peng [6] stated that water enrichment in ground strata could have a profound effect on coal mine roofs. More specifically, when the water is absorbed into the roof shale, the shale will relax because of decreased elasticity. These might be the reason why compressive strength and Young's modulus decrease under the water saturated condition. Nevertheless, the mechanisms behind the phenomena that the higher water content of specimens reduces the anisotropic effect and the rationale behind it are still unclear.

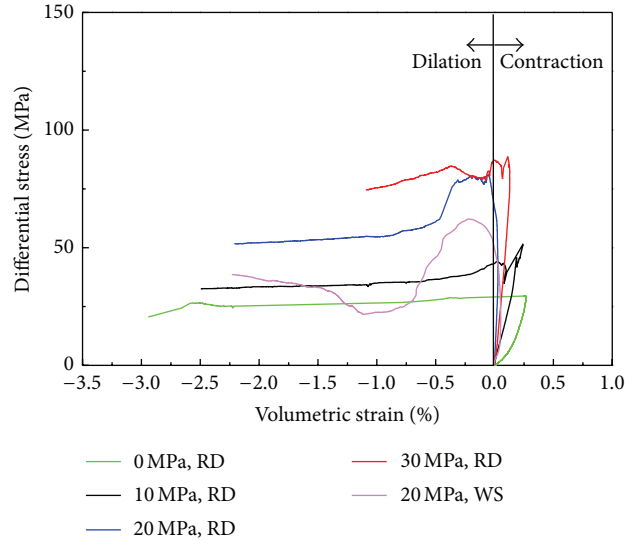
5.4. Failure Mechanism and Postfailure Behavior

5.4.1. Failure Modes. As stated in the previous sections, the mechanical properties of shale (i.e., compressive strength, Young's modulus, and axial strain at peak strength) exhibit obvious anisotropic characteristics, which are believed to be related to the failure mechanisms in shale. It was observed that brittle fractures are deformation characteristics of all specimens at all three confining pressures. Generally speaking, the fracture planes develop in two modes of brittle fractures, that is, sliding along laminations and shearing of rock material. Since the maximum confining pressure applied in this research was 30 MPa, which is insufficiently high to translate the failure mode from brittle to plastic flow or kink flow as reported in [4, 8]. Figure 14 shows all the samples after testing, whereas Figure 15 illustrates two typical modes of specimen failure.

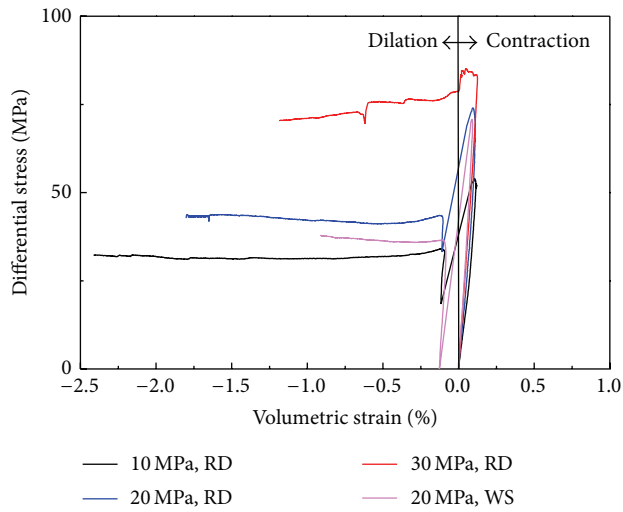
(1) Types of Fracture. There are two types of fracture (Figure 16). In the first type (Figure 16(a)), the laminations intersect one or both of the end surfaces of the specimen. In this case, when a fracture along the laminations occurs, it intersects one or both interfaces between the specimen end and the platen. As the test continues, the postfailure stress-strain curve fluctuates without losing strength (Figures 4(a), 4(b), and 4(f)). It finally drops down gradually as the test continues further. In the second type (Figure 16(b)), fractures occur in the shale matrix or along the laminations. In this case, both ends of the fracture are located on the free surface of the specimen without the constraint of the interface between the specimen ends and the platen. Consequently, its postfailure curve is a very rapid and sudden drop of strength (Figures 4(d) and 4(e)) is observed.



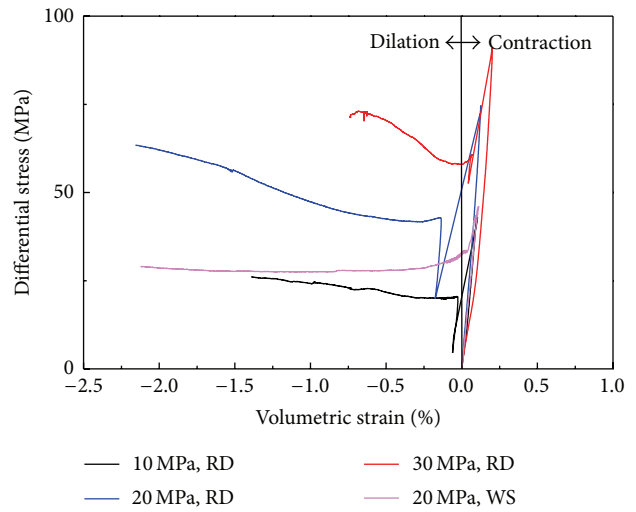
(a) $\beta = 0^\circ$



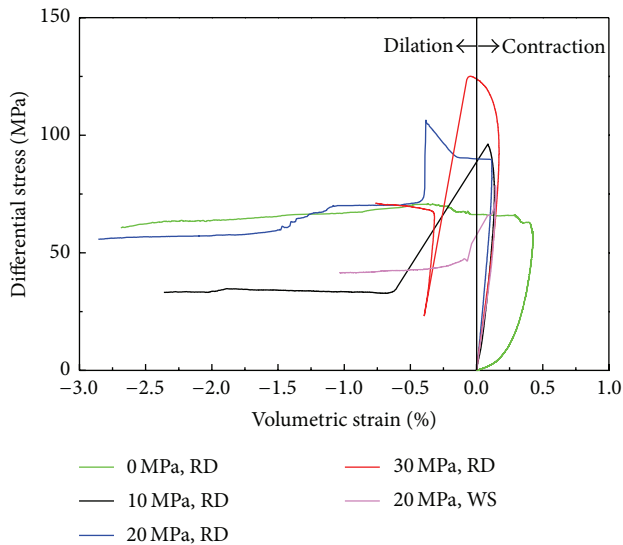
(b) $\beta = 15^\circ$



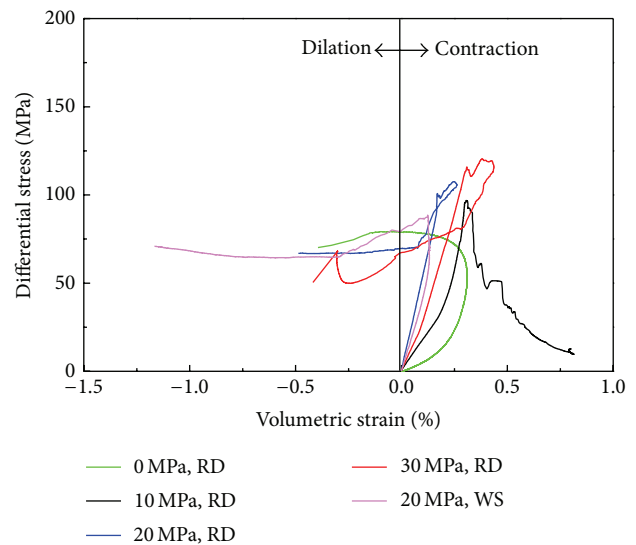
(c) $\beta = 30^\circ$



(d) $\beta = 45^\circ$



(e) $\beta = 60^\circ$



(f) $\beta = 75^\circ$

FIGURE II: Continued.

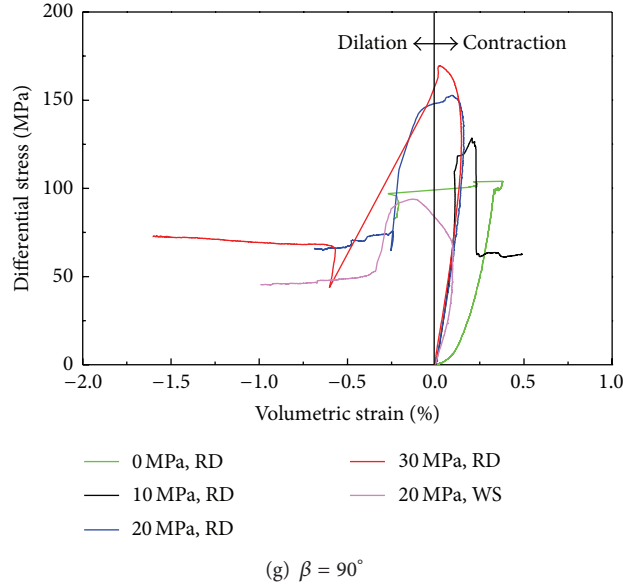


FIGURE 11: The differential stress-volumetric strain curves of dry and saturated shale samples of various angles, β , tested under different confining pressures.

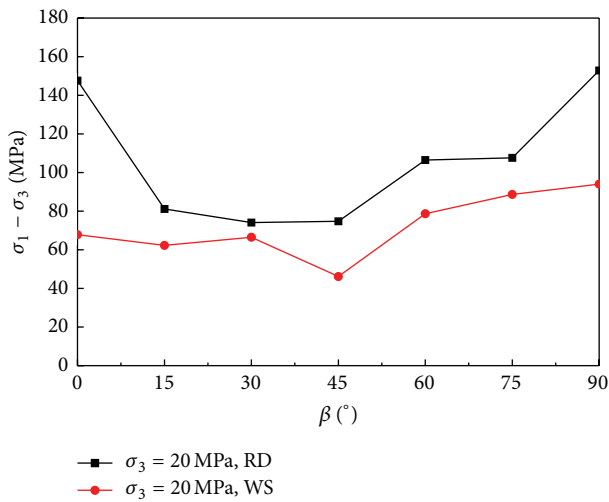


FIGURE 12: Comparison of the compressive strength of the room dried and water saturated specimens.

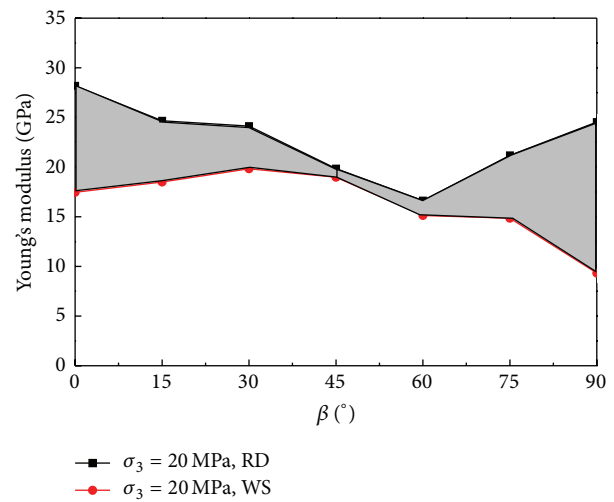


FIGURE 13: Comparison of the tangent Young modulus of the room dried and saturated specimens.

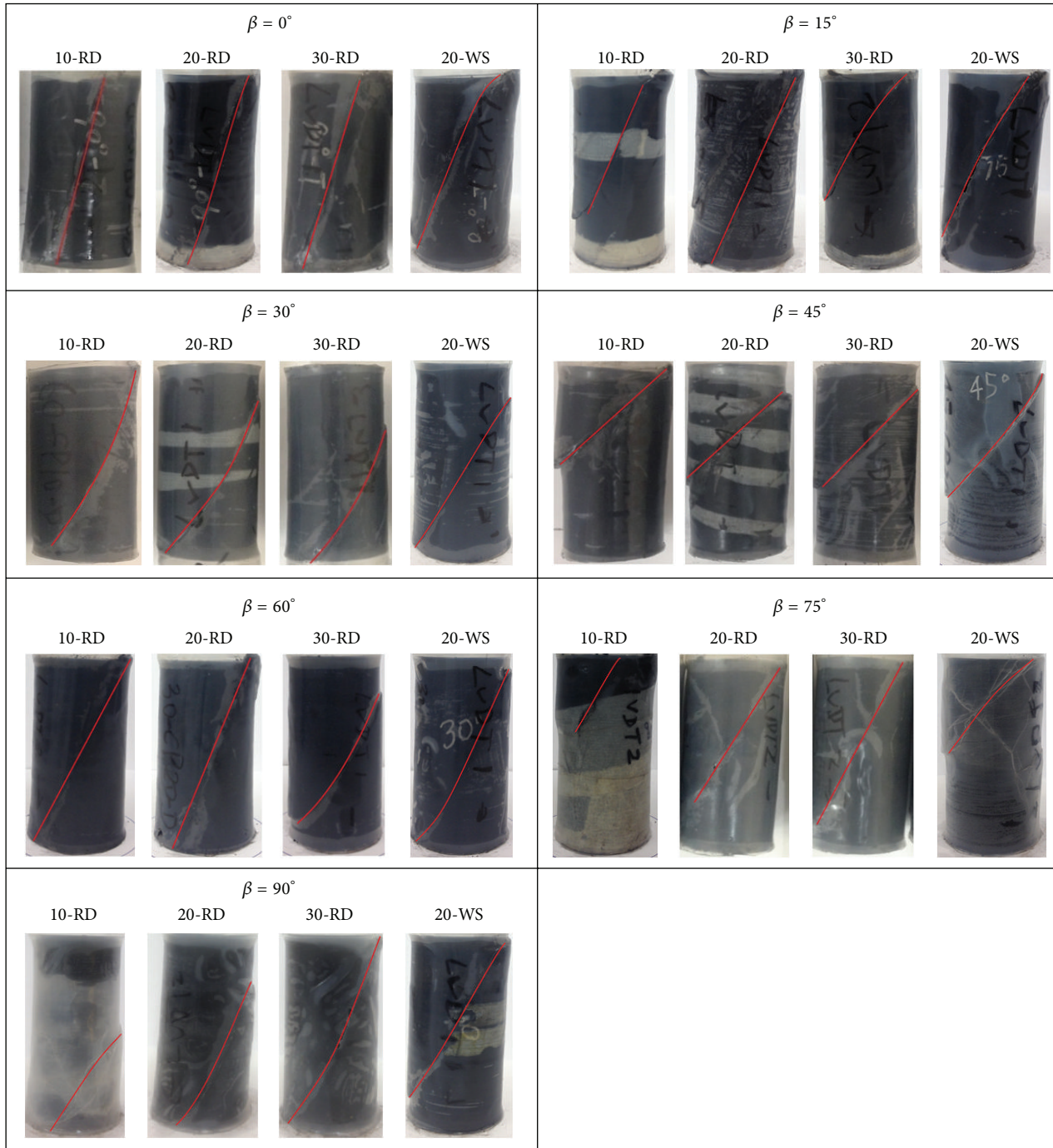
(2) *Fracture Developed along the Laminations.* For samples with β between 15 and 45° (Figures 4, 14, and 15(a)), specimens always failed suddenly along the lamination, because at failure the shear stress acting on the laminations exceeds their shear strength. Hence, the strength of samples with β between 15 and 45° was dictated by the shear strength of the laminations.

(3) *Fracture Developed across Rock Material.* For samples with $\beta = 0^\circ$ and between 60 and 90° (Figures 4, 14, and 15(b)), fractures developed in the rock material, which can be attributed to the fact that the shear stress acting on the laminations was smaller than the shear strength along

the laminations. Consequently, failure was dictated by the shale matrix instead of the laminations.

6. Conclusion

Coal measure shale is one of the most widely distributed rock materials in underground coal mines, and most ground control failures are related to coal measure shale. Although lots of research work have been done on the anisotropic behavior of different types of rocks or artificial materials, more detailed laboratory work on anisotropic strength and deformation behavior of coal measure shale, especially taking into consideration the effect of water content, is still needed



— Main fracture
 RD: room dried specimen
 WS: water saturated specimen

FIGURE 14: Photos of room dried samples at different β under various confining pressures after testing.

in order to understand better the mechanisms of many ground control failures. In this study, the uniaxial and triaxial compression tests have been conducted on samples of coal measure shale, under both room dried and water saturated conditions, to study the effect of anisotropy and water content

on the strength, deformability, and failure modes of coal measure shale.

Results of tests show that the strength and deformation behavior of room dried samples are strongly affected by the direction of the laminations with respect to that of the major

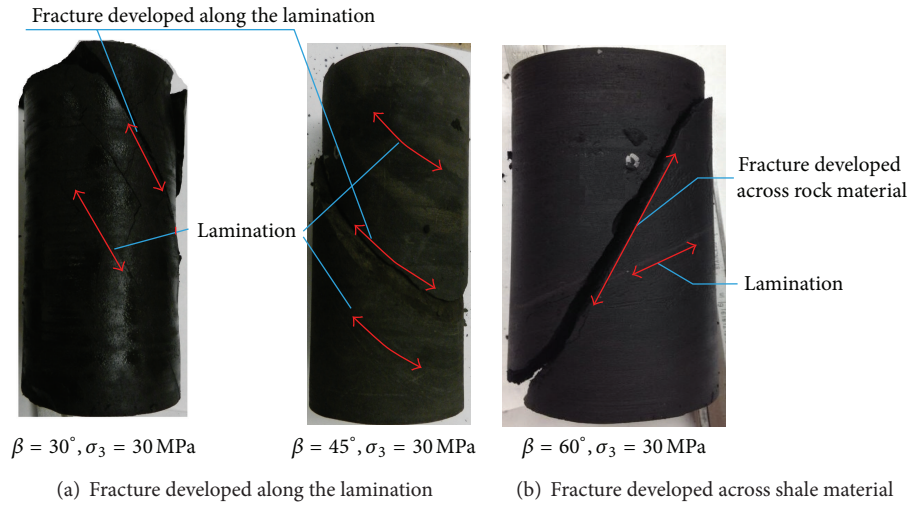


FIGURE 15: Photos showing two typical failure modes.

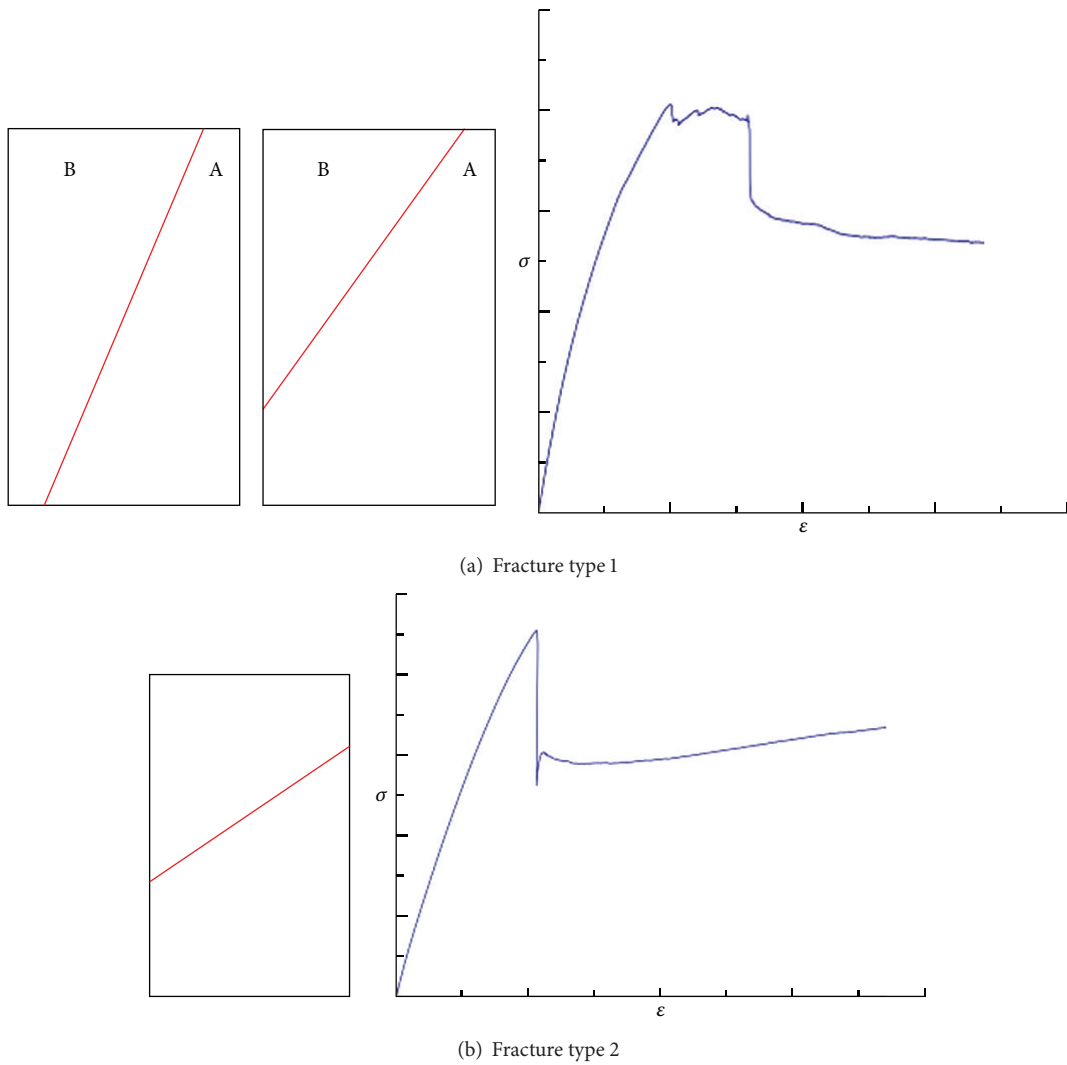


FIGURE 16: Type of fractures.

principal stress. The maximum strength always occurs at $\beta = 0^\circ$ or $\beta = 90^\circ$. Meanwhile, the minimum strength always occurs for samples with β between 30° and 45° . As the confining pressure increases, the compressive strength increases uniformly whereas the anisotropic effect of strength decreases. Based on the Mohr-Coulomb failure criterion, the cohesion ranges from 7.4 to 35.5 MPa with the higher values being found among samples with $\beta = 60^\circ$ – 90° . The tangent Young modulus also exhibits anisotropic behavior with respect to β with the maximum being for $\beta = 0^\circ$. Furthermore, as the confining pressure increases, Young's modulus only fluctuates slightly.

On the other hand, the impact of water content on compressive strength and deformation behavior is very evident. In comparison to room dried samples, the average compressive strength and Young's modulus reductions of water saturated samples are 28.9% and 26.1%, respectively, whereas the maximum reductions are 54% and 62%, respectively. Meanwhile, test results also indicate that these reductions are strongly related to the orientation angle (β). Water content has more effect on strength and Young's modulus when the applied load is perpendicular and parallel to the lamination orientation and has minimum effect when the orientation angle falls in the range of 30° – 45° . Furthermore, compared to room dried samples, the anisotropy of compressive strength and Young's modulus of water saturated samples is clearly reduced.

There are two types of failure mechanisms for shale: sliding along laminations and shearing of rock matrix. The two types of postfailure stress-strain curve are strongly dependent on the failure mechanism. One is a sudden and rapid drop down, while the other fluctuates before slopping down gently to the residual strength.

Conflict of Interests

The authors declare that there is no conflict of interests regarding the publication of this paper.

Acknowledgments

This study was sponsored by National High Technology Research and Development Program of China (no. 2012AA062100), National Natural Science Foundation of China (no. 51074164), the Program for New Century Excellent Talents in University of China (no. NCET-10-0770), and China Scholarship Council. The authors would like to express their sincere appreciation to Mr. Joe Andrews (Ark Land Company, WV, USA) and Mr. Kevin Andrews (Cardno MM&A, VA, USA) for their help in obtaining the samples and to Dr. Brijes Mishra, Mr. Xu Tang, and Mr. Priyesh Verma of West Virginia University for their contribution in this study.

References

- [1] S. S. Peng, *Ground Control Failures: A Pictorial View of Case Studies*, Syd S. Peng, Morgantown, WV, USA, 2007.
- [2] S. S. Peng, "Topical areas of research needs in ground control—a state of the art review on coal mine ground control," *Journal of China University of Mining & Technology*, vol. 44, no. 1, pp. 1–8, 2015.
- [3] W. Li, J. Bai, S. S. Peng, X. Wang, and Y. Xu, "Numerical modeling for yield pillar design: a case study," *Rock Mechanics and Rock Engineering*, vol. 48, no. 1, pp. 305–318, 2013.
- [4] F. A. Donath, "Effects of cohesion and granularity on deformational behavior of anisotropic rock," *Geological Society of America*, vol. 135, pp. 95–128, 1972.
- [5] H. Niandou, J. F. Shao, J. P. Henry, and D. Fourmaintraux, "Laboratory investigation of the mechanical behaviour of tour-nemire shale," *International Journal of Rock Mechanics and Mining Sciences*, vol. 34, no. 1, pp. 3–16, 1997.
- [6] E. M. van Eeckhout and S. S. Peng, "The effect of humidity on the compliances of coal mine shales," *International Journal of Rock Mechanics and Mining Sciences and*, vol. 12, no. 11, pp. 335–340, 1975.
- [7] M. E. Chenevert and C. Gatline, "Mechanical anisotropies of laminated sedimentary rocks," *The Society of Petroleum Engineers*, vol. 5, no. 1, pp. 67–77, 1965.
- [8] R. McLamore and K. E. Gray, "The mechanical behavior of anisotropic sedimentary rocks," *Journal of Manufacturing Science and Engineering*, vol. 89, no. 1, pp. 62–73, 1967.
- [9] A. Fahimifar, "Strength and deformation properties of a schist rock in Isfahan," *Iranian Journal of Science and Technology, Transaction B: Engineering*, vol. 28, no. 5, pp. 617–622, 2004.
- [10] M. H. B. Nasser, K. S. Rao, and T. Ramamurthy, "Anisotropic strength and deformation behavior of Himalayan schists," *International Journal of Rock Mechanics and Mining Sciences*, vol. 40, no. 1, pp. 3–23, 2003.
- [11] V. K. Singh, D. Singh, and T. N. Singh, "Prediction of strength properties of some schistose rocks from petrographic properties using artificial neural networks," *International Journal of Rock Mechanics and Mining Sciences*, vol. 38, no. 2, pp. 269–284, 2001.
- [12] T. Ramamurthy, "Strength and modulus responses of anisotropic rocks," *Comprehensive Rock Engineering*, vol. 1, pp. 313–329, 1993.
- [13] G. Khanlari, B. Rafiei, and Y. Abdilor, "Evaluation of strength anisotropy and failure modes of laminated sandstones," *Arabian Journal of Geosciences*, pp. 1–14, 2014.
- [14] Y. M. Tien, M. C. Kuo, and C. H. Juang, "An experimental investigation of the failure mechanism of simulated transversely isotropic rocks," *International Journal of Rock Mechanics and Mining Sciences*, vol. 43, no. 8, pp. 1163–1181, 2006.
- [15] Y. M. Tien and P. F. Tsao, "Preparation and mechanical properties of artificial transversely isotropic rock," *International Journal of Rock Mechanics and Mining Sciences*, vol. 37, no. 6, pp. 1001–1012, 2000.
- [16] Y. M. Tien and M. C. Kuo, "A failure criterion for transversely isotropic rocks," *International Journal of Rock Mechanics and Mining Sciences*, vol. 38, no. 3, pp. 399–412, 2001.
- [17] J. C. Jaeger, "Shear failure of anisotropic rocks," *Geological Magazine*, vol. 97, no. 1, pp. 65–72, 1960.
- [18] R. Nova, "The failure of transversely isotropic rocks in triaxial compression," *International Journal of Rock Mechanics and Mining Sciences and*, vol. 17, no. 6, pp. 325–332, 1980.
- [19] O. Cazacu, N. D. Cristescu, J. F. Shao, and J. P. Henry, "A new failure criterion for transversely isotropic rocks," *International Journal of Rock Mechanics and Mining Sciences*, vol. 3, no. 1, pp. 89–103, 1998.
- [20] H. Ding, X. Miao, F. Ju, X. Wang, and Q. Wang, "Strata behavior investigation for high-intensity mining in the water-rich coal

- seam,” *International Journal of Mining Science and Technology*, vol. 24, no. 3, pp. 299–304, 2014.
- [21] C. Meng, X. Li, Q. Yao, and J. Zhou, “Numerical research on stability control of roofs of water-rich roadway,” *International Journal of Mining Science and Technology*, vol. 24, no. 3, pp. 409–416, 2014.
- [22] Y. Zhang, S. Tu, Q. Bai, and J. Li, “Overburden fracture evolution laws and water-controlling technologies in mining very thick coal seam under water-rich roof,” *International Journal of Mining Science and Technology*, vol. 23, no. 5, pp. 693–700, 2013.
- [23] S. S. Peng, *Coal Mine Ground Control*, Syd S. Peng, Morgantown, WV, USA, 3rd edition, 2008.
- [24] G. M. Molinda, D. C. Oyler, and H. Gurgunli, “Identifying moisture sensitive roof rocks in coal mines,” in *Proceedings of the 25th International Conference on Ground Control in Mining*, pp. 57–64, West Virginia University, Morgantown, WV, USA, 2006.
- [25] E. M. van Eeckhout, *The effect of moisture on the mechanical properties of coal mine shales [Ph.D. thesis]*, University of Minnesota, Minneapolis, Minn, USA, 1974.
- [26] M. E. Chenevert, “Shale alteration by water adsorption,” *Journal of Petroleum Technology*, vol. 22, no. 9, pp. 1141–1148, 1970.
- [27] B. Vasárhelyi, “Some observations regarding the strength and deformability of sandstones in dry and saturated conditions,” *Bulletin of Engineering Geology and the Environment*, vol. 62, no. 3, pp. 245–249, 2003.
- [28] B. Vásárhelyi, “Statistical analysis of the influence of water content on the strength of the miocene limestone,” *Rock Mechanics and Rock Engineering*, vol. 38, no. 1, pp. 69–76, 2005.
- [29] B. Vásárhelyi and P. Ván, “Influence of water content on the strength of rock,” *Engineering Geology*, vol. 84, no. 1-2, pp. 70–74, 2006.
- [30] A. B. Hawkins and B. J. McConnell, “Sensitivity of sandstone strength and deformability to changes in moisture content,” *Quarterly Journal of Engineering Geology*, vol. 25, no. 2, pp. 115–130, 1992.
- [31] D. Li, L. N. Y. Wong, G. Liu, and X. Zhang, “Influence of water content and anisotropy on the strength and deformability of low porosity meta-sedimentary rocks under triaxial compression,” *Engineering Geology*, vol. 126, pp. 46–66, 2012.
- [32] Z. A. Erguler and R. Ulusay, “Water-induced variations in mechanical properties of clay-bearing rocks,” *International Journal of Rock Mechanics and Mining Sciences*, vol. 46, no. 2, pp. 355–370, 2009.
- [33] M. Talesnick and S. Shehadeh, “The effect of water content on the mechanical response of a high-porosity chalk,” *International Journal of Rock Mechanics and Mining Sciences*, vol. 44, no. 4, pp. 584–600, 2007.
- [34] ASTM D7012-10, *Standard Test Method for Compressive Strength and Elastic Moduli of Intact Rock Core Specimens Under Varying States of Stress and Temperatures*, ASTM International, West Conshohocken, Pa, USA, 2010.
- [35] B. H. G. Brady and E. T. Brown, *Rock Mechanics for Underground Mining*, Springer, Berlin, Germany, 3rd edition, 2006.

Research Article

Blasting Vibration Safety Criterion Analysis with Equivalent Elastic Boundary: Based on Accurate Loading Model

Qingwen Li,¹ Lan Qiao,¹ Gautam Dasgupta,² Siwei Ma,² Liping Wang,³ and Jianghui Dong⁴

¹The School of Civil and Environmental Engineering, University of Science and Technology Beijing, Beijing 100083, China

²Department of Civil Engineering and Engineering Mechanics, Columbia University, New York, NY 10027, USA

³School of Computer Science, Engineering and Mathematics, Flinders University, Adelaide, SA 5042, Australia

⁴School of Natural and Built Environments, University of South Australia, Adelaide, SA 5095, Australia

Correspondence should be addressed to Qingwen Li; qingwenli1118@gmail.com

Received 24 July 2014; Accepted 23 October 2014

Academic Editor: Caiping Lu

Copyright © 2015 Qingwen Li et al. This is an open access article distributed under the Creative Commons Attribution License, which permits unrestricted use, distribution, and reproduction in any medium, provided the original work is properly cited.

In the tunnel and underground space engineering, the blasting wave will attenuate from shock wave to stress wave to elastic seismic wave in the host rock. Also, the host rock will form crushed zone, fractured zone, and elastic seismic zone under the blasting loading and waves. In this paper, an accurate mathematical dynamic loading model was built. And the crushed zone as well as fractured zone was considered as the blasting vibration source thus deducting the partial energy for cutting host rock. So this complicated dynamic problem of segmented differential blasting was regarded as an equivalent elastic boundary problem by taking advantage of Saint-Venant's Theorem. At last, a 3D model in finite element software FLAC3D accepted the constitutive parameters, uniformly distributed mutative loading, and the cylindrical attenuation law to predict the velocity curves and effective tensile curves for calculating safety criterion formulas of surrounding rock and tunnel liner after verifying well with the in situ monitoring data.

1. Introduction

With the rapid infrastructure development in China, the improvement of control level on the blasting technique, and the well adaptability in various engineering, the blasting construction are used more and more widely; also, the drill and blast method has been becoming the most primary method in tunneling and underground space construction; in China, there are more than 95% mountain tunnel constructions which adopt the drill and blast method [1]. Also, the blasting is producing huge help on the engineering yet generating many adverse effects on existing structures. Also, many scholars have done a lot of researches on adverse effects [2–4]. Hence, predicting the vibration safety criterion has become an important and effective method for analyzing the adverse effects. Jiang and Zhou used the safety criterion method to analyze tunnel liner structure [5]. Karadogan et al. gave a damage criteria norm for blast-induced ground vibrations in Turkey [6]. Yang et al. studied the safety distance for secondary shotcrete in Jinping-II deep-buried tunnels [7].

Though many works have been done by all the world scholars, the most attempts were based on the monitoring data to summarize the empirical equation [8–18], which is restricted for the real engineering blasting vibration. At the same time, some new methods are used to analyze the blasting problem, such as the soft computing method [19], artificial neural networks method [20], MEMS-based commutation module, [21] and RES-based model [22]. But it should be based on large number of in situ monitoring data, not considering the effect of vibration frequency and duration.

The numerical simulation has become an important prediction method in the engineering, due to its high accuracy and less cost, as well as the fast development computer technique, to make many scholar use such ads ANSYS/LS-DYNA finite element software to solve the blasting vibration problems [23–29]. However, most models accepted the simplified triangle dynamic load, trapezoid dynamic load, or simplified data table which are not accurate enough for the blasting loading.

In blasting, the gas pressure in hole reached 50 to 100 thousand times atmosphere. The high gas pressure could crush the host rock around blast hole to form the crushed zone. And because of higher dynamic compressive strength, the crushed zone will consume large partial energy to make the shock wave attenuate very fast. After propagating a distance, the pressure cannot crush the host rock any more, to make the shock wave attenuate as stress wave. Then the surrounding rock would suffer radial compression to generate a strong radial movement to lead the rock shell expansion to cause the circular tensile stress. Also, the tensile stress tends to be greater than critical dynamic tensile strength which is usually less than 1/10 compression strength of rock masses, to lead to the radial fractures formed. After those radial fractures connected with crushed zone, the blasting gas which looked like a wedge entered the radial fractures to make them enlarge. Hence, the fractured zone would be formed which also could consume some energy to make the vibration wave attenuate as elastic seismic wave whose impact region was the elastic seismic zone.

In this paper, the accurate mathematical model of blasting loading was established on the analysis of the blasting pressure change, the blast hole volume expansion, the fracture development, and the blasting gas motion. All the blasting energy transformed to the kinetic energy of the host rock without considering energy loss, this energy was used to form the crushed zone and fractured zone, and the residual energy was used to produce the vibration in elastic seismic zone to propagate out. So the crushed zone and fractured zone were also regarded as the blasting vibration source by taking advantage of the unified mechanical and continuum damage mechanics thus deducting this partial energy for cutting host rock, and regarding the vibration wave on the elastic seismic zone as the cylindrical elastic seismic wave to attenuate along with radius direction [30].

For the far field vibration analysis, the separate blasting loading of each hole could meet Saint-Venant's theorem to be regarded as the uniformly distributed loading on its own segmentation cutting zone. Hence the complicated dynamic problem in segmented differential blasting turned into an initial equivalent elastic boundary problem alongside the uniformly distributed and the attenuation law. At last, a 3D model in finite element software FLAC3D accepted the parameters to predict the velocity curve and effective tensile curve for confirming safety criterion after verifying well with the in situ monitoring data.

2. Equivalent Boundary of Elastic Seismic Loading

Based on above analysis, for the far field vibration, after a distance propagating, the blasting wave would attenuate as the elastic seismic wave, and this elastic seismic wave followed a circular attenuation law along the radius direction. Also, the crushed zone and fractured zone were considered as blasting vibration source boundary by taking advantage of continuum damage mechanics theory and unified constitutive theory [30].

2.1. Seismic Elastic Velocity. During the blasting, assuming the host rock as non-compressible linear media, and all the blasting energy would transform to kinetic energy of host rock without any energy loss. So, according to dynamic gradient theory in the semi-infinite medium, the formula of the velocity can be shown as [31]

$$V = \sqrt{\frac{\rho_0 q}{8\rho_r v_s}} \frac{\bar{L}}{\bar{r} \sqrt{(\bar{r})^2 + (\bar{L}/2)^2}}, \quad (1)$$

where

$$v_s = \ln \frac{\bar{L} + \sqrt{1 + \bar{L}^2}}{-\bar{L} + \sqrt{1 + \bar{L}^2}}, \quad \bar{L} = \frac{L_0}{2r_0}, \quad \bar{r} = \frac{r}{2r_0}, \quad (2)$$

where V is the vibration rounded velocity, ρ_0 is the explosive density, q is the blasting energy, L_0 is the charging length, r_0 is radius of blast hole, and r is the propagated distance.

For a single blast hole in semi-infinite medium, the mainly destructional form of the crushed zone with the radius r_1 and for the fractured zone with radius r_2 , so the formula can be expressed as [32]

$$r_1 = \left(\frac{\rho_r c_p^2}{5\sigma_c} \right)^{1/2} \left(\frac{P}{\sigma_*} \right)^{1/4} r_0, \quad (3)$$

$$r_2 = \left[\frac{vP}{(1-v)\sigma_t} \right]^{1/\alpha} r_0,$$

where v is Poisson's ratio, c_p is the P-wave of rock mass, σ_c and σ_t are, respectively, the dynamic compressive strength and dynamic tensile strength of rock, σ_* is the static compressive strength, P is the blasting loading on the blast hole wall, and α is the attenuation coefficient of blasting vibration wave.

In above,

$$c_p^2 = \frac{\lambda + 2G}{\rho_r}, \quad \lambda = \frac{2Gv}{1-2v}, \quad (4)$$

where G is the shear modulus and ρ_r is the density of rock mass.

Experimental study showed that the radius of crushed zone is 3 to 5 times blast hole radius and 10 to 15 times for fractured zone [33].

2.2. Seismic Elastic Loading on Equivalent Boundary. For the elastic seismic loading, the attenuation functions of shock wave and stress wave with the time and displacement, to make the blasting loading $P(x, t)$ worked on the blast hole wall was shown as [34]

$$P_a(x, t) = P(x, t) \left(\frac{r_0}{r} \right)^\alpha, \quad (5)$$

where $P_a(x, t)$ is the blasting loading after attenuating along with distance in radius and α is the attenuation coefficient of vibration wave; in above formula, for the shock wave

$$\alpha = 2 + \frac{v}{1-v}, \text{ and for stress wave } \alpha = 2 - \frac{v}{1-v}. \quad (6)$$

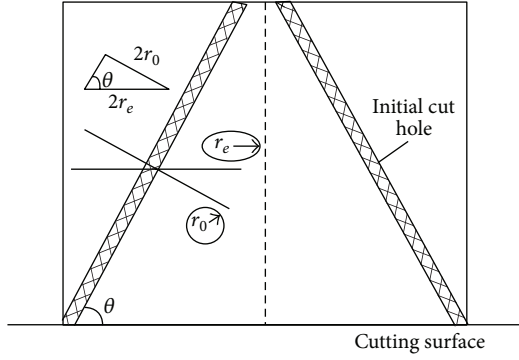


FIGURE 1: Initial cut hole with cutting surface.

For the underground space and tunneling blasting construction, there are, respectively, the initial cut hole, destruction rock hole, peripheral hole, and bottom hole arranged on the cutting surface, among, the initial cut holes were the inclined hole located in the center of cut surface, and the other holes were vertical hole surrounded the initial cut holes. Hence the blasting vibration must be a multiple and superimposed waves on cutting surface.

(1) *The Equivalent Blasting Loading of Initial Cut Zone.* According to the above formula, for elastic dynamic loading of single blast hole, for the initial cut hole with ignoring the overlapping influence and energy loss, the equivalent elastic loading can be shown as

$$P_{es}(x, t) = P(x, t) \left(\frac{r_0}{r_1} \right)^{2+v/(1-\nu)} \left(\frac{r_1}{r_2} \right)^{2-\nu/(1-\nu)}, \quad (7)$$

where $P_{es}(x, t)$ is dynamic load of single initial cut hole.

Assuming the angle between initial cut hole and cut surface is θ , so the projection of blast hole on the cut surface is ellipse with long radius r_e and the short radius r_0 (the radius of blast hole), as shown in Figure 1.

From the above relationship, we can know $r_e = r_0 / \sin \theta$. Usually, the initial cut hole was the first blasting segment, so the equivalent elastic dynamic load of initial cut section with considering the crushed zone and fractured zone as dynamic loading boundary was shown in Figure 2.

The equivalent elastic loading of all the initial cut holes by taking advantage of Saint-Venant's principle was shown as

$$P_e(x, t) = \frac{k_1 S_e}{S_{eq}} P(x, t) \left(\frac{r_0}{r_1} \right)^{2+v/(1-\nu)} \left(\frac{r_1}{r_2} \right)^{2-\nu/(1-\nu)}, \quad (8)$$

where $P_e(x, t)$ is equivalent elastic loading of all the initial cut holes, k_1 is the number of holes, S_e is the area of a single elliptic fractured zone with taking the 10 to 15 times blast hole's projection radius, and S_{eq} is the area of whole initial cut section.

(2) *The Equivalent Blasting Loading of Other Segments.* Except the initial cut holes, there was a free face due to last segmented blasting for other segments. And the free face make this segmented blasting could cut the whole rock mass between

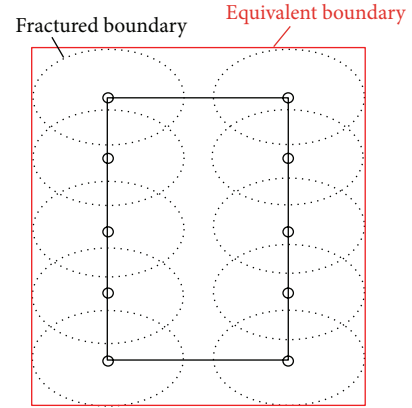


FIGURE 2: Equivalent boundary of initial cut zone.

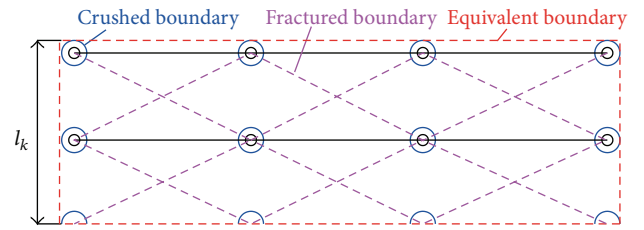


FIGURE 3: Equivalent boundary of other segments.

this segment and last segment, as shown in Figure 3. So taking $r_2 = l_k$, the formula is carried out as below:

$$P_e(x, t) = \frac{S_0}{S - S_{eq}} P(x, t) \left(\frac{r_0}{r_1} \right)^{2+v/(1-\nu)} \left(\frac{r_1}{l_k} \right)^{2-\nu/(1-\nu)}, \quad (9)$$

where S_0 is the area of a segmented blasting, S is the area of whole cut surface, and l_k is width of k th segmented blasting.

Based on the time interval of two segments, the total equivalent elastic loading of other segments was shown as

$$P_t(x, t) = \sum_{m=1}^{k=n} \frac{S_0}{S - S_{eq}} P(x, t + \tau_k) \left(\frac{r_0}{r_1} \right)^{2+v/(1-\nu)} \left(\frac{r_1}{l_k} \right)^{2-\nu/(1-\nu)}, \quad (10)$$

where n is the number of segments and τ_k is the time interval between two segments.

3. Continuum Damage Mechanics

For the host rock of tunnel, there was a damage zone due to internal stress redistribution and fracture extension. This damage made constitutive parameter become lower, which also generated impact on vibration wave propagation. The Canadian scholars measured that the main fracture extension depth is 0.5 m, and the maximum depth could reach 1.0 m with using in situ ultrasonic wave velocity testing technology [35]. So according to continuum damage mechanics theory,

the effective stress under damage condition can be expressed as [36]

$$\sigma_{ij}^* = \sigma_{ij}' (1 - D), \quad (11)$$

where σ_{ij}^* is the effective stress under damage condition, σ_{ij}' is effective stress of protolith, D is the scalar of damage condition, which can be carried out by Mazar damage model with two scalars being, respectively, tensile damage D_t and compression damage D_c , shown as [37]

$$D_c(\varepsilon_c) = 1 - e^{-\alpha_c(\varepsilon_c - \varepsilon_{c0})/\varepsilon_{c0}}, \quad (12a)$$

$$D_t(\varepsilon_t) = 1 - e^{-\alpha_t(\varepsilon_t - \varepsilon_{t0})/\varepsilon_{t0}}, \quad (12b)$$

where α_c and α_t are, respectively, compression and tensile coefficients, which depended on the material properties, for the rock, their value is usually 0.5, and ε_{c0} and ε_{t0} are, respectively, uniaxial compression and uniaxial tensile critical strain value. As shown below:

$$\varepsilon_c = \sqrt{\sum_{i=1,3} (\varepsilon_i^-)^2}, \quad (13a)$$

$$\varepsilon_t = \sqrt{\sum_{i=1,3} (\varepsilon_i^+)^2}, \quad (13b)$$

ε_i^- , ε_i^+ are, respectively, the negative and positive strains.

So, the damage scalar is the superposition of compression and tensile:

$$D = A_c D_c + A_t D_t, \quad A_c + A_t = 1, \quad (14)$$

$$A_c = \sum_{i=1,3} \frac{H_i [\varepsilon_i^- (\varepsilon_i^- + \varepsilon_i^+)]}{\bar{\varepsilon}_i^2}, \quad (15a)$$

$$A_t = \sum_{i=1,3} \frac{H_i [\varepsilon_i^+ (\varepsilon_i^- + \varepsilon_i^+)]}{\bar{\varepsilon}_i^2}, \quad (15b)$$

where $\bar{\varepsilon}_i^2 = \sum_{i=1,3} (\varepsilon_i^- + \varepsilon_i^+)^2$ is the effective strain, and when $x < 0$, $H[x] = 0$, and when $x > 0$, $H[x] = x$.

Based on above analysis, in the damage host rock, the formula of Young modulus between damage rock and original rock is

$$E^d = E_0 (1 - D), \quad (16)$$

where E^d is the Young modulus under damage rock and E_0 is Young modulus under original rock.

4. Equivalent Process of Blasting Loading

After blasting, the dynamic loading on the blast hole wall can make the volume of blast hole enlarged and the fracture expanded; also, the gas pressure and dynamic loading must be reduced with volume enlargement. At last, the explosion gas rapidly overflowed and the applied force decayed to zero with fracture development to connect each other.

Based on blasting mechanism, the process of blasting loading can be divided into four stages.

- (1) The first stage: the dynamic loading will increase with time till reaching the peak intensity of blasting.
- (2) The second stage: the blasting pressure will be reduced by the fracture expanding, the fillings moving, and the volume increasing before the filling was ejected from the hole.
- (3) The third stage: the explosive gas erupts quickly from the blast hole to lead to lower pressure after the filling was ejected.
- (4) The fourth stage: the explosive gas rapidly overflowed and the applied force decayed to zero when fractures develop to connect together.

4.1. The First Stage of Blasting. The dynamic loading will increase with time till reaching the peak intensity of blasting when the detonation gas wave propagated to the bottom section of blast hole after exploding. Many research works show that the initial peak blasting loading must have relationship to detonation wave pressure, and according to the Chapman-Jouguet model, the detonation wave pressure in an explosion can be guided by the widely known equation [34]

$$P_D = \frac{1}{\gamma + 1} \rho_0 V_D, \quad (17)$$

where P_D is the largest detonation wave pressure, ρ_0 is the density of explosive, V_D is detonation velocity, and γ is the ratio of the specific heats for the detonation gases; in this formula $\gamma = 3.0$.

The initial explosion pressure which was the explosion gas acted on the blast hole wall just after detonation is approximately the half of the detonation pressure for the coupled charge:

$$P_1 = \frac{\rho_0 V_D}{2(\gamma + 1)}. \quad (18)$$

For decoupled charges, the initial explosion pressure also had the relationship to the proportion between the blast hole diameter and the charge diameter, so the formula is

$$P_1 = \frac{\rho_0 V_D}{2(\gamma + 1)} \left(\frac{a}{b}\right)^{2\gamma}, \quad (19)$$

where a is the charge diameter and b is the blast hole diameter.

The rising time of loading was shown as

$$t_1 = \frac{L}{V_D}, \quad (20)$$

where L is the length of blast hole.

4.2. The Second Stage of Blasting. The blasting pressure will reduce with the fracture expanding, the filling moving, and the volume increasing of blast hole before the filling was

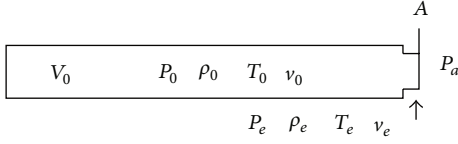


FIGURE 4: The equivalent structure of third stage.

ejected from the hole. So the volume of detonation gas with time can be expressed as

$$\Delta V(t) = 2\pi r(t) u(t) L dt + 2L \int_0^{L_a} \omega(\eta) d\eta + \frac{1}{4} \pi r(t)^2 y(t), \quad (21)$$

where $r(t)$ is the blast hole radius with time, $u(t)$ is the expansion velocity of blast hole wall, $\omega(\eta)$ is the width of fracture, and $y(t)$ is displacement of filling with time.

According to gas law, gas pressure with volume changed in detonation cavity can be shown as [5]

$$P_2 = A \left(1 - \frac{\omega}{R_1 V} \right) e^{-R_1 V} + B \left(1 - \frac{\omega}{R_2 V} \right) e^{-R_2 V} + \frac{\omega E_0}{(V)}. \quad (22)$$

Put the formula (21) into formula (22):

$$P_2(t) = A \left(1 - \frac{\omega}{R_1 (V_0 + \Delta V(t))} \right) e^{-R_1 (V_0 + \Delta V(t))} + B \left(1 - \frac{\omega}{R_2 (V_0 + \Delta V(t))} \right) e^{-R_2 (V_0 + \Delta V(t))} + \frac{\omega E_0}{(V_0 + \Delta V(t))}, \quad (23)$$

where V_0 is the initial volume of blast hole, A , B , R_1 , R_2 , and ω are all the explosive material parameter, and E_0 is initial energy of explosive.

4.3. The Third Stage of Blasting. The explosive gas erupts quickly out from the blast hole to lead to pressure getting lower after the filling was ejected or no filling blasting; according to gas dynamics theory, the blast hole in this period can be looked at as a bottle structure which follows the next assumptions, (a) because of the volume of blast hole was enlarged in last stage, which make the section of exit is smaller than inside, the shape of blast hole looks like a bottle; (b) because of very short time of reaction and better heat-insulating property of rock, the whole process are assumed as adiabatic process; (c) because of the very slow speed of volume expansion during last stage, the initial velocity of gas is zero at the beginning of this stage, so $v_0 = 0$, as shown in Figure 4.

In Figure 4, V_0 , P_0 , ρ_0 , T_0 , and v_0 are, respectively, the initial volume, pressure, density, temperature, and velocity. Also, P_e , ρ_e , T_e , and v_e are, respectively, the pressure, density, temperature, and velocity at the section of exit.

For this bottle structure, the inner pressure change of blast hole had the relationship with gas erupted statement; when $P_{cr}/P_a = 1$, the exit statement was critical condition, and the velocity of gas erupted was sound velocity; when $P_{cr}/P_a < 1$, the exit statement was subcritical condition, and the pressure at the exit was equal to air pressure $P_e = P_a$; when $P_{cr}/P_a > 1$, the exit statement was supercritical statement, and there was congested phenomenon at exit to make the velocity of gas also the sound velocity, $Ma = v_{cr}/v_s = 1$, where P_{cr} , v_{cr} are, respectively, critical statement of pressure and velocity.

According to isentropic gas formula, $P_{cr}/P_0 = (T_{cr}/T_0)^{\gamma/(\gamma-1)} = (2/(\gamma+1))^{\gamma/(\gamma-1)}$ to determine critical pressure value P_{cr} , where T_{cr} is the critical temperature, γ is the specific heat ratio of the gas, and $R = 297 \text{ J}/(\text{kg}\cdot\text{K})$ is the gas constant, so

$$\frac{P_{cr}}{P_0} = 0.3536. \quad (24)$$

Usually, the gas pressure in blast hole can reach $p_0 = (50000 \sim 10000) p_a$, so the critical pressure $p_{cr} \gg p_a$, which was supercritical statement to make the velocity of erupted gas be sound velocity.

Based on above analysis, the gas flow formula at the supercritical statement was

$$q_{mcr} = A \left(\frac{2}{\gamma+1} \right)^{(\gamma+1)/2(\gamma-1)} \sqrt{\gamma P_0 \rho_0}. \quad (25)$$

From time t to $t + dt$, based on the first law of thermodynamics with taking advantage of adiabatic process of gas in blast hole,

$$\frac{P}{\rho^\gamma} = \text{const}. \quad (26)$$

So,

$$\frac{P_e(t)}{\rho_e(t)^\gamma} = \frac{P_e(t+dt)}{\rho_e(t+dt)^\gamma}. \quad (27)$$

Put the formula (25) into formula (27):

$$\frac{P_e(t)}{\rho_e(t)^\gamma} = \frac{P_e(t+dt)}{\left(\rho_e(t) - (A/V_0) (2/(\gamma+1))^{\gamma/2(\gamma-1)} \sqrt{\gamma P_0 \rho_0} dt \right)^\gamma}. \quad (28)$$

So,

$$P_e(t+dt) = P_e(t) \left(\frac{\rho_e(t) - (A/V) (2/(\gamma+1))^{\gamma/2(\gamma-1)} \sqrt{\gamma P_0 \rho_0} dt}{\rho_e(t)} \right)^\gamma. \quad (29)$$

So, the formula of gas pressure change was

$$P_3(t+dt) = P_e(t+dt) = P_e(t) \left(1 - \frac{A}{V} \left(\frac{2}{\gamma+1} \right)^{\gamma/2(\gamma-1)} \frac{\sqrt{\gamma P_0 \rho_0}}{\rho_e(t)} dt \right)^\gamma. \quad (30)$$

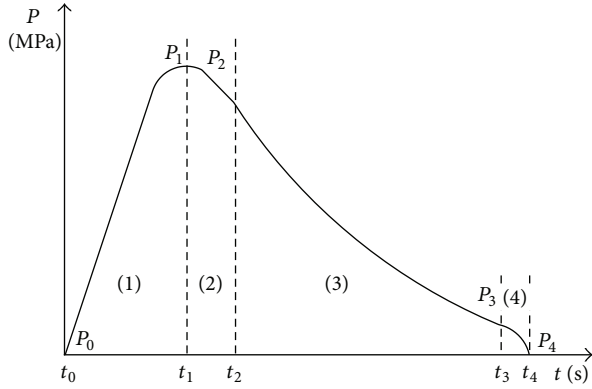


FIGURE 5: Blasting loading model.

4.4. The Fourth Stage of Blasting. The explosive gas rapidly overflows and the applied force decays to zero fast with fractures development to connect.

4.5. The Discipline of Loading. According the above separated analysis of blasting process, the blasting loading curve was shown as in Figure 5.

In Figure 5, t_0 is the beginning of blasting time, so $t_0 = 0$; the initial dynamic loading $P_0 = 0$; t_1 is the maximum blasting loading time, P_1 is the maximum blasting loading, t_2 is the time of fillings ejected, P_2 is the loading on the blast hole wall at that time, t_3 is the time just before fractures connect each other, P_3 is the loading on the blast hole wall at that time, t_4 is the end time of blasting, and $P_4 = 0$ is the gas pressure.

5. Project of Case Study

5.1. Engineering Introduction. The Chen-Chi West Connection Line Highway Tunnel, which was designed as a separate double tunnel each containing two lanes, was chosen as the case to be studied. The lengths of two tunnels are 1075 m and 1185 m, and the distance between them is between 18 m and 20 m. The cavern on the foothill region is 14 m wide and 12 m high. In this tunnel blasting, No. 2 rock emulsion explosive with diameter is 32 mm, length is 200 mm, and weight is 150 g was used. And positive multistage differential blasting method was taken by initial cut holes, destruction rock holes, peripheral holes, and bottom holes on the cutting surface. In working surface the distance between the holes was from 0.5 m to 0.7 m, the depth of the blast hole was 3.0 m, the charge length was 2.5 m without fillings, and the detonating cord across through the whole hole from opening to bottom. The blasting parameters were shown in Table 1, and the form of segments was shown in Figure 6 and interval time was shown in Table 2.

5.2. Constitutive Parameter. The formation lithology rock in the tunnel area is conglomerate, which belongs to the late Jurassic conglomerate, color is purple and structure is gravel with the diameter from 2 mm to 60 mm, and the gravels are cemented together with fillings to form the thick block layer. The compositions of the gravels are andesite, welded

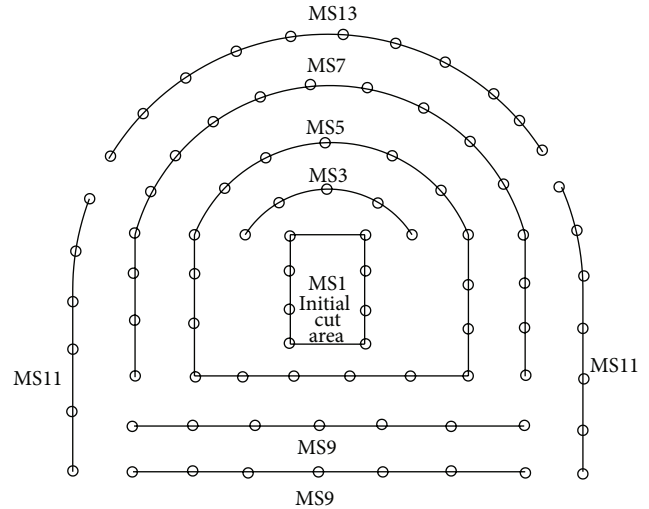


FIGURE 6: Blasting segmented situation.

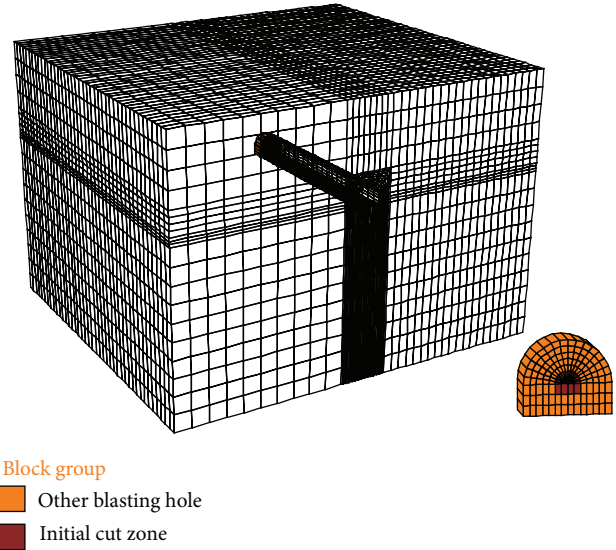


FIGURE 7: 3D model in numerical simulation.

tuff, rhyolite, and siliceous rocks, and for the fillings they are debris of rock, fine sand, quartz, feldspar, and some other stable mineral sand. The constitutive parameters are shown in Table 3.

6. Numerical Simulation Analysis

6.1. Simulation Model. Based on the actual engineering geology and structures, a 3D model was built in the finite element software of FLAC3D to accept the constitutive parameters, blasting load, and wave propagation parameters, as shown in Figure 7. The geometrical dimensions are length 228 m (X direction), width 203 m (Y direction), and height 159 m (Z direction). The finite element mesh consists of 386527 nodes and 372200 elements. And for the blasting zone, the group was between 100 m and 103 m (Y direction) after the cutting length 100 m, the initial cut hole zone was meshed

TABLE 1: Blasting parameters.

Charge diameter (mm)	Blast hole diameter (mm)	Holes number	Explosive density (kg/m ³)	Detonation velocity (m/s)
32	40	80	1000	3200

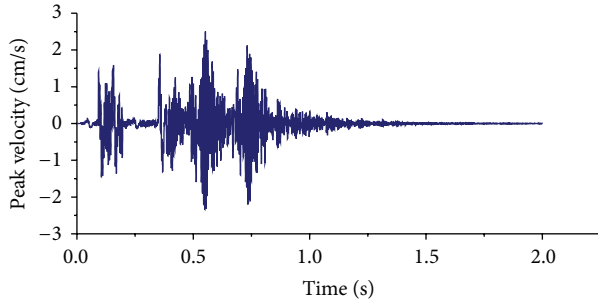


FIGURE 8: Simulated velocity curves in surrounding rock.

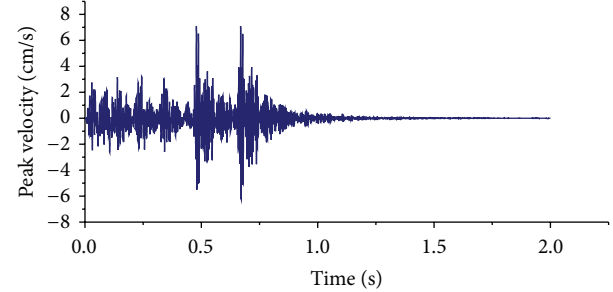


FIGURE 10: Velocity curves in surrounding rock.

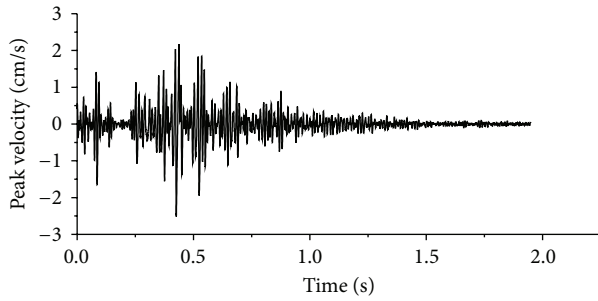


FIGURE 9: Monitored velocity curves in surrounding rock.

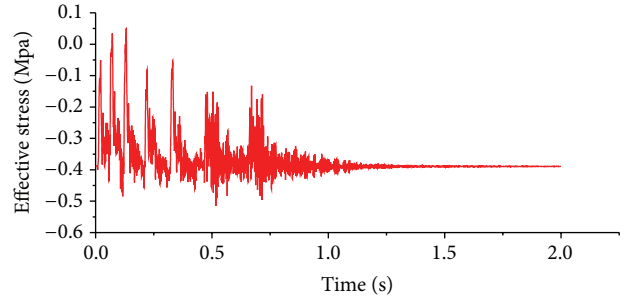


FIGURE 11: Tensile stress curves in surrounding rock.

TABLE 2: The time interval of every multistage.

MS1	MS3	MS5	MS7	MS9	MS11	MS13
0 ms	50 ms	110 ms	200 ms	310 ms	460 ms	650 ms

as 192 elements (brownish zone) and other worked zone was meshed as 606 elements (orange zone), also, as shown in Figure 7.

6.2. Dynamic Loading in Simulation. For the decoupled charge blasting, every stage pressure and arrival time were calculated by using above formulas. The detail values were shown in Table 4.

In the numerical simulation, it is difficult to determine the dumping of the rock mass directly, so, the field monitoring and calculation is necessary; in this paper, the dumping which was input into model was 0.015 based on the field monitoring and calculation repeatedly.

6.3. Verification of Simulation. In this simulation, the solve time was set to 2 s, and after 1284933 calculation steps, the curves of velocity were predicted from the model compared with 9 times field monitoring data at the same location. The simulation data and monitoring data were shown in Table 5, and the typical velocity curves were shown in Figures 8 and 9.

As shown in Figure 8, the predicted peak velocity was 2.505 cm/s compared with monitored peak velocity 2.51 cm/s which was obtained from Figure 9, so, the error rate is 2%; also, for those two curves, they had similar arrival time from 0.3 s to 0.7 s. From the error rate and similar arrival time, the simulation result in the surrounding rock was accurate enough for analysis. Also, for the other group data in Table 4, the error rates are from 0.5% to 23.1%, which all show that the simulation had the higher accurate results.

6.4. Predicted Results Analysis. After the simulation, the velocity curves and effective tensile stress curves with the distances 10 m, 20 m, 30 m, 50 m, and 80 m from the blasting point in surrounding rock and tunnel liner were obtained. The typical curves were shown in Figures 10–13.

For the surrounding rock, as shown in Figure 10, the peak velocity is 7.099. And the maximum effective tensile stress is 0.4502, which was shown in Figure 11. Also, for the tunnel liner, it is easy to learn that the peak velocity is 2.719 and maximum effective tensile stress is 0.7434 from Figures 12 and 13.

6.5. Conforming with Safety Criterion. The peak velocity and maximum effective stress can be obtained from the simulated model, which were shown in Table 6.

TABLE 3: Constitutive parameters of the rock.

Density (Kg/m ³)	Compressive strength (MPa)	Tensile strength (MPa)	Poisson's ratio	Cohesion (MPa)	Friction angle (MPa)	Compressive hardening coefficient (MPa)	Tensile hardening coefficient (MPa)
2820	75.5	3.0	0.2	4.5	38	0.26	0.33

TABLE 4: The detail value of every stage pressure and arrival time.

	P_D (MPa)	P_L (MPa)	P_0 (MPa)	P_1 (MPa)	P_2 (MPa)	P_3 (MPa)	P_4 (MPa)
Initial cut zone	2560	335.5	0	18.73	18.73	2.02	0
Other zones	2560	335.5	0	34.22	34.22	6.45	0
Arrival time (s)			$t_0 = 0$	$t_1 = 0.01$	$t_2 = 0.01$	$t_3 = 0.122$	$t_4 = 0.122$

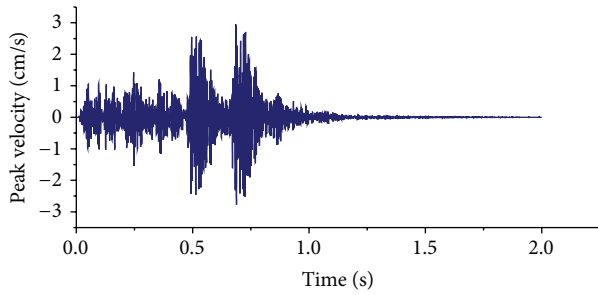


FIGURE 12: Velocity curves in tunnel liner.

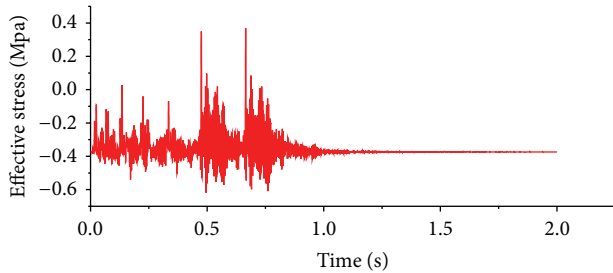


FIGURE 13: Tensile stress curves in tunnel liner.

Summarizing data in Table 6, the relationships between the effective tensile stress and peak velocity curves are, respectively, the safety criterion for the surrounding rock and tunnel liner, which were shown in Figures 14 and 15.

As shown in Figure 14, the safety criterion formula of the surrounding rock was

$$\sigma_t = 0.0363 (PPV)^2 - 0.25PPV + 0.4878, \quad R^2 = 0.991. \quad (31)$$

In this case study, the rock dynamic tensile strength is 4 MPa, so after calculating, when the PPV in the surrounding rock at the junction of tunnel arch and wall reaches 13.865 cm/s, the effective tensile stress will approach the maximum tensile strength.

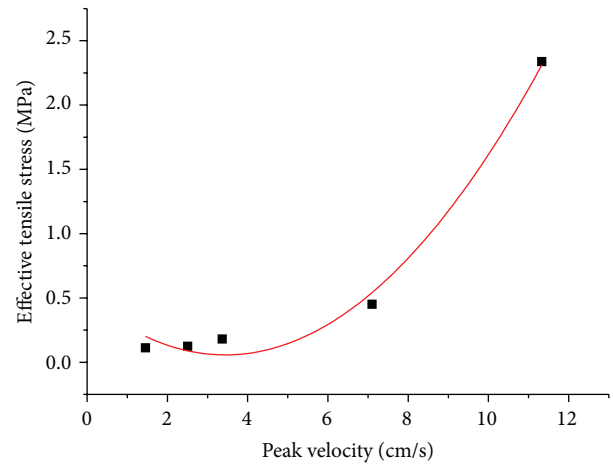


FIGURE 14: Safety criterion in surrounding rock.

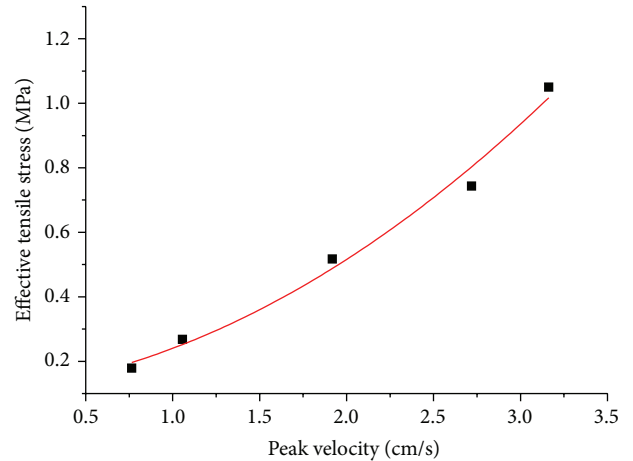


FIGURE 15: Safety criterion in tunnel liner.

As shown in Figure 15, the safety criterion formula was

$$\sigma_t = 0.0721 (PPV)^2 + 0.0593PPV + 0.1089, \quad R^2 = 0.988. \quad (32)$$

TABLE 5: The simulation and monitoring data of blasting vibration.

Date	Total charge (kg)	Distance (m)	Measured vertical PPV (cm/s)	Predicted vertical PPV (cm/s)	Error rate (%)
2013.5.18	240	64.3	1.263	1.293	+2.3
2013.5.22	240	58.8	1.519	1.644	+8.2
2013.5.24	240	57.2	1.705	1.771	+3.8
2013.5.27	240	54.8	1.999	1.998	-0.5
2013.6.02	240	50.0	2.505	2.510	+2
2013.6.03	240	53.2	2.248	2.176	-3.2
2013.6.11	240	57.2	2.304	1.771	-23.1
2013.6.12	240	58.8	1.582	1.641	+3.7
2013.6.14	240	62.3	1.747	1.403	-19.6

TABLE 6: Safety criterion data.

Distance (m)	Surrounding rock		Tunnel liner	
	Peak velocity (cm/s)	Maximum effective tensile stress (MPa)	Peak velocity (cm/s)	Maximum effective tensile stress (MPa)
10	11.33	2.337	3.162	1.050
20	7.099	0.4502	2.719	0.7434
30	3.370	0.1795	1.918	0.5172
50	2.505	0.1233	1.057	0.2677
80	1.455	0.1111	0.7643	0.1784

Also, for the tunnel liner, because there was a damage zone caused by excavated stress resilience and before blasts, the damage scale was $D = 0.2$ which was calculated by Mazar damage model based on the field fracture surveyed, so the safety criterion formula of the damage tunnel liner is

$$\sigma_t^* = \frac{0.0721 (\text{PPV})^2 + 0.0593\text{PPV} + 0.1089}{(1 - D)}. \quad (33)$$

The damage dynamic tensile strength was 3.2 MPa with the damage scale of $D = 0.2$, so, when the PPV in the tunnel liner at the junction of tunnel arch and wall reaches 6.213 cm/s, the effective tensile stress will approach the maximum tensile strength.

7. Conclusion

For the far field vibration analysis, based on the unified theory, the crushed zone and fractured zone can be regarded as blasting vibration source. Also, the wave propagation was essentially elastic. It was proved to be very accurate after comparing between the simulated velocity curves and the field monitoring data.

The accurate mathematic loading model was carried out by the analysis of the blasting pressure change, blast hole volume expansion, the fracture development, and the blasting gas motion; after well verification, this dynamic loading curve was more realistic and more accurate to the real loading, than other simplified loadings.

For the far field vibration analysis, the separated blasting loadings of each hole were regarded as uniformly distributed loading on its own segmented zone by taking advantage of

Saint-Venant theorem; it also met the requirement of analysis by comparing the monitoring data.

Based on the predicted velocity curves and effective tensile stress curves in surrounding rock and tunnel liner, the safety criterion field can be carried out to analyze the safety and stability of every point in field. And through adopting the continuum damage mechanics theory, the safety criterion of tunnel liner was more corresponding to the real situation.

Conflict of Interests

The authors declare that there is no conflict of interests regarding the publication of this paper.

Acknowledgments

This work has been supported by the research on the characteristics of rock high strain rate under dynamic load, NSFC (Natural Science Foundation of China, no. 51474016). Also, thanks are to Dr. Ming Cui and Dr. Miao Li for help in gathering the monitoring data.

References

- [1] W.-B. Lu, Y. Luo, M. Chen, and D.-Q. Shu, "An introduction to Chinese safety regulations for blasting vibration," *Environmental Earth Sciences*, vol. 67, no. 7, pp. 1951–1959, 2012.
- [2] D.-N. Lin, "The mitigation negative effect of tunnel-blasting-induced vibrations on constructed tunnel and buildings," *Journal of Coal Science and Engineering*, vol. 17, no. 1, pp. 28–33, 2011.

- [3] F. Ji, J. Lu, Y. Shi, and C. Zhou, "Mechanical response of surrounding rock of tunnels constructed with the TBM and drill-blasting method," *Natural Hazards*, vol. 66, no. 2, pp. 545–556, 2013.
- [4] M. Monjezi, H. A. Mohamadi, B. Barati, and M. Khandelwal, "Application of soft computing in predicting rock fragmentation to reduce environmental blasting side effects," *Arabian Journal of Geosciences*, vol. 7, no. 2, pp. 505–511, 2014.
- [5] N. Jiang and C. Zhou, "Blasting vibration safety criterion for a tunnel liner structure," *Tunnelling and Underground Space Technology*, vol. 32, pp. 52–57, 2012.
- [6] A. Karadogan, A. Kahrman, and U. Ozer, "A new damage criteria norm for blast-induced ground vibrations in Turkey," *Arabian Journal of Geosciences*, vol. 7, no. 4, pp. 1617–1626, 2014.
- [7] J. H. Yang, W. B. Lu, Z. G. Zhao, P. Yan, and M. Chen, "Safety distance for secondary shotcrete subjected to blasting vibration in Jinping-II deep-buried tunnels," *Tunnelling and Underground Space Technology*, vol. 43, pp. 123–132, 2014.
- [8] A. Ansell, "In situ testing of young shotcrete subjected to vibrations from blasting," *Tunnelling and Underground Space Technology*, vol. 19, no. 6, pp. 587–596, 2004.
- [9] M. Khandelwal, "Blast-induced ground vibration prediction using support vector machine," *Engineering with Computers*, vol. 27, no. 3, pp. 193–200, 2011.
- [10] Q. Liang, Y. An, L. Zhao, D. Li, and L. Yan, "Comparative study on calculation methods of blasting vibration velocity," *Rock Mechanics and Rock Engineering*, vol. 44, no. 1, pp. 93–101, 2011.
- [11] J.-H. Shin, H.-G. Moon, and S.-E. Chae, "Effect of blast-induced vibration on existing tunnels in soft rocks," *Tunnelling and Underground Space Technology*, vol. 26, no. 1, pp. 51–61, 2011.
- [12] R. Nateghi, "Prediction of ground vibration level induced by blasting at different rock units," *International Journal of Rock Mechanics & Mining Sciences*, vol. 48, no. 6, pp. 899–908, 2011.
- [13] M. Rezaei, M. Monjezi, S. G. Moghaddam, and F. Farzaneh, "Burden prediction in blasting operation using rock geomechanical properties," *Arabian Journal of Geosciences*, vol. 5, no. 5, pp. 1031–1037, 2012.
- [14] K. Dey and V. M. S. R. Murthy, "Prediction of blast-induced overbreak from uncontrolled burn-cut blasting in tunnels driven through medium rock class," *Tunnelling and Underground Space Technology*, vol. 28, no. 1, pp. 49–56, 2012.
- [15] Z. Wang, C. Fang, Y. Chen, and W. Cheng, "A comparative study of delay time identification by vibration energy analysis in millisecond blasting," *International Journal of Rock Mechanics and Mining Sciences*, vol. 60, pp. 389–400, 2013.
- [16] Q. Liang, J. Li, D. Li, and E. Ou, "Effect of blast-induced vibration from new railway tunnel on existing adjacent railway tunnel in Xinjiang, China," *Rock Mechanics and Rock Engineering*, vol. 46, no. 1, pp. 19–39, 2013.
- [17] H. Fu, L. N. Y. Wong, Y. Zhao, Z. Shen, C. Zhang, and Y. Li, "Comparison of excavation damage zones resulting from blasting with nonel detonators and blasting with electronic detonators," *Rock Mechanics and Rock Engineering*, vol. 47, no. 2, pp. 809–816, 2014.
- [18] L. Ahmed and A. Ansell, "Vibration vulnerability of shotcrete on tunnel walls during construction blasting," *Tunnelling and Underground Space Technology*, vol. 42, pp. 105–111, 2014.
- [19] M. Khandelwal, D. L. Kumar, and M. Yellishetty, "Application of soft computing to predict blast-induced ground vibration," *Engineering with Computers*, vol. 27, no. 2, pp. 117–125, 2011.
- [20] M. Monjezi, M. Ghafurikalajahi, and A. Bahrami, "Prediction of blast-induced ground vibration using artificial neural networks," *Tunnelling and Underground Space Technology*, vol. 26, no. 1, pp. 46–50, 2011.
- [21] J. Kim, S. Kwon, S. Park, and Y. Kim, "A MEMS-based commutation module with vibration sensor for wireless sensor network-based tunnel-blasting monitoring," *KSCE Journal of Civil Engineering*, vol. 17, no. 7, pp. 1644–1653, 2013.
- [22] F. Faramarzi, M. A. E. Farsangi, and H. Mansouri, "An RES-based model for risk assessment and prediction of backbreak in bench blasting," *Rock Mechanics and Rock Engineering*, vol. 46, no. 4, pp. 877–887, 2013.
- [23] M. Sazid and T. N. Singh, "Two-dimensional dynamic finite element simulation of rock blasting," *Arabian Journal of Geosciences*, vol. 6, no. 10, pp. 3703–3708, 2013.
- [24] X. Xia, H. B. Li, J. C. Li, B. Liu, and C. Yu, "A case study on rock damage prediction and control method for underground tunnels subjected to adjacent excavation blasting," *Tunnelling and Underground Space Technology*, vol. 35, pp. 1–7, 2013.
- [25] S. Sun, L. Yue, J. Wu, J. Liu, and J. Wei, "Case study on influence of step blast-excavation on support systems of existing service tunnel with small interval," *Advances in Mechanical Engineering*, vol. 2013, Article ID 257457, 13 pages, 2013.
- [26] J. Yang, W. Lu, M. Chen, P. Yan, and C. Zhou, "Microseism induced by transient release of in situ stress during deep rock mass excavation by blasting," *Rock Mechanics and Rock Engineering*, vol. 46, no. 4, pp. 859–875, 2013.
- [27] K.-I. Song, T.-M. Oh, and G.-C. Cho, "Precutting of tunnel perimeter for reducing blasting-induced vibration and damaged zone—numerical analysis," *KSCE Journal of Civil Engineering*, vol. 18, no. 4, pp. 1165–1175, 2014.
- [28] Y. G. Hu, W. Lu, M. Chen, P. Yan, and J. Yang, "Comparison of blast-induced damage between presplit and smooth blasting of high rock slope," *Rock Mechanics and Rock Engineering*, vol. 47, no. 4, pp. 1307–1320, 2014.
- [29] H. Yu, Y. Yuan, G. Yu, and X. Liu, "Evaluation of influence of vibrations generated by blasting construction on an existing tunnel in soft soils," *Tunnelling and Underground Space Technology*, vol. 43, pp. 59–66, 2014.
- [30] W. Lu, J. Yang, M. Chen, and C. Zhou, "An equivalent method for blasting vibration simulation," *Simulation Modelling Practice and Theory*, vol. 19, no. 9, pp. 2050–2062, 2011.
- [31] W. A. Hustrulid, *Blasting Principles for Open Pit Mining*, A.A. Balkema Publishers, Brookfield, Wis, USA, 1999.
- [32] A. H. XaHyKaeB, *Physical Process of Rock Blasting in Mining*, Mineral Press, Leningrad, Russia, 1974.
- [33] J. Mazars, "A description of micro- and macroscale damage of concrete structures," *Engineering Fracture Mechanics*, vol. 25, no. 5–6, pp. 729–737, 1986.
- [34] J. Henrych, *The Dynamics of Explosion and Its Use*, Elsevier Scientific Publishing Company, New York, NY, USA, 1979.
- [35] J. B. Martino and N. A. Chandler, "Excavation-induced damage studies at the underground research laboratory," *International Journal of Rock Mechanics and Mining Sciences*, vol. 41, no. 8, pp. 1413–1426, 2004.
- [36] X. Xue, W. Zhang, and X. Yang, "A damage mechanics model for porous media," *Geotechnical and Geological Engineering*, vol. 31, no. 2, pp. 817–825, 2013.
- [37] W. Zhang and Y. Cai, *Continuum Damage Mechanics and Numerical Applications*, Zhejiang University Press, Hangzhou, China, 2011.

Research Article

Dynamic Effect and Control of Key Strata Break of Immediate Roof in Fully Mechanized Mining with Large Mining Height

Yuan Yong, Tu Shihao, Zhang Xiaogang, and Li Bo

School of Mines, China University of Mining and Technology, Key Laboratory of Deep Coal Resource Mining, Ministry of Education, China-Australian Mining Research Center, Xuzhou, Jiangsu 221116, China

Correspondence should be addressed to Tu Shihao; 826192989@qq.com and Zhang Xiaogang; zxcumt90@163.com

Received 14 November 2014; Revised 12 March 2015; Accepted 14 March 2015

Academic Editor: Shimin Liu

Copyright © 2015 Yuan Yong et al. This is an open access article distributed under the Creative Commons Attribution License, which permits unrestricted use, distribution, and reproduction in any medium, provided the original work is properly cited.

This paper puts forward the concept of key strata in immediate roof (KSIF) and studied the dynamic effect and control mechanism of KSIF. The results show that KSIR controls the caving of its upper immediate roof strata; the break of KSIR has direct dynamic impact on its lower strata and this impact increases along with the increase of the thickness and hardness of the KSIR and the decrease of the distance to the working seam. The KSIR and main roof can easily form the bilayer structure “Cantilever-Masonry beam.” Support work load is affected by the position, thickness, and hardness of KSIR. The support work load increased on the condition of increase of the thickness and hardness of KSIR and the decrease of the distance to the face.

1. Introduction

In 2013, the coal production in China accounted for almost 1/2 of the total coal output in the world, and its coal production extracted from thick coal seams accounts for 40%~50% of national coal production. However, China is also the country with the largest number of mining disasters in all around the world [1, 2]. The number of people who died because of coal mine disasters is 1067, and 30.5% of those disasters are roof accidents. This situation means that it is quite important to control the mining safety in thick coal seams, especially about the control of roof stability because it significantly affects the safety of mining workers and equipment [3]. The common mining methods for thick coal seam with thickness more than 3.5 meters mining are fully mechanized mining with top coal caving (FMMTCC) and FMMLMH. Practice shows that recovery rates in FMMLMH are 10%~15% higher than FMMTCC. In recent years, with the development of mining equipment, FMMLMH technology has been widely applied in thick coal seam mining. As a type of high recovery ratio of mining technology with a promising future, FMMLMH has become a trend for coal seams less than 7.0 m thick [4].

Many problems exist in FMMLMH face such as large mining and caving height, intense ground pressure, poor coal wall stability, and difficulty in controlling rib spalling, and these problems have hindered the application of FMMLMH technology [5, 6].

Scholars have already done much work on roof structure characteristic of fully mechanized face and FMMTCC face, but research on roof structure characteristic of FMMLMH face is not sufficient [7]. Besides, the structure is always considered as a single layer structure of broken main roof. For example, the relation between mining height and caving zone, fractured zone has been studied [8]; analysis on the stability of main roof first break has been performed [9], the relationship between overlying movement and support has been studied [10], and how mining height affects the overlying structure has been analyzed [11]. With the increase of mining height, overlying fractured zone increases and bilayer structure forms in overlying structure have already drawn many scholars interests. Therefore, this paper puts forward the concept of key strata in immediate roof (KSIR) and its discrimination method. Reasonable support work load and dynamic effect of KSIR break have been studied and achieved several beneficial conclusions.

2. Dynamic Effect of KSIR in FMMLMH

2.1. Concept of KSIR. Figure 1 shows the occurrence characteristics of thick coal seams of several mining areas in China. In most cases, mudstone or mudstone strata above coal seam forms immediate roof; the thickness of these strata is almost equivalent to that of the coal seam. Above the immediate roof is the main roof. The overlying caving height increased with the increase of mining height. That is, the overlying caving height can reach 20 m when the mining height is 6 m. Therefore, under the condition of normal mining height, the break of main roof caves in gob and thus it cannot form a stable structure to bear the overlying weight. The position of stable structure is higher with the increase of mining height which means that, under the condition of normal fully mechanized mining and FMMTCC, the main roof cannot serve its function. Thus, we define that the strata between the stable masonry beam and the coal seam are immediate roof after mining the coal seam; the main roof is the strata that can form stable structure above the immediate roof. The thick hard strata that exist in the immediate roof and control the whole or part of the caving strata in FMMLMH face are KSIR.

2.2. Discrimination of KSIR

2.2.1. Discrimination Method and Procedure. The discrimination method of KSIR is based on the definition of KSIR and Key Strata Theory. The derivation procedure of KSIR is shown in Figure 2.

(1) *Estimation of Caving Height H_k .* H_k is calculated with the following equation [12] under gently inclined and inclined coal seams:

$$H_k = \frac{M}{K_k - 1}, \quad (1)$$

where M is mining height, m; K_k is average coefficients of bulk increase, 1.25~1.5.

(2) *Determination of Immediate Roof Height h_z .* h_z is approximate calculated according to the caving height:

$$h_z = H_k - \Delta_z, \quad (2)$$

where Δ_z is the space height between caving zone and stable structure, 1~3 m [13].

(3) *KSIR Positioning.* Assuming that immediate roof consists of n strata, based on the definition of immediate roof and article [14], the existence and position of KSIR are determined by the following process.

① *Positioning the Hard Strata.* This step starts with the first immediate roof stratum, from bottom to above, and calculates each stratum according to $E_{m+1}h_{m+1}^2 \sum_{i=1}^m h_i \gamma_i$ and $\gamma_{m+1} \sum_{i=1}^m E_i h_i^3$. If the result is in accord with (3), calculation stops; then from the first layer to the above, the $m + 1$ stratum is the first hard stratum. From the first hard stratum,

calculation continues with the above method to determine the second hard stratum; the rest can be done in the same method until the topmost hard stratum is positioned. One has

$$E_{m+1}h_{m+1}^2 \sum_{i=1}^m h_i \gamma_i > \gamma_{m+1} \sum_{i=1}^m E_i h_i^3. \quad (3)$$

If $m + 1 > n$, the calculation stops, which means KSIR does not exist; if $m + 1 \leq n$, continue the following step.

② *Examining the Hard Strata to Determine Whether They Are KSIR or Not.* According to the concept of KSIR, if there are j strata above the immediate roof deform synchronously, then the load which the $j + 1$ stratum imposes on the first hard stratum is

$$q_1|_j = \frac{E_1 h_1^3 \sum_{i=1}^{j+1} \gamma_i h_i}{\sum_{i=1}^{j+1} E_i h_i^3}, \quad (4)$$

where E_1 and E_i are the first and the i immediate roof stratum elasticity modulus, respectively, Mpa; h_1 and h_i are the thickness of the first and the i immediate roof stratum, respectively, m; γ_i is the volume-weight of the i layer, kN/m³. Consider

$$\text{If } q_1|_{j+1} < q_1|_j. \quad (5)$$

Then the j ($j + m \leq n$) immediate roof stratum is the KSIR, where $q_1|_{j+1}$ and $q_1|_j$ are the load imposed on the first layer from the calculation of the first layer to the $j + 1$ and the j layer.

KSIR does not exist if (5) cannot be established.

2.2.2. Application. The average mining height of No. 15104 working face in Shijiazhuang coal mine, Yangmei group, is 5.5 m. The overlying is mudstone, fine sandstone, and limestone. The caving height is 16.5 m according to (1) ($K_k = 1.3$). Considering deflection of the main roof, $\Delta_z = 1.5$ m; the thickness of immediate roof is 15 m according to (2). Based on the geogram of No. 15104 face, the immediate roof consists of three layers; their rock mechanics parameters are listed in Table 1. According to the above calculation methods, the second stratum is the hard stratum and also the KSIR.

2.3. Influence of KSIR on Roof Break. Based on No. 15104 face, influence of KSIR on roof break is studied by means of physical modelling.

2.3.1. Design of Physical Model

(1) *Similar Materials and Their Proportion.* The average coal seam thickness and its buried depth are 5.5 m and 480 m, respectively. Physical dimension of the model is Length \times width \times height = 2.5 m \times 0.2 m \times 1.3 m. The rest of overlying is replaced by water pressure, 0.06 Mpa. Based on the similar laws, geometric similarity ratio is $\alpha_l = 100$, volume-weight similarity ratio is $\alpha_r = 1.67$, time similarity ratio is $\alpha_t = 10$, and intensity similar ratio is $\alpha_R = \alpha_l \times \alpha_r = 167$. The main modelling material is sand, and cementing materials are

TABLE 1: Rock mechanics parameters of 15104 face.

Stratum number	Lithology	Thickness/m	Accumulated height/m	Elasticity modulus/Gpa	Unit weight/kN·m ⁻³	$E_{m+1}h^2_{m+1}\sum_{i=1}^m h_i\gamma_i$	$\gamma_{m+1}\sum_{i=1}^m E_i h_i^3$
4	Packsand	2	17	22.8	27.1	36334.1	175286.1
3	Sandy mudstone	3	15	7.24	26.2	20838.2	164343.2
2	Packsand	6	12	22.8	27.1	129029.8	36526.5
1	Mudstone	6	6	6.24	26.2		

TABLE 2: Modelling material ratio.

Lithology	Accumulated height/cm	Model height/cm	Layer volume/cm ³	Sand weight/kg	Gypsum weight/kg	CaCO ₃ weight/kg	Water weight/kg
Packsand	140	4.5	22500	32.8	3.9	2.2	4.6
Medium sandstone	135.5	5	25000	36.4	3.6	3	5.1
Sandy mudstone	130.5	6	30000	44.6	4.5	2.6	6
Packsand	124.5	4	20000	29.1	3.5	1.9	4.1
Medium sandstone	120.5	2	10000	14.6	1.5	1.2	2
Sandy mudstone	118.5	4	20000	29.8	3	1.7	4
Mudstone	114.5	7.5	37500	55.8	4.8	4	7.5
Coal	107	1	5000	7.4	0.5	0.6	1
Sandy mudstone	106	5.5	27500	40.9	4.1	2.4	5.5
Packsand	100.5	1	5000	7.3	0.9	0.5	1
Mudstone	99.5	10	50000	74.4	6.3	5.3	10
Coal	89.5	1.5	7500	11.2	0.8	1.0	1.5
Sandy mudstone	88	7.5	37500	55.8	5.7	3.2	7.5
Medium sandstone	80.5	5	25000	36.4	3.6	3	5.1
Limestone	75.5	3	15000	21.3	2.6	2.1	3.6
Sandy mudstone	72.5	6.5	32500	48.4	4.9	2.8	6.5
Packsand	66	5.5	27500	40.1	4.8	2.7	5.6
Mudstone	60.5	4.5	22500	33.5	2.9	2.4	4.5
Limestone	56	6	30000	42.5	5.1	4.3	7.3
Coal	50	1	5000	7.4	0.5	0.6	1
Sandy mudstone	49	6	30000	44.6	4.5	2.6	6
Mudstone	43	4.5	22500	33.5	2.9	2.4	4.5
Limestone	38.5	5	25000	35.4	4.3	3.5	6.1
Mudstone	33.5	6	30000	44.6	3.8	3.2	6
Packsand	27.5	2	10000	14.6	1.7	1	2
Sandy mudstone	25.5	3	15000	22.3	2.3	1.3	3
Packsand	22.5	6	30000	43.7	5.2	2.9	6.1
Mudstone	16.5	6	30000	44.6	3.8	3.2	6
15# coal	10.5	5.5	27500	40	4	2.6	5.2
Sandy mudstone	5	5	25000	37.3	3.6	2.5	4.7

CaCO₃ and gypsum. Mica powder is used between each layer to ensure bed separation. The modelling material ratio of each layer is shown in Table 2.

(2) *Model Design and Measurement Point Arrangement.* In order to analyze the roof break, stress distribution, and displacement characteristic, seven displacement meters are

installed in the fourth and eighth layer, respectively; eleven pressure cells are installed in the fifth and the twelfth layer, respectively. The arrangement is shown in Figure 3. Vertical stress is recorded by pressure cells; vertical displacement is recorded by YHD-50 displacement meters. This record equipment is monitored by TS3890A static resistance strain indicator.

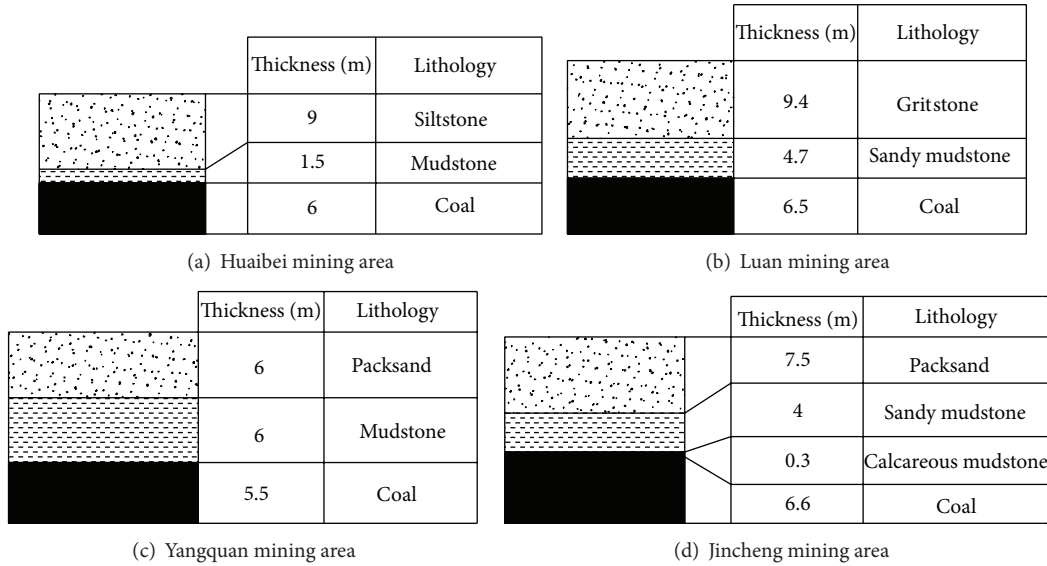


FIGURE 1: Typical thick coal seam occurrence characteristics in four mining areas.

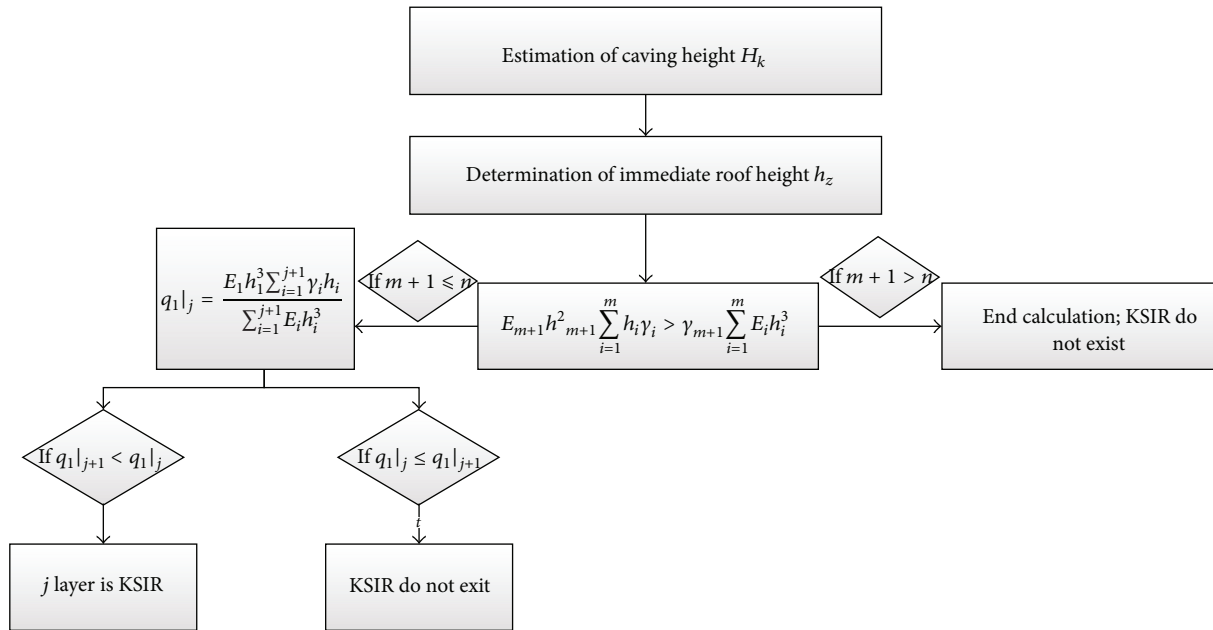


FIGURE 2: Derivation procedure of KSIR.

2.3.2. Modelling Results Analysis

(1) *Movement Characteristics of Overlying Strata.* Figure 4 shows the overlying movement characteristics along with the advancement. Figure 5 shows the height of caving zone and fractured zone along with the advancement.

Conclusions can be drawn from the above as follows.

① As the face advanced, caving height increased. When the advance distance is 75 m, caving height reached its peak, at approximate of 17 m; layers labeled 3~6 are in the caving zone.

Fractured height still increased as the face advanced. When the advance distance is 120 m, fractured height reached its peak, at about 77 m. ② Layers in caving zone are controlled by KSIR labeled number 4; when the advance distance is 70 m, layers number 5 and number 6 caved along with the break of KSIR and the caving has dynamic impact on the number 3 mudstone layer below the KSIR.

(2) *Overlying Displacement Characteristics.* Figure 6 shows the vertical displacement characteristics of different roof

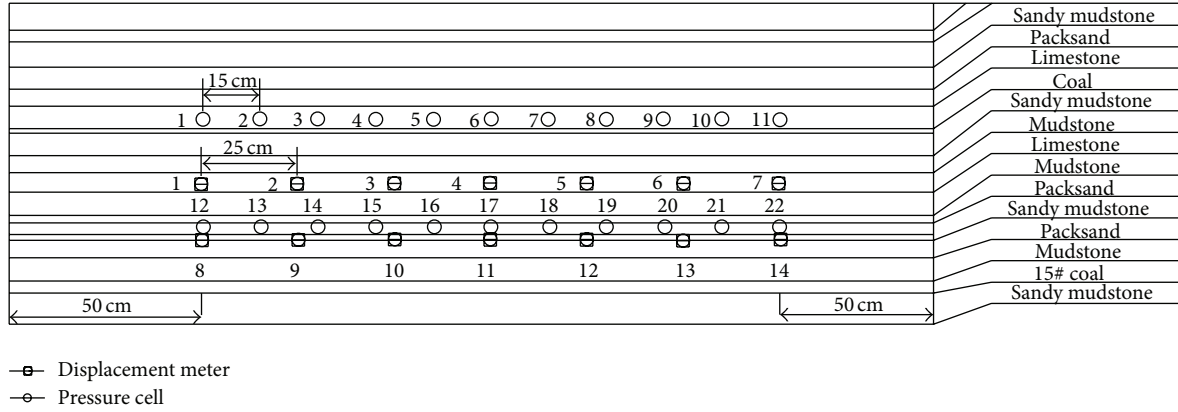


FIGURE 3: Model design and measurement point arrangement.

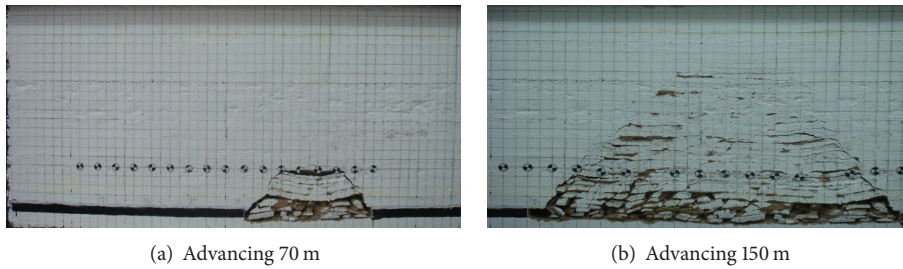


FIGURE 4: Overlying movement characteristics.

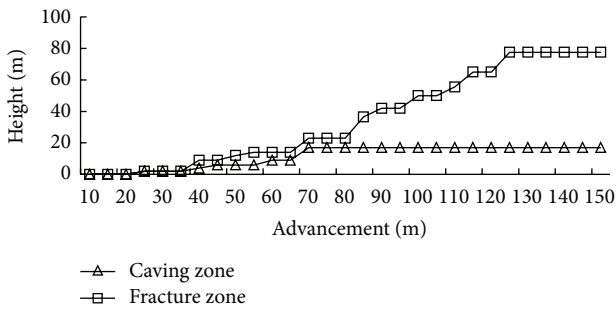


FIGURE 5: Height of caving zone and fractured zone along with the advancement.

layers. According to the figure, vertical displacement shows salutatory increase with the break of roof. The increase intervals of each point are in accord with its layer period break intervals. The displacement of middle measurement points is larger than that of the side points.

(3) *Stress Distribution Characteristics.* Figure 7 shows the mining-induced stress variation of each measurement point along with the advancement (points numbers 4, 8, 10, 13, and 17 are not included because of malfunction).

According to Figure 7, ① stress of points numbers 1, 11, 12, and 22 increased with face advancement and the higher the point position is, the larger the increase of the stress is. These

points are not in the caving zone; ② stress of points numbers 2~9 increased to the peak and then declined gradually. The peaking period is short. These points are in the fractured zone; ③ numbers 14~21 points are in the caving zone. The stress of these points increased to the peak and then declined gradually. The peaking period is relatively long. For example, stress peaking duration of numbers 16 and 21 points is 20 m and 10 m, respectively. This is because when KSIR broke, upper layers of numbers 5 and 6 caved into the gob; dynamic impact is strong and lasting.

2.3.3. *Effect on Distribution of Abutment Pressure of KSIR.*

Effect on distribution of abutment pressure of KSIR is studied by means of numerical simulations using UDEC^{2D}3.1. The existence of KSIR, the thickness of KSIR, and the position and hardness of KSIR are simulated to study the abutment pressure distribution with mining height of 5.5 m. According to (1), when mining height is 5.5 m, caving height is about 17 m. In order to facilitate comparison, the thickness of immediate roof and the main roof is 15 m and 5 m, respectively; the length and height of the models are 200 m and 56 m, respectively. The buried depth is 480 m. Since the model does not extend to the ground surface, vertical load of 10.85 MPa is applied to the model top to simulate the overburden up to the ground surface. The models are simulated using Mohr-Coulomb elements. Mechanical properties of each layer are presented in Table 3.

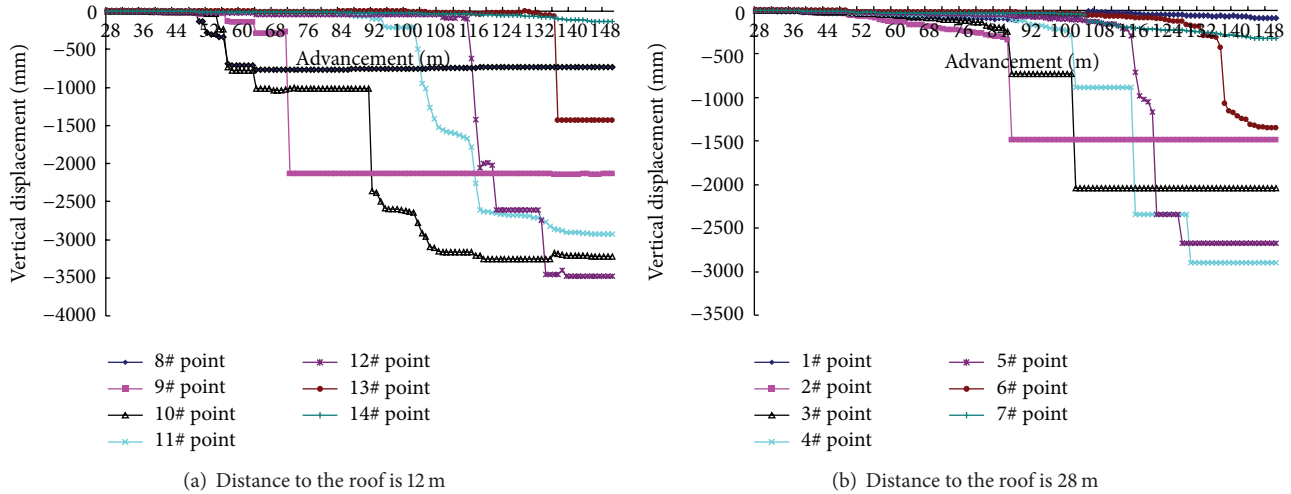


FIGURE 6: Roof vertical displacement along with advancement.

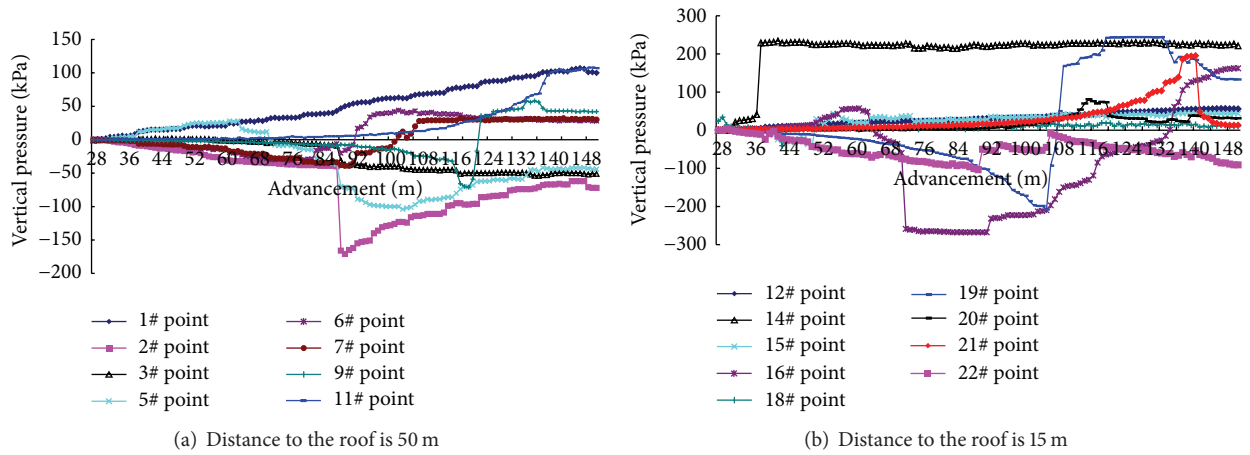


FIGURE 7: Vertical stress variation along with face advancement.

Figure 8 shows the effect of existence of KSIR on the distribution of abutment pressure when advancing 50 m. Figure 9(a) shows that the existence of KSIR increases the peak of abutment pressure, but it does not much affect the distance between peak stress position and coal wall and the influence scope of peak stress.

The thickness of KSIR in the model is 6 m. Three different positions of KSIR are simulated, and they are KSIR in the lower part of immediate roof (distance to the top of coal seam is 0 m), KSIR in the middle part of immediate roof (distance to the top of coal seam is 6 m), and KSIR in the upper part of immediate roof (distance to the top of coal seam is 12 m). Face advancement is 50 m. The distribution of abutment pressure is shown in Figure 8. According to Figure 9(b), ① the lower the KSIR position is, the larger the peak of abutment pressure is and the smaller the distance between peak position and coal wall is; ② if KSIR is in the lower part of immediate roof, there are no soft layers acting as cushion layer between KSIR and coal seam when extracting the coal seam. Thus, the

distribution of abutment pressure shows high-low oscillation because of KSIR break. Therefore, when extracting these coal seams, support should have antidynamic impact ability with certain yielding support columns.

Three different hardness coefficients ($f = 3$, $f = 9$, and $f = 15$) of KSIR models are simulated when KSIR is in the middle part of immediate roof. The distribution of abutment pressure under these three conditions is shown in Figure 9(c). With the increase of hardness coefficient, the peak of abutment pressure and the affected scope of abutment pressure increased. This phenomenon is in accord with site circumstance that the harder the roof is, the greater the strata behaviors are.

Three different thicknesses (3 m, 6 m, and 12 m) of KSIR models are simulated when KSIR is in the middle part of immediate roof. The distribution of abutment pressure under these three conditions is shown in Figure 9(d). With the increase of thickness, the peak of abutment pressure and the affected scope of abutment pressure increased. When

TABLE 3: Mechanical properties of numerical model.

Coal and rock mass	Bulk modulus K/GPa	Shear modulus G/GPa	Density $d/\text{kg}\cdot\text{m}^{-3}$	Friction angle/ $^\circ$	Cohesive force/ MPa	Tensile strength/ MPa
Overlying rock	3	2.3	2200	30	2	2
Main roof	10.1	8.2	2700	33	5.9	3
KISR	5.1	4.2	2500	33	3.9	3
Immediate roof	1.85	1.64	2000	24	1.1	1.19
15# coal seam	2.05	1.84	1400	25	1.85	0.89
Floor	10	8	2500	30	7	5

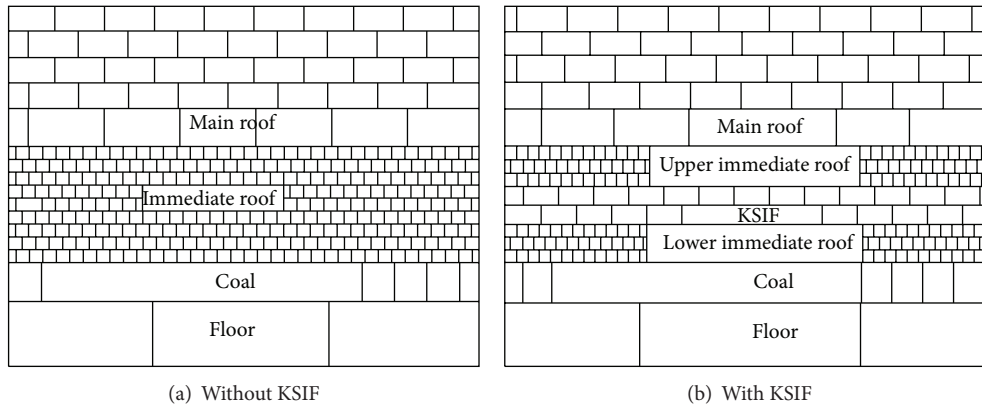


FIGURE 8: Simulation model of the existence of KSIR.

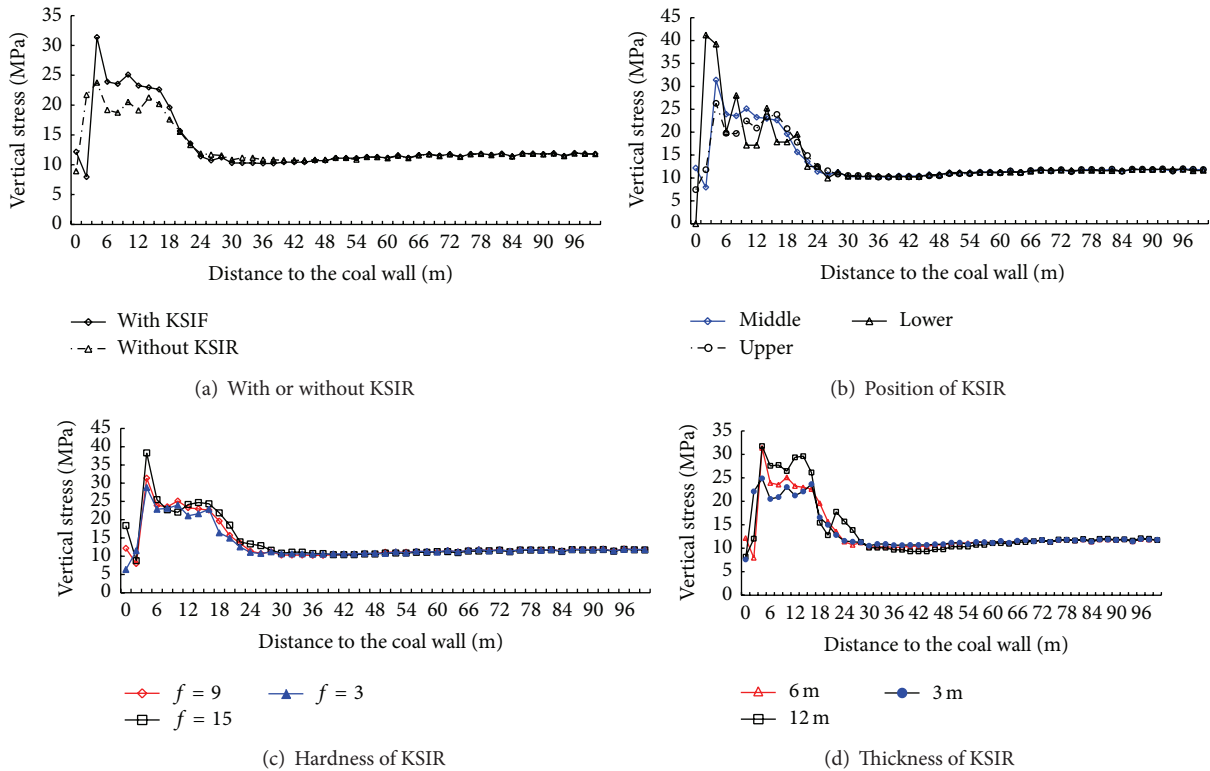


FIGURE 9: Effect on distribution of abutment pressure of KSIR.

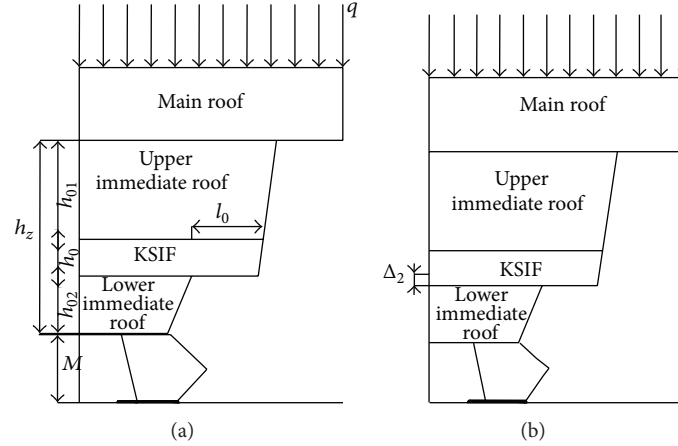


FIGURE 10: Dynamic load calculation model of KSIR.

the thickness of KSIR is 12 m, abutment pressure shows oscillation distribution.

3. Control of Dynamic Effect in FMMLMH Face

“Suspended roof” tends to be formed in FMMLMH face because of the existence of hard and thick KSIR. KSIR forms the cantilever beam structure. The break of KSIR and main roof can easily form the bilayer structure “Cantilever-Masonry beam.” The instability of cantilever beam structure causes dynamic impact of support; thus support accidents such as support pushed down can easily happen. Therefore, determination of support work load in FMMLMH should take KSIR dynamic impact into consideration, as is shown in Figure 10.

Take the most dangerous circumstance; for example, the crack of KSIR and main roof is on the coal wall. When KSIR breaks, from the position which the distance to the lower immediate roof is Δ_2 , KSIR does work to the lower immediate roof and support system. Under the dynamic impact, the sinkage of the lower immediate roof and support system is Δ_1 ; load (P) imposed on the support is

$$P = Q_1 + Q_2 + Q_3, \quad (6)$$

where Q_1 is static load of immediate roof, kN; Q_2 is addition load of main roof, kN; Q_3 is dynamic load of KSIR, kN.

3.1. Static Load of Immediate Roof. Static load of immediate roof (Q_1) is the immediate roof strata load beneath the KSIR; Q_1 is calculated with the following:

$$Q_1 = \gamma B l_k h_{01}, \quad (7)$$

where h_{01} is the thickness of immediate roof strata beneath the KSIR, m.

3.2. Addition Load of Main Roof. As the position of main roof is relatively far from the support and there are soft strata in

main roof which can absorb energy, these soft strata have poor ability of transporting energy. Thus, most of energy generated during the break of main roof has been absorbed. The addition load of main roof (Q_2) is generally calculated with multiple immediate roof loads. Q_2 can be represented by

$$Q_2 = (n - 1) \gamma l_k B h_z. \quad (8)$$

3.3. Dynamic Load of KSIR. Dynamic impact is a complicated physical process. Many aspects should be taken into account such as short action time, concentration and consumption of sound, and thermoenergy; if the dynamic impact is precisely analyzed, propagation effect of stress wave should be also considered. Thus, the calculation process is quite complicated and is difficult to the actual application. Therefore, we simplified several conditions as follows. ① The time between KSIR breaks and upper immediate roof breaks is 0. ② There is no springback when the broken KSIR touches the lower immediate roof. ③ There is no dissipation energy of sound and heat during impact process; the impact transports instantly through impacted body, and the impacted body obeys Hook’s law.

Based on the law of conservation of mechanical energy, kinetic energy E_k and potential energy E_p during the impact of KSIR break are all transferred into deformation energy V of the lower immediate roof. Consider

$$E_k + E_p = V. \quad (9)$$

The impact process does not affect the overlying movement above main roof; thus these overlying loads can be neglected. When lower immediate roof reaches its lowest position, the shrinking potential energy of KSIR is

$$E_p = Q_{kz} (\Delta_1 + \Delta_2), \quad (10)$$

where Q_{kz} is the weight of KSIR and upper immediate roof.

Initial velocity and final velocity of lower immediate roof during dynamic impact of KSIR break are the same, at 0. One has

$$E_k = 0. \quad (11)$$

As the impacted body obeys Hook law, the increased strain energy V can be represented as

$$V = \frac{1}{2}Q_3\Delta_2. \quad (12)$$

For the lower immediate roof, the relation between Q_3 and Δ_2 is

$$Q_3 = \frac{EA}{h_{01}}\Delta_2, \quad (13)$$

where E is elastic modulus of the lower immediate roof, MPa; A is hang areas of the lower immediate roof, m^2 .

Combined with (10), (11), (12), and (13), (9) can be transformed into

$$\frac{EA}{2h_{01}}\Delta_2^2 - Q_{kz}\Delta_2 - Q_{kz}\Delta_1 = 0. \quad (14)$$

Under the impact of KSIR break and static load of upper immediate roof, compression of the lower immediate roof (Δ_0) is

$$\Delta_0 = \frac{Q_{kz}h_{01}}{EA}. \quad (15)$$

Combining (14) with (15),

$$\Delta_2^2 - 2\Delta_0\Delta_2 - 2\Delta_0\Delta_1 = 0. \quad (16)$$

Solve the Δ_2 and neglect the negative root as follows:

$$\Delta_2 = \Delta_0 \left(1 + \sqrt{1 + \frac{2\Delta_1}{\Delta_0}} \right). \quad (17)$$

Combining (15) and (17) with (13),

$$Q_3 = Q_{kz} \left(1 + \sqrt{1 + \frac{2\Delta_1}{\Delta_0}} \right). \quad (18)$$

Label the C_d as

$$C_d = 1 + \sqrt{1 + \frac{2\Delta_1}{\Delta_0}}. \quad (19)$$

C_d is considered as the impact dynamic load coefficient [15, 16]; it means the increased load multiple of the impacted body during the roof descending process.

Combining (7), (8), (18), and (19) with (6),

$$P = \gamma B [h_{01}l_k + (n-1)h_zl_k + C_d(h_z - h_{01})(l_0 + l_k)], \quad (20)$$

where l_0 is the hanging length of KSIR.

3.4. Discussion. Based on (19), when $\Delta_0 = 0.2$ m, the relation between C_d and Δ_1 is shown in Figure 11(a); when $\Delta_1 = 0.1$ m, the relation between K_d and Δ_0 is shown in Figure 11(b). According to Figure 10, dynamic impact can be alleviated by reducing the descending height of broken KSIR and by increasing the compressibility of support column.

In field practice, increasing the setting load can reduce the separation between the lower part of immediate roof and KSIF; if there is no separation at all, $\Delta_1 = 0$ and $C_d = 2$.

Actually, part of the impact energy is consumed because of the existence of the lower part of immediate roof and the compressible elastic characteristic of support. Thus, dynamic impact is alleviated. Generally, the value of C_d is 1~2. The harder the KSIF and the closer the distance to the support are, the greater the dynamic impacts of the broken KSIR are, and vice versa.

(1) Effect of the Hanging Length of KSIF. Based on (20), the relation between support force and the hanging length of KSIR is shown in Figure 11 when $l_k = 5.5$ m, $h_{01} = 6$ m, $h_z = 15$ m, $n = 1.5$, $\gamma = 25$ kN/m³, and $B = 1.75$ m.

Figure 12 indicates that, with the increase of l_0 , dynamic impact to the lower part of immediate roof increased; thus greater support resistance is needed. When the hanging length is 10 m, support with working resistance over 10000 kN can also be crushed. Therefore, hanging length should be controlled to protect support under the circumstances that the roof is relatively hard or the immediate roof is thin.

(2) Effect of the Position of KSIF

- When $h_z = h_{01}$, KSIF is the main roof, which means there are no hard strata in immediate roof. Support work force is calculated with (7).
- When $h_{01} = 0$, the lower part of immediate roof does not exist. Supports contact with KISR directly, which equals mining under hard roof. Equation (20) can be transformed into

$$P = \gamma B h_z [(n-1)l_k + C_d(l_0 + l_k)]. \quad (21)$$

Equation (21) shows that the support load is mainly affected by the hanging length of KSIF.

- When $h_{01} = mh_z$ ($0 < m < 1$), this means KSIF exist in immediate roof. Consider

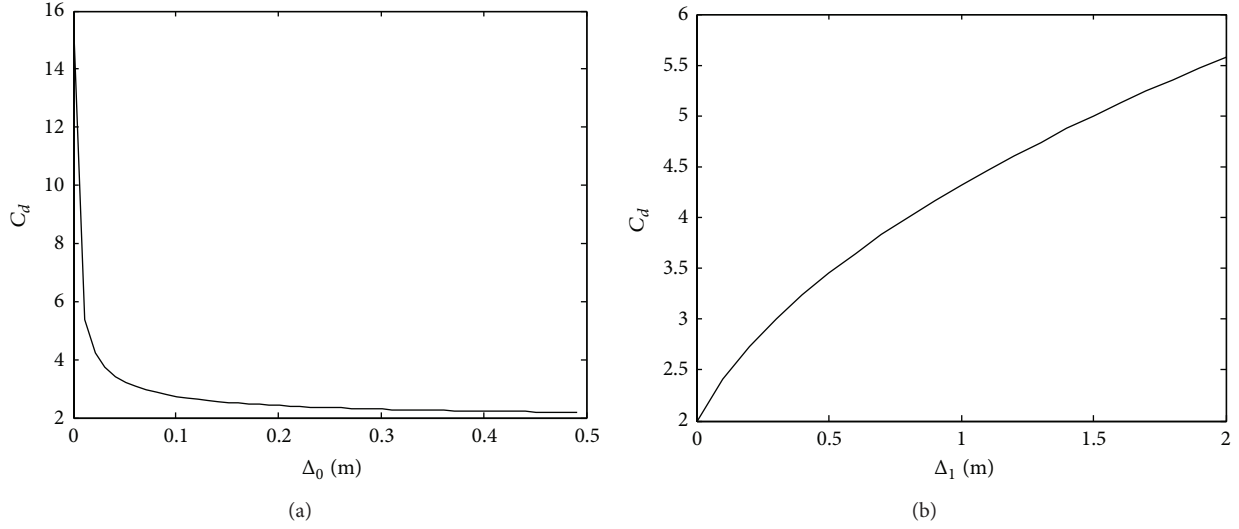
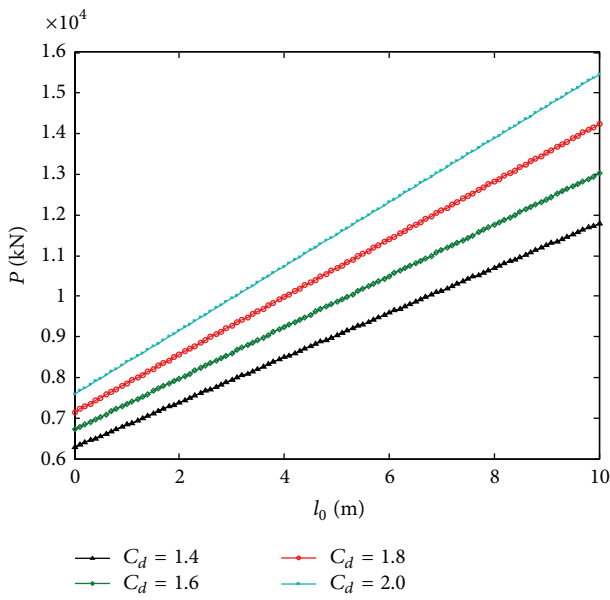
$$P = \gamma B h_z [ml_k + (n-1)l_k + C_d(1-m)(l_0 + l_k)]. \quad (22)$$

Equation (22) shows that the support load is mainly affected by the position and the hanging length of KSIF.

4. Application

Based on the working conditions of No. 15104 working face of Shijiazhuang coal mine, support work force can be achieved ($P = 7382.8$ kN) according to (20) when $l_k = 5.5$ m, $l_0 = 2$ m, $l_z = 15$ m, $h_{01} = 6$, $n = 1.5$, $\gamma = 25$ kN/m³, and $B = 1.75$ m. ZY8000/26/56 shield hydraulic support is adopted in the face. The mine pressure behavior is shown in Figure 13.

Conclusions can be drawn from Figure 12 that ① the first weighing steps in lower part, middle part, and upper part of working face are 36 m, 34 m, and 38 m; the average periodic weighing intervals are 17 m, 17 m, and 19 m; the average

FIGURE 11: The relation between C_d and Δ_1 , Δ_0 .FIGURE 12: The relation between P and l_0 , C_d .

weighing distances are 4.3 m, 3.7 m, and 3.8 m; the average dynamic load factors are 1.43, 1.53, and 1.48, respectively; ② the average dynamic load of the working face is 1.48. Overall, the selection of support in this face is reasonable although there are some safety valves in upper face supports activated due to roof fall caused by the crushed gas tail roadway.

5. Conclusion

- (1) Large mining and caving height are the basic characteristics of FMMLMH face. The strata between masonry beam structure and coal seam are defined as immediate roof; the main roof is the strata which can form the stable structure above the immediate

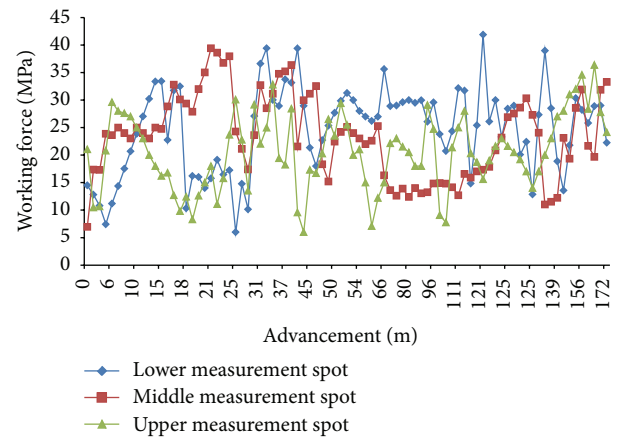


FIGURE 13: Support work force of No. 15104 face.

roof. This paper defines KSIF as the strata which can control the caving of the immediate roof and also puts forward the discrimination methods and procedures.

- (2) KSIR controls the movement of the upper immediate roof and has dynamic impact on the lower part of immediate roof when it breaks. The dynamic impact increases along with the increase of the thickness and hardness of KSIR and the decrease of the distance to the working seam.
- (3) With the existence of KSIR, KSIR and main roof can easily form the bilayer structure “Cantilever-Masonry beam” in FMMLMH face. Support work load under this condition is affected by the position, thickness, and hardness of KSIR. Based on (20), the above achievements are successfully applied in the support selection in No. 15104 face of Shijiazhuang coal mine.

Conflict of Interests

The authors declare that there is no conflict of interests regarding the publication of this paper.

Acknowledgments

Financial support for this work is provided by the Priority Academic Program Development of Jiangsu Higher Education Institutions and the Fundamental Research Funds for the Central Universities (2014QNB32).

References

- [1] P. Wu, H. Chen, and R. Long, "Relationship between coal output and safety in China," *Disaster Advances*, vol. 5, no. 4, pp. 551–556, 2012.
- [2] X. P. Yuan, "The characters and trend of accidents in the coal mining in China," *Disaster Advances*, vol. 5, no. 4, pp. 866–869, 2012.
- [3] S. H. Tu, Y. Yuan, Z. Yang, X. T. Ma, and Q. Wu, "Research situation and prospect of fully mechanized mining technology in thick coal seams in China," *Procedia Earth and Planetary Science*, vol. 1, no. 1, pp. 35–40, 2009.
- [4] J. F. Ju and J. L. Xu, "Structural characteristics of key strata and strata behaviour of a fully mechanized longwall face with 7.0m height chocks," *International Journal of Rock Mechanics and Mining Sciences*, vol. 58, pp. 46–54, 2013.
- [5] Y. Yuan, S.-H. Tu, Y. Wang, X.-T. Ma, and Q. Wu, "Discussion on key problems and countermeasures of fully mechanized mining technology with high mining height," *Coal Science and Technology*, vol. 38, no. 1, pp. 4–8, 2010.
- [6] J. Xu and J. Ju, "Structural morphology of key stratum and its influence on strata behaviors in fully-mechanized face with super-large mining height," *Chinese Journal of Rock Mechanics and Engineering*, vol. 30, no. 8, pp. 1547–1556, 2011.
- [7] Y. Yong, *Stability Control Mechanism of Support-Surrounding Rocks at Fully Mechanized Mining Face with Great Cutting Height*, China University of Mining & Technology, Xuzhou, China, 2011.
- [8] P.-L. Gong and Z.-M. Jin, "Study on the structure characteristics and movement laws of overlying strata with large mining height," *Journal of the China Coal Society*, vol. 29, no. 1, pp. 7–11, 2004.
- [9] Y.-P. Fu, X.-M. Song, P.-W. Xing, G.-C. Yan, and Z.-J. Li, "Stability analysis on main roof key block in large mining height workface," *Journal of the China Coal Society*, vol. 34, no. 8, pp. 1027–1031, 2009.
- [10] H.-J. Hao, J. Wu, Y. Zhang, and Z.-B. Yuan, "Balance structure of main roof and its action to immediate roof in large cutting height workface," *Journal of the China Coal Society*, vol. 29, no. 2, pp. 137–141, 2004.
- [11] C. Y. Liu and M. G. Qian, "Stability and control of immediate roof of fully mechanized coal face," in *Proceedings of the International Conference on Ground Control in Mining*, pp. 123–127, The University of West Virginia, Morgantown, WV, USA, 1990.
- [12] L.-M. Dou, X.-Z. Zou, S.-G. Cao et al., *Surrounding Rock Control of Coal Mine*, China University of Mining and Technology Press, Xuzhou, China, 2010.
- [13] H.-Z. Zhao and Q.-S. Song, "Development of hydraulic support for super great mining height," *Journal of Mining & Safety Engineering*, vol. 27, no. 3, pp. 265–269, 2007.
- [14] M.-G. Qian, X.-X. Miao, J.-L. Xu et al., *Theory of Key Strata in Ground Control*, China University of Mining and Technology Press, Xuzhou, China, 2003.
- [15] J.-C. Wang, *Theory and Technology of Thick Coal Seam Mining*, Metallurgical Industry Press, Beijing, China, 2009.
- [16] X.-R. Jia, *Ground Control*, China University of Mining and Technology Press, Xuzhou, China, 2011.

Research Article

Acoustic Emission Behavior of Rock-Like Material Containing Two Flaws in the Process of Deformation Failure

Quan-Sheng Liu,^{1,2} Jie Xu,¹ Bin Liu,² and Jing-Dong Jiang¹

¹*School of Civil Engineering, Wuhan University, Wuhan, Hubei 430072, China*

²*Institute of Rock and Soil Mechanics, Chinese Academy of Sciences, Wuhan, Hubei 430071, China*

Correspondence should be addressed to Quan-Sheng Liu; liuqs@whrsm.ac.cn

Received 17 October 2014; Revised 14 February 2015; Accepted 17 February 2015

Academic Editor: Shimin Liu

Copyright © 2015 Quan-Sheng Liu et al. This is an open access article distributed under the Creative Commons Attribution License, which permits unrestricted use, distribution, and reproduction in any medium, provided the original work is properly cited.

Many sudden disasters (such as rock burst) by mining extraction originate in crack initiation and propagation. Meanwhile a large number of shock waves are produced by rock deformation and failure. With the purpose of investigating crack coalescence and failure mechanism in rock, experimental research of rock-like materials with two preexisting flaws was performed. Moreover, the AE technique and photographic monitoring were adopted to clarify further the procedure of the crack coalescence and failure. It reveals that AE location technique can record the moments of crack occurrences and follow the crack growth until final failure. Finally, the influence of different flaw geometries on crack initiation strength is analyzed in detail. This research provides increased understanding of the fracture mechanism of mining-induced disasters.

1. Introduction

With the development of underground engineering excavating technology, more and more new equipment and new strategies are applied into mining industry. However, the capacity of mining disaster prevention and mitigation cannot meet the productivity demands. Many sudden disasters (such as rock burst) by mining extraction originate in the linkage of preexisting flaws due to the initiation, propagation, and interaction of new cracks and existing fractures. Meanwhile a large number of shock waves are produced by rock deformation and failure. Therefore, it is very urgent and important to understand the mining-induced shock waves during crack initiation, coalescence, and failure of rock material.

Many experimental investigations [1–4] have been carried out on enhancing the understanding of crack coalescence. The experimental results indicated that the mechanical behaviors of rock failure were closely bound up with the geometries of flaws. Meanwhile, the coalescence behavior of cracks is of great importance and difficulty. Following the development of test research, rock-like materials gain more attention and have been widely studied.

Vásárhelyi and Bobet [5], Sagong and Bobet [6], Zhou et al. [7], and Zhu et al. [8] have investigated the crack coalescence behavior by loading rock-like materials with different flaw geometries. Wong and Einstein [9] carried out an experimental study on cracking and coalescence behavior with molded gypsum and marble samples, which showed that the cracking processes and macroscopic deformation were bound up with the underlying microscopic change. Based on the combination of numerical simulations and experiments, Haeri et al. [10] have investigated the crack coalescence mechanism and propagation paths according to Mode I and Mode II stress intensity factors. In order to research the effect of flaw angle and distribution density on the failure characteristics, Pu and Cao [11] have performed experimental study on rock-like samples with prefabricated closed multiflows. In accordance with cracking behaviors in modeled gypsum and Carrara marble samples, Wong and Einstein [12] have obtained seven different crack types. The reason for choosing rock-like materials is threefold: first, a large number of samples can be easily prepared; second, a wide range of brittle rocks can be represented; third, many

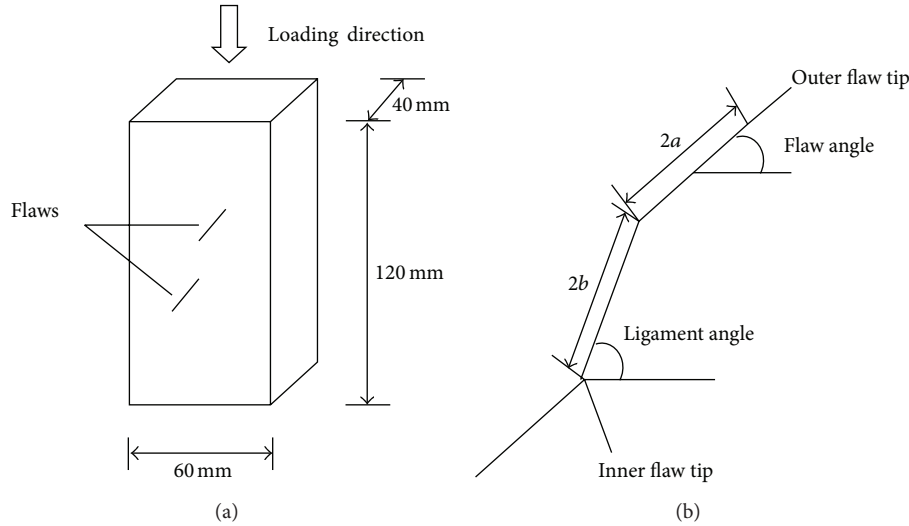


FIGURE 1: Sample with two flaws. (a) Overall view and (b) geometry of the flaws.

of previous experimental results can be compared with the current investigation.

Acoustic emission technique (AE) has the capability to efficiently reflect the initiation and coalescence of cracks by tracing the mining-induced shock waves, which has been widely applied to many studies [13, 14] of crack behavior in the rock material. With the purpose of better understanding frost weathering mechanisms of rocks, Duca et al. [15] conducted an experimental study on the stored elastic energy by AE technique, which was released accompanied by the growth of microcracks during freezing tests. A series of AE location tests were carried out by Ting et al. [16] under unloading conditions, which indicated that energy increasing rate and AE space-time evolution rules during strength failure process were dependent on the unloading rates. Jouniaux et al. [17] studied the fracturing and slip behaviors of the samples containing a preexisting macroscopic healed joint, which showed that precursory localization of microfractures in the final rupture plane had been observed in the early stage of deformation by AE technique. Based on the analysis of AE parameters in microcracking activity, Vidya Sagar et al. [18] found the AE behavior characteristics of each stage were linked closely with the number and distribution of microcracks. In order to identify the characteristics of crack coalescence behaviors in sandstone samples, Yang et al. [19–21] adopted the AE technique to record the real-time crack coalescence process of the samples in the whole loading course. All studies show that AE has the capacity to efficiently highlight the moments of crack occurrences and follow the crack growth until final failure.

With the purpose of figuring out the strength failure mechanism and crack coalescence behavior in rock materials, AE technique and photographic monitoring were used in the uniaxial compression tests for samples containing two parallel flaws. Moreover, the whole process of the real-time crack coalescence was also recorded by tracing mining-induced shock waves in the whole loading course, which

was not carried out in rock-like materials previously. In this paper, the researching emphasis centralizes in investigating the effect of the geometry (flaw angle and ligament angle) on the strength failure mechanism of rock-like materials and in studying real-time crack coalescence process under uniaxial compression on the foundation of photographic monitoring and AE technique combination.

2. Sample Materials and Experimental Techniques

2.1. Sample Preparation. The samples were made of high-strength gypsum and water-cement ratio is 1. The size and flaw geometry of the samples are shown in Figure 1. Each sample was cast in a mold with internal dimensions of 60 mm × 40 mm × 120 mm. Meanwhile, the open flaws were produced with different-sized metallic shims, which are 0.2 mm in thickness, 60 mm in length, and 10–30 mm in width. In order to further investigate the influence of flaw geometry on the crack coalescence behavior, different geometries of two parallel flaws were chosen, which were set by varying inclination angle (α and β) while keeping two constants ($2a = 14$ mm and $2b = 16$ mm). Two flaw inclination angles were used: 45° and 75°; six ligament angles were used: 45°, 60°, 75°, 90°, 105°, and 120°.

To obtain the physicochemical parameters of the rock-like materials, uniaxial and biaxial compression tests were done with the standard cylindrical samples of 50 mm in diameter and 100 mm in length and Brazilian splitting tests were done with the samples of 50 mm in diameter and 50 mm in length. The physicochemical parameters of intact samples are shown in Table 1.

2.2. Test Equipment. A servo-controlled hydraulic testing machine, namely, RMT-150C (Figure 2(a)), was used in the experiment, which can perform well in load or displacement control. The maximum capacity of RMT-150C was 1 MN and

TABLE 1: The physico-mechanical parameters of intact samples.

σ_c (MPa)	σ_t (MPa)	E (GPa)	c	φ ($^\circ$)	ρ (g/cm ³)	P-wave velocity (m/s)	S-wave velocity (m/s)
5.45	0.90	1.30	2.44	9.03	0.84	3123	2657

Note: σ_c = uniaxial compressive strength, σ_t = tensile strength, φ = internal friction angle, c = cohesive force, and ρ = density.

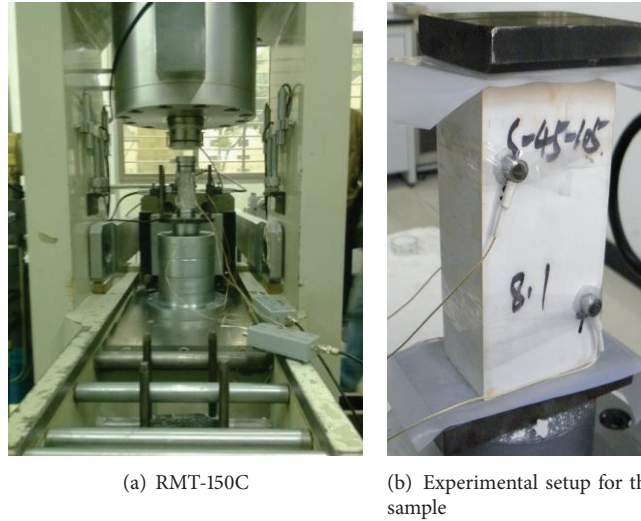


FIGURE 2: RMT-150C testing system and experimental setup of samples.

all the real-time data were recorded and analyzed in time. The samples were loaded in the displacement-controlled condition and the strain rate was set as 1×10^{-3} mm/s. In addition, two rigid steel blocks were placed between the testing samples and loading frame. With the purpose of decreasing the influence of the friction effects and obtaining more accurate testing results, plastic cushions were placed between the end face of samples and rigid steel blocks, as shown in Figure 2(b).

A multichannel, high-speed AE testing system, namely, PCI-2, was used to acquire the real-time AE information, which was manufactured by American Physical Acoustic Corporation (Figure 3(a)). The AE system has become mature as a technique for monitoring the crack growth in rock materials, which is composed of AE transducers, preamplifier, signal acquisition, and so on. In this study, AE signals were amplified by 40 dB, and the amplitude threshold, the sampling frequency, and the sampling length were set at 18 mV, 2.5 MHz, and 8192, respectively. Eight Nano-30 type sensors are used to acquire AE signals, of which the operating frequency is 100–400 kHz. Each sensor was equipped with a 1220A-AST type preamplifier. The sensors were fixed on rock faces by plastic tapes and Vaseline was used for coupling, as shown in Figure 3(b). Before the test, a pencil lead break (PLB) was conducted to check out coupling quality of the acoustic emission sensor with the specimen and correct the AE location system, shown in Figure 3(b). If the amplitude value tested by one AE sensor was above 95 dB, the sensor could be considered to have a good coupling quality with the specimen. If the location of the AE event tested by AE setup was close to the actual location, this system could achieve the demand of position control. Otherwise the PLB tests should

be repeated and setup parameters should be modified until the location has met the requirements. Besides, the velocity of longitudinal wave and transverse wave is 3123 m/s and 2657 m/s, respectively.

3. Strength and Deformation Behavior

Take flaw angles $\alpha = 45^\circ$ and $\alpha = 75^\circ$, for example; the uniaxial compression curves for the samples containing two flaws are shown in Figure 4. It can be found that flaw angle α and ligament angle β make a great difference in the strength and deformation properties of rock-like materials, and the detailed influence will be analyzed in the following.

3.1. Relationship between Stress and Strain for the Samples with Different Flaw Geometries. The relationship between stress and strain for the samples containing two parallel flaws can go through approximately four classic stages, that is, flaw closure, elastic deformation, crack initiation and propagation, and strain-softening.

At the initial stage of the stress-strain curves, the downward concave and nonlinear characteristics are clearly observed, which result from the closure of some primary pores and voids at low stress levels and are defined as flaw closure. Moreover the better consistency of the rigidity for all samples at this stage lies in the better homogeneity of tested materials. With the increase of stress, the relationship of stress and strain is at the stage where the linear stress-strain behavior of flawed samples keeps unchanged although there are some irrecoverable processes, which is defined as elastic deformation. Moreover, the slope of the line at elastic deformation stage is dependent distinctly on ligament angle

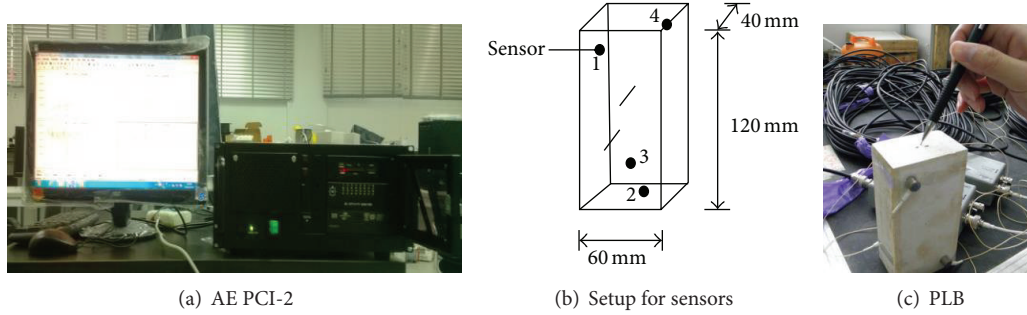


FIGURE 3: AE PCI-2 acoustic emission system.

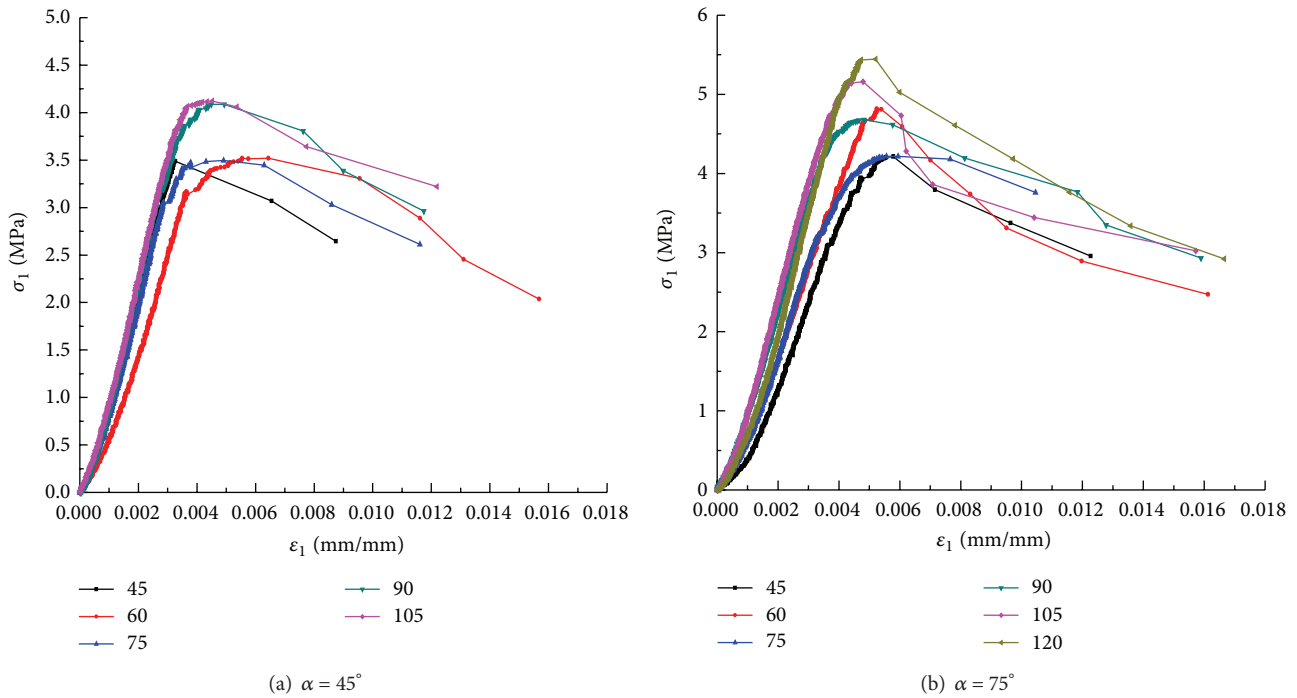


FIGURE 4: Axial stress-strain curves of the samples, in which (a) and (b), respectively, show the flaw angles $\alpha = 45^\circ$ and $\alpha = 75^\circ$ ($\sigma_1 =$ axial stress and $\epsilon_1 =$ axial strain) (black, red, blue, dark cyan, magenta, and dark yellow correspond to 45° , 60° , 75° , 90° , 105° , and 120° of ligament angle β , resp.).

β . In accordance with Figure 4, it is clear that the slope of the line increases with the increase of ligament angle β . Nevertheless, at the stage of crack initiation and propagation, new cracks will initiate and propagate from the tips of the preexisting flaws, which result from stress concentration. Therefore the stress-strain curve shows distinctly nonlinear deformation before peak strength point. From Figure 4, it is clear that the peak strength of samples with ligament angle $\beta = 105^\circ$ or 120° is obviously greater than that of others, so one can conclude that it is more difficult to fail for overlapping flaw geometries ($\beta \geq 90^\circ$) than nonoverlapping ones ($\beta \leq 90^\circ$). When the relationship of stress and strain develops into the strain-softening stage, the macroscopic crack occurs and then the postpeak behavior shows a slower fall.

3.2. Effect of Different Flaw Geometries on Mechanical Parameters of Samples. In order to investigate the influence of

different flaw geometries on the strength and deformation behaviors, the mechanical parameters of the samples under uniaxial compression are discussed in detail, which are shown in Figure 5.

The uniaxial compressive strength of intact sample is 5.450 MPa. Corresponding to the uniaxial strength of the integrity sample, for the samples with $\alpha = 45^\circ$ or $\alpha = 75^\circ$, the average reduction extent of uniaxial compressive strength is 32.02% or 12.76%, respectively. According to Figure 5(a), the uniaxial compressive strength of the samples containing flaw angle $\alpha = 75^\circ$ is greater than that of samples containing flaw angle $\alpha = 45^\circ$; therefore, one can conclude that the samples with flaw angle $\alpha = 75^\circ$ have the ability to bear greater pressure. Moreover, when the β angle is increased from 45 to 75 degrees and from 45 to 90 degrees for α angles of 75 and 45 degrees, respectively, the uniaxial compressive strength keeps almost unchanged. Then it begins to increase with increasing

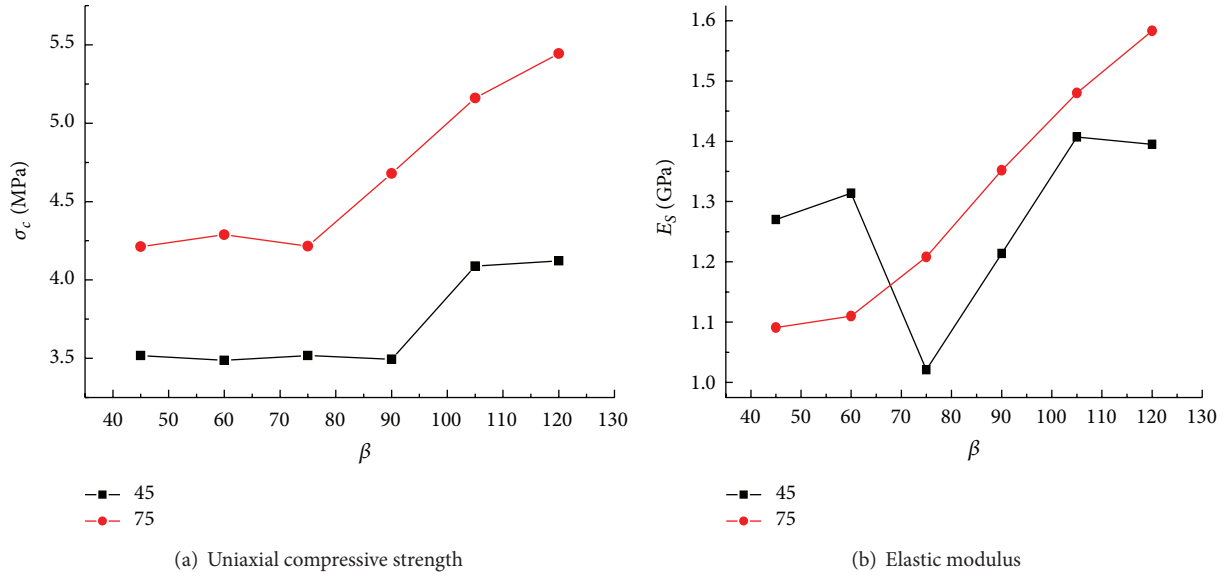


FIGURE 5: Effect of flaw angle and ligament angle on mechanical parameters of samples.

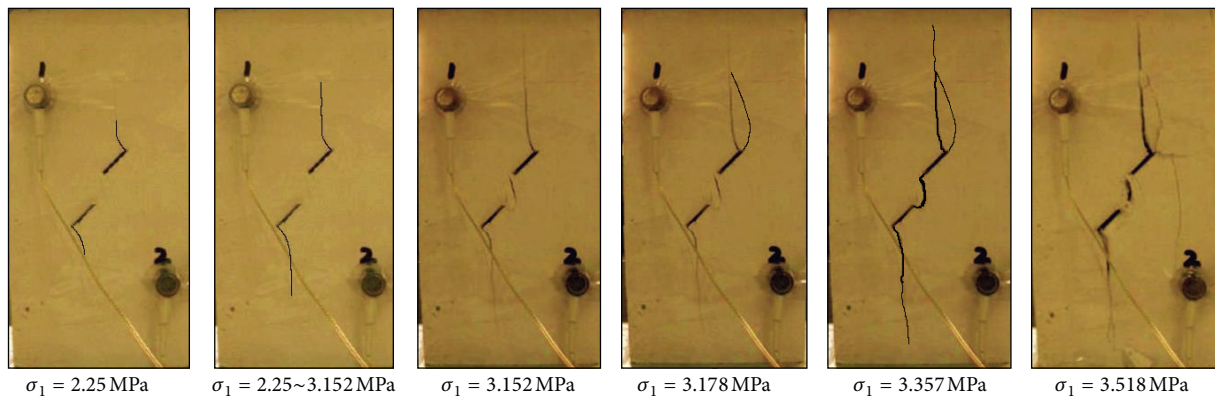


FIGURE 6: Real-time recording of crack coalescence process for flawed sample ($\alpha = 45^\circ$ and $\beta = 75^\circ$).

of ligament angle and the demarcation point is $\beta = 90^\circ$ for $\alpha = 45^\circ$ and $\beta = 75^\circ$ for $\alpha = 75^\circ$.

In accordance with Figure 5(b), the change rule of the elastic modulus is different from that of uniaxial compressive strength shown in Figure 5(a). For the samples with $\alpha = 45^\circ$, there is a distinct valley when $\beta = 75^\circ$; then the elastic modulus increases with the increasing ligament angle. However, the elastic modulus of the samples with $\alpha = 75^\circ$ keeps an increasing trend from beginning to end, which has a demarcation point at $\beta = 60^\circ$ because of the different slope of increase.

From the above analysis, one can conclude that the mechanical parameters of the samples with $\alpha = 75^\circ$ are greater than those with $\alpha = 45^\circ$, which shows that the flaw angle makes a significant difference on the strength and deformation behaviors. In addition, when $\beta \geq 90^\circ$, all mechanical parameters increase with increasing ligament angle, which shows that the overlapping flaw geometries have contributed more to the stability of the samples.

4. Real-Time Recording and Analysis of Crack Coalescence Process for Flawed Samples

Besides AE energy technique, the AE location-based technology and photographic monitoring were also adopted to illuminate further the characteristics of crack coalescence behaviors in flawed samples under uniaxial compression. It is generally known that the located AE events directly reflect the time-space distribution of the catastrophic fracture within the samples. Based on the combined results, the real-time recording and analysis of crack coalescence process for flawed samples are shown in detail as in Figure 6.

In accordance with Figures 6, 7, and 8, the crack coalescence process of the sample containing two preexisting flaws ($\alpha = 45^\circ$ and $\beta = 75^\circ$) in real time was analyzed in detail. Before point A ($\sigma_1 = 2.25 \text{ MPa} = 64\% \sigma_c$) as shown in Figures 7 and 8, the stress concentration is too small to reach the material strength, so that there is no crack initiation at the tips of flaws. For the moment, the average modulus is 1.09 GPa.

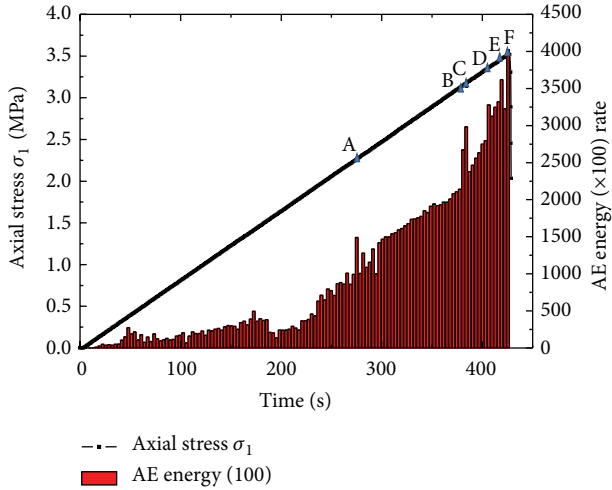


FIGURE 7: Relation between AE energy rate and time of flawed sample ($\alpha = 45^\circ$ and $\beta = 75^\circ$).

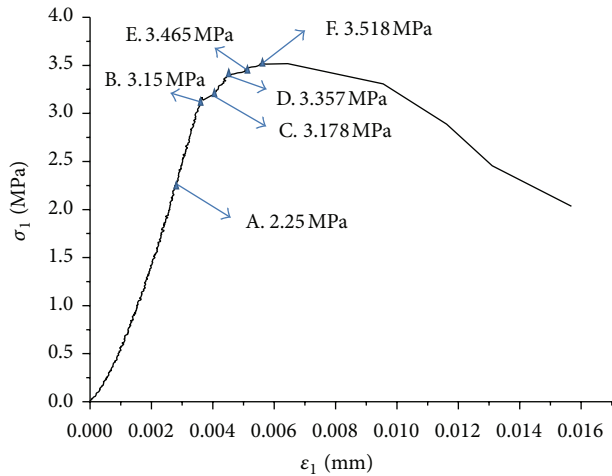


FIGURE 8: Several important points in stress-strain curve for flawed sample ($\alpha = 45^\circ$ and $\beta = 75^\circ$).

But a wing crack begins to initiate from the outer tips of the preexisting flaws as soon as the sample is loaded to point A, which is identified by AE energy shown in Figure 7. With the axial stress increasing, the wing crack further lengthens and continues to expand along the direction of loading. Due to some minor damage of structural supports inside the material, the average modulus (1.0 GPa) becomes a little lower than the elastic modulus 1.09 GPa. When the sample is loaded to the first yielding point B ($\sigma_1 = 3.152 \text{ MPa} = 89.6\% \sigma_c$), a vertical tensile crack occurs rapidly in the bridge in one second, which can be observed from the AE energy shown in Figure 7. At this time, the axial stress undergoes a minor drop to 3.074 MPa from 3.152 MPa. However it is more and more difficult for the wing crack to continue propagating because of the limitation of sample boundary. As time grows, the axial supporting capacity of the sample becomes increasingly great. At the moment of axial stress loaded to point C ($\sigma_1 = 3.178 \text{ MPa} = 90.3\% \sigma_c$), the second

wing crack initiates from the outer tip of the upper flaw. What is more, the average modulus ($\sim 0.262 \text{ GPa}$) becomes significantly lower than previous elastic modulus, which results from the serious damage of structural supports inside the materials. When the sample was loaded to the second yielding point D ($\sigma_1 = 3.357 \text{ MPa} = 95.4\% \sigma_c$), two shear cracks emanate concurrently from the internal tips of two flaws, which indicates that the coalescence occurs. This moment is captured by the AE technology, as shown in Figure 7. During this loading process, it is much in evidence that the axial supporting capacity turns into growing slowly compared to previous period. In addition, the critical decline of average modulus ($\sim 0.096 \text{ GPa}$) is largely due to serious damage of structural supports inside the materials. Afterwards, with the sample being loaded to 3.465 MPa ($98.5\% \sigma_c$), surface spalling starts to appear on the surface of the sample, which can be obviously observed from Figure 6. When the sample is loaded to 3.518 MPa ($100\% \sigma_c$), at this moment, the first wing crack develops rapidly to the edge of the sample in one second, which leads to the strength failure. At the same time, the axial supporting capacity reduces to 2.035 MPa.

The crack coalescence process of flawed sample in real time can be confirmed and characterized by virtue of AE location technique as well, as shown in Figure 9. At the beginning of load, the AE events are so little that no rules can be obtained. When the sample is loaded to 2.25 MPa (point A), more AE events are observed at the outer tips of preexisting flaws, indicating that wing crack occurs. At the moment, the number of AE events only accounts for 6.9% of the total. Afterwards, with the increasing axial stress, a red zone can be distinctly observed in the bridge, which indicates the vertical tensile crack occurs. However the continuous increasing stress leads the AE events to increase rapidly. At this moment of about 406 s (corresponding axial stress is 3.357 MPa), the coalescence occurs, which is shown in Figure 9(e). Meanwhile, the proportion of AE events has risen to 79.3%. When the sample is loaded to 3.518 MPa (corresponding time is 425 s), a vertical red zone can be observed through the whole sample, which results from the failure of the sample (Figure 9(g)).

By adopting the combination of photographic monitoring and AE technique, the crack coalescence behavior and failure process of all other samples with different flaw geometries were also recorded in real time. One can conclude that each bigger elastic modulus decline in all the compression curves signifies a bigger crack initiation, which is also accompanied by greater amplifying AE energy and more AE location events. Figure 10 summarizes the stress of first crack initiation, which also is called crack initiation strength.

According to Figure 10, we can draw the conclusion that the crack initiation strength is linked closely with flaw angle and ligament angle. To explain in concrete terms, the crack initiation strength in the sample with $\alpha = 75^\circ$ is higher than that with $\alpha = 45^\circ$ for each ligament angle except $\beta = 45^\circ$; that is, the initiation of first crack in the sample with $\alpha = 45^\circ$ is easier than that with $\alpha = 75^\circ$. In addition, for the sample with $\alpha = 45^\circ$, the crack initiation strength showed a trend of fluctuations when the ligament angle was lower than 90° . When the ligament angle increased from 45° to 60° ,

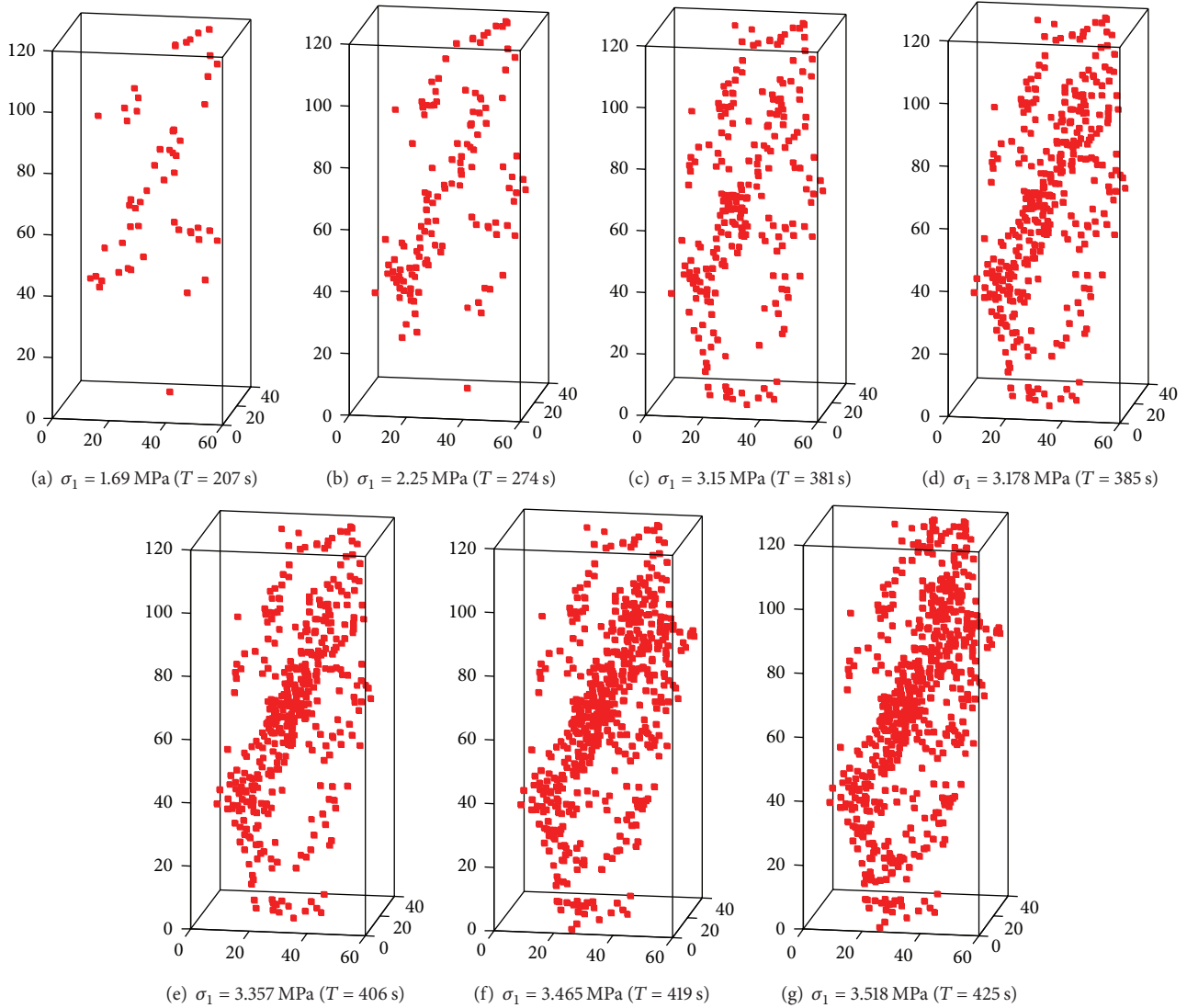


FIGURE 9: The AE location for cracks initiating and propagating in flawed sample ($\alpha = 45^\circ$ and $\beta = 75^\circ$).

the crack initiation strength increased from 3.1 MPa to 3.25 MPa. Then it decreased to 3.17 MPa at $\beta = 75^\circ$ and 3.12 MPa at $\beta = 90^\circ$. After that the crack initiation strength increased with the increase of ligament angle. Similarly, for the sample with $\alpha = 75^\circ$, the crack initiation strength was 4.52 MPa at $\beta = 60^\circ$. Then it decreased to 3.8 MPa at $\beta = 75^\circ$. After that it increased to the maximum value of 5.15 MPa at $\beta = 120^\circ$. What is more, we can come to a conclusion that the first crack in the sample with smaller ligament angle is easier to initiate than that with larger ligament angle on the whole. Particularly for the sample with overlapping flaw geometries ($\beta \geq 90^\circ$), the crack initiation strength is distinctly higher than that of nonoverlapping flaw geometries ($\beta \leq 90^\circ$).

5. Conclusions

This study focused on the influence of the geometry (flaw angle and ligament angle) on the strength failure mechanism

of rock-like materials and analyzed real-time crack coalescence process by tracing mining-induced shock waves on basis of AE technique. It provides better understanding of the fracture mechanism of mining-induced disasters. The main conclusions of this study are the following.

- (1) Compared with intact sample, the flawed samples fail with lower strengths, which is closely related to the flaw angle α and ligament β . The mechanical parameters of the samples with $\alpha = 75^\circ$ are greater than those with $\alpha = 45^\circ$. When $\beta \geq 90^\circ$, all mechanical parameters increase with increasing ligament angle, which shows that the overlapping flaw geometries have contributed more to the stability of the samples.
- (2) The crack coalescence behavior and strength failure process of the samples with different flaw geometries are recorded in real time by tracing induced shock waves. Each bigger elastic modulus decline in all the compression curves signifies a bigger crack initiation,

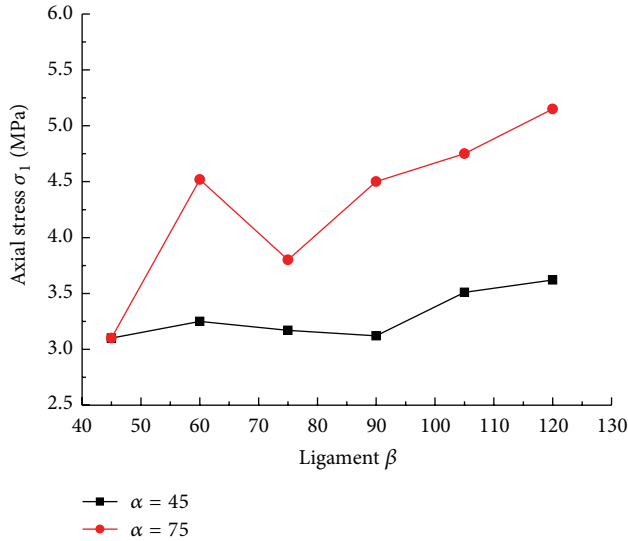


FIGURE 10: Crack initiation strength of the samples with different geometries.

which is also accompanied by greater amplifying AE energy and more AE location events.

- (3) The crack initiation strength is linked closely with flaw angle and ligament angle. The crack initiation strength in the sample with $\alpha = 75^\circ$ is higher than that with $\alpha = 45^\circ$ for each ligament angle except $\beta = 45^\circ$; that is, the initiation of first crack in the sample with $\alpha = 45^\circ$ is easier than that with $\alpha = 75^\circ$. Moreover, the initiation of first crack in the sample with smaller ligament angle is easier than that with larger ligament angle on the whole. Particularly for the sample with overlapping flaw geometries ($\beta \geq 90^\circ$), the crack initiation strength is distinctly higher than that of nonoverlapping flaw geometries ($\beta \leq 90^\circ$).

Conflict of Interests

The authors declare that there is no conflict of interests regarding the publication of this paper.

Acknowledgments

Financial supports from the National Basic Research Program of China (973 Program) Grant no. 2014CB046904 and the National Natural Science Foundation of China Grant nos. 41130742 and 51474205 are gratefully acknowledged.

References

- [1] G. Chen, J. Kemeny, and S. S. Harpalani, "Fracture propagation and coalescence in marble plates with pre-cut notches under compression," *International Journal of Rock Mechanics and Mining Sciences*, vol. 30, p. 279, 1993.
- [2] H. Jiefan, C. Ganglin, Z. Yonghong, and W. Ren, "An experimental study of the strain field development prior to failure of a marble plate under compression," *Tectonophysics*, vol. 175, no. 1-3, pp. 269-284, 1990.
- [3] L. N. Y. Wong and H. Einstein, "Fracturing behavior of prismatic specimens containing single flaws," in *Proceedings of the 41st US Rock Mechanics Symposium (Golden Rocks '06)*, Omni Press, Golden, Colo, USA, June 2006.
- [4] L. G. Zhao, J. Tong, and M. C. Hardy, "Prediction of crack growth in a nickel-based superalloy under fatigue-oxidation conditions," *Engineering Fracture Mechanics*, vol. 77, no. 6, pp. 925-938, 2010.
- [5] B. Vásárhelyi and A. Bobet, "Modeling of crack initiation, propagation and coalescence in uniaxial compression," *Rock Mechanics and Rock Engineering*, vol. 33, no. 2, pp. 119-139, 2000.
- [6] M. Sagong and A. Bobet, "Coalescence of multiple flaws in a rock-model material in uniaxial compression," *International Journal of Rock Mechanics and Mining Sciences*, vol. 39, no. 2, pp. 229-241, 2002.
- [7] X. P. Zhou, H. Cheng, and Y. F. Feng, "An experimental study of crack coalescence behaviour in rock-like materials containing multiple flaws under uniaxial compression," *Rock Mechanics and Rock Engineering*, vol. 47, no. 6, pp. 1961-1986, 2013.
- [8] W. S. Zhu, W. Z. Chen, and J. Shen, "Simulation experiment and fracture mechanism study on propagation of Echelon pattern cracks," *Acta Mechanica Solida Sinica*, vol. 19, pp. 355-360, 1998.
- [9] L. N. Y. Wong and H. H. Einstein, "Crack coalescence in molded gypsum and Carrara marble. Part I. Macroscopic observations and interpretation," *Rock Mechanics and Rock Engineering*, vol. 42, no. 3, pp. 475-511, 2009.
- [10] H. Haeri, K. Shahriar, M. F. Marji, and P. Moarefvand, "Cracks coalescence mechanism and cracks propagation paths in rock-like specimens containing pre-existing random cracks under compression," *Journal of Central South University*, vol. 21, no. 6, pp. 2404-2414, 2014.
- [11] C.-Z. Pu and P. Cao, "Failure characteristics and its influencing factors of rock-like material with multi-fissures under uniaxial compression," *Transactions of Nonferrous Metals Society of China*, vol. 22, no. 1, pp. 185-191, 2012.
- [12] L. N. Y. Wong and H. H. Einstein, "Systematic evaluation of cracking behavior in specimens containing single flaws under uniaxial compression," *International Journal of Rock Mechanics and Mining Sciences*, vol. 46, no. 2, pp. 239-249, 2009.
- [13] A. Zang, F. C. Wagner, S. Stanchits, G. Dresen, R. Andresen, and M. A. Haidekker, "Source analysis of acoustic emissions in Aue granite cores under symmetric and asymmetric compressive loads," *Geophysical Journal International*, vol. 135, no. 3, pp. 1113-1130, 1998.
- [14] X. Lei, K. Kusunose, M. V. M. S. Rao, O. Nishizawa, and T. Satoh, "Quasi-static fault growth and cracking in homogeneous brittle rock under triaxial compression using acoustic emission monitoring," *Journal of Geophysical Research B: Solid Earth*, vol. 105, no. 3, pp. 6127-6139, 2000.
- [15] S. Duca, C. Occhiena, and L. Sambuelli, "A procedure to determine the optimal sensor positions for locating AE sources in rock samples," *Rock Mechanics and Rock Engineering*, vol. 48, no. 2, pp. 481-493, 2014.
- [16] A. Ting, Z. Ru, L. Jianfeng, and R. Li, "Space-time evolution rules of acoustic emission location of unloaded coal sample at different loading rates," *International Journal of Mining Science and Technology*, vol. 22, no. 6, pp. 847-854, 2012.
- [17] L. Jouniaux, K. Masuda, X. Lei et al., "Comparison of the microfracture localization in granite between fracturation and

- slip of a preexisting macroscopic healed joint by acoustic emission measurements,” *Journal of Geophysical Research B: Solid Earth*, vol. 106, no. 5, pp. 8687–8698, 2001.
- [18] R. Vidya Sagar, R. V. Prasad, B. K. Raghun Prasad, and M. V. M. S. Rao, “Microcracking and fracture process in cement mortar and concrete: a comparative study using acoustic emission technique,” *Experimental Mechanics*, vol. 53, no. 7, pp. 1161–1175, 2013.
- [19] S. Q. Yang and H. W. Jing, “Strength failure and crack coalescence behavior of brittle sandstone samples containing a single fissure under uniaxial compression,” *International Journal of Fracture*, vol. 168, no. 2, pp. 227–250, 2011.
- [20] S. Q. Yang, Y. H. Dai, L. J. Han, and Z. Q. Jin, “Experimental study on mechanical behavior of brittle marble samples containing different flaws under uniaxial compression,” *Engineering Fracture Mechanics*, vol. 76, no. 12, pp. 1833–1845, 2009.
- [21] S.-Q. Yang, “Crack coalescence behavior of brittle sandstone samples containing two coplanar fissures in the process of deformation failure,” *Engineering Fracture Mechanics*, vol. 78, no. 17, pp. 3059–3081, 2011.